Physics of Atomic Nuclei, Vol. 63, No. 11, 2000, pp. 1865–1873. Translated from Yadernaya Fizika, Vol. 63, No. 11, 2000, pp. 1957–1965.

NUCLEI
Theory

Langevin Description of Mass Distributions of Fragments Originating from the Fission of Excited Nuclei

D. V. Vanin[1)], P. N. Nadtochy[1)], G. I. Kosenko*, and G. D. Adeev[1)]

Joint Institute for Nuclear Research, Dubna, Moscow oblast, 141980 Russia

Received July 26, 1999; in final form, December 8, 1999

Abstract—A stochastic approach to fission dynamics is proposed. The approach, which is based on Langevin equations, is used to calculate the mass distributions of fragments originating from the fission of excited nuclei. The effect of viscosity and light-particle emission on the variance of mass distributions is studied. The results of the calculations based on the above approach reveal that, in order to obtain a simultaneous description of mass-distribution parameters and the multiplicities of prescission particles, it is necessary to use sufficiently large values of nuclear viscosity both for the one-body and for the two-body viscosity mechanism, anomalously large values of the viscosity coefficient being required in the latter case. *© 2000 MAIK "Nauka/Interperiodica".*

1. INTRODUCTION

In recent years, a vast body of experimental data has been accumulated by studying the observed distributions of fission fragments (mass, energy, and angular distributions) for various values of compound-nucleus parameters, such as the excitation energy, the angular momentum, and the fissility parameter Z^2/A. A major part of this data set was systematized and analyzed in [1–3]. A theoretical interpretation of the mechanism of formation of the distributions of fission fragments on the basis of a dynamical description remains one of the unsolved problems in the physics of fission. Among several theoretical schemes [4–8] used to describe the dynamics of fission treated as a nonequilibrium process, the stochastic approach [7, 8] based on Langevin equations is the most promising and the most popular one at present.

In [9–12], the parameters of the energy distribution of fission fragments were calculated, together with the multiplicities of prescission neutrons, on the basis of stochastic Langevin equations used as dynamical equations. The results of these calculations proved to be in satisfactory agreement with experimental data. On the other hand, there had been no studies until recently devoted to a detailed analysis of the parameters of fragment mass distributions on the basis of Langevin equations.

The results of the first calculations of the fragment mass distributions within a scheme where Langevin equations are used as dynamical equations can be found in [13]. However, the calculations in [13] relied on a simplified model, so that the results obtained there can claim only for a qualitative description of experimental data. Indeed, the emission of light particles was disregarded in [13], but this phenomenon is peculiar to the reactions under investigation. The mechanism and the magnitude of nuclear viscosity that lead to the best description of experimental data were not determined there either.

In the present study, we give an account of the results obtained from a calculation of the fragment mass distributions that is based on the Langevin equations and analyze the effect of the emission of prescission light particles and of the type and magnitude of nuclear viscosity on the computed parameters of the mass distributions in question.

For our investigation, we have chosen heavy-ion reactions [3, 14] that were investigated experimentally in detail and which lead to the formation of compound nuclei with excitation energies $E^* \geq 50$ MeV (temperatures $T \geq 1$ MeV). This makes it possible to neglect shell effects and the nucleon-pairing effect in calculating the potential energy of the nucleus and the transport coefficients in dynamical equations.

The calculation in [13] was performed for a wide range of nuclei ($Z^2/A \simeq 21$–40) within two versions of the liquid-drop model, that with a sharp boundary of the nuclear surface and that with a diffuse boundary [15]. The initial conditions for the Langevin equations were chosen on the ridge separating the ground state from the fission valley of the nucleus in accordance with the idea of the transition state.

For the present calculations, the initial conditions were chosen to correspond to the ground state of the compound nucleus (in the liquid-drop model, this is a sphere). At such initial conditions, however, the higher the barrier, the larger is the time required for relevant calculations, since the fission possibility P_f decreases exponentially with increasing fission-barrier height B_f ($P_f \sim \exp[-B_f/T]$). In order to reduce the calculation time, we decided on three reactions that lead to the for-

[1)] Omsk State University, pr. Mira 55A, Omsk, 644077 Russia.
* e-mail: kosenko@nrsun.jinr.dubna.ru

mation of nuclei having a barrier height not greater than 7 MeV. Our results are compared with those from [13]. The present study also aims at clarifying the effect of the magnitude and type of nuclear viscosity. In addition, we consider the changes suffered by the mass distributions when nucleon exchange between the two parts of the fissile nucleus (that is, between the would-be fragments) is taken into account in the mass-asymmetric component of the viscosity tensor as determined within the one-body dissipation mechanism.

2. DESCRIPTION OF THE MODEL

In describing nuclear surfaces, we restrict ourselves to axisymmetric shapes using the two-parameter family of Cassini ovaloids that was proposed in [16]. In cylindrical coordinates, the shape of the nuclear surface is specified by the equation

$$\rho_s^2 = \sqrt{\frac{1}{c_v^4} + 4\frac{\varepsilon}{c_v^2}(z - \kappa|z|)^2} - \frac{\varepsilon}{c_v^2} - z^2, \qquad (1)$$

where z is the coordinate along the symmetry axis; ρ is a coordinate orthogonal to the z axis; ρ_s is the ρ value at the nuclear surface; ε and κ are the collective coordinates associated with the elongation and mass asymmetry, respectively; and c_v is a scale factor that is responsible for the conservation of the nuclear volume. In the symmetric case ($\kappa = 0$), the nuclear surface corresponds to mirror-symmetric shapes known as Cassini ovaloids [17, 18]; for $\kappa > 0$, we are dealing with asymmetric shapes. The condition $\varepsilon < \frac{1}{2}(1+\kappa)^{-2}$ leads to a set of axisymmetric ovaloids; for $\frac{1}{2}(1+\kappa)^{-2} < \varepsilon < \frac{1}{2}(1-\kappa)^{-2}$, Eq. (1) describes a pearlike surface; and the inequality $\varepsilon > \frac{1}{2}(1-\kappa)^{-2}$ leads to asymmetric bodies featuring the neck coordinate of $z_{\text{neck}} = 0$. At $\varepsilon = 1$ and any value of κ, the neck radius vanishes, and this is considered as the simplest condition of the scission of a continuous shape into fragments. At the same time, it is sometimes assumed (see [19–21]) that scission occurs at some critical value of the deformation corresponding to a relatively thick neck.

The evolution of collective degrees of freedom was considered in a stochastic approach [19, 22] as the motion of a Brownian particle in a heat bath formed by single-particle degrees of freedom of the fissile nucleus being considered. For the case of N collective coordinates, the set of relevant Langevin equations has the form

$$\begin{aligned} \dot{q}_i &= \mu_{ij} p_j, \\ \dot{p}_i &= -\frac{1}{2} p_j p_k \frac{\partial \mu_{jk}}{\partial q_i} - \frac{\partial F}{\partial q_i} - \gamma_{ij}\mu_{jk} p_k + \theta_{ij}\xi_j, \\ i, j, k &= 1, \ldots, N, \end{aligned} \qquad (2)$$

where $\mathbf{q} = (\varepsilon, \kappa)$ stands for the set of collective coordinates; $\mathbf{p} = (p_\varepsilon, p_\kappa)$ represents the momenta conjugate to them; $F(\mathbf{q})$ is the free energy of the system being considered; $m_{ij}(\|\mu_{ij}\| = \|m_{ij}\|^{-1})$ is the inertia tensor; γ_{ij} is the friction tensor; $\theta_{ij}\xi_j$ is a random force; and θ_{ij} is its amplitude, which is related to the diffusion tensor D_{ij} by the equation

$$D_{ij} = \theta_{ik}\theta_{kj}. \qquad (3)$$

The diffusion tensor in turn obeys the Einstein relation

$$D_{ij} = T\gamma_{ij}. \qquad (4)$$

The random variable ξ_j possesses the following statistical properties:

$$\begin{aligned} \langle \xi_i \rangle &= 0, \\ \langle \xi_i(t_1)\xi_j(t_2) \rangle &= 2\delta_{ij}\delta(t_1 - t_2). \end{aligned} \qquad (5)$$

The angular brackets in (5) denote averaging over a statistical ensemble.

We note that, instead of the free energy $F(\mathbf{q}, T) = V(\mathbf{q}) - a(\mathbf{q})T^2$, the potential energy was used in [13] to determine the conservative force in the Langevin equation (2). The use of the free energy is one of the significant improvements in the model proposed in [13]. In order to calculate the free energy, we took the level-density parameter $a(\mathbf{q})$ depending on the collective coordinates, its definition being given below.

As was mentioned above, the potential energy was calculated within two versions of the liquid-drop model. We used the Myers–Swiatecki parameters [23] for the liquid-drop model with a sharp boundary and the Sierk parameters [24] for the liquid-drop model with a diffuse boundary.

The inertia tensor was calculated within the Werner–Wheeler approximation for an irrotational flow of an incompressible liquid (see [25]).

In order to describe the dissipation of the collective kinetic energy into the internal energy, we assumed two friction mechanisms, a two-body and a one-body one (as in [25] and [26], respectively). The calculation was performed by the so-called wall + window formula

$$\begin{aligned} \gamma_{ij} = \frac{1}{2}\rho_m \bar{\nu}\Bigg\{ & \frac{\partial R}{\partial q_i}\frac{\partial R}{\partial q_j}\Delta\sigma + k_s\pi\Bigg[\int_{z_{\min}}^{z_{\text{neck}}} \left(\frac{\partial \rho_s^2}{\partial q_i} + \frac{\partial \rho_s^2}{\partial z}\frac{\partial D_1}{\partial q_i}\right) \\ & \times \left(\frac{\partial \rho_s^2}{\partial q_j} + \frac{\partial \rho_s^2}{\partial z}\frac{\partial D_1}{\partial q_j}\right)\left(\rho_s^2 + \left(\frac{1}{2}\frac{\partial \rho_s^2}{\partial z}\right)^2\right)^{-1/2} dz \\ & + \int_{z_{\text{neck}}}^{z_{\max}} \left(\frac{\partial \rho_s^2}{\partial q_i} + \frac{\partial \rho_s^2}{\partial z}\frac{\partial D_2}{\partial q_i}\right)\left(\frac{\partial \rho_s^2}{\partial q_j} + \frac{\partial \rho_s^2}{\partial z}\frac{\partial D_2}{\partial q_j}\right) \\ & \times \left(\rho_s^2 + \left(\frac{1}{2}\frac{\partial \rho_s^2}{\partial z}\right)^2\right)^{-1/2} dz\Bigg]\Bigg\}, \end{aligned} \qquad (6)$$

where ρ_m is the nuclear density, $\bar{v}$ is the mean velocity of intranuclear nucleons, $\Delta\sigma$ is the area of the window (that is the neck between the two would-be fragments), R is the distance between the centers of mass of the two would-be fragments, D_1 and D_2 are the positions of their centers of mass with respect to the center-of-mass coordinate of the entire system, $z_{\min}$ and $z_{\max}$ are the left and the right boundary of the nuclear surface, z_{neck} is the neck coordinate, and k_s is the coefficient that takes into account the reduction of the contribution from the wall formula [27].

Apart from (6), the calculations relied on the so-called full formula for one-body viscosity [28, 29],

$$\gamma_{ij} = (6) + \frac{16}{9}\frac{\rho_m \bar{v}}{\Delta\sigma}\frac{\partial V_1}{\partial q_i}\frac{\partial V_1}{\partial q_j}, \tag{7}$$

where V_1 is the volume of one of the would-be fission fragments. The additional term is associated with the flow of nucleons through the neck connecting two parts of the nucleus. This correction was evaluated by two methods in the studies of Feldmeier [28] and Randrup and Swiatecki [29].

The initial conditions for the dynamical equations (2) were preset in the following way. In [13], the initial values of the collective coordinates were chosen on the line of the ridge separating the ground state of the compound nucleus from the fission valley, as was done in [12]; the momentum distribution was set to that in equilibrium. In this case, the distribution function has the form

$$P(\mathbf{q}_0, \mathbf{p}_0) \sim \exp\left\{-\frac{V(\mathbf{q}_0) + E_{\text{coll}}(\mathbf{q}_0, \mathbf{p}_0)}{T}\right\}, \tag{8}$$

where $E_{\text{coll}}(\mathbf{q}, \mathbf{p}) = \frac{1}{2}\sum_{i,j}\mu_{ij}(\mathbf{q})p_i p_j$ is the kinetic energy of the collective motion of the nucleus and $V(\mathbf{q}_0)$ is the deformation-dependent potential energy of the nucleus on the ridge line (it is reckoned from the ground-state energy). Numerically, the initial values $\mathbf{q}_0$ and $\mathbf{p}_0$ were chosen on the basis of the Neumann method. In order to choose the initial conditions in the ground state, the distribution with respect to the collective coordinates was assumed to be of the delta-function type, $P(\mathbf{q}_0) \sim \delta(\mathbf{q} - \mathbf{q}_{\text{g.s.}})$. In the nuclear-shape parametrization used, this corresponds to the collective-coordinate values of $\varepsilon_0 = 0$ and $\kappa_0 = 0$. The momentum distribution then has the form $P(\mathbf{p}_0) \sim \exp(-E_{\text{coll}}(\mathbf{q}_0, \mathbf{p}_0)/T)$.

Over the entire trajectory of the motion of the nucleus to the scission line in the collective-coordinate space, we used the energy-conservation law in the form

$$E^* = E_{\text{int}} + E_{\text{coll}} + V(\mathbf{q}) + E_{\text{evap}}(t), \tag{9}$$

where E^* is the total excitation energy of the compound nucleus (in the input reaction channel, it is determined by the incident-ion energy and by the difference of the sum of the masses of colliding nuclei and the mass of the compound system), E_{int} is the excitation energy of single-particle degrees of freedom of the compound nucleus (internal energy), and $E_{\text{evap}}(t)$ is the nucleus excitation energy that light particles have carried away by the instant t.

The probabilities of light-particle emission were determined from the compound-nucleus widths with respect to decays through the corresponding channels. The decay widths were calculated within the statistical model on the basis of the formulas [30]

$$\Gamma_j = \frac{g_j m_j}{(\pi\hbar)^2}\frac{1}{\rho_0(E_{\text{int}}^{(0)})} \times \int_{V_j}^{E_{\text{int}}^{(j)} - B_j} \sigma_{\text{inv}}^{(j)}(E)\rho_j(E_{\text{int}}^{(j)} - B_j - E)E\,dE, \tag{10}$$

where $j = n, p, d, t, {}^3\text{He}$, and α, and

$$\Gamma_\gamma = \frac{1}{(\pi\hbar c)^2}\frac{1}{\rho_0(E_{\text{int}}^{(0)})}\int_0^{E_{\text{int}}^{(0)}} \sigma_\gamma(E)\rho_\gamma(E_{\text{int}}^{(0)} - E)E^2\,dE. \tag{11}$$

Here, g_j, m_j, B_j, and V_j are, respectively, the spin factor, the mass, the binding energy, and the Coulomb barrier for the jth particle; ρ_0 is the density of single-particle levels in the compound nucleus; ρ_j and ρ_γ are the densities of single-particle levels in the residual nucleus after the emission of the jth particle and of a photon, respectively; $\sigma_{\text{inv}}^{(j)}$ is the cross section for the absorption of the jth particle by the residual nucleus (inverse cross section); σ_γ is the cross section for dipole-photon absorption; and $E_{\text{int}}^{(0)}$ and $E_{\text{int}}^{(j)}$ are the internal energies of, respectively, the original and the residual nucleus, with the nucleon-pairing energy being included.

In calculating the density of excited levels, we also included collective effects by using formulas from [30].

Apart from this, we took into account the effect of nuclear deformation and the effect of the internal energy of the nucleus on the level-density parameter

$$a = \tilde{a}\left\{1 + \frac{\delta W[1 - \exp(-\gamma E_{\text{int}})]}{E_{\text{int}}}\right\}, \tag{12}$$

$$\tilde{a} = \alpha A + \beta A^{2/3} B_s.$$

Here, $\alpha = 0.09$, $\beta = -0.04$, $\gamma = 0.07$, and B_s is the surface-energy functional depending on the collective coordinates. For a simple estimate of the shell correction δW, we took that from [31].

The nuclear temperature T used in the calculations was determined according to the expression

$$T = \left(\frac{d\ln\rho(E_{\text{int}})}{dE_{\text{int}}}\right)^{-1}. \tag{13}$$

Table 1. Results of theoretical calculations performed within two versions of the liquid-drop model for the reaction $^{12}C + {}^{232}Th \longrightarrow {}^{244}Cm$ (E_{lab} = 97 MeV)

Coefficient	Liquid drop with a sharp boundary [23]					Liquid drop with a diffuse boundary [24]				
	Light-particle emission					Light-particle emission				
	is disregarded		is taken into account			is disregarded		is taken into account		
	σ_M^2	t_{sc}	σ_M^2	t_{sc}	$\langle n_{pre}\rangle$	σ_M^2	t_{sc}	σ_M^2	t_{sc}	$\langle n_{pre}\rangle$
One-body viscosity mechanism										
$k_s = 0.25$	211	33.9	185	33.6	1.89	315	27.7	235	26.8	4.06
$k_s = 0.5$	218	38.3	190	38.0	2.04	324	31.1	245	29.9	4.26
$k_s = 1.0$	221	46.7	188	46.5	2.29	348	38.3	253	37.3	4.60
Two-body viscosity mechanism										
$\nu = 0.02$	226	4.02	163	3.51	0.574	278	3.0	277	2.57	0.867
$\nu = 0.10$	211	16.8	164	20.0	2.30	248	11.38	244	10.5	2.64
$\nu = 0.25$	206	39.9	153	46.0	3.30	256	24.9	216	25.8	4.0

Note: According to [14], the experimental values are σ_M^2 = 319 (amu)^2 (L = 0) and $\langle n_{pre}\rangle$ = 2.6. Here and in Tables 2 and 3 below, σ_M^2, t_{sc}, and the coefficient of two-body viscosity (ν) are measured in (amu)^2, 10^{-21} s, and 10^{-21} MeV s fm^{-3} units, respectively.

Our procedure for combining the statistical model and the dynamical approach was as follows. The partial decay widths Γ_j were determined at each step of integration of the Langevin equations (2) according to (10) and (11). On the basis of their sum, we then calculated the mean lifetime of the compound nucleus before the emission of any light particle, $\tau_{tot} = \hbar/\sum_j \Gamma_j$. In the interval [0, 1] we further generated an equiprobably distributed random number ξ, which was compared with the ratio τ/τ_{tot} (τ is the time step of integration of the Langevin equation). If the condition $\xi < \tau/\tau_{tot}$ was satisfied, it was assumed that some light particle was emitted [32]. A particular particle species was chosen by a Monte Carlo procedure in accordance with the probability of compound-nucleus decay through a specific channel by using the calculated decay widths Γ_j.

3. DISCUSSIONS OF THE RESULTS AND CONCLUSIONS

For the reaction $^{12}C + {}^{232}Th \longrightarrow {}^{244}Cm$ (E_{lab} = 97 MeV), the calculations that employed the initial conditions on the ridge and the friction tensor defined by (6), which disregarded light-particle evaporation, and which assumed zero angular momentum L of the compound nucleus yielded the values of σ_M^2 = 200 (amu)^2 and $t_{sc} = 45.5 \times 10^{-21}$ s for the variance of the mass distribution and for the mean time of motion to the scission line within the liquid-drop model with a sharp boundary and the values of σ_M^2 = 311 (amu)^2 and $t_{sc} = 35.6 \times 10^{-21}$ s for the analogous quantities within the liquid-drop model with a diffuse boundary. For the same reaction, a variation in the initial conditions that corresponds to choosing initial coordinates near the ground state, all other conditions being the same [L = 0, one-body viscosity calculated by formula (6) with k_s = 1, no light-particle emission], does not change significantly the variance of the mass distribution: σ_M^2 = 204 (amu)^2 and $t_{sc} = 53.9 \times 10^{-21}$ s within the model with a sharp boundary and σ_M^2 = 309 (amu)^2 and $t_{sc} = 38.2 \times 10^{-21}$ s within the model with a diffuse boundary. This might have been expected for heavy nuclei because the ridge line separating the ground state from the fission valley is offset by quite a large distance from the scission line, so that the evolution before the saddle point does not affect significantly the parameters of the mass distribution, only increasing the mean time it takes for a nucleus to reach the scission line.

A more pronounced effect is observed when, in calculating the friction tensor, we include the additional term that corresponds to nucleon exchange between the two parts of the compound system [see Eq. (7)]. In this case, the variance of the mass distribution increases noticeably (by 10–15%, depending on the model used). [The calculated values of σ_M^2 and t_{sc} for the reaction $^{12}C + {}^{232}Th \longrightarrow {}^{244}Cm$ (E_{lab} = 97 MeV) are presented in Table 1.] The reason behind this increase is that the value of the mass-asymmetric component of the viscosity tensor as calculated by formula (7) exceeds the corresponding value calculated by formula (6), especially near the scission point (see Fig. 1*a*). This quenches the motion along the mass-asymmetric coordinate, on one

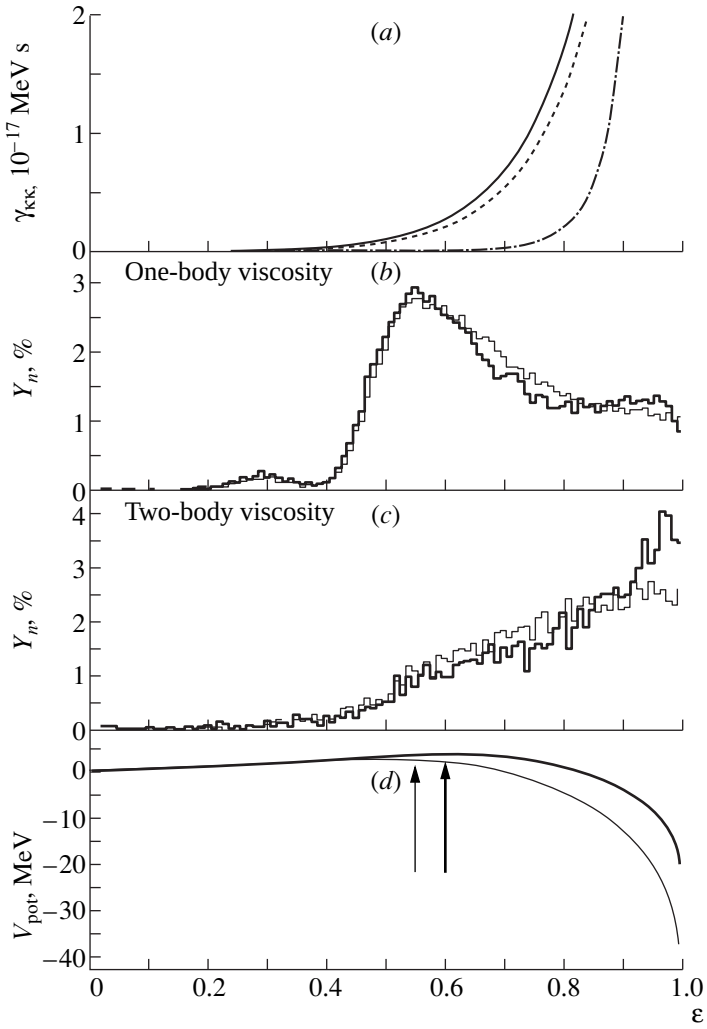

Fig. 1. Various features of the fission process at $\kappa = 0$ versus the parameter ε for the compound nucleus ^{244}Cm: (*a*) friction-tensor component $\gamma_{\kappa\kappa}$ represented by the dash-dotted curve for the two-body mechanism of viscosity with coefficient $\nu = 0.02 \times 10^{-21}$ MeV s fm^{-3}, the dashed curve for the one-body mechanism computed by formula (6) with $k_s = 1$, and the solid curve for the one-body mechanism computed by formula (7); (*b*, *c*) percent yield of prescission fission neutrons (in relation to their total number) that was calculated within two versions of the liquid-drop model (that which assumes a sharp boundary of a nucleus [23] and which leads to the results shown by the thick-line histogram and that which assumes a diffuse boundary of a nucleus [24] and which leads to the results shown by the thin-line histogram) by using, respectively, the one-body (with $k_s = 1$) and the two-body (with $\nu = 0.02 \times 10^{-21}$ MeV s fm^{-3}) viscosity mechanism; and (*d*) potential-energy profiles represented by the thick curve for the model of a nuclear liquid drop having a sharp boundary and the thin curve for the model of a nuclear liquid drop having a diffuse boundary (arrows indicate the position of the fission barrier).

hand, and intensifies fluctuations along it, on the other hand. As a result, the variance of the mass distribution increases.

Another significant factor that affects the parameters of the mass distribution is the inclusion of the evaporation of prescission light particles. Since the technical aspect of combining the dynamical model of fission with the static model of light-particle emission was described above, we present here only the main results.

Light-particle emission from the compound nucleus affects the variance of the fission-fragment mass distribution in two ways: (i) a variation in the nucleonic composition of the fissile nucleus must increase the scatter of the fission-fragment masses; (ii) the emitted particles take away some part of the excitation energy of the compound system, whereby the nuclear temperature is reduced and so therefore are fluctuations of the collective degrees of freedom, including fluctuations of the mass-asymmetric coordinate. The concerted effect of the two factors leads to a decrease in the variance of the mass distribution (this decrease may be as large as 30%) and in its mean value. As an illustration of the particle-emission effect on the shape of the fission-fragment mass distribution, two mass distributions computed on the basis of the one-body viscosity mechanism with $k_s = 1$ for the reaction involving the com-

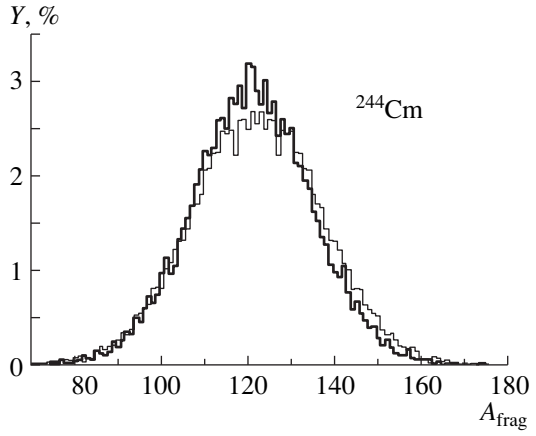

Fig. 2. Example of the fission-fragment mass distributions in the reaction $^{12}C + ^{232}Th \longrightarrow ^{244}Cm$ at $E_{lab} = 97$ MeV that were calculated by using the one-body viscosity mechanism with $k_s = 1$ on the basis of the model of a nuclear liquid drop having a diffuse boundary [24]: (thin-line histogram) results obtained without allowance for light-particle emission and (thick-line histogram) results obtained with allowance for light-particle emission.

pound nucleus ^{244}Cm are shown in Fig. 2, where the thin- and the thick-line histograms represent, respectively, the yield of fragments in the calculation without light-particle emission (the distribution is symmetric with respect to $A_{CN}/2$ in this case) and the analogous yield obtained with allowance for this process. These distributions are normalized to the total number of fission fragments (so-called normalization to 200%).

In order to clarify the viscosity type realized in the fission process, we performed our calculations for the reactions

$$^{12}C + ^{232}Th \longrightarrow ^{244}Cm \ (E_{lab} = 97 \text{ MeV}),$$

$$^{16}O + ^{249}Cf \longrightarrow ^{265}Sg \ (E_{lab} = 145 \text{ MeV}),$$

$$^{16}O + ^{208}Pb \longrightarrow ^{224}Th \ (E_{lab} = 108 \text{ MeV}).$$

The characteristics of fission (the variance of mass distribution, the mean time it takes for a nucleus to reach the scission line, and the mean number of prescission neutrons) that were calculated within two versions of the liquid-drop model—that with a sharp boundary [23] and that with a diffuse boundary [24]—are quoted in Tables 1–3. In all these results, the statistical error is about 1%. This estimate is based on the fact that, for each nucleus and each viscosity value, we analyzed the evolution of approximately 10^4 trajectories.

As can be seen from the tables, the type of viscosity mechanism affects significantly the value of the variance and its qualitative dependence on the magnitude of viscosity. If we use the one-body mechanism of viscosity, the variance of mass distribution increases slightly (this increase is more pronounced in the model with a diffuse boundary than in the model with a sharp boundary) with increasing reduction coefficient k_s. In the case of two-body viscosity, the increase in the coefficient of two-body viscosity ν leads to a decrease in the variance of the mass distribution. In all probability, this behavior is due to the different coordinate dependences of the friction-tensor components. By way of illustration, the component $1a$ as a function of the collective coordinate ε is presented in Fig. $1a$ at $\kappa = 0$ (symmetric shapes)—this component has a greater bearing on the variance of the mass distribution. The tensor of two-body viscosity increases sharply only near the scission line, while the value of one-body viscosity is significant even near the fission barrier ($\varepsilon = 0.5$–0.6). If the coefficient of the two-body viscosity is $\nu = 0.02 \times 10^{-21}$ MeV s fm^{-3}, prescission neutrons are therefore evaporated only immediately prior to scission. In this case, the mean number of prescission neutrons is modest. The increase in the coefficient ν by a factor of 12.5 significantly increases the number of prescission fission neutrons (by a factor of 3 to 7). Here, a noticeable

Table 2. Results of theoretical calculations performed within two versions of the liquid-drop model for the reaction $^{16}O + ^{208}Pb \longrightarrow ^{224}Th$ ($E_{lab} = 108$ MeV)

Coefficient	Liquid drop with a sharp boundary [23]			Liquid drop with a diffuse boundary [24]		
	σ_M^2	t_{sc}	$\langle n_{pre} \rangle$	σ_M^2	t_{sc}	$\langle n_{pre} \rangle$
One-body viscosity mechanism						
$k_s = 0.25$	148	67.8	0.8	208	50.8	2.69
$k_s = 0.5$	146	76.9	0.878	214	56.9	2.80
$k_s = 1.0$	146	86.7	0.967	221	66.7	2.99
Two-body viscosity mechanism						
$\nu = 0.02$	156	7.06	0.233	234	3.86	0.955
$\nu = 0.10$	135	40.8	1.113	197	19.3	1.69
$\nu = 0.25$	126	102.6	1.768	184	49.1	2.65

Note: According to [14], the experimental values are $\sigma_M^2 = 180$ (amu)^2 ($L = 0$) and $\langle n_{pre} \rangle = 2.5$.

Table 3. Results of theoretical calculations performed within two versions of the liquid-drop model for the reaction $^{16}O + ^{249}Cf \longrightarrow ^{265}Sg$ (E_{lab} = 145 MeV)

Coefficient	Liquid drop with a sharp boundary [23]			Liquid drop with a diffuse boundary [24]		
	σ_M^2	t_{sc}	$\langle n_{pre}\rangle$	σ_M^2	t_{sc}	$\langle n_{pre}\rangle$
One-body viscosity mechanism						
k_s = 0.25	224	15.9	1.81	272	14.1	4.14
k_s = 0.5	227	18.1	2.0	283	16.1	4.43
k_s = 1.0	227	22.8	2.38	317	20.1	4.93
Two-body viscosity mechanism						
ν = 0.02	269	2.30	0.668	310	1.75	0.805
ν = 0.10	238	7.76	2.094	287	5.59	2.42
ν = 0.25	223	18.6	3.44	265	13.5	4.01

Note: According to [14], the experimental values are σ_M^2 = 506 (amu)^2 (L = 0) and $\langle n_{pre}\rangle$ = 4.1.

part of the neutrons is evaporated not only prior to scission but also along the entire descent from the barrier to the scission point, as in the case of one-body viscosity. Because of the increase in neutron emission, the temperature of the compound system decreases, and so therefore does the variance of the mass distribution. This effect is similar to the simple inclusion of particle emission in the computational scheme by proceeding in the same way as was described above. In the case of the one-body dissipation mechanism, the viscosity value is high even at k_s = 0.25, and the cooling of the system via particle evaporation attains its limit here (a major part of the excitation energy of the nucleus is converted into its internal energy and is carried away by light particles), so that no significant increase in the number of prescission particles occurs at k_s = 1. A slight increase in the variance of the mass distribution is explained here by the growth of fluctuations of the mass-asymmetric coordinate, which are dependent on the nuclear viscosity.

It should be recalled that the choice of version of the liquid-drop model is also of importance. Within the model of a liquid drop having a diffuse boundary, the fission barrier is higher, whereas the descent in energy from the saddle point to the scission point is longer. As a result, the fission time always proves to be less in this model than in the model of a liquid drop with a sharp boundary, whereas the variance of the mass distribution is greater. The mean multiplicity of neutrons in the model of a liquid drop with a sharp boundary is almost everywhere one-half as great as that in the model where the drop boundary is smeared. This is determined by the potential-energy drop between the saddle and the scission point in the models being discussed: the higher this drop, the greater the collective-motion-energy fraction that can be converted into the internal energy, whereby the emission of particles is facilitated.

In order to explain the distinctions between the prescission-neutron multiplicities as obtained by using the different viscosity mechanisms, we invoke data in Figs. 1 and 3. From Fig. 1*a*, it can clearly be seen that one-body viscosity [dashed curve and solid curve, the

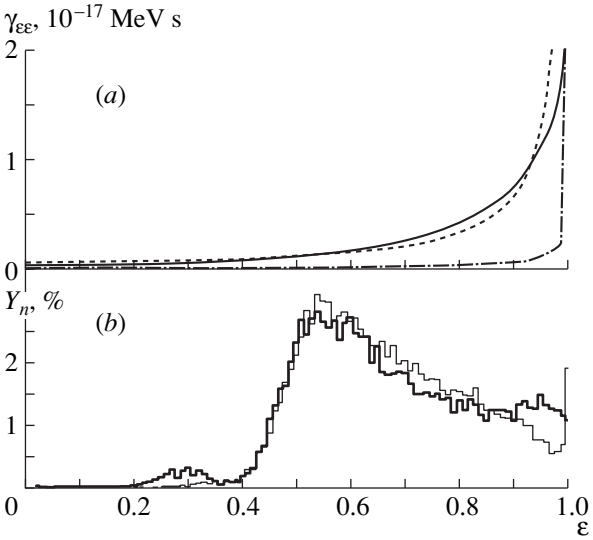

Fig. 3. Various features of the fission process at κ = 0 versus the parameter ε for the compound nucleus ^{244}Cm: (*a*) friction-tensor component $\gamma_{\varepsilon\varepsilon}$ represented by the dash-dotted curve for the two-body mechanism of viscosity with coefficient $\nu = 0.02 \times 10^{-21}$ MeV s fm^{-3}, the dotted curve for the two-body mechanism with coefficient $\nu = 0.25 \times 10^{-21}$ MeV s fm^{-3}, and the solid curve for the one-body mechanism computed by formula (7) with k_s = 1 and (*b*) percent yield of prescission fission neutrons (in relation to their total number) that was calculated within two versions of the liquid-drop model (that which assumes a sharp boundary of a nucleus [23] and which leads to the results shown by the thick-line histogram and that which assumes a diffuse boundary of a nucleus [24] and which leads to the results shown by the thin-line histogram) by using the two-body viscosity mechanism with $\nu = 0.25 \times 10^{-21}$ MeV s fm^{-3}.

latter being computed with allowance for the additional term in (7)] grows faster than two-body viscosity (dash-dotted curve for $\nu = 0.02 \times 10^{-21}$ MeV s fm^{-3}). Figures 1*b* and 1*c* show the percentage of neutrons emitted at a given value of the nucleus-elongation coordinate ε for one- and for two-body viscosity, respectively. For the symmetric case, the shape of the potential energy is presented in Fig. 1*d*. From Figs. 1*b* and 1*c*, it can be seen that, in the case of one-body viscosity, the evaporation of neutrons is enhanced faster and begins earlier, the peak being in the region of the saddle point. By this instant, a significant part of the energy has been dissipated; apart from this, the system moves in this region rather slowly. Upon passing the saddle, the probability of evaporation approaches a constant that is determined by the transfer of the collective energy to the internal energy during the descent from the saddle to the scission point. For two-body viscosity, the pattern is somewhat different. By the instant when the system reaches the barrier, the viscosity is still low; therefore, the internal energy and the number of evaporated neutrons are not large. Upon passing the saddle point, viscosity sharply grows, which leads to an increase in the probability of neutron evaporation in this region.

In this study, we used three values of the coefficient ν of two-body viscosity. The relationship between one- and two-body viscosity changes with increasing ν, (Fig. 3*a*). Two-body viscosity begins to grow earlier and appears to be commensurate with one-body viscosity. This is noticeably reflected in the dependence of the neutron-evaporation probability on the elongation coordinate ε (Fig. 3*b*)—it becomes similar to that in the one-body case. Here, the mean values of the neutron multiplicities are nearly equalized in the two cases. As has already been mentioned, such changes in two viscosity lead to qualitatively different types of behavior of σ_M^2 with increasing viscosity in the two-body and in the one-body case.

For one of the main results obtained from the present calculations and quoted in the tables, we indicate that the experimental data on the variances of the mass distributions and on the multiplicities of prescission particles can be described on the basis of both the one- and the two-body mechanism of nuclear viscosity, but the magnitude of nuclear viscosity must be high in either case. In order to achieve satisfactory agreement with experimental data, one therefore has to use an anomalously large viscosity value in the case of the two-body mechanism ($\nu \sim 0.25 \times 10^{-21}$ MeV s fm^{-3}). In this case, however, the coefficient ν is more than 12 times as great as that which was extracted from the description of the mass–energy distributions in [33] and six times as great as that which was used by a Japanese group in [8]. A similar conclusion was drawn by Blocki *et al.* [34]. In view of all this, the possibility of consistently describing the mass–energy distribution and the multiplicity of prefission neutrons at the above value of ν is questionable.

Here, we do not present the energy distributions of fission fragments. This is because, in calculating such distributions, it is necessary to invoke, in addition to the elongation and the mass-asymmetry parameter, a third collective coordinate that is responsible for the formation of a neck in the nuclear shape (neck parameter). In order to describe completely mass–energy distributions, we must therefore employ a three-parameter family of fissile-nucleus shapes—in other words, relevant calculations must be performed within three-dimensional Langevin dynamics. Such investigations are presently under way.

ACKNOWLEDGMENTS

We are grateful to our colleagues A.Ya. Rusanov and V.S. Salamatin for stimulating discussions and constructive criticism. D.V. Vanin is indebted to the directorate of the Laboratory for Nuclear Reactions at the Joint Institute for Nuclear Research for the opportunity to work at that laboratory over the period of time it took to complete this investigation.

REFERENCES

1. Yu. Ts. Oganessian and Yu. A. Lazarev, in *Treatise on Heavy Ion Science*, Ed. by D. A. Bromley (Plenum, New York, 1985), Vol. 4, p. 3.
2. F. Gönnenwein, in *Nuclear Fission Process*, Ed. by C. Wagemans (CRC, Boca Raton, 1991), p. 287.
3. M. G. Itkis and A. Ya. Rusanov, Fiz. Élem. Chastits At. Yadra **29**, 389 (1998) [Phys. Part. Nucl. **29**, 160 (1998)].
4. J. W. Negele *et al.*, Phys. Rev. C **17**, 1098 (1978).
5. F. Berger, M. Curod, and D. Cogny, Nucl. Phys. A **429**, 23c (1984).
6. P. Bonche, S. E. Koonin, and J. W. Negele, Phys. Rev. C **13**, 1226 (1976).
7. H. J. Krappe, in *Proceedings of the International Workshop on Dynamical Aspects of Nuclear Fission, Smolenice, Slovakia, 1991*, Ed. by J. Kristiak and B. I. Pustylnik (Joint Inst. for Nuclear Research, Dubna, 1992), p. 51.
8. Y. Abe, S. Ayik, P.-G. Reinhard, and E. Suraud, Phys. Rep. **275**, 49 (1996).
9. T. Wada, N. Carjan, and Y. Abe, Nucl. Phys. A **538**, 283c (1992).
10. G.-R. Tillack *et al.*, Phys. Lett. B **296**, 296 (1992).
11. J. Bao, Y. Zhuo, and X. Wu, Z. Phys. A **352**, 321 (1995).
12. G. I. Kosenko, I. G. Cagliari, and G. D. Adeev, Yad. Fiz. **60**, 404 (1997) [Phys. At. Nucl. **60**, 334 (1997)].
13. D. V. Vanin, G. I. Kosenko, and G. D. Adeev, Phys. Rev. C **59**, 2114 (1999).
14. A. Ya. Rusanov, M. G. Itkis, and V. N. Okolovich, Yad. Fiz. **60**, 773 (1997) [Phys. At. Nucl. **60**, 683 (1997)].
15. H. J. Krappe, J. R. Nix, and A. J. Sierk, Phys. Rev. C **20**, 992 (1979).
16. G. D. Adeev and P. A. Cherdantsev, Phys. Lett. B **39**, 485 (1972); Yad. Fiz. **18**, 741 (1973) [Sov. J. Nucl. Phys. **18**, 381 (1973)].

17. V. S. Stavinskiĭ, N. S. Rabotnov, and A. A. Seregin, Yad. Fiz. **7**, 1051 (1968) [Sov. J. Nucl. Phys. **7**, 631 (1968)]; V. V. Pashkevich, Nucl. Phys. A **169**, 275 (1971).
18. R. W. Hasse and W. D. Myers, *Geometrical Relationships of Macroscopic Nuclear Physics* (Springer-Verlag, Berlin, 1988).
19. M. Brack *et al.*, Rev. Mod. Phys. **44**, 320 (1972).
20. U. Brosa, S. Grossmann, and A. Müller, Phys. Rep. **197**, 167 (1990).
21. K. T. R. Davies, R. A. Managan, J. R. Nix, and A. J. Sierk, Phys. Rev. C **16**, 1890 (1977).
22. H. A. Kramers, Physica (Utrecht) **7**, 284 (1940).
23. W. D. Myers and W. J. Swiatecki, Ark. Fys. **36**, 343 (1967).
24. A. J. Sierk, Phys. Rev. C **33**, 2039 (1986).
25. K. T. R. Davies, A. J. Sierk, and J. R. Nix, Phys. Rev. C **13**, 2385 (1976).
26. J. Blocki *et al.*, Ann. Phys. (N.Y.) **113**, 330 (1978); A. J. Sierk and J. R. Nix, Phys. Rev. C **21**, 982 (1980).
27. J. R. Nix and A. J. Sierk, in *Proceedings of the International School–Seminar on Heavy Ion Physics, Dubna, 1986*, Ed. by M. I. Zarubina and E. V. Ivashkevich (Joint Inst. for Nuclear Research, Dubna, 1987), p. 453; *Proceedings of the 6th Adriatic Conference on Nuclear Physics: Frontiers of Heavy Ion Physics, Dubrovnik, Yugoslavia, 1987*, Ed. by N. Cindro *et al.* (World Sci., Singapore, 1990), p. 333.
28. H. Feldmeier, Rep. Prog. Phys. **50**, 915 (1987).
29. J. Randrup and W. J. Swiatecki, Nucl. Phys. A **429**, 105 (1984).
30. A. S. Iljinov, M. V. Mebel, *et al.*, Nucl. Phys. A **543**, 517 (1992).
31. W. D. Myers and W. J. Swiatecki, Nucl. Phys. **81**, 1 (1966).
32. N. D. Mavlitov, P. Fröbrich, and I. I. Gontchar, Z. Phys. A **342**, 195 (1992).
33. G. D. Adeev *et al.*, Fiz. Élem. Chastits At. Yadra **19**, 1229 (1988) [Sov. J. Part. Nucl. **19**, 529 (1988)].
34. J. Blocki, R. Planeta, J. Brzychczyk, and K. Grotowski, Z. Phys. A **341**, 307 (1992).

Translated by A. Isaakyan

Physics of Atomic Nuclei, Vol. 63, No. 11, 2000, pp. 1874–1884. Translated from Yadernaya Fizika, Vol. 63, No. 11, 2000, pp. 1966–1977.

NUCLEI
Theory

Properties of Isovector 1^+ States in $A = 28$ Nuclei and Nuclear Muon Capture

V. A. Kuz'min* and T. V. Tetereva[1), **]

Joint Institute for Nuclear Research, Dubna, Moscow oblast, 141980 Russia

Received August 13, 1999; in final form, February 15, 2000

Abstract—A method is proposed for taking into account, in a calculation of partial rates of muon capture by nuclei, experimental information about strength functions for Gamow–Teller and isovector $M1$ transitions. The method, which amounts to choosing an orthogonal transformation that acts in the subspace of wave functions for excited states, requires neither modifying transition operators nor introducing effective charges. The matrix of the above transformation is constructed as a product of the matrices of reflection in a plane. All calculations are performed on the basis of the multiparticle shell model. Numerical results are obtained for isovector states in $A = 28$ nuclei. Strength functions for Gamow–Teller and isovector $M1$ transitions in ^{28}Si are considered, and the lifetimes of 1^+ states in ^{28}Al and the branching fractions for gamma decays of this state are calculated. Owing to taking into account experimental information about the properties of isovector states, the branching fractions for the γ decays of the 1^+ state at 2.201 MeV in ^{28}Al are successfully described for the first time. The above transformation of the wave functions changes substantially the distribution of partial rates of allowed muon capture by a ^{28}Si nucleus among the 1^+ states of the final nucleus ^{28}Al in relation to the results of the calculations with the eigenfunctions of the Hamiltonian of the multiparticle shell model. The muon-capture rates calculated with the transformed functions agree well with experimental data. © *2000 MAIK "Nauka/Interperiodica".*

1. INTRODUCTION

The results of two independent measurements of a correlation between the momentum of the neutrino produced in the capture of polarized negative muons by a ^{28}Si nucleus and the momentum of the photon emitted in the γ decay of an excited state of the daughter nucleus are known at present [1, 2]. The authors of these studies considered the same allowed partial transition

$$\mu^- + {}^{28}\mathrm{Si}(0^+_{\mathrm{g.s.}}) \longrightarrow \nu_\mu + {}^{28}\mathrm{Al}(1^+_3, 2201).$$

A comparison of the values that they obtained for the $\gamma\nu$-correlation coefficient with the results of the theoretical calculations from [3–5] led to the conclusion that induced pseudoscalar weak muon interaction with intranuclear nucleons is suppressed to a considerable extent in relation to estimates based on the hypothesis of a partial conservation of the axial current (PCAC). Table 1 displays the g_P/g_A values obtained from a comparison of the correlation coefficients measured in [1, 2] with the results of the theoretical studies quoted above. Another experiment determined the ratio of the rates of muon capture from the hyperfine-splitting states of the ^{23}Na muonic atom, and a comparison of those results with theoretical predictions yielded $g_P/g_A = 7.6 \pm 2.1$ [6], a value that is consistent with the PCAC hypothesis. Such a great distinction between the values of g_P/g_A is quite unexpected, especially as the ^{28}Si and ^{23}Na nuclei are close to each other in mass number; therefore, it could be thought that the coupling constants for induced pseudoscalar interaction would be nearly identical in the two cases. It should be noted that, in [5, 6], nuclear matrix elements of the effective Hamiltonian for ordinary muon capture were computed within the same multiparticle shell model [7] employing the full *sd*-shell space and the parametrization of the shell Hamiltonian from [8]. However, the partial transitions being discussed have one important distinction. The experiment reported in [6] dealt with the allowed transition $3/2^+, 1/2 \longrightarrow 1/2^+, 3/2$. (Nuclear states are classified in terms of the total spin, parity, and isospin—that is, J^π, T.) Calculations reveal that the above partial transition is dominated by the single-particle transition $d_{5/2} \longrightarrow d_{5/2}$. As a result, the matrix ele-

Table 1. Ratio g_P/g_A obtained from a comparison of the measured and calculated angular-correlation factors

Calculation	Experiment	
	[1]	[2]
[3]	3.4 ± 1.0	5.3 ± 2.0
[4]	2.0 ± 1.6	4.2 ± 2.5
[5]	-2.8 ± 1.6	0.0 ± 3.2

[1)] Institute of Nuclear Physics, Moscow State University, Vorob'evy gory, Moscow, 119899 Russia.
* e-mail: kuzmin@thsun1.jinr.dubna.su
** e-mail: tetereva@thsun1.jinr.dubna.su

ment of the operator $j_0(\nu r)\sigma t^-$ (in the notation adopted in [9, 10], this is the [101] matrix element) makes a leading contribution, determining the partial rate of nuclear muon capture; therefore, the results of the calculations prove to be quite reliable. In the case of the $0^+_{g.s.} \longrightarrow 1^+_3$ transition, which was considered in the experiment with ^{28}Si, there is no dominant matrix element, since the single-particle transition $d_{5/2} \longrightarrow d_{3/2}$, which has the greatest amplitude in the single-particle transition density, is suppressed by the $d_{3/2} \longrightarrow d_{5/2}$ transition going in the opposite direction. In the absence of a leading matrix element, the rate of nuclear muon capture is determined by the interference of several small matrix elements, including velocity-dependent ones. In this case, a theoretical description becomes much less reliable, so that a further investigation of the properties of excited states of the daughter nucleus is highly desirable.

Theoretically, isovector $J^\pi = 1^+$ states in $A = 28$ nuclei were studied in [11] on the basis of the multiparticle shell model by using the full *sd*-shell space, the energies of single-particle nucleon states and two-particle matrix elements of interaction between valence nucleons being taken from [8]. The results obtained in [11] can be summarized as follows. The calculated excitation energies and lifetimes of low-lying 1^+ states comply with experimental data. However, the branching fractions for γ decays of the 1^+ state at 2.201 MeV in ^{28}Al could not be reproduced.

Experimentally, the properties of isovector 1^+ states in $A = 28$ nuclei were studied in [12], [13], and [14] by using the relevant (e, e'), (p, n), and $(^3\mathrm{He}, t)$ reactions, respectively. Lüttge *et al.* [12] compared their experimental excitation-energy distributions of the $M1$ strengths ($M1$ strength functions) with the distributions calculated on the basis of the shell model employing the Hamiltonian from [8] and arrived at the conclusion that the theoretical distribution of the quantities $B(M1)$, reduced probabilities of $M1$ transitions, do not agree with the experimental distribution. For the majority of states, the computed values of $B(M1)$ considerably exceed the corresponding experimental values, but this is not so for the 11.445-MeV state, which corresponds to the third eigenstate of the shell-model Hamiltonian—here, the theoretical value of $B(M1)$ is much less than the experimental result. The theoretical total strength of the transitions falls considerably short of the experimental value. In [13], the strength function for Gamow–Teller σt^+ transitions was extracted from the measured cross sections for the reaction ^{28}Si $(p, n)^{28}$Al. In just the same way as in the case of $M1$ transitions, the theoretical total strength of Gamow–Teller transitions exceeded considerably the experimental value. For the transition to the 1^+ state at 2.10 MeV in ^{28}P, however—this state corresponds to the third eigenstate of the Hamiltonian from [8]—the theoretical reduced probability of the Gamow–Teller transition, $B(\mathrm{GT})$, proved to be much less than the corresponding experimental value.

The hypothesis that the isospin is conserved in nuclei makes it possible to combine isovector 1^+ states in ^{28}Al, ^{28}Si, and ^{28}P into isotopic triplets. The table establishing the correspondence can be found in [11]. From this table, it can be seen that the 1^+ level at 2.201 MeV in ^{28}Al—this level is populated in the $\gamma\nu$ correlation experiment using ^{28}Si—belongs to the same triplet as the 11.445-MeV level in ^{28}Si and the 2.10-MeV level in ^{28}P (for the last two, the theoretical strengths of Gamow–Teller and $M1$ transitions proved to be smaller than the corresponding experimental values). The transitions from the ^{28}Si ground state, whose isospin is equal to zero, to the isotopic-triplet states can be described in terms of rank-1 isotopic tensor operators. In the matrix elements of these operators, we can single out the isospin-projection dependence, thereby going over to matrix elements reduced in isospin (doubly reduced matrix elements). If the same isospin-reduced matrix elements had appeared in the amplitudes for electron scattering, (p, n) reactions, and muon capture, it would have been possible to use the amplitudes determined in one of the processes to describe other processes. However, the transition operators for different properties are different. We can extract the square of the matrix element $\langle 1^+, 1|||\sigma t|||0^+, 0\rangle$ from data on (p, n) reactions and the square of the matrix element $\langle 1^+, 1|||g_s^{\mathrm{IV}}\sigma + g_l^{\mathrm{IV}} l|||0^+, 0\rangle$ from data on $M1$ transitions; at the same time, the partial amplitude of muon capture involves the matrix elements $\langle 1^+, 1|||j_0(\nu r)\sigma t|||0^+, 0\rangle$, $\langle 1^+, 1|||j_2(\nu r)[Y_2, \sigma]_1 t|||0^+, 0\rangle$, $\langle 1^+, 1|||j_1(\nu r)[Y_1, \nabla]_1 t|||0^+, 0\rangle$, and $\langle 1^+, 1|||j_1(\nu r)Y_1(\sigma\nabla)t|||0^+, 0\rangle$. In describing muon capture, the quantities $B(M1)$ and $B(\mathrm{GT})$ are therefore used primarily to assess the degree to which the features of partial transitions are reproduced. From this point of view, the fact that the calculations considerably underestimate the strengths of $M1$ and Gamow–Teller transitions to the third eigenstate of the Hamiltonian in relation to experimental data (although the theoretical total strengths of the transitions in question considerably exceed the experimental values) evinces inadequacy of the theoretical description of the features of the level being discussed. In addition, it should be borne in mind that the wave functions were obtained by diagonalizing the shell-model Hamiltonian in the full *sd*-shell space and that a way to improve this description within a consistent theory has yet to be found.

It such a situation, it would be desirable that calculations of nuclear muon capture invoke available experimental information about Gamow–Teller and $M1$ strengths. With this aim in view, we propose introducing, in calculations of muon capture, phenomenological corrections via an orthogonal transformation of the wave functions of J^π, $T = 1^+$, 1 excited states. A key point here is the following. The parameters of the transformation must be chosen in such a way as to ensure

agreement in form—that is, a full consistency apart from a numerical factor—between Gamow–Teller and $M1$ strength functions calculated with the transformed wave functions and their experimental counterparts. Since the transformation in question is orthogonal, the resulting wave functions will be orthogonal to one another and will be normalized in just the same way as the original wave functions. Moreover, the space of states is neither contracted nor expanded, and the total Gamow–Teller and $M1$ strengths remain unchanged. Under the transformations of the wave functions, the transition strength can only be redistributed among excited states. Thereby, all the problems concerning the excess of the theoretical total strengths of Gamow–Teller and $M1$ transitions over the experimental values remain beyond the scope of the present study. Since the new wave functions are linear combinations of functions characterized by the same values of the total spin, parity, and isospin (J^π, $T = 1^+$, 1), we have J^π, $T = 1^+$, 1 for them. In calculating the features of muon capture, the proposed method makes it possible to take into account a major piece of available experimental information about Gamow–Teller and $M1$ strength functions. In a sense, this method represents a generalization of the two-level scheme popular in nuclear spectroscopy.

The present article consists of the Introduction (Section 1), four main sections, and the Conclusion. In Section 2, we consider the auxiliary mathematical problem of transforming vectors by means of reflections in a plane. In Section 3, we analyze in detail Gamow–Teller and $M1$ transitions and construct the transformation matrix for the relevant wave functions. In Section 4, the transformed wave functions are used to describe the features of the γ decays of 1^+ states in ^{28}Al. Section 5 is devoted to partial rates of muon capture in ^{28}Si. There, we also compare the results of the calculations with recent experimental data. The basic results of this study are summarized in the Conclusion.

2. MATHEMATICAL DETAILS

For the wave functions of excited states, it is necessary to find an orthogonal transformation that reproduces the form of the experimental strength functions for Gamow–Teller and $M1$ transitions from the ground state, whose quantum numbers are 0^+, 0, to 1^+, 1 excited states. We begin by discussing the auxiliary problem of transforming one specific N-dimensional vector into another specific N-dimensional vector.

2.1. Transformation of Wave functions and Transition Amplitudes

We denote by ϕ_k ($k = 1, \ldots, N$) the set of wave functions of the chosen excited states. We assume that these functions are normalized and are orthogonal. With the aid of a unitary transformation U, we construct a new set of functions,

$$\psi_k = U_{k,k'}\phi_{k'} \quad (k = 1, 2, \ldots, N). \tag{1}$$

Owing to unitarity of the transformation U, the resulting functions ψ_k are also normalized and orthogonal. The matrix element of the operator O responsible for the transition between the ground state characterized by the wave function Φ and the excited state described by the wave function ψ_k is given by

$$\langle \psi_k | O | \Phi \rangle = U^*_{k,k'} \langle \phi_{k'} | O | \Phi \rangle = \langle \phi_{k'} | O | \Phi \rangle U^\dagger_{k',k}. \tag{2}$$

Thus, the vector of the amplitudes for the transitions from the Φ state to the transformed states ψ_k is obtained by applying the unitary transformation $U^\dagger$ to the vector of the amplitudes for transitions to the original state ϕ_k. The transformation $U^\dagger$ is the Hermitian conjugate of the transformation U. Relation (2) considerably simplifies the problem of seeking the transformation in (1) since, owing to this relation, the problem of seeking the transformation of a vector whose components are multiparticle wave functions reduces to seeking the transformation of the much simpler vector composed of transition amplitudes representing conventional numbers. In the overwhelming majority of cases, transition amplitudes are real numbers; therefore, we can require that the elements of the U matrix be real-valued and that the matrix itself be orthogonal.

2.2. Structure of the Orthogonal Matrix

A general orthogonal matrix of dimension N can be determined in terms of $N(N-1)/2$ real-valued parameters. If we consider nine or ten excited states, we must therefore specify 36 or 45 parameters. As a result, we have nine or ten equations of the type in (2) for determining 36 or 45 unknown quantities, so that the problem is underdetermined. For this reason, we employ orthogonal matrices of a special form that depend on a smaller number of parameters.

The simplest orthogonal transformation of a vector is the reflection with respect to a plane [15, 16]. Any vector v can be decomposed into the sum of two vectors, $v = u + w$; of these, one, u, belongs to a preset plane, while the other, w, is orthogonal to it. The reflection with respect to this plane reverses the direction of the vector w, transforming the vector v into the vector $v' = u - w$. Under this transformation, the length of the vector v is conserved, $|v| = |v'|$, the square of this length being $|v|^2 = |u|^2 + |w|^2 = v_1^2 + v_2^2 + \ldots + v_N^2 = v_k v_k$. Therefore, two arbitrarily preset vectors u and v of the same length ($|u| = |v|$) can be transformed into each other by means of the reflection with respect to the plane that passes through the origin of coordinates and which is orthogonal to the vector $u - v$. This plane is determined by the equation

$$(u_i - v_i)x_i = 0. \tag{3}$$

The transformation matrix then has the form

$$R_{i,j} = \delta_{i,j} - 2\frac{(u_i - v_i)(u_j - v_j)}{|u - v|^2}. \tag{4}$$

The matrix in (4) is symmetric—that is, $R_{i,j} = R_{j,i}$—and is orthogonal, $\tilde{R}R = RR = I$, I being an identity matrix. For any pair of vectors u and v of the same length, the above transformation of reflection is unique since it is specified by Eq. (3) (equation of a plane), where the coordinates of the vector $u - v$ appear to be parameters. The number of independent parameters is equal to the dimensionality of the vector space, where we implement the transformation in question.

In order to construct the matrix transforming the wave functions of excited states, it is sufficient to know two vectors composed of transition amplitudes. The values calculated theoretically for the transition amplitudes within multiparticle shell model are the coordinates of one vector. The other vector must be composed of the experimental transition amplitudes.

3. GAMOW–TELLER AND $M1$ STRENGTH FUNCTIONS

In order to find transformation matrices, we need two vectors formed by the amplitudes for transitions to the chosen excited states. The square of the length of each vector is equal to the transition strength (theoretical or experimental one) summed over all chosen excited states.

We begin by considering the vector of theoretical amplitudes. Since we are interested here in a transformation that reproduces only the shape of the experimental strength function, it is legitimate to use a vector of unit norm in constructing the required transformation matrix. Let the vector $(t_1, \ldots, t_N)$ be composed of theoretical Gamow–Teller amplitudes normalized by the condition $t_k t_k = 1$. The relative signs of the coordinates of the vector t are determined by the relative phases of the wave functions for the excited states being considered.

3.1. Experimental Amplitudes and Searches for the Most Appropriate Transformation

Problems to be overcome in dealing with experimental amplitudes are much more intricate. From experimental data, it is possible to extract only the transition strength—that is, the square of the modulus of the transition amplitude. We denote by e_k the strength of Gamow–Teller transition to the kth chosen excited state of spin–parity 1^+. The absolute value of the amplitude for this transition is $|f_k| = \sqrt{e_k}$. By using these amplitudes, we construct the vector $\tilde{f} = (f_1, \ldots, f_N)$. The square of its length represents the total strength of the transitions to all chosen states, $s^2(f) = |f|^2 = e_1 + \ldots + e_N$. The sign of each amplitude f_k remains unknown. Therefore, we have to consider all possible distributions of the signs of the amplitudes forming the vector f. For each distribution of signs in the vector f, there exists an individual reflection matrix (4),

$$R(f, t)_{i,j} = \delta_{i,j} - 2\frac{(f_i - s(f)t_i)(f_j - s(f)t_j)}{|f - s(f)t|^2}. \quad (5)$$

For the strength of the relevant Gamow–Teller transitions, the vector of theoretical amplitudes that is transformed with the aid of this matrix yields the distribution that is coincident in form with the experimental Gamow–Teller strength function. By using only one strength function, it is therefore impossible single out the most appropriate transformation among the emerging set.

There arises a natural criterion for choosing an optimum transformation if, along with the Gamow–Teller strength function, we consider the $M1$ strength function. The transformation (1) of the wave functions entails the transformation (2) of the transition amplitudes; therefore, the amplitudes of $M1$ transitions also transform in terms of the matrix $R(f, t)$. The distinctions between the operators of Gamow–Teller and $M1$ transitions result in that the vectors composed of the amplitudes for these transitions are linearly independent. This is true both for the vectors constructed from the experimental amplitudes and for the vectors constructed from the theoretical amplitudes. In general, the new $M1$ strength function obtained with the aid of $R(f, t)$ does not coincide with the experimental strength function for $M1$ transitions. This can be deduced from the fact that the scalar product of two vectors is invariant under orthogonal transformations. Generally, the scalar product of the vectors composed of the theoretical Gamow–Teller and $M1$ amplitudes is not equal to the scalar product of the vectors composed of experimental Gamow–Teller and $M1$ amplitudes. In an attempt at fully reconstructing the form of the Gamow–Teller strength function, the form of the $M1$ strength function will therefore be reproduced with some error. Accordingly, the version characterized by the smallest root-mean-square deviation will be taken to be the best one.

Making one step further, we can reduce the distinctions between the forms of the resulting theoretical and the experimental $M1$ strength function, by applying an additional transformation that is of the type in (4) and which acts in the subspace orthogonal to the vector formed by the theoretical Gamow–Teller amplitudes and to the vector formed by the experimental Gamow–Teller amplitudes. What has already been obtained for the excitation-energy distribution of the Gamow–Teller strength remains invariant under this additional transformation.

3.2. Calculation of Strength Functions for Gamow–Teller and M1 Transitions

The theoretical and experimental Gamow–Teller and $M1$ strength functions to be used in the ensuing

Table 2. Properties of isovector 1^+ states in the $A = 28$ nuclei: Gamow–Teller and $M1$ strength functions calculated on the basis of the shell model and data obtained by experimentally studying the reactions ^{28}Si$(p, n)^{28}$P and ^{28}Si$(e, e')^{28}$Si

k	1	2	3	4	5	6	7	8	9	10
Results of the calculations										
$E_k - E_1$ [MeV]	0.0	0.38	0.71	1.83	2.16	2.56	3.56	3.80	4.21	4.70
E_k [MeV]	10.81	11.19	11.52	12.64	12.97	13.37	14.37	14.61	15.02	15.51
b(GT)	0.822	0.262	0.862	−0.783	0.014	−0.355	0.798	−0.574	−0.426	0.342
$b(M1)$	1.232	0.733	1.750	−1.178	0.162	−0.091	0.957	−0.712	0.629	0.538
B(GT)	0.676	0.069	0.744	0.613	0.000	0.126	0.637	0.330	0.182	0.117
$B(M1)$	1.518	0.538	3.064	1.387	0.026	0.008	0.917	0.507	0.395	0.290
Experimental distributions of the Gamow–Teller strength according to data on the reaction ^{28}Si$(p, n)^{28}$P [13]										
$E_k - E_1$ [MeV]	0.0	0.34	0.85	1.69		2.62	3.34	3.77	4.30	4.64
E_k [MeV]	1.25	1.59	2.10	2.94		3.87	4.59	5.02	5.55	5.91
B(GT)	0.198	0.109	0.956	0.146		0.163	0.410	0.137	0.092	0.090
Error	0.002	0.002	0.005	0.003		0.002	0.004	0.041	0.004	0.003
Experimental distributions of the $M1$ strength according to data on the reaction ^{28}Si$(e, e')^{28}$Si [12]										
$E_k - E_1$ [MeV]	0.0	0.26	0.80	1.69			3.39		4.50	4.86
E_k [MeV]	10.64	10.90	11.45	12.33			14.03		15.15	15.50
$B(M1)$	0.30	0.90	4.42	0.87			0.37		0.23	0.26
Error	0.04	0.02	0.20	0.06			0.02		0.02	0.03

Note: The following notation is used in the table: B(GT) and $B(M1)$ are the reduced probabilities of Gamow–Teller and $M1$ transitions, respectively, while b(GT) and $b(M1)$ are the corresponding transition amplitudes normalized by the conditions $B(\mathrm{GT}) = b^2(\mathrm{GT})$ and $\mathrm{B}(M1) = b^2(M1)$.

analysis are displayed in Table 2. In the calculations, we made use of the Hamiltonian from [8]. The multiparticle wave functions, the energies of the states involved, and the amplitudes of the Gamow–Teller and $M1$ transitions were calculated with the aid of the codes presented in [7].

The first part of the table quotes the results obtained by calculating the following features of the first ten excited states whose spin–parity and isospin are J^π, $T = 1^+, 1$: the excitation energies and the amplitudes and reduced probabilities of the relevant Gamow–Teller and $M1$ transitions from the $0^+, 0$ state at the lowest energy (ground state of ^{28}Si nucleus). The excitation energies given there are reckoned from the ground-state energy of ^{28}Si.

The wave functions of the J^π, $T = 1^+, 1$ states characterized by the isospin projection of $T_3 = 1$ represent the 1^+ states in ^{28}P, which manifest themselves as resonances in the charge-exchange (p, n) reaction at intermediate energies. The cross section for this reaction is proportional to B(GT). The resonance-state energies and the B(GT) values obtained by experimentally studying the reaction ^{28}Si$(p, n)^{28}$P [13] are displayed in the second part of Table 2. Presented there are all states that occur at excitation energies below 6 MeV and which were observed experimentally. The energies of the states are reckoned from the ground-state energy of the ^{28}P nucleus. The states at energies in excess of 6 MeV saturate only an insignificant fraction of the observed Gamow–Teller strength; moreover, their spin values are not known precisely. In total, the experimentally detected strength of Gamow–Teller transitions to states at excitation energies below 12.6 MeV amounts to 2.595. The states listed in Table 2 saturate 2.301 of this strength. The total theoretical strength of Gamow–Teller transitions that corresponds to the first ten 1^+ states is 3.492.

The wave functions characterized by J^π, $T = 1^+, 1$ and by $T_3 = 0$ describe the isovector 1^+ states in ^{28}Si. These states are excited in inelastic electron scattering, the values of $B(M1)$ being extracted from the relevant experimental cross sections. Listed in the last part of Table 2 are experimental data from [12] on the excitation-energy distribution of the strength of isovector $M1$ transitions. We display all isovector states discovered in the excitation-energy range between 10.5 and 15.5 MeV.

The following comment on the 10.64-MeV state indicated in the first column of Table 2 is in order here. As a matter of fact, two states at energies 10.597 and 10.725 MeV were discovered experimentally in place of this state. Usually, they are considered as superpositions of one isovector and one isoscalar 1^+ state [17]. It can easily be shown that, in this case, the total strength of $M1$ transitions to the two states in question is equal to the sum of the strengths of $M1$ transitions to the input

Table 3. Transformation matrix

	1	2	3	4	6	7	8	9	10
1	0.952	0.024	−0.293	−0.013	−0.080	−0.032	−0.003	0.006	0.001
2	0.023	0.988	0.146	0.004	0.030	0.014	−0.005	−0.003	−0.001
3	−0.293	0.146	−0.885	0.021	−0.153	−0.149	0.248	0.042	0.011
4	−0.013	0.004	0.021	0.903	−0.340	−0.050	−0.258	−0.002	−0.005
6	−0.080	0.030	−0.153	−0.340	−0.216	−0.194	−0.877	−0.004	−0.018
7	−0.032	0.014	−0.150	−0.050	−0.194	0.961	−0.116	0.002	−0.002
8	−0.003	−0.005	0.248	−0.258	−0.877	−0.116	0.299	−0.011	−0.015
9	0.006	−0.003	0.043	−0.002	−0.004	0.002	−0.011	0.999	−0.000
10	0.001	−0.001	0.011	−0.005	−0.018	−0.002	−0.015	−0.000	1.000

isovector and isoscalar 1^+ states. The calculations performed within the multiparticle-shell model based on the Hamiltonian from [8] reveal that the strength of the isoscalar $M1$ transition is one to two orders of magnitude less than the strength of the isovector $M1$ transition. Disregarding the strength of the isoscalar $M1$ transition, we can therefore calculate the energy of the input isovector state as the weighted mean of the energies of the observed states, $\dfrac{E_1B_1(M1)+E_2B_2(M1)}{B_1(M1)+B_2(M1)}$. The resulting energy of the isovector state and the total strength of the transitions are quoted in Table 2.

The sum of the experimental $B(M1)$ values listed in Table 2 is equal to 7.360 nuclear magnetons. The sum of the corresponding theoretical values is 8.623. The calculations were performed with free gyromagnetic ratios, but effective magnetic charges were not introduced.

Let us contrast the states observed experimentally against the eigenfunctions of the shell model. For this purpose, we compare the energies of these states with the eigenvalues of the Hamiltonian of the multiparticle shell model. Such a comparison is considerably simplified if we consider excitation energies reckoned from the energy of the first excited state—that is, the differences $E_k - E_1$, which are also given in Table 2. With the aid of these differences, the eigenfunctions of the Hamiltonian of the multiparticle shell model can be put into correspondence to states discovered experimentally quite unambiguously, whereby we arrive at the conclusion that the energies of the states in question are described remarkably well on the basis of the multiparticle shell model implemented with the Hamiltonian proposed in [8].

From Table 2, we can see that there are eigenfunctions of the Hamiltonian—for example, the fifth function in this table—that have no counterparts in the experimental spectrum measured so far. This may be due to extremely small theoretical values of $B(\mathrm{GT})$ and $B(M1)$. In what follows, we take no account of this state because no manifestations of it have been found experimentally. The state corresponding to the sixth function was discovered in the (p, n) reaction; its analog at 13.31 MeV in ^{28}Si has not yet been recorded in inelastic electron scattering, although it manifested itself in inelastic proton scattering [18]. According to the explanation given in [12], this is because the spin magnetic current and the orbital magnetic current compensate each other in the $M1$ transition to the state being discussed. The calculations with the Hamiltonian from [8] that were performed in [12] reproduced this effect successfully.

Thus, we arrive at the conclusion that the shell model qualitatively reproduces the basic features of the excitation-energy distributions of the Gamow–Teller and $M1$ strengths—in other words, small experimental values of the relevant cross sections correspond to small theoretical values of $B(\mathrm{GT})$ and $B(M1)$. However, the theoretical distributions of the transition strength among states whose contribution saturates a major part of the entire transition strength differ substantially from the analogous experimental distributions. In particular, the $B(\mathrm{GT})$ and $B(M1)$ values calculated for transitions to the third isovector 1^+ states are noticeably less than the relevant experimental values; at the same time, the theoretical values of the total strength of Gamow–Teller and $M1$ transitions are much greater than the experimental values. The distinctions between the theoretical and experimental strength functions are illustrated graphically in [12, 13]. The transformation of the wave functions that is proposed in the present study is aimed at removing this discrepancy.

The resulting matrix that represents the entire transformation and which appears to be the product of two reflection matrices is given in Table 3, which also quotes the number of the Hamiltonian eigenfunctions subjected to mixing. The matrix in question is symmetric since the reflections are performed with respect mutually orthogonal planes, whence it follows that the matrices of these reflections commute. Basically, the numbers appearing on the principal diagonal of the matrix are close to unity in absolute value. The sixth and eighth states, whose experimental counterparts

Table 4. Distributions of the Gamow–Teller and $M1$ strengths in ^{28}Si according to the calculations with the transformed wave functions for excited states

k	1	2	3	4	6	7	8	9	10
B(GT)	0.300	0.165	1.451	0.222	0.247	0.622	0.208	0.140	0.137
$B(M1)$	0.445	1.044	4.641	0.764	0.258	0.620	0.234	0.286	0.330

Table 5. Lifetimes of the 1^+ states in ^{28}Al (in units of 10^{-15} s)

k	E_k, MeV	a	b	E_k', MeV	a'	b'	c	Experimental data
1	1.373	239	152	10.810	184	117	235	320 ± 50
2	1.620	465	531	11.192	285	279	590	120 ± 60
3	2.201	66	44	11.519	70	48	65	65 ± 35
4	3.105	21	12	12.643	17	10	22	
5	3.542	9.7	9.8	12.970	9.1	9.2	7.9	
6	4.115	0.94	7.0	13.771	1.1	8.6	0.9	
7	4.846	0.69	0.88	14.374	0.64	0.80	0.7	
8	5.017	1.2	0.48	14.605	1.0	0.41		
9	5.435	0.94	0.93	15.024	0.77	0.76		
10	5.919	1.8	1.8	15.507	1.5	1.5		

Note: In columns a, b, and c, we display, respectively, the results calculated with the Hamiltonian from [8], the results calculated with the transformed wave functions for 1^+ states, and the results of the calculations performed by Endt and Booten [11] (these authors relied on the Hamiltonian from [8]). The experimental values presented here are quoted according [11]. The results given in columns a' and b' were obtained by using the excitation energies as calculated with the Hamiltonian from [8], in which case these excitation energies were reckoned from the ground-state energy of ^{28}Si.

were discovered only in the (p, n) reaction, are virtually interchanged. In the remaining cases, the main component is conserved—other states are admixed to it insignificantly.

Knowing the transformation matrix, we can use expression (2) to calculate the amplitudes for $M1$ and Gamow–Teller transitions and, after that, to evaluate the corresponding reduced probabilities $B(M1)$ and B(GT). The resulting strength functions for Gamow–Teller and $M1$ transitions are quoted in Table 4. The values found for B(GT) must be multiplied by 0.66 in order to obtain the experimental values from Table 2; that is, the form of the experimental strength function for Gamow–Teller transitions has been faithfully reproduced. The ratios of the experimental values of $B(M1)$ to the corresponding values from Table 4 vary between 0.67 and 1.5, whence we see that, as might have been expected, the form of the $M1$ strength function is described in this way only approximately.

4. GAMMA DECAYS OF 1^+ STATES IN ^{28}Al

As an additional check upon the wave functions obtained here, we will calculate the lifetimes of the 1^+ states in ^{28}Al and the branching fractions for their decays.

Not only does the transformation (1) of the wave functions change the matrix elements of the operators that are responsible for transitions between 1^+ states and states of different spin–parities, but it also affects, as can be seen from Eq. (2), the matrix elements of the operators for transitions within 1^+, 1 states themselves:

$$\langle \phi_k | O | \phi_l \rangle \longrightarrow \langle \psi_k | O | \psi_l \rangle = U_{l,l'} \langle \phi_{k'} | O | \phi_{l'} \rangle U^{\dagger}_{k',k}. \quad (6)$$

As a result, the gamma-decay lifetimes of isovector 1^+ states and the relevant branching fractions also change.

For the 1^+ states in ^{28}Al, Table 5 displays the lifetimes computed with the original wave functions and the wave functions (or transition amplitudes) transformed with the aid of the matrix from Table 3. Also quoted in Table 5 are experimental data from [11, 17]. In our calculations, we took into account the $J^\pi = 0^+$, 1^+, 2^+, and 3^+ states of the ^{28}Al nucleus and used experimental values of the energies of excited states in those cases where these energies are known. This is because the rates of electromagnetic transitions depend greatly on the transition energy [19], and the precision of 0.1–0.2 MeV achieved in calculating the energies of nuclear states is insufficient at transition energies of 1 to 2 MeV. With increasing gamma-transition energy, the effect of this uncertainty is reduced. In all probability, Endt and Booten [11] also performed their calculations with the experimental values of the excitation energies. Table 5 additionally presents the results of our calculations employing purely theoretical values of the excitation energies. By comparing these two versions, we can easily notice that, at low transition energies, even comparatively small variations in the energies of excited levels

Table 6. Branching fractions for the gamma decays of 1^+ states in ^{28}Al

E_i, MeV	J^π_f	$3^+_{g.s.}$	2^+_1	0^+_1	3^+_1	1^+_1	1^+_2	2^+_2	2^+_3	1^+_3	2^+_4	0^+_2	1^+_4
	E_f	0.000	0.031	0.972	1.014	1.372	1.620	1.623	2.139	2.201	2.486	3.012	3.105
1.372	*a*	4.4	73.2	22.4									
	b	2.9	75.8	21.3									
	c	4.4	74	22									
	Expt.	4.7(3)	55(1)	40(1)									
1.620	*a*	3.8	77.6	18.0		0.5							
	b	4.2	58.7	36.7		0.3							
	c	4.7	93	2.1									
	Expt.	6	92	<2									
2.201	*a*	0.2	2.1	80.4		14.5		2.6					
	b	0.0	63.3	35.2		1.4							
	c	0.2	2.2	80.1		14		2.7					
	Expt.	<6	79(3)	16(2)		<3		<5					
3.105	*a*	0.5	41.4	30.5	0.1	0.4	3.7	17.7	1.3	0.3	4.1		
	b	0.2	76.1	2.6	0.0	1.2	4.9	7.4	3.7	0.1	3.7		
	c	0.5	43	32	0.2	0.4	3.8	18	1.4	0.3			
	Expt.		75(3)							25(3)			
3.542	*a*	1.6	30.2	25.7		11.9	1.5	22.2	2.6	0.0	4.1		
	b	1.6	30.4	25.8		11.1	1.6	22.3	2.7	0.1	4.2		
4.115	*a*	0.0	52.3	36.0		3.2	2.7	0.1	4.4	0.1	0.6		
	b	0.1	9.9	2.1		30.0	0.1	18.5	26.1	5.0	6.3		
4.846	*a*	0.1	77.0	1.2		4.9	4.5	2.1	1.2	5.1	0.2	2.0	1.1
	b	0.2	71.8	0.3		4.6	5.3	4.3	0.3	8.2	0.8	3.1	0.4
5.017	*a*	0.3	36.5	29.0		7.9	0.8	4.9	3.4	0.0	12.1	1.3	0.3
	b	0.1	56.4	36.1		0.4	0.9	0.7	0.3	1.4	0.2	0.0	2.3
5.435	*a*	1.1	1.1	14.0	0.3	11.0	0.0	61.5	0.2	0.3	4.0	0.4	0.6
	b	1.1	1.0	12.0	0.3	8.2	0.3	61.7	0.6	4.0	4.0	0.5	0.7
5.919	*a*	13.2	15.7			34.2	6.8	3.6	10.6	0.2	0.2	3.3	0.4
	b	12.0	15.1			36.1	6.3	3.7	10.5	0.5	0.3	3.5	0.2

Note: The results displayed in rows *a*, *b*, and *c* correspond to the same versions of the calculations as those used to obtain the values in the columns of Table 5 that have the same labels.

cause a sizable scatter in the lifetime values. Also given in the table for the sake of comparison are the results of the calculations from [11].

The branching fractions for the gamma decays of the 1^+ states in ^{28}Al are given in Table 6. A comparison of the results of the calculations with experimental data reveals that the transformation of the wave functions for the 1^+ states leads above all to an enhancement of the rate of the transitions to the 2^+_1 state at 0.031 MeV from the $1^+_{1,3}$ states and to a reduction of the rate of the transition from the 1^+_2 level. As a result, the agreement between the experimental and theoretical lifetimes of the $1^+_{1,2}$ levels becomes poorer. For the 1^+_3 level, the lifetime of 44×10^{-15} s obtained from a calculation with the transformed wave functions (column *b*) is close to the values of $(38.3 \pm 2.8) \times 10^{-15}$ and $[60.8 \pm 3.4\ (\text{stat.}) \pm 9.1\ (\text{syst.})] \times 10^{-15}$ reported in [1] and [2], respectively. Concurrently, the correct relationship between the intensities of the transitions from the $1^+_{3,4}$ states to the 2^+_1 and 0^+_1 states is recovered. Previously, the calculations within the multiparticle shell model were unable to describe these branching fractions [11, 20].

Investigation of the branching fractions for the gamma decays of excited 1^+ states of ^{28}Al is necessary for analyzing experiments measuring partial muon capture by ^{28}Si nuclei, including relevant polarization experiments [1, 2]. Of particular importance may prove to be gamma transitions to the 2.201-MeV state from higher lying 1^+ states populated in muon capture.

In connection with our analysis of the lifetimes and branching fractions, the following comment is in order. The procedure used here to take into account experi-

mental data on strength functions implies that the ground states are well described by the multiparticle shell model and that the discrepancies between the theoretical and the experimental strength functions are due exclusively to uncertainties in the wave functions for excited 1^+ states. By transforming the wave functions for excited states in such a way as to reproduce the experimental strength functions, we simultaneously make an attempt at partly compensating for the possible flaws in describing the ground state. The total Gamow–Teller and $M1$ strengths can be computed as the expectation values of specific two-particle operators over the ground state. Therefore, a considerable excess of the theoretical values of the total transition strength over the corresponding experimental values evinces inadequacy of the description of the ground state.

5. MUON-CAPTURE RATES FOR ALLOWED PARTIAL TRANSITIONS

The rate of ordinary muon capture accompanied by the $J_i \longrightarrow J_f$ partial transition is given by [9, 10]

$$\Lambda^{\mathrm{OMC}} = V \sum_{J=|J_f-J_i|}^{J_f+J_i} [M_J^2(-J) + M_J^2(J+1) + M_J^2(-J-1) + M_J^2(J)], \tag{7}$$

where the abbreviation "OMC" in the superscript on the left-hand side denotes ordinary muon capture. The independent nuclear amplitudes $M_J(\kappa)$ describe muon capture from the $s_{1/2}$ state in the process where a neutron is produced in the state characterized by the spherical quantum number κ and where the total angular momentum J is transferred to the nucleus. The general formulas for computing these amplitudes can be found in [9, 10]. The expression for calculating the factor V is presented in [10]. For the allowed $0^+ \longrightarrow 1^+$ transition, the only nonzero amplitudes are

$$M_1(-1) = \sqrt{\frac{2}{3}}\left\{-\left(G_A - \frac{1}{3}G_P\right)[101] + \frac{\sqrt{2}}{3}G_P[121] - \frac{g_A}{M}[011p] + \sqrt{\frac{2}{3}}\frac{g_V}{M}[111p]\right\},$$

$$M_1(2) = \sqrt{\frac{2}{3}}\left\{-\frac{\sqrt{2}}{3}G_P[101] + \left(G_A - \frac{2}{3}G_P\right)[121] + \sqrt{2}\frac{g_A}{M}[011p] + \sqrt{\frac{1}{3}}\frac{g_V}{M}[111p]\right\}, \tag{8}$$

which represent sums of the products of the weak form factors

$$G_A = g_A(q^2) - [g_V(q^2) + g_M(q^2)]\frac{E_\nu}{2M},$$
$$G_P = [g_P(q^2) - g_A(q^2) - g_V(q^2) - g_M(q^2)]\frac{E_\nu}{2M} \tag{9}$$

and the multiparticle matrix elements

$$[101] = \sqrt{\frac{3}{4\pi}}\left\langle J_f \left\| \sum_{k=1}^{A} \varphi_\mu(r_k) j_0(\nu r_k)\sigma_k t_k^- \right\| J_i \right\rangle \frac{1}{\sqrt{2J_f+1}},$$

$$[121] = \sqrt{\frac{3}{4\pi}} \times \left\langle J_f \left\| \sum_{k=1}^{A} \varphi_\mu(r_k) j_2(\nu r_k)[Y_2(\hat{r}_k), \sigma_k]_1 t_k^- \right\| J_i \right\rangle \frac{1}{\sqrt{2J_f+1}},$$

$$[111p] = \sqrt{\frac{3}{4\pi}} \times \left\langle J_f \left\| \sum_{k=1}^{A} \varphi_\mu(r_k) j_1(\nu r_k)[Y_1(\hat{r}_k), \nabla_k]_1 t_k^- \right\| J_i \right\rangle \frac{1}{\sqrt{2J_f+1}}, \tag{10}$$

$$[011p] = \sqrt{\frac{1}{4\pi}} \times \left\langle J_f \left\| \sum_{k=1}^{A} \varphi_\mu(r_k) j_1(\nu r_k) Y_1(\hat{r}_k)(\sigma_k \nabla_k) t_k^- \right\| J_i \right\rangle \frac{1}{\sqrt{2J_f+1}}.$$

Here, $\varphi_\mu(r)$ is the bound-muon wave function. The main difficulty encountered in analyzing partial rates of ordinary muon capture is associated with uncertainties in these nuclear matrix elements. Of prime importance often appears to be the [101] matrix element; in the limit of vanishing neutron energy, it comes to be proportional to the Gamow–Teller matrix element $\langle J_f \| \sigma t^\pm \| J_i \rangle$, which is known from the theory of beta decay. The nuclear matrix elements in (10) depend on the neutrino energy—that is, on the energy of the final state of the nucleus. In calculating the capture rates, we will therefore transform, instead of the nuclear matrix elements in (10) and the amplitudes in (8), the single-particle transition densities defined as the spin- and isospin-reduced matrix elements of the tensor product of the nucleon creation and annihilation operators between multiparticle wave functions [21],

$$D(\Delta J, \Delta T, \alpha\alpha', f, i) = \frac{\langle J_f, T_f \| [a_\alpha^\dagger \otimes \tilde{a}_{\alpha'}]^{(\Delta J, \Delta T)} \| J_i T_i \rangle}{\sqrt{(2\Delta J+1)(2\Delta T+1)}}. \tag{11}$$

Under the transformation in (1), the single-particle transition densities will therefore change according to

Table 7. Partial rates of muon capture (in units of 10^3 s^{-1}) and nuclear matrix elements computed with (*a*) the original and (*b*) the transformed single-particle transition densities (data for ^{28}Si)

		k, number of an 1^+ excited state									
		1	2	3	4	5	6	7	8	9	10
Λ_k^{OMC}	*a*	29.9	3.1	34.1	26.1	0.02	3.1	20.6	11.5	8.2	3.5
	b	12.8 ± 0.2	7.6 ± 0.2	63.6 ± 2.4	11.2 ± 0.5		8.5 ± 0.4	18.7 ± 0.2	7.3 ± 2.1	6.6 ± 0.2	4.2 ± 0.1
Expt.	[23]		12.9 ± 2.1	62.8 ± 7.4	14.7 ± 2.6						
[101]	*a*	0.039	0.012	0.041	−0.037	0.001	−0.017	0.039	−0.028	−0.021	0.017
	b	0.027	0.019	−0.057	−0.022		0.024	0.039	0.023	−0.018	0.018
[121]	*a*	−0.006	0.000	−0.005	0.006	0.001	−0.002	0.001	0.001	0.006	0.004
	b	−0.004	−0.001	0.007	0.005		−0.002	0.002	−0.001	0.005	0.004
[111*p*]	*a*	−0.004	0.011	0.012	0.003	0.005	0.017	−0.012	0.008	0.002	−0.001
	b	−0.008	0.012	−0.007	−0.004		−0.010	−0.017	−0.009	0.002	0.001
[011*p*]	*a*	−0.016	−0.007	−0.017	0.017	0.001	0.007	−0.019	0.015	0.012	−0.005
	b	−0.011	−0.010	0.025	0.010		−0.013	−0.020	−0.008	0.011	−0.005

(2). The muon-capture rates calculated with the original and with the transformed wave functions of excited states are quoted in Table 7. In calculating the nuclear matrix elements in (10), we used $\varphi_\mu(r)$ values averaged over the nuclear volume [10]. The amplitudes in (8) were computed with the values of $g_A = -1.263$ and $g_P/g_A = 7.0$. Of particular interest is the muon-capture process involving the excitation of the 1_3^+ 2.201-MeV state, which was studied in the experiments reported in [1, 2]. The calculation with transformed functions revealed that, in muon capture, this state is populated at the highest rate and that the corresponding capture rate exceeds the total rate of capture into all other 1^+ states. The greatest matrix elements are [101] and [011*p*]. The remaining matrix elements are much less. The [101] matrix element is related to the Gamow–Teller matrix element, whose value can be tested in (*p*, *n*) reactions. No direct means for testing the values of the [011*p*] matrix element has been proposed thus far. In [22], it was shown that the g_P/g_A value extracted from data of the correlation experiments reported in [1, 2] is extremely sensitive to the theoretical value of the ratio [011*p*]/[101].

The experimental values of B(GT) and $B(M1)$ serve as parameters of the orthogonal transformation in the space spanned by the wave functions for excited states. Therefore, it is desirable to consider the possible effect of uncertainties in the values of B(GT) and $B(M1)$ on the results that we obtained. Let us estimate the root-mean-square error in the values calculated for partial rates of muon capture. For this purpose, we address Eq. (7). The error in B_k(GT)—we denote it by δB_k (GT)—can affect only the quantity $S = M_1^2(-1) + M_1^2(2)$. For each partial transition, the root-mean-square error in the theoretical capture rate is then given by

$$\delta\Lambda = V\delta S,$$

where

$$\delta S \approx \sqrt{\sum_{k=1}^{N}\left[\left(\frac{\partial S}{\partial B_k(\mathrm{GT})}\delta B_k(\mathrm{GT})\right)^2 + \left(\frac{\partial S}{\partial B_k(M1)}\delta B_k(M1)\right)^2\right]}.$$

The partial derivatives appearing in the expression for δS can be calculated analytically or estimated with the aid of a finite-difference approximation of the form

$$\frac{df}{dx} \approx \frac{f(x+h) - f(x-h)}{2h}.$$

This is the way in which we have calculated the values that are presented in Table 7 for the errors in the theoretical values of Λ_k^{OMC}.

The partial rates of ordinary muon capture by *sd*-shell nuclei were measured by Goringe *et al.* [23]. Their results concerning ^{28}Si are also quoted in Table 7. A comparison of those data with the results of our calculations demonstrates that the wave functions constructed for the excited states in such a way as to reproduce the shapes of the Gamow–Teller strength functions make it possible to describe quite accurately the partial rates of muon capture as well. In the case of the 1_3^+ state, the theoretical value of the ordinary-muon-capture rate is very close with the experimental result. This is because this transition is dominated by the spin-flip matrix element [101]. That the theoretical values of muon-capture rates are close to their experimental

counterparts highlights the following contradiction. The matrix elements of the Gamow–Teller transitions as extracted from data on the reaction ^{28}Si(p, n)^{28}Al prove to be suppressed in relation to the theoretical estimates [according to Tables 2 and 4, we have $B_{\text{exp}}(\text{GT}) = 0.66B_{\text{theor}}(\text{GT})$]. At the same time, the agreement between the theoretical (version *b*) and the experimental partial rates suggests that, in muon capture, there is no suppression of the spin matrix element [101]. Obviously, only further investigations can clarify the reasons behind this discrepancy.

6. CONCLUSION

We have proposed an approach that makes it possible to take into account, in calculating the partial rates of muon capture by nuclei, experimental information about the strength functions for Gamow–Teller and isovector $M1$ transitions. The approach consists in choosing an orthogonal transformation in the subspace of the wave functions for excited states in such a way that the Gamow–Teller and $M1$ strength functions calculated with the transformed wave functions coincide in form with the corresponding experimental strength functions. No modifications of the transition operators are required within this approach. This point is of importance since the operators of Gamow–Teller and $M1$ transitions differ from the operators of the effective Hamiltonian for ordinary muon capture. In the present study, we have set forth a method for constructing the matrix of such a transformation in terms of reflections with respect to a plane. All calculations have been performed on the basis of the multiparticle shell model. The numerical results have been obtained for isovector states in A =28 nuclei. In particular, we have considered the strength functions for Gamow–Teller and isovector $M1$ transitions in ^{28}Si, calculated the gamma-decay lifetimes of those 1^+ states in ^{28}Al that can be excited in ordinary muon capture by ^{28}Si, and found the relevant branching fractions. By using experimental information in the way outlined above, we have been able to describe correctly, for the first time, the branching fractions for the gamma decay of the 1^+ state at 2.201 MeV in ^{28}Al.

It has been shown that, upon applying the transformation of the wave functions that has been introduced in the present article, the distribution of the partial rates of allowed muon capture by ^{28}Si among the final 1^+ states of ^{28}Al changes substantially in relation to the results of the calculations employing the original eigenfunctions of the Hamiltonian of the multiparticle shell model. The rates of ordinary muon capture that have been calculated with $g_A = -1.263$ comply well with experimental data, being very close to them for the strongest transition.

ACKNOWLEDGMENTS

We are grateful to T.P. Gorringe, who called our attention to the problem of theoretically investigating the rates of allowed muon capture, and to A.A. Ovchinnikova and K. Junker for stimulating discussions on the problems considered in this study.

REFERENCES

1. V. B. Brudanin *et al.*, Nucl. Phys. A **587**, 577 (1995).
2. B. A. Moftah *et al.*, Phys. Lett. B **395**, 157 (1997).
3. S. Ciechanowicz, Nucl. Phys. A **267**, 472 (1976).
4. R. Parthasarathy and V. N. Sridhar, Phys. Rev. C **23**, 861 (1981).
5. K. Junker, V. A. Kuz'min, A. A. Ovchinnikova, and T. V. Tetereva, in *Proceedings of the IV International Symposium on Weak and Electromagnetic Interactions in Nuclei, Osaka, June 1995* (World Sci., Singapore, 1995), p. 394.
6. T. P. Gorringe *et al.*, Phys. Rev. Lett. **72**, 3472 (1994).
7. B. A. Brown, A. Etchegoyen, and W. D. M. Rae, MSU Cyclotron Laboratory Report No. 524, 1986.
8. B. H. Wildenthal, Prog. Part. Nucl. Phys. **11**, 5 (1984).
9. M. Morita and A. Fujii, Phys. Rev. **118**, 606 (1960).
10. V. V. Balashov and R. A. Eramzhyan, At. Energy Rev. **5**, 3 (1967).
11. P. M. Endt and J. G. L. Booten, Nucl. Phys. A **555**, 499 (1993).
12. C. Lüttge *et al.*, Phys. Rev. C **53**, 127 (1996).
13. B. D. Anderson *et al.*, Phys. Rev. C **43**, 50 (1991); P. von Neumann-Cosel *et al.*, Phys. Rev. C **55**, 532 (1997).
14. Y. Fujita *et al.*, Phys. Rev. C **55**, 1137 (1997).
15. E. Cartan, *Leçons sur la théorie des spineurs* (Paris, 1938; Inostrannaya Literatura, Moscow, 1947).
16. A. S. Householder, *The Theory of Matrices in Numerical Analysis* (Blaisdel, New York, 1964).
17. P. M. Endt, Nucl. Phys. A **521**, 1 (1990).
18. G. M. Crawley *et al.*, Phys. Rev. C **39**, 311 (1989).
19. A. Bohr and B. R. Mottelson, *Nuclear Structure* (Benjamin, New York, 1969), Vol. 1.
20. E. Boshitz, V. A. Kuz'min, A. A. Ovchinnikova, and T. V. Tetereva, Soobshch. Ob'edin. Inst. Yad. Issled., Dubna, No. R4-94-427 (1994).
21. B. A. Brown and B. H. Wildenthal, At. Data Nucl. Data Tables **33**, 347 (1985).
22. K. Junker, V. A. Kuz'min, A. A. Ovchinnikova, and T. V. Tetereva, Preprint No. PSI-PR-99-14 (Paul Scherrer Institut, Switzerland, June 1999).
23. T. P. Gorringe *et al.*, Phys. Rev. C **60**, 055501 (1999).

Translated by A. Isaakyan

Physics of Atomic Nuclei, Vol. 63, No. 11, 2000, pp. 1885–1888. Translated from Yadernaya Fizika, Vol. 63, No. 11, 2000, pp. 1978–1981.

NUCLEI
Theory

New Formula for Calculating Coulomb Energies in the Liquid-Drop Model

R. S. Kurmanov[1)], G. I. Kosenko*, and G. D. Adeev[2)]

Joint Institute for Nuclear Research, Dubna, Moscow oblast, 141980 Russia

Received July 26, 1999; in final form, December 8, 1999

Abstract—A new transformation of double volume integrals into double surface integrals is presented. A simple regular method for deriving integrands in a surface integral is proposed. This method is used to calculate the Coulomb energy of a nucleus within the model of a liquid drop with a sharp boundary. Numerical results obtained on the basis of the new formula are compared with those calculated by one of the formulas employed previously.© *2000 MAIK "Nauka/Interperiodica".*

1. INTRODUCTION

Over a few decades, the liquid-drop model has been extensively used in nuclear physics. Proposed by Ya. Frenkel [1] and by N. Bohr and J.A. Wheeler [2], when nuclear physics was still in its infancy, it also forms a basis for the shell-correction approach of Strutinsky [3, 4]. Within the liquid-drop model, the energy of a nucleus is given by

$$E_{\rm tot}^{\rm LD} = B_{\rm S}^{\rm LD}E_{\rm S}^{(0)} + B_{\rm Coul}^{\rm LD}E_{\rm Coul}^{(0)} + B_{\rm R}^{\rm LD}E_{\rm R}, \qquad (1)$$

where the first, the second, and the third term stand for, respectively, the surface, the Coulomb, and the rotational energy of the nucleus being considered; the dimensionless quantities $B_{\rm S}^{\rm LD}$, $B_{\rm Coul}^{\rm LD}$, and $B_{\rm R}^{\rm LD}$ are functionals dependent on the nuclear shape; $E_{\rm S}^{(0)}$ and $E_{\rm Coul}^{(0)}$ are, respectively, the surface and the Coulomb energy of the corresponding spherical nucleus; and E_R is the angular-momentum-dependent component of the rotational energy. In dealing with nuclear energies within this framework, the quantity $B_{\rm Coul}^{\rm LD}$ requires the most cumbersome calculations. In this study, we propose a new method for calculating this quantity.

2. FORMULATING AND SOLVING THE PROBLEM

By definition, the Coulomb energy is expressed in the term of a sextuple integral,

$$E_{\rm Coul} = E_{\rm Coul}^{(0)}B_{\rm Coul}^{\rm LD} = E_{\rm Coul}^{(0)}\frac{15}{32\pi^2}\int dVdV'\frac{1}{|\mathbf{r}-\mathbf{r}'|}, \qquad (2)$$

which is calculated over the volume of the nucleus. Hereafter the radius of the corresponding spherical nucleus is used as a unit of length.

Since it is necessary to evaluate many times the Coulomb energy and its derivatives with respect to collective coordinates in dynamical calculations like those from [5–7], there arises the pressing problem of optimizing existing computational methods and formulas implementing these methods. The relevant calculations can be considerably simplified if we assume that the charge is uniformly distributed over the nuclear volume. In this connection, we would like to mention the well-known method that was proposed in [8, 9] and which relies on a transformation of the double volume integral appearing in Eq. (2) into a double surface integral where integration is performed over the nuclear surface and where the nuclear shape depends on parameters. Thus, the integral proves to be a functional of the nuclear-surface shape. By going over to a surface integral, we get rid of two integrations with the result that the relevant integral assumes the form

$$\int dVdV'\frac{1}{\sigma} = -\frac{1}{6}\int(d\mathbf{S}\cdot\boldsymbol{\sigma})(d\mathbf{S}'\cdot\boldsymbol{\sigma})\frac{1}{\sigma}, \qquad (3)$$

where $\boldsymbol{\sigma} = \mathbf{r} - \mathbf{r}'$ and $\sigma = |\mathbf{r} - \mathbf{r}'|$. The price that we have had to pay for this simplification is that the integrand becomes more involved. Indeed, the scalar products $(d\mathbf{S}\cdot\boldsymbol{\sigma})$ and $(d\mathbf{S}'\cdot\boldsymbol{\sigma})$ generate an additional dependence on the angle between the normal to an element of the integration surface and the vector $\boldsymbol{\sigma}$. On the other hand, a scalar quantity having dimensions of energy can be obtained by multiplying two surface elements. {Unfortunately, this possibility was not explored by Davies and Sierk [8], who obtained integral formulas for calculating the Coulomb functional $B_{\rm Coul}$—see Eqs. (2.24)–(2.26) in [8].} The unknown integrand $f(\sigma)$ in the transformation

$$\int dVdV'\frac{1}{\sigma} = \int(d\mathbf{S}\cdot d\mathbf{S}')\,f(\sigma) \qquad (4)$$

will then depend on σ, the modulus of the difference of the relevant radius vectors.

[1)] Omsk State University of Railway Transport, pr. Marksa 35, Omsk, 644046 Russia.
[2)] Omsk State University, pr. Mira 55A, Omsk, 644077 Russia.
* e-mail: kosenko@nrsun.jinr.dubna.su

Mathematically, the problem is formulated as follows: it is necessary to find an appropriate function $f(\sigma)$ in the simplest way. If, for example, Eq. (3) is used to perform surface integration, the relevant integrand is constructed by means of a procedure involving a Fourier transformation followed by a determination of the Fourier transform via a transition to the relevant complex plane. This procedure is quite regular, but it is not efficient when there is an arbitrary integrable function in the double volume integral.

On the other hand, the use of Gauss' theorem for the gradient of a function [10] makes it possible to recast Eq. (4) into the form

$$\int (d\mathbf{S}\cdot d\mathbf{S}')\, f(\sigma) = \int dV'(d\mathbf{S}\,\mathrm{grad}_{\mathbf{r}'})\, f(\sigma). \qquad (5)$$

The right-hand side of Eq. (5) involves a volume integral where the scalar product of the gradient operator and the remaining second surface integral appears in the integrand. Applying Gauss' theorem for the divergence of a vector, we obtain the double volume integral

$$\int dV'(d\mathbf{S}\,\mathrm{grad}_{\mathbf{r}'})\, f(\sigma) = \int dV dV' \mathrm{div}_{\mathbf{r}}\mathrm{grad}_{\mathbf{r}'} f(\sigma), \qquad (6)$$

where the integrand has the form of the scalar product of two del operators differentiating an unknown function with respect to the different variables.

That Eq. (6) must be satisfied for an arbitrary integration surface dictates that the integrand on the left-hand side of Eq. (4) be equal to the integrand on the right-hand side of Eq. (6); that is,

$$\mathrm{div}_{\mathbf{r}}\mathrm{grad}_{\mathbf{r}'} f(|\mathbf{r}-\mathbf{r}'|) = \frac{1}{|\mathbf{r}-\mathbf{r}'|}. \qquad (7)$$

Introducing the notation $\boldsymbol{\sigma}$ for the difference of the vector variables $\mathbf{r}$ and $\mathbf{r}'$, $\boldsymbol{\sigma} = \mathbf{r} - \mathbf{r}'$, we can represent the differential operator on the left-hand side of Eq. (7) in the form

$$-\mathrm{div}_{\mathbf{r}}\mathrm{grad}_{\mathbf{r}} f(|\mathbf{r}-\mathbf{r}'|) = -\Delta_{\mathbf{r}} f(|\mathbf{r}-\mathbf{r}'|) = -\Delta_{\boldsymbol{\sigma}} f(\sigma). \qquad (8)$$

Combining Eqs. (7) and (8), we arrive at Poisson's equation

$$-\Delta_{\boldsymbol{\sigma}} f(\sigma) = \rho(\sigma), \qquad (9)$$

where $\rho(\sigma) = 1/\sigma$.

Since the charge "density" $\rho(\sigma)$ is spherically symmetric, the "potential" $f(\sigma)$ must have the same symmetry. Going over to spherical coordinates, we obtain

$$-\frac{1}{\sigma^2}\frac{d}{d\sigma}\left[\sigma^2\frac{d}{d\sigma}f(\sigma)\right] = \rho(\sigma). \qquad (10)$$

Upon the substitution

$$f(\sigma) = \frac{u(\sigma)}{\sigma}, \qquad (11)$$

Eq. (10) takes the form

$$-\frac{1}{\sigma}\frac{d^2}{d\sigma^2}u(\sigma) = \frac{1}{\sigma}. \qquad (12)$$

A general solution to Eq. (12) is given by

$$u(\sigma) = -\frac{\sigma^2}{2} + C_1\sigma + C_2. \qquad (13)$$

Setting $C_1 = C_2 = 0$, we arrive at $f(\sigma) = -\sigma/2$.

Thus, we have transformed the above double volume integral into a double surface integral; that is,

$$\int dV dV' \frac{1}{\sigma} = -\frac{1}{2}\int (d\mathbf{S}\cdot d\mathbf{S}')\sigma. \qquad (14)$$

We further test Eq. (14) analytically for the case of spherical symmetry. A simple integration then yields

$$-\frac{1}{2}\int (d\mathbf{S}\cdot d\mathbf{S}')\sigma = \frac{32\pi^2}{15}. \qquad (15)$$

Substituting (14) and (15) into (2), we find that $B_{\mathrm{Coul}}^{\mathrm{LD}}$ is equal to unity is this case, as it must for a spherical nucleus.

Let us now rewrite the expression that we have obtained for $B_{\mathrm{Coul}}^{\mathrm{LD}}$ in terms of cylindrical coordinates. Restricting our consideration to axisymmetric nuclear shapes—that is, assuming that $\rho = \rho(z)$, where $\rho(z)$ is a profile function whose rotation about the symmetry axis z specifies a nuclear surface—we obtain

$$B_{\mathrm{Coul}}^{\mathrm{LD}} = -\frac{15}{64\pi^2}\int (d\mathbf{S}\cdot d\mathbf{S}')|\mathbf{r}-\mathbf{r}'| = -\frac{15}{32\pi}\int_{z_{\min}}^{z_{\max}} dz \int_{z'_{\min}}^{z'_{\max}} dz'$$
$$\times \int_0^{2\pi} d\phi \left\{ \rho(z)\rho(z')\cos\phi + \rho(z)\frac{d\rho(z)}{dz}\rho(z')\frac{d\rho(z')}{dz'} \right\} \qquad (16)$$
$$\times \{\rho^2(z) + \rho^2(z') - 2\rho(z)\rho(z')\cos\phi + (z-z')^2\}^{1/2}.$$

If we have the implicit dependences $\rho(x)$ and $z(x)$, Eq. (16) takes the form

$$-\frac{15}{64\pi^2}\int (d\mathbf{S}\cdot d\mathbf{S}')|\mathbf{r}-\mathbf{r}'|$$
$$= -\frac{15}{32\pi}\int_{-1}^{1} dx \int_{-1}^{1} dx' \int_0^{2\pi} d\phi \left\{ \rho(x)\rho(x')\cos\phi \frac{dz(x)}{dx}\frac{dz(x')}{dx'} \right.$$
$$\left. + \rho(x)\frac{d\rho(x)}{dx}\rho(x')\frac{d\rho(x')}{dx'} \right\}$$
$$\times \{\rho^2(x) + \rho^2(x') - 2\rho(x)\rho(x')\cos\phi + [z(x)-z(x')]^2\}^{1/2}.$$

We now proceed to discuss our numerical results; concurrently, we determine the accuracy that the above formula ensures and assess the time required for the calculations on its basis. The numerical results obtained for B_{Coul} by using Eq. (16) can be compared with those that

Results for the functional $B_{\mathrm{Coul}}^{\mathrm{LD}}$ that were calculated by the Lawrence formula (17), along with the results obtained by the new formula (16)

c	Eq. (17), $N = 32$	Eq. (16), $N = 32$	Difference ($\times 10^{-5}$)	Eq. (17), $N = 96$	Eq. (16), $N = 96$	Difference ($\times 10^{-5}$)
1.00	0.999999	1.00001	−1.64	0.99999999	1.0000006	−6.26
1.01	0.999977	0.99999	−1.66	0.99997771	0.9999783	−6.35
1.02	0.999911	0.99992	−1.69	0.99991133	0.9999119	−6.44
1.03	0.999801	0.99981	−1.71	0.99980155	0.9998022	−6.54
1.04	0.999649	0.99966	−1.74	0.99964902	0.9996496	−6.64
1.05	0.999454	0.99947	−1.77	0.99945435	0.9994550	−6.75
1.06	0.999218	0.99923	−1.79	0.99921811	0.9992188	−6.85
1.07	0.998940	0.99895	−1.82	0.99894084	0.9989415	−6.97
1.08	0.998623	0.99864	−1.85	0.99862304	0.9986237	−7.08
1.09	0.998265	0.99828	−1.88	0.99826517	0.9982658	−7.20
1.10	0.997867	0.99788	−1.91	0.99786765	0.9978683	−7.32
1.11	0.997430	0.99745	−1.95	0.99743087	0.9974316	−7.45
1.12	0.996955	0.99697	−1.98	0.99695520	0.9969559	−7.58
1.13	0.996440	0.99646	−2.02	0.99644095	0.9964417	−7.71
1.14	0.995888	0.99590	−2.05	0.99588843	0.9958892	−7.84
1.15	0.995297	0.99531	−2.09	0.99529790	0.9952987	−7.98
1.16	0.994669	0.99469	−2.12	0.99466959	0.9946704	−8.13
1.17	0.994003	0.99402	−2.16	0.99400371	0.9940045	−8.27
1.18	0.993300	0.99332	−2.20	0.99330044	0.9933012	−8.42
1.19	0.992559	0.99258	−2.24	0.99255991	0.9925607	−8.58
1.20	0.991782	0.99180	−2.28	0.99178227	0.9917831	−8.74
1.21	0.990967	0.99099	−2.32	0.99096760	0.9909684	−8.90
1.22	0.990115	0.99013	−2.37	0.99011599	0.9901169	−9.06
1.23	0.989227	0.98925	−2.41	0.98922748	0.9892284	−9.23
1.24	0.988302	0.98832	−2.46	0.98830210	0.9883030	−9.40
1.25	0.987339	0.98736	−2.50	0.98733985	0.9873408	−9.58
1.26	0.986340	0.98636	−2.55	0.98634073	0.9863417	−9.76
1.27	0.985304	0.98533	−2.60	0.98530469	0.9853056	−9.94
1.28	0.984231	0.98425	−2.65	0.98423169	0.9842327	−10.1
1.29	0.983121	0.98314	−2.70	0.98312165	0.9831226	−10.3
1.30	0.981974	0.98200	−2.75	0.98197449	0.9819755	−10.5

Note: Here, c is the elongation parameter in the $\{c, h, \alpha\}$ parametrization and N is the number of nodes in integration by the Gauss method.

are calculated on the basis of the Lawrence formula [11] (see also [12])

$$B_{\mathrm{Coul}}^{\mathrm{LD}} = \frac{15}{4\pi}\int_{z_{\min}}^{z_{\max}} dz \int_{z_{\min}}^{z} dz' \int_{0}^{\pi} d\phi \frac{\rho^2 \rho'^2 \sin^2\phi}{z - z' + f}, \qquad (17)$$

where $f = \sqrt{(z-z')^2 + \rho^2 + \rho'^2 - 2\rho\rho'\cos\phi}$ and $\rho' = \rho(z')$. The Lawrence formula was extensively used in dynamical calculations within the liquid-drop model [13], despite the fact that, here—as in (16)—it is necessary to calculate a triple integral in order to estimate the functional B_{Coul}.

According to [8], other formulas for calculating the functional B_{Coul} that involve total elliptic integrals of the first and the second kind [4, 8, 14] in the integrand require using effective high-precision methods [15] for estimating elliptic integrals. Landen's method (arithmetic–geometric mean) [14, 16, 17] is not appropriate for this [8]. This is the reason why, despite an additional integration, the Lawrence formula, as well as formulas for B_{Coul} in terms of double integrals (see, for example,

[14]), is widely used in numerical calculations performed in the theory of fission.

Our new formula is also advantageous in that, in contrast to similar formulas from [9, 11, 12], it has no singularities in the integrand. Since such singularities must be avoided in numerical calculations, this feature of our formula is of great value.

In order to perform numerical calculations on the basis of Eq. (16), we chose the popular $\{c, h, \alpha\}$ parametrization [4] of the nuclear surface and set $h = \alpha = 0$ for the sake of simplicity, varying only the nuclear-elongation parameter c. The triple integrals in Eqs. (16) and (17) were calculated by Gauss' quadrature formulas with 32 and 96 nodes. The results are quoted in the table, where we can see that the values calculated by the two formulas differ only in the fifth significant digit when integration is performed with 32 nodes and in the seventh digit when integration is performed with 96 nodes. The example of a sphere ($c = 1$, $B_{\mathrm{Coul}}^{\mathrm{LD}} = 1$) demonstrates clearly that our formula overestimates the exact result, whereas the formula employed previously underestimates it. We also note that computations on the basis of the new formula require 10–15% less machine time, depending on the parametrization of the nuclear shape.

3. CONCLUSION

A new transformation of double volume integrals into double surface integrals has been presented. A simple regular method for deducing the integrands in the surface integral has been proposed: it is sufficient to perform only two integrations of the function entering into the volume integral. The new formula does not require applying special numerical techniques, since the integrand in it is free from singularities. Our method has been used to calculate the Coulomb energy of a nucleus within the model of a liquid drop with a sharp boundary. The results of this calculation have been compared with those obtained according to one of the formulas employed previously. For the Coulomb functional, the new formula ensures a reasonably high precision that increases with the number of nodes in the integration. Calculations by the new formula consume 10–15% less machine time than calculations by the formulas used so far.

ACKNOWLEDGMENTS

We are grateful to V.V. Pashkevich for stimulating discussions and enlightening comments.

REFERENCES

1. Ya. Frenkel, Zh. Éksp. Teor. Fiz. **9**, 641 (1939); Phys. Rev. **55**, 987 (1939).
2. N. Bohr and J. A. Wheeler, Phys. Rev. **56**, 426 (1939).
3. V. M. Strutinsky, Nucl. Phys. A **95**, 420 (1967); **122**, 1 (1968).
4. M. Brack, J. Damgaard, A. S. Jensen, *et al.*, Rev. Mod. Phys. **44**, 320 (1972).
5. J. R. Nix and W. J. Swiatecki, Nucl. Phys. **71**, 1 (1965); J. R. Nix, Nucl. Phys. A **130**, 241 (1969).
6. K. T. R. Davies, A. J. Sierk, and J. R. Nix, Phys. Rev. C **13**, 2385 (1976).
7. G. I. Kosenko, I. I. Gonchar, O. I. Serdyuk, and N. I. Pischasov, Yad. Fiz. **55**, 920 (1992) [Sov. J. Nucl. Phys. **55**, 514 (1992)].
8. K. T. R. Davies and A. J. Sierk, J. Comput. Phys. **18**, 311 (1975).
9. H. J. Krappe, J. R. Nix, and A. J. Sierk, Phys. Rev. C **20**, 992 (1979).
10. G. A. Korn and T. M. Korn, *Mathematical Handbook for Scientists and Engineers* (McGraw-Hill, New York, 1968; Nauka, Moscow, 1984).
11. J. N. P. Lawrence, Phys. Rev. B **139**, 1227 (1965).
12. R. W. Hasse and W. D. Myers, *Geometrical Relationships of Macroscopic Nuclear Physics* (Springer-Verlag, Berlin, 1988).
13. R. W. Hasse, Nucl. Phys. A **118**, 577 (1968); Nucl. Phys. A **128**, 605 (1969).
14. V. M. Strutinsky, N. Ya. Lyashenko, and N. A. Popov, Nucl. Phys. **46**, 639 (1963).
15. W. J. Cody, J. Math. Comp. **19**, 105 (1965).
16. S. Frankel and S. N. Metropolis, Phys. Rev. **72**, 914 (1947).
17. *Handbook of Mathematical Functions*, Ed. by M. Abramowitz and I. A. Stegun (Dover, New York, 1965; Nauka, Moscow, 1979).

Translated by R. Tyapaev

Physics of Atomic Nuclei, Vol. 63, No. 11, 2000, pp. 1889–1894. Translated from Yadernaya Fizika, Vol. 63, No. 11, 2000, pp. 1982–1987.

NUCLEI
Theory

Special Analytic Properties of the Amplitude for Scattering on the Woods–Saxon Potential

Yu. V. Orlov

Institute of Nuclear Physics, Moscow State University, Vorob'evy gory, Moscow, 119899 Russia

Received June 18, 1999; in final form, October 6, 1999

Abstract—It is shown that the *s*-wave partial amplitude $f(k)$ for scattering on the real-valued Woods–Saxon potential $V(r) = -V_0/[1 + \exp((r - R)/d)]$ has very special analytic properties: the trajectories of the poles of the function $k\cot\delta$ [of the zeros of the amplitude $f(k)$] coincide with the lines of the dynamical singularities [spurious poles of $f(k)$], so that the zeros and the poles compensate each other. In contrast to what is obtained for Yukawa-like potentials, the scattering length does not vanish here at zero energy. The results reported in this article were obtained analytically under the assumption that $\exp(-R/d) \ll 1$. The problem of revealing the poles of the function $k\cot\delta$ in a partial-wave analysis of neutron scattering on nuclei is discussed.© *2000 MAIK "Nauka/Interperiodica".*

1. INTRODUCTION

For analytic Yukawa-like potentials whose asymptotic behavior is given by

$$V(r) \longrightarrow \text{const} \cdot r^b \exp(-\mu r), \quad \mu > 0, \quad b \geq -2, \quad (1)$$

a quantum-mechanical theorem on the symmetry of bound and virtual states was formulated and proven in [1]. According to this theorem, the positions of the points where the trajectories of these levels intersect the lines of dynamical singularities of a partial-wave amplitude as a function of the interaction strength $g = K_0^2/\mu^2$ (where $K_0^2 = 2mV_0/\hbar^2$, V_0 being the potential-well depth) exhibit mirror symmetry with respect to the zero-momentum axis. Later on, this theorem was proven analytically for the Woods–Saxon potential [2], which is extensively used in nuclear physics. Thereby, it was shown that the theorem on the discrete symmetry of bound and virtual levels also holds for potentials irregular in the region $\mathrm{Re}\, r > 0$. In [3], it was proven that, for Yukawa-like potentials, the above theorem of symmetry has a corollary according to which the trajectories of the poles of the function $k\cot\delta$ [or of the zeros of the *s*-wave amplitude $f(k)$] intersect the lines of dynamical singularities of the partial-wave S matrix at the same symmetry points through which the trajectories of bound and virtual levels pass. The corollary proven in [3] was illustrated by considering the examples of the Yukawa and Hulthén potentials.

In deriving the above statements, use was made of the fact that the scattering length as a function of the interaction strength passes through zero smoothly changing from $+\infty$ to $-\infty$ in the interval between the neighboring critical values of the interaction strength that are defined as those at which a virtual state becomes a bound state (an important property of the scattering length indeed). However, that this property is not universal. It is shown in the present study that, in the case of the real-valued Woods–Saxon potential, the scattering length does not vanish at any parameter value. Nonetheless, the above corollary of the theorem of symmetry remains valid. Moreover, it is proven that, for the same potential, the trajectories of the zeros of $f(k)$ merely coincide with the lines of dynamical singularities (spurious poles). Thus, the dynamical poles and the zeros compensate each other completely. To the best of my knowledge, this is a unique property of a partial-wave amplitude, and it leads to important corollaries. One of these is that, for the Woods–Saxon potential, the trajectory of the pole of $k\cot\delta$ [zero of $f(k)$] as a function of the interaction strength does not intersect the zero-momentum axis (this is in sharp contrast to what was found for potentials of the Yukawa type). Thus, the pole of the function $k\cot\delta$ cannot come arbitrarily close to the physical region ($E \geq 0$). For this reason, the Woods–Saxon potential cannot be used, for example, to describe the features of the doublet *nd* system at low energies within a two-body model. In this connection, we discuss the possibility of revealing the pole of the function $k\cot\delta$ in the partial-wave analysis of neutron–nucleus scattering. Below, we use the system of units where $\hbar = c = 1$.

2. BEHAVIOR OF THE TRAJECTORIES OF $k\cot\delta$ AND COROLLARY OF THE THEOREM OF SYMMETRY FOR THE WOODS–SAXON POTENTIAL

We begin by recalling the proof of the theorem of symmetry for the Woods–Saxon potential

$$V(r) = -V_0/\left[1 + \exp\left(\frac{r - R}{d}\right)\right]. \quad (2)$$

1063-7788/00/6311-1889$20.00

In contrast to the potentials for which the theorem of symmetry was proven in [1]—those potentials are analytic in the region $\mathrm{Re}\, r > 0$—the potential given by (2), albeit showing the required asymptotic behavior given by (1), has an infinite number of poles in the complex plane of r, the coordinates of the poles being $\mathrm{Re}\, r = R$ and $\mathrm{Im}\, r = \pm\pi(2\nu + 1)d$, where ν is an arbitrary integer.

The well-known analytic solution to the problem in the s wave for the Woods–Saxon potential was used in [2] to prove the required statements. Let us introduce the notation

$$\beta^2 = -2mEd^2 = \lambda^2 d^2, \quad \gamma^2 = 2mV_0 d^2 = K_0^2 d^2, \\ \alpha^2 = \gamma^2 - \beta^2 = 2md^2(V_0 + E), \quad k^2 = 2mE, \tag{3}$$

where E is the energy of the relative motion of colliding particles, while m is the reduced mass of the system.

We now investigate the analytic properties of the s-wave partial amplitude, representing it as

$$f(k) = (2ik)^{-1}[F(-k) - F(k)]/F(k), \tag{4}$$

where $F(k)$ is the s-wave Jost function. The expression for this function in the potential (2) is known. In particular, the Jost function can be found from the asymptotic representation of the radial wave function for the problem of scattering on the Woods–Saxon potential. The relevant expansion can be found, for example, in [4] (below, we correct misprints occurring there). For the scattering of a particle with a momentum k on a spherically symmetric potential $V(r)$, the radial wave function has the form (see, for example, [5])

$$\Psi(k, r) = [F(-k)\, f(-k, r) - F(k)\, f(k, r)]/2ikrF(k), \tag{5}$$

where $f(+k, r)$ and $f(-k, r)$ stand for the Jost solutions whose asymptotic forms are $\exp(-ikr)$ and $\exp(ikr)$, respectively. For the scattering problem in question, the S matrix is given by

$$S(k) = F(-k)/F(k). \tag{6}$$

After some simple algebra, we find that the explicit expression for $F(k)$ in the Woods–Saxon potential has the form

$$F(k) = c^{-i\beta}(1-c)^{i\alpha} \\ \times F(i(\alpha+\beta), i(\alpha+\beta)+1; 2i\beta+1; c), \tag{7}$$

where $c = (1 + \exp(-R/d))^{-1}$ and $F(s, t; u; z)$ is a hypergeometric function (for its definition and properties, see, for example, [6]). This function can be calculated with the aid of the hypergeometric series

$$F(s, t; u; z) = 1 + (st/u \cdot 1)z \\ + (s(s+1)t(t+1)/u(u+1) \cdot 1 \cdot 2)z^2 + \ldots. \tag{8}$$

The convergence of this series in (7) is ensured by the inequality $c = (1 + \exp(-R/d))^{-1} < 1$.

The analytic properties of the Jost function $F(k)$ and, accordingly, of the scattering amplitude $f(k)$ (4) can be established on the basis of expressions (7) and (8). For example, it can easily be seen that the dynamical singularities of $F(\pm k)$ are spurious poles occurring on the imaginary axis of the complex-valued momentum k ($k = i\lambda$) at values satisfying the well-known equation

$$\beta = \lambda d = \pm l/2, \quad l = 1, 2, \ldots. \tag{9}$$

The pole character of the dynamical singularities is associated with the fact that the Woods–Saxon potential (2) has the asymptotic form (1) at $b = 0$. By way of example, we indicate that the Hulthén potential

$$V(r) = -V_0/[\exp(\mu r) - 1] \tag{10}$$

has the same asymptotic behavior. In connection with the theorem being discussed, the properties of the trajectories of the zeros and poles of $f(k)$ for the Hulthén potential were considered in detail elsewhere [3].

Since the hypergeometric series in (7) converges very slowly for $\exp(-R/d) \ll 1$ (this is so, for example, in neutron–nucleus interactions), it is reasonable to transform the hypergeometric function by going over from the argument $z = c$ to the argument $z = 1 - c = \exp(-R/d)/[1 - \exp(-R/d)] \cong \exp(-R/d)$. The next step consists in retaining only the first term in the expansion of the hypergeometric function whose argument is $z = 1 - c$ (this first term is equal to unity), as was done in [4]. In this approximation, the Jost solution assumes the form {see Eq. (64.12) in [4]}[1)]

$$f(-k, r) = (y(r))^{\beta}\Gamma(2\beta+1) \\ \times \{[\Gamma(-2i\alpha)/\Gamma(\beta+1-i\alpha)\Gamma(\beta-i\alpha)](1-y(r))^{i\alpha} \\ + [\Gamma(2i\alpha)/\Gamma(\beta+1+i\alpha)\Gamma(\beta+i\alpha)](1-y(r))^{-i\alpha}\}, \tag{11}$$

where $y(r) = [1 + \exp((r - R)/d)]^{-1}$ and $\Gamma(z)$ is the Euler gamma function. The wave function in (5) must be bounded at $r = 0$. The boundary condition at the origin leads to the Jost function in the form

$$F(k) = f(-k, 0). \tag{12}$$

Thus, we can see that, in order to obtain the explicit expression for $F(k)$, the value of the function $y(r)$ at the origin,

$$y(0) = [1 + \exp(-R/d)]^{-1}, \tag{13}$$

must be substituted into (11). The poles of the scattering amplitude for bound and virtual states correspond to the equalities $F(k) = 0$ and $F(-k) = 0$, respectively. The pole position for a bound state is determined by the transcendental equation (see, for example, [4, Eq. (64.16)])

$$\frac{\alpha R}{d} - \sum_{n=1}^{\infty}\left(\arctan\frac{2\alpha}{n} - 2\arctan\frac{\alpha}{n+\beta}\right) \\ + \arctan\frac{\alpha}{\beta} = l\pi, \tag{14}$$

[1)] In Eq. (11), there appears the factor $(y(r))^{\beta}$, which is absent from (64.12) in [4].

where l is an arbitrary integer. The equation for a virtual pole differs from (14) by the obvious substitution $\beta \longrightarrow -\beta$ and has the form ($\beta > 0$)

$$\frac{\alpha R}{d} - \sum_{n=1}^{\infty}\left(\arctan\frac{2\alpha}{n} - 2\arctan\frac{\alpha}{n-\beta}\right) - \arctan\frac{\alpha}{\beta} = l\pi. \quad (15)$$

The proof of the theorem of symmetry in [2] relied on the fact that, at the points where the trajectories intersect the lines of the dynamical singularities, $\beta = |\lambda d| = \nu/2$ (ν is an integer), Eq. (15) goes over to Eq. (14) (only the integer l on the right-hand side of the equation changes).

The positions of the zeros of $f(k)$ are determined by the obvious condition $F(k) - F(-k) = 0$, which leads to the transcendental equation

$$\arctan(\alpha/\beta) + \sum_{n=1}^{\infty}[\arctan(\alpha/(n+\beta)) - \arctan(\alpha/(n-\beta))] = \pm l\pi/2, \quad l = 0, 1, 2, \ldots. \quad (16)$$

It can easily be shown that Eq. (16) is the difference of Eqs. (14) and (15), whence it immediately follows that the above corollary of the theorem of symmetry is valid: symmetry points lying at the intersection of the lines of the dynamical singularities of the S matrix and the trajectories of the poles corresponding to bound and virtual states also belong to the trajectories of the zeros of the amplitude $f(k)$ (or of the poles $k\cot\delta$).

It is interesting to note that the parameter R does not appear in Eq. (16), which determines the trajectory of the pole of $k\cot\delta$. Moreover, it can be shown that the transcendental equation (16), which has a rather complicated form, has an unexpectedly simple solution for the unknown β as a function of γ. This equation is satisfied at β values corresponding to condition (9) such that $\beta(=\lambda d)$ does not depend on $\gamma(=K_0 d)$ either. Here, the intersection of the trajectories of the zeros of the amplitude $f(k)$ (or of the poles of $k\cot\delta$) and the lines of the dynamical singularities implies their coincidence.

Thus, we can see that, in the case of the Woods–Saxon potential, there is an unusual, possibly unique, situation in potential scattering: the trajectories of the dynamical singularities (spurious poles of the S matrix) merely coincide with the trajectories of the zeros of the amplitude $f(k)$.

In quantum scattering theory, it is well known that the poles of the s-wave partial scattering amplitude $f(k)$ for bound states are simple, and it was emphasized in [3] that the corollary deduced from the theorem of symmetry and discussed here is consistent with the above statement of quantum scattering theory. By way of example, we indicate that, in the case of the Hulthén potential, the spurious pole is compensated by the zero of $f(k)$ at the symmetry point, which appears to be a point of triple intersection where the trajectory of the position of the bound level as a function of the interaction strength intersects the dynamical-singularity line. But in the case of the Woods–Saxon potential, the s-wave partial scattering amplitude $f(k)$ has neither dynamical spurious poles nor zeros because they compensate one another completely (see above). Thus, we conclude that, in contrast to what was obtained for Yukawa-like potentials, which were considered previously, the amplitude $f(k)$ for the real-valued Woods–Saxon potential has no poles in the complex plane other than those that correspond to bound, virtual, and resonance states. The zeros of the Jost function $F(k)$ correspond to these poles [$F(k) = 0$]. With the aid of (4), (7), and (13), the scattering length [$a = -f(0)$] can be represented as

$$a \cong -(2/K_0) \times\left\{1 + 2(K_0 d)^2\sum_{n=1}^{\infty}[n^2 + (K_0 d)^2]^{-1}\right\}/(\sin\phi\cos\phi), \quad (17)$$

$$\phi = K_0 R - \sum_{n=1}^{\infty}[\arctan(2K_0 d/n) - 2\arctan(K_0 d/n)].$$

From these expressions, it can clearly be seen that the scattering length a cannot vanish, since the numerator in (17) is a positive definite function if the Woods–Saxon potential is real (that is, K_0 is real). At the same time, the behavior of the scattering length at parameter values corresponding to interaction-strength values close to the critical one at which a virtual level becomes a bound level—that is, when $\cos\phi = 0$ [see (14)]—has a character peculiar to quantum mechanics: the scattering length undergoes an infinite jump, changing sign. In contrast to what was observed for Yukawa-like potentials, there is, however, another singular point in (17), that which corresponds to $\sin\phi = 0$. Here, the scattering length changes sign in the interval between two critical points, as it does in the case of Yukawa-like potentials, but this sign reversal is not smooth as for Yukawa potentials—this proceeds via an infinite jump in a. For each interval between the critical values of the parameters of the Woods–Saxon potential, the modulus of $|a|$ has a nonzero minimum, so that the scattering length cannot be arbitrarily close to zero. The minimum value $|a|_{\min} = A_{\min}$ is achieved for R values at which $\sin 2\phi = 1$ (that is, at $\phi = \pi/4 + n\pi$), $|a/d|_{\min}$ being dependent only on the scaled parameter $\gamma = K_0 d$.

For $d \longrightarrow 0$, the Woods–Saxon potential reduces to a rectangular well, for which s-wave scattering length is given by the well-known expression (see, for example, [4])

$$a_0 = R(1 - (K_0 R)^{-1}\tanh(K_0 R)); \quad (18)$$

that is, $a_0 > 0$ for any interaction strength, provided that the potential is real-valued.

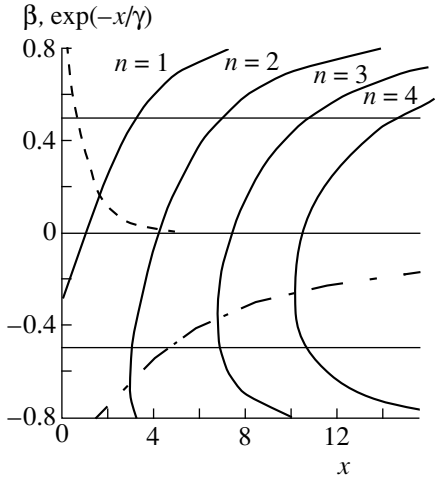

Fig. 1. Trajectories of the *s* levels in the Woods–Saxon potential (thick solid lines). The scaled argument $x = K_0R$ and the scaled function $\beta = \lambda d$ are plotted along the coordinate axes. The graph of the function $\exp(-x/\gamma) = \exp(-R/d)$ is depicted by the dashed line. The positions of the dynamical singularities at $\beta = \pm 0.5$ are shown by thin horizontal lines. Higher order poles of the scattering amplitude occur at the intersections of the dash-dotted line and the trajectories of the levels (see main body of the text). The calculations were performed at the fixed value of $\gamma = K_0 d = 0.903$, which corresponds to the parameter values of $V_0 = 40$ MeV and $d = 0.65$ fm.

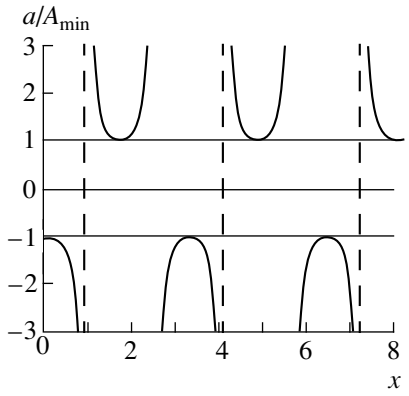

Fig. 2. Scattering length a as a function of the interaction strength $x = K_0R$. The parameter γ was set to the same value as that used to calculate the data displayed in Fig. 1. The scaled quantity $a/A_{\min}$ is plotted along the ordinate. The positions of the critical values of x ($\cos\varphi = 0$) that correspond to a transformation of a virtual into a bound level are indicated by vertical dashed lines.

It should be recalled that, for the case of the Woods–Saxon potential, expressions (14)–(17) were derived in the approximation $\exp(-R/d) \ll 1$. In order to refine the results of the calculations, the hypergeometric series in (8) can be evaluated with allowance for higher powers of $z = c - 1$. However, the above approximation is quite good even for relatively light nuclei. By way of example, we indicate that, at parameter values of $R \geq 3$ fm and $d \approx 0.65$ fm, which are peculiar to this region of nuclei, we have $\exp(-R/d) \leq 0.01$.

3. NUMERICAL RESULTS

The trajectories of bound and virtual levels were calculated here in order to illustrate the above results. The function $\lambda = \lambda_n(\mu)$ [n is the principal quantum number (number of a level) and $\mu = d^{-1}$] was calculated in [2] with the parameter set from [7] for the case of neutron scattering on a ^{208}Pb nucleus ($V_0 = 46.232$ MeV, $R = 7.347$ fm, $2m/\hbar^2 = 0.04824$ MeV^{-1} fm^{-2}). In contrast to the study of Gareev *et al.* [7], who varied the potential depth V_0 and fixed the value of $d^{-1} = 1.587$ fm^{-1} ($d \cong 0.63$ fm), the quantity varied in [2] was μ. Here, we consider the dependence $\beta = \beta(x)$, $x = K_0R$. The quantity $\gamma = K_0d$ is fixed at the value of $\gamma = 0.903$, which is in reasonably good agreement with the optical-model parameters for low-energy neutron–nucleus scattering. The results of the calculations based on Eqs. (14) and (15) are illustrated in Fig. 1. In these equations, summations can be truncated at $n > N = 1000$, whereby the required accuracy is ensured. It can be seen that the points occurring at the intersections of the trajectories and the straight lines of the dynamical singularities ($\lambda d = \pm 1/2$) form pairs symmetric with respect to the point $\lambda = 0$, as they must according to the theorem of symmetry. Figure 1 also displays the curve that was obtained with the aid of the pole-order equation {see Eq. (17) from [2]). At the points where this curve intersects the trajectories of virtual levels, the relevant S matrix has second-order poles. Two trajectories—one that appears to be a continuation of the trajectory of a bound state to the unphysical list and the other that comes from the region of virtual lines—meet at each such point. Either trajectory satisfies Eq. (15), and the two actually form one continuous line. That these trajectories approach each other, coming from opposite directions as the parameter x (equal to K_0R) is changed monotonically, is reflected in that the derivative $d\beta/dx$ tends to infinity at the above pole-order points. Finally, the graph of the function $\exp(-x/\gamma) = \exp(-R/d) \ll 1$ is also depicted in Fig. 1, illustrating, for $x \geq 3$, the applicability range of the approximation $\exp(-R/d) \ll 1$ adopted here. By definition, the binding energy ε cannot be greater than V_0, whence it follows that $\beta < \gamma$. From the behavior of the trajectories in Fig. 1, it can be seen that, with increasing R, levels corresponding to various values of the principal quantum number ($n = 1, 2, 3, 4, \ldots$) are accumulated near the bottom of the potential well.

The results of the calculations for the function $a/A_{\min}$ versus the scaled interaction-strength parameter $x = K_0R$ are displayed in Fig. 2 at the same fixed value of $\gamma = K_0d$ as in Fig. 1. These data exhibit the special features in the behavior of the scattering length for the case of the Woods–Saxon potential that were discussed in Section 2. The critical values of the argument x that correspond to a transformation of a virtual into a bound level ($\cos\phi = 0$) are shown by vertical dashed lines. A

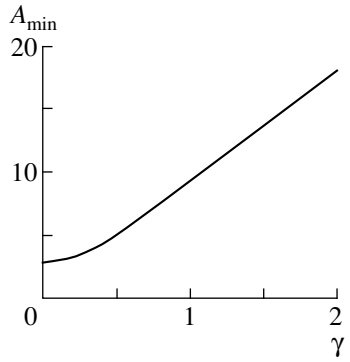

Fig. 3. Minimal absolute value of the scattering length, $A_{min} = |a|_{min}$, as a function of the strength of the Woods–Saxon potential, $\gamma = K_0 d$. The quantity K_0 is fixed at 1.389 fm^{-1} in accordance with the chosen value of $V_0 = 40$ MeV.

periodic character of the interaction-strength dependence of the scattering length is quite conventional and is associated with a change in the number of a level. The dependence of the scattering length on the radius R of the Woods–Saxon potential is determined entirely by the denominator on the right-hand side of Eq. (17). The discontinuities at the x points where $\sin\phi = 0$—they are shown in Fig. 2 by vertical solid lines—proved to be quite unexpected. For Yukawa-like potentials, the scattering length changes monotonically in this region from $+\infty$ to $-\infty$, passing through zero. As can be seen from Fig. 2, $|a/A_{min}| \geq 1$.

Figure 3 shows the results of the calculations for the minimal absolute value of the scattering length, $A_{min} = |a|_{min}$, versus $\gamma = K_0 d$. The graph presented there illustrates all that was said above about the special features of the behavior of the scattering length for the Woods–Saxon potential that distinguish this case from that of Yukawa-like potentials.

4. CONCLUSION

As was indicated in [3], the emergence of a pole in the function $k\cot\delta$ [that is, a zero in the amplitude $f(k)$] at real negative values of energy ($E < 0$) is not accidental; this is quite typical of Yukawa-like potentials, for which the trajectories of this pole are periodically replicated as the principal quantum number is increased. That the poles of $k\cot\delta$ manifest themselves very rarely in partial-wave analyses of nuclear processes may be due to the fact that, as can be seen from the examples of the Yukawa and Hulthén potentials, the trajectory of such a pole intersects the zero-momentum axis at a right angle (infinite derivative at the intersection point). As a result, small variations in the interaction strength move such a pole away from the physical region ($E \geq 0$); therefore, it can be missed in a partial-wave analysis. Near a pole of the above type, the formula that appears in the conventional effective-range approximation ($k\cot\delta = -1/a + r_0 k^2/2$) must be replaced by a modified formula of effective-range theory,

$$k\cot\delta = (C_0 + C_2 k^2 + C_4 k^4)/(1 + k^2/k_0^2). \qquad (19)$$

The results obtained in the present study—in particular, the absence of poles in the function $k\cot\delta$—imply that no such poles must appear in an analysis of experimental data within the optical model featuring the Woods–Saxon potential. As was indicated in the Introduction, one of the conclusions from the present consideration is that, in contrast to what is obtained for the family of analytic Yukawa-like potentials, which lead to a monotonic change in the scattering length a from $-\infty$ to ∞ as the interaction strength increases in the interval between the critical values, the scattering length in the Woods–Saxon potential vanishes nowhere.

The results of the present study explicitly demonstrate that the Woods–Saxon potential, which is very popular in nuclear physics, cannot be applied, for example, to describing the low-energy ($E \leq 0$) features of the doublet *nd* system, for which the pole of $k\cot\delta$ has been reliably established. This follows both from the results of an analysis of experimental data within the generalized effective-range theory based on Eq. (19) (see, for example, [8]) and from theoretical calculations relying on the Faddeev equations, as well as from calculations within the *N*/*D* method and within the two-body model employing various potentials of the Yukawa type (see [3] and references therein). All calculations on the basis of the Faddeev equations lead to a smooth variation of the doublet *nd* scattering length in the vicinity of zero as we go over from one model of nucleon–nucleon forces to another (with sign reversal). This is the main reason behind the existence of well-known correlations between the doublet *nd* scattering length and other low-energy features of the *nd* system [in particular, the binding energies of the bound and the virtual triton (T and T^*, respectively)].

Although the Woods–Saxon potential is widely used in optical-model calculations, it cannot be considered as the only acceptable potential for describing, for example, neutron scattering on nuclei (especially light nuclei). In this connection, it would be of interest to reconsider the results of partial-wave analyses of experimental data on low-energy neutron–nucleus scattering with a special emphasis on searches for a pole of $k\cot\delta$ at negative energies. Should such a pole be discovered, this would imply the need for modifying optical potentials, and this is a point of great practical interest for the physics of slow neutrons and for astrophysics.

For $E \longrightarrow 0$, the potential becomes real-valued, since the optical model goes over to the shell model. The formulas obtained above can be generalized to the case of a complex-valued potential, but this is beyond the scope of the present article.

ACKNOWLEDGMENTS

This work was supported by the Foundation Russian Universities—Fundamental Research (project no. 5368, 1998).

REFERENCES

1. Yu. V. Orlov, Phys. Lett. B **163**, 25 (1985).
2. Yu. V. Orlov and L. I. Nikitina, Yad. Fiz. **49**, 701 (1989) [Sov. J. Nucl. Phys. **49**, 434 (1989)].
3. Yu. V. Orlov and L. I. Nikitina, Yad. Fiz. **61**, 833 (1998) [Phys. At. Nucl. **61**, 750 (1998)].
4. S. Flügge, *Practical Quantum Mechanics* (Springer-Verlag, Berlin, 1971; Mir, Moscow, 1974), Vol. 1.
5. R. G. Newton, *Scattering Theory of Waves and Particles* (Springer-Verlag, New York, 1982, 2nd ed.; Mir, Moscow, 1969).
6. I. S. Gradshteyn and I. M. Ryzhik, *Table of Integrals, Series, and Products* (Nauka, Moscow, 1971; Academic, New York, 1980).
7. F. A. Gareev, S. A. Goncharov, V. I. Kukulin, and V. M. Krasnopol'skiĭ, Preprint No. R4-12002, OIYaI (Joint Institute for Nuclear Research, Dubna, 1978).
8. I. V. Simenog, A. I. Sitnichenko, and D. V. Shapoval, Yad. Fiz. **45**, 60 (1987) [Sov. J. Nucl. Phys. **45**, 37 (1987)].

Translated by A. Isaakyan

Physics of Atomic Nuclei, Vol. 63, No. 11, 2000, pp. 1895–1902. Translated from Yadernaya Fizika, Vol. 63, No. 11, 2000, pp. 1988–1995.

NUCLEI
Theory

Possibility of Choosing between Different Types of Nucleon–Nucleon Interaction on the Basis of Data on Hard Bremsstrahlung in the Process $pp \longrightarrow pp\gamma$ at Beam Energies in the Range 350–500 MeV

V. A. Knyr[1)], V. G. Neudatchin*, and N. A. Khokhlov[1)]

Institute of Nuclear Physics, Moscow State University, Vorob'evy gory, Moscow, 119899 Russia

Received April 1, 1999; in final form, February 22, 2000

Abstract—Previously reported results on the differential cross sections for the process $pp \longrightarrow pp\gamma$ occurring at beam-proton energies of 280, 350, and 450 MeV and involving the emission of hard photons are supplemented with the results of calculations at 400 and 500 MeV. The emerging pattern suggests that, in the energy range E_0 = 450–500 MeV, an experiment detecting hard photons from this reaction, in which case outgoing protons escape at small angles on the different sides of the beam direction, will be very sensitive to the type of nucleon–nucleon potential (meson-exchange potentials versus the Moscow potential). The energy of E_0 = 400 MeV is not optimal for this purpose because the sensitivity is higher even at E_0 = 350 MeV. The possibility of distinguishing between the types of nucleon–nucleon potentials through examining the transverse analyzing power $A_y(\theta_\gamma)$, which reflects the correctness of taking into account spin effects, is studied. This analyzing power is found to exhibit comparatively small changes in response to introducing short-range oscillations in the *S* and *P* waves instead of the repulsive-core-induced vanishing of the wave function at small distances. © *2000 MAIK "Nauka/Interperiodica"*.

1. INTRODUCTION

Although a great number of studies on the short-range part of the nucleon–nucleon interaction—and in general, the baryon–baryon interaction—have been performed over the past two decades, advances in understanding its origin have been very slow. Moreover, there remain three different concepts in these realms.

The first concept assumes meson-exchange potentials involving a repulsive core [1–4]. The second is based on models of the Skyrme type [5], which are close to the concept of meson-exchange potentials in practical aspects. The third relies on quark models of the nucleon, where gluon perturbative interaction between quarks [6, 7]–or, more recently, various nonperturbative interactions [8, 9]—takes the place of meson exchange at small distances between nucleons. The majority of calculations performed within the third concept yielded results close to those obtained on the basis of meson-exchange potentials, but these potentials are treated there as a phenomenological device.

However, there is a markedly different result. On the basis of the symmetry properties of six-quark systems, it was found in [7, 10] that there are attraction channels in nucleon–nucleon systems. By way of example, we indicate that, in the case of color-magnetic *qq* interaction of $\lambda\lambda\sigma\sigma$ symmetry, such an attraction is induced by the excitation of the $s^4p^2[42]_X[42]_{CS}$ quark configurations in the *S* and *D* waves and the $s^3p^3[33]_X[51]_{CS}$ quark configurations in the *P* and *F* waves. These configurations become energetically favorable [7] when the amplitude of the above *qq* interaction is sufficiently large (for projection onto baryon–baryon channels, see [10–13]). In the case of $\sigma\sigma\tau\tau$ symmetry, which was discussed in connection with the models of instanton-induced interactions [8], the Young diagram $[42]_{CS}$ is replaced by $[42]_{ST}$, etc. On the basis of this concept, the model of the phenomenological Moscow nucleon–nucleon potential was proposed in [14–19]. Instead of a repulsive core in the *S* and *P* waves, this model introduces a wave function that has a node associated with excited quark configurations [7, 10–13]—that is, the resulting potential is deep and involves forbidden states. This approach provided a viable description of the properties of the deuteron and of low-energy nucleon–nucleon scattering [15–17]. Also, an overall pattern of the differential cross sections and polarizations for nucleon–nucleon scattering at energies up to 5 or 6 GeV was closely reproduced on its basis for the first time [20]. Later, the idea that excited quark configurations of the above type play a leading role in the region where the two deuteron nucleons overlap led to the conclusion [11, 12] that the deuteron includes a rich set of baryon–baryon configurations. Of course, this set

[1)] Khabarovsk State Technological University, Khabarovsk, Russia.
* e-mail: neudat@anna19.npi.msu.su

is dominated by the *np* component, but, in the order of importance, it is followed by the $NN^*(3/2^-, 1/2^-)$ component characterized by *P*-wave relative motion, the *S*-wave NN^* component, the $NN^*(1/2^+$, Roper) component (their probabilities are somewhat less than 1%), etc.; there is, however, no $\Delta\Delta$ component. This prediction was confirmed by an analysis of polarization data on $d + p$ scattering at $E_d = 7$ GeV [21]: it appeared that, in the deuteron, a sizable $N^*(3/2^-, 1/2^-)N$ component corresponding to *P*-wave relative motion and substantially affecting polarization transfer is necessary.

In view of the above, investigations into the physics behind the Moscow potential within nonperturbative QCD must be supplemented with searches for a reliable means to distinguish between alternative potentials, those that feature a repulsive core (meson-exchange potentials), on one hand, and those that feature a node in the wave function (Moscow potential), on the other hand. It should be considered that scattering data alone—even if they are available over a very wide energy interval—are insufficient because, as was indicated quite correctly in [22], the repulsive-core leading to an r^{-2} behavior at small distances can yield *S*- and *P*-wave phase shifts that are less than the respective phase shifts for the Moscow potential by π. However, such a pronounced phase difference is unobservable in elastic scattering.

The required means was found in [18], where the differential cross section for hard bremsstrahlung in the process $pp \longrightarrow pp\gamma$ was found, for the first time, to be highly sensitive to the potential type (meson-exchange potentials versus Moscow potential) at the easily available beam energies of $E_0 = 350$ and 450 MeV (in the laboratory frame), where exchange currents are immaterial for hard photons [23–25]. Here, we continue this investigation, considering, along with the differential cross sections, the transverse analyzing power A_y and extending, in calculating the differential cross sections and the above analyzing power, the kinematical region, which now includes large proton emission angles and the beam energies of $E_0 = 400$ and 500 MeV. {In [26], it was shown that, in the case of meson-exchange potentials, relativistic corrections are less than 20% in the region being studied; therefore, we apply the nonrelativistic approach, but there are reasons to believe that relativistic effects for the Moscow potential are more pronounced (see below).} All this enables us to disclose more fully the pattern of the effects under consideration for future experiments.

2. DESCRIPTION OF THE FORMALISM

As in [18], we employ here the coordinate representation. The amplitude A_{if} for the transition from the initial (i) to the final (f) state can represented in the form [18]

$$\delta(\mathbf{P}_i - \mathbf{P}_f + \mathbf{k})A_{if} = 2\sqrt{4\pi}\int d^3\mathbf{x}\langle\psi_f|\mathbf{J}(\mathbf{x})\cdot\boldsymbol{\varepsilon}|\psi_i\rangle\exp(-i\mathbf{k}\cdot\mathbf{x}), \quad (1)$$

where $\boldsymbol{\varepsilon}$ is the photon polarization vector and the current density has the form

$$\mathbf{J}(\mathbf{x}) = -\frac{i}{2}\sum_{i=1,2}\frac{e}{m}[\delta(\mathbf{x}-\mathbf{r}_i)\nabla_i + \nabla_i\delta(\mathbf{x}-\mathbf{r}_i)] + \sum_{i=1,2}\mu\,\mathrm{curl}(\delta(\mathbf{x}-\mathbf{r}_i)\boldsymbol{\sigma}_i), \quad (2)$$

μ being the proton magnetic moment.

Using the wave functions for the two-proton system in the form

$$\psi_i(\mathbf{r}_1, \mathbf{r}_2) = (2\pi)^{3/2}\exp(i\mathbf{P}_i\cdot\mathbf{R})\varphi(\mathbf{p}_i, \mathbf{r}),$$
$$\int d^3\mathbf{r}\bar{\varphi}(\mathbf{p}_1, \mathbf{r})\varphi(\mathbf{p}_2, \mathbf{r}) = \delta(\mathbf{p}_1 - \mathbf{p}_2) \quad (3)$$

(the form for the final-state wave function is similar, with i replaced by f), we consider, by way of example, the calculation of the component appearing on the right-hand side of Eq. (1) and corresponding to that term in (2) which involves $\delta(\mathbf{x}-\mathbf{r}_1)\nabla_1$. Substituting this term into the expression on the right-hand side of (1), we obtain

$$\begin{aligned}
&\int d^3\mathbf{r}_1 d^3\mathbf{r}_2\bar{\psi}_f(\mathbf{r}_1, \mathbf{r}_2)(\nabla_1\cdot\boldsymbol{\varepsilon})\psi_i(\mathbf{r}_1, \mathbf{r}_2)\exp(-i\mathbf{k}\cdot\mathbf{r}_1)\\
&= \int d^3\mathbf{R}d^3\mathbf{r}\exp(-i\mathbf{P}_f\cdot\mathbf{R})\bar{\varphi}_f(\mathbf{p}_f, \mathbf{r})\left(\frac{1}{2}\nabla_R - \nabla_r\right)\cdot\boldsymbol{\varepsilon}\\
&\times\exp(i\mathbf{P}_i\cdot\mathbf{R})\varphi(\mathbf{p}_i, \mathbf{r})\exp\left(-i\mathbf{k}\cdot\left(\mathbf{R} - \frac{1}{2}\mathbf{r}\right)\right)\\
&= \mathrm{const}\times\left[\frac{i}{2}\boldsymbol{\varepsilon}\cdot(\mathbf{P}_i - \mathbf{k})\delta(\mathbf{P}_i - \mathbf{P}_f - \mathbf{k})\right.\\
&\times\int d^3\mathbf{r}\bar{\varphi}_f(\mathbf{p}_f, \mathbf{r})\varphi_i(\mathbf{p}_i, \mathbf{r})\exp\left(\frac{i}{2}\mathbf{k}\cdot\mathbf{r}\right) - \delta(\mathbf{P}_i - \mathbf{P}_f - \mathbf{k})\\
&\left.\times\int d^3\mathbf{r}\bar{\varphi}_f(\mathbf{p}_f, \mathbf{r})(\boldsymbol{\varepsilon}\cdot\nabla_r)\varphi_i(\mathbf{p}_i, \mathbf{r})\exp\left(\frac{i}{2}\mathbf{k}\cdot\mathbf{r}\right)\right].
\end{aligned} \quad (4)$$

In the initial-state c.m. frame, where $\mathbf{P}_i = \mathbf{0}$ and $\mathbf{P}_f = -\mathbf{k}$, the first term in the last expression vanishes since the gauge of the electromagnetic field is chosen in such a way that $\boldsymbol{\varepsilon}\cdot\mathbf{k} = 0$. In the final-state c.m. frame, where $\mathbf{P}_f = \mathbf{0}$ and $\mathbf{P}_i = \mathbf{k}$, this term also vanishes. Considering similarly other terms on the right-hand side of Eq. (1), we obtain

$$A_{if} = 16(\pi)^3\sqrt{\pi}m \times\left(\frac{e}{im}\mathbf{M}^{\mathrm{el}} + \mu^1\mathbf{M}^{\mathrm{mag}} + \mu^2\mathbf{M}^{\mathrm{mag}}\right)\cdot\boldsymbol{\varepsilon}, \quad (5)$$

where

$$\mathbf{M}^{\mathrm{el}} = \int d^3\mathbf{r}(\exp(-i\mathbf{k}\cdot\mathbf{r}/2) - \exp(i\mathbf{k}\cdot\mathbf{r}/2)) \times(\overline{\varphi_f(\mathbf{r})}\nabla\varphi_i(\mathbf{r}) - \varphi_i(\mathbf{r})\nabla\overline{\varphi_f(\mathbf{r})}), \quad (6)$$

$$^1\mathbf{M}^{\mathrm{mag}} = \int d^3\mathbf{r}\overline{\varphi_f(\mathbf{r})}[\mathbf{k}\times(\boldsymbol{\sigma}_1+\boldsymbol{\sigma}_2)]\varphi_i(\mathbf{r}) \times(\exp(-i\mathbf{k}\cdot\mathbf{r}/2)+\exp(i\mathbf{k}\cdot\mathbf{r}/2)), \quad (7)$$

$$^2\mathbf{M}^{\mathrm{mag}} = \int d^3\mathbf{r}\overline{\varphi_f(\mathbf{r})}[\mathbf{k}\times(\boldsymbol{\sigma}_1-\boldsymbol{\sigma}_2)]\varphi_i(\mathbf{r}) \times(\exp(-i\mathbf{k}\cdot\mathbf{r}/2)-\exp(i\mathbf{k}\cdot\mathbf{r}/2)), \quad (8)$$

where $^1\mathbf{M}^{\mathrm{mag}}$ is diagonal in spin $S = 1$, while $^2\mathbf{M}^{\mathrm{mag}}$ is off-diagonal. The wave functions $\varphi_i(\mathbf{r})$ and $\varphi_f(\mathbf{r})$ correspond to the motion of nucleons in the field of the Moscow potential or a meson-exchange potential describing their interaction. These functions are expanded in terms of partial waves (in even and odd l values for singlet and triplet waves, respectively); the resulting expressions for the amplitudes in (6)–(8) are very cumbersome, but they involve one-dimensional integrals [18] calculable numerically. Omitting the expressions for the differential cross sections from [18], we present only the necessary formulas for the analyzing power A_y, which is traditionally defined as

$$P_yA_y = \frac{\sigma_\uparrow-\sigma_\downarrow}{\sigma_\uparrow+\sigma_\downarrow},$$

where P_y is the degree of proton-beam polarization, while $\sigma_\uparrow$ and $\sigma_\downarrow$ are the cross sections for, respectively, the up and the down orientation of the initial-proton spin with respect to the y axis, which is orthogonal to the reaction plane in coplanar geometry.

The general expression for the analyzing power from [27],

$$A_y = \frac{\mathrm{tr}(\sigma_yA_{if}\overline{A_{if}})}{\mathrm{tr}(A_{if}\overline{A_{if}})}, \quad (9)$$

can be rewritten in the form [27]

$$A_y = i\frac{T_{12}^2-T_{22}^2}{T_{11}^2+T_{22}^2}. \quad (10)$$

Here, the subscripts 1 and 2 denote the projections +1/2 and –1/2 of the incident-nucleon spin onto the momentum direction and

$$T_{ab}^2 = \sum_{m_2m_3m_4}(\langle m_3m_4|\mathbf{M}|am_2\rangle\langle m_3m_4|\mathbf{M}|bm_2\rangle^* - \frac{1}{k^2}\langle m_3m_4|\mathbf{k}\cdot\mathbf{M}|am_2\rangle\langle m_3m_4|\mathbf{k}\cdot\mathbf{M}|bm_2\rangle^*, \quad (11)$$

where $\mathbf{k}$ is the photon momentum and where the basis $|m_1m_2\rangle$ is used instead of the basis $|Sm\rangle$.

3. DIFFERENTIAL CROSS SECTIONS AND ANALYZING POWER IN THE EXTENDED KINEMATICAL REGION

In our calculations, we employed the same nucleon–nucleon potentials as in [18] and, in addition, the refined version of the Moscow potential from [19] (the results based on this, last, version exhibit virtually no difference from those calculated by using the preceding version from [17, 18]).

Supplementing the results obtained in [18] for the beam energies of E_0 = 280, 350, and 450 MeV, we present here the differential cross sections for the process $pp \longrightarrow pp\gamma$ at E_0 = 400 and 450 MeV (see Figs. 1 and 2, respectively). On the basis of the overall pattern, we conclude that, as the beam energy increases from E_0 = 280 MeV, the sensitivity of the $pp \longrightarrow pp\gamma$ experiment being discussed to the type of nucleon–nucleon potential does not become monotonically higher. Indeed, a comparison of the results presented in Fig. 1 with the corresponding cross sections from [18] demonstrates that a high sensitivity (different shapes of the differential-cross-section curves for potentials of the two types, with the cross-section values at maxima being a few times greater for the Moscow potential than for meson-exchange potentials) that is peculiar to the energy of E_0 = 350 MeV and, especially, to the energy of E_0 = 450 MeV, is much lower than at the energy of E_0 = 400 MeV. At this, last, energy value, it is acceptable for only one pair of angles, $\theta_1 = 20°$ and $\theta_2 = 10°$, of the four pairs considered here.

The angular dependence of the differential cross section results from a complicated interference pattern. In the present study, we only conclude that the energy of E_0 = 400 MeV is not optimal for reliably testing the off-shell behavior of nucleon–nucleon potentials, not addressing the separate question of whether the above unfavorable feature of the cross section at E_0 = 400 MeV is associated with the fact that this is the energy at which the S-wave phase shift $\delta_0(E)$ for pp scattering passes through the value of 180° (0° if the phase shift is defined traditionally).

Let us now proceed to discuss the results presented in Fig. 2. At E_0 = 500 MeV—in contrast to the preceding case—the general sensitivity of the differential cross section for the process $pp \longrightarrow pp\gamma$ to the type of nucleon–nucleon potential is at approximately the same level as that found in [18] at E_0 = 450 MeV. This especially concerns the region of small angles—$\theta_1 = 10°$, $\theta_2 = 5°$ and $\theta_1 = 10°$, $\theta_2 = 10°$—where the cross section calculated with the Moscow potential at the maxima is approximately four times as large as that for meson-exchange potentials. Even for somewhat larger angles of $\theta_1 = 20°$ and $\theta_2 = 10°$, which can be more convenient experimentally, the cross-section ratio at the maxima is still quite large (2 to 3). Thus, we conclude that, at E_0 = 450 and 500 MeV, there are kinematical conditions—which can be varied, as is suggested by the data in Fig. 2 and by the relevant results from [18]—such that, on the basis of experimental data obtained under these conditions, it is possible to find out reliably which of the two qualitatively different types of nucleon–nucleon potential describes the actual interac-

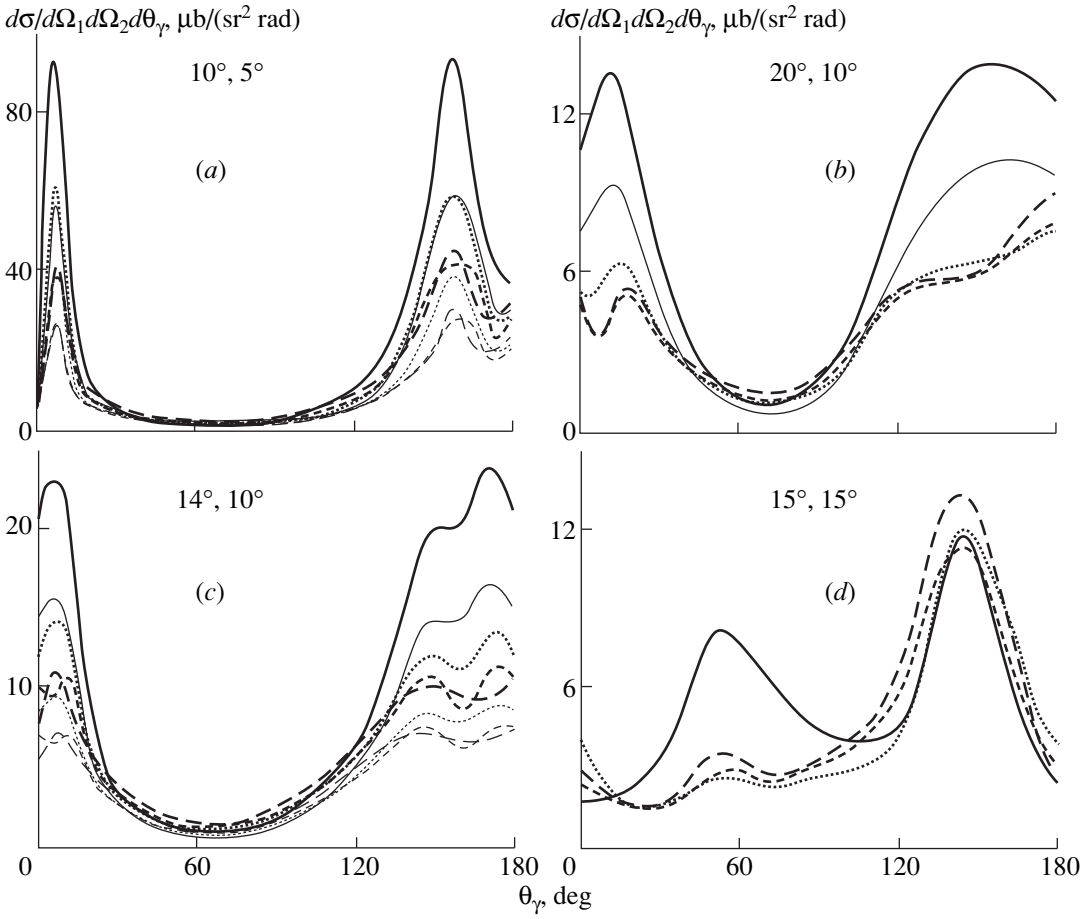

Fig. 1. Differential cross section as a function of the laboratory photon emission angle θ_γ with respect to the beam direction for the beam-proton energy of E_0 = 400 MeV at various angles θ_1 and θ_2 (indicated in the figures) of proton emission on the different sides of the beam direction. The results are presented for (solid curve) the Moscow potential, (dotted curve) the supersymmetric partner (the photon emission angle is reckoned ni the same direction at the angle θ_2) to the Moscow potential, (long dashes) the Paris potential, and (short dashes) the Hamada–Johnston potential). Thick and thin curves were computed, respectively, in the c.m. frame of two initial protons and in the c.m. frame of two final protons.

tion more adequately (in principle, such experimental data may also favor an intermediate version—that is, a nonlocal nucleon–nucleon potential [6, 28] for which the wave function to the left of a node is shallower than the wave function in the local potential).

The above possibility of distinguishing between the types of potential is based on the following two observations. The first is that, under the aforementioned kinematical conditions, the different types of nucleon–nucleon potential lead to different shapes of the differential cross section as a function of the photon emission angle θ_γ. The second is that the corresponding cross sections differ considerably in absolute value: at the maxima, the cross section obtained with the Moscow potential is a few times as large as that calculated with meson-exchange potentials. Our recommendation is to perform relevant measurements at E_0 = 450 and 500 MeV. Recently, Yasuda *et al.* [29] reported data on the process $pp \longrightarrow pp\gamma$ at E_0 = 390 MeV, but this is not an optimal energy value (see above). Moreover, these measurements were performed for the angles of $\theta_1 = \theta_2 = 26°$, which are also unfavorable: the energies of the emitted photons are not as high as is possible in this region, and meson-exchange currents and a virtual Δ isobar are expected to make maximum contributions (under the kinematical conditions proposed here and illustrated in Fig. 1, the role of these effects is negligible [23–25]). Despite all the above, the cross section measured for the forward hemisphere is nearly twice as large as that predicted in the theory involving meson-exchange nucleon–nucleon potentials and taking into account the important contribution of meson-exchange currents. This can be considered as preliminary evidence in favor of the Moscow potential, which yields larger cross-section values, and as a further motivation for performing the proposed experiments, which are thought to be free from the complicating effect of meson-exchange currents.

Two important comments are in order here.

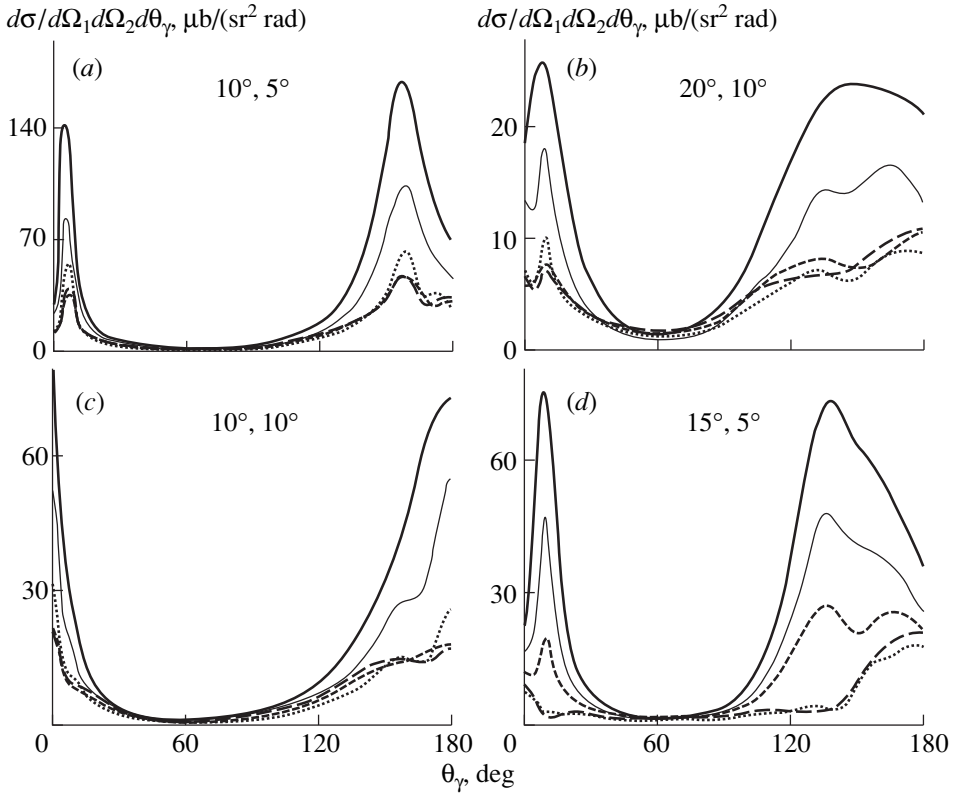

Fig. 2. As in Fig. 1, but for the laboratory beam-proton energy of E_0 = 500 MeV. When thin curves prove to be close to thick ones, the former are not presented.

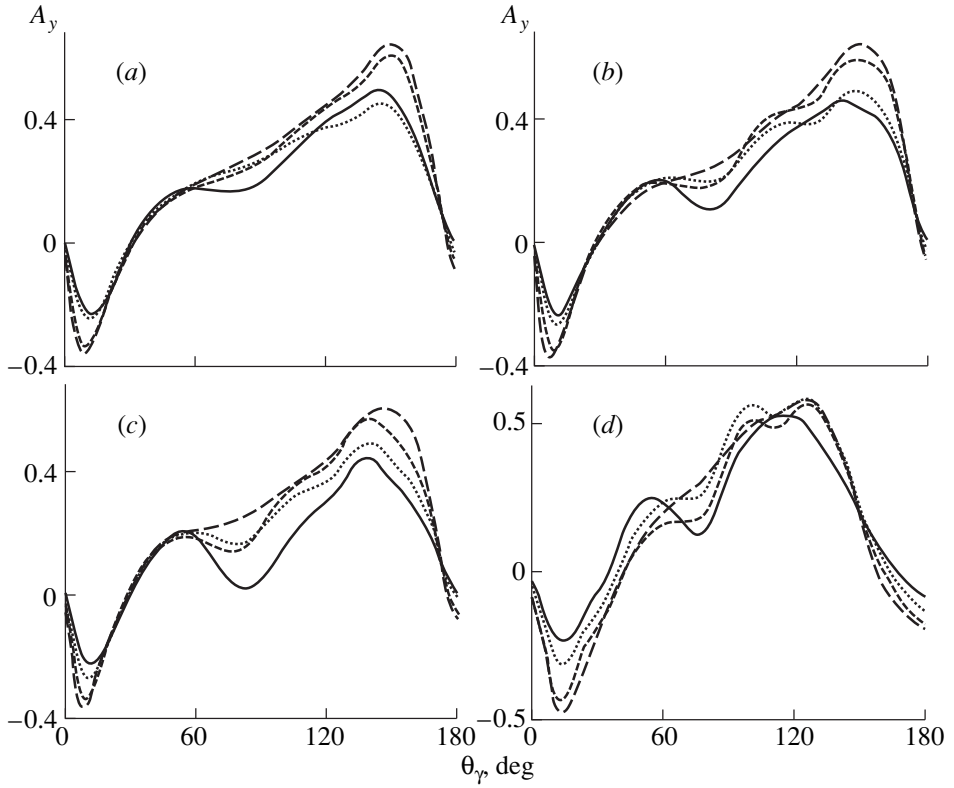

Fig. 3. Transverse analyzing power A_y as a function of the photon-emission angle θ_γ under various kinematical conditions: (*a*) E_0 = 350 MeV, θ_1 = 14°, and θ_2 = 10°; (*b*) E_0 = 400 MeV, θ_1 = 14°, and θ_2 = 10°; (*c*) E_0 = 450 MeV, θ_1 = 14°, and θ_2 = 10°; and (*d*) E_0 = 350 MeV, θ_1 = 20°, and θ_2 = 10°. The rest of the notation is identical to that in Fig. 1.

(i) Instead of measuring small values of the angle θ_2, which are inconvenient experimentally, the quantities E_1 and θ_γ or E_γ can be measured in coincidence at a given angle θ_1 (in coplanar geometry, there are three two-dimensional momenta in the final state, but only three of the six quantities are independent because of energy–momentum conservation). By selecting their values corresponding to the hardest photons, we directly meet the main criterion for choosing optimum kinematical conditions that ensure a high sensitivity to the type of nucleon–nucleon potential and which correspond to small values of θ_2.

(ii) That the broad energy range from 280 to 500 MeV is covered in our analysis makes it possible to trace carefully the changes that the distinctions between our nonrelativistic results derived in the c.m. frames of two initial- and final-state protons reveal in response to variations in the energy E_0. The data displayed in Figs. 1 and 2, together with the results from [18], show that, while being insignificant at E_0 = 280 MeV, the above difference increases with energy E_0—it is about 40% at E_0 = 500 MeV, which is a limiting energy for a nonrelativistic treatment. An analysis at higher energies would be uncertain for yet another reason: the nucleon–nucleon potentials compared here were fitted to the phase shifts up to E_0 = 300–400 MeV.

One more point is worthy of note. By and large, the contribution of meson-exchange currents and of an intermediate delta isobar increases with increasing beam energy [30], but it remains small in the kinematical region of the hardest photons even at E_0 = 500 MeV [25].

Let us now address the analyzing power. Figure 3 shows our results for it over the entire energy range E_0 = 350–500 MeV studied here. Of course, we are interested in the case of small angles θ_1 and θ_2. We see that, in contrast to the differential cross section, the analyzing power A_y is but weakly sensitive to the type of nucleon–nucleon potential. Spin effects are close for the two types of potential, so that the pursued difference is due entirely, as was indicated above, to the distinctions between the shapes of the radial dependences of the wave functions. Nevertheless, an experiment corresponding to Fig. 3 will be of importance—should the theory be confirmed—as a check upon the correctness of taking into account spin effects.

4. CONCLUSION

Although much attention has been given in the literature to the reaction $pp \longrightarrow pp\gamma$ and to allied processes—in addition to the studies reported in [23–27, 29, 30], we would like to mention the analysis of Gerasimov *et al.* [31], who considered the possibility of revealing a dibaryon resonance in the process $pp \longrightarrow pp\gamma\gamma$ [31]—reactions leading to hard-photon emission and occurring at energies somewhat higher than those used previously have not been studied experimentally throughout the 1990s. Earlier experiments explored small angles θ_1 and θ_2 at E_0 = 280 MeV [32] or the region of insufficiently hard photons (that is, large angles θ_1 and θ_2) at higher E_0 energies. At the same time, the aforementioned relevant experiments with hard photons could have been performed because proton energies of E_0 = 400–500 MeV had been available and because the required experimental procedures have been developed [32]. In all probability, the pessimistic conclusions of the previous theoretical studies [23–25]—these conclusions were summarized in [33]—that different meson-exchange potentials [1–4] cannot be distinguished on the basis of data on hard bremsstrahlung in the process $pp \longrightarrow pp\gamma$ (from the data in Figs. 1 and 2 and from the results presented in [18], we can see that the Paris potential [1] and the Hamada–Johnston potential [34], which was proposed much earlier, yield virtually indistinguishable results for the reaction in question) had a discouraging effect. We hope that our results, which extend the conceptual framework behind the problem of comparing different types of nucleon–nucleon potential, together with the new preliminary experimental result from [29], will inspire a renewed interest in the problem considered here.

In general, the validity of the Moscow potential and of the quark concepts behind it can be tested along various lines. In [18], the processes $d + \gamma \longrightarrow n + p$, $d + A \longrightarrow N^* + X$, and $^2\mathrm{H}(e, e'p)N^*$ at energies of a few GeV, (N^* is an orbitally excited nucleon corresponding to the s^4p^2 quark configuration in the deuteron [12]), were mentioned in this connection. In addition to the photodisintegration reaction $d + \gamma \longrightarrow n + p$ [34], the quasielastic-knockout processes $^2\mathrm{H}(p, 2p)n$ [35–37] and $^2\mathrm{H}(e, e'p)n$ [38–40] were also studied experimentally, the proton momentum distribution being measured up to the momentum of q = 0.7 GeV/c in the last case. In order to take consistently into account final-state interaction, which is very strong at high recoil momenta [41], so that the simplified treatment of this interaction in [35] is questionable, it is desirable to analyze these reactions by using the Moscow potential. Finally, a new partial-wave analysis extended to the energy of E_{lab} = 2.5 GeV was reported in [42]. This makes it possible to refine the results obtained in [20], where the phase shifts for nucleon–nucleon scattering were theoretically extrapolated to high energies on the basis of the Moscow potential with allowance for absorption, which increases with energy, and to test the stability of the partial-wave analysis itself at energies as high as some 2 GeV.

ACKNOWLEDGMENTS

We are grateful to Profs. S.B. Gerasimov and A.I. Titov for a stimulating discussion on the general potential of the $pp \longrightarrow pp\gamma$ method.

This work was supported in part by the Russian Foundation for Basic Research (project no. 96-02-18072).

REFERENCES

1. L. Lacombe, B. Loiseau, J. M. Richard, *et al.*, Phys. Rev. C **21**, 861 (1980).
2. R. Machleidt, K. Holinde, and Ch. Elster, Phys. Rep. **149**, 1 (1987).
3. V. G. J. Stoks, R. A. M. Klomp, C. P. F. Terheggen, and J. J. de Swart, Phys. Rev. C **49**, 2950 (1994).
4. R. B. Wiringa, V. G. J. Stoks, and R. Schiavilla, Phys. Rev. C **51**, 38 (1995).
5. H. Yinlu, M. Guangjin, L. Zhuxia, and Z. Yizhong, Phys. Rev. C **50**, 961 (1994); T. Gisiger and M. B. Paranjape, Phys. Rev. D **51**, 3034 (1995); G. Holzwarth and R. Machleidt, Phys. Rev. C **55**, 1088 (1997).
6. A. Faessler, F. Fernández, G. Lubeck, and K. Shimizu, Nucl. Phys. A **402**, 555 (1983); Y. Fujiwara and K. T. Hecht, Nucl. Phys. A **462**, 621 (1987); F. Myhrer and J. Wroldsen, Rev. Mod. Phys. **60**, 629 (1988).
7. I. T. Obukhovsky, V. G. Neudatchin, and Y. F. Smirnov, Phys. Lett. B **88**, 231 (1979); V. G. Neudachin, I. T. Obukhovskiĭ, and Yu. F. Smirnov, Fiz. Élem. Chastits At. Yadra **15**, 1165 (1984) [Sov. J. Part. Nucl. **15**, 519 (1984)].
8. M. Oka and S. Takeuchi, Phys. Rev. Lett. **63**, 1780 (1989); H. G. Weber, in *Proceedings of the XI International Seminar "Relativistic Nuclear Physics and QCD," Dubna, 1992*, Ed. by A. M. Baldin and V. V. Burov (Joint Institute for Nuclear Research, Dubna, 1994), p. 542; Z.-Y. Zhang, A. Faessler, U. Straub, and L. Ya. Glozman, Nucl. Phys. A **578**, 573 (1994).
9. A. M. Kusainov, V. G. Neudatchin, and I. T. Obukhovsky, Phys. Rev. C **44**, 2343 (1991).
10. V. G. Neudatchin, Yu. F. Smirnov, and R. Tamagaki, Prog. Theor. Phys. **58**, 1072 (1977); Yu. F. Smirnov, I. T. Obukhovskiĭ, V. G. Neudachin, and R. Tamagaki, Yad. Fiz. **27**, 860 (1978) [Sov. J. Nucl. Phys. **27**, 456 (1978)].
11. E. V. Kuznetsova, Yu. F. Smirnov, and Yu. M. Tchuvil'sky, Izv. Akad. Nauk Kaz. SSR, Ser. Fiz.-Mat., No. 2, 3 (1979).
12. L. Ya. Glozman, V. G. Neudatchin, and I. T. Obukhovsky, Phys. Rev. C **48**, 389 (1993).
13. L. Ya. Glozman and E. I. Kuchina, Phys. Rev. C **49**, 1149 (1994).
14. V. G. Neudatchin, I. T. Obukhovsky, and Yu. F. Smirnov, Phys. Lett. B **43**, 13 (1973); V. G. Neudatchin, I. T. Obukhovsky, V. I. Kukulin, and N. F. Golovanova, Phys. Rev. C **11**, 128 (1975).
15. V. I. Kukulin, V. N. Pomerantsev, V. M. Krasnopol'sky, and P. V. Sazonov, Phys. Lett. B **135**, 20 (1984); V. I. Kukulin, V. M. Krasnopol'skiĭ, V. N. Pomerantsev, and P. B. Sazonov, Yad. Fiz. **43**, 559 (1986) [Sov. J. Nucl. Phys. **43**, 355 (1986)].
16. V. M. Krasnopol'sky, V. I. Kukulin, and V. N. Pomerantsev, Izv. Akad. Nauk SSSR, Ser. Fiz. **51**, 898 (1987).
17. V. I. Kukulin and V. N. Pomerantsev, Prog. Theor. Phys. **88**, 159 (1992).
18. V. G. Neudatchin, N. A. Khokhlov, A. M. Shirokov, and V. A. Knyr, Yad. Fiz. **60**, 1086 (1997) [Phys. At. Nucl. **60**, 971 (1997)].
19. V. I. Kukulin, V. N. Pomerantsev, A. Faessler, *et al.*, Phys. Rev. C **57**, 535 (1998); **59**, 3021 (1999).
20. V. G. Neudatchin, N. P. Yudin, Yu. L. Dorodnykh, and I. T. Obukhovsky, Phys. Rev. C **43**, 2499 (1991).
21. M. P. Rekalo and I. M. Sitnik, Phys. Lett. B **356**, 434 (1995); B. Kuehn, C. F. Perdrisat, and E. A. Strokovsky, Yad. Fiz. **58**, 1898 (1995) [Phys. At. Nucl. **58**, 1795 (1995)]; A. P. Kobushkin, A. I. Syamtomov, and L. Ya. Glozman, Yad. Fiz. **59**, 833 (1996) [Phys. At. Nucl. **59**, 795 (1996)]; A. P. Kobushkin, A. I. Syamtomov, and L. Ya. Glozman, in *Proceedings of the 3rd International Symposium "Deuteron-95," Dubna, 1995*, Ed. by A. M. Baldin and V. V. Burov, JINR E2-96-100 (Dubna, 1996), p. 285; L. S. Azhgirey, Yu. T. Borzunov, E. V. Chernych, *et al.*, in *Proceedings of the XII International Seminar "Relativistic Nuclear Physics and QCD," Dubna, 1994*, Ed. by A. M. Baldin and V. V. Burov, JINR E1-2-97-79 (Dubna, 1997), p. 174; V. P. Ladygin, N. M. Piskunov, I. M. Sitnik, *et al.*, in *Proceedings of the XII International Seminar "Relativistic Nuclear Physics and QCD," Dubna, 1994*, Ed. by A. M. Baldin and V. V. Burov, JINR E1-2-97-79 (Dubna, 1997), p. 178; Yu. N. Uzikov, Fiz. Élem. Chastits At. Yadra **29**, 1405 (1998) [Phys. Part. Nucl. **29**, 583 (1998)].
22. D. Baye, Phys. Rev. Lett. **58**, 2738 (1987); F. Michel and G. Reidemeister, Z. Phys. A **329**, 385 (1988).
23. M. Jetter and H. W. Fearing, Phys. Rev. C **51**, 1666 (1995).
24. J. A. Eden and M. F. Gari, Phys. Lett. B **347**, 187 (1995); Phys. Rev. C **53**, 1102 (1996).
25. F. de Jong and K. Nakayama, Phys. Rev. C **52**, 2377 (1995).
26. G. H. Martinus, O. Scholten, and J. A. Tjon, Phys. Rev. C **56**, 2945 (1997).
27. R. L. Workman and H. W. Fearing, Phys. Rev. C **34**, 780 (1986).
28. P. J. Siemens and A. P. Vischer, Ann. Phys. (N.Y.) **238**, 129 (1995); **238**, 167 (1995).
29. K. Yasuda, H. Akiyoshi, T. Hotta, *et al.*, Phys. Rev. Lett. **82**, 4775 (1999).
30. V. V. Shklyar, B. Kampfer, B. L. Reznik, and A. I. Titov, Nucl. Phys. A **628**, 255 (1998).
31. S. B. Gerasimov, S. N. Ershov, and A. S. Khrykin, Yad. Fiz. **58**, 911 (1995) [Phys. At. Nucl. **58**, 844 (1995)].
32. K. Michaelian, P. Kitching, D. A. Hutcheon, *et al.*, Phys. Rev. D **41**, 2689 (1990); B. V. Przewoski, H. O. Meyer, H. Nann, *et al.*, Phys. Rev. C **45**, 2001 (1992).
33. H. W. Fearing, Phys. Rev. Lett. **81**, 758 (1998).
34. T. Hamada and L. D. Johnston, Nucl. Phys. **34**, 382 (1962).
35. P. Anthony, R. G. Arnold, J. Arrington, *et al.*, AIP Conf. Proc. **338**, 678 (1995); J. E. Belz, D. H. Potterveld, P. Anthony, *et al.*, Phys. Rev. Lett. **74**, 646 (1995); R. Crawford, J. Ahrens, S. Altieri, *et al.*, Nucl. Phys. A **603**, 303 (1996).
36. C. E. Perdrisat and V. Punjabi, Phys. Rev. C **42**, 1899 (1990); E. Cheng, C. F. Perdrisat, K. Beard, *et al.*, Phys. Lett. B **284**, 210 (1992); C. F. Perdrisat and V. Punjabi, in *Proceedings of the XI International Seminar "Relativistic Nuclear Physics and QCD," Dubna, 1992*, Ed. by

A. M. Baldin and V. V. Burov, JINR E1, 2-97-79 (Dubna, 1994), p. 491.

37. J. Erohuml, Z. Fodor, P. Koncz, *et al.*, Phys. Rev. C **50**, 2687 (1994).
38. L. L. Frankfurt, E. Piasetsky, M. Sargsyan, and M. I. Strikman, Phys. Rev. C **51**, 890 (1995).
39. J. F. J. van der Brand, Few-Body Syst., Suppl. **7**, 151 (1994); B. H. Schoch, Few-Body Syst., Suppl. **7**, 144 (1994); G. van der Steenhoven, in *Proceedings of the 3rd International Symposium "Deuteron-95," Dubna, 1995*, Ed. by A. M. Baldin and V. V. Burov, JINR E2-96-100 (Dubna, 1996), p. 291.
40. V. V. Kotlyar, Yu. P. Mel'nik, and A. V. Shebeko, Fiz. Élem. Chastits At. Yadra **26**, 192 (1995) [Phys. Part. Nucl. **26**, 79 (1995)].
41. A. Bianconi, S. Jeschonnek, N. N. Nikolaev, and B. G. Zacharov, Phys. Rev. C **53**, 576 (1996).
42. R. A. Arndt, C. H. Oh, I. I. Strakovsky, *et al.*, Phys. Rev. C **56**, 3005 (1997); M. Matsuda, Nucl. Phys. A **631**, 436c (1998).

Translated by R. Tyapaev

Physics of Atomic Nuclei, Vol. 63, No. 11, 2000, pp. 1903–1906. From Yadernaya Fizika, Vol. 63, No. 11, 2000, pp. 1996–1999.

NUCLEI
Theory

Form of the Long-Range Potential Observed in Fast-Neutron Scattering by Heavy Nuclei*

Yu. N. Pokotilovski**

Joint Institute for Nuclear Research, Dubna, Moscow oblast, 141980 Russia

Received May 26, 1999; in final form, July 23, 1999

Abstract—It is shown that the discrepancy between the results obtained for different neutron-energy ranges, when the neutron polarizability is derived from data on neutron scattering, can be removed if one assumes that a strong-interaction long-range potential of van der Waals ($\sim r^{-6}$) or of Casimir and Polder ($\sim r^{-7}$) is observed in fast-neutron scattering. This strong-interaction long-range potential possibly has some experimental confirmation in elastic *pp* scattering. *© 2000 MAIK "Nauka/Interperiodica".*

There is a strong contradiction between the values of the neutron electric polarizability α_n that are obtained from experiments on elastic neutron scattering by heavy nuclei in different energy ranges: $\alpha_n \le 2 \times 10^{-3}$ fm^3 from experiments at neutron energies $E_n \le 40$ keV, and $\alpha_n \ge 10^{-1}$ fm^3 from measurements with neutrons in the energy range from about 0.5 to a few MeV. The first results do not contradict modern theoretical models [1], in which $\alpha_n \sim 1 \times 10^{-3}$ fm^3, but the second one seems overly large, exceeding expectations by two orders of magnitude.

Measurements of the neutron electric polarizability at low energies of scattered neutrons are based on the specific form of the Born amplitude for neutron scattering in the r^{-4} polarization potential

$$U_{\rm pol} = -\alpha_n (Ze)^2/2r^4, \text{ for } r > R; \quad U_{\rm pol} = 0, \text{ for } r < R, \tag{1}$$

where Ze is nuclear electric charge and R is the electric radius of the nucleus. For the sake of simplicity, we will further set long-range potentials to zero within nuclei, since this does not change significantly the results of this consideration. In the Born approximation, the scattering amplitude for the potential (1) has the form

$$f_{\rm pol} = \alpha_n \left(\frac{Ze}{\hbar}\right)^2 \frac{m}{2R}\left[\frac{\sin x}{x} + \cos x - x\int_x^\infty \frac{\sin t}{t}dt\right], \tag{2}$$

where m is the neutron mass and $x = qR$, q being a neutron scattering vector. In the limit $x \ll 1$, we have

$$f_{\rm pol} = \alpha_n \left(\frac{Ze}{\hbar}\right)^2 \frac{m}{R}\left[1 - \frac{\pi}{4}x + \frac{1}{6}x^2 + O(x^4)\right]. \tag{3}$$

It was shown by Thaler [2] that, owing to the second term in the neutron polarization scattering amplitude—this term is linear in q—the differential cross section for neutron–nucleus scattering must contain a term linear in the neutron wave vector k because of the interference of the nuclear and polarization amplitudes. The angular distribution of neutrons,

$$\sigma(\theta) = \frac{\sigma_t}{4\pi}[1 + \omega_1 P_1(\cos\theta) + \omega_2 P_2(\cos\theta) + \ldots], \tag{4}$$

involves the quantity

$$\omega_1 = -\alpha_n \frac{\pi}{5}\left(\frac{Ze}{\hbar}\right)^2 \frac{2m}{a}k, \tag{5}$$

which is linear in k (a is the neutron scattering length).

The measurements of the angular distribution of neutrons scattered by heavy nuclei [3] in the energy range 0.6–26 keV, together with the earlier measurements [4] in the energy range 50–160 keV [4], yielded $\alpha_n \le 10^{-2}$ fm^3.

It is evident that, because of neutron polarizability, the total neutron–nucleus cross section must contain a term linear in k:

$$\sigma_s(k) = \sigma_0 + ak + bk^2 + \ldots . \tag{6}$$

Precise measurements of total neutron cross sections and the coherent scattering lengths for Pb and Bi [5] yielded

$$\alpha_n = (0.8 \pm 1.0) \times 10^{-3} \text{ fm}^3. \tag{7}$$

The result of the measurements of the total cross section for neutron scattering by heavy nuclei in the energy region up to 40 keV [6, 7] resulted in

$$\alpha_n = (1.20 \pm 0.15 \pm 0.20) \times 10^{-3} \text{ fm}^3. \tag{8}$$

A reconsideration [8] of the experiments reported in [6, 7] led to the conclusion that $\alpha_n \le 2 \times 10^{-3}$ fm^3.

On the other hand, neutron scattering by heavy nuclei in the MeV energy range demonstrates signifi-

* This article was submitted by the author in English.

** e-mail: pokot@nf.jinr.ru

cant deviations from the results of optical-model calculations with allowance for Schwinger (spin–orbit) scattering. For example, the cross sections measured in [9] are systematically larger than the calculated cross sections at the smallest angles. The authors of [9] did not propose any explanation of this disagreement, and the measurements were not continued.

In a series of experiments and careful optical-model calculations, the authors of [10] showed that the great variety of data on neutron scattering in the MeV energy range (total cross sections, angular distributions, and especially small-angle scattering) are described much better if, in addition to the general short-range Woods–Saxon potential and the Schwinger interaction, the polarization term with a neutron polarizability factor as large as $\alpha_n \simeq (1\text{–}2) \times 10^{-1}$ fm^3 is included in the potential of neutron–nucleus interaction, which is two orders of magnitude greater than the value expected from reasonable calculations [1] and the measured restrictions [5–7].

What is the way to reconcile these two contradicting results? It is possible that some more refined model of neutron–nucleus interaction allowing for the Schwinger term and "reasonable" neutron polarizability is able to describe data in the MeV energy range. However, it may be possible that some other potential of the $\sim r^{-n}$ type with $n > 4$—for example, with $n = 6$ (van der Waals) or $n = 7$ (Casimir–Polder) affects neutron scattering in the MeV energy range.

The possibility of a strong long-range interaction between hadrons was discussed two decades ago by using various approaches (see, for example, [11] and references therein) with mostly negative results and without any firm final conclusion. On the other hand, there are persistent indications of a strong attractive potential of the r^{-n} form with n between 6 and 7 (see [12] and references therein) that follow from a sophisticated analysis of elastic pp scattering in the MeV energy range. A similar long-range strong interaction might be observed in neutron–nucleus scattering in the MeV energy range in just the same way as it was (possibly) observed between hadrons.

It turns out that, in the experiments that were reported in [3, 5–7] and which were performed at low energies (more precisely, at $x \ll 1$), these potentials could hardly be observed. The reason for this is that the only signal of the long-range interaction at low energies ($x \ll 1$) that distinguishes it from a short-range interaction is a noneven term in the expansion of the first-order Born amplitude.

In the first Born approximation, the scattering amplitudes for long-range potentials of the form

$$U(r) = -U_R\left(\frac{R}{r}\right)^n, \text{ for } r > R; \qquad U(r) = 0, \text{ for } r < R, \tag{9}$$

where R is the radius of the nucleus, can be represented as

$$f_5 = \frac{2mU_R R^3}{\hbar^2} \times \left[\frac{\sin x}{3x} + \frac{\cos x}{6} - x\frac{\sin x}{6} - \frac{x^2}{6}\int_x^\infty \frac{\cos t}{t}dt\right] \tag{10}$$

for $n = 5$, as

$$f_6 = \frac{2mU_R R^3}{\hbar^2}\left[\frac{\sin x}{4x} + \frac{\cos x}{12} - x\frac{\sin x}{24} - x^2\frac{\cos x}{24} + \frac{x^3}{24}\int_x^\infty \frac{\sin t}{t}dt\right] \tag{11}$$

for $n = 6$, and as

$$f_7 = \frac{2mU_R R^3}{\hbar^2}\left[\frac{\sin x}{5x} + \frac{\cos x}{20} - x\frac{\sin x}{60} - x^2\frac{\cos x}{120} + x^3\frac{\sin x}{120} + \frac{x^4}{120}\int_x^\infty \frac{\cos t}{t}dt\right] \tag{12}$$

for $n = 7$.

In the limit $x \ll 1$, these amplitudes are

$$f_5(x \ll 1) = \frac{2mU_R R^3}{\hbar^2}\left[\frac{1}{2} - \left(\frac{11}{36} - \frac{\ln\gamma}{6}\right)x^2 + \frac{1}{6}x^2\ln x + O(x^4)\right], \tag{13}$$

$$f_6(x \ll 1) = \frac{2mU_R R^3}{\hbar^2}\left[\frac{1}{3} - \frac{1}{6}x^2 + \frac{\pi}{48}x^3 + \frac{1}{80}x^4 + O(x^6)\right], \tag{14}$$

$$f_7(x \ll 1) = \frac{2mU_R R^3}{\hbar^2}\left[\frac{1}{4} - \frac{1}{12}x^2 + \left(\frac{137}{720} - \frac{\ln\gamma}{120}\right)x^4 - \frac{1}{120}x^4\ln x + O(x^6)\right], \tag{15}$$

where $\gamma \simeq 1.781$ is the Euler constant. It can be seen that the only noneven power of the x term in the expansion of the Born amplitude for an r^{-5} potential is $x^2\ln x$. For an r^{-6} potential, the only odd term is x^3; and the term characteristic of a long-range r^{-7} interaction is $x^4\ln x$. The short-range potentials yield only even powers of x. For the potential of an r^{-2n} form, expansion of the Born amplitude yields the single odd term proportional to x^{2n-3}; for the potential of an $r^{-(2n+1)}$ form, the noneven term

is $x^{2(n-1)}\ln x$. Quantitative estimations for $x = 0.2$ yield the result that these terms are more than two orders of magnitude lower than the linear term in the decomposition of the Born amplitude for an r^{-4} potential. Therefore, in low-energy experiments ($x \ll 1$), it is virtually impossible to recognize the presence of an r^{-n} long-range potential with $n \geq 5$, even if it is as large as two orders of magnitude greater than the potential due to neutron polarizability (1) with $\alpha_n \simeq 10^{-3}$ fm^3.

The scattering amplitudes in the first Born approximation (3) and (10)–(12) for $n = 4$–7 generally behave similarly in the range $x < 5$ where the amplitudes are not small, differing only by a factor which does not change significantly. The same is true for the first five to six Born scattering phases for these potentials in the MeV neutron energy range. This means that it is possible that the large potential of the r^{-4} type inferred from fast-neutron scattering in [10] may in fact be the potential r^{-n} with $n = 6$ or $n = 7$ but of larger magnitude at $r = R$.

Better confirmation or rejection of this viewpoint requires detailed computations with the most flexible nuclear optical potential and inclusion of long-range potentials of the r^{-n} type with different n in order to find out what kind of long-range potential better satisfies the description of all the data on fast-neutron scattering. These computations are now in progress. The tentative calculations of neutron-scattering cross sections in the MeV energy range for the Woods–Saxon potential with the addition of long-range potentials r^{-n} with different n between 4 and 7 yield a small difference in the form of angular distributions and total cross section.

For example, the figure illustrates the result of calculation of the neutron elastic scattering cross section for the Woods–Saxon potential with the addition of long-range potential (9) with $n = 4$ (corresponding to neutron electric polarizability $\alpha_n = 0.15$ fm^3 inferred from the experiments [10]) and $n = 6$. The value U_R (14) for the latter was chosen to reach the best similarity in the behavior of the elastic cross section for these potentials.

$d\sigma_{WS}/d\Omega$ is the cross section for the Woods–Saxon potential with parameters pertinent to the ^{208}Pb nucleus [10], i.e., $V_0 = 43.2$ MeV, $W_0 = 3.8$ MeV, $V_{SO} = 11.7$ MeV (the depths of the real, imaginary, and spin–orbit parts of the potential, respectively); $R_0 = R_0' = 7.64$ fm is the radius of the real, imaginary, and spin–orbit components; $r_0 = r_0' = 1.29$ fm; the diffusivity of the real and spin–orbit components $a = 0.425$ fm; and the diffusivity of the imaginary component $a' = 0.475$ fm.

$d\sigma_4/d\Omega$ is the cross section for the Woods–Saxon potential plus the potential of (9) with $n = 4$ and $U_R = 213$ keV, and $d\sigma_6/d\Omega$ is the cross section for the Woods–Saxon potential plus the potential of (9) with $n = 6$ and $U_R = 300$ keV.

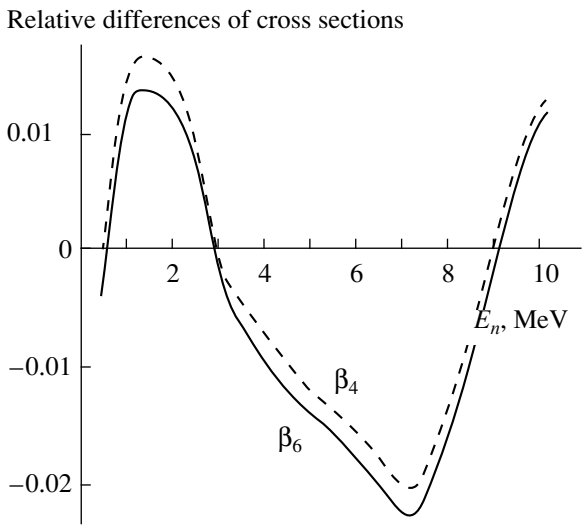

Energy dependence of the relative effects of long-range interactions in elastic-scattering cross section $\beta_4 = \left(\frac{d\sigma_{WS}}{d\Omega} - \frac{d\sigma_4}{d\Omega}\right) \Big/ \frac{d\sigma_{WS}}{d\Omega}$ and $\beta_6 = \left(\frac{d\sigma_{WS}}{d\Omega} - \frac{d\sigma_6}{d\Omega}\right) \Big/ \frac{d\sigma_{WS}}{d\Omega}$. The scattering angle is $\theta = 5°$.

It is seen that the relative difference of the effect that these two long-range potentials have on cross sections is very small.

ACKNOWLEDGMENTS

I am grateful Mrs. S.V. Konnova and Dr. V.V. Lyuboshitz for their assistance in the computations.

REFERENCES

1. G. Breit and M. L. Rustgi, Phys. Rev. **114**, 830 (1959); A. Kanazawa, Nucl. Phys. **24**, 524 (1961); P. Hecking and G. F. Bertsch, Phys. Lett. B **99**, 237 (1981); H. Krivine and J. Navarro, Phys. Lett. B **171**, 331 (1986); V. Bernard, B. Hiller, and W. Weise, Phys. Lett. B **205**, 16 (1988); R. Weiner and W. Weise, Phys. Lett. B **159**, 85 (1985); G. G. Bunatyan, Yad. Fiz. **55**, 3196 (1992) [Sov. J. Nucl. Phys. **55**, 1781 (1992)].
2. R. M. Thaler, Phys. Rev. **114**, 827 (1959).
3. Yu. A. Alexandrov, G. S. Samosvat, Z. Sereeter, and Tsoi Gen Sor, Pis'ma Zh. Éksp. Teor. Fiz. **4**, 196 (1966) [JETP Lett. **4**, 134 (1966)].
4. M. D. Goldberg, V. M. May, and J. R. Stehn, BNL-400 (1962, 2nd ed.), Vol. II.
5. L. Koester, W. Washkowski, and J. Meyer, Z. Phys. A **329**, 229 (1988).
6. J. Schmiedmayer, H. Rauch, and P. Riehs, Phys. Rev. Lett. **61**, 1065 (1988).
7. J. Schmiedmayer, P. Riehs, J. A. Harvey, and N. W. Hill, Phys. Rev. Lett. **66**, 1015 (1991).
8. V. G. Nikolenko and A. B. Popov, Preprint No. E3-92-254, OIYaI (Joint Institute for Nuclear Research, Dubna,

1992); in *Proceedings of the 8th International Symposium on Capture Gamma Ray Spectroscopy, Frieburg, 1993*, p. 812; T. L. Enik, L. V. Mitsyna, V. G. Nikolenko, *et al.*, Yad. Fiz. **60**, 648 (1997) [Phys. At. Nucl. **60**, 567 (1997)].

9. L. Drigo, C. Manduchi, G. Moschini, *et al.*, Nuovo Cimento A **13**, 867 (1973); V. Giordano, C. Manduchi, M. T. Russo-Manduchi, and G. F. Segato, Nucl. Phys. A **302**, 83 (1978).
10. G. V. Anikin and I. I. Kotukhov, Yad. Fiz. **12**, 1121 (1970) [Sov. J. Nucl. Phys. **12**, 614 (1971)]; Yad. Fiz. **14**, 269 (1971) [Sov. J. Nucl. Phys. **14**, 152 (1972)]; At. Énerg. **60**, 51, 54 (1986); in *Proceedings of the International Conference on Neutron Physics, Kiev, 1987*, Vol. 2, p. 139; Yad. Fiz. **49**, 101 (1989) [Sov. J. Nucl. Phys. **49**, 64 (1989)]; I. I. Kotukhov, Doctoral Dissertation in Mathematical Physics (Obninsk, 1990).
11. G. Feinberg and J. Sucher, Phys. Rev. D **20**, 1717 (1979).
12. T. Sawada, Int. J. Mod. Phys. **11**, 5365 (1996).

Physics of Atomic Nuclei, Vol. 63, No. 11, 2000, pp. 1907–1909. Translated from Yadernaya Fizika, Vol. 63, No. 11, 2000, pp. 2000–2002.

NUCLEI
Theory

Inelastic p^4He Interaction in Nonequilibrium Cosmological Nucleosynthesis

E. V. Sedelnikov

Institute of Mathematical Modeling, Russian Academy of Sciences, Miusskaya pl. 4a, Moscow, 125047 Russia

Received April 2, 1999; in final form, September 30, 1999

Abstract—The current status of experimental data on inelastic p^4He scattering is reviewed, and the cross sections for respective channels are roughly estimated. These estimates make it possible to compute the amounts of ^{3}He, ^{3}H, and *d* nuclei produced in nonequilibrium cosmological nucleosynthesis to a precision of 10%. Investigation of inelastic p^4He scattering by using the method of accelerated ^{4}He nuclei at $E_p \sim 75$ MeV is of particular interest for cosmological applications because this allows one to achieve a higher precision in calculating nonequilibrium cosmological nucleosynthesis.

1. INTRODUCTION

An extra production of light nuclei in the interactions of high-energy protons and antiprotons with a cosmological plasma in the early Universe is one of the problems that arises in investigating nonequilibrium cosmological nucleosynthesis. Here, a particle is considered as a nonequilibrium object if its energy far exceeds the mean thermal energy of particles of the cosmological plasma in equilibrium.

A high-energy proton or antiproton interacting with the cosmological plasma, which consists predominantly of protons and ^{4}He nuclei, generates a secondary proton cascade. Secondary protons, as well as the primary proton, break up ^{4}He nuclei, thereby producing nonequilibrium ^{3}He, ^{3}H, and *d* nuclei, which may generate Li and Be nuclei through collisions with primary ^{4}He nuclei. That light nuclei are additionally formed by the above mechanism can be used to obtain information about the physics of the early Universe. For example, constraints on the parameters of the Grand Unified Theories [1] and on the concentration of the primary black holes [2] can be derived from the requirement that the number of deuterons and the number of ^{3}He nuclei produced in nonequilibrium nucleosynthesis be consistent with their abundances in the present Universe. At the same time, nonequilibrium cosmological nucleosynthesis can be considered as the possible source of evolution of the chemical composition in the early Universe. As a result, there may arise either small corrections to the initial concentrations or a significant effect distorting the outcome of primary nucleosynthesis to the extent that a new chemical composition of the early Universe is formed. The above assumption presents an as-yet-unresolved problem.

As a continuation of investigations into nonequilibrium cosmological nucleosynthesis that were performed in [3], new calculations taking into account currently available experimental data were reported in [4] for nucleosynthesis processes featuring protons and antiprotons. (The effect of electromagnetic processes on nonequilibrium cosmological nucleosynthesis is not considered here because this requires a dedicated analysis of features peculiar to such processes.) The energetic-proton-induced breakup of a ^{4}He nucleus is a key process in nonequilibrium cosmological nucleosynthesis. It was shown in [4] that, at primary-particle energies in the region $E_{p,\bar{p}} > 2$ GeV, ^{3}He, ^{3}H, and *d* nuclei are produced primarily by the secondary proton cascade developing in the cosmological plasma, the probability of ^{4}He breakup induced by this cascade taking maximum values at $E \sim 75$ MeV. The present analysis revealed that the uncertainties in computing the numbers of product nuclei depend primarily on the error in determining the cross sections for the channels of inelastic p^4He interaction and that these uncertainties are estimated at 8–10%.

2. MODEL OF INELASTIC p^4He INTERACTION

Experimental data on the cross sections for inelastic channels of p^4He scattering are displayed in the figure.

The reaction $p^4\text{He} \longrightarrow d^3\text{He}$ has received the most comprehensive study. A vast body of consistent and precise data is available for this channel, ensuring a reliable fit to the relevant cross section.

The experimental data reported in [10, 12] make it possible to describe accurately the reactions $p^4\text{He} \longrightarrow {}^3\text{He}X$, $p^4\text{He} \longrightarrow dX$, and $p^4\text{He} \longrightarrow ddX$ at energies in the region $E_p > 0.2$ GeV. In these experiments, the method that employed accelerated ^{4}He nuclei incident on a proton target permitted an efficient separation of the channels of inelastic p^4He interaction. (In the present study, we everywhere quote relevant kinetic

1063-7788/00/6311-1907$20.00

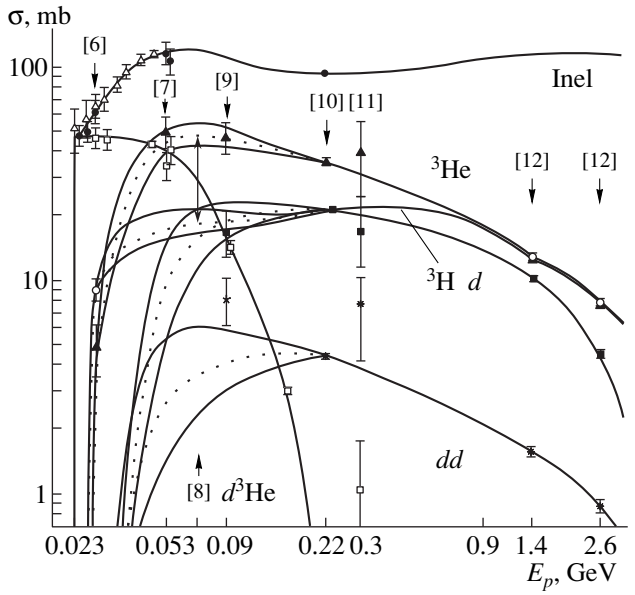

Cross sections for the inelastic channels of p^4He interaction. Points represent experimental data on (closed circles) the total inelastic cross section and on the (open boxes) d^3He, (closed triangles) ^{3}He*X*, (open circles) ^{3}H*X*, (closed boxes) *dX*, and (asterisks) *ddX* channels. The data from [5] on the total inelastic cross sections are shown by open triangles. An arrow near a reference to experimental data indicates that the quoted study contains data on a few channels at the corresponding proton energy. The remaining data were borrowed from [13]. For energies in the region $E_p < 0.22$ GeV, three types of approximation of the cross section—upper and lower bounds (solid curves) and the basic version (dotted curves) are shown for all channels under study, with the exception of $p^4\text{He} \longrightarrow d^3\text{He}$.

energies of protons in the rest frame of the nucleus.) More recent data on the yields of ^{3}He and ^{3}H nuclei (not shown in the figure)—they are summarized in the review article of Meyer [13]—are much less accurate and contradict the results reported in [10, 12]. The situation around the yield of tritium is less clear. An attempt was made in [13] to develop a model for inelastic p^4He interaction on the basis of available data. In estimating relevant cross sections, it was additionally assumed that $\sigma_{^3\text{He}}/\sigma_{^3\text{H}} = \sigma_{pn}/\sigma_{pp}$. This assumption leads to an excess of the yield of ^{3}H over the yield of ^{3}He in the energy range 0.6–2.7 GeV, where $\sigma_{pn} < \sigma_{pp}$ [14]. However, this prediction is inconsistent with the new data from [10, 12]. It would be of interest to test the above relation at $E_p \sim 0.9$ GeV (an energy value at which the ratio σ_{pn}/σ_{pp} approaches its minimum) in an experiment similar to that described in [8] or in an experiment based on the method of accelerated ^{4}He nuclei. The calculations show that the number of ^{3}He nuclei generated in the processes of nonequilibrium cosmological nucleosynthesis is less affected by small uncertainties in the cross section for the reaction $p^4\text{He} \longrightarrow {}^3\text{H}X$ in the energy range $E_p \sim 0.6$–1.4 GeV than by similar uncertainties at energies in the region $E_p < 0.2$ GeV.

At energies below 0.2 GeV data summarized in [13] do not exhaust the entire body of available experimental information: there are also data of Sourkes *et al.* [5] on the total cross sections for inelastic scattering and data of Pasechnik *et al.* [8], who measured the ratio $\dfrac{\sigma_{p^4\text{He}\to{}^3\text{He}X}}{\sigma_{p^4\text{He}\to{}^3\text{H}X}}$ to a precision higher than in any other study (the reactions $p^4\text{He} \longrightarrow {}^3\text{He}X$ and $p^4\text{He} \longrightarrow {}^3\text{H}X$ were explored there under the same kinematical conditions); however, the absolute cross-section values are not presented in [8] because they were measured less precisely. The results obtained in [8, 10, 12] allow one to construct a reliable fit to the ratio $k(E) = \dfrac{\sigma_{p^4\text{He}\to{}^3\text{He}X}}{\sigma_{p^4\text{He}\to{}^3\text{H}X}}$ and to use it in the following to evaluate the relevant cross sections. The function $k(E)$ determined from the data at energies in excess of 70 MeV can be extrapolated to the region of lower energies, as low as those at which near-threshold effects come into play. In estimating the cross sections for the reactions $p^4\text{He} \longrightarrow {}^3\text{He}X$ and $p^4\text{He} \longrightarrow {}^3\text{H}X$ in the near-threshold domain, it is therefore reasonable to rely on the data from [6], which still remain the most precise in this domain. The total inelastic cross section, that was estimated in [6] as the sum of all measured cross sections for individual channels agrees well with data from [5].

The cross section for the process $p^4\text{He} \longrightarrow {}^3\text{He}X$ in the energy range $E_p \sim 40$–100 MeV was derived from the data that were reported [7, 9] and which were revised and corrected in [13]. The corrected data of Cairns *et al.* [7] are consistent with the results obtained in [5].

Experimental data on the reactions $p^4\text{He} \longrightarrow dX$ and $p^4\text{He} \longrightarrow ddX$ for energies in the region $E_p <$ 0.2 GeV can be found only in [9]. The experiments reported in [9] and in [11] were performed by using the same facility (Wilson chamber) under the same conditions. As can be seen from the figure, the cross section for the reaction $p^4\text{He} \longrightarrow ddX$ as determined in [11] proved to be larger than what was obtained from the more accurate data presented in [10]. In view of the above, there is every reason to believe that same is true for the data from [9]. In estimating the cross sections for the reactions $p^4\text{He} \longrightarrow dX$ and $p^4\text{He} \longrightarrow ddX$, it is reasonable to use the cross section for the reaction $p^4\text{He} \longrightarrow 3p2n$ (not shown in the figure) and to consider that, at energies below the pion-production threshold, the sum of the five cross sections discussed above must be equal to the total inelastic cross section extracted from the data obtained in [5].

The results of the calculations based on the above considerations on inelastic p^4He scattering, which take into account available experimental data, are presented

in the figure (curves). For proton energies in excess of E_p = 0.22 GeV, the cross section for the reaction $p^4\mathrm{He} \longrightarrow d^3\mathrm{He}$, as well as those for other channels, was fitted unambiguously. For energies below this value, we give upper and lower bounds on the cross sections for various channels of inelastic p^4He scattering and present the basic version of the approximation of the cross sections. The estimates of the cross sections for the reactions $p^4\mathrm{He} \longrightarrow {}^3\mathrm{He}X$ and $p^4\mathrm{He} \longrightarrow {}^3\mathrm{H}X$ are correlated: if some type of estimate is adopted for one reaction (for example, an upper bound), then the same type must be used for the other reaction. The main source of uncertainties for $E_p < 0.2$ GeV is associated with the estimates of the cross sections for the reactions $p^4\mathrm{He} \longrightarrow dX$ and $p^4\mathrm{He} \longrightarrow ddX$. However, the fact that the channel $p^4\mathrm{He} \longrightarrow d^3\mathrm{He}$ makes a leading contribution to the inelastic cross section at energies in the region $E_p < 80$ MeV significantly reduces the error in the total yield of deuterium and ^{3}He in p^4He scattering at low energies.

The proposed approximations of the cross sections for the channels discussed above differ substantially from one another. Nevertheless, they make it possible to compute the number of nuclei generated in nonequilibrium cosmological nucleosynthesis to a precision of 10% owing to a large contribution of the thoroughly studied channel $p^4\mathrm{He} \longrightarrow d^3\mathrm{He}$ at low energies. It should be emphasized that the energy range $E_p \sim 40$–100 MeV, where the uncertainties in the estimates of the cross sections for the channels of inelastic p^4He scattering are quite large, is of prime interest for cosmological applications because the probability of the breakup of the ^{4}He nucleus by a proton from the secondary cascade reaches a maximum in this domain (at $E \sim 75$ MeV) [4].

Investigation of the channels of the inelastic breakup of the ^{4}He nucleus at energies in the region $E_p < 0.2$ GeV is of interest for exploring the chain of subsequent nuclear reactions of nonequilibrium cosmological nucleosynthesis. Nonequilibrium fragments (^{3}He, ^{3}H, and d) can interact with ^{4}He nuclei, thereby producing ^{6,7}Li and ^{7}Be nuclei, whose yields are determined by the energy spectra of outgoing fragments. For the most part, these fragments appear to be spectators undergoing thermalization within a short time. For this reason, investigation of the high-momentum tail of the distribution of fragments by the method used in [12] at 1.4 and 2.6 GeV is of particular interest.

3. CONCLUSION

The proposed estimates of the cross sections for the inelastic channels of p^4He interaction permit computing, to a precision of about 10%, the yields of ^{3}He, ^{3}H, and d nuclei originating from nonequilibrium cosmological nucleosynthesis triggered by high-energy protons and antiprotons ($E_p > 0.2$ GeV). The uncertainties are due to the absence of reliable experimental data on the inelastic channels of p^4He interaction for energies $E_p < 0.2$ GeV. Experiments with accelerated ^{4}He nuclei at $E_p \sim 75$ MeV could remedy this flaw, whereby the accuracy in computing the yields of light elements from nonequilibrium cosmological nucleosynthesis would be improved considerably.

ACKNOWLEDGMENTS

I am grateful to V.I. Kukulin and L.A. Kondratyuk for stimulating discussions and assistance in work.

REFERENCES

1. M. Yu. Khlopov and V. M. Chechetkin, Fiz. Élem. Chastits At. Yadra **18**, 627 (1987) [Sov. J. Part. Nucl. **18**, 267 (1987)]; M. Yu. Khlopov and A. D. Linde, Phys. Lett. B **138**, 265 (1984); V. M. Chechetkin, M. Yu. Khlopov, M. G. Sapozhnikov, and Ya. B. Zeldovich, Phys. Lett. B **118**, 329 (1982); V. M. Chechetkin, M. Yu. Khlopov, and M. G. Sapozhnikov, Riv. Nuovo Cimento **5**, 1 (1982).
2. Ya. B. Zel'dovich, A. A. Starobinskiĭ, M. Yu. Khlopov, and V. M. Chechetkin, Pis'ma Astron. Zh. **3**, 208 (1977) [Sov. Astron. Lett. **3**, 110 (1977)]; E. V. Sedel'nikov, Pis'ma Astron. Zh. **22**, 889 (1996) [Astron. Lett. **22**, 797 (1996)].
3. Yu. L. Levitan, I. M. Sobol', M. Yu. Khlopov, and V. M. Chechetkin, Yad. Fiz. **47**, 168 (1988) [Sov. J. Nucl. Phys. **47**, 109 (1988)]; M. Yu. Khlopov, Yu. L. Levitan, E. V. Sedel'nikov, and I. M. Sobol', Yad. Fiz. **57**, 1466 (1994) [Phys. At. Nucl. **57**, 1393 (1994)]; E. V. Sedel'nikov, S. S. Filippov, and M. Yu. Khlopov, Yad. Fiz. **58**, 280 (1995) [Phys. At. Nucl. **58**, 235 (1995)]; E. V. Sedel'nikov, Yu. L. Levitan, and I. M. Sobol', Preprint No. 1, IMM RAN (Institute of Mathematical Modeling, Russian Academy of Sciences, 1996).
4. E. V. Sedel'nikov, Pis'ma Zh. Éksp. Teor. Fiz. **69**, 609 (1999) [JETP Lett. **69**, 645 (1999)].
5. A. M. Sourkes, A. Houdayer, W. T. H. van Oers, *et al.*, Phys. Rev. C **13**, 451 (1976).
6. A. F. Wickersham, Phys. Rev. **107**, 1050 (1957).
7. D. J. Cairns, T. C. Griffith, G. J. Lush, *et al.*, Nucl. Phys. **60**, 369 (1964).
8. M. V. Pasechnik, V. B. Shostak, A. D. Fursa, *et al.*, Yad. Fiz. **54**, 616 (1991) [Sov. J. Nucl. Phys. **54**, 373 (1991)].
9. P. E. Tannenwald, Phys. Rev. **89**, 508 (1953).
10. S. K. Abdullin, A. V. Blinov, I. A. Vanyushin, *et al.*, Yad. Fiz. **56** (4), 204 (1993) [Phys. At. Nucl. **56**, 536 (1993)]; A. V. Blinov, V. E. Grechko, S. M. Zombikovskiĭ, *et al.*, Yad. Fiz. **58**, 1814 (1995) [Phys. At. Nucl. **58**, 1713 (1995)].
11. W. H. Innes, Report UCRL-8040 (Univ. of California Radiation Laboratory, 1957).
12. H. Braun, J. Hlavacova, V. V. Glagolev, *et al.*, Yad. Fiz. **59**, 2001 (1996) [Phys. At. Nucl. **59**, 1928 (1996)].
13. J. P. Meyer, Astron. Astrophys., Suppl. Ser. **7**, 417 (1972).
14. D. V. Bugg, D. C. Salter, G. H. Stafford, *et al.*, Phys. Rev. **146**, 980 (1966).

Translated by R. Rogalyov

Physics of Atomic Nuclei, Vol. 63, No. 11, 2000, pp. 1910–1922. Translated from Yadernaya Fizika, Vol. 63, No. 11, 2000, pp. 2003–2015.

NUCLEI
Theory

Elastic and Inelastic Proton Scattering on ^{7}Li Nuclei within Diffraction Theory

M. A. Zhusupov and E. T. Ibraeva

Institute of Experimental and Theoretical Physics, Al'Farabi Kazakh State National University, Tole-bi 96a, Almaty, 480012 Kazakhstan

Received April 20, 1999; in final form, November 29, 1999

Abstract—On the basis of Glauber diffraction theory, the differential cross sections and analyzing powers are calculated for elastic and inelastic (to the $J^\pi = \frac{1}{2}^-$ level at $E^* = 0.48$ MeV) proton scattering on ^{7}Li nuclei at $E_p = 0.2$, 0.6, and 1.0 GeV. In this calculation, the ^{7}Li wave function is taken in the αt model. The sensitivity of our results to variations in the parameters of the elementary pN and $p\alpha$ amplitudes is investigated. Effects induced by multiple scattering on the target-nucleus clusters are shown to play a significant role. Theoretical results are found to comply well with experimental data available only at $E_p = 0.2$ GeV. © *2000 MAIK "Nauka/Interperiodica".*

1. INTRODUCTION

Systematic experimental data on the scattering of protons with energies in excess of 100 MeV on ^{7}Li nuclei were obtained by a group from the Gustav Werner Institute (Uppsala, Sweden) [1], where the domestic synchrocyclotron was used for this investigation, and by a group from the Institute de Physique Nucléaire (Orsay, France) [2]. The former group measured only angular distributions for inelastic proton scattering on light nuclei (up to ^{16}O), while the latter determined the angular distributions and polarizations both for elastic and for inelastic scattering (for the range of light nuclei extending up to ^{14}N). Also, calculations within the plane-wave optical model were performed in [2]. Since then, these data have been refined over and over again, and one of the latest studies [3] presents the differential cross sections and analyzing powers A_y at $E_p = 200$ MeV that were measured at the synchrocyclotron of Indiana University (IUCF). These experimental data were analyzed within the microscopic folding model and within the distorted-wave approximation.

Here, we calculate the differential cross section and the analyzing power A_y within the Glauber theory of multiple scattering. If the free hadron–nucleon amplitude and the wave function for the target nucleus are known, this theory is advantageous in direct calculations of elastic- and inelastic-scattering processes.

To some extent, the application of Glauber theory at energies of about a few hundred MeV without taking into account corrections for the internal motion of nucleons and for deviations from the eikonal propagation of the incident beam may seem questionable. However, investigations of corrections to Glauber theory—in particular, those in [4–6]—revealed that different corrections are mutually canceled to a considerable extent. For example, Wallace [4] showed that noneikonal corrections and corrections for the Fermi motion of intranuclear nucleons have opposite signs and cancel; Kolybasov and Marinov [5] estimated all corrections for the case of scattering on a deuteron and clarified the physical grounds for the high accuracy of the eikonal approach at relatively low energies, where different nonadiabatic effects are partly compensated and where they even vanish for a local nucleon–nucleon potential. With the aim of assessing the effect of partial nucleon deconfinement in a nucleus (a very delicate phenomenon indeed) on the behavior of cross sections, Sapersteĭn and Starodubskiĭ [6] analyzed the differential cross section for elastic proton scattering within Glauber theory. Although those authors did not draw definitive conclusions, they were able to set constraints on the magnitude of relevant swelling.

The ^{7}Li nucleus was investigated by many authors within various models, including the Cohen–Kurath model [3], the shell model involving LS coupling [7], and the cluster model [8–10]. In the study of Glover *et al.* [3], the ^{7}Li wave function was represented in the form of a nuclear density as the sum of two components, a spherical (ρ_0^m) and a quadrupole (ρ_2^m) one. Among other things, those authors demonstrated the importance of taking into account the quadrupole component in calculating both the differential cross sections and the analyzing powers. The results of the calculations were compared with experimental data and with the results of previous calculations for the ^{6}Li nucleus [11]. Since the ^{6}Li nucleus is spherically symmetric, the contribution of the quadrupole density component is not very important for it.

1063-7788/00/6311-1910$20.00

In contrast to [3], we use here the ^{7}Li wave function derived on the basis of the αt cluster model [9] with the Wood–Saxon potential whose parameters are set to values recommended in [12]. This wave function makes it possible to reproduce faithfully static features and electromagnetic form factors at low momentum transfers. Similar wave functions for the Buck potential were calculated in [10]. Later, Dubovichenko and Dzhazairov-Kakhramanov [13] obtained wave functions on the basis of potentials involving forbidden states; their results proved to be in perfect agreement with the conclusions presented in [9, 10] and with the static features computed in those studies. Thus, we can see that nothing radically new emerged from the use of eight adjustable parameters in [13] (instead of three in [12]).

An important point in the present study is that we take into account spin–orbit interaction in the scattering process. Although it was shown in number of studies (see [14–16]) that the inclusion of spin–orbit interaction leads to insignificant changes in the cross section (mainly, in the region of diffraction minima and at large scattering angles), polarization features, which are more sensitive to model parameters and to the scattering mechanism than the differential cross section, cannot be computed without this.

In this study, the differential cross sections and the analyzing power A_y calculated for elastic and inelastic (to the $J^\pi = \frac{1}{2}^-$ level at $E^* = 0.48$ MeV) proton scattering are analyzed as functions of the parameters of the elementary pN and $p\alpha$ amplitudes and as functions of the contributions from the multiple scattering and rescattering of incident protons on the target-nucleus clusters. The objective of this study is to systematize, at the proton energies used, the parameters of the pN and $p\alpha$ amplitudes as extracted from the literature. That such data, especially the spin-dependent parameters of the elementary amplitudes, are incomplete and show considerable scatter restricts severely the potential of the theory.

2. FUNDAMENTALS OF FORMALISM

Let us proceed to calculate the matrix element or the amplitude for elastic p^7Li scattering in the Glauber diffraction theory of multiple scattering. The quantum numbers of the ^{7}Li nucleus are $J^\pi = (3/2)^-$, $T = 1/2$, and $L = 1$ in the ground state and $J^\pi = (1/2)^-$, $T = 1/2$, and $L = 1$ in the first excited state. Within the αt cluster model, the ^{7}Li wave functions can be represented as

$$\psi_{^7\mathrm{Li}} = \langle LM_L SM_S | JM_j \rangle \Phi_\alpha \Phi_t \Phi_{\alpha t} \chi_{\frac{1}{2}M_S}, \qquad (1)$$

where $\chi_{\frac{1}{2}M_S}$ is the spin function and Φ_α, Φ_t, and $\Phi_{\alpha t}$ are the wave functions of the alpha particle, of the triton, and of their relative motion, respectively. In the form of expansions in terms of the Gaussian basis, these wave functions are given by

$$\Phi_\alpha = N_\alpha \sum_j C_j \exp(-\alpha_j R_\alpha^2), \qquad (2)$$

$$\Phi_t = N_t \sum_k C_k \exp\left(-\frac{1}{2}\alpha_k \sum_{l=1}^{3} (\mathbf{r}_l - \mathbf{R}_t)^2\right), \qquad (3)$$

$$\Phi_{\alpha t} = R^L Y_{LM}(\hat{\mathbf{R}}) N_{\alpha t} \sum_i C_i \exp(-\alpha_i R^2), \qquad (4)$$

where N_α, N_t, and $N_{\alpha t}$ are the relevant normalization factors; $C_{i(j,k)}$ and $\alpha_{i(j,k)}$ are the expansion coefficients, whose values were borrowed from [17] for alpha particles, from [18] for t, and from [9] for αt; $\mathbf{R}_\alpha$ and $\mathbf{R}_t$ are the c.m. coordinates of the alpha particle and of the triton; $\mathbf{r}_l$ stands for the single-particle coordinates of the triton nucleons; and $\mathbf{R}$ is the coordinate of the relative motion of the alpha particle and the triton in the ^{7}Li nucleus ($\mathbf{R} = \mathbf{R}_\alpha - \mathbf{R}_t$).

The Glauber multiple-scattering operator can be represented in the factorized form

$$\Omega = \Omega_\alpha + \Omega_t - \Omega_\alpha \Omega_t, \qquad (5)$$

where Ω_α is the operator of scattering on the alpha particle, Ω_t is the operator of scattering on the triton, and $\Omega_\alpha \Omega_t$ is the operator of multiple scattering on the two clusters of the target nucleus. It is well known that the operators Ω_i are expressed in terms of the profile functions, which in turn involve the elementary pN amplitudes. In considering scattering on the alpha particle, we disregard its internal structure and, instead of the elementary pN amplitudes, use the elementary $p\alpha$ amplitude with the parameters fitted to experimental data. This approach is validated in detail elsewhere [19, 20].

Thus, the alpha-particle wave function in the form (2) depends only on the c.m. coordinates of the alpha particle ($\mathbf{R}_\alpha$); in contrast, the triton wave function (3) involves the single-particle coordinates ($\mathbf{r}_i$) of the triton nucleons. In Glauber theory, scattering occurs in the plane orthogonal to the incident-proton beam (in the xy plane if the z axis is aligned with the beam distribution, as is usually done), whence it follows that all vectors appearing in the operator Ω are two-dimensional and that the vectors appearing in the wave function are three-dimensional. Two-dimensional vectors will be either labeled with a tilde, $\mathbf{a} = \{\tilde{\mathbf{a}}, a_z\}$, or denoted by the Greek letter $\boldsymbol{\rho}$ carrying a corresponding subscript, $\mathbf{r}_i \equiv \{\boldsymbol{\rho}_i, z_i\}$. (The Greek letter $\boldsymbol{\rho}$ without any subscript will stand for the impact parameter.) In accordance with this, we have

$$\Omega_\alpha = \omega_\alpha(\boldsymbol{\rho} - \boldsymbol{\rho}_\alpha) = \frac{1}{2\pi i k}\int d^2\mathbf{q} \exp(-i\mathbf{q}\cdot(\boldsymbol{\rho} - \boldsymbol{\rho}_\alpha)) f_{p\alpha}(q), \qquad (6)$$

where

$$f_{p\alpha}(q) = f^c_{p\alpha}(q) + f^s_{p\alpha}(q)\boldsymbol{\sigma}\cdot\mathbf{n}. \qquad (7)$$

Table 1. Parameters of the $p\alpha$ amplitude

E_p, GeV	$\sigma_{p\alpha}$, fm^2	$\varepsilon^c_{p\alpha}$	$\beta^c_{p\alpha}$, fm^2	t_1, fm^{-2}	t_2, fm^{-2}	$\varepsilon^s_{p\alpha}$	D_s	$\beta^c_{p\alpha}$, fm^2	t_3, fm^{-2}	t_4, fm^{-2}	References	Set number
0.2	10.8	0.645	0.867	2.48 + *i*2.54							[20]	1
0.2	8.908	0.357	0.5055	10.09 – *i*5.16	4.530 + *i*1.256	–0.127	10.312	1.071	1.593 – *i*1.302	12.03 + *i*2.22	[15]	2
0.56	12.3	0.083	0.550	6.41 + *i*1.15							[20]	3
0.60	12.3	0.03	0.56	6.2 + *i*1.1							[20]	4
1.0	15.2	–0.5	1.254			–0.31	0.16	1.85			[19]	5
1.0	15.2	–0.2	1.188			–0.2	0.15	1.769			[19]	6
1.03	12.7	–0.189	0.652	5.61 + *i*1.17							[20]	7
1.05	15.3	–0.200	0.622	5.93 + *i*1.22							[20]	8

Here, $f^c_{p\alpha}$ and $f^s_{p\alpha}$ are, respectively, the central and the spin–orbit component of the elementary $p\alpha$ amplitude; **n** is a unit vector orthogonal to the scattering plane, $\mathbf{n} = \mathbf{k}\times\mathbf{k}'/|\mathbf{k}\times\mathbf{k}'|$; and $\boldsymbol{\sigma}$ is the Pauli spin matrix of the scattered proton. As was shown in [15], the diffraction pattern of proton scattering on alpha particles at energies about a few hundred MeV is described well by the parametrization [up to values of $q^2 = 0.8$ (GeV/c)^2]

$$f^c_{p\alpha}(q) = \frac{k\sigma_{p\alpha}}{4\pi}(i+\varepsilon^c_{p\alpha})\left(1-\frac{q^2}{t_1}\right)\left(1-\frac{q^2}{t_2}\right)\exp(-\beta^c_{p\alpha}q^2/2), \tag{8}$$

$$f^s_{p\alpha}(q) = \frac{k\sigma_{p\alpha}}{4\pi}(i+\varepsilon^s_{p\alpha}) \times D_s\sqrt{\frac{q^2}{4m^2}}\left(1-\frac{q^2}{t_3}\right)\left(1-\frac{q^2}{t_4}\right)\exp(-\beta^s_{p\alpha}q^2/2), \tag{9}$$

where m is the nucleon mass and q is the momentum transfer. The parameters of the elementary $p\alpha$ amplitude are quoted in Table 1. By substituting (8) and (9) into (6) and performing relevant integration, we obtain

$$\Omega^\nu_\alpha = G^\nu V^\nu \exp[-\lambda^\nu_\alpha(\boldsymbol{\rho}-\boldsymbol{\rho}_\alpha)^2], \tag{10}$$

where $\nu = c, s$, and where

$$\lambda^\nu_\alpha = \frac{1}{2\beta^\nu_{p\alpha}}, \quad G^c = \frac{F^c_1}{ik\beta^c_{p\alpha}}, \quad G^s = \frac{2F^s_1}{k(\beta^s_{p\alpha})^2}\boldsymbol{\sigma}\cdot\mathbf{n},$$
$$F^\nu_1 = \frac{k\sigma_{p\alpha}}{4\pi}(i+\varepsilon^\nu_{p\alpha}), \quad F^c_2 = -\frac{1}{t_1}-\frac{1}{t_2},$$
$$F^s_2 = -\frac{1}{t_3}-\frac{1}{t_4}, \quad F^c_3 = \frac{1}{t_1t_2}, \quad F^s_3 = \frac{1}{t_3t_4}, \tag{11}$$
$$V^c = F^c_4 + F^c_5(\boldsymbol{\rho}-\boldsymbol{\rho}_\alpha)^2 + F^c_6(\boldsymbol{\rho}-\boldsymbol{\rho}_\alpha)^4,$$
$$F^c_4 = \frac{2F^c_2}{\beta^c_{p\alpha}} + \frac{8F^c_3}{(\beta^c_{p\alpha})^2}, \quad F^c_5 = -\left(\frac{F^c_2}{(\beta^c_{p\alpha})^2} + \frac{8F^c_3}{(\beta^c_{p\alpha})^3}\right),$$
$$F^c_6 = \frac{F^c_3}{(\beta^c_{p\alpha})^4},$$
$$V^s = F^s_4(\boldsymbol{\rho}-\boldsymbol{\rho}_\alpha) + F^s_5(\boldsymbol{\rho}-\boldsymbol{\rho}_\alpha)^3 + F^s_6(\boldsymbol{\rho}-\boldsymbol{\rho}_\alpha)^5, \tag{12}$$
$$F^s_4 = \frac{1}{2} - \frac{2F^s_2}{\beta^s_{p\alpha}} - \frac{12F^s_3}{(\beta^s_{p\alpha})^2}, \quad F^s_5 = \frac{F^s_2}{2(\beta^s_{p\alpha})^2} + \frac{6F^s_3}{(\beta^s_{p\alpha})^3},$$
$$F^s_6 = -\frac{F^s_3}{2(\beta^s_{p\alpha})^4}.$$

Unfortunately, there are no data in the literature on the parameters of the pt amplitudes; for this reason, scattering on a triton will be considered as a process occurring on three constituent nucleons. With allowance for all multiplicities of scattering, the Glauber operator Ω_t then becomes

$$\Omega_t = \omega_1+\omega_2+\omega_3-\omega_1\omega_2-\omega_1\omega_3 - \omega_2\omega_3+\omega_1\omega_2\omega_3, \tag{13}$$

where ω_i can be represented in a form similar to that given by Eqs. (6) and (7) with the substitution of the pN amplitudes for the $p\alpha$ amplitude. Breaking down the elementary pN amplitudes into the central and spin–orbit components, we represent these two in the standard way as [21]

$$f^c_{pN} = \frac{k\sigma_{pN}}{4\pi}(i+\varepsilon^c_{pN})\exp(-\beta^c_{pN}q^2/2), \tag{14}$$

$$f^s_{pN} = \frac{k\sigma_{pN}}{4\pi}qD_s(i+\varepsilon^s_{pN})\exp(-\beta^s_{pN}q^2/2), \tag{15}$$

where the subscripts $N = 1$ and 2 correspond to the proton and the neutron, respectively. The parameters of the amplitudes are quoted in Table 2.

Substituting (14) and (15) into the formula corresponding to (6) and performing two-dimensional integration with respect to q, we obtain

$$\omega^c_i(\boldsymbol{\rho}-\boldsymbol{\rho}_i) = F^c_N\exp[-(\boldsymbol{\rho}-\boldsymbol{\rho}_i)^2\lambda^c_N], \tag{16}$$

Table 2. Parameters of the *pN* amplitude

E_p, GeV	*pN*	σ_{pN}, fm^2	ε^c_{pN}	β^c_{pN}, fm^2	D_s, fm	ε^s_{pN}	β^s_{pN}, fm^2	References	Set number
0.185	*pp*	2.5	1.22	0.529				[22]	1
	pn	4.77	0.84	0.697					
0.2	*pp*	2.19	−0.068	0.103				[23]	2
	pn	4.10	5.199	0.0534					
0.2	*pp*	2.36	1.15	0.65				[24]	3
	pn	4.20	0.71	0.68				[25]	
0.398	*pp*	2.56	0.584	$0.564 - i0.61$	0.674	0.102	$0.316 + i0.0.024$	[19]	4
	pn	3.332	0.108	$0.612 - i0.486$	0.441	0.431	$0.40 - i0.054$		
0.6	*pp*	4.00	1.11	0.022				[23]	5
	pn	3.75	1.712	−0.0122					
0.6	*pp*	3.7	−0.48	0.097				[27]	6
	pn	3.6	−0.36	0.115					
0.6	*pp*	3.96	0.24	0.11				[21]	7
	pn	3.66	−0.295	0.175					
0.6	*ppn**	3.7	−0.1	0.12	3.0	1.0	0.6	[26]	8
0.6	*pp*	3.61	0.378	0.1				[22]	9
	pn	3.6	−0.205	0.111					
1.0	*ppn**	4.356	−0.3	0.187	0.21	0.364	0.298	[30]	10
1.0	*pp*	4.75	−0.1	0.23	0.16	−0.3	0.75	[29]	11
	pn	4.04	−0.4	0.16	0.16	−0.3	0.75		
1.0	*pp*	4.75	−0.05	0.109				[22]	12
	pn	4.04	−0.4	0.109					
1.0	*pp*	4.75	−0.1	0.24	0.14	−0.6	0.6	[28]	13
	pn	4.04	−0.45	0.24	0.14	−0.6	0.6		
1.0	*pp*	4.75	−0.05	0.21				[6]	14
	pn	4.04	−0.5	0.21					
1.0	*pp*	4.72	−0.09	0.09				[21]	15
	pn	3.92	−0.46	0.12					
1.0	*pp*	4.75	1.99	−0.0112				[23]	16
	pn	4.02	2.133	−0.404					
1.0	*pp*	4.75	−0.05	0.182				[24]	17
	pn	4.00	−0.5	0.182				[25]	
1.0	*ppn**	4.356	−0.3	0.187	0.202	0.413	0.333	[30]	18
1.0	*ppn**	4.356	−0.3	0.26	0.213	0.3	$0.467 + i0.297$	[31]	19
1.0	*pp*	4.75		0.25	0.1	15	0.75	[32]	20
	pn	3.85		0.25	0.1	15	0.75		
1.0	*pp*	4.75		0.25	5.5	0.2	1.25	[32]	21
	pn	3.85		0.25	5.5	0.2	1.25		
1.0	*pp*	4.75	−0.33	0.182				[34]	22
	pn	4.00	−0.33	0.182					
1.0	*pp*	4.75	−0.06	0.182				[35]	23
	pn	4.00	−0.4	0.182					
1.04	*pp*	4.75	−0.1	0.24				[33]	24
	pn	4.04	−0.4	0.17					
1.05	*ppn**	4.4	−0.27	0.25	2.3	0.7	0.6	[26]	25

Note: Asterisks label cases where the parameters of the *pp* and *pn* amplitudes are identical.

where $F_N^c = \frac{\sigma_{pN}}{4\pi\beta_{pN}}(i + \varepsilon_{pN}^c)$ and $\lambda_N^c = \frac{1}{2\beta_{pN}^c}$, and

$$\omega_i^s(\boldsymbol{\rho} - \boldsymbol{\rho}_i) = (\boldsymbol{\rho} - \boldsymbol{\rho}_i)F_N^s \exp[-(\boldsymbol{\rho} - \boldsymbol{\rho}_i)^2\lambda_N^s], \quad (17)$$

where $F_N^s = \frac{\sigma_{pN}D_s}{8\pi(\beta_{pN}^s)^2}(i + \varepsilon_{pN}^s)$ and $\lambda_N^s = \frac{1}{2\beta_{pN}^s}$.

Inserting (16) and (17) into (13), we can represent the central and the spin component of the Glauber operator Ω_t as

$$\Omega_t^c = \sum_{N=1}^{3} F_N^c \exp[-(\boldsymbol{\rho} - \boldsymbol{\rho}_N)^2\lambda_N^c]$$

$$- \sum_{N<N'=1}^{3} F_N^c F_{N'}^c \exp[-(\boldsymbol{\rho} - \boldsymbol{\rho}_N)^2\lambda_N^c - (\boldsymbol{\rho} - \boldsymbol{\rho}_{N'})^2\lambda_{N'}^c] \quad (18)$$

$$+ (F_n^c)^2 F_p^c \exp[-(\boldsymbol{\rho} - \boldsymbol{\rho}_1)^2\lambda_n^c - (\boldsymbol{\rho} - \boldsymbol{\rho}_2)^2\lambda_n^c$$

$$- (\boldsymbol{\rho} - \boldsymbol{\rho}_3)^2\lambda_p^c],$$

$$\Omega_t^s = \boldsymbol{\sigma}\cdot\mathbf{n}\sum_{N=1}^{3} F_N^s(\boldsymbol{\rho} - \boldsymbol{\rho}_N)\exp[-(\boldsymbol{\rho} - \boldsymbol{\rho}_N)^2\lambda_N^s]$$

$$- \sum_{N<N'=1}^{3} F_N^s F_{N'}^s(\boldsymbol{\rho} - \boldsymbol{\rho}_N)\cdot(\boldsymbol{\rho} - \boldsymbol{\rho}_{N'})$$

$$\times \exp[-(\boldsymbol{\rho} - \boldsymbol{\rho}_N)^2\lambda_N^s - (\boldsymbol{\rho} - \boldsymbol{\rho}_{N'})^2\lambda_{N'}^s] \quad (19)$$

$$+ (F_n^s)^2 F_p^s(\boldsymbol{\rho} - \boldsymbol{\rho}_1)(\boldsymbol{\rho} - \boldsymbol{\rho}_2)\cdot(\boldsymbol{\rho} - \boldsymbol{\rho}_3)$$

$$\times \exp[-(\boldsymbol{\rho} - \boldsymbol{\rho}_1)^2\lambda_n^s - (\boldsymbol{\rho} - \boldsymbol{\rho}_2)^2\lambda_n^s - (\boldsymbol{\rho} - \boldsymbol{\rho}_3)^2\lambda_p^s],$$

where $N, N' = 1, 2$ correspond to n and $N, N' = 3$ correspond to p.

Within Glauber theory, the scattering amplitude (or the relevant matrix element) can be written as

$$M(\mathbf{q}) = \frac{ik}{2\pi}\int d^2\boldsymbol{\rho}\prod_{\nu=1}^{4} d\mathbf{r}_\nu \exp(i\mathbf{q}\cdot\boldsymbol{\rho})\delta(\mathbf{R}_7)\langle\psi_{^7\mathrm{Li}}|\Omega|\psi_{^7\mathrm{Li}}\rangle, \quad (20)$$

where r_ν stands for the single-particle coordinates of the nucleons and of the nucleon cluster (alpha particle) in the target nucleus; $\mathbf{k}$ and $\mathbf{k}'$ are the c.m. momenta of, respectively, the incident and the emitted proton; and $\mathbf{q}$ is the momentum transfer in the reaction, $\mathbf{q} = \mathbf{k} - \mathbf{k}'$. In the particular case of elastic scattering, we have $k = k'$ and $|\mathbf{q}| = 2k\sin(\theta/2)$, where θ is the incident-proton scattering angle.

Since the Glauber operator Ω in (5) depends on the elementary $p\alpha$ and pN amplitudes and since each of these two is broken into the sum of the central and the spin–orbit term [see Eq. (7)], Ω also appears as the sum of two terms,

$$\Omega = \Omega^c + \Omega^s. \quad (21)$$

Substituting (21) into (20), we obtain the expression for the total amplitude in the form

$$M(\mathbf{q}) = M^c(\mathbf{q}) + M^s(\mathbf{q}), \quad (22)$$

where the quantities $M^c(\mathbf{q})$ and $M^s(\mathbf{q})$ are calculated by formula (20), where Ω is replaced by Ω^c and Ω^s, respectively. In terms of the amplitude in (22), the differential cross section and the analyzing power (or polarization) can be expressed in a conventional way as

$$\frac{d\sigma}{d\Omega} = \frac{1}{2J+1}|M(\mathbf{q})|^2, \quad (23)$$

$$A_y = P = \frac{2\,\mathrm{Re}[M^c(\mathbf{q})M^{s*}(\mathbf{q})]}{|M^c(\mathbf{q})|^2 + |M^s(\mathbf{q})|^2}. \quad (24)$$

In order to proceed further, it is necessary to go over, in the wave functions and in the operators, from the single-particle nucleon coordinates $\{\mathbf{r}_1, \mathbf{r}_2, \mathbf{r}_3, \mathbf{R}_\alpha\}$ to the Jacobi coordinates $\{\mathbf{a}, \mathbf{b}, \mathbf{R}_t, R_\alpha\}$; the relation between these two sets of coordinates can be represented as

$$\mathbf{a} = \mathbf{r}_1 - \mathbf{r}_2, \quad \mathbf{b} = \frac{\mathbf{r}_1 + \mathbf{r}_2}{2} - \mathbf{r}_3,$$
$$\mathbf{R}_t = \frac{1}{3}\sum_{i=1}^{3}\mathbf{r}_i, \quad \mathbf{R}_\alpha = \frac{1}{4}\sum_{i=4}^{7}\mathbf{r}_i. \quad (25)$$

The inverse transformations yield

$$\mathbf{r}_1 = \mathbf{R}_t + \frac{\mathbf{b}}{3} + \frac{\mathbf{a}}{2}, \quad \mathbf{r}_2 = \mathbf{R}_t + \frac{\mathbf{b}}{3} - \frac{\mathbf{a}}{2},$$
$$\mathbf{r}_3 = \mathbf{R}_t - \frac{2}{3}\mathbf{b}. \quad (26)$$

The expressions for the coordinate of the relative motion, $\mathbf{R}$, and for the coordinate of the center of mass of the nucleus as a discrete unit, $\mathbf{R}_7$, are given by

$$\mathbf{R} = \mathbf{R}_\alpha - \mathbf{R}_t, \quad (27)$$

$$\mathbf{R}_7 = \frac{1}{7}\sum\mathbf{r}_i = \frac{3}{7}\mathbf{R}_t + \frac{4}{7}\mathbf{R}_\alpha. \quad (28)$$

Going over in operators (18) and (19) from the single-particle nucleon coordinates to the Jacobi coordinates by formulas (26) and performing some transformations, we can further represent the operator Ω_t as the sum

$$\Omega_t^\nu = \sum_{m=1}^{7} g_m^\nu \exp(-c_m^\nu\rho^2 - d_m^\nu\rho_t^2 - e_m^\nu\tilde{b}^2 - f_m^\nu\tilde{a}^2$$
$$+ h_m^\nu\boldsymbol{\rho}\cdot\boldsymbol{\rho}_t + k_m^\nu\boldsymbol{\rho}\cdot\tilde{\mathbf{b}} + n_m^\nu\boldsymbol{\rho}\cdot\tilde{\mathbf{a}} + m_m^\nu\boldsymbol{\rho}_t\cdot\tilde{\mathbf{b}} \quad (29)$$

$$+ l_m^{\nu}\boldsymbol{\rho}_t\cdot\tilde{\mathbf{a}} + s_m^{\nu}\tilde{\mathbf{a}}\cdot\tilde{\mathbf{b}}).$$

Summation over m in (29)—that is, over the multiplicity of scattering on the triton-cluster nucleons, with m = 1–3, 4–6, and 7 corresponding to single, double, and triple scattering, respectively—is equivalent to the summation over N and N' in (18) and (19). In the following, we disregard the term $\omega_1\omega_2\omega_3$, which is associated with triple collisions, in the spin–orbit operator Ω_t^s because, as was shown in [14, 36], its contribution to the matrix element is approximately two orders of magnitude less than the contribution of single and double collisions. The expressions for the coefficients g_m^{ν}, c_m^{ν}, …, and s_m^{ν} are presented in the Appendix.

We begin by calculating the central matrix element $M^c(\mathbf{q})$. For this, we go over in (20) from the single-particle coordinates to the Jacobi coordinates according to (26). Upon integrating the matrix element with respect to $\mathbf{R}_7$ with the aid of a delta function and taking into account (27) and (28), we obtain

$$\mathbf{R}_\alpha = -\frac{3}{4}\mathbf{R}_t, \quad \mathbf{R} = \mathbf{R}_\alpha - \mathbf{R}_t = -\frac{7}{4}\mathbf{R}_t. \tag{30}$$

In terms of the Jacobi coordinates, the wave functions (2)–(4) become

$$\Phi_\alpha = N_\alpha\sum C_j\exp\left(-\alpha_j\frac{9}{16}R_t^2\right),$$

$$\Phi_t = N_t\sum C_k\exp\left[-\frac{1}{2}\alpha_k\left(\frac{a^2}{2}+\frac{2b^2}{3}\right)\right], \tag{31}$$

$$\Phi_{\alpha t} = -\frac{7}{4}R_tY_{LM}(\hat{\mathbf{R}}_t)N_{\alpha t}\sum C_i\exp\left(-\alpha_i\frac{49}{16}R_t^2\right).$$

With allowance for (30), the operator Ω_α in (10) can be recast into the form

$$\Omega_\alpha^{\nu} = G^{\nu}V^{\nu}\exp\left[-\lambda_\alpha^{\nu}\left(\rho^2+\frac{9}{16}\rho_t^2+\frac{3}{2}\boldsymbol{\rho}\cdot\boldsymbol{\rho}_t\right)\right], \tag{32}$$

where the expressions for V^{ν}, which are specified by (11) and (12), assume the form

$$V^c = \left\{F_4^c + F_5^c\left(\rho^2+\frac{3^2}{4^2}\rho_t^2+\frac{3}{2}\rho\rho_t\right)\right.$$
$$\left. + F_6^c\left[\rho^4+\left(\frac{3}{4}\rho_t\right)^4+\frac{3^3}{2^3}(\rho\rho_t)^2+3\boldsymbol{\rho}^3\cdot\boldsymbol{\rho}_t+\frac{3^3}{4^2}\boldsymbol{\rho}\cdot\boldsymbol{\rho}_t^3\right]\right\}, \tag{33}$$

$$V^s = F_4^s\left(\boldsymbol{\rho}+\frac{3}{4}\boldsymbol{\rho}_t\right)+F_5^s\left(\boldsymbol{\rho}^3+\frac{3^2}{4}\rho^2\boldsymbol{\rho}_t+\frac{3^3}{4^2}\boldsymbol{\rho}\rho_t^2\right.$$
$$\left.+\frac{3^3}{4^3}\boldsymbol{\rho}_t^3\right)+F_6^s\left(\boldsymbol{\rho}^5+\frac{3\cdot5}{4}\rho^4\boldsymbol{\rho}_t+\frac{3^2\cdot5}{4\cdot2}\boldsymbol{\rho}^3\rho_t^2\right. \tag{34}$$
$$\left.+\frac{3^3\cdot5}{4^2\cdot2}\rho^2\boldsymbol{\rho}_t^3+\frac{3^4\cdot5}{4^4}\boldsymbol{\rho}\rho_t^4+\frac{3^5}{4^5}\boldsymbol{\rho}_t^5\right).$$

Substituting (30) and (31) into the matrix element (20), we obtain

$$M^c(\mathbf{q}) = C_1\int d^2\boldsymbol{\rho}e^{i\mathbf{q}\cdot\boldsymbol{\rho}}d\mathbf{R}_t d\mathbf{a}d\mathbf{b}$$
$$\times\exp(-\nu_{1k}a^2-\nu_{2k}b^2-\nu_{3i}R_t^2)\Omega^c$$
$$\times\sum_{\substack{M_LM_L'\\M_SM_S'}}\left\langle 1M_L\frac{1}{2}M_S\middle|\frac{3}{2}M_J\right\rangle\left\langle 1M_L'\frac{1}{2}M_S'\middle|\frac{3}{2}M_J'\right\rangle \tag{35}$$
$$\times\langle R_tY_{1M_L}(\hat{\mathbf{R}}_t)\big|R_tY_{1M_L'}(\hat{\mathbf{R}}_t)\rangle\left\langle\chi_{\frac{1}{2}M_S}\middle|\chi_{\frac{1}{2}M_S'}\right\rangle,$$

where

$$C_1 = \frac{ik}{2\pi}N_t^2N_\alpha^2N_{\alpha t}^2\left(\frac{7}{4}\right)^2\sum_{kk'}C_kC_{k'}\sum_{jj'}C_jC_{j'}\sum_{ii'}C_iC_{i'},$$

$$\nu_{1k} = \frac{1}{4}(\alpha_k+\alpha_{k'}), \quad \nu_{2k} = \frac{1}{3}(\alpha_k+\alpha_{k'}),$$

$$\nu_{3i} = \frac{49}{16}(\alpha_i+\alpha_{i'})+\frac{9}{16}(\alpha_j+\alpha_{j'}).$$

Calculating separately the factor appearing in the matrix element and depending on the angular-momentum projections, we find for the case of elastic scattering that

$$\sum_{\substack{M_LM_L'\\M_SM_S'}}\left\langle 1M_L\frac{1}{2}M_S\middle|\frac{3}{2}M_J\right\rangle\left\langle 1M_L'\frac{1}{2}M_S'\middle|\frac{3}{2}M_J'\right\rangle$$
$$\times\langle R_tY_{1M_L}(\hat{\mathbf{R}}_t)\big|R_tY_{1M_L'}(\hat{\mathbf{R}}_t)\rangle \tag{36}$$
$$= \frac{3}{4\pi}[k_1x_t^2+k_2y_t^2+k_3z_t^2],$$

where $k_1 = \frac{4}{3}-\frac{2}{\sqrt{3}}$, $k_2 = \frac{4}{3}+\frac{2}{\sqrt{3}}$, $k_3 = \frac{4}{3}$, $x_t = R_{tx}$, $y_t = R_{ty}$, and $z_t = R_{tz}$.

For inelastic scattering, the analogous factor is

$$\sum_{\substack{M_LM_L'\\M_SM_S'}}\left\langle 1M_L\frac{1}{2}M_S\middle|\frac{1}{2}M_J\right\rangle\left\langle 1M_L'\frac{1}{2}M_S'\middle|\frac{1}{2}M_J'\right\rangle$$
$$\times\langle R_tY_{1M_L}(\hat{\mathbf{R}}_t)\big|R_tY_{1M_L'}(\hat{\mathbf{R}}_t)\rangle = \frac{1}{\pi}[x_t^2-x_tz_t]. \tag{37}$$

Because the operators Ω_α and Ω_t depend only on the two-dimensional components of the corresponding vectors, we represent the integral in (35) as the product

of the factors depending on the longitudinal (z) and transverse (ρ) components:

$$M^c(\mathbf{q}) = C_1\frac{3}{4\pi}\int d^2\boldsymbol{\rho}\, d\boldsymbol{\rho}_t\, d\tilde{\mathbf{a}}\, d\tilde{\mathbf{b}} \times \exp(-\nu_{1k}\tilde{a}^2 - \nu_{2k}\tilde{b}^2 - \nu_{3i}\rho_t^2 + i\mathbf{q}\boldsymbol{\rho})\Omega^c \times \int dz_t\, da_z\, db_z \exp(-\nu_{1k}a_z^2 - \nu_{2k}b_z^2 - \nu_{3i}z_t^2) \times [k_1x_t^2 + k_2y_t^2 + k_3z_t^2]. \quad (38)$$

Integration with respect to z projections is performed with the aid of standard formulas from [37]. The result is

$$\int dz_t\, da_z\, db_z \exp(-\nu_{1k}a_z^2 - \nu_{2k}b_z^2 - \nu_{3i}z_t^2) \times [k_1x_t^2 + k_2y_t^2 + k_3z_t^2] = (k_1x_t^2 + k_2y_t^2)\frac{\pi^{3/2}}{\sqrt{\nu_{1k}\nu_{2k}\nu_{3i}}} + k_3\frac{\pi^{3/2}}{2\nu_{3i}\sqrt{\nu_{1k}\nu_{2k}\nu_{3i}}}.$$

If we use symmetric kinematics, then $k_1x_t^2 + k_2y_t^2 = k_3\rho_t^2$, where $\rho_t^2 = \sqrt{x_t^2 + y_t^2}$; in this case, integration with respect to ρ_t in (38) will be simplified considerably. Substituting (5) into (38), we obtain

$$M^c(\mathbf{q}) = M_1(\Omega_\alpha^c) + M_2(\Omega_t^c) - M_3(\Omega_\alpha^c\Omega_t^c), \quad (39)$$

where the first and the second term determine proton scattering on the alpha particle and on the triton, respectively, while the third term determines the rescattering of the incident beam on all the clusters and nucleons constituting the ^{7}Li nucleus. Inserting the explicit expressions for operators (29) and (32) into each matrix element in (39), we obtain an expression in the form of the sum of multidimensional integrals of the Poisson type, which are calculated analytically with the aid of the formula [38]

$$\int d^2\boldsymbol{\rho}_1 d^2\boldsymbol{\rho}_2 d^2\boldsymbol{\rho}_3 \exp[-sb_1^2 - tb_2^2 - ub_3^2 + e\boldsymbol{\rho}_1\cdot\boldsymbol{\rho}_2 + f\boldsymbol{\rho}_1\cdot\boldsymbol{\rho}_3 + g\boldsymbol{\rho}_2\cdot\boldsymbol{\rho}_3 + h_1\mathbf{q}_1\cdot\boldsymbol{\rho}_1 + h_2\mathbf{q}_2\cdot\boldsymbol{\rho}_2 + h_3\mathbf{q}_3\cdot\boldsymbol{\rho}_3] = \frac{\pi^3}{\Delta}\exp\left(-\frac{\tau}{\Delta}\right), \quad (40)$$

where

$$\Delta = \begin{vmatrix} s & -\frac{l}{2} & -\frac{f}{2} \\ -\frac{l}{2} & t & -\frac{g}{2} \\ -\frac{f}{2} & -\frac{g}{2} & u \end{vmatrix},$$

$$\tau = \begin{vmatrix} s & -\frac{l}{2} & -\frac{f}{2} & -\frac{h_1\mathbf{q}_1}{2} \\ -\frac{l}{2} & t & -\frac{g}{2} & -\frac{h_2\mathbf{q}_2}{2} \\ -\frac{f}{2} & -\frac{g}{2} & u & -\frac{h_3\mathbf{q}_3}{2} \\ -\frac{h_1\mathbf{q}_1}{2} & -\frac{h_2\mathbf{q}_2}{2} & -\frac{h_3\mathbf{q}_3}{2} & 0 \end{vmatrix}.$$

If the integrand additionally contains a polynomial of nth degree (33), the integrals are calculated by means of differentiation with respect to the corresponding parameters in the original expression (40). The ensuing calculations do not involve difficulties of a fundamental nature, but the final expressions are rather cumbersome and are not presented here for this reason.

Let us go over to calculating the spin-dependent matrix elements. Substituting the wave functions (2)–(4) and the expression for Ω^s into the matrix element (20) and performing integration with respect to $\mathbf{R}_\alpha$ with the aid of the delta function $\delta(\mathbf{R}_7)$, we arrive at

$$M^s(\mathbf{q}) = C_1\int d^2\boldsymbol{\rho}\, d\mathbf{a}\, d\mathbf{b}\, d\mathbf{R}_t \times \exp(-\nu_{1k}a^2 - \nu_{2k}b^2 + \nu_{3i}R_t^2)\Omega^s \times \sum_{\substack{M_LM_L' \\ M_SM_S'}} \left\langle 1M_L\tfrac{1}{2}M_S\middle|\tfrac{3}{2}M_J\right\rangle\left\langle 1M_L'\tfrac{1}{2}M_S'\middle|\tfrac{3}{2}M_J'\right\rangle \times \langle R_tY_{1M_L}(\hat{\mathbf{R}}_t)\big|R_tY_{1M_L'}(\hat{\mathbf{R}}_t)\rangle\left\langle\chi_{\frac{1}{2}M_S}\middle|\boldsymbol{\sigma}\cdot\mathbf{n}\middle|\chi_{\frac{1}{2}M_S'}\right\rangle. \quad (41)$$

Calculating the spin part of the matrix element separately, we obtain [39]

$$\left\langle\chi_{\frac{1}{2}M_S}\middle|\boldsymbol{\sigma}\cdot\mathbf{n}\middle|\chi_{\frac{1}{2}M_S'}\right\rangle = 2\left\langle\tfrac{1}{2}M_S\middle|\mathbf{s}\cdot\mathbf{n}\middle|\tfrac{1}{2}M_S'\right\rangle = 2\sqrt{\pi}\sum_\mu(-1)^{1-\mu}\left\langle 1\mu\tfrac{1}{2}M_S'\middle|\tfrac{1}{2}M_S\right\rangle Y_{1-\mu}(\hat{\mathbf{n}}). \quad (42)$$

Considering that $\theta_n = \frac{\pi}{2}$, since $\mathbf{n}$ is orthogonal to the plane spanned by the vectors $\mathbf{k}$ and $\mathbf{k}'$, we arrive at the expression for the matrix element in the form

$$\left\langle\tfrac{1}{2}M_S\middle|\mathbf{s}\cdot\mathbf{n}\middle|\tfrac{1}{2}M_S'\right\rangle = \begin{cases} 0, & M_S = M_S' \\ \frac{1}{2}(\cos\varphi_n - i\sin\varphi_n), & M_S = \frac{1}{2},\quad M_S' = -\frac{1}{2} \\ \frac{1}{2}(\cos\varphi_n + i\sin\varphi_n), & M_S = -\frac{1}{2},\quad M_S' = \frac{1}{2}. \end{cases} \quad (43)$$

By using this result and performing summation over the projections of the angular momenta, we obtain

$$\sum_{\substack{M_L M_L' \\ M_S M_S'}} \left\langle 1M_L \frac{1}{2} M_S \middle| \frac{3}{2} M_J \right\rangle \left\langle 1M_L' \frac{1}{2} M_S' \middle| \frac{3}{2} M_J' \right\rangle \times \langle R_t Y_{1M_L}(\hat{\mathbf{R}}_t) | R_t Y_{1M_L'}(\hat{\mathbf{R}}_t) \rangle \left\langle \chi_{\frac{1}{2}M_S} \middle| \boldsymbol{\sigma} \cdot \mathbf{n} \middle| \chi_{\frac{1}{2}M_S'} \right\rangle = f(x_t, y_t) + f(z_t), \quad (44)$$

where

$$f(x_t, y_t) = (k_4 x_t^2 + k_5 y_t^2)\cos\varphi_n + k_6 x_t y_t \sin\varphi_n,$$
$$f(z_t) = k_6 z_t^2 \cos\varphi_n,$$
$$k_4 = \frac{1}{\sqrt{3}} - \frac{2}{3}, \quad k_5 = \frac{1}{\sqrt{3}} + \frac{2}{3}, \quad k_6 = \frac{2}{3}. \quad (45)$$

The ensuing calculations are analogous to those for the central component of the amplitude with the only difference that the number of terms in the matrix element increases substantially because of the polynomials appearing in the operators Ω_t^s and Ω_α^s.

3. DISCUSSION OF THE RESULTS

The formulas that were derived in the preceding section make it possible to calculate the differential cross sections for elastic and inelastic proton scattering on ^{7}Li at E_p = 0.2, 0.6, and 1.0 GeV and the corresponding analyzing powers.

Figure 1 illustrates the behavior of the differential cross sections versus the incident-proton energy. Curves *1*, *2*, *3*, *4*, and *5* represent the differential cross sections computed at energies of 0.2, 0.4, 0.6, 0.8, and 1.0 GeV, respectively. The figure shows how the diffractive structure of the cross sections manifests itself with increasing energy: at 0.2 GeV, the cross section decreases monotonically (as a function of the scattering angle), while, at 1.0 GeV, we clearly see three shallow minima. As the energy increases further, the first minimum in the differential cross section is shifted to the region of smaller angles, while the magnitude of the differential cross section at $\theta = 0°$ is determined by the total scattering cross section, which depends on $\sigma_{p\alpha}$ and σ_{pN} (see Tables 1, 2).

The differential cross sections as functions of the parameters of the (*a*–*c*) *pN* and (*d*) $p\alpha$ amplitudes are displayed in Fig. 2 for three values of the incident-proton energy. In Fig. 2*a* (E_p = 0.2 GeV), curves *1*, *2*, and *3* correspond to the parameter sets 1, 2, and 3 from Table 2. The experimental data are better described with set no. 1 than with set no. 2 (as can be seen from Table 2, set no. 2 involves the overly large value of ε_{pN}^c = 5.199). It turns out that, for angles $\theta > 35°$–$40°$, the parameter set no. 2 is at odds with experimental data. In Fig. 2*b*, we present the same result, but at E_p = 0.6 GeV. The parameter sets 5, 6, 7, and 8 from Table 2 correspond to curves *1*, *2*, *3*, and *4*, respectively. All curves show maxima and minima at the same positions. Basically, the curves differ in the depths of the minima and in their behavior for $\theta > 40°$. As was indicated in [14, 22], the depths of the minima are controlled by the parameter ε_{pN}^c—the greater the value of this parameter, the shallower the minima. This is clearly seen in Fig. 2 as well, from a comparison of curve *1* (ε_{pp} = 1.11, ε_{pn} = 1.712) with curves *2* (ε_{pp} = –0.48, ε_{pn} = –0.36), *3* (ε_{pp} = 0.24, ε_{pn} = –0.295), and *4* ($\varepsilon_{pp} = \varepsilon_{pn}$ = –0.1). The results of the calculations with the parameter sets 7 and 9 are similar. In Fig. 2*c*, we have the same pattern at E_p = 1.0 GeV. Because of a great variety of the parameters at this energy, we performed calculations with several options. The parameter sets 10, 11, and 12 from Table 2 correspond to curves *1*, *2*, and *3*, respectively. It should be emphasized that, again, all the curves show minima and maxima at the same positions, differing only in absolute values at these minima and maxima. The dependence of the minima on the parameter ε_{pN}^c is clearly seen in the figure (we have $\varepsilon_{pp} = \varepsilon_{pn}$ = –0.3 for curve *1* and ε_{pp} = –0.05 and ε_{pn} = –0.4 for curve *3*). The parameters of the $p\alpha$ amplitudes correspond to set no. 7 from Table 1. The differential cross sections as functions of the parameters of the $p\alpha$ amplitudes are displayed in Fig. 2*d* at E_p = 1.0 GeV. Curves *1*, *2*, and *3* were calculated with the parameter sets 8, 7, and 5 from Table 1, respectively. (Curve *3* in Fig. 2*c* corresponds to curve *2* in Fig 2*d*, since the calculation was performed with the set no. 12 of the parameters of the *pN* amplitude.) A somewhat different pattern can be seen in Fig. 2*d*. Curves *1* and *2* differ insignificantly, mainly because of the difference in $\sigma_{p\alpha}$ (12.7 and 15.3 fm^2 for

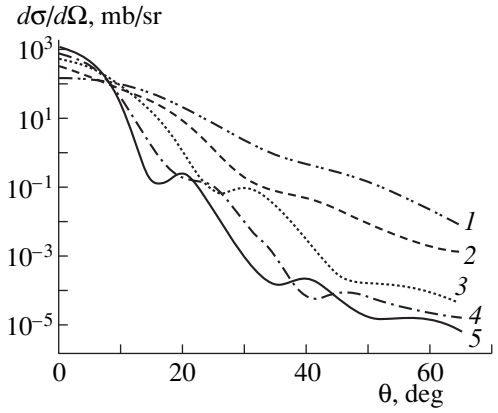

Fig. 1. Differential cross section as a function of the scattering angle at the incident-proton energies of E_p = (*1*) 0.2, (*2*) 0.4, (*3*) 0.6, (*4*) 0.8, and (*5*) 1.0 GeV.

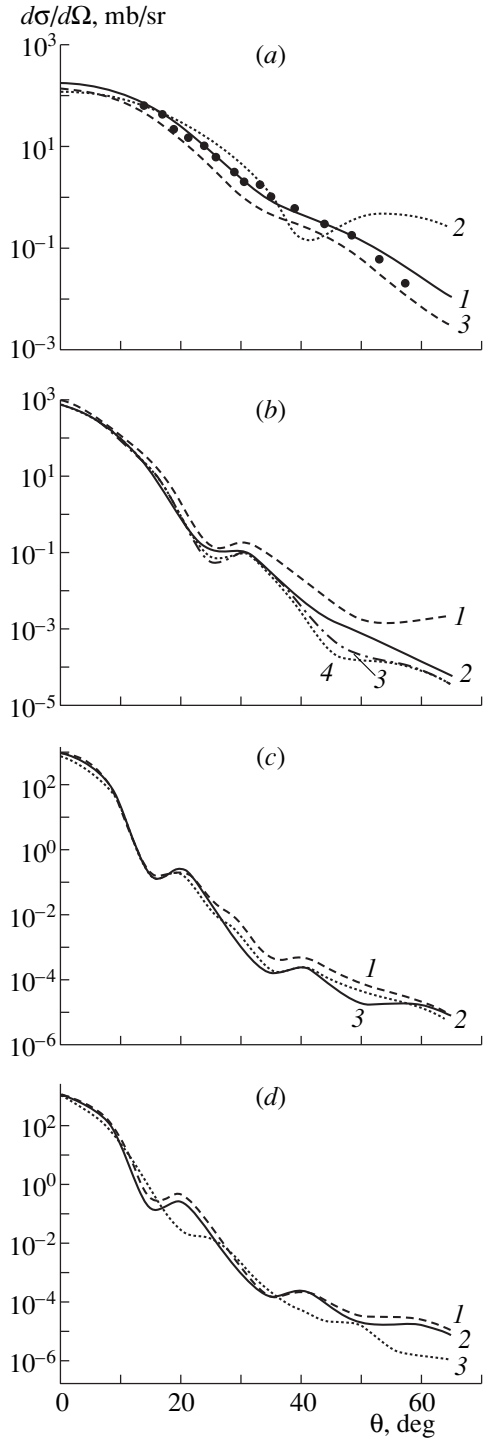

Fig. 2. Differential cross section as a function of the scattering angle for various sets of the parameters of the (*a*–*c*) *pN* and (*d*) *p*α amplitudes at the incident-proton energies of (*a*) E_p = 0.2 GeV (curves *1*, *2*, and *3* were calculated with the parameter sets 1, 2, and 3 from Table 2, respectively; the experimental data were borrowed from [3]); (*b*) E_p = 0.6 GeV (curves *1*, *2*, *3*, and *4* were calculated with the parameter sets 5, 6, 7, and 8 from Table 2, respectively); (*c*) E_p = 1.0 GeV (curves *1*, *2*, and *3* were calculated with the parameter sets 10, 11, and 12 from Table 2); and (*d*) E_p = 1.0 GeV (curves *1*, *2*, and *3* were calculated with the parameter sets 8, 7, and 5 from Table 1, respectively).

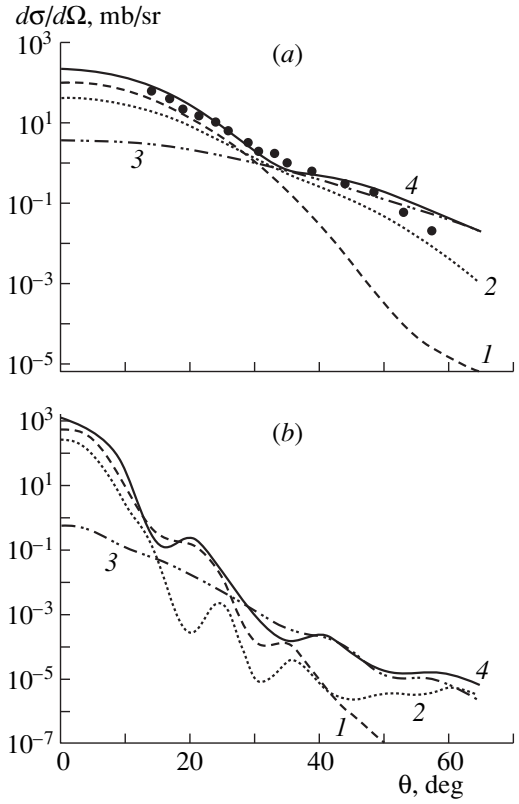

Fig. 3. Contributions of various multiplicities of scattering to the differential cross section at E_p = (*a*) 0.2 and (*b*) 1.0 GeV. Curves *1*, *2*, and *3* represent the contributions from, respectively, scattering on the alpha particle, scattering on the triton, and rescattering on the two clusters, while curve *4* shows the total contribution.

curves *1* and *2*, respectively). Beginning from the second maximum—that is, for θ > 20°—curve *3* is in antiphase with curves *1* and *2*. For want of experimental data at this energy, no definitive conclusions can be drawn unfortunately as to the quality of these parameter sets; however, the amplitude for set 5 differs qualitatively from the amplitudes for sets 7 and 8—in the amplitude corresponding set 5, there is no $(1 - q^2/t_1)$ pole. As was shown in [20], this pole ensures a better fit to the differential cross section for proton scattering on ^{4}He at high momentum transfers (which correspond to large scattering angles). This naturally affects the behavior of the differential cross section for proton scattering on ^{7}Li nuclei.

In Figs. 3*a* and 3*b*, the individual contributions of various multiplicities of scattering to the differential cross section are shown at two values of the proton energy. These contributions were determined by formula (39). Curves *1*, *2*, and *3* in Figs. 3*a* and 3*b* represent the contributions of, respectively, the first (scattering on the alpha-particle cluster), the second (scattering on the triton), and the third (rescattering on the two

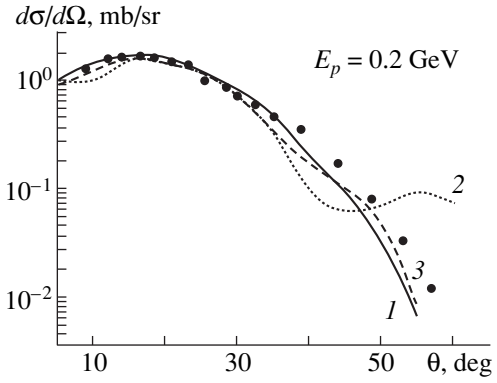

Fig. 4. Differential cross section for inelastic p^7Li scattering to the E^* = 0.48 MeV level as a function of the scattering angle for various values of the parameters of the *pN* amplitude. Curves *1*, *2*, and *3* were calculated with the parameter sets 1, 2, and 3 from Table 2, respectively. The experimental data were borrowed from [3].

clusters) term in (39) [$\frac{d\sigma}{d\Omega} = \frac{1}{2J+1}|M_1(\Omega_\alpha^c)|^2$, $\frac{d\sigma}{d\Omega} = \frac{1}{2J+1}|M_2(\Omega_t^c)|^2$, and $\frac{d\sigma}{d\Omega} = \frac{1}{2J+1}|M_3(\Omega_\alpha^c\Omega_t^c)|^2$, respectively]; finally, curve *4* depicts their total contribution to the cross section, $\frac{d\sigma}{d\Omega} = \frac{1}{2J+1}|M_1(\Omega_\alpha^c) + M_2(\Omega_t^c) - M_3(\Omega_\alpha^c\Omega_t^c)|^2$. From the figures, it can be seen that, at small angles, the main contribution to the differential cross section comes from scattering on the α and *t* clusters; the contribution from rescattering at θ = 0° is two orders of magnitude smaller, but it begins to approach the first two in absolute value at θ ≈ 30° and becomes dominant at large angles. This was confirmed in [14, 22, 36], where it was shown that, as the multiplicity of scattering grows, the absolute value of the amplitude decreases, but the rate of their decrease diminishes concurrently, so that higher multiplicities begin dominate over lower ones at specific angles. The regions where these contributions become commensurate are known as the interference regions. This is clearly manifested, for example, in Fig. 3*a*, where the minimum is smoothed, however, because the cross section is equal to the sum of three terms—each amplitude is complex-valued, and summation of the real and imaginary parts can lead either to a constructive (when the partial contributions are added) or to a destructive (when they are suppressed) interference. It should be noted here that, as can be seen from the results presented in Figs. 3*a* and 3*b*, it is impossible to describe satisfactorily the differential cross section by taking into account only single (even single and double) scattering. It is necessary to include all multiplicities of scattering on a cluster formed by nucleons (triton in our case) or to choose a realistic *px* amplitude if the cluster

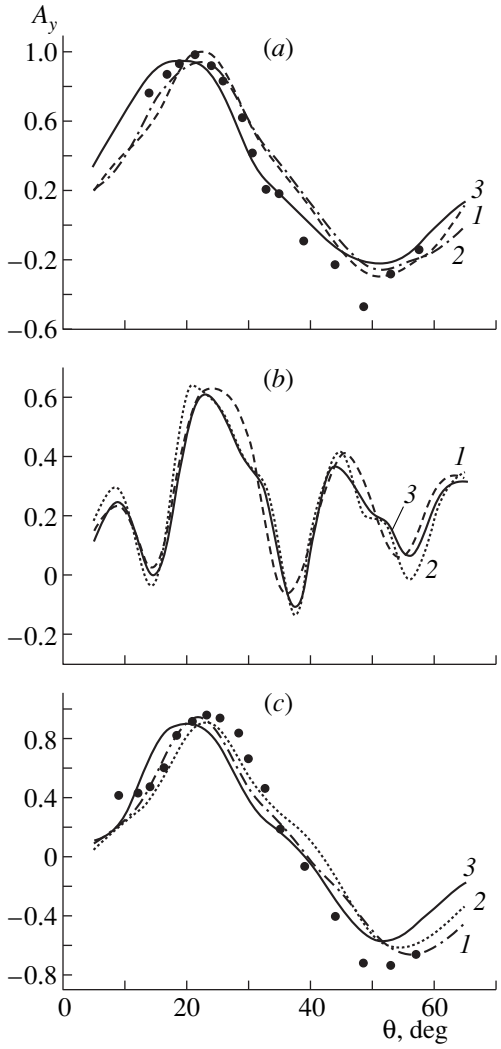

Fig. 5. Analyzing power A_y for (*a*, *b*) elastic and (*c*) inelastic proton scattering on ^{7}Li nuclei at (*a*, *c*) E_p = 0.2 GeV (curves *1*, *2*, and *3* were calculated with, respectively, the sets 1, 3, and 4 of the parameters of the *pN* amplitude from Table 2) and (*b*) E_p = 1.0 GeV (curves *1*, *2*, and *3* were calculated with, respectively, the sets 10, 11, and 13 of the parameters of the *pN* amplitude from Table 2). The experimental data were borrowed from [3].

is considered as a structureless system (alpha particle in our case).

The differential cross sections for inelastic proton scattering on ^{7}Li nuclei at E_p = 0.2 GeV are shown in Fig. 4 for three sets of the *pN* amplitudes. Curves *1*, *2*, and *3* were calculated with the amplitude sets 1, 2, and 3, respectively. It was indicated above that, for elastic scattering, the calculations with the parameter sets 1 and 3 yield close results (the parameters themselves are close, too). At the same time, the parameters from set 2 differ sharply in the values of ε_{pN}^c and β_{pN}^c from those in sets 1 and 3. This is reflected in the behavior of curve *2*—it describes experimental data less well than curves *1* and *3*.

In Fig. 5, the calculated analyzing powers for elastic (Figs. 5*a*, 5*b*) and inelastic (Fig. 5*c*) proton scattering at E_p = 0.2 GeV (Figs. 5*a*, 5*c*) and E_p = 1.0 GeV (Fig. 5*b*) are depicted for various values of the parameters of the *pN* amplitude. At E_p = 0.2 GeV, we used set 2 from Table 1 for the parameters of the *pN* amplitude. For the *pN* amplitude, we took the parameter sets 1 (curve *1*), 3 (curve *2*), and 4 (curve *3*) from Table 2; here, the spin–isospin parameters for sets 1 and 3 were chosen to be identical to those for set 4, but it should be borne in mind that this is not quite correct at the incident-proton energy of 0.2 GeV. Since no fitting was performed for the parameters of the spin–orbit component of the amplitude (this is postponed to a future study), the resulting qualitative agreement between the calculated analyzing power and experimental data from [3] can be thought to be quite good both for elastic and for inelastic scattering. At E_p = 1.0 GeV, there are a few equivalent sets of the parameters of the spin–orbit *pN* and *p*α amplitudes (see Tables 1, 2); unfortunately, there are no experimental data in this region. Nevertheless, we have calculated the analyzing power at E_p = 1.0 GeV, the results being plotted in Fig. 5*b*. Here, we have used the parameter set 6 (Table 1) for the *p*α amplitude and sets 10 (curve *1*), 11 (curve *2*), and 13 (curve 3) from Table 2 for the *pN* amplitudes. All three curves are sufficiently close to one another—the maxima, the minima, and the numbers of oscillations are virtually coincident for them, only slight distinctions between the absolute values being observed. We note that the minima of A_y correlate with the minima of the differential cross sections, a regularity that is also observed for scattering on other nuclei [19, 20, 22]. Curve *1* is more symmetric, possibly because the parameters of the *pp* and *pn* amplitudes are identical in this set (no. 10).

4. CONCLUSIONS

A systematic analysis of the differential cross sections and of the analyzing power A_y for p^7Li scattering at various energies of incident protons cannot be performed because of paucity of experimental data. However, some conclusions can be drawn from currently available information.

(i) The diffractive pattern of elastic scattering manifests itself more clearly with increasing energy of incident particles. This is one of the reasons why, at E_p = 0.2 GeV, a diffractive pattern appears neither in scattering on the ^{6}Li nucleus [10] nor in scattering on the ^{7}Li nucleus [3], despite the fact that the former and the latter are, respectively, spherically symmetric ($Q \sim 0$) and asymmetric ($Q \sim 40$ mb). Hence, only at sufficiently high energies ($E \sim 0.6$–1.0 GeV) can we say that the diffraction minimum is filled owing to the contribution of the quadrupole component.

(ii) For $E_p < 1$ GeV, it is illegitimate to take into account only single collisions in calculating the differential cross section and the analyzing power A_y. It is necessary either to include all multiplicities of scattering on nucleons or to use a well-fitted (realistic) elementary *px* amplitude, which effectively incorporates contributions from multiple collisions.

(iii) It is well known that data on the differential cross sections and on the analyzing power A_y can be used as a test for the parameters of the *px* amplitudes. In particular, such a test can reject parameters that do not correspond to experimental data. In our case, this concerns the parameter set for the *pN* amplitude from [23] with the unusually large ratio of the real part of the amplitude to its imaginary part ($\varepsilon^c_{pn} = 5.199$). Here, we do not draw definitive conclusions from the calculation of the analyzing power, taking our calculations to be preliminary, because we did not fit the parameters of the *pN* amplitude at E_p = 0.2 GeV. Moreover, it was indicated in [38] that, in order to refine the parameters of the elementary amplitudes, it is necessary to analyze all observables of proton–nucleus scattering, including the spin-rotation function Q_0, because it is the spin-rotation function that exhibits the greatest variations upon going over from one set of proton–nucleon amplitudes to another.

APPENDIX

The coefficients in the operator Ω^c_t determined by formula (29) at $\nu = c$ are given by

$$g^c_m = (F^c_n, F^c_n, F^c_p, -(F^c_n)^2, -F^c_nF^c_p, -F^c_nF^c_p, (F^c_n)^2F^c_p),$$

$$c^c_m = (\lambda^c_n, \lambda^c_n, \lambda^c_p, 2\lambda^c_n, \lambda^c_{np}, \lambda^c_{np}, (2\lambda^c_n + \lambda^c_p)),$$

$$e^c_m = \left(\frac{1}{9}\lambda^c_n, \frac{1}{9}\lambda^c_n, \frac{4}{9}\lambda^c_p, \frac{2}{9}\lambda^c_n, \left(\frac{1}{9}\lambda^c_n + \frac{4}{9}\lambda^c_p\right), \left(\frac{2}{9}\lambda^c_n + \frac{4}{9}\lambda^c_p\right)\right),$$

$$f^c_m = \left(\frac{1}{4}\lambda^c_n, \frac{1}{4}\lambda^c_n, 0, \frac{1}{2}\lambda^c_n, \frac{1}{4}\lambda^c_n, \frac{1}{4}\lambda^c_n, \frac{1}{2}\lambda^c_n\right),$$

$$h^c_m = (2\lambda^c_n, 2\lambda^c_n, 2\lambda^c_p, 4\lambda^c_n, 2\lambda^c_{np}, 2\lambda^c_{np}, (4\lambda^c_n + 2\lambda^c_p)),$$

$$k^c_m = \left(\frac{2}{3}\lambda^c_n, \frac{2}{3}\lambda^c_n, -\frac{4}{3}\lambda^c_p, \frac{4}{3}\lambda^c_n, \left(\frac{2}{3}\lambda^c_n - \frac{4}{3}\lambda^c_p\right), \left(\frac{2}{3}\lambda^c_n - \frac{4}{3}\lambda^c_p\right), \left(\frac{4}{3}\lambda^c_n - \frac{4}{3}\lambda^c_p\right)\right),$$

$$n^c_m = (\lambda^c_n, -\lambda^c_n, 0, 0, \lambda^c_n, -\lambda^c_p, 0),$$

$$l^c_m = (-\lambda^c_n, \lambda^c_n, 0, 0, -\lambda^c_n, \lambda^c_n, 0),$$

$$m^c_m = \left(-\frac{2}{3}\lambda^c_n, -\frac{2}{3}\lambda^c_n, \frac{4}{3}\lambda^c_p, -\frac{4}{3}\lambda^c_n, \left(-\frac{2}{3}\lambda^c_n + \frac{4}{3}\lambda^c_p\right), \left(-\frac{2}{3}\lambda^c_n + \frac{4}{3}\lambda^c_p\right), \left(-\frac{4}{3}\lambda^c_n + \frac{4}{3}\lambda^c_p\right)\right),$$

$$s_m^c = \left(-\lambda_n^c, \lambda_n^c, 0, 0, -\frac{1}{3}\lambda_n^c, \frac{1}{3}\lambda_n^c, 0\right).$$

The coefficients in the operator Ω_t^s determined by formula (29) at $\nu = s$ can be represented as

$$g_m^s = \boldsymbol{\sigma}\cdot\mathbf{n}[\xi_m(\boldsymbol{\rho}-\boldsymbol{\rho}_t), \alpha_m\tilde{\mathbf{b}}, \beta_m\tilde{\mathbf{a}}, \varphi_m(\rho^2+\rho_t^2),$$
$$\gamma_m b^2, \delta_m a^2, \varepsilon_m\boldsymbol{\rho}\cdot\boldsymbol{\rho}_t, -\varsigma_m\boldsymbol{\rho}\cdot\tilde{\mathbf{b}}, -\varsigma_m\boldsymbol{\rho}_t\cdot\tilde{\mathbf{b}}, \theta_m\boldsymbol{\rho}\cdot\tilde{\mathbf{a}},$$
$$-\theta_m\boldsymbol{\rho}_t\cdot\tilde{\mathbf{a}}, \mu_m\tilde{\mathbf{a}}\cdot\tilde{\mathbf{b}}],$$

$$\xi_m = (F_n^s, F_n^s, F_p^s, 0, 0, 0),$$

$$\alpha_m = \left(-\frac{1}{3}F_n^s, -\frac{1}{3}F_n^s, \frac{2}{3}F_p^s, 0, 0, 0\right),$$

$$\theta_m = \frac{1}{2}F_p^sF_n^s(0, 0, 0, 0, 1, 1),$$

$$\beta_m = -\frac{1}{2}F_n^s(1, 1, 0, 0, 0, 0),$$

$$\varphi_m = -(0, 0, 0, (F_n^s)^2, -F_n^sF_p^s, -F_n^sF_p^s),$$

$$\gamma_m = \frac{1}{9}(0, 0, 0, -(F_n^s)^2, 2F_n^sF_p^s, 2F_n^sF_p^s),$$

$$\delta_m = \frac{1}{4}(F_n^s)^2(0, 0, 0, 1, 0, 0, 0),$$

$$\varepsilon_m = 2(0, 0, 0, (F_n^s)^2, F_n^sF_p^s, F_n^sF_p^s),$$

$$\varsigma_m = \frac{1}{3}(0, 0, 0, 2(F_n^s)^2, F_n^sF_p^s, F_n^sF_p^s),$$

$$\mu_m = \frac{1}{3}F_n^sF_p^s(0, 0, 0, 0, 1, -1),$$

$$c_m^s = (\lambda_n^s, \lambda_n^s, \lambda_p^s, 2\lambda_n^s, \lambda_{np}^s, \lambda_{np}^s), \quad d_m^s = c_m^s,$$

$$e_m^s = \left(\frac{1}{9}\lambda_n^s, \frac{1}{9}\lambda_n^s, \frac{4}{9}\lambda_p^s, \frac{2}{9}\lambda_n^s, \left(\frac{1}{9}\lambda_n^s + \frac{4}{9}\lambda_p^s\right), \left(\frac{1}{9}\lambda_n^s + \frac{4}{9}\lambda_p^s\right)\right),$$

$$f_m^s = \left(\frac{1}{4}\lambda_n^s, \frac{1}{4}\lambda_n^s, 0, \frac{1}{2}\lambda_n^s, \frac{1}{4}\lambda_n^s, \frac{1}{4}\lambda_n^s\right),$$

$$h_m^s = (2\lambda_n^s, 2\lambda_n^s, 2\lambda_p^s, 4\lambda_n^s, 2\lambda_{np}^s, 2\lambda_{np}^s),$$

$$k_m^s = \left(\frac{2}{3}\lambda_n^s, \frac{2}{3}\lambda_n^s, -\frac{4}{3}\lambda_p^s, \frac{4}{3}\lambda_n^s, \left(\frac{2}{3}\lambda_n^s - \frac{4}{3}\lambda_p^s\right),\right.$$
$$\left.\left(\frac{2}{3}\lambda_n^s - \frac{4}{3}\lambda_p^s\right)\right),$$

$$n_m^s = (\lambda_n^s, -\lambda_n^s, 0, 0, \lambda_n^s, -\lambda_n^s),$$

$$m_m^s = \left(-\frac{2}{3}\lambda_n^s, -\frac{2}{3}\lambda_n^s, \frac{4}{3}\lambda_p^s, -\frac{4}{3}\lambda_n^s, -\left(\frac{2}{3}\lambda_n^s - \frac{4}{3}\lambda_p^s\right),\right.$$
$$\left.-\left(\frac{2}{3}\lambda_n^s - \frac{4}{3}\lambda_p^s\right)\right),$$

$$l_m^s = (-\lambda_n^s, \lambda_n^s, 0, 0, -\lambda_n^s, \lambda_n^s),$$

$$s_m^s = \left(-\frac{1}{3}\lambda_n^s, \frac{1}{3}\lambda_n^s, 0, 0, -\frac{1}{3}\lambda_n^s, \frac{1}{3}\lambda_n^s\right),$$

where $\lambda_{np}^\nu = \lambda_n^\nu + \lambda_p^\nu$.

REFERENCES

1. D. Hasselgren, P. U. Renberg, O. Sundberg, and G. Tibell, Nucl. Phys. **69**, 81 (1965).
2. B. Geoffrion, N. Marty, M. Morlet, *et al.*, Nucl. Phys. A **116**, 209 (1968).
3. C. W. Glover, C. C. Foster, P. Schwandt, *et al.*, Phys. Rev. C **43**, 1664 (1991).
4. S. J. Wallace, Phys. Rev. C **12**, 179 (1975).
5. V. M. Kolybasov and M. S. Marinov, Usp. Fiz. Nauk **109**, 137 (1973) [Sov. Phys. Usp. **16**, 53 (1973)]; V. M. Kolybasov, Pis'ma Zh. Éksp. Teor. Fiz. **46**, 139 (1987) [JETP Lett. **46**, 173 (1987)].
6. É. E. Sapershteĭn and V. E. Starodubskiĭ, Yad. Fiz. **46**, 69 (1987) [Sov. J. Nucl. Phys. **46**, 44 (1987)].
7. J. Lichtenstadt, J. Alster, M. A. Moinester, *et al.*, Phys. Lett. B **121**, 377 (1983); **219**, 394 (1989); **244**, 173 (1990).
8. H. Kanada, Q. K. K. Liu, and Y. C. Tang, Phys. Rev. C **22**, 813 (1980).
9. S. B. Dubovichenko and M. A. Zhusupov, Izv. Akad. Nauk Kaz. SSR, Ser. Fiz.-Mat. **4**, 44 (1984).
10. B. Buck, R. A. Baldock, and A. Rubio, J. Phys. G **11**, L11 (1985); B. Buck and A. C. Merchant, J. Phys. G **14**, L211 (1988).
11. C. W. Glover, C. C. Foster, P. Schwandt, *et al.*, Phys. Rev. C **41**, 2487 (1990).
12. V. G. Neudatchin and Yu. F. Smirnov, in *Modern Problems in Optics and Nuclear Physics* (Naukova Dumka, Kiev, 1974), p. 225.
13. S. B. Dubovichenko and A. V. Dzhazairov-Kakhramanov, Yad. Fiz. **56** (2), 87 (1993) [Phys. At. Nucl. **56**, 195 (1993)]; **57**, 784 (1994) [**57**, 733 (1994)].
14. G. D. Alkhazov, V. V. Anisovich, and P. É. Volkovitskiĭ, *Diffraction Interactions of Hadrons with Nuclei at High Energies* (Nauka, Leningrad, 1991).
15. Tan Zhen-Qiang and Ruan Wen-Ying, Nucl. Phys. A **514**, 295 (1990).
16. M. A. Zhusupov and E. T. Ibraeva, Yad. Fiz. **61**, 51 (1998) [Phys. At. Nucl. **61**, 46 (1998)].
17. L. G. Dakhno and N. N. Nikolaev, Nucl. Phys. A **436**, 653 (1985).
18. S. B. Dubovichenko and M. A. Zhusupov, Izv. Akad. Nauk Kaz. SSR, Ser. Fiz.-Mat. **4**, 64 (1987).
19. Yu. A. Berezhnoĭ, V. P. Mikhaĭlyuk, and V. V. Pilipenko, Izv. Akad. Nauk SSSR, Ser. Fiz. **57**, 1953 (1981); Yad.

Fiz. **55**, 1885 (1992) [Sov. J. Nucl. Phys. **55**, 1044 (1992)].
20. Li Quing-run and Zhou Jin-li, J. Phys. G **17**, 663 (1991).
21. L. Ray, Phys. Rev. C **19**, 1855 (1979); **20**, 1857 (1979).
22. A. G. Sitenko and I. S. Dotsenko, Yad. Fiz. **17**, 67 (1973) [Sov. J. Nucl. Phys. **17**, 35 (1973)]; Fiz. Élem. Chastits At. Yadra **4**, 546 (1973) [Sov. J. Part. Nucl. **4**, 231 (1973)].
23. D. K. Hasell, A. Bracco, H. P. Gubler, *et al.*, Phys. Rev. C **34**, 236 (1986).
24. I. M. A. Tag Eldin *et al.*, J. Phys. G **16**, 1051 (1990).
25. G. J. Igo *et al.*, Rev. Mod. Phys. **50**, 523 (1978).
26. J. P. Auger *et al.*, Nucl. Phys. A **262**, 372 (1976).
27. J. Fain *et al.*, Nucl. Phys. A **262**, 413 (1976).
28. B. L. Birbrair *et al.*, Yad. Fiz. **28**, 625 (1978) [Sov. J. Nucl. Phys. **28**, 321 (1978)].
29. G. D. Alkhasov, S. L. Belostotsky, E. A. Damaskinsky, *et al.*, Phys. Lett. B **85**, 43 (1979).
30. G. Faldt and I. Hulthage, J. Phys. G **4**, 363 (1978).
31. C. H. Gustaffson and E. Lambert, Ann. Phys. (N.Y.) **111**, 304 (1978).
32. J. P. Auger *et al.*, J. Phys. G **7**, 1627 (1981).
33. G. D. Alkhazov, V. E. Starodubskiĭ, *et al.*, Preprint No. 449, LIYaF (Leningrad Nuclear Physics Institute, Leningrad, 1978).
34. W. Czyz, L. Lesniak, and H. Walek, Nucl. Phys. B **19**, 125 (1970).
35. H. Lesniak and L. Lesniak, Nucl. Phys. B **38**, 221 (1972).
36. M. A. Zhusupov and E. T. Ibraeva, Izv. Akad. Nauk, Ser. Fiz. **60** (5), 169 (1996).
37. I. S. Gradshteyn and I. M. Ryzhik, *Table of Integrals, Series, and Products* (Fizmatgiz, Moscow, 1963; Academic, New York, 1980).
38. V. V. Pilipenko and A. P. Soznik, Yad. Fiz. **44**, 369 (1986) [Sov. J. Nucl. Phys. **44**, 235 (1986)].
39. D. A. Varshalovich, A. N. Moskalev, and V. K. Khersonskii, *Quantum Theory of Angular Momentum* (Nauka, Leningrad, 1975; World Sci., Singapore, 1988).

Translated by A. Isaakyan

Physics of Atomic Nuclei, Vol. 63, No. 11, 2000, pp. 1923–1926. Translated from Yadernaya Fizika, Vol. 63, No. 11, 2000, pp. 2016–2019.

ELEMENTARY PARTICLES AND FIELDS
Experiment

Potential of Deep-Underwater Neutrino Telescopes for Recording Muons from Charm Decay

V. A. Naumov, T. S. Sinegovskaya, and S. I. Sinegovsky
Irkutsk State University, ul. Lermontova 126, Irkutsk, 664033 Russia
Received October 7, 1999; in final form, February 15, 2000

Abstract—Within several models of charm production in hadron–nucleus interactions, it is shown that prompt-muon fluxes at the depths of operating and designed neutrino telescopes (1–4 km) can in principle be measured in experiments with a high detection threshold. © *2000 MAIK "Nauka/Interperiodica".*

1. INTRODUCTION

Not only is charm production in hadron interactions at energies $E \gg 1$ TeV a phenomenon of interest for particle physics, it also has an important application in high-energy astronomy—namely, atmospheric neutrinos from the decays of charmed hadrons (predominantly, D, D^*, and Λ_c) produced in the interactions of cosmic rays with the Earth's atmosphere appear to be the main source of background in detecting (quasi)diffuse fluxes of neutrinos of astrophysical and cosmological origin [1]. The flux of atmospheric muons genetically related to neutrinos is a natural tool for testing charm-production models and for more precisely estimating the background of atmospheric neutrinos [2].

Direct spectrometric measurements of muon fluxes with ground-based arrays have not yet covered the muon-energy region above 20 TeV for nearly horizontal fluxes and the region above 3 TeV for vertical fluxes. The statistical significance of these measurements is insufficient for extracting quantitative information about the contribution of muons from charm decay—that is, prompt muons. The potential of underground experiments is considerably higher, but there is a natural limit here caused by irregularities in the density and chemical composition of rock around the facility used, by a limited detector volume, etc. Therefore, it is pertinent to recall important advantages of deep-underwater Cherenkov facilities, such as a high degree of homogeneity of the absorbing medium (water, ice) and a large sensitive volume, and to discuss prospects for neutrino telescopes like AMANDA [3], Baikal NT [4], and NESTOR [5] in the problem of measuring prompt-muon fluxes. It is important to assess depths, threshold energies, and zenith angles appropriate for experimental measurements aimed at reliably identifying the contribution of prompt muons and—as an eventual goal, if achievable in principle—for establishing the most adequate models of charm production.

In this article, we discuss the results obtained by calculating the flux of high-energy muons ($E_\mu \gtrsim 1$ TeV) at sea level and its transformation at large depths in water (between 1 and 20 km). The differential cross sections for charm production in nucleon and pion interactions with light nuclei were calculated within the model of quark–gluon strings (QGS model also known as QGSM) [6], the recombination quark–parton model (RQPM) [7], and the model [8] that is based on perturbative QCD with allowance for nonleading contributions of order α_s^3 and which employs, at the stage of hadronization, nonperturbative fragmentation functions [9].

2. ATMOSPHERIC MUONS AT SEA LEVEL

For various zenith angles θ, the energy spectra of muons from pion and kaon decays (π-, K-muons in the following) were calculated on the basis of the nuclear-cascade model [10] refined in [2, 11]. The parametrization proposed in [12] was chosen for the spectrum of primary cosmic rays. The same nuclear-cascade model was used to compute the prompt-muon contributions within the QGSM and the QPRM. The predictions of the QCD-based model [8] were obtained within the less detailed nuclear-cascade model and only for nearly vertical directions. The resulting distinctions can be neglected, however, against more significant uncertainties associated with known arbitrariness in choosing parameters of the QCD-based model like μ_R [the energy scale specifying the renormalized charge $\alpha_s \sim 1/\ln(\mu_R/\Lambda_{\rm QCD})$] and μ_F (the factorization scale separating perturbative dynamics from the infrared region) and the parton distributions in the nucleon. In all cases, the differential widths with respect to the inclusive semileptonic decays of D and Λ_c were calculated on the basis of the simple method proposed in [7].

The calculated differential spectra of muons at sea level, $D_\mu(E_\mu, \theta)$, for two zenith-angle values of $\theta = 0°$ and 89° are displayed in Fig. 1, along with experimental data from [13–18]. All quoted data, with the exception of those from [13] (MUTRON spectrometer), were obtained by applying various methods to processing the results of underground experiments. A detailed com-

1063-7788/00/6311-1923$20.00

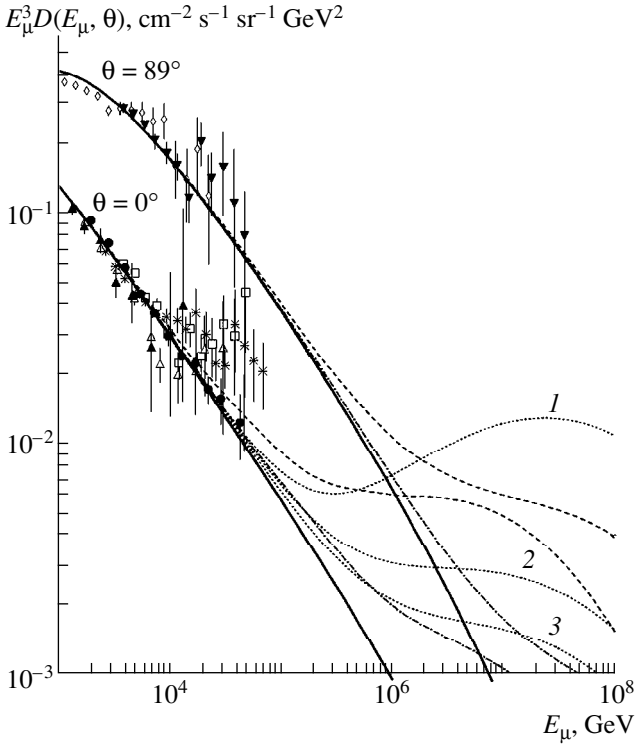

Fig. 1. Vertical and nearly horizontal fluxes of muons at sea level. The experimental data were borrowed from (◊) [13] (89°), (□, ▼) [14], (∗) [15], (●) [16], (▲) [17], and (△) [18]. The results of the calculations taking into account only π-, *K*-muons are shown by solid curves. The results including the prompt-muon contribution were computed on the basis of the (dashed curves) RQPM, (dash-dotted curves) QGSM and (dotted curves) QCD-based model from [8] (the figures 1, 2, and 3 on the dotted curves correspond to the QCD-1, QCD-2, and QCD-3 versions, respectively).

parison with experimental data at sea level was presented in [2, 19].

The RQPM predicts a relatively fast variation of the exponent of the muon spectrum. We denote by $E_\mu^c(\theta)$ the energy at which the contributions of ordinary muons from (π and *K* decays) and prompt muons become equal. Within the RQPM, we have $E_\mu^c(0°) \approx$ 150 TeV and $E_\mu^c(89°) \approx 1$ PeV. According to the QCD-based model developed in [8], the contribution of prompt muons begins to dominate in the total muon flux at higher energies. Specific values of $E_\mu^c(\theta)$ depend heavily on the choice of the parton distributions and other model parameters. In Fig. 1, curve *1* represents the results obtained for the so-called MRSD model of the parton distributions [20] with $\mu_F = 2\mu_R = 2m_c$; while curves *2* and *3* correspond to the CTEQ3 model [21] with $\mu_F = 2\mu_R = 2m_c$ and $\mu_F = \mu_R = m_c$, respectively. Below, these versions will carry the labels QCD-1, QCD-2, and QCD-3. In all three cases, the *c*-quark mass m_c was set to 1.3 GeV. Within the QCD-1 model, the critical energies $E_\mu^c(\theta)$ are numerically close to those obtained within the RQPM, while, within QCD-3, they are close to the QGSM predictions [$E_\mu^c(0°) \approx 850$ TeV, $E_\mu^c(89°) \approx 5$ PeV]. In order to distinguish experimentally the versions of the QCD-based model by using sea-level muon data, it is necessary to cover energies $E_\mu \gtrsim 100$ TeV.

From Fig. 1, we can see that, for $E_\mu > 10$–20 TeV, none of the models being discussed can reproduce the data from the experiment with x-ray-emulsion chambers evolved at Moscow State University [14] and from the experiment with the Frèjus underground detector [15]; at the same time, none is ruled out by recent LVD results (Gran Sasso) [16]. As a matter of fact, the remaining experimental data presented in Fig. 1 furnish no new arguments in favor of or against the models in question. This paradoxical situation clearly demonstrates that new experiments at significantly higher energies are required. Such experiments can be performed only with large deep-underwater telescopes.

3. UNDERWATER SPECTRA AND ANGULAR DISTRIBUTIONS OF MUONS

In order to calculate the transformation of the muon spectrum at large depths in water, we used the analytic method developed in [22]. For the boundary spectrum that decreases sufficiently fast with increasing energy, this method allows us to solve approximately the kinetic equation with a collision integral that takes into account the actual energy dependences of the differential cross sections for radiative losses (e^+e^- production, bremsstrahlung) and of the cross sections for photonuclear muon interaction. The calculation was tested by comparing the numerical results it yields with the entire body of available data on muon absorption in rock of various compositions and in water [2], as well as with data on the muon angular distributions measured at the NT-36 and AMANDA-B4 facilities (see [4] and [3], respectively) for low recording thresholds [23].

The calculated integral spectra $I_\mu(>E_\mu, h, \theta)$ of ordinary and prompt muons under water are displayed in Fig. 2 versus (*a*) the energy E_μ, (*b*) the depth *h* along the vertical, and (*c*, *d*) $\cos\theta$ at fixed values of the other variables. Figures 2*a*, 2*c*, and 2*d* display the results obtained on the basis of the QCD-2 version, while Fig. 2*b* shows the relevant results for all three versions of the QCD-based model.

A reliable identification of the prompt-muon contribution can be expected if there is an intersection of the curves for prompt and for π-, *K*-muons, in which case the number of events is doubled with respect to that which is expected for π-, *K*-muons. It should be noted that the curves describing the angular distributions can intersect twice, as in the case of the RQPM at a depth of $h = 1.15$ km (Fig. 2*d*). This occurs if the prompt-

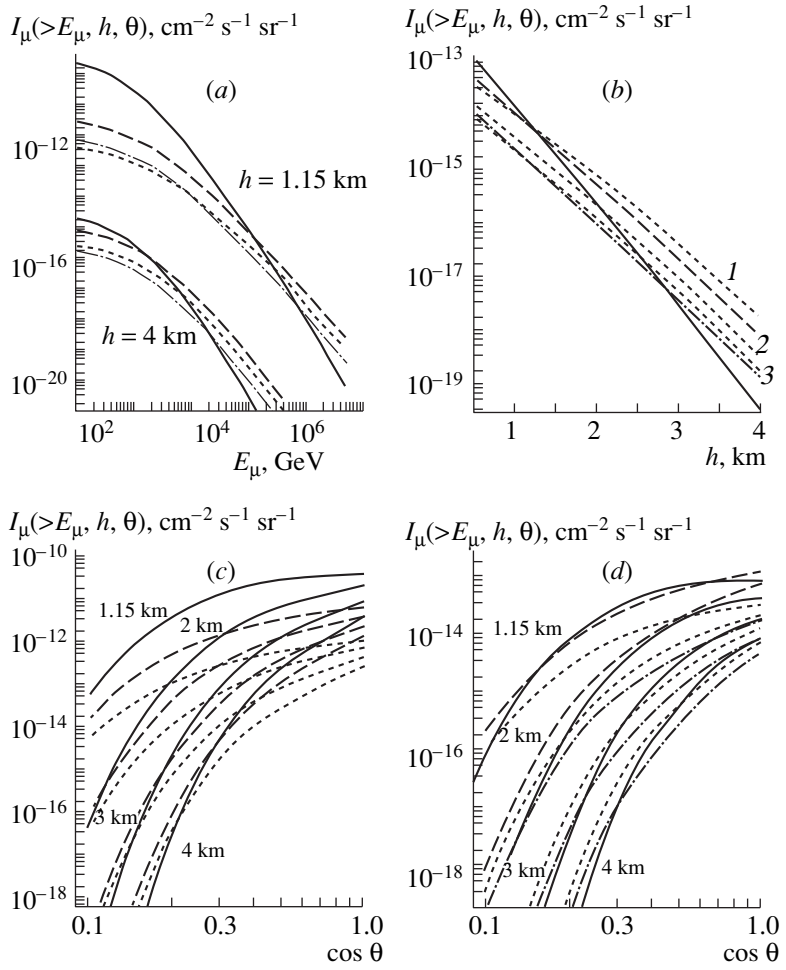

Fig. 2. Results of calculations for muon fluxes at depths of 1–4 km under water: (*a*) integrated energy spectra at a zenith angle of $\theta = 78.46°$ ($\sec\theta = 5$); (*b*) fluxes of muons with energies $E_\mu \geq 100$ TeV as functions of the vertical depth h at $\sec\theta = 5$; (*c*) zenith-angle distributions for $E_\mu \geq 10$ TeV at the depths of h = 1.15, 2, 3, and 4 km; and (*d*) as in Fig. 2*c*, but for $E_\mu \geq 100$ TeV. The contribution of π-, *K*-muons is shown by solid curves. The prompt-muon contributions calculated on the basis of the RQPM, the QGSM, and the QCD-based model from [8] are depicted by dashed, dash-dotted, and dotted curves, respectively.

muon contribution at a given depth exceeds the contribution of π-, *K*-muons even at the vertical and is due to the fact that the factor of angular enhancement at sea level is significantly higher for π-, *K*-mesons than for prompt muons.

From Fig. 2, we can see that the coordinates of the points where the spectra of π-, *K*-muons and of prompt muons intersect are highly model-dependent. By way of example, we indicate that, at $\sec\theta = 5$, the minimal and the maximal predictions of the models in question for the prompt-muon flux at the intersection points differ by three orders of magnitude (Fig. 2*b*). On the basis of this fact, one can in principle test charm-production models experimentally and, in particular, set constraints on the parameters of the QCD-based model.

At a detection threshold of $E_\mu \sim 1$ TeV, only telescopes arranged at depths of 3 to 4 km (for example, NESTOR) can ensure a reliable identification of prompt muons for $\theta \lesssim 80°$. An order of magnitude increase in the threshold (Fig. 2*c*) would permit one to address such a problem with the under-ice telescope AMANDA ($h \approx 2$ km), but at larger zenith angles of $\theta \gtrsim 85°$. At the threshold of $E_\mu = 10$ TeV, experiments at the NESTOR can be performed for smaller angles, whereby one achieves an increase in statistics and a reduction of the background from π-, *K*-muons. The higher threshold of $E_\mu = 100$ TeV (Figs. 2*b*, 2*d*) provides the possibility of detecting prompt muons at the Baikal neutrino telescope as well (h = 1.15 km). At a fixed value of θ, the energy $E_\mu^c(\theta)$ at which the prompt-muon contribution doubles the total flux is significantly less at the depth of NESTOR than at the depth of the Baikal neutrino telescope (by a factor of 35 to 60 at $\sec\theta = 5$). For example, the QCD-2 version predicts

$E_\mu^c \approx 8$ TeV for the NESTOR facility and $E_\mu^c \approx 300$ TeV for the Baikal neutrino telescope. Nevertheless, the flux $I_\mu(>E_\mu^c, h, \theta)$ is nearly one order of magnitude greater in the latter case. This example illustrates a more general statement. In future experiments aimed at detecting muons from charm decay, facilities located at a small depth (1 to 2 km) may prove to be preferable, in some respects, to those located at larger depths, provided that the energy detection threshold and the range of zenith angles are chosen appropriately ($E_\mu \sim 100$ TeV and 70°–80°, respectively), all other conditions being the same.

ACKNOWLEDGMENTS

This work was supported by the Ministry for General and Professional Education of the Russian Federation within the program Universities of Russia—Basic Research (project no. 015.02.01.04).

REFERENCES

1. S. Barwick, F. Halzen, D. Lowder, *et al.*, J. Phys. G **18**, 225 (1992); L. Nellen, K. Manheim, and P. L. Biermann, Phys. Rev. D **47**, 5270 (1993); T. K. Gaisser, F. Halzen, and T. Stanev, Phys. Rep. **258**, 173 (1995); G. C. Hill, Astropart. Phys. **6**, 215 (1997).
2. E. V. Bugaev, A. Misaki, V. A. Naumov, *et al.*, Phys. Rev. D **58**, 054001 (1998).
3. AMANDA Collab. (S. Hundertmark), in *Proceedings of the 26th International Cosmic Ray Conference, Salt Lake City, 1999*, Vol. 2, p. 12; AMANDA Collab. (E. Andres, P. Askebjer, S. W. Barwick, *et al.*), astro-ph/9906203; AMANDA Collab. (C. Spiering), astro-ph/9906205.
4. Baikal Collab. (I. A. Belolaptikov, L. B. Bezrukov, B. A. Borisovets, *et al.*), Astropart. Phys. **7**, 263 (1997).
5. NESTOR Collab. (E. Anassontzis *et al.*), in *Proceedings of the Baikal School on Fundamental Physics, Astrophysics, and Physics of the Microcosm, Irkutsk, 1998*, Ed. by V. A. Naumov *et al.* (Irkutsk. Gos. Univ., Irkutsk, 1998), p. 105; NESTOR Collab. (S. Bottai), in *Proceedings of the 26th International Cosmic Ray Conference, Salt Lake City, 1999*, Vol. 2, p. 456.
6. A. B. Kaĭdalov and O. I. Piskunova, Yad. Fiz. **43**, 1545 (1986) [Sov. J. Nucl. Phys. **43**, 994 (1986)].
7. E. V. Bugaev, V. A. Naumov, S. I. Sinegovsky, and E. S. Zaslavskaya, Nuovo Cimento C **12**, 41 (1989).
8. L. Pasquali, M. H. Reno, and I. Sarcevic, Phys. Rev. D **59**, 034020 (1999).
9. P. Nason, S. Dawson, and R. K. Ellis, Nucl. Phys. B **303**, 607 (1988); **327**, 49 (1989); M. L. Mangano, P. Nason, and G. Ridolfi, Nucl. Phys. B **373**, 295 (1992); M. L. Mangano, Preprint No. CERN-TH/97-328 (Geneva, 1997); hep-ph/9711337.
10. A. N. Vall, V. A. Naumov, and S. I. Sinegovskiĭ, Yad. Fiz. **44**, 1240 (1986) [Sov. J. Nucl. Phys. **44**, 806 (1986)].
11. V. A. Naumov, T. S. Sinegovskaya, and S. I. Sinegovsky, Nuovo Cimento A **111**, 129 (1998).
12. S. I. Nikol'skiĭ, Ĭ. N. Stamenov, and S. Z. Ushev, Zh. Éksp. Teor. Fiz. **87**, 18 (1984) [Sov. Phys. JETP **60**, 10 (1984)]; S. I. Nikol'skiĭ, in *Problems in Cosmic Ray Physics*, Ed. by A. E. Chudakov *et al.* (Nauka, Moscow, 1987), p. 169.
13. S. Matsuno, F. Kajino, Y. Kawashima, *et al.*, Phys. Rev. D **29**, 1 (1984).
14. G. T. Zatsepin, N. P. Il'ina, N. N. Kalmykov, *et al.*, Izv. Akad. Nauk, Ser. Fiz. **58** (12), 119 (1994).
15. W. Rhode, Nucl. Phys. B (Proc. Suppl.) **35**, 250 (1994).
16. LVD Collab. (M. Aglietta, B. Alpat, E. D. Alyea, *et al.*), Phys. Rev. D **58**, 092005 (1998).
17. F. F. Khalchukov *et al.*, in *Proceedings of the 19th International Cosmic Ray Conference, La Jolla, 1985*, Vol. 8, p. 12.
18. V. N. Bakatanov, Yu. F. Novosel'tsev, R. V. Novosel'tseva, *et al.*, Yad. Fiz. **55**, 2107 (1992) [Sov. J. Nucl. Phys. **55**, 1169 (1992)].
19. T. S. Sinegovskaya, in *Proceedings of the Second Baikal School in Fundamental Physics: Interaction of Radiations and Fields with Matter, Irkutsk, September 13–18, 1999*, Ed. by Yu. N. Denisyuk and A. N. Maslova (Irkutsk. Gos. Univ., Irkutsk, 1999), vol. 2, p. 598.
20. A. D. Martin, W. J. Stirling, and R. G. Roberts, Phys. Lett. B **306**, 145 (1993).
21. CTEQ Collab. (H. Lai *et al.*), Phys. Rev. D **51**, 4763 (1995).
22. V. A. Naumov, S. I. Sinegovsky, and E. V. Bugaev, Yad. Fiz. **57**, 439 (1994) [Phys. At. Nucl. **57**, 412 (1994)].
23. V. A. Naumov, T. S. Sinegovskaya, and S. I. Sinegovsky, in *Proceedings of the Second Baikal School in Fundamental Physics: Interaction of Radiations and Fields with Matter, Irkutsk, September 13–18, 1999*, Ed. by Yu. N. Denisyuk and A. N. Malova (Irkutsk. Gos. Univ., Irkutsk, 1999), vol. 2, p. 621.

Translated by E. Kozlovskiĭ

Physics of Atomic Nuclei, Vol. 63, No. 11, 2000, pp. 1927–1935. Translated from Yadernaya Fizika, Vol. 63, No. 11, 2000, pp. 2020–2028.

ELEMENTARY PARTICLES AND FIELDS
Experiment

Simple Method for Solving Transport Equations Describing the Propagation of Cosmic-Ray Nucleons in the Atmosphere

V. A. Naumov and T. S. Sinegovskaya
Irkutsk State University, ul. Lermontova 126, Irkutsk, 664033 Russia
Received September 21, 1999; in final form, January 12, 2000

Abstract—A simple and efficient method is proposed for solving transport equations that describe the propagation of cosmic-ray protons and neutrons in the atmosphere at high energies. It is shown that, upon taking into account a non-power-law character of the primary spectrum, a growth of total cross sections for inelastic nucleon–nucleus interactions, and violation of scaling in such interactions, the effective absorption ranges of nucleons come to be dependent not only on energy but also on the depth in the atmosphere. The results of the calculations are compared with available experimental data. © *2000 MAIK "Nauka/Interperiodica".*

1. INTRODUCTION

Measurements of the fluxes of secondary cosmic-ray protons and neutrons can furnish valuable information about primary cosmic radiation and about the interactions of nucleons and nuclei at high energies. In order to extract this information from experimental data, it is necessary, among other things, to be able to calculate the nucleon absorption ranges, which are functionals of the spectrum of primary cosmic rays and of inclusive and total cross sections for inelastic interactions and which also depend, in general, on energy and the depth in the atmosphere. An exact analytic solution to the problem can be obtained only within very simple models of the primary spectrum and interaction cross sections, but such models are very unrealistic just because of their simplicity. In the present study, a straightforward method is proposed for approximately solving one-dimensional transport equations describing the propagation of cosmic-ray nucleons. This method, which is applicable at sufficiently high energies, does not rely on any unrealistic assumptions about the shape of the primary spectrum or about the form of differential and total cross sections for nucleon–nucleus interactions. With some qualifications (see Section 2), a solution to the transport equations can be found to a precision as high as is desirable and for an arbitrary depth, whereby nucleon fluxes can be studied at sea level even for inclined directions.[1)]

Basically, the idea of the method consists in reducing the integro-differential transport equation to a nonlinear integral equation for a so-called Z factor, a quantity that is directly related to the effective absorption range. After that, the equation for the Z factor is solved by mere iterations. Within this method, even the lowest approximation has a rather high accuracy. The efficiency of the method has already been demonstrated in solving the problem of muon-neutrino transfer in a dense medium with $h \gg \lambda_\nu(E)$ [1] (λ_ν is the distance that a neutrino travels prior to interaction)—that is, in a situation where conventional numerical methods, including the Monte Carlo method, either are inapplicable or require enormous amounts of machine time. By invoking some natural physical assumptions, the method can be modified to render it appropriate for solving the problems of transport of high-energy nuclei, muons, and other mesons in the atmosphere and in dense media.

2. BASIC ASSUMPTIONS OF THE NUCLEAR-CASCADE MODEL

We are interested here in the differential energy spectra of cosmic-ray protons and neutrons at energies that are so high that proton energy losses by ionization and by the excitation of air atoms, geomagnetic effects, and effects associated with a three-dimensional character of the cascade process (in particular, scattering) can be disregarded. The one-dimensional approximation assumes a sharp anisotropy of the angular distribution of secondary particles formed in inelastic interactions of nucleons and nuclei and is justified at nucleon momenta p much greater than $\langle p_T \rangle \approx 0.4$ GeV/c. Owing to the fact that the energy spectrum of cosmic rays decreases fast (and, as a consequence, to the predominant role of $p_T \ll p_L$ processes in the development of the cascade), as well as to a high degree of isotropy of primary radiation, the range where the one-dimensional

[1)] We recall that the depth of the atmosphere along the vertical direction is $h_0 \simeq 1030$ g/cm$^2 \simeq 11.4\lambda_N^*$, where $\lambda_N^* = 90$ g/cm^2 is the characteristic range that a nucleon travels in air prior to undergoing interaction. The depth of the atmosphere along the horizontal direction exceeds $440\lambda_N^*$. Therefore, the flux of nucleons arriving from nearly horizontal directions is completely determined by integration of small deflections in inelastic nuclear interactions, multiple Coulomb scattering, and elastic scattering, as well as by the contributions from reactions induced by long-range particles, whence it follows that it is meaningless, in this case, to consider a one-dimensional formulation of the problem. For small zenith angles ϑ, the above effects can be taken into account as corrections to a solution of one-dimensional transport equations.

1063-7788/00/6311-1927$20.00

approximation is valid broadens considerably for directions close to the vertical direction.

In the present study, we use the standard superposition model for nucleus–nucleus interactions. Since the range of a nucleus decreases fast with increasing atomic number A, it is assumed in this model that the $A > 1$ nuclei of primary cosmic rays fragment completely in upper layers of the atmosphere; therefore, the integrated spectrum of nuclei with energies in excess of $\mathscr{E}$ can be approximated by an equivalent summary spectrum of Z protons and $A - Z$ neutrons with energies $E \geq \mathscr{E}/A$. At low and intermediate energies (especially at energies below the geomagnetic threshold), this model is overly rough—approaches having a firmer basis and taking explicitly into account the interactions of cosmic-ray nuclei must be used to compute the nucleonic components of the cascade (see, for example, [2]).

The superposition model is used for want of more rigorous models for describing the interactions of high-energy nuclei and also for want of detailed empirical data. At high energies, the applicability of this model is eventually justified by the smallness of the relevant contribution to the total flux of secondary nucleons.

Yet another important approximation that will be used below consists in the disregard of processes that lead to the production of nucleon–antinucleon pairs in meson–nucleus collisions. At not overly large depths or at modest energies[2)] (or when both these conditions are satisfied), the contribution to the nucleon flux from such processes is immaterial for the following reasons: (i) There are no mesons in primary cosmic radiation; hence, their flux in upper layers of the atmosphere is much smaller than the nucleon flux. (ii) The differential cross sections for $\pi A \longrightarrow N\bar{N}X$, $KA \longrightarrow N\bar{N}X$, etc., reactions are much smaller than the differential cross sections for $NA \longrightarrow N'X$ reactions. (iii) Only a small fraction of mesons with $E \lesssim E_M^{\mathrm{cr}}(\vartheta)$ have time to interact with nuclei prior to undergoing decay. However, the total cross sections for inelastic NA interactions exceed cross sections for the interactions of light mesons with nuclei by about 30%. At a sufficiently large depth, $h = h_M(E, \vartheta)$, and for $E \gtrsim E_M^{\mathrm{cr}}(\vartheta)$, the flux of mesons M therefore becomes equal to the flux of nucleons of the same energy. For $h \gg h_M(E, \vartheta)$, the contribution of nucleon-generation processes in MA interactions (predominantly $\pi^{\pm}A \longrightarrow N\bar{N}X$ processes) can be disregarded no longer [3]. Thus, the formalism used here is applicable for depth values satisfying the condition $h \lesssim h_\pi(E, \vartheta)$. As a matter of fact, this region is sufficiently broad for describing the entire body of currently available data on the nucleonic component of high-energy cosmic rays in the atmosphere and at sea level. In particular, it covers completely the region of the effective generation of muons and neutrinos ($h \lesssim 500$ g/cm^2).

Within the above assumptions, the problem of calculating the differential energy spectra of protons, $D_p(E, h)$, and of neutrons, $D_n(E, h)$, at a depth h reduces to solving the set of one-dimensional transport equations

$$\left[\frac{\partial}{\partial h} + \frac{1}{\lambda_N(E)}\right] D_p(E, h)$$

$$= \frac{1}{\lambda_N(E)} \int_E^\infty \frac{1}{\sigma_{NA}^{\mathrm{in}}(E)} \frac{d\sigma_{pp}(E, E_0)}{dE} D_p(E_0, h)\, dE_0 \qquad (1)$$

$$+ \frac{1}{\lambda_N(E)} \int_E^\infty \frac{1}{\sigma_{NA}^{\mathrm{in}}(E)} \frac{d\sigma_{np}(E, E_0)}{dE} D_n(E_0, h)\, dE_0,$$

$$\left[\frac{\partial}{\partial h} + \frac{1}{\lambda_N(E)}\right] D_n(E, h)$$

$$= \frac{1}{\lambda_N(E)} \int_E^\infty \frac{1}{\sigma_{NA}^{\mathrm{in}}(E)} \frac{d\sigma_{nn}(E, E_0)}{dE} D_n(E_0, h)\, dE_0 \qquad (2)$$

$$+ \frac{1}{\lambda_N(E)} \int_E^\infty \frac{1}{\sigma_{NA}^{\mathrm{in}}(E)} \frac{d\sigma_{pn}(E, E_0)}{dE} D_p(E_0, h)\, dE_0$$

with the boundary conditions

$$D_p(E, 0) = D_p^0(E), \quad D_n(E, 0) = D_n^0(E), \qquad (3)$$

where $D_p^0(E)$ and $D_n^0(E)$ are the differential energy spectra of protons and neutrons at the boundary of the atmosphere—we emphasize that, according to the superposition model, these spectra include both primary protons and the products of the fragmentation of cosmic-ray nuclei.

In Eqs. (1) and (2), we have used the notation

$$\frac{d\sigma_{NN'}(E, E_0)}{dE} = 2\pi \int_0^{p_T^{\max}} \frac{p_T}{p_L} \left(E \frac{d^3\sigma_{NN'}}{d^3p}\right) dp_T;$$

where $Ed^3\sigma_{NN'}/d^3p$ is the invariant differential cross section for the inclusive reaction $NA \longrightarrow N'X$ (A is the nucleus of an air atom, while X is the system of all undetected secondaries, including the products of the decay of the nucleus A); E_0 is the total energy of the incident nucleon N; E is the total energy; p_T and p_L are the components of the momentum $\mathbf{p}$ of the final nucleon N'; and $\lambda_N(E) = 1/(N_0\sigma_{NA}^{\mathrm{in}}(E))$ is the distance that a nucleon travels prior to undergoing interaction[3)] (N_0 is the number of nuclei A per gram of air). Within

[2)] More specifically, we mean here energies E not greater than $E_M^{\mathrm{cr}}(\vartheta)$, the zenith-angle-dependent critical energy of the meson M—in particular, we have $E_{\pi^\pm}^{\mathrm{cr}}(0°) \approx 115$ GeV, $E_{K_L^0}^{\mathrm{cr}}(0°) \approx 206$ GeV, and $E_{K^\pm}^{\mathrm{cr}}(0°) \approx 857$ GeV.

[3)] In the following, we assume that $\sigma_{pA}^{\mathrm{in}} = \sigma_{nA}^{\mathrm{in}}$.

NN kinematics, the quantity $p_T^{\max}$ is determined by the condition

$$E^* \le \frac{s - s_X^{\min} + M}{2\sqrt{s}},$$

where E^* is the energy of the inclusive particle in the c.m. frame of colliding nucleons, while $s_X^{\min}$ is the minimum value of the square of the invariant mass of the X system. Disregarding the cumulative kinematical region, which does not play a significant role in the development of the nuclear cascade, we obtain

$$p_T^{\max} = \sqrt{\frac{2ME(E-M)(1-x)}{E - Mx}},$$

where $x = E/E_0$ is the total-energy fraction carried away by the nucleon N' and M is the nucleon mass.

The approximate isotopic symmetry of *NA* interactions makes it possible to reduce the set of Eqs. (1) and (2) to two independent equations for the linear combinations

$$N_\pm(E, h) = D_p(E, h) \pm D_n(E, h).$$

After some simple algebra, these equations can be represented in the form

$$\left[\frac{\partial}{\partial h} + \frac{1}{\lambda_N(E)}\right] N_\pm(E, h) = \frac{1}{\lambda_N(E)} \int_0^1 \Phi_\pm(x, E) N_\pm(E/x, h) \frac{dx}{x^2}, \quad (4)$$

where

$$\Phi_\pm(x, E) = \frac{E}{\sigma_{NA}^{\text{in}}(E)} \left[\frac{d\sigma_{pp}(E, E_0)}{dE} \pm \frac{d\sigma_{pn}(E, E_0)}{dE}\right]_{E_0 = E/x}.$$

3. *Z*-FACTOR METHOD

We define

$$N_\pm(E, h) = N_\pm(E, 0) \exp\left[-\frac{h}{\Lambda_\pm(E, h)}\right]. \quad (5)$$

The functions $\Lambda_\pm(E, h)$ will be referred to as effective absorption ranges, but this term applies, strictly speaking, only to Λ_+—as to Λ_-, it is a quantity that characterizes the rate at which the intensity of the proton component of the nucleon flux and the intensity of its neutron component equalize. It is also convenient to introduce the auxiliary dimensionless functions $Z_\pm(E, h)$ (Z factors) that are related to $\Lambda_\pm(E, h)$ and $\lambda_N(E)$ by the equation

$$\frac{1}{\Lambda_\pm(E, h)} = \frac{1 - Z_\pm(E, h)}{\lambda_N(E)}. \quad (6)$$

In just the same way as the absorption ranges, the Z factors contain full information about the kinetics of nucleons in a medium. From the transport equation (4) and from the definitions in (5) and (6), it immediately follows that $0 < Z_+(E, h) < 1$. In general, the function $Z_-(E, h)$ must not be of a fixed sign. Taking into account the behavior of the actual primary spectrum of cosmic rays and considering that, almost everywhere in the relevant kinematical domain, regeneration processes ($pA \longrightarrow pX$ and $nA \longrightarrow nX$) dominate over charge-exchange processes ($pA \longrightarrow nX$ and $nA \longrightarrow pX$), we can nevertheless show that it also satisfies the inequality $0 < Z_-(E, h) < 1$. Moreover, it can easily be proven that $Z_-(E, h) < Z_+(E, h)$ and, hence, $\Lambda_-(E, h) < \Lambda_+(E, h)$.

Substituting (5) and (6) into the transport equation (4), we find that the Z factors satisfy the equation

$$\left(\frac{\partial}{\partial h} + \frac{1}{h}\right) Z_\pm(E, h) = \frac{1}{h} \int_0^1 \eta_\pm(x, E) \Phi_\pm(x, E) \exp\left[\frac{h}{\Lambda_\pm(E, h)} - \frac{h}{\Lambda_\pm(E/x, h)}\right] dx, \quad (7)$$

where

$$\eta_\pm(x, E) = \frac{N_\pm(E/x, 0)}{x^2 N_\pm(E, 0)}. \quad (8)$$

Since the actual primary spectrum decreases much faster than E^{-2} over the entire energy range of our interest, we have $0 \le \eta_\pm(x, E) \le 1$ and $\eta_\pm(0, E) = 0$. In particular, we note that, for such spectra and purely power-law boundary spectra of protons and neutrons [$D_{p,n}^0(E) \sim E^{-\gamma+1}$], we have $\eta_\pm(x, E) = x^{\gamma-1}$.

Integrating (7) by parts, we find that the Z factors satisfy the integral equation

$$Z_\pm(E, h) = \frac{1}{h} \int_0^h dh' \int_0^1 \eta_\pm(x, E) \Phi_\pm(x, E) \exp[-h' D_\pm(x, E, h')] dx, \quad (9)$$

where

$$D_\pm(x, E, h) = \frac{1 - Z_\pm(E/x, h)}{\lambda_N(E/x)} - \frac{1 - Z_\pm(E, h)}{\lambda_N(E)}.$$

Although this equation is nonlinear, it is much more convenient to solve it by an iterative process than the original transport equation (4). The rate at which the iterative process converges depends on the choice of the zero-order approximation. The simplest choice is

$$Z_\pm^{(0)}(E, h) = 0,$$

in which case

$$D_\pm^{(0)}(x, E, h) \equiv \mathcal{D}(x, E) = \frac{1}{\lambda_N(E/x)} - \frac{1}{\lambda_N(E)} \quad (10)$$

is independent of h; in the first approximation, we then have

$$Z_{\pm}^{(1)}(E, h) = \int_0^1 \eta_{\pm}(x, E)\Phi_{\pm}(x, E) \times \left\{\frac{1 - \exp[-h\mathcal{D}(x, E)]}{h\mathcal{D}(x, E)}\right\}dx. \quad (11)$$

Let us first address the case of small depths. Considering that, in the integrand on the right-hand side of (11), the small-x region is cut off by the factor $\eta_{\pm}(x, E)$, we can formally expand the braced expression in powers of h. This yields

$$Z_{\pm}^{(1)}(E, h) = \int_0^1 \eta_{\pm}(x, E)\Phi_{\pm}(x, E) \times \left[1 - \frac{h\mathcal{D}(x, E)}{2} + \ldots\right]dx. \quad (12)$$

The leading term of the expansion in (12),

$$\mathcal{J}_{\pm}(E) \equiv Z_{\pm}(E, 0) = \int_0^1 \eta_{\pm}(x, E)\Phi_{\pm}(x, E)dx, \quad (13)$$

represents an obvious generalization of Zatsepin's classical formula [4], which was first obtained within the simplest assumptions (power-law primary spectrum, scaling of invariant inclusive cross sections, invariability of $\sigma_{NA}^{\text{inel}}$ with energy)[4)] and which has been used so far in many analytic calculations of nuclear-cascade processes in the atmosphere.

Let us now consider the opposite limiting case of large h. Taking into account the known growth of $\sigma_{pA}^{\text{inel}}(E)$ with energy and using Eqs. (10) and (12), we can easily show that $\lim_{h\to\infty} Z_{\pm}^{(0)}(E, h) = 0$. Under quite general assumptions, it can also be proven that $\lim_{h\to\infty} Z_{\pm}(E, h) = 0$; therefore, the absorption ranges $\Lambda_{\pm}(E, h)$ coincide with the free range $\lambda_N(E)$ at sufficiently large depths. We will not present here the proof of this statement because it is of purely academic interest for the reasons indicated above (disregard of three-dimensional effects, of energy losses, and of the contribution of nucleons from meson–nucleus interactions). What only counts is that, with increasing depth, Z_+ and Z_- decrease, which means that the relative contribution of regeneration processes is reduced. As a consequence, the energy spectra of nucleons become steeper with increasing depth.

Thus, even the first-approximation expression (11) for the Z factors has a correct asymptotic behavior both at small and at large values of h. With the aid of expression (12), we can reproduce approximate analytic results of some studies that took into account (within one model or another) the growth of σ_{NA}^{in} with energy (see, for example, [3, 5]).

Obviously, the recursion relations for the nth approximation ($n > 0$) are given by

$$Z_{\pm}^{(n)}(E, h) = \frac{1}{h}\int_0^h dh' \int_0^1 \eta_{\pm}(x, E)\Phi_{\pm}(x, E) \times \exp[-h' D_{\pm}^{(n-1)}(x, E, h')]dx, \quad (14)$$

$$D_{\pm}^{(n)}(x, E, h) = \frac{1 - Z_{\pm}^{(n)}(E/x, h)}{\lambda_N(E/x)} - \frac{1 - Z_{\pm}^{(n)}(E, h)}{\lambda_N(E)}. \quad (15)$$

A numerical analysis has revealed that, even in the case of the simplest choice of $Z_{\pm}^{(0)} = 0$, the rate at which the iterative algorithm specified by Eqs. (14) and (15) converges is quite sufficient for practical uses. However, it can be improved (on average or locally—that is, for preset intervals of E and h values) by choosing the zero-order approximation more appropriately. To illustrate, we note that, in view of the inequalities $0 < Z_{\pm}(E, h) \leq \mathcal{J}_{\pm}(E)$, it is reasonable to set $Z_{\pm}^{(0)}(E, h) = \mathcal{J}_{\pm}(E)/2$, which considerably improves convergence on average.

4. INPUT DATA AND NUMERICAL RESULTS

4.1. Primary Spectrum

In order to describe the spectrum and the chemical composition of primary cosmic rays, we employ two empirical models proposed by Nikolsky, Stamenov, and Ushev [6] (NSU model)[5)] and by Erlykin, Krutikova, and Shabel'ski [8] (EKS model). In either model, the nuclear component of cosmic rays was broken down into five groups of nuclei—those having the A values of 1, 4, 15, 26, and 51 in the NSU model and those having the A values of 1, 4, 15, 27, and 56 in the EKS model—and the integrated spectrum was parametrized as

$$I(>\mathcal{E}) = I_0\left(\frac{\mathcal{E}}{E_1}\right)^{-\gamma}\sum_A B_A\left(\frac{\mathcal{E}}{E_{100}}\right)^{\kappa_A}\left(1 + \frac{\delta_A\mathcal{E}}{AE_1}\right)^{-\kappa}, \quad (16)$$

where $\mathcal{E}$ is the energy of a nucleus, $E_1 = 1$ GeV, $E_{100} = 100$ GeV, and $\kappa = 0.4$; the remaining parameters were taken to be $I_0 = 1.16$ cm^{-2} s^{-1} sr^{-1}, $\gamma = 1.62$, $B_1 = 0.40$,

[4)] It can easily be verified that, under the above assumptions, $Z_{\pm} = \int_0^1 x^{\gamma-1}\Phi_{\pm}(x)dx = \text{const}$ is an exact solution to Eq. (9).

[5)] In [7], the predictions of the NSU model were contrasted against experimental data for $\mathcal{E} \geqslant 100$ GeV/nucleon that had been obtained prior to 1993.

$B_4 = 0.21$, $B_{15} = 0.14$, $B_{26} = 0.13$, $B_{51} = 0.12$, $\delta_1 = 3 \times 10^{-7}$, $\delta_{A \geq 4} = 6 \times 10^{-6}$, and $\kappa_A = 0$ in the NSU model and $I_0 = 2.02$ cm^{-2} s^{-1} sr^{-1}, $\gamma = 1.70$, $B_1 = 0.41$, $B_4 = 0.22$, $B_{15} = 0.13$, $B_{27} = 0.14$, $B_{56} = 0.10$, $\delta_1 = 6 \times 10^{-7}$, $\delta_{A \geq 4} = 10^{-5}$, $\kappa_1 = \kappa_4 = 0$, and $\kappa_{15} = \kappa_{27} = \kappa_{56} = 0.04$ in the EKS model.

For the equivalent differential spectra of protons and neutrons, we find with the aid of (16) that

$$D_p^0(E) = D_1(E) + \frac{1}{2}\sum_{A \geq 4} D_A(E),$$

$$D_n^0(E) = \frac{1}{2}\sum_{A \geq 4} D_A(E),$$

$$D_A(E) = \frac{(\gamma - \kappa_A) I_0 B_A}{(1 + \delta_A E/E_1)^{\kappa} A^{\gamma - 1 - \kappa_A} E_1} \left(\frac{E}{E_1}\right)^{-(\gamma+1)} \times \left(\frac{E}{E_{100}}\right)^{\kappa_A} \left[1 + \frac{\kappa \delta_A}{(\gamma - \kappa_A)(E_1/E + \delta_A)}\right].$$

These models cannot provide a quantitative description of the primary spectrum at energies above 10^8–10^9 GeV/nucleon. However, the contribution from this energy region to the total number of events that are of interest for experiments aimed at measuring individual components of secondary cosmic rays (including experiments devoted to deep-underwater detection of muons and neutrinos) is insignificant. In order to simplify the calculations, we therefore introduced an ad hoc soft cutoff of the primary spectrum[6)] by replacing the functions $D^0_{p,n}(E)$ in the boundary conditions (3) by $D^0_{p,n}(E)\phi(E/E_c)$, where $\phi(t)$ is a dimensional function that satisfies the conditions $\phi(t) = 1$ for $t \ll 1$ and $\phi(t) = 0$ for $t \geq 1$. The explicit form of this function is immaterial as long as we are interested in energies E much lower than E_c and in not overly large depths h. Below, we set $E_c = 3 \times 10^{10}$ GeV.

4.2. Cross Sections for NA Interactions

Available data on the total inelastic cross section $\sigma^{\text{in}}_{pA}(E)$ (both data collected at accelerators and data extracted from cosmic-ray experiments) are described reasonably well by the empirical dependence

$$\sigma^{\text{inel}}_{pA}(E) = \sigma_0 - \theta(E - E_*) \times \left[\sigma_1 \ln\left(\frac{E}{E_1}\right) - \sigma_2 \ln^2\left(\frac{E}{E_1}\right)\right], \quad (17)$$

where $\theta(E - E_*)$ is the conventional Heaviside step function and $E_* = 45.4$ GeV. Below, we use expression (17) with the parameter values of $\sigma_0 = 290 \pm 5$ mb, $\sigma_1 = 8.7 \pm 0.5$ mb, and $\sigma_2 = 1.14 \pm 0.05$ mb, which were found in [10].

[6)] As a matter of fact, this cutoff roughly simulates the Greisen–Zatsepin–Kuz'min effect, which is due to the interaction of extragalactic cosmic rays with relic microwave radiation [9].

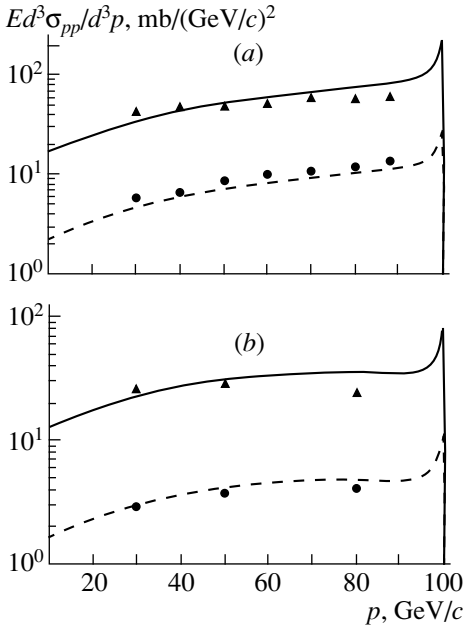

Fig. 1. Invariant inclusive cross sections calculated for the reactions (solid curves) $pC \longrightarrow pX$ and (dashed curves) $pp \longrightarrow pX$ within the model from [11] at $p_0 = 100$ GeV/c and the p_T values of (*a*) 0.3 and (*b*) 0.5 GeV/c. The experimental data on the reactions (▲) $pC \longrightarrow pX$ and (●) $pp \longrightarrow pX$ were borrowed from [12].

For the normalized inclusive cross sections $(1/\sigma^{\text{in}}_{pA})d^3\sigma_{pp}/d^3p$ and $(1/\sigma^{\text{in}}_{pA})d^3\sigma_{pn}/d^3p$, we took semiempirical formulas proposed by Kimel' and Mokhov [11] and modified slightly here. In these formulas, the free parameters were determined by fitting the entire body of available accelerator data on the interactions of projectile nucleons with various nuclear targets at $p_0 = 3$–1500 GeV/c and 0.45 GeV/$c \lesssim p \leq p_0$ (where p_0 is the projectile-nucleon momentum in the laboratory frame). All the ensuing calculations were performed with the parameter values that correspond to a beryllium target. According to [11], however, the normalized differential cross sections depend only slightly on the target atomic number, so that the results obtained here are valid for other light nuclei as well, including the nuclei of air atoms.

The calculated invariant cross section $Ed^3\sigma_{pp}/d^3p$ as a function of p at $p_0 = 100$ GeV/c (in the laboratory frame) and two fixed values of p_T (0.3 and 0.5 GeV/c) is displayed in Fig. 1, along with experimental data from [12] that were obtained with hydrogen and carbon targets. The values of $\sigma^{\text{inel}}_{pp}$ and $\sigma^{\text{inel}}_{pC}$, which are necessary for a normalization, were borrowed from [13]. The differential cross section $d\sigma_{pp}/dx_{\text{F}}$ for the reaction

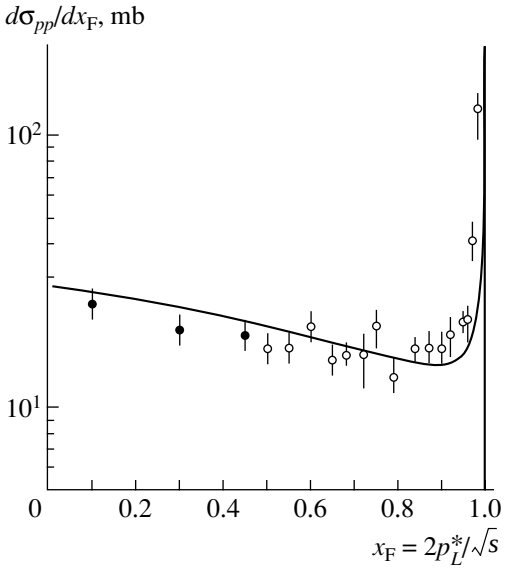

Fig. 2. Inclusive differential cross section $d\sigma_{pp}/dx_F$ calculated for the reaction $pp \longrightarrow pX$ within the model from [11] at $\sqrt{s}$ = 62 GeV. The experimental data were borrowed from [14].

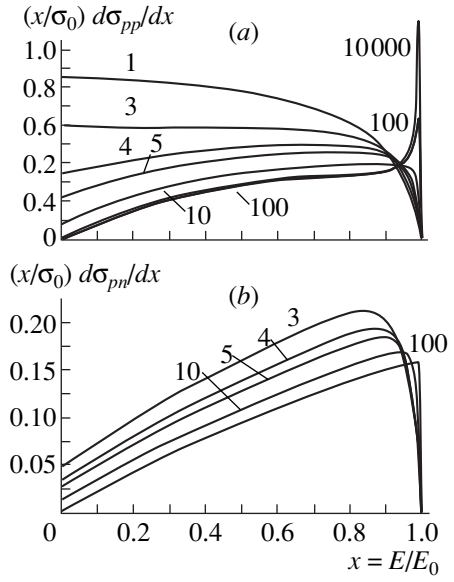

Fig. 3. Normalized differential cross sections calculated for the reactions (*a*) $pA \longrightarrow pX$ and (*b*) $pA \longrightarrow nX$ according to the model proposed in [11]. The numbers on the curves indicate the kinetic energy of the secondary nucleon, $E_{kin} = E - M$, in GeV.

$pp \longrightarrow pX$ at the ISR energy ($\sqrt{s}$ = 62 GeV) is shown in Fig. 2 versus $x_F = 2p_L^*/\sqrt{s}$, where p_L^* is the longitudinal momentum of the leading proton in the c.m. frame. The data of two ISR experiments were borrowed from [14]. As can be seen from the figures presented here, the model proposed in [11] describes accelerator data fairly well. It should also be noted that, over a broad kinematical region, the predictions of this model for the cross sections describing *pp* and *pA* interactions are numerically close to the results obtained on the basis of the two-component dual parton model as implemented within the last version of the DPMJET II.5 code [15].

The cross sections $(x/\sigma_0)d\sigma_{pp}(x, E)/dx$ and $(x/\sigma_0)d\sigma_{pn}(x, E)/dx$ calculated within the model proposed in [11] are displayed in Fig. 3 for several values of the kinetic energy of secondary nucleons E_{kin}. From this figure, we can see that, for $E_{kin} \gtrsim 100$ GeV, the differential cross sections come to be virtually independent of energy everywhere, with the exception of a narrow diffraction region for the reaction $pA \longrightarrow pX$, where the cross section $d\sigma_{pp}/dx$ grows with energy. In other words, the Kimel'–Mokhov model leads to Feynman scaling at high energies. Because of a descending character of the primary spectrum, the contribution from the diffraction region to the *Z* factors is far from negligible. In order to avoid an unphysically fast growth of $d\sigma_{pp}/dx$ in the region around $x \sim 1$ at ultrahigh energies, we assumed that, for $E_0 > 10^6$ GeV, this cross section becomes scale-invariant over the entire kinematical region. However, it is rather difficult to validate this assumption because there are no reliable experimental data for $E_0 \gtrsim 10^6$ GeV.

4.3. Results of the Calculations

The calculations were performed for the energy range between 5 and 3×10^{10} GeV at $h \leq 4 \times 10^3$ g/cm^2. It should be noted that, at $h \sim 10^3$ g/cm^2, the energy lost by protons in the nucleon cascade must be taken into account up to E = 25–30 GeV. By way of example, we indicate that, at E = 10 GeV, the relevant correction is about 20% for protons and about 6% for neutrons [16]. Moreover, the models adopted here for the primary spectrum and for the chemical composition become too crude even for $E \lesssim 100$ GeV. In order to match our results with the results of the more detailed analysis from [16], the method used here was extrapolated to the region of low energies. In the absence of experimental data on the fluxes of secondary nucleons arriving from inclined directions, the calculations for depths of $h > 10^3$ g/cm^2 can be used at present only to test convergence of the iterative algorithm.

In order to perform a multidimensional numerical integration, which is necessary for a numerical implementation of the method, use was made here of the adaptive cubature algorithm proposed by Genz and Malik [17]; a fast algorithm relying on standard local *B* splines of second degree on an equidistant mesh was employed to approximate and interpolate intermediate functions of one and two variables.

At all values of *E* and *h*, the iterative process converges fast: five to six iterations are sufficient for calcu-

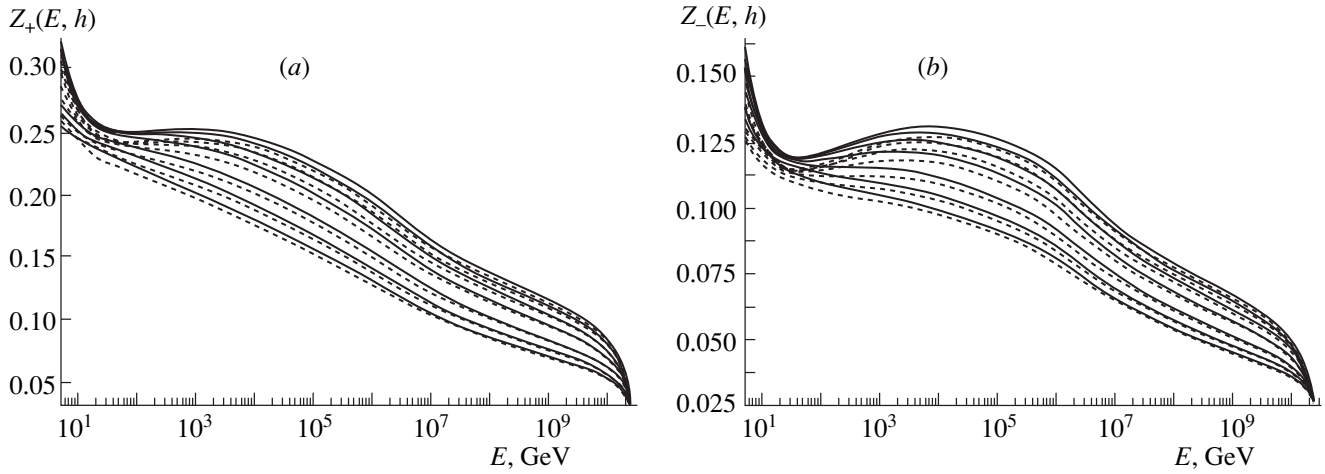

Fig. 4. (*a*) Z_+ and (*b*) Z_- as functions of energy at the depth values of h = 10, 200, 500, 1000, 2000, 3000, and 4000 g/cm^2. The energy dependences displayed in this figure were computed on the basis of the (solid curves) NSU and (dashed curves) EKS models of the primary spectrum (see main body of the text). The Z factors are seen to decrease with increasing h.

lating the Z factors to a precision not poorer than 10^{-3}–10^{-4}. At moderate depths, $h \lesssim 300$ g/cm^2, even the first approximation ensures a precision of a few percent, which is sufficient for many applications of the theory—in particular, for calculating the fluxes of atmospheric muons and neutrinos.

Figure 4 illustrates the energy dependences of the Z factors calculated within the two models of the primary spectrum at h = 10, 200, 500, 1000, 2000, 3000, and 4000 g/cm^2. It is quite natural that the Z factors computed with the harder primary spectrum of the NSU model prove to be systematically greater at all values of E and h. Although the relevant relative difference does not exceed some 4% and decreases with energy, it is significant at $h \gg \lambda_N(E)$ since nucleon fluxes depend exponentially on the combinations $hZ_\pm(E, h)/\lambda_N(E)$. The observed strong dependence of $Z_\pm$ on E and h is caused by the following three effects: (i) a non-power-law dependence of the primary spectrum, (ii) the energy dependence of the total inelastic cross section, and (iii) violation of Feynman scaling.

Local minima that appear in the region $E \lesssim E_* \simeq$ 45 GeV are due to the beginning of growth of $\sigma_{NA}^{\text{inel}}(E)$ [see Eq. (17)]. At not overly large depths, the character of the energy dependence changes at $E \gtrsim 10^6$, which is associated with the artificially introduced freezing of the growth of the quasielastic peak in the reactions $pA \longrightarrow pX$ and $nA \longrightarrow nX$. Finally, the vanishing of the Z factors at $E = E_c = 3 \times 10^{10}$ GeV is due to a fall-down of the primary spectrum for $E > E_c$.

The calculated differential energy spectra of nucleons ($D_p + D_n$), protons (D_p), and neutrons (D_n) at various values of the depth in the atmosphere are displayed in Figs. 5 and 6, along with experimental data from [18–28].

The calculations were based on two models of the primary spectrum (NSU and EKS). Figure 6 also shows the results of the Monte Carlo calculation from [24] for sea level. Data on the spectra of nucleons for $h \leq$ 530 g/cm^2 (Fig. 5) were obtained from an analysis of photon spectra in extensive air showers (see [29]) and are therefore model-dependent to a considerable extent. Nonetheless, our calculations relying on either model of the primary spectrum are by and large consistent

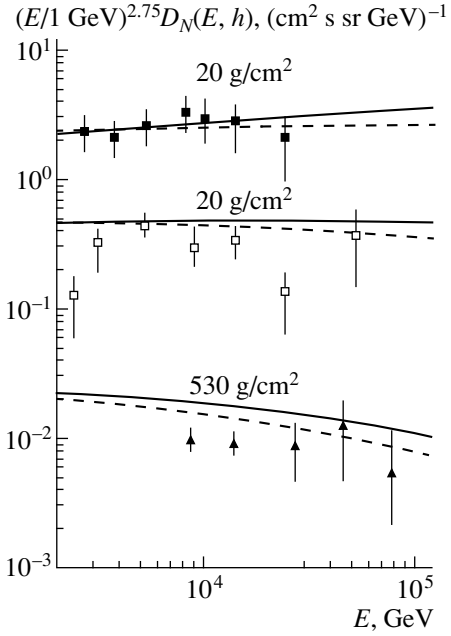

Fig. 5. Differential energy spectra of nucleons at the depth values of h = 20, 200, and 530 g/cm^2. Points represent experimental data from (■) [18], (□) [19], and (▲) [20]. Curves depict the results of our calculations employing the (solid curves) NSU and (dashed curves) EKS models of the primary spectrum (see main body of the text).

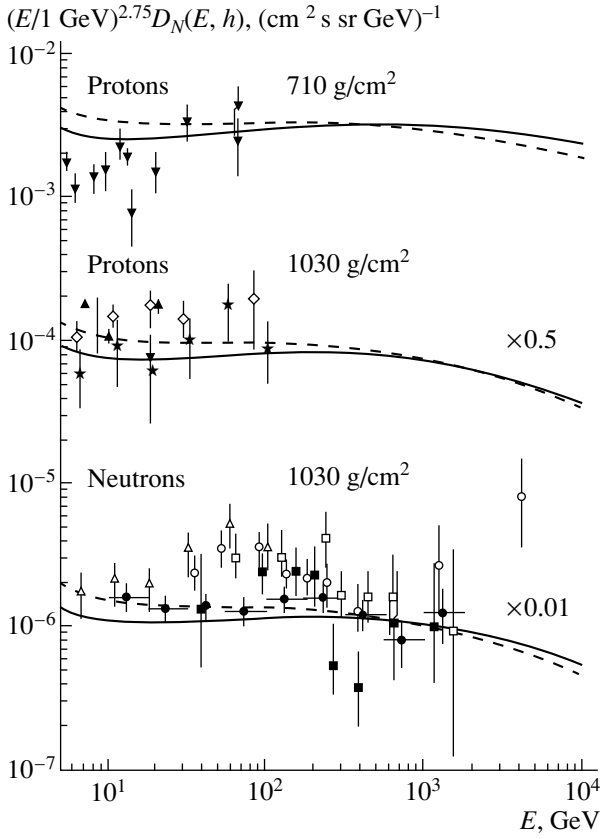

Fig. 6. Differential energy spectra of protons (h = 710, 1030 g/cm^2) and neutrons (h = 1030 g/cm^2). Points represent experimental data from (▼) [21], (◇) [22], (▲) [23], (★, △) [24], (○) [25], (□) [26], (■) [27], and (●) [28]. Curves depict the results of our calculations employing the (solid curves) NSU and (dashed curves) EKS models of the primary spectrum (see main body of the text). The experimental and calculated results at sea level for protons and neutrons were multiplied by 0.5 and 0.01, respectively.

with this data sample. The most pronounced discrepancies have been observed in a comparison with the results presented in [19]. In our opinion, the estimate of the nucleon energy in [19] on the basis of the formula $E_N \approx 3E_\gamma$ is too crude and leads to a systematic underestimation of nucleon fluxes. Direct measurements of the proton energy spectra in mountains and at sea level are very fragmentary (see Fig. 6), and we can here speak only about qualitative agreement with the results of the calculations. Estimates reveal (see also [3]) that the inclusion of nucleon-production processes in meson–nucleus interactions can increase the vertical flux of nucleons at sea level by no more than 10% at E = 1 TeV and by no more than 15% at E = 10 TeV, but this increase is much smaller, in either case, than uncertainties in the *NA* cross sections and in the spectrum of primary cosmic rays. Experimental data on the neutron component at sea level are vaster, but they are contradictory. The results of our calculations are in good agreement with data from recent measurements at a prototype of the KASKADE facility in Karlsruhe [28]. As can be seen from Fig. 6, data from [28] at $E \lesssim 1$ TeV are described much better by the calculation with the EKS primary spectrum than by the calculation with the NSU primary spectrum.

It can be hoped that further experiments to study the nucleonic component of secondary cosmic rays will allow a more detailed test of the method and of the models for the primary spectrum and for nucleon–nucleus interactions.

ACKNOWLEDGMENTS

We are grateful to S.I. Sinegovsky for stimulating discussions.

This work was financially supported by the Ministry for Higher Education of the Russian Federation within the program Universities of Russia—Fundamental Research (grant no. 015.02.01.04).

REFERENCES

1. V. A. Naumov and L. Perrone, Astropart. Phys. **10**, 239 (1999).
2. V. A. Naumov, Issled. Geomagn., Aéron. Fiz. Solntsa **69**, 82 (1984); É. V. Bugaev and V. A. Naumov, Preprint No. P-0401, IYaI AN SSSR (Institute for Nuclear Research, Academy of Sciences of USSR, Moscow, 1985).
3. A. N. Vall, V. A. Naumov, and S. I. Sinegovskiĭ, Yad. Fiz. **44**, 1240 (1986) [Sov. J. Nucl. Phys. **44**, 806 (1986)]; E. V. Bugaev, A. Misaki, V. A. Naumov, *et al.*, Phys. Rev. D **58**, 054001 (1998).
4. G. T. Zatsepin, in *Problems in Cosmic-Ray Physics* (Inst. Yad. Issled. Akad. Nauk SSSR, Moscow, 1978), p. 189.
5. N. L. Grigorov, Yad. Fiz. **25**, 788 (1977) [Sov. J. Nucl. Phys. **25**, 419 (1977)]; L. V. Volkova, G. T. Zatsepin, and L. A. Kuz'michev, Yad. Fiz. **29**, 1252 (1979) [Sov. J. Nucl. Phys. **29**, 645 (1979)]; I. P. Ivanenko and T. M. Roganova, *Cascade Showers Induced by Ultra-high-Energy Particles* (Nauka, Moscow, 1983); J. Bellandi, L. M. Mundim, J. Dias de Deus, and R. M. J. Covolan, J. Phys. G **18**, 579 (1992).
6. S. I. Nikol'skiĭ, Ĭ. N. Stamenov, and S. Z. Ushev, Zh. Éksp. Teor. Fiz. **87**, 18 (1984) [Sov. Phys. JETP **60**, 10 (1984)]; S. I. Nikol'skiĭ, in *Problems in Cosmic-Ray Physics*, Ed. by A. E. Chudakov *et al.* (Nauka, Moscow, 1987), p. 169.
7. E. V. Bugaev, V. A. Naumov, S. I. Sinegovsky, *et al.*, in *Proceedings of the RIKEN International Workshop on Electromagnetic and Nuclear Cascade Phenomena in High and Extremely High Energies, Tokyo, RIKEN, 1994*, Ed. by M. Ishihara and A. Misaki, p. 264.
8. A. D. Erlykin, N. P. Krutikova, and Yu. M. Shabel'skiĭ, Yad. Fiz. **45**, 1075 (1987) [Sov. J. Nucl. Phys. **45**, 668 (1987)].
9. K. Greisen, Phys. Rev. Lett. **16**, 748 (1966); G. T. Zatsepin and V. A. Kuz'min, Pis'ma Zh. Éksp. Teor. Fiz. **4**, 114 (1966) [JETP Lett. **4**, 78 (1966)].
10. H. H. Mielke, M. Föller, J. Engler, and J. Knapp, J. Phys. G **20**, 637 (1994).

11. L. R. Kimel' and N. V. Mokhov, Izv. Vyssh. Uchebn. Zaved., Fiz., No. 10, 17 (1974); L. R. Kimel' and N. V. Mokhov, Vopr. Dozim. Zashch. Izluch. **14**, 41 (1975).
12. D. S. Barton, G. W. Brandenburg, W. Busza, *et al.*, Phys. Rev. D **27**, 2580 (1983).
13. Particle Data Group (C. Caso *et al.*), Eur. Phys. J. C **3**, 1 (1998).
14. ISR Collab. (M. Basile *et al.*), Lett. Nuovo Cimento **41**, 298 (1984).
15. J. Ranft, hep-ph/9911213.
16. É. V. Bugaev and V. A. Naumov, Issled. Geomagn., Aéron. Fiz. Solntsa **73**, 198 (1985); É. V. Bugaev and V. A. Naumov, Preprint No. P-0385, IYaI AN SSSR (Institute for Nuclear Research, Academy of Sciences of USSR, Moscow, 1985).
17. A. C. Genz and A. A. Malik, J. Comput. Appl. Math. **6**, 295 (1980).
18. P. Fawler *et al.*, Nature **209**, 567 (1966).
19. A. V. Apanasenko and M. N. Shcherbakova, Izv. Akad. Nauk SSSR, Ser. Fiz. **32**, 372, 374 (1968).
20. C. Aguirre, A. Trepp, C. R. Mejía, *et al.* (Brazilian–Japanese Emulsion Group), Can. J. Phys. **46**, 660 (1968).
21. N. M. Kocharyan, G. S. Saakyan, and Z. A. Kirakosyan, Zh. Éksp. Teor. Fiz. **35**, 1335 (1958) [Sov. Phys. JETP **8**, 933 (1958)].
22. G. Brooke and A. W. Wolfendale, Proc. Phys. Soc. London **84**, 843 (1964).
23. I. S. Diggory, J. R. Hook, I. A. Jenkins, and K. E. Turver, J. Phys. A **7**, 741 (1974).
24. M. Lumme, M. Nieminen, J. Peltonen, *et al.*, J. Phys. G **10**, 683 (1984).
25. F. Ashton and R. B. Coats, J. Phys. A **1**, 169 (1968).
26. F. Ashton, J. King, É. A. Mamidzhanyan, and N. I. Smith, Izv. Akad. Nauk SSSR, Ser. Fiz. **33**, 1557 (1969).
27. F. Ashton, N. I. Smith, J. King, and E. A. Mamidzhanian, Acta Phys. Acad. Sci. Hung. **29** (3), 25 (1970); A. Liland, in *Proceedings of the 20th International Cosmic Ray Conference, Moscow, 1987*, Vol. 5, p. 295.
28. H. Kornmayer, H. H. Mielke, J. Engler, and J. Knapp, J. Phys. G **21**, 439 (1995).
29. N. L. Grigorov, I. D. Rapoport, and V. Ya. Shestoperov, *High-Energy Particles in Cosmic Rays* (Nauka, Moscow, 1973).

Translated by A. Isaakyan

Physics of Atomic Nuclei, Vol. 63, No. 11, 2000, pp. 1936–1942. Translated from Yadernaya Fizika, Vol. 63, No. 11, 2000, pp. 2029–2035.

ELEMENTARY PARTICLES AND FIELDS
Theory

Phase of $\phi\omega$ Interference due to Unitarity Corrections to the Amplitude of $\phi\omega$ Mixing

N. N. Achasov* and A. A. Kozhevnikov

Institute of Mathematics, Siberian Division, Russian Academy of Sciences, Universitetskii pr. 4, Novosibirsk, 630090 Russia

Received July 22, 1999; in final form, November 29, 1999

Abstract—The phase of $\phi\omega$ interference in the reaction $e^+e^- \longrightarrow \pi^+\pi^-\pi^0$ near the energy of the $\phi(1020)$ peak is calculated within an approach that is virtually independent of the model for $\phi\omega$ mixing. A comparison with the phase measured recently (with a poor precision) shows that the deviation of the measured result from the expected value of 180° is associated largely with the effect of the right shoulder of the $\omega(782)$ peak in the region of the $\phi(1020)$ peak. The ω width at the energy equal to the ϕ mass is within the interval 120–200 MeV. The effect of the $\phi\omega$-state-induced unitarity corrections to the ϕ and ω coupling constants on the phase of $\rho\pi$ interference is considered in detail. *© 2000 MAIK "Nauka/Interperiodica".*

1. INTRODUCTION

For the phase of $\phi\omega$ interference, a recent measurement of the cross section for the reaction $e^+e^- \longrightarrow \pi^+\pi^-\pi^0$ at energies near the $\phi(1020)$ resonance with the KMD-2 detector yielded the value of $\chi_{\phi\omega} = 162° \pm 17°$ [1]. The analysis of these data properly allowed for the phases of the complex propagators for the ϕ and ω mesons. In other words, the cross section was fitted in terms of the expression

$$\sigma_{3\pi} \propto \left| \frac{1}{m_\omega^2 - s - i\sqrt{s}\Gamma_\omega(s)} + \frac{A\exp(i\chi_{\phi\omega})}{m_\phi^2 - s - i\sqrt{s}\Gamma_\phi(s)} \right|^2, \quad (1.1)$$

where A is a real positive number. Hereafter, s stands for the square of the total c.m. energy. It is hoped that the accuracy in measuring the $\phi\omega$ phase by the SND and KMD-2 detectors installed at the VEPP-2M storage ring in Novosibirsk will be substantially improved in the near future. Mention should also be made of the DAΦNE facility, which is expected to produce formidable numbers of ϕ mesons, so that prospects for achieving there a high precision of the relevant measurements are optimistic too. The central value of the $\chi_{\phi\omega}$ phase in [1] is somewhat surprising because it differs significantly from the standard value of 180°, which is predicted by many theoretical approaches based on the $SU(3)$ flavor group and by the simplest quark models featuring real-valued coupling constants [2]. The value obtained for the phase explains the experimental observation [1, 3] that the minimum of $\phi\omega$ interference in the energy dependence of the cross section for the reaction $e^+e^- \longrightarrow \pi^+\pi^-\pi^0$ occurs to the right of the ϕ resonance.

The objective of the present study is to demonstrate that the phase $\chi_{\phi\omega}$ can be calculated by a method that is virtually independent of the $\phi\omega$-mixing model used to describe the decay process $\phi \longrightarrow \rho\pi$. As will be seen below, this is associated with a subtle cancellation of the contributions from the $\rho\pi$ state to the $\phi\omega$-mixing amplitude, $\phi \longrightarrow \omega \longrightarrow \rho\pi$, and to the direct transition $\phi \longrightarrow \rho\pi$. We will show that the deviation of $\chi_{\phi\omega}$ from 180° is explained predominantly by finite-width effects. A precise measurement of the above phase would contribute to a reliable validation of the procedure for extrapolating the excitation curve of the $\omega(782)$ resonance up to energies corresponding to the ϕ-meson mass.

The ensuing exposition is organized as follows. In Section 2, we give a brief account of basic models used to explain the decay process $\phi \longrightarrow \rho\pi$. In Section 3, we present the expressions that describe the leading corrections to the $\phi\omega$-mixing amplitude and to the constants of ϕ and ω coupling to the $\rho\pi$ state and which satisfy the unitarity condition. In Section 4, we calculate the phase of $\phi\omega$ interference in the reaction $e^+e^- \longrightarrow \pi^+\pi^-\pi^0$. Our results and conclusions are summarized in Section 5.

2. BASIC MODELS OF THE DECAY PROCESS $\phi \longrightarrow \rho\pi$

The formalism required for analyzing the pattern of $\phi\omega$ interference in the reaction $e^+e^- \longrightarrow \pi^+\pi^-\pi^0$ was developed in [4–6], where the reader can also find necessary details. Here, we restrict ourselves to briefly mentioning the most significant points. The problem of assessing the extent to which $\omega(782)$ and $\phi(1020)$ represent the ideal mixture of the states

$$\begin{aligned} \omega^{(0)} &= (u\bar{u} + d\bar{d})/\sqrt{2}, \\ \phi^{(0)} &= s\bar{s} \end{aligned} \quad (2.1)$$

emerged almost simultaneously with the discovery of these resonances [7]. The point is that the decay process

* e-mail: achasov@math.nsc.ru

$\phi \longrightarrow \rho\pi \longrightarrow \pi^+\pi^-\pi^0$, which violates the Okubo–Zweig–Iizuka (OZI) rule [7–9], is usually considered as evidence for a small admixture of nonstrange quarks in the φ-meson wave function; that is,

$$\phi(1020) = s\bar{s} + \varepsilon_{\phi\omega}(u\bar{u} + d\bar{d})/\sqrt{2}, \qquad (2.2)$$

where the φω-mixing amplitude is described by the complex mixing parameter $\varepsilon_{\phi\omega} \equiv \varepsilon_{\phi\omega}(s)$, $|\varepsilon_{\phi\omega}| \ll 1$. This parameter in turn is expressed in terms of an off-diagonal element of the polarization mixing operator according to the relation

$$\varepsilon_{\phi\omega} = -\frac{\mathrm{Re}\Pi_{\phi\omega} + i\mathrm{Im}\Pi_{\phi\omega}}{\Delta M^2_{\phi\omega}(s)}, \qquad (2.3)$$

where

$$\Delta M^2_{\phi\omega}(s) = \Delta m^{(0)2}_{\phi\omega} - i\sqrt{s}[\Gamma^{(0)}_{\phi}(s) - \Gamma^{(0)}_{\omega}(s)] \qquad (2.4)$$

with $\Delta m^{(0)2}_{\phi\omega} = m^{(0)2}_{\phi} - m^{(0)2}_{\omega}$. Hereafter, $m^{(0)}_V$ and $\Gamma^{(0)}_V$ are, respectively, the mass and the width of the ideally mixed state (2.1), all quantities carrying superscript (0) referring to this state. In the following, this mechanism is called the model of strong φω mixing. In QCD, the real part of the mixing operator, $\mathrm{Re}\Pi_{\phi\omega}$, is nonzero either owing to the perturbative three-gluon state [10, 11] shown in Fig. 1*a* or owing to nonperturbative effects [12] that are illustrated in Fig. 2*b*. However, the contribution of the diagram in Fig. 1*a* is small and has a wrong sign (see [10, 11])—namely, the minimum in the cross section for the reaction $e^+e^- \longrightarrow \pi^+\pi^-\pi^0$ is predicted to occur on the left of the φ resonance, in disagreement with experimental data from [1, 3]. At the same time, the calculation of $\varepsilon_{\phi\omega}$ on the basis of the diagram in Fig. 1*b* [12] can yield at best an order-of-magnitude estimate. The contribution of the single-photon state to $\mathrm{Re}\Pi_{\phi\omega}$ is two orders of magnitude less than what is required for explaining the partial width with respect to the decay $\phi \longrightarrow 3\pi$.

The direct transition in Fig. 1*c*, in which case $\mathrm{Re}\, g^{(0)}_{\phi\rho\pi} \neq 0$ and $\mathrm{Re}\Pi_{\phi\omega} \equiv 0$, is an alternative to the commonly adopted mechanism of φω mixing. As a matter of fact, this is the well-known Appelquist–Politzer mechanism [13], which was introduced to explain the violation of the OZI rule in the decays of heavy quarkonia into light hadrons and which is extrapolated in the present case to the region of energies around the φ-meson mass. It was demonstrated in [6] that the direct transition makes a significant contribution to the amplitude for the decay process $\phi \longrightarrow \rho\pi$. The order-of-magnitude estimates of $\mathrm{Re}\, g^{(0)}_{\phi\rho\pi}$ from [6] comply with the value obtained from the partial width with respect to the decay $\phi \longrightarrow 3\pi$. Hereafter, this mechanism will be referred to as the model of weak φω mixing. Of course, either version represents a limiting case, and we cannot rule out intermediate situations where the above mechanisms are both operative.

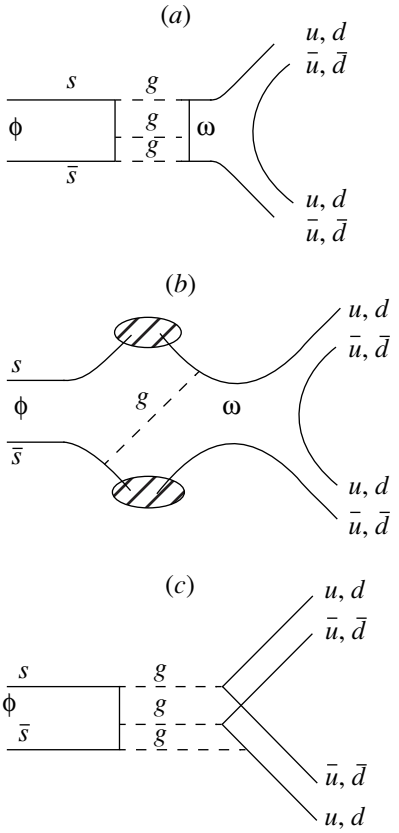

Fig. 1. The models of the decay $\phi(1020) \longrightarrow \rho(770)\pi$: (*a*) φω mixing owing to the three-gluon mechanism, (*b*) φω mixing owing to nonperturbative QCD effects (shaded regions denote quark condensates), and (*c*) direct decay $\phi \longrightarrow \rho\pi$ owing to three-gluon mechanism (*g* stands for a gluon).

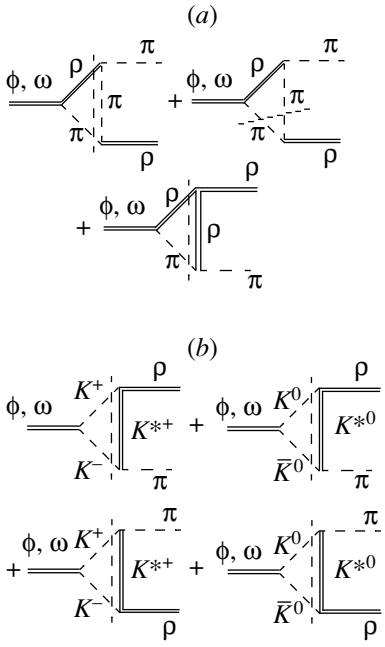

Fig. 2. Contributions to $2\mathrm{Im}\, g^{(0)}_{\phi(\omega)\rho\pi}$ from (*a*) the ρπ intermediate state and (*b*) the $K\bar{K}$ intermediate state.

3. UNITARITY CORRECTIONS TO THE COUPLING CONSTANTS AND TO THE φω-MIXING AMPLITUDE

In contrast to $\mathrm{Re}\, g^{(0)}_{\phi\rho\pi}$ and $\mathrm{Re}\Pi_{\phi\omega}$, which are hardly calculable, the corresponding imaginary parts can easily be evaluated with the aid of the unitarity condition. The main contribution to $2\mathrm{Im}\, g^{(0)}_{\phi(\omega)\rho\pi}$ comes from the diagrams in Fig. 2. The sum of the first two diagrams can be calculated by using the results from [14, 15] that were generalized by allowing for the one-pion-exchange form factor $\exp(-\lambda_\pi|t - m_\pi^2|)$. Isolating the factor $\mathrm{Re}\, g^{(0)}_{\phi(\omega)\rho\pi}$, we then arrive at

$$\Phi_{\rho\pi}(s, m^2) = -\frac{g^2_{\rho\pi\pi}}{8\pi\sqrt{s}q_f^3}\int\limits_{2m_\pi}^{\sqrt{s}-m_\pi} d\mu \frac{2\mu^2\Gamma(\rho \longrightarrow \pi\pi, \mu)}{\pi|D_\rho(\mu^2)|^2} \times\left\{(q_i q_f)^2 \mathrm{P}.\int\limits_{-1}^{+1} dx \frac{1-x^2}{a+x}\exp[2(-\lambda_\pi)q_i q_f|a+x| - 1] + \Phi_0(s, m^2, \mu^2)\right\}, \quad (3.1)$$

where P. denotes the principal-value prescription for the integral; m and μ are the invariant masses of the final and the intermediate ρ meson, respectively; the ρ-meson propagator is given by

$$1/D_\rho(\mu^2) = [m_\rho^2 - \mu^2 - i\mu\Gamma(\rho \longrightarrow \pi\pi, \mu)]^{-1},$$

and the function

$$\Phi_0(s, m^2, \mu^2) = (q_i q_f)^2\left(2a + \ln\left|\frac{a+1}{a-1}\right|\right) + (q_{\pi\pi}q_f)^2\left(2b + \ln\left|\frac{b+1}{b-1}\right|\right)$$

represents the contribution of the first two diagrams in Fig. 2*a* in the limit of zero slope of the one-pion exchange form factor [14, 15]. In the above expressions, we have used the notation

$$a = (\mu^2/2 - E_i E_f)/q_i q_f, \quad b = m(E_i + E_f - E_\rho)/2q_{\pi\pi}q_f, \quad (3.2)$$

where

$$q_i = q(\sqrt{s}, m_\pi, \mu), \quad E_i = E(\sqrt{s}, m_\pi, \mu), \quad q_f = q(\sqrt{s}, m_\pi, m), \quad E_f = E(\sqrt{s}, m_\pi, m), \quad q_{\pi\pi} = q(m, m_\pi, m_\pi), \quad E_\rho = E(\sqrt{s}, \mu, m_\pi). \quad (3.3)$$

Here, the expressions for the energy and for the momentum are given by

$$E(M, m_1, m_2) = (M^2 + m_1^2 - m_2^2)/2M,$$
$$q(M, m_1, m_2) = \{[M^2 - (m_1 + m_2)^2][M^2 - (m_1 - m_2)^2]\}^{1/2}/2M. \quad (3.4)$$

The decay kinematics of the first two diagrams in Fig. 2*a* results in a very weak dependence of their contribution on λ_π. This is because the contribution of the cut across the ππ lines is significant and is independent of λ_π (for details see [14, 15]). A numerical calculation yields $\Phi_{\rho\pi}(m_\phi^2, m_\rho^2) = 0.44$, 0.45, 0.47, and 0.49 at $\lambda_\pi =$ 0, 1, 2, and 4 GeV^{-2}, respectively. The weak change with increasing λ_π is due to the fact that the contributions of the first two diagrams in Fig. 2*a* have opposite signs at $\sqrt{s} < 1.1$ GeV. Numerically, the contribution of the third diagram in Fig. 2*a* at $\sqrt{s} = m_\phi$ is -3.4×10^{-2}, provided that the slope parameter for ρ exchange is $\lambda_\pi = 2$ GeV^{-2}. This value was chosen from the requirement that, to within 10%, the ππ phase shift at the energy value being considered be determined by the phase of the ρ-meson propagator, as is indeed the case. Hence, the contribution of the third diagram in Fig. 2*a* can be neglected against the contribution of the first two diagrams. The contribution of the diagram in Fig. 2*b* is determined by the $K\bar{K}$ intermediate state with K^* exchange. In the case of the φ meson, this contribution is given by

$$\Phi_{K\bar{K}}(s, m^2) = g_{\phi K\bar{K}} g_{K^{*+}K^+\pi^0} g_{K^{*+}K^+\rho^0}\frac{q^2_{K\bar{K}}}{8\pi\sqrt{s}q_{\rho\pi}} \times\int\limits_{-1}^{+1} dx \frac{1-x^2}{a_{K\bar{K}} + x}\exp[2\lambda_{K^*}q_{K\bar{K}}q_{\rho\pi}(a_{K\bar{K}} + x)], \quad (3.5)$$

where $a_{K\bar{K}} = (m_K^2 - m_{K^*}^2 + m^2)/2q_{K\bar{K}}q_{\rho\pi}$, $q_{K\bar{K}} = q(\sqrt{s}, m_K, m_K)$, and $q_{\rho\pi} = q(\sqrt{s}, m, m_\pi)$. In the case of the ω meson, expression (3.5) must be multiplied by the $SU(3)$ factor of $-1/\sqrt{2}$. We also note that, according to $SU(3)$, the coupling constants are related as $g_{K^{*+}K^+\rho^0} = g_{\omega\rho\pi}/2$. The effect of nonzero $\Phi_{K\bar{K}}$ is numerically small for the ω meson. In the case of the φ meson, this effect expressed in terms of the phase of the coupling constant $g_{\phi\rho\pi}$ is at first glance enhanced by the factor $g_{\omega\rho\pi}/g_{\phi\rho\pi} \simeq 18$. Even in this case, however, the contribution of the $K\bar{K}$ intermediate state at $\sqrt{s} = 1020$ (1050) MeV is 6% (18%) of the φρπ total effective coupling constant. These values were obtained at $\lambda_{K^*} = 0$ and $m = m_\rho$. The more realistic value of $\lambda_{K^*} = 1$ GeV^{-2} [it is considered

here that the average of $\Phi_{K\bar{K}}(s, m^2)$ over the mass spectrum of the ππ system must enter into the expression for the phase of φω interference—see expression (4.3) below] leads to a further reduction of the above estimates by a factor of about 2. Since the leading unitarity correction $\Phi_{\rho\pi} \neq 0$ is relatively large, it is necessary to take into account the rescattering chain in Fig. 2*a* entirely. This can be done by a method similar to that of solving the Dyson equation for the vertex function. Making use of all the above considerations, we can represent the constants of φ and ω coupling to ρπ as

$$\begin{aligned} g^{(0)}_{\phi\rho\pi}(s, m^2) &\simeq \mathrm{Re}\, g^{(0)}_{\phi\rho\pi}/[1 - i\Phi_{\rho\pi}(s, m^2)] \\ &\quad + i\Phi_{K\bar{K}}(s, m^2), \\ g^{(0)}_{\omega\rho\pi}(s, m^2) &\simeq \mathrm{Re}\, g^{(0)}_{\omega\rho\pi}/[1 - i\Phi_{\rho\pi}(s, m^2)]. \end{aligned} \tag{3.6}$$

Of course, $\mathrm{Re}\, g^{(0)}_{\phi(\omega)\rho\pi}$ must be determined from the partial width with respect to the decay $\phi(\omega) \longrightarrow \pi^+\pi^-\pi^0$ on the mass shell of the φ(ω) meson. It is clear from (3.6) that the most significant contribution to the imaginary parts of the coupling constants drops out from their ratio owing to the ρπ intermediate states. It should be borne in mind, however, that the nonzero quantity $\Phi_{\rho\pi}$ enters into the expression for the 3π partial decay widths of the φ and ω mesons [14, 15]; that is,

$$\Gamma(\omega, \phi \longrightarrow \pi^+\pi^-\pi^0, s) = [\mathrm{Re}\, g^{(0)}_{\omega,\phi\rho\pi}]^2 W(s)/4\pi, \tag{3.7}$$

where the decay phase space is given by

$$\begin{aligned} W(s) &= \frac{1}{2\pi}\int\limits_{2m_\pi}^{\sqrt{s}-m_\pi} dm m^2 \Gamma_{\rho\pi\pi}(m^2) q^2_{\rho\pi}(m) \int\limits_{-1}^{1} dx(1 - x^2) \\ &\times \left| \frac{1}{D_\rho(m^2)Z(m^2)} + \frac{1}{D_\rho(m^2_+)Z(m^2_+)} + \frac{1}{D_\rho(m^2_-)Z(m^2_-)} \right|^2. \end{aligned} \tag{3.8}$$

Expression (3.8) involves the squares of the invariant masses of the charged ρ mesons. For these masses, we have

$$m^2_\pm = (s + 3m^2_\pi - m^2)/2 \pm 2x q_{\rho\pi} q_{\pi\pi}\sqrt{s}/m, \tag{3.9}$$

where $q_{\rho\pi} = q(\sqrt{s}, m, m_\pi)$ and $q_{\pi\pi} = q(m, m_\pi, m_\pi)$ must be calculated according to (3.4), while $Z(m^2) = 1 - i\Phi_{\rho\pi}(s, m^2)$. The effect of the nonzero $\Phi_{K\bar{K}}$ on the partial width with respect to the decay $\phi \longrightarrow 3\pi$ is negligible.

The most significant unitarity corrections to the mixing amplitude, $\mathrm{Im}\Pi_{\phi\omega}$, are determined by the $K\bar{K}$ and ρπ intermediate states and are given by

$$\begin{aligned} \mathrm{Im}\Pi_{\phi\omega} &= \sqrt{s}[\mathrm{Re}\, g^{(0)}_{\phi\rho\pi}\Gamma(\omega \longrightarrow \pi^+\pi^-\pi^0, s)/\mathrm{Re}\, g^{(0)}_{\omega\rho\pi} \\ &\quad - \Gamma(\phi \longrightarrow K\bar{K}, s)/\sqrt{2}]. \end{aligned} \tag{3.10}$$

For the sake of completeness, it should be noted that, although the effect of nonzero $\Phi_{\rho\pi}$ is of importance for ωρ interference in the $\pi^+\pi^-$ mass spectrum [14, 15], we can simulate it in calculating the 3π partial decay width (at a given value of $\sqrt{s}$) in terms of the form factor

$$C_{\rho\pi}(s) = [1 + (R_{\rho\pi}m_\omega)^2]/(1 + R^2_{\rho\pi}s) \tag{3.11}$$

and introduce this form factor in the $\omega \longrightarrow \rho\pi$ vertex via the substitution $g_{\omega\rho\pi} \longrightarrow g_{\omega\rho\pi}C_{\rho\pi}(s)$ [14]. The contributions to the unitarity correction from the $\pi^0\gamma$ and ηγ radiative states do not exceed, respectively, 4 and 2% of the contribution of the $K\bar{K}$ intermediate state. These values are well below the accuracy of the quark-model predictions that is necessary for obtaining relations between the constants of φ and ω couplings to the $K\bar{K}$ pair. For the accuracy of the calculation, we adopt the conservative estimate of 20%, so that the contribution of radiative states can be disregarded.

4. PHASE OF THE φω INTERFERENCE IN THE REACTION $e^+e^- \longrightarrow \pi^+\pi^-\pi^0$

Taking into account the above features of the decay $e^+e^- \longrightarrow \pi^+\pi^-\pi^0$, we can represent the cross section for the reaction $\phi \longrightarrow \pi^+\pi^-\pi^0$ in the form [4, 5]

$$\begin{aligned} \sigma_{3\pi}(s) &= \frac{4\pi\alpha^2 W(s)}{s^{3/2}} \\ &\times \left| \frac{g_{\gamma\omega}g_{\omega\rho\pi}}{m^2_\omega - s - i\sqrt{s}\Gamma_\omega(s)} + \frac{g_{\gamma\phi}g_{\phi\rho\pi}}{m^2_\phi - s - i\sqrt{s}\Gamma_\phi(s)} \right|^2, \end{aligned} \tag{4.1}$$

where

$$\begin{aligned} g_{\gamma\omega} &= g^{(0)}_{\gamma\omega} - \varepsilon_{\phi\omega}g^{(0)}_{\gamma\phi}, \\ g_{\gamma\phi} &= g^{(0)}_{\gamma\phi} + \varepsilon_{\phi\omega}g^{(0)}_{\gamma\omega}, \\ g_{\omega\rho\pi} &= \mathrm{Re}\, g^{(0)}_{\omega\rho\pi} - \varepsilon_{\phi\omega}\mathrm{Re}\, g^{(0)}_{\phi\rho\pi} \simeq \mathrm{Re}\, g^{(0)}_{\omega\rho\pi}, \\ g_{\phi\rho\pi} &= \mathrm{Re}\, g^{(0)}_{\phi\rho\pi} + \varepsilon_{\phi\omega}\mathrm{Re}\, g^{(0)}_{\omega\rho\pi} + i\langle\Phi_{K\bar{K}}(s)\rangle. \end{aligned} \tag{4.2}$$

In expressions (4.2), the coupling constants for the physical states of total widths $\Gamma_{\phi,\omega}(s)$ are expressed in terms of the coupling constants for ideally mixed states. The quantity

$$\langle\Phi_{K\bar{K}}(s)\rangle = \int\limits_{2m_\pi}^{\sqrt{s}-m_\pi} d\mu \frac{2\mu^2\Gamma_\rho(\mu)}{\pi|D_\rho(\mu^2)|^2}\Phi_{K\bar{K}}(s, \mu^2) \tag{4.3}$$

corresponds to averaging over the ππ mass spectrum—that is, to approximately taking into account the invariant-mass dependence of $\Phi_{K\bar{K}}$. Quantitatively, this leads to a 33% reduction of $\Phi_{K\bar{K}}$ with respect to the relevant value at the ρ-meson mass. We note that the quantity

$$g^{(0)}_{\gamma V} = m^{(0)2}_V / f^{(0)}_V, \tag{4.4}$$

where $V = \omega, \phi$, is the amplitude of the transition $\gamma \longrightarrow V^{(0)}$ and that the quantity $f_V^{(0)}$ appears in the expression for the leptonic width of the ideally mixed state $V^{(0)}$ as

$$\Gamma(V^{(0)} \longrightarrow e^+e^-, m_V^{(0)2}) = \frac{4\pi\alpha^2 m_V^{(0)}}{3 f_V^{(0)2}} \qquad (4.5)$$

($\alpha = 1/137$ is the QED fine-structure constant). If all coupling constants and the parameter of $\phi\omega$ mixing in relation (4.1) were real-valued, the phase of $\phi\omega$ interference would be determined by the sign of the ratio

$$R_0 = g^{(0)}_{\gamma\phi} g_{\phi\rho\pi} / g^{(0)}_{\gamma\omega} g_{\omega\rho\pi}. \qquad (4.6)$$

At the same time, the position of the interference minimum in the energy dependence of the cross section for the reaction $e^+e^- \longrightarrow \pi^+\pi^-\pi^0$, as given by the expression

$$s_{\min}^{1/2} = \left(\frac{m_\phi^2 + R_0 m_\omega^2}{1 + R_0}\right)^{1/2}, \qquad (4.7)$$

was experimentally determined to be $s_{\min}^{1/2} = 1.05$ GeV [1, 3]. This corresponds to the value of $R_0 = -0.13$, whence we obtain the canonical phase value of 180°. From the arguments presented in Section 3, it follows, however, that, because of unitarity corrections, the coupling constants and the mixing amplitudes develop sizable imaginary parts. A comparison of expressions (1.1) and (4.1) [see also (4.2)] shows that a significant additional phase $\Delta\chi_{\phi\omega}$ stems from the phase of the following combination of the coupling constants that enter into relation (4.2):

$$r \equiv \frac{g_{\phi\rho\pi}}{g_{\omega\rho\pi}} = \frac{g^{(0)}_{\phi\rho\pi}(s)}{g^{(0)}_{\omega\rho\pi}(s)} + \varepsilon_{\phi\omega}(s) \simeq \frac{\Delta m^2_{\phi\omega}}{\Delta M^2_{\phi\omega}(s)}\left(\frac{\mathrm{Re} g^{(0)}_{\phi\rho\pi}}{\mathrm{Re} g^{(0)}_{\omega\rho\pi}} - \frac{\mathrm{Re}\Pi_{\phi\omega}}{\Delta m^2_{\phi\omega}} + i\frac{\sqrt{s}\Gamma_{\phi KK}(s)}{\sqrt{2}\Delta m^2_{\phi\omega}}\right) + i\langle\Phi_{K\bar{K}}(s)\rangle / \mathrm{Re} g^{(0)}_{\omega\rho\pi}. \qquad (4.8)$$

Here, $\Delta m^2_{\phi\omega} = m^2_\phi - m^2_\omega$, while $\Delta M^2_{\phi\omega}(s)$ is determined by expression (2.4). To within 5%, the masses and the widths of the ideally mixed states appearing in the expression for $\varepsilon_{\phi\omega}$ have been replaced in Eq. (4.8) [and will be replaced in Eq. (4.9) below] by the masses and the widths of the physical vector mesons. We note that the combination $\mathrm{Re} g^{(0)}_{\phi\rho\pi}/\mathrm{Re} g^{(0)}_{\omega\rho\pi} - \mathrm{Re}\Pi_{\phi\omega}/\Delta m^2_{\phi\omega}$ on the right-hand side of Eq. (4.8) determines the 3π partial decay width of the ϕ meson. Hence, it takes the same value in the two models of $\phi\omega$ mixing that have been mentioned in Section 2. The correction to the phase due to taking into account terms with nonzero $\varepsilon_{\phi\omega}$ in the $\gamma\phi(\omega)$ transition amplitude is $\Delta\chi_{\phi\omega} = 1.4°$, which is below the adopted accuracy of the calculation. Therefore, the result for $\chi_{\phi\omega}$ is virtually independent of the mixing model.

Let us first obtain a rough estimate of the deviation of the phase from 180° at the energy value equal to the ϕ-meson mass. In doing this, we neglect unitarity corrections to the ω and ϕ coupling constants. For the deviation in question, we then arrive at

$$\Delta\chi_{\phi\omega} \simeq \arctan\frac{m_\phi \Gamma_{\phi KK}/\Delta m^2_{\phi\omega}}{\sqrt{2}(\mathrm{Re} g^{(0)}_{\phi\rho\pi}/\mathrm{Re} g^{(0)}_{\omega\rho\pi} - \mathrm{Re}\Pi_{\phi\omega}/\Delta m^2_{\phi\omega})} - \tan^{-1}\frac{m_\phi[\Gamma_\omega(m_\phi) - \Gamma_\phi]}{\Delta m^2_{\phi\omega}}. \qquad (4.9)$$

The first term in (4.9) contributes $6° \pm 1°$ to $\chi_{\phi\omega}$, the uncertainty being determined by a 20% accuracy of the $SU(3)$ predictions for the constants of coupling to the $K\bar{K}$ state. The contribution of the second term is opposite in sign to the contribution of the first term and strongly depends on the ω-meson width at the energy value equal to the ϕ-meson mass, $\Gamma_\omega(m_\phi)$. When $R_{\rho\pi}$ is changed from 0 to 1 GeV^{-2} (this corresponds to changing the ω width at the ϕ-meson mass from 200 to 120 MeV) in (3.11), the contribution of the second term changes from –26° to –13°. Larger values of $R_{\rho\pi}$ would violate the description of data on the reaction $e^+e^- \longrightarrow \pi^+\pi^-\pi^0$ at energies above the $\phi(1020)$-meson mass. Indeed, the fits from [16] yield $R_{\rho\pi} = 0.8^{+0.6}_{-0.3}$ GeV^{-2}.

The results of a more precise calculation are as follows. In addition to the aforementioned uncertainty in the $SU(3)$ predictions, the error of the calculation includes the uncertainties in the slopes of the form factors that appear in the amplitudes of the unitarity condition. (i) If we take into account effects of $\rho\pi$ rescatterings, $\Phi_{\rho\pi} \neq 0$, then a variation of λ_π in the interval from 0 to 4 GeV^{-2} leads to a small variation of 0.5° in the phase $\chi_{\phi\omega}$. A variation of λ_{K^*} in the same interval changes the phase by about 2°. Upon taking into account a 20% uncertainty in the $SU(3)$ predictions for $\mathrm{Im}\Pi_{\phi\omega}$, the total error becomes some ±3°. This result is much more precise than available data accurate to $\Delta\chi_{\phi\omega} = \pm 17°$ [1] and is commensurate with the accuracy expected in future. The calculated phase depends on the form factor (3.11), which restricts an overly fast growth of the ω-meson width with energy. With allowance for the above uncertainties in the calculations, the result for the phase of $\phi\omega$ interference is $\chi_{\phi\omega} = 165° \pm 3°$ at $R_{\rho\pi} = 0$ and $\chi_{\phi\omega} = 172° \pm 3°$ at $R_{\rho\pi} = 1$ GeV^{-2}. The existing error in the measurement [1] of the phase $\chi_{\phi\omega}$ admits a large interval for $R_{\rho\pi}$; however, the expected reduction of the uncertainty to ±10° would permit setting the more stringent constraint $R_{\rho\pi} \lesssim 2$ GeV^{-2}; a further improvement of the accuracy would open the possibility of reliably determining this parameter. (ii) If we do not take into account effects of $\rho\pi$ rescatterings in the 3π decay width, we arrive at $\chi_{\phi\omega} = 162° \pm 4°$ at $R_{\rho\pi} = 0$

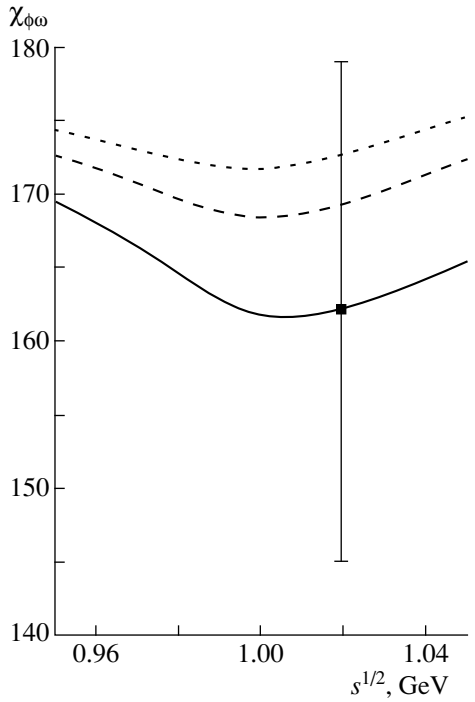

Fig. 3. Phase of the φω interference as a function of energy for the case where rescattering effects are disregarded in the 3π decay width (see main body of the text). The solid, the dashed, and the dotted curve represent the results obtained at $R_{\rho\pi} = 0$, 1, and 2 GeV^{-2}, respectively. The experimental point was borrowed from [1].

and $\chi_{\phi\omega} = 170° \pm 4°$ at $R_{\rho\pi} = 1$ GeV^{-2} (within the aforementioned uncertainties in the calculation).

Unfortunately, the difference of the predictions of the models of strong and weak φω mixing for the phase $\chi_{\phi\omega}$ at the energy value equal to the φ-meson mass is as small as 0.6°. This value cannot be tested experimentally at present. On the other hand, the mixing models in question yield different predictions for the $e^+e^- \longrightarrow \pi^+\pi^-\pi^0$ cross sections at energies around the φω interference minimum [5] because the contribution of the $K\bar{K}$ intermediate state, which affects the imaginary parts of the coupling constants and of the amplitude of φω mixing, strongly depends on energy. At the energy value equal to the φ-meson mass, the contribution of the $K\bar{K}$ state is within the uncertainties in the calculation, but it grows with energy, so that the additional phase from this contribution could be measurable near the φω minimum [5]. Therefore, the study of $\chi_{\phi\omega}$ as a function of energy (this dependence is displayed in Fig. 3) is of considerable interest.

5. CONCLUSION

We have analyzed the possible contributions to the φω-interference phase $\chi_{\phi\omega}$ measured in the reaction $e^+e^- \longrightarrow \pi^+\pi^-\pi^0$. It has been established that the imaginary part of the φω mixing parameter—this imaginary part is determined primarily by the ρπ intermediate state—is the main reason for the experimentally observed deviation of $\chi_{\phi\omega}$ from 180° [1]. However, this result is not quite obvious. The point is that the far right shoulders of resonance curves are usually considered as some substitute for the unknown background in the reaction cross section. Information about the φω-interference phase, which is suggested by data from the experiment reported in [1], but which must be measured more precisely in order to refine this information, is also of value since it demonstrates the applicability of field-theoretical calculations to such complicated systems as hadron resonances. A confirmation of the deviation observed in [1] would imply that the right shoulder of the ω resonance is significant at energy values around the φ-meson mass, which is offset from the center of the ω peak by a distance of 28 widths of the peak. Such an effect can hardly be interpreted in terms of a conventional nonresonance background. The validity of this point of view could be tested by studying the energy dependence of the phase of φω interference (see Fig. 3). In addition to the measurement of the phase $\chi_{\phi\omega}$, more precise measurements of the cross section for the reaction $e^+e^- \longrightarrow \pi^+\pi^-\pi^0$ in the energy interval between the ω and φ peaks are required. Such measurements would enable a reliable determination of the parameter $R_{\rho\pi}$, which enters into expression (3.11). The calculation has revealed that, at $\sqrt{s} = 900$ (950) MeV, the cross section calculated with $R_{\rho\pi} = 1$ GeV^{-2} is 20% (28%) smaller than the cross section calculated with $R_{\rho\pi} = 0$. Such measurements would also contribute to confirming that the heavier ω' and ω'' resonances do not play a significant role for $\sqrt{s} \lesssim m_\phi$.

ACKNOWLEDGMENT

We are grateful to M.N. Achasov for stimulating discussions.

REFERENCES

1. R. R. Akhmetshin *et al.*, Phys. Lett. B **434**, 426 (1998).
2. N. N. Achasov, A. A. Kozhevnikov, and G. N. Shestakov, Pis'ma Zh. Éksp. Teor. Fiz. **21**, 497 (1975) [JETP Lett. **21**, 229 (1975)].
3. S. I. Dolinsky *et al.*, Phys. Rep. **202**, 99 (1991).
4. N. N. Achasov, M. S. Dubrovin, V. N. Ivanchenko, *et al.*, Yad. Fiz. **54**, 1097 (1991) [Sov. J. Nucl. Phys. **54**, 664 (1991)]; N. N. Achasov *et al.*, Int. J. Mod. Phys. A **7**, 3187 (1992).
5. N. N. Achasov and A. A. Kozhevnikov, Yad. Fiz. **55**, 3086 (1992) [Sov. J. Nucl. Phys. **55**, 1726 (1992)]; Part. World **3**, 125 (1993).
6. N. N. Achasov and A. A. Kozhevnikov, Phys. Rev. D **52**, 3119 (1995); Yad. Fiz. **59**, 153 (1996) [Phys. At. Nucl. **59**, 144 (1996)].
7. S. Okubo, Phys. Lett. **5**, 165 (1963).

8. G. Zweig, CERN report 8419/TH412, 1964 (unpublished).
9. J. Iizuka, Prog. Theor. Phys., Suppl. **37/38**, 21 (1966).
10. J. Arafune, M. Fukugita, and Y. Oyanagy, Phys. Lett. B **70**, 221 (1977).
11. B. V. Geshkenbein and B. L. Ioffe, Nucl. Phys. B **166**, 340 (1980).
12. M. A. Shifman, A. I. Vainshtein, and V. I. Zakharov, Nucl. Phys. B **147**, 448 (1979).
13. T. Appelquist and H. D. Politzer, Phys. Rev. Lett. **34**, 43 (1975).
14. N. N. Achasov and A. A. Kozhevnikov, Yad. Fiz. **56** (9), 191 (1993) [Phys. At. Nucl. **56**, 1261 (1993)]; Int. J. Mod. Phys. A **9**, 527 (1994).
15. N. N. Achasov and A. A. Kozhevnikov, Phys. Rev. D **49**, 5773 (1994).
16. N. N. Achasov and A. A. Kozhevnikov, Yad. Fiz. **60**, 2212 (1997) [Phys. At. Nucl. **60**, 2029 (1997)]; Phys. Rev. D **57**, 4334 (1998).

Translated by Kobrinsky

Physics of Atomic Nuclei, Vol. 63, No. 11, 2000, pp. 1943–1948. Translated from Yadernaya Fizika, Vol. 63, No. 11, 2000, pp. 2036–2040.

ELEMENTARY PARTICLES AND FIELDS
Theory

Pion-Pair Production on a Proton by Photons in the Energy Region of Nucleon-Resonance Excitation

M. Ripani[1)], V. I. Mokeev[1)], M. Battaglieri[1)], B. S. Ishkhanov[2)], E. N. Golovach[1)], M. V. Osipenko[2)], G. Ricco[1), 3)], M. Anghinolfi[1)], V. V. Sapunenko[1)], M. Taiuti[1)], and G. V. Fedotov[2)]

Institute of Nuclear Physics, Moscow State University, Vorob'evy gory, Moscow, 119899 Russia

Received June 21, 1999; in final form, March 3, 2000

Abstract—A model is proposed for describing the production of $\pi^+\pi^-$ pairs by real and virtual photons on protons in the energy region of nucleon-resonance excitation. The invariant-mass distributions of the $\pi^+\pi^-$ and π^+p systems at the photon point are calculated. The results are compared with available experimental data. *© 2000 MAIK "Nauka/Interperiodica".*

1. INTRODUCTION

Investigation of the structure of hadrons in photon-induced exclusive reactions is an important line of modern inquiries into the physics of elementary particles and nuclei. The advent of continuous electron accelerators opened qualitatively new possibilities for further advances in these realms. At the moment, a vast experimental program of investigations into nucleon resonances is being performed at TJNAF [1]. Experiments studying the exclusive channel of $\pi^+\pi^-$ production [2, 3] constitute an important part of this program. The point is that such experiments will furnish information about the Q^2 dependence of the electromagnetic form factors for nucleon resonances of masses in excess of 1.6 GeV, which is currently not known. The two-pion channel is promising for seeking "missing" resonances that are predicted in quark models [4, 5], but which have not been observed experimentally. Observing missing resonances or reliably establishing upper bounds on their existence would provide a test for the foundations of modern quark models.

Their competition of a great number of nonresonance mechanisms, which results in a significant contribution of nonresonance processes, presents one of the main difficulties in investigating nucleon resonances in the exclusive channel of pion-pair production by photons. In the situation where it is necessary to describe a large number of various nonresonance mechanisms, the problem of extracting electromagnetic form factors for nucleon resonances becomes very involved. In order to determine these form factors, one needs models that relate them to measured cross sections.

An approach to describing pion-pair production by photons on a proton in the energy region of nucleon-resonance excitation was proposed in [6, 7]. This approach takes into account dominant resonance and nonresonance mechanisms that are described on the basis of meson–baryon interaction with effective vertex functions in terms of tree diagrams. The objective of the phenomenological description developed here is to establish relationships between quintuple-differential cross sections measured in complete kinematics for pion-pair production in photon–proton collisions and the helicity amplitudes for nucleon-resonance excitation, which are denoted by $A_{1/2}(Q^2)$, $A_{3/2}(Q^2)$, and $C_{1/2}(Q^2)$. From a comparison of experimental data and the cross sections calculated within the model used, one can deduce information about the nucleon-resonance contribution to the exclusive channel of pion-pair production by photons. The developed model makes it possible to perform a comparative analysis of various approaches to determining electromagnetic form factors for nucleon resonances, thereby obtaining information about the validity of the description of the structure of the nucleon and its excited states N^* in the transition region between quark confinement and the asymptotic freedom of quarks. By varying the amplitudes $A_{1/2}(Q^2)$, $A_{3/2}(Q^2)$, and $C_{1/2}(Q^2)$ treated as free parameters, we can reconstruct the electromagnetic form factors by imposing the requirement of the best fit to the measured quintuple-differential cross sections for the reaction $\gamma_{r,v}p \longrightarrow \pi^+\pi^-p$.

Model approaches to describing the main quasi-two-body channels $\gamma_{r,v}p \longrightarrow \pi^-\Delta^{++}$ and $\gamma_{r,v}p \longrightarrow \rho p$ of pion-pair production by photons were developed in [6–9]. In the present study, we propose a description of the

[1)] Istituto Nazionale di Fisica Nucleare, Sezione di Genova, Genova, Italy.
[2)] Department of Physics, Moscow State University, Vorob'evy gory, Moscow, 119899 Russia.
[3)] Università di Genova, via Dodecaneso 33, I-16146 Genova, Italy.

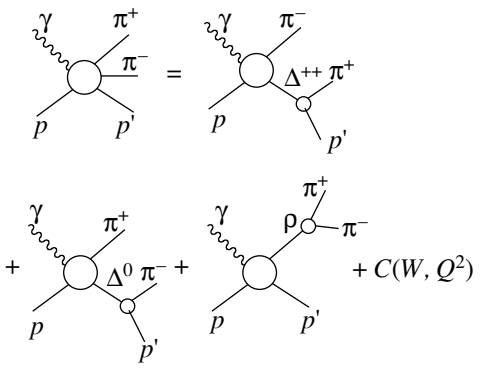

Fig. 1. Mechanisms of the reaction $\gamma_{r,v}p \longrightarrow \pi^+\pi^-p$.

three-body channel $\gamma_{r,v}p \longrightarrow \pi^+\pi^-p$. The results of our calculations are compared with data obtained at the photon point in experiments employing a bubble chamber [10, 11].

For the majority of nucleon resonances with masses above 2.0 GeV, the electromagnetic form factors for the majority of nucleon resonances are known quite well [12], which makes it possible to validate the proposed model description of pion-pair production by photons through a comparison of the calculated and measured cross sections for the above exclusive channel at the photon point.

2. DESCRIPTION OF THE REACTIONS $\gamma_{r,v}p \longrightarrow \pi^+\pi^-p$

2.1. Relationship between the Reaction Amplitudes and Cross Sections

In order to calculate the cross sections for the three-body process in question, we rely here on the standard formalism [13] employing the convolution of the leptonic ($L_{\mu\nu}$) and hadronic ($W_{\mu\nu}$) tensors and invoke the results from [14] for the three-body phase space. The final three-particle state will be described in terms of the following variables: the invariant mass of the π^+p system, s_{π^+p}; the invariant mass of the $\pi^+\pi^-$ system, $s_{\pi^+\pi^-}$; the proton emission angle with respect to the photon momentum, θ_p; the angle between the scattering plane and the plane spanned by the momenta of the proton and the photon, ϕ_p; and the angle between the plane spanned by the momenta of the proton and the photon and the plane spanned by the momenta of the pions forming the $\pi^+\pi^-$ pair, α.

By using these kinematical variables, the quintuple-differential cross section for the reaction $\gamma_{r,v}p \longrightarrow \pi^+\pi^-p$ can be represented in the form

$$d^5\sigma = \left[\frac{1}{4K_L M_N}\right]\left[(4\pi\alpha)\frac{1-\varepsilon}{-Q^2}\frac{1}{2}L_{\mu\nu}W^{\mu\nu}\right]\left[\frac{d\tau}{(2\pi)^5 \times 32W^2}\right], \quad (1)$$

$$d\tau = ds_{\pi^+p}\,ds_{\pi^+\pi^-}\,d\Omega_p\,d\alpha,$$

$$d\Omega_p = \sin\theta_p\,d\theta_p\,d\phi_p,$$

where ε and Q^2 are, respectively, the polarization and the squared 4-momentum of the photon, M_N is the proton mass; W is the total energy of the proton and photon in the reaction c.m. frame; and

$$K_L = \frac{W^2 - M_N^2}{2M_N}, \quad (2)$$

is the equivalent photon momentum.

The tensor $L_{\mu\nu}$ was calculated within QED [13]. Information about the dynamics of the channel being investigated and about the structure of the participant particles is entirely contained in the hadronic tensor $W^{\mu\nu}$, which appears to be a bilinear combination of the hadronic currents J_μ and J_ν,

$$W^{\mu\nu} = \frac{1}{2}\sum_{\lambda_p\lambda_f} J_\mu^*(\lambda_p, \lambda_f)J_\nu(\lambda_p, \lambda_f). \quad (3)$$

The hadronic currents are dependent on the initial-state-proton helicity λ_p and on the helicities of the final-state particles, λ_f, and are related to the reaction amplitudes in the helicity representation as

$$\varepsilon_\mu(\lambda_\gamma)J^\mu(\lambda_p\lambda_f) = \langle\lambda_f|T|\lambda_\gamma\lambda_p\rangle, \quad (4)$$

where $\varepsilon_\mu(\lambda_\gamma)$ is the polarization vector of the photon whose helicity is λ_γ. The first bracketed factor in (1) is the invariant flux of the incident photons; the last factor corresponds to the phase space of three final-state particles.

2.2. Mechanisms of the Reaction $\gamma p \longrightarrow \pi^+\pi^-p$

The Dalitz plots for the invariant masses of the $\pi^+\pi^-$, π^-p, and π^+p pairs produced in the reaction $\gamma p \longrightarrow \pi^+\pi^-p$ show bands corresponding to the production of Δ^{++}, Δ^0, and ρ in the intermediate state, which subsequently decay through the channels $\Delta^{++} \longrightarrow \pi^+p$, $\Delta^0 \longrightarrow \pi^-p$, and $\rho \longrightarrow \pi^+\pi^-$, respectively. Therefore, the mechanism of the reaction $\gamma_{r,v}p \longrightarrow \pi^+\pi^-p$ can be described as a combination of three quasi-two-body processes in Fig. 1. We assumed that the amplitude $C(W, Q^2)$ of all the remaining processes is independent of the kinematical variables that describe the final-state particles and determined this amplitude by fitting the Dalitz plots for the invariant masses of $\pi^+\pi^-$ and π^+p systems. The amplitude $C(W, Q^2)$ then can depend on W and Q^2. We approximated the Dalitz distributions independently for each pair of individual W and Q^2 values. In the tree approximation, a detailed analysis of the contributions from the large number of various mechanisms to the reaction $\gamma p \longrightarrow \pi^+\pi^-p$ at $W < 1.6$ GeV in terms of the meson–baryon degrees of freedom was performed in [15] at the photon point. According to the calculations presented there, the entire set of processes not shown in Fig. 1 does not reveal features in this kinematical region that depend on the kinematical variables of the

final state, so that the above approximation is quite reasonable. More detailed information about mechanisms other than those in Fig. 1 can be obtained from a comparison of the results of the calculation of all possible two-dimensional correlation distributions in the reaction $\gamma p \longrightarrow \pi^+\pi^- p$ ($s_{\pi^+\pi^-}$ and $s_{\pi^+ p}$, $s_{\pi^+\pi^-}$ and θ_p, $s_{\pi^+ p}$ and θ_p, $s_{\pi^+\pi^-}$ and α, $s_{\pi^+ p}$ and α, and α and θ) with the experimental data. The absence of special features in the distributions representing differences between the calculated and the measured cross sections would be evidence in favor of the validity of the approximation used, while the presence of such features would suggest that it is necessary to introduce mechanisms other than those in Fig. 1. Hereafter, the set of all processes not shown in Fig. 1 will be referred to as the three-body phase space. The relative contribution of quasi-two-body processes depends on W. In the region $W < 1.7$ GeV, the dominant contribution comes from the reaction $\gamma p \longrightarrow \pi^-\Delta^{++}$, while, in the region $W > 1.9$ GeV, the contributions of the reactions $\gamma p \longrightarrow \pi^-\Delta^{++}$ and $\gamma p \longrightarrow \rho p$ are commensurate. The contribution of the quasi-two-body reaction $\gamma p \longrightarrow \pi^+\Delta^0$ never saturates more than 10% of the cross section.

The amplitudes of the processes in Fig. 1 were calculated in the Breit–Wigner approximation. The total amplitude of the reaction $\gamma p \longrightarrow \pi^+\pi^- p$ has the form

$$\begin{aligned}\langle \pi^+\pi^-\lambda_{p'}|T|\lambda_\gamma\lambda_p\rangle &= \sum_{\lambda_{\Delta^{++}}} \frac{\langle \lambda_{\Delta^{++}}\pi^-|T|\lambda_\gamma\lambda_p\rangle\langle \pi^+\lambda_{p'}|T|\lambda_{\Delta^{++}}\rangle}{s_{\pi^+ p} - M_\Delta^2 - i\Gamma_\Delta(s_{\pi^+ p})M_\Delta} \\ &+ \sum_{\lambda_{\Delta^0}} \frac{\langle \lambda_{\Delta^0}\pi^+|T|\lambda_\gamma\lambda_p\rangle\langle \pi^-\lambda_{p'}|T|\lambda_{\Delta^0}\rangle}{s_{\pi^- p} - M_\Delta^2 - i\Gamma_\Delta(s_{\pi^- p})M_\Delta} \\ &+ \sum_{\lambda_\rho} \frac{\langle \lambda_\rho\lambda_{p'}|T|\lambda_\gamma\lambda_p\rangle\langle \pi^+\pi^-|T|\lambda_\rho\rangle}{s_{\pi^+\pi^-} - M_\rho^2 - i\Gamma_\rho(s_{\pi^+\pi^-})M_\rho} + C(W, Q^2),\end{aligned} \tag{5}$$

where $\langle \lambda_{\Delta^{++}}\pi^-|T|\lambda_\gamma\lambda_p\rangle$, $\langle \lambda_{\Delta^0}\pi^+|T|\lambda_\gamma\lambda_p\rangle$, and $\langle \lambda_\rho\lambda_{p'}|T|\lambda_\gamma\lambda_p\rangle$ are the amplitudes of the quasi-two-body reactions $\gamma_{r,v}p \longrightarrow \pi^-\Delta^{++}$, $\gamma_{r,v}p \longrightarrow \pi^+\Delta^0$, and $\gamma_{r,v}p \longrightarrow \rho p'$, respectively; $\langle \pi^+\lambda_{p'}|T|\lambda_{\Delta^{++}}\rangle$, $\langle \pi^-\lambda_{p'}|T|\lambda_{\Delta^0}\rangle$, and $\langle \pi^+\pi^-|T|\lambda_\rho\rangle$ are the amplitudes of the decay processes $\Delta^{++} \longrightarrow \pi^+ p$, $\Delta^0 \longrightarrow \pi^- p$, and $\rho \longrightarrow \pi^+\pi^-$, respectively; M_Δ and $\Gamma_\Delta(s_{\pi p})$ are the Δ mass and width; M_ρ and $\Gamma_\rho(s_{\pi^+\pi^-})$ are the ρ mass and width; and $C(W, Q^2)$ is the amplitude of three-body phase space.

A detailed account of the models for describing the amplitudes of the quasi-two-body processes $\gamma p \longrightarrow \pi^-\Delta^{++}$ and $\gamma p \longrightarrow \rho p$ is given in [6–9]. Here, we restrict ourselves to presenting basic features of the approach used to calculate the quasi-two-body amplitudes. The amplitudes of the processes $\gamma p \longrightarrow \pi^-\Delta^{++}$, $\gamma p \longrightarrow \pi^+\Delta^0$, and $\gamma p \longrightarrow \rho p$ were taken to be superpositions of a nucleon-resonance excitation in the s channel of a photon–proton collision and nonresonance mechanisms. The nonresonance amplitudes of the reactions $\gamma p \longrightarrow \pi^-\Delta^{++}$ and $\gamma p \longrightarrow \pi^+\Delta^0$ were represented in terms of the minimal set of Born diagrams proposed in [16]. The new elements in the approach developed in [6–9] were the following. The electromagnetic form factor for the pion according to the data on one-pion electroproduction from [17] and the form factor for the $\pi N\Delta$ vertex from the analysis of the data on nucleon–nucleon scattering [18] were used to describe the interaction between the virtual photon and the virtual pion in the t-channel of the pion-in-flight exchange diagram. The approach took into account particle interactions in the initial and the final state with open inelastic channels on the basis of the method proposed in [9] and employed the results obtained in [19] from an analysis of data on the amplitudes of pion–nucleon interaction. Allowances for channel-coupling effects are of importance for describing cross sections in the region $W > 1.6$ GeV, where, because of the competition between many open inelastic channels, the cross sections are sizably modified in view of channel coupling. The nonresonance processes in the channel $\gamma p \longrightarrow \rho p$ were described on the basis of the diffraction vector-dominance model [20].

Excitations of nucleon resonances in photon–proton collisions were taken into account in the Breit–Wigner approximation. The model included all reliably established nucleon resonances of masses below 2.0 GeV. The helicity electromagnetic amplitudes $A_{1/2}$ and $A_{3/2}$ for nucleon-resonance excitation at the photon point were taken from [12]. The amplitudes of the strong decays of nucleon resonances through the $\pi\Delta$ and ρp channels were described by using the results of the analysis from [19].

The approach proposed in [6–9] faithfully reproduces the entire body of available data [10, 11] on the total cross sections and angular distributions for the quasi-two-body channels $\gamma p \longrightarrow \pi^-\Delta^{++}$ and $\gamma p \longrightarrow \rho p$.

The amplitudes of Δ and ρ decays were calculated on the basis of effective Lagrangians, the effect of the internal structure of particles being taken into account by introducing the vertex form factors

$$\begin{aligned}\langle \lambda_{p'}\pi|T|\lambda_\Delta\rangle &= g_{\Delta\pi p}\frac{F(s_{\pi p})}{F(M_\Delta^2)}\bar{u}_p p_{\mu p} u_{\mu\Delta}, \\ \langle \pi^+\pi^-|T|\lambda_p\rangle &= g_{\rho\pi^+\pi^-}\frac{F(s_{\pi^+\pi^-})}{F(M_\rho^2)}\varepsilon_\mu^0(p_{\pi^+} - p_{\pi^-})_\mu,\end{aligned} \tag{6}$$

where $\bar{u}_p$, $u_{\mu\Delta}$, and ε_ρ are the Dirac spinor, the Rarita–Schwinger spin–tensor, and the polarization vector describing p, Δ, and ρ, respectively; $p_{\mu p}$, $p_{\mu\pi^+}$, and $p_{\mu\pi^-}$ are the 4-momenta of the proton, the π^+ meson, and the

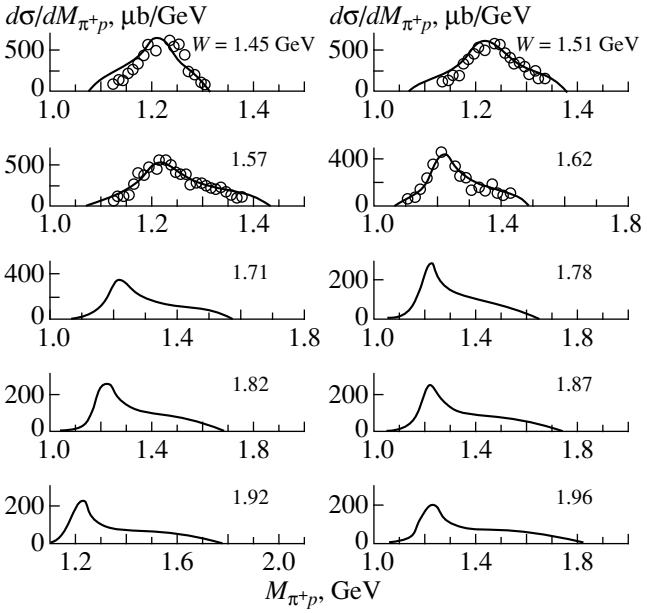

Fig. 2. Calculated and measured [11] invariant-mass distributions of the π^+p system. The three-body phase space was taken to be an adjustable parameter.

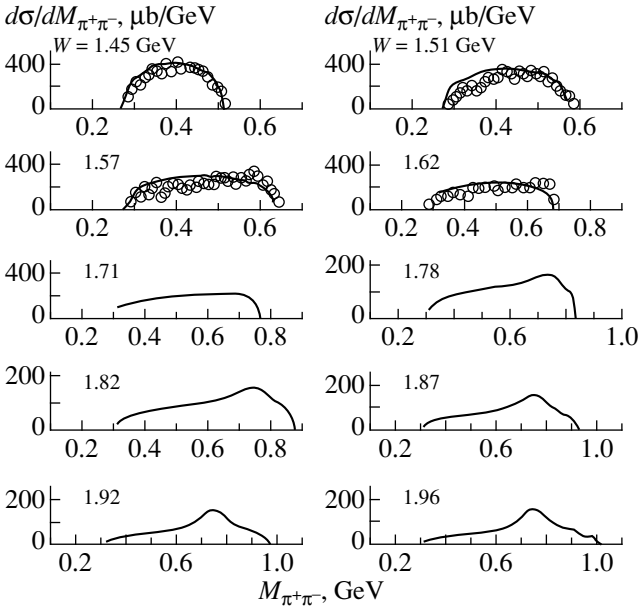

Fig. 3. Calculated and measured [11] invariant-mass distributions of the $\pi^+\pi^-$ system. The three-body phase space was taken to be an adjustable parameter.

π^- meson, respectively; and $F(s_{\pi^+\pi^-})$ and $F(s_{\pi p})$ are the form factors in the $\rho\pi\pi$ and $\Delta\pi p$ vertices. These form factors, which depend on the invariant masses of the π^+p, π^-p, and $\pi^+\pi^-$ systems from the decay processes $\Delta^{++} \longrightarrow \pi^+p$, $\Delta^0 \longrightarrow \pi^-p$, and $\rho \longrightarrow \pi^+\pi^-$, respectively, were borrowed from the analysis of data on pion–nucleon scattering [21]. The effective coupling constants $g_{\Delta\pi p}$ and $g_{\rho\pi^+\pi^-}$ were determined by fitting, to the measured decay widths, the results of the calculations with the amplitudes in (6) at the resonance point defined as the point at which the invariant mass of the final-state particles is equal to the mass of the decaying particle. In order to use the form factors from [21] in the amplitudes given by (6), it is necessary to calculate the contractions of the spin–tensors at the resonance point and to introduce the factor $1/F(s_{\pi^+\pi^-} = M_\rho^2)$ or $1/F(s_{\pi p} = M_\Delta^2)$.

3. RESULTS

Within the approach described above, we calculated the quintuple-differential cross sections for the reaction $\gamma p \longrightarrow \pi^+\pi^-p$ at the photon point for W values that lie in the interval from the threshold to 2 GeV and which corresponds to excitation energies of nucleon resonances. By appropriately integrating these quintuple-differential cross sections, we then obtained the invariant-mass distributions $d\sigma/dM_{\pi^+\pi^-}$ and $d\sigma/dM_{\pi^+p}$, which were compared with experimental data from [10, 11]. For each value of W, the three-body phase space $C(W, Q^2)$ was varied in order to fix its value on the basis of the best simultaneous fit to the two invariant-mass distributions mentioned immediately above. The calculated invariant-mass distributions $d\sigma/dM_{\pi^+p}$ and $d\sigma/dM_{\pi^+\pi^-}$ are displayed in Figs. 2 and 3, respectively, along with the relevant experimental data from [10, 11]. The amplitude that describes processes forming the three-body phase space and which is determined from a fit to these data is shown in Fig. 4 as a function of W.

From Figs. 2 and 3, it can be seen that, by and large, the proposed approach provides a satisfactory description of the invariant-mass distributions $d\sigma/dM_{\pi^+p}$ and $d\sigma/dM_{\pi^+\pi^-}$. The greatest distinctions between the calculated and the measured cross sections are observed at W = 1.45 and 1.57 GeV. It should be noted that it is the region of W values where the shape of the Δ line must induce the most pronounced effects, but available experimental information about the form factor in the $\pi N\Delta$ vertex is insufficient for describing the line shape unambiguously. That our fits to all experimental invariant-mass distributions of the $\pi^+\pi^-$ and π^+p systems proved to be satisfactory over the energy region of nucleon-resonance excitation and that the fits to the entire body of data on the quasi-two-body channels $\gamma p \longrightarrow \pi^-\Delta^{++}$ and $\gamma p \longrightarrow \rho p$ are of a reasonably good quality indicate that the developed approach can be applied to analyzing data on the exclusive channel $\gamma p \longrightarrow \pi^+\pi^-p$ with the aim of determining the contributions and the properties of nucleon resonances. Figures 2 and 3 display the model predictions for the

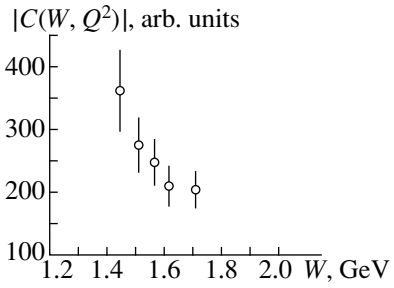

Fig. 4. Absolute value of the amplitude of the processes constituting the three-body phase space as a function of *W*. The results displayed in this figure were obtained from a simultaneous fit to the invariant-mass distributions of the π^+p and $\pi^+\pi^-$ systems.

invariant-mass distributions of the π^+p and $\pi^+\pi^-$ systems in the region $W > 1.7$ GeV. In this region of *W* values, the three-body phase space was determined by extrapolating the values extracted from the data presented in [10, 11] for $W < 1.7$ GeV. A comparison of the results of calculations for $W > 1.7$ GeV with the TJNAF data measured with beams of real photons would enable one to explore the contributions from high-lying nucleon resonances to photoproduction on a proton target and to obtain data on possible manifestations of as-yet-unobserved nucleon resonances.

It is clear from Fig. 4 that the amplitude of the three-body phase space is a monotonically decreasing function of *W*. This suggests that some additional mechanisms making the greatest contribution at low *W* are operative. Presently, a detailed investigation of the exclusive two-pion channel in photon-induced reactions is being performed at TJNAF [2, 3, 7]. An analysis of data on all two-dimensional correlations of kinematical variables ($s_{\pi^+\pi^-}$ and s_{π^+p}, $s_{\pi^+\pi^-}$ and θ_p, s_{π^+p} and θ_p, $s_{\pi^+\pi^-}$ and α, s_{π^+p} and α, and α and θ) would furnish important information, which could be used, in particular, to construct diagrams that describe the mechanisms of the processes under study.

4. CONCLUSION

We have developed a phenomenological approach to describing pion-pair production by photons on protons in the energy region of nucleon-resonance excitation. The reaction $\gamma p \longrightarrow \pi^+\pi^-p$ has been considered as a combination of the quasi-two-body processes $\gamma p \longrightarrow \pi^-\Delta^{++}$, $\gamma p \longrightarrow \pi^+\Delta^0$, and $\gamma p \longrightarrow \rho p$. The entire set of remaining processes has been treated in the approximation of the amplitude $C(W, Q^2)$, which is independent of the kinematical variables of the final state, but which can depend on *W* and Q^2. This amplitude has been determined by fitting experimental data on the invariant-mass distributions of the final-state particles.

The proposed approach relates the measured quintuple-differential cross sections for the reaction $\gamma p \longrightarrow \pi^+\pi^-p$ to the electromagnetic form factors $A_{1/2}(Q^2)$, $A_{3/2}(Q^2)$, and $C_{1/2}(Q^2)$ for nucleon resonances. That the invariant-mass distributions of the $\pi^+\pi^-$ and π^+p systems at the photon point have been described here quite well and that the entire body of available data on the integrated cross sections and on the angular distributions for the quasi-two-body channels $\gamma p \longrightarrow \pi^-\Delta^{++}$ and $\gamma p \longrightarrow \rho p$ were faithfully reproduced in [6–9] suggests that the developed approach as applied to data analysis has a rich potential for extracting information about the contributions of nucleon resonances to the exclusive channel $\gamma p \longrightarrow \pi^+\pi^-p$.

The developed approach would make it possible to predict the nucleon-resonance contributions to the differential cross sections for the virtual-photon-induced reactions $\gamma_v p \longrightarrow \pi^+\pi^-p$. The observation of kinematical regions characterized by the most spectacular manifestations of nucleon resonances is of importance for planning experiments and for data processing in investigations of the structure of nucleon resonances in exclusive reactions featuring virtual photons.

ACKNOWLEDGMENTS

We are grateful to Profs. V. Burkert (Jefferson Laboratory), S. Dytman (Pittsburgh University), and N.C. Mukhopadhyay (Rensselaer Polytechnic Institute) for interest in this study and support and to Prof. N.P. Zotov (Institute of Nuclear Physics, Moscow State University) for stimulating discussions and enlightening comments. We are also indebted to Prof. S. Simula (Istituto Nazionale di Fisica Nucleare, Sezione di Roma III) for support and for the opportunity to discuss our results at the ECT*/JLAB Workshop, Trento, Italy, May 18–29, 1998.

REFERENCES

1. V. D. Burkert, in *Proceedings of Joint ECT*/JLAB Workshop, Trento, Italy, May 18–29, 1998*, Few-Body Syst., Suppl. **7**, 1 (1999).
2. V. D. Burkert, M. Ripani, *et al.*, CEBAF Experiment E-93-006.
3. M. Ripani, Nucl. Phys. A **623**, 110c (1997).
4. R. Koniuk and N. Isgur, Phys. Rev. D **21**, 1868 (1980).
5. S. Capstick and W. Roberts, Phys. Rev. D **49**, 4570 (1994).
6. V. Mokeev *et al.*, in *Proceedings of Joint ECT*/JLAB Workshop, Trento, Italy, May 18–29, 1998*, Few-Body Syst., Suppl. **19**, 293 (1999).
7. M. Ripani, in *Proceedings of Joint ECT*/JLAB Workshop, Trento, Italy, May 18–29, 1998*, Few-Body Syst., Suppl. **19**, 284 (1999).
8. M. Anghinolfi *et al.*, Yad. Fiz. **62**, 1522 (1999) [Phys. At. Nucl. **62**, 1437 (1999)].

9. M. Anghinolfi, M. Battglieri, E. N. Golovach, *et al.*, Yad. Fiz. **63**, 85 (2000) [Phys. At. Nucl. **63**, 76 (2000)].
10. ABBHHM Collab., Phys. Rev. **175**, 1669 (1968).
11. Cambridge Bubble Chamber Group, Phys. Rev. **155**, 1447 (1967).
12. Particle Data Group, Phys. Rev. D **54**, 1 (1996).
13. E. Amaldi, S. Fubini, and G. Furlan, Springer Tracts Mod. Phys. **83**, 162 (1979).
14. D. J. Herdon and P. Soding, Phys. Rev. D **11**, 3165 (1975).
15. J. A. Gómez-Tejedor and E. Oset, Nucl. Phys. A **571**, 667 (1994).
16. D. Luke and P. Soding, Springer Tracts Mod. Phys. **59**, 39 (1971).
17. C. J. Bebek *et al.*, Phys. Rev. D **17**, 1693 (1978).
18. R. Machleidt, K. Holinde, and Ch. Elster, Phys. Rep. **149**, 1 (1987).
19. D. M. Manley and E. M. Salesky, Phys. Rev. D **45**, 4002 (1992).
20. D. G. Cassel *et al.*, Phys. Rev. D **24**, 2787 (1981).
21. R. S. Longacre *et al.*, Phys. Rev. D **17**, 1795 (1978).

Translated by M. Kobrinsky

Physics of Atomic Nuclei, Vol. 63, No. 11, 2000, pp. 1949–1955. Translated from Yadernaya Fizika, Vol. 63, No. 11, 2000, pp. 2041–2047.

ELEMENTARY PARTICLES AND FIELDS
Theory

Annihilation of a Neutrino Pair into a Muon–Positron Pair in a Magnetic Field

A. V. Borisov, V. A. Guseinov[1)], and N. B. Zamorin
Moscow State University, Vorob'evy gory, Moscow, 119899 Russia
Received July 21, 1999; in final form, November 15, 1999

Abstract—The cross section for the process $\nu_\mu + \bar{\nu}_e \longrightarrow \mu^- + e^+$ in a constant magnetic field is calculated with allowance for muon and positron polarizations. The asymptotic behavior of the cross section as a function of the kinematical and the field parameter is investigated in the case where a high-energy neutrino (antineutrino) is scattered by a low-energy antineutrino (neutrino). The effect of a weak field is especially important near the threshold for the free process. The spectrum and the total cross section for the process in a strong field differ markedly from the corresponding characteristics of the free process. Possible astrophysical applications are considered. © *2000 MAIK "Nauka/Interperiodica".*

1. Investigation of neutrino–lepton processes makes it possible to deduce detailed information about the structure of weak currents in a pure form not complicated by strong-interaction effects [1]. These processes play an important role in astrophysics [2]. The inverse muon decay $\nu_\mu + e^- \longrightarrow \mu^- + \nu_e$, a purely leptonic process that is caused by the charged weak current (*W*-boson exchange), has been investigated experimentally since the late 1970s [3, 4]. Within the Standard Model, the cross section for this process was calculated in [5] with allowance for one-loop radiative corrections. For astrophysical applications, it is of great interest to take into account the effect of strong external electromagnetic fields on electroweak processes. For example, magnetic fields of neutron stars can be as large as $H \gtrsim H_0 = m_e^2 c^3/e\hbar = 4.41 \times 10^{13}$ G [6]. Fields of $H \sim 10^{15}$–10^{17} G are generated in supernova explosions (see, for example, [7]). We note that, even in laboratory experiments with beams of high-energy particles traversing single crystals, it is necessary to take into account strong internal electrical fields ($E \lesssim 10^{-4}H_0$) [8]. Inverse muon decay in a constant crossed field ($\mathbf{E} \cdot \mathbf{H} = \mathbf{E}^2 - \mathbf{H}^2 = 0$) was investigated in [9, 10]; the case of a magnetic field was considered in [11, 12]. In the present study, we calculate the cross section for the process

$$\nu_\mu + \bar{\nu}_e \longrightarrow \mu^- + e^+. \tag{1}$$

In a constant crossed field, this process is related to muon decay by the crossing-symmetry equation. Here, we study characteristic polarization effects associated with the direction specified by the external field and with the weak-current structure. Presently, various processes induced by the inelastic scattering of ultrahigh-energy cosmic (anti)neutrinos on low-energy relic (anti)neutrinos in the Milky Way Galaxy are considered as possible sources of high-energy cosmic rays (see, for example, [13]).

2. By using the four-fermion approximation of the Weinberg–Salam Standard Model and the Fierz identity [1], the amplitude of the process in (1) can be represented in the form

$$S_{fi} = \frac{4G_F}{\sqrt{2}} \frac{\bar{\nu}(k')\gamma_L^\alpha u(k)}{2L^3(\omega\omega')^{1/2}} J_\alpha(q), \tag{2}$$

where G_F is the Fermi constant; $u(k)$ and $\nu(k')$ are the bispinors of the massless neutrinos ν_μ and antineutrinos $\bar{\nu}_e$ with 4-momenta $k = (\omega, \mathbf{k})$ and $k' = (\omega', \mathbf{k}')$ ($k^2 = k'^2 = 0$), respectively; $q = k + k' = (E, \mathbf{q})$; $\gamma_L^\alpha = \gamma^\alpha(1 + \gamma^5)/2$ are the left components of the Dirac matrices; $\gamma^5 = -i\gamma^0\gamma^1\gamma^2\gamma^3$; and L is the normalization length. The charged-lepton current is given by

$$\begin{aligned} J^\alpha(q) &= \int d^4x e^{-iqx} \overline{\psi_{n'}^{(+)}}(x)\gamma_L^\alpha \psi_n^{(-)}(x) \\ &= 2\pi\delta(\varepsilon' + \varepsilon - E) j^\alpha(\mathbf{q}), \end{aligned} \tag{3}$$

where the muon wave functions $\psi_{n'}^{(+)}$ and the positron (negative-frequency electron) wave functions $\psi_n^{(-)}$ are exact solutions to the Dirac equation in a constant magnetic field and where the delta function expresses the energy-conservation law in a time-independent field. We use the pseudo-Euclidean metric with signature (+ – – –) and the system of units where $\hbar = c = 1$.

By using Eqs. (2) and (3), we represent the cross section for the process in the general form (compare

[1)] Nakhichevan State University, Nakhichevan, Azerbaijan.

with [12])

$$\sigma = \frac{8\pi}{L^3}\frac{G_F^2}{k'k}\sum_{f',f}\delta(\varepsilon'+\varepsilon-E)[(k'j^*)(kj) + (k'j)(kj^*) - (k'k)(j^*j) - i\varepsilon^{\alpha\beta\mu\nu}j^*_\alpha j_\beta k'_\mu k_\nu], \quad (4)$$

where summation is performed over the sets of four muon quantum numbers $f' = (n', p'_z, s', \zeta')$ and four positron quantum numbers $f = (n, p_z, s, \zeta)$. These numbers have the following meaning [14]: $n = 0, 1, 2, \ldots$ is the principal quantum number (number of the Landau level); $-\infty < p_z < \infty$ is the projection of the 3-momentum onto the direction of the magnetic field aligned with the z axis; $s = 0, 1, 2, \ldots$ is the radial quantum number that corresponds to the axisymmetric gauge of the 4-potential of the magnetic field,

$$A^\mu = \left(0, -\frac{1}{2}yH, \frac{1}{2}xH, 0\right); \quad (5)$$

and $\zeta = \pm 1$ is the spin quantum number specifying the particle polarization (see below). The energy spectrum of a particle in a magnetic field is degenerate in s and ζ,

$$\varepsilon' = (m_\mu^2 + 2eHn' + p_z'^2)^{1/2}, \qquad \varepsilon = (m_e^2 + 2eHn + p_z^2)^{1/2}, \quad (6)$$

where $e > 0$ is the positron charge.

By using the explicit form of the wave functions for charged leptons in a magnetic field in the gauge specified by Eq. (5) (see [14]), we find that the components of the current in (3) can be represented as

$$\begin{pmatrix} j^0 \\ j^1 \\ j^2 \\ j^3 \end{pmatrix} = 2\exp\left[i(n-n')\left(\varphi+\frac{\pi}{2}\right)\right] \times \frac{2\pi}{L}\delta(p_z+p'_z-q_z)I_{ss'}\begin{pmatrix} F_0 \\ F_1\cos\varphi + iF_2\sin\varphi \\ F_1\sin\varphi - iF_2\cos\varphi \\ F_3 \end{pmatrix}, \quad (7)$$

$$\begin{pmatrix} F_0 \\ F_3 \end{pmatrix} = l'_2 l_2 I_{nn'} \pm l'_1 l_1 I_{n-1,n'-1}, \qquad \begin{pmatrix} F_1 \\ F_2 \end{pmatrix} = l'_1 l_2 I_{n,n'-1} \pm l'_2 l_1 I_{n-1,n'}, \quad (8)$$

where $I_{ss'}$ and $I_{nn'}$ are known Laguerre functions [14] of the argument

$$x = \frac{q_\perp^2}{2eH}, \quad q_\perp^2 = q_x^2 + q_y^2, \quad (9)$$

while φ is the azimuthal angle of the vector $\mathbf{q}$ ($\cos\varphi = q_x/q_\perp$, $\sin\varphi = q_y/q_\perp$). The quantities l_k ($k = 1, 2$) in (8) are expressed in terms of the spin coefficients C_i ($i = \overline{1,4}$) in the positron (more precisely, negative-frequency-electron) wave functions,

$$l_1 = \frac{1}{2}(C_1 - C_3), \quad l_2 = \frac{1}{2}(C_2 - C_4), \quad (10)$$

while l'_k refer to a muon. The explicit expressions for them depend on the choice of the lepton polarization operator (integral of the motion in a given external field); the wave function is an eigenfunction of this operator; the spin number ζ is a normalized eigenvalue [14];

$$\mu_3\psi = \frac{\varepsilon_\perp}{m}\zeta\psi, \qquad h\psi = \zeta p\psi. \quad (11)$$

Here, the transverse-polarization operator

$$\mu_3 = \Sigma_3 + i\gamma^0\gamma^5(\boldsymbol{\Sigma}\times\mathbf{P})_z = \frac{\varepsilon}{m}\gamma^0(\Sigma_3 + \gamma^5 p_z) \quad (12)$$

determines the projection of the lepton spin onto the direction of the magnetic field $\mathbf{H}$, $\varepsilon_\perp = (\varepsilon^2 - p_z^2)^{1/2}$, and $\mathbf{P} = -i\nabla + e\mathbf{A}$ is the momentum operator.

The longitudinal polarization is associated with the helicity operator

$$h = \boldsymbol{\Sigma}\cdot\mathbf{P} = \gamma^5(m\gamma^0 - \varepsilon), \quad (13)$$

and $p = (\varepsilon^2 - m^2)^{1/2}$. We note that the operator equalities (12) and (13) are valid in the class of functions ψ satisfying the Dirac equation (the general theory of polarization operators in external fields is developed in [14, 15]). The interactions of the lepton anomalous magnetic moment representing the radiative correction to the Dirac moment destroy the longitudinal polarization (quite fast under the actual conditions in storage rings), but the operator in (12) remains an integral of the motion [14]. For this reason, we consider below only transverse polarization.

3. We restrict ourselves to the case where a neutrino and an antineutrino approach each other from opposite directions in the plane orthogonal to the field $\mathbf{H}$. Since the problem in an external field possesses axial symmetry, the choice of the x axis along the collision axis imposes no constraints on the generality of our consideration. Accordingly, the 4-momenta in the neutrino pair are then taken to be

$$k = \omega(1, 1, 0, 0), \quad k' = \omega'(1, -1, 0, 0), \quad (14)$$

in which case $q_y = q_z = 0$ and the angle φ in (7) is

$$\varphi = \begin{cases} 0, & \omega > \omega', \\ \pi, & \omega' > \omega. \end{cases} \quad (15)$$

Taking into account (14), (15), and (7), we express the cross section (4) in terms of the functions in (8) as

$$\sigma^{(\pm)} = \frac{8}{\pi} G_F^2 eH \sum_{\zeta,\zeta'} \sum_{n,n'} \int dp_z \delta(\varepsilon + \varepsilon' - E)(F_3 \pm F_2)^2, \quad (16)$$

where the upper and the lower sign in the superscript refer to the cases of $q_x = \omega - \omega' > 0$ and $q_x < 0$, respectively. In deriving (16), we have used the conservation of the z component of the momentum [see Eq. (7)] and the known formula for summation over radial quantum numbers [14],

$$\sum_{s,s'} I_{ss'}^2 = \frac{eH}{2\pi} L^2.$$

The case of a collision between a high-energy neutrino (antineutrino) and a low-energy antineutrino (neutrino) is of interest for astrophysical applications. Suppose that the energy of the $\nu_\mu \bar{\nu}_e$ pair, $E = \omega + \omega'$, and the momentum transfer $q_\perp = |\omega - \omega'|$ are both much greater than m_μ and that the magnetic-field strength satisfies the condition $H \ll H_\mu = m_\mu^2/e$. The main contribution to the total cross section for process (16) then comes from the final-lepton states having large quantum numbers, $n, n' \gg 1$ (high Landau levels); for the Laguerre functions $I_{nn'}$ in (8), we can therefore use the well-known semiclassical asymptotic form in terms of the relativistic parameter $\gamma^{-1} = m_\mu/E \ll 1$ [14],

$$\begin{pmatrix} I_{nn'}(x) \\ dI_{nn'}(x)/dx \end{pmatrix} \equiv \begin{pmatrix} I \\ I' \end{pmatrix} \simeq \frac{(-1)^{n'}}{\sqrt{\pi}} \gamma^{-1} (v\bar{v})^{-1/2} \begin{pmatrix} w^{1/3}\Phi(y) \\ \gamma^{-1} w^{2/3} \Phi'(y) \end{pmatrix},$$

$$I_{n,n'-1} \simeq -I - \frac{1}{\bar{v}} I', \quad I_{n-1,n'} \simeq I + \frac{1}{v} I',$$

$$I_{n-1,n'-1} \simeq -I - \frac{1}{v\bar{v}} I', \quad (17)$$

$$w = 2\kappa v\bar{v}, \quad \bar{v} = 1 - v,$$

where

$$\Phi(y) = \frac{1}{\sqrt{\pi}} \int_0^\infty dt \cos\left(yt + \frac{t^3}{3}\right) \quad (18)$$

is the Airy function of the argument

$$y = (2\kappa v\bar{v})^{-2/3} (v + \delta^2 \bar{v} - \lambda v\bar{v} + \tau^2), \quad (19)$$

and $\Phi'(y) = d\Phi(y)/dy$. In (19), we have introduced the field, the kinematical, and the mass parameter (κ, λ, and δ, respectively)

$$\kappa = \frac{e}{m_\mu^3} [-(F_{\alpha\beta} q^\beta)^2]^{1/2} = \frac{q_\perp}{m_\mu} \frac{H}{H_\mu} \simeq \frac{eHE}{m_\mu^3},$$

$$\lambda = \frac{q^2}{m_\mu^2} = \frac{4\omega\omega'}{m_\mu^2}, \quad \delta = \frac{m_e}{m_\mu}, \quad (20)$$

and the spectral and the angular variable (v and τ, respectively)

$$v = \frac{\chi}{\chi + \chi'} \simeq \frac{\varepsilon}{\varepsilon + \varepsilon'}, \quad \tau = \frac{e q^\alpha \tilde{F}_{\alpha\beta} p^\beta}{m_\mu^4 (\chi + \chi')} \simeq \frac{p_z}{m_\mu}, \quad (21)$$

where

$$\chi = \frac{e}{m_\mu^3} [-(F_{\alpha\beta} p^\beta)^2]^{1/2} \simeq \frac{eH\varepsilon}{m_\mu^3}, \quad \chi' = \chi(p \longrightarrow p'),$$

$F_{\alpha\beta} = \partial_\alpha A_\beta - \partial_\beta A_\alpha$ is the strength tensor of an external magnetic field, and $\tilde{F}_{\alpha\beta} = \frac{1}{2} \varepsilon_{\alpha\beta\lambda\sigma} F^{\lambda\sigma}$ is its dual counterpart. We note that $v \in (0, 1)$ and that, in the ultrarelativistic approximation adopted here ($\gamma = E/m_\mu \gg 1$), $\tau \in (-\infty, \infty)$.

Since the motion of leptons is semiclassical, summation over the quantum numbers n and n' in (16) can be replaced by integration according to the relation [see (6)]

$$dndn' = \frac{\varepsilon\varepsilon' d\varepsilon d\varepsilon'}{(eH)^2}.$$

After that, the integral with respect to ε' is removed by the delta function. Further, we go over to the variables v and τ (21). As a result, we derive the cross section for the process at fixed lepton polarizations ζ' and ζ in the form

$$\sigma^{(\pm)}(\zeta', \zeta) = \frac{8}{\pi} G_F^2 \frac{m_\mu^2}{\kappa} \gamma^4 \int_0^1 dv v\bar{v} \int_{-\infty}^\infty d\tau (\tilde{F}_3 \pm \tilde{F}_2)^2, \quad (22)$$

where the upper and the lower sign in the superscript refer to the kinematical conditions $\omega \gg \omega'$ and $\omega \ll \omega'$, respectively, and $\tilde{F}_i$ is the semiclassical asymptotic form of the function F_i.

The expressions for $\tilde{F}_i$ in (22) can be obtained by substituting (17) into (8) and retaining only the first, linear, terms of the expansion in the small parameter γ^{-1} in the spin coefficients C_i and C_i' [see Eqs. (8) and (10)]. In doing this, it should be considered that $\omega\omega' \lesssim m_\mu^2$ ($\lambda \sim \gamma^0$) and that

$$\frac{m_e}{\varepsilon} = \gamma^{-1} \frac{\delta}{v}, \quad \frac{m_\mu}{\varepsilon'} = \gamma^{-1} \frac{1}{\bar{v}},$$

$$\frac{p_z}{\varepsilon} = \gamma^{-1} \frac{\tau}{v}, \quad \frac{p_z'}{\varepsilon'} = -\gamma^{-1} \frac{\tau}{\bar{v}},$$

the main contribution to the total cross section (22) coming from the region specified by inequalities $v \lesssim 1$ and $|\tau| \lesssim 1$. Further, we note that, in fact, the mass parameter [see (20)] is small, $\delta \simeq 4.8 \times 10^{-3}$, and that it is on the same order of magnitude as radiative corrections (about $\alpha/\pi \sim 10^{-3}$), which are disregarded in this

study. To the precision adopted here, we therefore set this parameter to zero below.

Finally, we find that, in terms of the spectral and the angular variable, the cross sections for the production of transversely polarized leptons [see (12)] are given by

$$\begin{pmatrix}\sigma^{(+)}(\zeta',\zeta)\\ \sigma^{(-)}(\zeta',\zeta)\end{pmatrix} = \frac{G_F^2}{\pi^2}m_\mu^2\int_0^1 dv\begin{pmatrix}\bar{v}/v\\ v/\bar{v}\end{pmatrix}\int_{-\infty}^{\infty}d\tau\Big[(2\tilde{\kappa})^{-1/3} \times\begin{pmatrix}\tau^2\\ 1+\tau^2+2\zeta'\tau\end{pmatrix}\Phi^2(y)+(2\tilde{\kappa})^{1/3}\begin{pmatrix}1\\ 1\end{pmatrix}\Phi'^2(y) + 2\begin{pmatrix}-\tau\\ \zeta'+\tau\end{pmatrix}\Phi(y)\Phi'(y)\Big], \quad (23)$$

where $\tilde{\kappa} = \kappa v\bar{v}$ and the argument of the Airy functions is determined by (19) at $\delta = 0$.

The cross sections (23), which are expressed in terms of the invariant parameters (20) and the variables in (21), is applicable (in the ultrarelativistic approximation) in an arbitrary constant field $F_{\mu\nu}$ of strength F much less than $H_\mu = m_\mu^2/e$ [see (12)], the spin numbers ζ' and ζ being eigenvalues of the corresponding invariant spin operator (see [12, 15]). The conditions under which the above generalization to the case of two-body processes in an external field is applicable are analyzed in [16] (see also Section 6 below).

4. The integrands in (23) determine the differential cross sections $d^2\sigma^{(\pm)}/dvd\tau$. The asymmetric dependence on the angular variable τ and the spin variables ζ and ζ' is due to P and C nonconservation in weak interactions and to the choice of kinematical conditions (compare with [12])—an ultrarelativistic muon and an ultrarelativistic positron are emitted at small angles (not greater than γ^{-1}) with respect to the direction of the high-energy-(anti)neutrino momentum.

In order to investigate the spectral distribution $d\sigma^{(\pm)}/dv$, we perform integration with respect to the variable τ by using the relations

$$\int_{-\infty}^{\infty}d\tau\Phi^2(y) = \sqrt{\pi}\cdot 2^{-2/3}b^{-1/2}\Phi_1(z),$$

$$\int_{-\infty}^{\infty}d\tau\tau^2\Phi^2(y) = \sqrt{\pi}\cdot 2^{-5/3}b^{-3/2}[\Phi'(z)+z\Phi_1(z)], \quad (24)$$

$$\int_{-\infty}^{\infty}d\tau\Phi'^2(y) = -\sqrt{\pi}\cdot 2^{-7/3}b^{-1/2}[3\Phi'(z)+z\Phi_1(z)],$$

where the arguments are $y = x + a\tau^2$, $z = 2^{2/3}x$, and $b = 2^{2/3}a$ and where $\Phi_1(z) = \int_z^\infty dt\Phi(t)$. The relations in (24) were derived with the aid of the well-known relations for the Airy functions {see [17, ch. 5, formulas (46), (48), (58)]}.

From expressions (23), (24), and (19), we obtain

$$\begin{pmatrix}\sigma^{(+)}(\zeta',\zeta)\\ \sigma^{(-)}(\zeta',\zeta)\end{pmatrix} = \frac{G_F^2}{\pi^{3/2}}m_\mu^2\int_0^1 dv\begin{pmatrix}\bar{v}/v\\ v/\bar{v}\end{pmatrix} \times\Big[\begin{pmatrix}-(v/2)(1-\lambda\bar{v})\\ (\bar{v}/2)(1+\lambda v)\end{pmatrix}\Phi_1(z)-\tilde{\kappa}^{2/3}\begin{pmatrix}1\\ 1\end{pmatrix}\Phi'(z) + \tilde{\kappa}^{1/3}\begin{pmatrix}0\\ -\zeta'\end{pmatrix}\Phi(z)\Big]. \quad (25)$$

The integrands in expression (25) represent the spectral distributions $d\sigma^{(\pm)}/dv$, the argument of the Airy functions being

$$z = (\kappa v\bar{v})^{-2/3}v(1-\lambda\bar{v}). \quad (26)$$

For the free process (in the absence of an external field, $\kappa = 0$), we find the spectral distributions in the form

$$\begin{pmatrix}d\sigma_0^{(+)}(\zeta',\zeta)/dv\\ d\sigma_0^{(-)}(\zeta',\zeta)/dv\end{pmatrix} = \frac{G_F^2}{2\pi}m_\mu^2\begin{pmatrix}-\bar{v}(1-\lambda\bar{v})\\ v(1+\lambda v)\end{pmatrix}\theta(\lambda\bar{v}-1). \quad (27)$$

These expressions follow from (25) for $\kappa \longrightarrow 0$ with allowance for the weak limit

$$\lim_{A\to\infty}\Phi_1(Ax) = \sqrt{\pi}\theta(-x),$$

where $\theta(x) = (1+\mathrm{sgn}x)/2$ is the Heaviside step function. The range of the spectral variable v in (27) is determined from the condition $\lambda\bar{v} - 1 \geq 0$, which yields

$$0 \leq v \leq v_1 = 1 - 1/\lambda. \quad (28)$$

From (28), it can be seen that, in the absence of a field, reaction (1) has a threshold; that is, the kinematically allowed region is

$$\lambda > 1. \quad (29)$$

According to the general theory developed in [16], the external-field effect on the process allowed in the absence of a field as well is determined by the parameter

$$\eta = \kappa/|\lambda - 1|. \quad (30)$$

Let us investigate the qualitative characteristics of the spectra given by (25) in the limiting cases of $\eta \ll 1$ and $\eta \gg 1$ by using the known properties of the Airy functions [17].

For $\eta \ll 1$ (weak field) and $\lambda > 1$, oscillations are superimposed on the smooth free spectra (27) in the region determined by (28), and these oscillations grow

as v approaches its boundaries. In the region $v_1 \le v \le 1$, which is forbidden at $\eta = 0$, the differential cross section $d\sigma^{(\pm)}/dv$ decreases fast as we go away from the point v_1 [for $v \longrightarrow 1$, it is proportional to $\exp(-2/3\kappa\bar{v})$].

At $\eta \gg 1$ (strong field) and $\lambda > 1$, the region of oscillations is comparatively narrow.

At $\lambda < 1$, the free process (1) is forbidden, and there are no oscillations in the spectra. In a weak field, the spectra are exponentially small in this case over the entire interval $0 \le v \le 1$.

The above features of the spectra are typical of all processes proceeding in the absence of external fields as well—in particular, of inverse muon decay [12] and of the Compton effect in a magnetic field [16].

5. Let us consider the asymptotic behavior of the total cross section for the process.

At $\kappa \ll 1$ and $\lambda > 1$, it follows from (26) that we can use the weak asymptotic expansions of the Airy functions (see, for example, [10, 12]),

$$\begin{aligned}\Phi(Ax) &= \sqrt{\pi}A^{-1}\delta(x) + O(A^{-4}),\\ \Phi'(Ax) &= \sqrt{\pi}A^{-2}\delta'(x) + O(A^{-5}),\\ \Phi_1(Ax) &= \sqrt{\pi}\left[\theta(-x) + \frac{1}{3}A^{-3}\delta''(x)\right] + O(A^{-6}),\end{aligned} \tag{31}$$

where $A \gg 1$ and $\delta(x) = d\theta(x)/dx$ is a delta function. In our case, $A = \kappa^{-2/3}$ and

$$x(v) = (v\bar{v})^{-2/3}v(1-\lambda\bar{v}). \tag{32}$$

Let us substitute (31) into (25) and perform integration with respect to v by using the relations

$$\int_0^1 dv f(v)\theta(-x) = \int_0^{v_1} dv f(v),$$

$$\int_0^1 dv\,\delta^{(n)}(x)f(v) = (-1)^n\frac{d^n}{dx^n}[v'f(v)]\Big|_0^{v_1},$$

where $v' = dv(x)/dx$; $v = v(x)$ is the function inverse to $x(v)$ (32); and $\delta^{(n)}(x) = d^n\delta(x)/dx^n$, $n = 1, 2$. In the above relations, we have considered that $x'(0) < 0$ and $x'(v_1) > 0$. The derivatives d^nv/dx^n ($n = 1, 2, 3$) are calculated by differentiating, with respect to x, the left- and the right-hand side of the equation $x = x(v)$, which determines the function $v(x)$ implicitly.

To terms of order κ^2 inclusive, we eventually obtain the asymptotic expressions

$$\begin{aligned}\begin{pmatrix}\sigma^{(+)}(\zeta',\zeta)\\ \sigma^{(-)}(\zeta',\zeta)\end{pmatrix} &= \frac{G_F^2}{4\pi}m_\mu^2\left[F_0(\lambda)\begin{pmatrix}1\\1\end{pmatrix}\right.\\ &\left. + 4\frac{\kappa}{\lambda-1}\begin{pmatrix}0\\ -\zeta'(1-1/\lambda)^2\end{pmatrix} + \left(\frac{\kappa}{\lambda-1}\right)^2\begin{pmatrix}F_+(\lambda)\\ F_-(\lambda)\end{pmatrix}\right],\end{aligned} \tag{33}$$

where

$$\begin{aligned}F_0(\lambda) &= \frac{1}{3}(2\lambda+1)\left(1-\frac{1}{\lambda}\right)^2,\\ F_+(\lambda) &= -\frac{8}{3}\left(1+\frac{3}{\lambda^2}-\frac{2}{\lambda^3}\right),\\ F_-(\lambda) &= -\frac{8}{3}\left(1-\frac{2}{\lambda}\right)\left(1-\frac{1}{\lambda}\right)^2.\end{aligned} \tag{34}$$

From (33), it can be seen that, in accord with (30), the external-field effect on the process is described by the parameter $\kappa/(\lambda-1)$. This effect is stronger for polarized particles than for unpolarized particles, being of the first and of the second order in κ, respectively. In a relatively weak field ($\kappa \ll 1$) such that the relation $\kappa \gtrsim \lambda - 1$ nevertheless holds, the cross section for the process differs markedly from the cross section for the free process, the latter being very small near the threshold [$F_0 = 0$ at $\lambda = 1$; see (34)]. From (33), it follows that, for $\omega \gg \omega'$ ($\omega' \gg \omega$), we predominantly have the generation of muons (positrons) whose spins are aligned with (opposite to) the direction of the magnetic field **H**—that is, $\zeta = +1$ ($\zeta' = -1$). This effect is similar to the Sokolov–Ternov effect, the radiative polarization of electrons and positrons in a magnetic field due to synchrotron radiation [14].

For $\lambda < 1$, the free process (at $\kappa = 0$) is forbidden. In a weak field ($\eta \ll 1$), the cross section for process (1) is exponentially small, which is characteristic of all processes that have a threshold in the absence of a field [17]. In this case, the argument of the Airy function is very large ($z \gg 1$), so that we asymptotically have

$$\Phi(z) \simeq \frac{1}{2}z^{-1/4}\exp\left(-\frac{2}{3}z^{3/2}\right).$$

By using this asymptotic expression and the method of steepest descent and taking into account a finite value of the mass parameter ($\delta \ll 1$), we can easily obtain

$$\sigma \sim \kappa\exp\left(-\sqrt{3}\delta\frac{1-\lambda}{\kappa}\right).$$

For $\eta \gg 1$ and $\kappa \gg 1$ (strong field), the main contribution to the integrals in (25) comes from the region $|z| \ll 1$. If only the leading terms are retained in the asymptotic expressions in κ, the integrands can be simplified by setting there

$$\begin{aligned}\Phi(z) \simeq \Phi(0) &= 3^{-1/6}\frac{\Gamma(1/3)}{2\sqrt{\pi}},\\ \Phi'(z) \simeq \Phi'(0) &= -3^{1/6}\frac{\Gamma(2/3)}{2\sqrt{\pi}}.\end{aligned}$$

Upon evaluating the remaining standard integrals with respect to v, we obtain the strong-field asymptotic

expressions for the cross sections (25) in the form

$$\begin{pmatrix}\sigma^{(+)}(\zeta',\zeta)\\ \sigma^{(-)}(\zeta',\zeta)\end{pmatrix} = \frac{G_F^2}{4\pi^3}m_\mu^2\left[c_2(3\kappa)^{2/3}\begin{pmatrix}1\\1\end{pmatrix} + c_1(3\kappa)^{1/3}\begin{pmatrix}0\\-\zeta'\end{pmatrix}\right],$$
$$c_2 = \frac{15}{14}\Gamma^4\left(\frac{2}{3}\right), \quad c_1 = \frac{2}{5}\Gamma^4\left(\frac{1}{3}\right). \tag{35}$$

As in the case of a weak field [see Eq. (16)], we see that, for $\omega \gg \omega'$ ($\omega' \gg \omega$), there is a predominant production of positrons (muons) polarized in the direction parallel (antiparallel) to the external field **H**.

6. In the above analysis [see Eq. (2)], we have made use of the four-fermion approximation for the amplitude of process (1). As in the absence of an external field, the relative smallness of the momentum transfer—$|q^2| \ll m_W^2$, where m_W is the *W*-boson mass—is the necessary condition of its applicability. Taking into account (20), we obtain the kinematical constraint

$$\lambda \ll (m_W/m_\mu)^2 \simeq 6\times 10^5. \tag{36}$$

In an external field, however, there arises an additional condition: changes in the particle momentum over the formation length for the process, l_f, must be much less than m_W. In a strong field ($\kappa \gg 1$), this length is independent of the particle mass and is given by [17, 18]

$$l_f \sim [-(eF_{\alpha\beta}q^\beta)^2]^{1/6}/eH.$$

As a result, we find that the field parameter κ [see Eq. (20)] must be constrained as

$$\kappa \ll (m_W/m_\mu)^3 \simeq 4.4\times 10^8. \tag{37}$$

In our case, the condition in (36) is obviously satisfied since the semiclassical asymptotic expressions used for the Laguerre functions $I_{nn'}(x)$ (17) are valid [14] when the argument x is close to the transition point $x_0 = (\sqrt{n} + \sqrt{n'})^2 = (p_\perp + p'_\perp)^2/2eH$,

$$x/x_0 - 1 = O(\gamma^{-2})$$

or [see Eqs. (9), (6), and (14)]

$$q^2 = q_0^2 - q_\perp^2 \lesssim \gamma^{-2}E^2 = m_\mu^2;$$

that is, we have [see Eq. (20)] $\lambda \lesssim 1$.

Following [16], we will now show that the basic results deduced here under the kinematical conditions chosen in a special way [see Eq. (14)] can be used in a more general case. The cross section for the two-body process (1) in an arbitrary constant field $F_{\alpha\beta}$ for arbitrary directions of the neutrino momenta depends on eight independent invariant parameters (for unpolarized particles). These are the quantities κ and λ, which were already defined in (20), and

$$f_1 = \frac{e}{m_\mu^2}[|F_{\alpha\beta}F^{\alpha\beta}|/2]^{1/2}, \quad f_2 = \frac{e}{m_\mu^2}[|F_{\alpha\beta}\tilde{F}^{\alpha\beta}|/2]^{1/2},$$
$$f_3 = \frac{e}{m_\mu^4}|k_\alpha F^{\alpha\beta}k'_\beta|, \quad f_4 = \frac{e}{m_\mu^4}|k_\alpha \tilde{F}^{\alpha\beta}k'_\beta|, \tag{38}$$
$$f_5 = \frac{e}{m_\mu^3}[-(F^{\alpha\beta}k'_\beta)^2]^{1/2}, \quad f_6 = \frac{e}{m_\mu^3}[|k^\alpha F_{\alpha\beta}F^{\beta\gamma}k'_\gamma|]^{1/2}.$$

We note that, in a purely magnetic field, $f_1 = H/H_\mu$ and $f_2 = 0$. Suppose that the parameters in (38) satisfy the conditions

$$f_i \ll \kappa, \quad f_i \ll \lambda, \quad f_i \ll 1 \quad (i = 1\text{–}6). \tag{39}$$

They are fulfilled for field strengths $F \ll H_\mu$, high energies of a neutrino pair (for markedly different energies of its components), and at not overly small angles between the ultrarelativistic-(anti)neutrino 3-momentum **k** and the field-strength vectors **E** and **H**. By virtue of (39), the general expression for the cross section can be approximated by the simpler two-parameter formula

$$\sigma(\kappa, \lambda, f_1, \ldots, f_6) \simeq \sigma(\kappa, \lambda, 0, \ldots, 0).$$

Thus, our results expressed in terms of the invariant parameters κ and λ are applicable not only to the case of kinematics specified by (14) but also in the rather general case specified by (39).

Let us consider the possibilities for observing the external-field effect on process (1). Muon neutrinos of energy $\omega \simeq 20$ GeV are used in experimental investigations of inverse muon decay [4]. Our results are applicable if the energies ω' of electron antineutrinos obey the condition

$$\omega' \ll m_\mu^2/\omega \lesssim 1 \text{ MeV}$$

at $\omega \gtrsim 10$ GeV. Such energies ω' correspond to the lower limit on the reactor- and solar-(anti)neutrino energies recorded by conventional methods [2]. Let us set $H = 10^8$ G (this can be pulsed magnetic fields or effective single-crystal fields [8]) and $E = \omega + \omega' \simeq \omega = 20$ GeV. The field parameter is then given by [see (20)]

$$\kappa \simeq \frac{\omega}{m_\mu}\frac{H}{H_\mu} \simeq 10^{-8},$$

where we have used the value of $H_\mu = m_\mu^2/e \simeq 1.9\times 10^{18}$ G. From (30), it follows that, in this case, the external-field effect becomes sizable in a narrow region of λ values lying near the free-process threshold: $\lambda \simeq 1$, $|\lambda - 1| \lesssim 10^{-8}$ [see (33), (34)]. However, the observation of the effect under laboratory conditions is complicated by a relatively low density of neutrino beams and by small dimensions of the interaction region. For this reason, we will focus on astrophysical conditions.

As was indicated in Section 1, much attention is being given at present to the possibility that high-energy cosmic rays are generated in the annihilation of ultrahigh-energy neutrinos on low-energy galactic relic antineutrinos (see [13] and references therein). Assuming that relic (anti)neutrinos are massless, we estimate their energy (that is, the temperature of relic radiation) at $\omega' \sim 2\ \mathrm{K} \simeq 1.7 \times 10^{-4}$ eV. Our results are valid in the region of cosmic-neutrino energies,

$$\omega \lesssim m_\mu^2/\omega' \lesssim 10^{20}\ \mathrm{eV}.$$

For the field parameter, we then have

$$\kappa \lesssim 10^{-7}\,(H/1\ \mathrm{G}). \qquad (40)$$

The mean-galactic magnetic field is overly weak: $H \sim 10^{-6}$ G and $\kappa \lesssim 10^{-13}$. However, compact objects in the Milky Way Galaxy can develop strong fields [19]. The surface fields of white dwarfs take values of $H \lesssim 10^9$ G, in which case expression (40) yields $\kappa \lesssim 10^2$. The dipole fields of neutron stars are $H \lesssim 10^{13}$ G. For these fields, $\kappa \lesssim 10^6$ [the condition in (37) is satisfied in this case], and the cross section for process (1) in a magnetic field is much larger than the cross section for the free process owing to the factor [see Eq. (35)]

$$F(\kappa) = (3\kappa)^{2/3} \lesssim 10^4.$$

Thus, process (1) can be a source of high-energy charged leptons; in the vicinity of strongly magnetized stars, their spectral distributions and total fluxes can differ considerably [see Eq. (25)] from the corresponding values in the regions where the field can be disregarded [see (27)]. We note that, despite the relatively small dimensions of neutron stars, they may modify sizably the energy spectra of cosmic rays owing to the large-scale pulsar-wind effect (see, for example, [20]).

ACKNOWLEDGMENTS

We are grateful to a reviewer for constructive criticism.

REFERENCES

1. L. B. Okun, *Leptons and Quarks* (Nauka, Moscow, 1990; North-Holland, Amsterdam, 1984).
2. J. N. Bahcall, *Neutrino Astrophysics* (Cambridge Univ. Press, Cambridge, 1989; Mir, Moscow, 1993).
3. N. Armenise *et al.*, Phys. Lett. B **84**, 137 (1979).
4. P. Vilain *et al.*, Preprint No. CERN-PPE/96-01 (Geneva, 1996).
5. D. Yu. Bardin and V. A. Dokuchaeva, Nucl. Phys. B **287**, 839 (1987).
6. V. M. Lipunov, *Astrophysics of Neutron Stars* (Nauka, Moscow, 1987).
7. G. S. Bysnovatyi-Kogan, Astron. Astrophys. Trans. **3**, 287 (1993).
8. V. N. Baĭer, V. M. Katkov, and V. M. Strakhovenko, Itogi Nauki Tekh., Ser.: Puchki Zaryazhennykh Chastits Tverd. Tela **4**, 57 (1992).
9. V. A. Lyul'ka, Yad. Fiz. **39**, 680 (1984) [Sov. J. Nucl. Phys. **39**, 431 (1984)].
10. A. V. Borisov, L. V. Morozova, and M. K. Nanaa, Izv. Vyssh. Uchebn. Zaved., Fiz., No. 12, 106 (1992).
11. A. V. Borisov and V. A. Guseinov, Yad. Fiz. **57**, 496 (1994) [Phys. At. Nucl. **57**, 466 (1994)].
12. A. V. Borisov, V. A. Guseinov, and O. S. Pavlova, Yad. Fiz. **61**, 103 (1998) [Phys. At. Nucl. **61**, 94 (1998)].
13. D. Fargion and B. Mele, astro-ph/9902024; J. J. Blanco-Pillado, R. A. Vázquez, and E. Zas, astro-ph/9902266.
14. A. A. Sokolov and I. M. Ternov, *Radiation from Relativistic Electrons* (Nauka, Moscow, 1983; AIP, New York, 1986).
15. V. G. Bagrov, D. M. Gitman, I. M. Ternov, *et al.*, *Exact Solutions of Relativistic Wave Equations* (Nauka, Novosibirsk, 1982; Kluwer, Dordrecht, 1990).
16. I. M. Ternov, V. Ch. Zhukovskiĭ, and A. V. Borisov, *Quantum Processes in Strong External Fields* (Mosk. Gos. Univ., Moscow, 1989).
17. V. I. Ritus, Tr. Fiz. Inst. Akad. Nauk SSSR **111**, 5 (1979).
18. V. O. Papanyan and V. I. Ritus, Tr. Fiz. Inst. Akad. Nauk SSSR **168**, 120 (1986).
19. G. G. Raffelt, *Stars as Laboratories for Fundamental Physics* (Univ. of Chicago Press, Chicago, 1996).
20. M. Giller and W. Michalak, in *Proceedings of the International Conference "Relativistic Jets in AGNs," Kraków, May 27–30, 1997* (Kraków, 1997), p. 189.

Translated by A. Isaakyan

Physics of Atomic Nuclei, Vol. 63, No. 11, 2000, pp. 1956–1962. Translated from Yadernaya Fizika, Vol. 63, No. 11, 2000, pp. 2048–2054.

ELEMENTARY PARTICLES AND FIELDS
Theory

W-Boson Mass Operator in an External Magnetic Field at High Temperatures

V. V. Skalozub* and A. V. Strelchenko

Dnepropetrovsk State University, pr. Gagarina 72, Dnepropetrovsk, 320625 Ukraine

Received July 1, 1999; in final form, February 11, 2000

Abstract—By the Schwinger proper-time method, the one-loop contribution to the *W*-boson mass operator is calculated in a constant magnetic field at high temperatures. The static limit is investigated. By averaging the mass operator over the physical states of a vector particle, the temperature-dependent radiative corrections to the *W*-boson energy spectrum are obtained at high magnetic fields ($eH/M^2 \gg 1$) for various values of the spin projection onto the field direction. These corrections are found to be positive. In particular, the correction to the ground-state level stabilizes the *W*-boson vacuum state at high temperatures. *© 2000 MAIK "Nauka/Interperiodica".*

1. INTRODUCTION

The *W*-boson mass operator in a constant magnetic field H and zero temperature was calculated and investigated in [1, 2]. Among other things, this makes it possible to reveal the role of radiative corrections in the problem of stabilization of the *W*-boson vacuum. The problem consists in the following. In the ground state of the spectrum, the mode $E^2(0) = P_3^2 + M^2 - eH$, where P_3 is the momentum projection onto the field direction, M is the particle mass, and e is the electric charge, becomes unstable (tachyonic) for fields $H > H_0 = M^2/e$ [2]. In the tree approximation, the evolution of the mode leads to *W*- and *Z*-boson condensation [3–5]. As soon as radiative corrections are included, the threshold for the emergence of instability is shifted with the result that the spectrum is stabilized if the Higgs boson mass and the *W*-boson masses are related in a specific way. At nonzero temperatures, the condensation of these fields was also studied in [3] within some approximations. However, temperature-dependent radiative corrections to the *W*-boson spectrum have not yet been investigated. In [6], for example, it was assumed that the *W*-boson vacuum state is stabilized by the Debye mass $m_T^2 \approx e^2T^2$, which is generated only in the longitudinal components of gauge fields, but the point is that the tachyonic mode represents a transverse state resulting from the interaction of a spin with a magnetic field.

In the present study, we calculate and investigate in part the *W*-boson mass operator in a constant magnetic field at high temperatures. The imaginary-time formalism is used here to take into account temperature. As in the case of the calculation at zero temperature from [1], we rely here on the proper-time method. In general, the use of this method runs into difficulties associated with the need for performing summation over discrete imaginary frequencies. However, this method is quite appropriate in the high-temperature region, where it is sufficient to take into account only the ($l = 0$) static modes [7]. As will be shown in Section 2, the procedure for implementing the Schwinger proper-time method is virtually identical to that in the case of $T = 0$ [8].

We average the mass operator over *W*-boson physical states $|n, \sigma\rangle$, where n and σ are, respectively, the number of the Landau level and the spin variable. The functions $\langle n, \sigma|M|n, \sigma\rangle$ determine temperature-dependent radiative corrections to the energy spectrum in an external magnetic field. The square of the effective mass of a vector particle is given by $M^2(H, T) = M^2 - eH + \langle n = 0, \sigma = +1|M|n = 0, \sigma = +1\rangle$. If the quantity $\langle M\rangle_{n=0,\sigma=+1}$ is positive, the *W*-boson vacuum is stabilized by the radiative corrections to the effective mass. At high temperatures, stabilization of this type may occur in strong fields ($eH \gg M^2$) as well.

The ensuing exposition is organized as follows. We calculate the *W*-boson mass operator in Section 2 and perform averaging of the expression for the mass operator over *W*-boson physical states in Section 3. In Section 4, we derive asymptotic expressions for the averaged mass operator in the limit of strong magnetic fields and high temperatures. Our basic results are discussed in Section 5.

2. MASS OPERATOR

Let us consider a simple model of electroweak interactions that is based on the spontaneously broken gauge symmetry $SU(2) \longrightarrow U(1)$. The relevant Lagrangian has the form

$$L = -\frac{1}{4}(G^a_{\mu\nu})^2 + \frac{1}{2}(D_\mu\phi)^2 + \frac{m_0^2}{2}\phi^2 - \frac{\lambda}{4}\phi^4, \qquad (1)$$

* e-mail: skalozub@ff.dsu.dp.ua

1063-7788/00/6311-1956$20.00

where $G^a_{\mu\nu} = \partial_\mu A^a_\nu - \partial_\nu A^a_\mu + g\epsilon^{abc}A^b_\mu A^c_\nu$ and $D^{ab}_\mu = \partial_\mu\delta^{ab} + g\epsilon^{abc}A^c_\mu$.

This model is described in detail elsewhere [2]. As the result of a spontaneous breakdown of symmetry, the charged components $W^\pm_\mu = \frac{1}{\sqrt{2}}(A^1_\mu \pm iA^2_\mu)$ acquire the mass $M = g\Phi_0$, where $\Phi_0 = m_0/\sqrt{\lambda}$ is the vacuum expectation value of the scalar field; as to the component $A_\mu = A^3_\mu$, it remains massless, playing the role of an electromagnetic field. We also identify the gauge coupling g with the electric charge: $g \equiv e$. For the sake of definiteness, the external magnetic field is assumed to be aligned with the third axis of the system of Cartesian coordinates, $H = H_3$. The relevant potential of this field is chosen to be $A^{\text{ext}}_\mu = (0, 0, Hx, 0)$, H = const. In order to quantize the fields being studied, we make use of the gauge condition

$$\partial_\mu W^{\pm\mu} - ieA^{\text{ext}}_\mu W^{\pm\mu} - M\phi^\pm = 0, \qquad (2)$$

where $\phi^\pm = \frac{1}{\sqrt{2}}(\phi^1 \pm i\phi^2)$ are charged Goldstone fields. As a matter of fact, the model being considered represents a massive regularization of Yang–Mills theory; in the limit $M \longrightarrow 0$, it reproduces all relevant results. Results concerning Weinberg–Salam theory can be derived with the aid of relevant algebraic transformations (for more details, see [2]).

In the one-loop approximation, the *W*-boson mass operator is determined by the standard set of diagrams in Fig. 1 [1, 2], where double lines represent the Green's functions for charged particles—specifically, the Green's functions $G_{\mu\nu}(x, y)$ for the vector particles $W^\pm_\mu$ (solid double lines shaded in between), the Green's function $G(x, y)$ for the Goldstone particles (solid double lines closed in between), and the Green's function $\Delta(x, y)$ for charged ghost components $\chi^\pm$ (dashed double line shaded in between). Thin wavy, thin solid, and thin dashed lines correspond to a radiated photon A^R, a neutral Higgs scalar η, and a neutral ghost component χ^3, respectively. In the operator form, the relevant expressions for the above Green's functions are given by

$$G_{\mu\nu}(P) = -[P^2 + M^2 + 2ieF_{\mu\nu}]^{-1},$$

$$G(P) = \Delta(P) = -[P^2 + M^2]^{-1}.$$

In order to calculate the mass operator, we make use of the proper-time representation and the Schwinger operator formalism. The *W*-boson mass operator in a magnetic field at nonzero temperatures can be represented as

$$M_{\mu\nu} = \frac{e^2}{\beta}\sum_{k_4}\int\frac{d^3k}{(2\pi)^3}[M^\eta_{\mu\nu}(k, p) + M^W_{\mu\nu}(k, p)], \qquad (3)$$

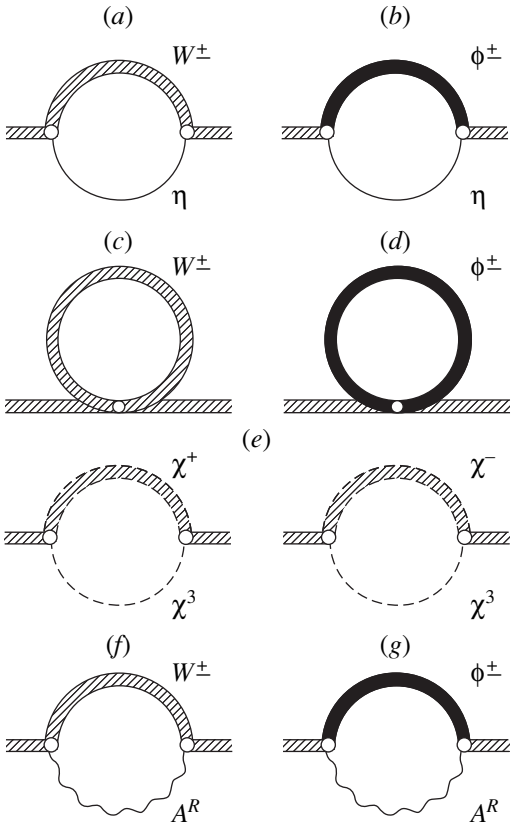

Fig. 1. *W*-boson mass operator in the one-loop approximation.

where

$$M^\eta_{\mu\nu}(k, p) = (k^2 + m^2)^{-1}$$
$$\times[(2k-p)_\mu G(p-k)(2k-p)_\nu - 4M^2 G_{\mu\nu}(p-k)],$$

$$M^W_{\mu\nu}(k, p) = k^{-2}\{\Gamma_{\mu\alpha,\rho}G_{\alpha\beta}(p-k)\Gamma_{\nu\beta,\rho}$$
$$+ (p-k)_\mu\Delta(p-k)k_\nu + k_\mu\Delta(p-k)(p-k)_\nu$$
$$+ M^2\delta_{\mu\nu}G(p-k) + k^2[G_{\mu\nu}(p-k) - 2G_{\nu\mu}(p-k)$$
$$+ \delta_{\mu\nu}G_{\rho\rho}(p-k)]\},$$

$$\Gamma_{\mu\alpha,\rho} = \delta_{\mu\alpha}(2p-k)_\rho + \delta_{\alpha\rho}(2k-p)_\mu + \delta_{\mu\rho}(p+k)_\alpha;$$

$\beta = 1/T$; $k_4 = 2\pi l/\beta$, $l = 0, \pm1, \pm2, \ldots$; and $P_\mu = i\partial_\mu + eA^{\text{ext}}_\mu$ by definition. The first term in the bracketed expression on the right-hand side of (3) stands for the contribution of the neutral Higgs scalar η (diagrams in Figs. 1*a*, 1*b*), while the second term represents the gauge sector (diagrams in Figs. 1*c*–1*h*). As was indicated in Section 1, we restrict our consideration to the case of the high-temperature limit; in (3), this limit corresponds to the $l = 0$ term in the sum over k_4 (see the review article of Kalashnikov [7]). This case can be treated by directly applying the standard computational

procedure developed for the case of zero temperature. For the details of the relevant calculations, the reader is referred to [1, 2]. Highlighted below are only the basic points peculiar to the case of $k_4 = 0$. For the sake of definiteness, let us consider the first term in the bracketed expression on the right-hand side of (3), $M^{\eta}_{\mu\nu}(k, p)$.

In order to perform three-dimensional integration with respect to k in (3), it is necessary to introduce a proper time for each propagator appearing in $M^{\eta}_{\mu\nu}(k, p)$ and to represent the product of the propagators in the form

$$D_{\eta}(k)G(p-k) = -\int_0^1 du \int_0^{\infty} ds s e^{-s\chi(u)},$$

where

$$\chi(u) = (1-u)\bar{k}^2 + u(\bar{p}-\bar{k})^2 + (1-u)m^2 + u(M^2 + 2ieF),$$

m being the mass of the neutral scalar field. The k_4-dependent part of the "Hamiltonian" is equal to zero. Three-dimensional integration with respect to k is performed with the aid of a transition to the conjugate variable ξ_i,

$$[\xi_i, k_j] = i\delta_{ij}.$$

By using the eigenstate of the operator ξ_i as determined by the condition $\xi_i' = 0$, the three-dimensional integral with respect to k can be represented as

$$\int \frac{d^3k}{(2\pi)^3} f(\bar{k}) = \langle \xi' = 0 | f(\bar{k}) | \xi' = 0 \rangle.$$

Further, the Hamiltonian $\Re(u) = (1-u)\bar{k}^2 + u(\bar{p} - \bar{k})^2$ is integrated according to the procedure described in [8]. The eventual result takes the form

$$\langle e^{-s\Re} k_i \rangle = \langle e^{-s\Re} \rangle \left(\frac{A}{D}\bar{p}\right)_i,$$

$$\langle e^{-s\Re} k_i k_j \rangle = \langle e^{-s\Re} \rangle \left[\left(\frac{A}{D}\bar{p}\right)_i \left(\frac{A}{D}\bar{p}\right)_j - ie\left(\frac{F}{D^T}\right)_{ij}\right],$$

where

$$A = e^{2ieuFs} - 1, \quad D = A + 2ieFs(1-u),$$

$$\langle e^{-s\Re} \rangle = \frac{1}{(4\pi s)^{3/2}} \left[\det\left(\frac{D}{2ieFs}\right)\right]^{-1/2} e^{-s\Phi_0},$$

$$\Phi_0 = u\bar{p}^2 - \bar{p}\left[\frac{1}{2ieFs}\ln\left(-\frac{D}{D^T}\right)\right]\bar{p}.$$

The distinction between the cases of a nonzero and zero temperature consists in the difference of the dimensionalities of the relevant integrals. This is reflected in the power to which the parameter s is raised and which represents the dimensionality of the integral: the factor $s^{-3/2}$ comes from the three-dimensional integral corresponding to $T \neq 0$, whereas the factor s^{-2} arises in the case of $T = 0$ [8]. The result for the scalar sector has the form

$$M^{\eta}_{ij} = \frac{2\alpha}{\sqrt{\pi}\beta} \int_0^1 du \int_0^{\infty} ds s^{-1/2} \left[\det\left(\frac{D}{2ieFs}\right)\right]^{-1/2} \times e^{-s\Phi_0} e^{-s[(1-u)m^2 + uM^2]} [K_{ij} - M^2(A^T + I)_{ij}], \quad (4)$$

where

$$K_{ij} = \left[\left(\frac{A}{D} - Bu\right)\bar{p}\right]_i \left[\left(\frac{A}{D} - u\right)\bar{p}\right]_j - ie\left(\frac{F}{D^T}\right)_{ij}.$$

The relevant result for the gauge sector is given by

$$M^{W}_{ij} = \frac{2\alpha}{\sqrt{\pi}\beta} \int_0^1 du \int_0^{\infty} ds s^{-1/2} \left[\det\left(\frac{D}{2ieFs}\right)\right]^{-1/2} \times e^{-s\Phi_0} e^{-suM^2} M_{ij}(s, u),$$

$$M_{ij}(s,u) = 2(A^T + I)_{ij}\bar{p}\left[\frac{TA^T(A + 2 + 2A^T) + 2(A^T)^2}{DD^T} + 2(A^T + I)\right]\bar{p} + [2(A^T - A) + 4\cosh^2 x] \times \left[\left(\frac{A}{D}\bar{p}\right)^T \left(\frac{A}{D}\bar{p}\right) - ie\,\mathrm{tr}\left(\frac{F}{D^T}\right)\right] + \left[\left(\frac{A}{D} - Bu\right)\bar{p}\right]_i \times \left\{\left[2(A + A^T) - 3A\frac{T}{D} + 2A^T\frac{A}{D}\right]\bar{p}\right\}_j + \left\{\left[3A\frac{T}{D} + \frac{D^T}{D} + (2A^T + A)B + \frac{A^2}{D}\right]\bar{p}\right\}_i \left[\left(\frac{A}{D} - u\right)\bar{p}\right]_j + ie\,\mathrm{tr}\left[\frac{F(2AA^T - I)}{D^T}\right] - 2ieA^T_{ij}\,\mathrm{tr}\left(\frac{FA^T}{D^T}\right) + 8(1 + 2\sinh^2 x)K_{ij} - \left[\left(\frac{2AT + A^TA}{D} + A^T\right)\bar{p}\right]_i \times \left\{\left[\frac{A}{D}(2T + 1) - u\right]\bar{p}\right\}_j + \left[\frac{A(2T-1)}{D}\bar{p}\right]_i \times \left[\left(AB + \frac{A^2}{D}\right)\bar{p}\right]_j + ie\left[\frac{(2A^2 - A^T - 6A)F}{D^T}\right]_{ij} + \delta_{ij}\left\{\bar{p}^2 + M^2 + \bar{p}\left[A^T + (A^T + I)\frac{A}{D}\right.\right. \quad (5)$$

$$+\frac{(A^T+T)(A^T+I)(A+D)}{DD^T}\Bigg]\Bigg\}$$

$$+ie\left\{\frac{F[4A^T+(A^T)^2-2A]}{D^T}\right\}_{ij},$$

where $T = 2ieFs(u-1)$.

3. AVERAGING OVER PHYSICAL STATES

In order to find radiative corrections to the *W*-boson energy spectrum, it is necessary to define the mass shell for a vector particle in an external magnetic field at high temperatures. In the static case, the mass shell is specified by the equations

$$[(\bar{p}^2+M^2)\delta_{ij}+2ieF_{ij}^{\text{ext}}]W_j^- = 0,$$
$$p_iW_i^- = 0, \quad \phi^- = 0, \tag{6}$$

where $i, j = 1, 2, 3$ and where the term p_4W_4 vanishes since $p_4 = 0$ for static modes. If the magnetic field is constant, it is convenient to choose basic states in such a way that the tensor F_{ij} is diagonal in this basis, in which case F_{ij} plays the role of the operator projecting spins onto the field direction. State vectors are normalized by the condition

$$\langle n, \sigma|n', \sigma'\rangle = \delta_{nn'}\delta_{\sigma\sigma'},$$

where $n, n' = 0, 1, 2, 3, \ldots$ and $\sigma, \sigma' = 0, \pm 1$.

The eigenvalues of the operators F, $\bar{p}^2$, and $p_\perp^2$ in these states are

$$F = iH\sigma,$$
$$\bar{p}^2 = -M^2+2eH\sigma, \quad p_\perp^2 = (2n+1)eH.$$

In order to find the quantity $\langle n, \sigma|M|n, \sigma\rangle$, it is also necessary to evaluate the expectation value of the operator $(\bar{p}\bar{p})$ over the $|n, \sigma\rangle$ states. The result is

$$\langle n, \sigma|\bar{p}\bar{p}|n, \sigma\rangle = \frac{1}{2}(2n+1-\sigma)eH.$$

The averaged expressions for the mass operator can be represented as

$$\langle n, \sigma|M_{ij}^{\eta}|n, \sigma\rangle = \frac{2\alpha}{\sqrt{\pi}\beta}\int_0^1 du\int_0^\infty \frac{dx}{\sqrt{x}}[euH\Delta]^{-1/2}$$
$$\times\exp\left[-xu\frac{M^2}{eH}-\frac{x(1-u)}{u}\frac{m^2}{eH}\right]$$
$$\times\exp\{-(2n+1)[\rho-x(1-u)]-2y(1-u)\}$$
$$\times[K(y)-M^2e^{2y}], \tag{7}$$

$$\langle n, \sigma|M_{ij}^{W}|n, \sigma\rangle = \frac{\alpha}{2\sqrt{\pi}\beta}\int_0^1 du\int_0^\infty \frac{dx}{\sqrt{x}}(euH\Delta)^{-1/2}$$
$$\times\exp\{-(2n+1)[\rho-x(1-u)]-2y(1-u)\}M(x, u), \tag{8}$$

where $x = euHs$, $y = x\sigma$,

$$\tanh\rho = \frac{(1-u)\sinh x}{(1-u)\cosh x+u\dfrac{\sinh x}{x}},$$

$$\Delta = (1-u)^2+2u(1-u)\frac{\sinh 2x}{2x}+u^2\frac{\sinh^2 x}{x^2}.$$

The explicit expressions for $M(x, u)$ and $K(y)$ are given in the Appendix.

4. ASYMPTOTIC EXPANSION OF THE MASS OPERATOR IN A STRONG MAGNETIC FIELD

The expressions for the averaged mass operator that were obtained in Section 3 are investigated here in the limiting case of strong magnetic fields and high temperatures: $eH/M^2 \gg 1$, $eH/T^2 \ll 1$.

The integrands in expressions (7) and (8) involve the factor $\exp\left(-xu\dfrac{m^2}{eH}\right)$, whence it follows that, in the case of $eH \gg M^2$, the main contributions to the relevant integrals come from the region where $u \sim 1$ and $x \gg 1$. In order to find the relevant asymptotic expressions, we will need the relations

$$\Delta \sim \frac{u^2}{4x^2}e^{2x} \quad (u \longrightarrow 1, x \gg 1),$$
$$\Delta^{-1/2}\exp\{-(2n+1)[\rho-x(1-u)]-2y(1-u)\} \tag{9}$$
$$\sim \frac{x}{u\sinh x}e^{-\lambda x(1-u)}\exp[2nx(1-u)],$$
$$x \gg 1,$$

where we set $\lambda = 1, -3$, and -1 for $\sigma = +1, -1$, and 0, respectively. Without loss of generality, the calculations can be performed in the reference frame where $p_3 = 0$. For the case of the gauge sector, which is described by expression (A.1), we now present terms contributing to the integral in (8) for each value of the spin projection:

$$M^{\sigma=+1}(x, u) = 4e^{2x}(2n+1)eH$$
$$+2e^{2x}eH\left[2A(x)-\frac{u^2A^2(x)}{2x^2\Delta}\right]+4(\sinh 2x+\cosh^2 x)$$

$$\times\left[(2n+1)eH\frac{u^2\sinh^2 x}{x^2\Delta}+eH\frac{u^2\sinh 2x}{2x^2\Delta}\right]$$
$$+eH(8\sinh^2 x+1)\frac{u^2\sinh^2 x}{2x^2\Delta}$$
$$+2neH\left\{-\frac{u^2\sinh^2 x}{x^2\Delta}A(x)D(-x)\right.$$
$$+A(-x)\left[2\frac{A(-x)}{D(-x)}-\frac{u^2\sinh^2 x}{x^2\Delta}\right]$$
$$\left.+\frac{1}{2}uA(-x)\left[1+\frac{A(x)}{D(x)}\right]\right\}$$
$$+8(1+2\sinh^2 x)\frac{eH}{D(-x)}+neH\left\{4\sinh^2 x+\left[\frac{A(x)}{D(x)}\right.\right.$$
$$\left.+\frac{A(-x)}{D(-x)}\right]\cosh 2x+2\frac{u^2\sinh^2 x}{x^2\Delta}\cosh 2x\Bigg\}$$
$$+eH[2+A(x)]+A^2(-x)\frac{eH}{D(-x)},$$

$$M^{\sigma=-1}(x,u)=-4(\sinh 2x-\cosh^2 x)$$
$$\times\left[(2n+1)eH\frac{u^2\sinh^2 x}{x^2\Delta}+eH\frac{u^2\sinh 2x}{2x^2\Delta}\right]+2(n+1)eH$$
$$\times\left\{\frac{u^2\sinh 2x}{2x^2\Delta}[A(-x)+ue^{2x}D(x)][1-D(x)]\right\}$$
$$+neH\left\{4\sinh^2 x+\left[\frac{A(x)}{D(x)}+\frac{A(-x)}{D(-x)}\right]\cosh 2x\right.$$
$$\left.+2\frac{u^2\sinh^2 x}{x^2\Delta}\cosh 2x\right\}+8(1+2\sinh^2 x)\frac{eH}{D(x)}$$
$$+eH(8\sinh^2 x+1)\frac{u^2\sinh 2x}{2x^2\Delta}+eH[-2+A(x)]$$
$$+[A^2(x)+3A(x)+2A^2(-x)-8A(-x)]\frac{eH}{D(x)},$$

$$M^{\sigma=0}(x,u)=4(2n+1)eH$$
$$+4\cosh^2 x\left[(2n+1)eH\frac{u^2\sinh 2x}{2x^2\Delta}+eH\frac{u^2\sinh^2 x}{x^2\Delta}+\frac{u}{2x}\right]$$
$$+eH(8\sinh^2 x+1)\frac{u^2\sinh 2x}{2x^2\Delta}$$
$$+neH\left\{\left[\frac{A(x)}{D(x)}+\frac{A(-x)}{D(-x)}\right]\cosh 2x\right.$$
$$\left.+4\sinh^2 x+2\frac{u^2\sinh^2 x}{x^2\Delta}\cosh 2x\right\}+16\sinh^2 x\frac{eH}{2x}.$$

Performing integration with allowance for (9), we obtain

$$\begin{aligned}\langle n,\sigma=+1|M^W|n,\sigma=+1\rangle&=\alpha\sqrt{eH}T[12.6+6n+i(5+24n)],\\ \langle n,\sigma=-1|M^W|n,\sigma=-1\rangle&=\alpha\sqrt{eH}T[14+6n+i(9.69+2n)],\\ \langle n,\sigma=0|M^W|n,\sigma=0\rangle&=\alpha\sqrt{eH}T[13+10n+6i(1+n)].\end{aligned}\qquad(10)$$

By using expression in (A.2) and evaluating the integral in (7), we arrive at

$$\begin{aligned}\langle n,\sigma=+1|M^\eta|n,\sigma=+1\rangle&=\alpha\sqrt{eH}T(1.15+4i),\\ \langle n,\sigma=-1|M^\eta|n,\sigma=-1\rangle&=4\alpha\sqrt{eH}T,\\ \langle n,\sigma=0|M^\eta|n,\sigma=0\rangle&=-4\frac{M^2}{eH}\alpha\sqrt{eH}T.\end{aligned}\qquad(11)$$

From (10) and (11), it can be seen that the real part of $\langle M\rangle$ is positive in the ground state and in excited states. The emergence of the imaginary part in $\langle M\rangle$ is due to nonanalyticity of some terms in the integrands on the right-hand sides of (7) and (8) for $x\longrightarrow\infty$. The choice of an integration contour that ensures convergence of the integrals with respect to x for these terms generated the imaginary parts in expressions (10) and (11), which describe a transition to a state occurring at a lower energy.

5. DISCUSSION OF THE RESULTS

Let us now consider the effective mass of the W boson. With the aid of Eqs. (10) and (11), we obtain

$$\begin{aligned}M^2(H,T)&=M^2-eH\\ &+\mathrm{Re}\langle n=0,\sigma=+1|M|n=0,\sigma=+1\rangle\\ &=M^2-eH+13.75\alpha T\sqrt{eH}.\end{aligned}\qquad(12)$$

From (12), it can be seen that the quantity $M^2(H,T)$ is positive for sufficiently high temperatures. On this basis, we can conclude that, for $T\gg(eH)^{1/2}$, the radiative correction to the W-boson ground state stabilizes the vacuum. Here, the stabilizing mass depends on the

field strength and vanishes at $H = 0$, as it must in the one-loop approximation [7].

Let us compare our results on the role of radiative corrections to the *W*-boson mass in an external field at nonzero temperatures with the results presented by Elmfors and Persson [9], who relied on the weak-field approximation. The basic conclusion drawn by those authors is that, for the ground state $|n = 0, \sigma = +1\rangle$, radiative corrections to the mass at nonzero temperatures in an external field vanish, which is in a glaring contradiction with expression (12). The reason behind this contradiction is rooted in the computational procedure adopted in [9], where the field dependence is introduced in $\langle M\rangle$ exclusively via the *W*-boson wave functions in a magnetic field and where the mass operator is replaced by its field-independent asymptotic expression for high temperatures. It is obvious that this approximation cannot be applied to the case of weak fields, since it fails to reproduce the result at $T = 0$, where the anomalous-magnetic-moment contribution to the *W*-boson energy must manifest itself in weak fields [1]. In the case of weak fields, the contribution of gH is taken into account both via the *W*-boson external lines and via the term featuring the magnetic moment of the *W* boson.

The above results are of interest for cosmology. We imply that, if a magnetic field was present in the Universe in the era of an electroweak phase transition—as is often discussed in the literature (see, for example, [6, 10])—the radiative mass of the *W* bosons determines the dynamical mechanism of vacuum stabilization, both in the case of a broken vacuum phase and in the case of the restored vacuum phase. If the magnetic field is spontaneously generated at a nonzero temperature, it is given by $(eH)^{1/2} \sim g^2T$ in the one-loop approximation (see [11, 12]). Therefore, the square of the effective mass is about g^4T^2 for the restored phase, in which case $M = 0$. Moreover, it is positive owing to a large coefficient in the radiative mass (12). In the one-loop approximation, we thereby arrive at a self-consistent pattern where, at high temperatures, there spontaneously arises a magnetic field, which is stabilized by the radiative mass of charged gauge fields.

APPENDIX

The explicit expression obtained upon averaging the mass operator over physical states has the form

$$
\begin{aligned}
M(x,u) = 2e^{2y}\Bigg\{ & neH\Bigg[8\sinh^2 x - \frac{u^2}{x^2\Delta}\\
&\times\Bigg(\frac{4x(1-u)}{u}\cosh 3x\sinh x\\
&+ 8\sinh 2x\sinh^2 x\Bigg)\Bigg] + eH\Bigg[2A(x) - \frac{u^2A(x)}{2x^2\Delta}\Bigg(A(x)\\
&- \frac{x(1-u)}{u}(A(x) + 2\cosh 2x)\Bigg)\Bigg] - 2up_3^2 + 2\bar{p}^2\Bigg\}\\
&+ 4(\sinh 2y + \cosh^2 x)\Bigg\{up_3^2 + (2n+1)eH\frac{u^2\sinh^2 x}{x^2\Delta}\\
&+ eH\frac{u^2}{4x^2\Delta}\Bigg[2\sinh 2x + \frac{4x(1-u)}{u}\Bigg] + \frac{ueH}{2x}\Bigg\}\\
&+ eH\Bigg\{2A(-y)\frac{u(1-u)}{x}\frac{\cosh 2x}{\Delta}\\
&+ \frac{u^2(8\sinh^2 x + 1)}{2x^2\Delta}\Bigg[\sinh 2x + \frac{4x(1-u)}{u}\Bigg] + \frac{u}{2x}\Bigg\}\\
&+ neH\Bigg\{4\sinh^2 x + N(x) + N(-x) + \frac{u^2\sinh^2 x}{x^2\Delta}\\
&\times\Bigg[2\cosh 2x + \frac{4x(1-u)}{u}\sinh 2x\Bigg]\Bigg\} + (2n + 1 - \sigma)eH\\
&\times\Bigg\{\frac{A^2(y) + (1 - 4\sinh^2 y)e^{-2y}D(-y) + 2\dfrac{y}{u}(1-u)A(y)}{D(y)}\\
&\times\Bigg[\frac{A(y)}{D(y)} - u\Bigg] + \frac{u^2\sinh^2 y}{y^2\Delta(y)}[A(y) + ue^{-2y}D(y)][1 - D(-y)]\\
&+ \Bigg[\frac{4(1-u)u\sinh^2 y}{y\Delta(y)} - \frac{u^2\sinh^2 y}{y^2\Delta(y)} + u\frac{A(y)}{D(y)}\Bigg]\\
&\times\Bigg[A(-y) + e^{2y}y\frac{1-u}{u}\Bigg] - \Bigg[(1 + e^{2y})\frac{A(-y)}{D(-y)}\\
&+ A(-y)\frac{u^2\sinh^2 y}{y^2\Delta(y)}\Bigg]\Bigg[\frac{1}{2} - \frac{y}{u}(1-u)\Bigg]\\
&+ \frac{u}{2}\Bigg[1 + e^{2y} + \frac{u^2\sinh^2 y}{y^2\Delta(y)}D(-y)\Bigg]\Bigg\} + 8(1 + \sinh^2 y)K(y)\\
&+ u(2+u)p_3^2 + \frac{eH\sigma}{D(-y)}[8A(y) - 2A(-y) - A^2(-y)\\
&- 2A^2(y)] + 2eH\sigma + eH\Bigg\{A(x) - \frac{A(x)}{D(-x)}\\
&+ e^{-2x}\Bigg[1 - \frac{2x}{u}(1-u)\Bigg]\Bigg[\frac{A(x)}{D(x)} + \frac{u^2\sinh^2 x}{x^2\Delta}\Bigg]\Bigg\},
\end{aligned}
\tag{A.1}
$$

where

$$\Delta(y) = (1-u)^2 + 2u(1-u)\frac{\sinh 2y}{2y} + u^2\frac{\sinh^2 y}{y^2},$$

$$\Delta \equiv \Delta(x),$$

$$K(y) = \frac{1}{2}(2n+1-\sigma)\left[-u^2 e^{-2y}\frac{D(-y)}{D(y)} - 2u\frac{A(y)}{D(y)} + \frac{u^2\sinh^2 y}{y^2\Delta(y)}\right] + \frac{eH\sigma}{\Delta(-y)}, \quad \text{(A.2)}$$

$$N(x) = \frac{A(x)}{D(x)}\left[2\cosh 2x - \frac{e^{-2x}2x}{u}(1-u)\right],$$

$$A(y) = e^{-2y} - 1, \quad D(y) = A(y) - \frac{2y}{u}(1-u).$$

REFERENCES

1. V. S. Vanyashin, Yu. Yu. Reznikov, and V. V. Skalozub, Yad. Fiz. **33**, 429 (1981) [Sov. J. Nucl. Phys. **33**, 227 (1981)].
2. V. V. Skalozub and V. S. Vanjashin, Fortschr. Phys. **40**, 759 (1992).
3. V. V. Skalozub, Yad. Fiz. **45**, 1708 (1987) [Sov. J. Nucl. Phys. **45**, 1058 (1987)].
4. J. Ambjorn and P. Olesen, Int. J. Mod. Phys. A **5**, 4252 (1990).
5. S. MacDowell and O. Tornquist, Phys. Rev. D **45**, 3833 (1992).
6. K. Enquist and P. Olesen, Phys. Lett. B **324**, 195 (1994).
7. O. K. Kalashnikov, Fortschr. Phys. **32**, 325 (1984).
8. J. Schwinger, Phys. Rev. D **7**, 1696 (1973).
9. P. Elmfors and D. Persson, Nucl. Phys. B **538**, 309 (1999).
10. M. Giovanini and M. Shaposhnikov, Phys. Rev. D **57**, 2186 (1998).
11. A. O. Starinets, A. S. Vshivtsev, and V. Ch. Zhukovskii, Phys. Lett. B **322**, 403 (1994).
12. V. V. Skalozub, Int. J. Mod. Phys. A **11**, 5643 (1996).

Translated by A. Isaakyan

Physics of Atomic Nuclei, Vol. 63, No. 11, 2000, pp. 1963–1968. Translated from Yadernaya Fizika, Vol. 63, No. 11, 2000, pp. 2055–2060.

ELEMENTARY PARTICLES AND FIELDS
Theory

Primakoff Effect: Synchrotron and Coulomb Mechanisms of Axion Emission

V. V. Skobelev*
Moscow State Industry University, Moscow, Russia
Received April 9, 1999; in final form, November 22, 1999

Abstract—The Primakoff effect–induced radiative emission of axions by an alternating electromagnetic field, $F_a \longrightarrow \gamma a$, is considered for the first time. The synchrotron mechanism and the Coulomb mechanism—in the latter case, the alternating field is formed when a charge executes an infinite motion in the field of a Coulomb center—are considered as specific examples. The contributions of these effects to the axion emissivity of magnetic neutron stars and of the Sun are estimated. *© 2000 MAIK "Nauka/Interperiodica".*

1. INTRODUCTION

The axion is one of pseudoscalar particles (omion, arion, etc.) whose existence is suggested both by some theoretical considerations and by an analysis of astrophysical data (primarily by the analysis of the hidden-mass problem). Namely, the axion as a Goldstone boson in the Peccei–Quinn scheme [1] provides a natural explanation of the exact *CP* invariance of strong interactions, while the axion condensate formed at early stages of Universe evolution could constitute a major part of cold dark matter. This explains why interest in the possibility of experimentally detecting the axion [2–4] and in investigations into axion interactions [5, 6], including interactions under extreme conditions (for example, in the presence of strong external electromagnetic fields [7–9]), has quickened in the last decade. Hopes for experimentally identifying axions are pinned primarily on implications of the Primakoff effect—that is, on direct axion–photon coupling described by the Lagrangian (hereafter, we use the system of units where $e^2 = \alpha = 1/137$)

$$\mathcal{L} = -\frac{g_\gamma}{16\pi} F^{\mu\nu}\tilde{F}_{\mu\nu} a, \qquad (1)$$

where $\tilde{F}_{\mu\nu} = \frac{1}{2}\varepsilon_{\mu\nu\alpha\beta}F^{\alpha\beta}$ is the dual of the electromagnetic-field strength tensor and

$$g_\gamma = -\frac{\alpha c_\gamma}{2\pi f} \qquad (1a)$$

is the coupling constant. The dimensionless parameter c_γ is on the order of unity, its specific value depending on the axion model used; the parameter f represents the energy scale at which Peccei–Quinn symmetry is broken [1, 10]. The possible value of g_γ in energy units is quite small (not greater than 10^{-10} GeV^{-1}), which corresponds to the concept of an invisible axion.

The axion mass is also rather small: it can lie in the interval

$$10^{-5} \lesssim m \lesssim 10^{-2}\ \text{eV}, \qquad (2)$$

whose boundaries were determined on the basis of astrophysical data [6].

From the form of the Lagrangian in (1), it follows that an axion can be produced in the interactions of real photons with an alternating external field F_a (diagram in Fig. 1*a*) or as the result of the transformation of an external field with a nonzero Fourier transform in the spacelike region of momentum transfer into a γa pair (diagram in Fig. 1*b*). The first mechanism has been vigorously discussed in the literature [2], while the second mechanism has thus far attracted no attention, to the best of my knowledge.

In the present study, we will analyze general regularities of the process $F_a \longrightarrow \gamma a$ (Section 2) and consider specific cases where the alternating field is formed by a charge moving along a circle (Section 3)

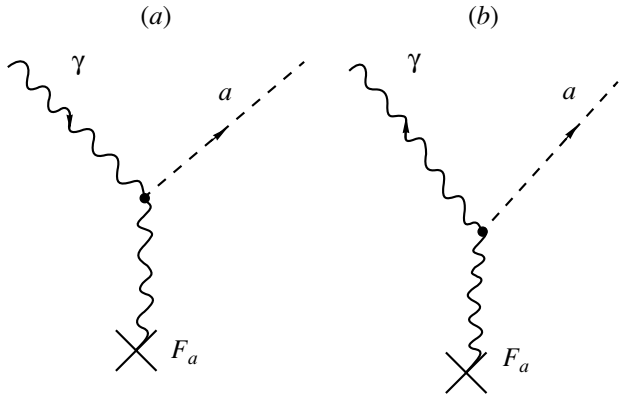

Fig. 1.

* e-mail: v_skobelev@hotmail.com

and in the field of a Coulomb center (Section 4). For a special version of the ultrarelativistic motion of an electron in a magnetic field, results are presented in Section 3 for the probability and for the intensity of synchrotron radiation $e \longrightarrow e\gamma a$ in terms of invariant field parameters. In Section 5, we discuss the astrophysical aspects of the issue, comparing the implications of the above mechanism and of the mechanism of axion generation through the channel represented by the diagram in Fig. 1*a*.

2. INVARIANT CHARACTERISTICS OF RADIATIVE AXION EMISSION

Making the substitution $F \longrightarrow F_a + F$ in (1), where F_a and F are the strength tensors of the alternating and the radiative field, respectively, and performing some simple transformations, we find that the total probability of the emission of an axion and a photon as expressed in terms of an integral with respect to the momentum transfer k can be represented in the form

$$W = \frac{g_\gamma^2}{2(2\pi)^7}\int d^4k[\tilde{F}_a(k)\tilde{F}_a^*(k)]_{\mu\nu}J^{\mu\nu}, \qquad (3)$$

where $F_a(k)$ is the Fourier transform of F_a and

$$J^{\mu\nu} = \int\frac{d^3p}{2p_0}\int\frac{d^3\kappa}{2\kappa_0}\kappa^\mu\kappa^\nu\delta(k-p-\kappa), \qquad (3a)$$

p and κ being, respectively, the axion and the photon momentum.

The expression for the invariant probability W can be further simplified with the aid of the relations

$$(\tilde{F}_a\tilde{F}_a^*)_{\mu\nu} = (F_aF_a^*)_{\mu\nu} + \frac{1}{2}g_{\mu\nu}F^a_{\alpha\beta}F_a^{*\alpha\beta}, \qquad (4a)$$

$$J^{\mu\nu} = \frac{\pi(k^2-m^2)^3}{24k^6}(4k^\mu k^\nu - k^2g^{\mu\nu}), \qquad (4b)$$

and the Maxwell equation

$$k_\mu F^a_{\sigma\nu} + k_\nu F^a_{\mu\sigma} + k_\sigma F^a_{\nu\mu} = 0. \qquad (4c)$$

This yields

$$W = \frac{g_\gamma^2}{96(2\pi)^6}\int_\Gamma d^4k\frac{(k^2-m^2)^3}{k^4}F^a_{\alpha\beta}(k)F_a^{*\beta\alpha}(k), \qquad (5)$$

where the invariant region of integration is given by

$$\Gamma = \left\{\begin{array}{l} k^2 \geq m^2 \\ k_0 > 0 \end{array}\right\}.$$

The mean 4-momentum of the emitted axion, $\langle p_\alpha\rangle$, is obtained from (3) by introducing the factor $(k-\kappa)_\alpha$ in the integrand on the right-hand side of (3a). Further transformations are similar to those performed above. The result is

$$\langle p_\alpha\rangle = \frac{g_\gamma^2}{192(2\pi)^6} \times\int_\Gamma d^4k\frac{(k^2-m^2)^3}{k^6}(k^2+m^2)F^a_{\alpha\beta}(k)F_a^{*\beta\alpha}k_\alpha. \qquad (6)$$

Obviously, the mean value of the total radiated 4-momentum, $\langle k_\alpha\rangle$, can be obtained from (5) by introducing k_α in the integrand.

An equivalent representation of expressions (5) and (6) in terms of the currents generating the field F_a is obtained via the substitution

$$F^a_{\alpha\beta}(k)F_a^{*\beta\alpha}(k) \longrightarrow -\frac{32\pi^2}{k^2}j_\alpha(k)j^{*\alpha}(k). \qquad (7)$$

If the field F_a is generated by a classical pointlike charge Q, the components of this field are determined by the well-known Lienard–Wiechert potentials, in which case the above expressions are valid only if the radiation recoil is disregarded—that is, under the condition

$$\langle k_0\rangle \ll E_Q, \qquad (8)$$

where E_Q is the energy of the charge. This condition is rather weak and is obviously satisfied in the cases considered below.

3. SYNCHROTRON MECHANISM OF RADIATIVE AXION EMISSION

In the case where a charge Q executes an ultrarelativistic motion along a circle of radius R with a frequency ω, the Fourier transforms of the potentials can be chosen as

$$A_0^a(k) = \frac{8\pi^2Q}{k^2\omega}J_\nu(z), \qquad (9)$$

$$\left\{\begin{array}{l} A_1^a(k) \\ A_2^a(k) \end{array}\right\} = \frac{8\pi^2QR}{k^2}\left\{\left(\begin{array}{c}\cos\varphi\\ \sin\varphi\end{array}\right)\frac{\nu}{z}J_\nu(z) + i\left(\begin{array}{c}\sin\varphi\\ -\cos\varphi\end{array}\right)J'_\nu(z)\right\},$$

$$A_3^a(k) = 0,$$

where $\nu = k_0/\omega \gg 1$, θ and φ are spherical angles of the vector $\mathbf{k}$, the third axis is taken to be orthogonal to the plane of motion, and the argument z of the Bessel functions is given by

$$z = R|\mathbf{k}|\sin\theta. \qquad (10)$$

Substituting expression (9) for A^a_α into F^a and into (5) and performing some transformations, we obtain

the probability of radiative axion emission per unit time (the probability divided by the period $2\pi/\omega$) in the form

$$W_T = \frac{g_\gamma^2 Q^2 \omega^3}{6(2\pi)^2}\int_0^1 d\bar{\nu}\bar{\nu}^2\int_0^1 d\cos\theta \times \int_{\tilde{m}/(1-\bar{\nu}^2)^{1/2}}^{\infty} d\nu\nu^3\left[1-\frac{\tilde{m}^2}{\nu^2(1-\bar{\nu}^2)}\right]^3 \times\left[\left(\frac{1}{\bar{\nu}^2\sin^2\theta}-1\right)J_\nu^2(z)+J_\nu'^2(z)\right]. \quad (11)$$

Here and below (in this section), we set all powers of the speed v to unity, when possible, and introduced the notation

$$\bar{\nu} = |\mathbf{k}|/k_0, \quad \tilde{m} = m/\omega, \quad z = v\nu\bar{\nu}\sin\theta, \quad (12)$$

In addition, it is assumed that the integral with respect to ν is dominated by the contribution of higher harmonics with

$$\nu_{\text{eff}} \gg 1. \quad (13)$$

The integrals in (11) can be calculated analytically at some specific values of the parameter $\tilde{m}$.

(i) $\tilde{m} \gg 1$. In this case, the condition in (13) is satisfied automatically. Under the additional constraints

$$\nu_{\text{eff}} \gg (1-v^2\bar{\nu}^2\sin^2\theta)_{\text{eff}}^{-3/2}, \quad (14a)$$

$$\bar{\nu}_{\text{eff}}, (\sin\theta)_{\text{eff}} \approx 1, \quad (14b)$$

it is reasonable to approximate the Bessel functions involved as [12]

$$J_\nu \approx (2\pi\nu\sqrt{\varepsilon})^{-1/2}\exp\left(-\frac{\nu}{3}\varepsilon^{3/2}\right), \quad \varepsilon = 1-v^2\bar{\nu}^2\sin^2\theta. \quad (15)$$

Making the change of variable in the integral with respect to ν as

$$\nu = x\frac{\tilde{m}}{(1-\bar{\nu}^2)^{1/2}}, \quad (16)$$

we arrive at the intermediate result

$$W_T \approx \frac{g_\gamma^2 Q^2\omega^3\tilde{m}^3}{6\pi^3}\int_0^1\frac{d\bar{\nu}}{(1-\bar{\nu}^2)^{3/2}} \times\int_0^1 d\cos\theta\left(\frac{1-\bar{\nu}^2\sin^2\theta}{\varepsilon^{1/2}}+\varepsilon^{1/2}\right)\int_1^\infty dx(x-1)^3e^{-cx}, \quad (17)$$

$$c = \frac{2}{3}\frac{\tilde{m}\varepsilon^{3/2}}{(1-\bar{\nu}^2)^{1/2}}.$$

From the analysis of the last expression, it follows that, in the case of ultrarelativistic motion, the condition in (14b) is satisfied; taking into account (14a), we find that the approximation used in item (i) is valid under the condition

$$\tilde{m}\left(\frac{m_Q}{E_Q}\right)^2 \gg 1, \quad (18)$$

where m_Q and E_Q are, respectively, the mass and the energy of the charge Q. Since

$$\langle k_0\rangle \sim \nu_{\text{eff}}\omega \sim m\left(\frac{E_Q}{m_Q}\right),$$

the condition in (8), which justifies the disregard of recoil, assumes the form

$$\frac{m}{m_Q} \ll 1 \quad (19)$$

and always holds in view of the smallness of the axion mass [see the constraints in (2)].

An approximate integration in (17) yields

$$W_T \approx \left(\frac{2}{3}\right)^{3/2}\frac{g_\gamma^2Q^2\omega^3}{3(2\pi)^2\tilde{m}^2}\left(\frac{E_Q}{m_Q}\right)^9\exp\left[-\sqrt{3}\tilde{m}\left(\frac{m_Q}{E_Q}\right)^2\right]; \quad (20)$$

that is, we can conclude with allowance for (18) that, in the region being considered, W_T is exponentially small.

If the charge Q is taken to be an electron moving in a constant uniform magnetic field, the right-hand side of Eq. (20) can be expressed in terms of the field-strength tensor F and the electron 4-momentum q in the standard form

$$W_T \approx \left(\frac{2}{3}\right)^{3/2}\frac{g_\gamma^2\alpha m_e^6}{3(2\pi)^2m^2q_0}\chi^5\exp\left[-\sqrt{3}\frac{(m/m_e)}{\chi}\right], \quad (21)$$

where

$$\chi = \frac{\sqrt{e^2(qF^2q)}}{m_e^3}, \quad \frac{m}{m_e} \gg \chi. \quad (21a)$$

A similar exponential dependence in the region specified by Eq. (21a) is also obtained in precise quantum calculations of the processes $e \longrightarrow e\nu\bar{\nu}$ and $e \longrightarrow ea$ in an external field [8, 13] (the last effect is possible in the presence of direct axion–fermion coupling).

The results for the intensity of axion emission that are given by (20) and (21) can be obtained from expression (6) by means of similar operations leading to

$$S_a \approx \frac{g_\gamma^2Q^2\omega^4}{3^{5/2}\pi^2\tilde{m}}\left(\frac{E_Q}{m_Q}\right)^{10}\exp\left[-\sqrt{3}\tilde{m}\left(\frac{m_Q}{E_Q}\right)^2\right], \quad (22)$$

$$S_a \approx \frac{g_\gamma^2\alpha m_e^5}{3^{5/2}\pi^2m}\chi^5\exp\left[-\sqrt{3}\frac{(m/m_e)}{\chi}\right]. \quad (23)$$

(ii) $\tilde{m} \ll 1$. In this case, we can set $\tilde{m} = 0$ and approximate the Bessel functions involved by Macdonald functions, as was done in the classical problem of synchrotron radiation [14]. The momentum-transfer distribution obtained from the general expression (11) then takes the form

$$W_T = \frac{2}{9}\frac{g_\gamma^2 Q^2 \omega^3}{(2\pi)^4}\int_0^1 d\bar{\nu}\int_0^1 d\cos\theta\int_0^\infty d\nu\nu^3 \times\left[\varepsilon(1-\bar{\nu}^2\sin^2\theta)K_{1/3}^2\left(\frac{\nu}{3}\varepsilon^{3/2}\right)+\varepsilon^2 K_{2/3}^2\left(\frac{\nu}{3}\varepsilon^{3/2}\right)\right]. \quad (24)$$

After some simple algebra, we obtain the integrated probability of the process per unit time. The result is

$$W_T = \frac{13Q^2 g_\gamma^2 \omega^3}{3^{5/2}\cdot 32(2\pi)^2}\left(\frac{E_Q}{m_Q}\right)^5. \quad (25)$$

As in the problem of synchrotron radiation, we obtain $\nu_{\text{eff}} \sim \left(\frac{E_Q}{m_Q}\right)^3$, and the condition justifying the disregard of recoil can be represented as

$$\left(\frac{\omega}{m_Q}\right)\left(\frac{E_Q}{m_Q}\right)^2 \ll 1. \quad (26)$$

For the process $e \longrightarrow e\gamma a$ in a magnetic field, the result corresponding to (25) assumes the form

$$W_T = \frac{13\alpha g_\gamma^2 m_e^4}{3^{5/2}\cdot 32(2\pi)^2 q_0}\chi^3, \quad \chi \ll 1. \quad (27)$$

In the case being considered, the intensity of axion emission is given by

$$S_a = \frac{g_\gamma^2 Q^2 \omega^4}{72(2\pi)^2}\left(\frac{E_Q}{m_Q}\right)^8. \quad (28)$$

For the process $e \longrightarrow e\gamma a$ in a magnetic field, the analogous result is

$$S_a = \frac{g_\gamma^2 \alpha m_e^4}{72(2\pi)^2}\chi^4. \quad (29)$$

The χ dependence in expressions (27) and (29) coincides with the corresponding result from [8] for the process $e \longrightarrow ea$.

4. COULOMB MECHANISM OF RADIATIVE AXION EMISSION

In this section, we consider radiative axion emission by the alternating field generated by a classical charge Q_1 executing a nonrelativistic infinite motion in the field of an immobile Coulomb center of charge Q_2, assuming for the sake of definiteness that $Q_1Q_2 < 0$. In the ensuing calculations, we will use the representation of the probability in (5) in terms of currents by involving the substitution in (7). The relevant Fourier components of the current density can be obtained from the equation for the trajectory in [11] and are given by

$$\begin{aligned} j_1 &= i\pi Q_1 g H_{i\nu}^{(1)'}(i\nu\varepsilon),\\ j_2 &= i\pi Q_1 g\frac{\sqrt{\varepsilon^2-1}}{\varepsilon}H_{i\nu}^{(1)}(i\nu\varepsilon),\\ j_3 &= 0,\\ j_0 &= (k_1 j_1 + k_2 j_2)/k_0, \end{aligned} \quad (30)$$

where $H_p^{(1)}(x)$ and $H_p^{(1)'}(x)$ are, respectively, a Hankel function of the first kind and its derivative with respect to the argument; μ is the mass of the charge Q_1; and v_0 and ρ is its velocity at infinity and its impact parameter; for the sake of brevity, use has also been made of the notation

$$\nu = \frac{k_0\alpha_{12}}{\mu v_0^3}, \quad \alpha_{12} = |Q_1Q_2|, \quad \varepsilon = \sqrt{1+\frac{\mu^2 v_0^4\rho^2}{\alpha_{12}^2}}, \quad g = \frac{\alpha_{12}}{\mu v_0^2}. \quad (31)$$

The derivation of the expressions in (30) was performed under the condition

$$k_0\alpha_{12} \ll \mu v_0^2 \quad (32a)$$

(k_0 is the total energy of the emitted axion and photon), which is in fact satisfied if recoil can be disregarded:

$$k_0 \ll \frac{\mu v_0^2}{2}. \quad (32b)$$

With the aid of relations (30) and (31), the probability of the process can be represented as

$$W = \frac{g_\gamma^2\alpha_1 g^2}{48(2\pi)^2}\int_\Gamma d^4k\frac{(k^2-m^2)^3}{k^6}\left\{[H_{i\nu}^{(1)'}(i\nu\varepsilon)]^2\left(1-\frac{k_1^2}{k_0^2}\right) - \frac{\varepsilon^2-1}{\varepsilon^2}[H_{i\nu}^{(1)}(i\nu\varepsilon)]^2\left(1-\frac{k_2^2}{k_0^2}\right)\right\}, \quad (33)$$

$$\alpha_1 = Q_1^2.$$

Here, the integral with respect to the spatial components of k,

$$N = \frac{3}{\pi k_0^3}\int d^3k\frac{(k^2-m^2)^3}{k^6}\left(1-\frac{k_{1,2}^2}{k_0^2}\right),$$

$$|\mathbf{k}| \le \sqrt{k_0^2-m^2},$$

is given by

$$N = \sqrt{s}\left[21 - 8s - \frac{49}{5}s^2 - \frac{3}{2\sqrt{s}}(1-s)(7+2s-s^2)\ln\frac{1+\sqrt{s}}{1-\sqrt{s}}\right], \quad (34)$$

$$s = 1 - \frac{m^2}{k_0^2}.$$

Physically, the differential cross section for inelastic scattering on a Coulomb center is a more appropriate feature of the process. By definition, we have

$$\frac{d\sigma}{dk_0} = \int_0^\infty \frac{dW}{dk_0} \times 2\pi\rho d\rho.$$

Using the above relations, we obtain

$$\frac{d\sigma}{dk_0} = \frac{g_\gamma^2 \alpha_1 \alpha_{12}^3 k_0^2}{288\mu^3 v_0^5} N\left|H_{i\nu}^{(1)}(i\nu)H_{i\nu}^{(1)'}(i\nu)\right|, \quad (35)$$

where the quantity ν is given by the first relation in (31).

The asymptotic representations of expression (35) are determined by the threshold and the high-energy (in the axion mass) behavior of the factor

$$N = \begin{cases} \frac{64}{105}s^{9/2}, & s \longrightarrow 0 \\ \frac{16}{5}, & s \longrightarrow 1 \end{cases} \quad (36)$$

and by the asymptotic expressions for the Hankel functions at large and small ν [these cases can be consistent with the approximation specified by (32a) and (32b) since ν is the product of the small quantity $\frac{k_0\alpha_{12}}{\mu v_0^2}$ and the large quantity v_0^{-1}] in terms of elementary functions. For the product of the Hankel functions in (35), the required asymptotic forms are

$$\left|H_{i\nu}^{(1)}(i\nu)H_{i\nu}^{(1)'}(i\nu)\right| = \begin{cases} \frac{4}{\pi\sqrt{3}\nu}, & \nu \gg 1 \\ \frac{4}{\pi^2\nu}\left[\ln\frac{2}{\nu} - C\right], & \nu \ll 1, \end{cases} \quad (37)$$

where C is the Euler constant.

For the case of unlike charges being considered, the total cross section cannot be estimated correctly because use is made here of the low-energy approximation. However, the cutoff exponential factor $\exp(-2\pi\nu)$ appears in (35) under the condition $Q_1Q_2 > 0$, and the two conditions in (32a) and (32b) are satisfied in the effective region of integration if the additional constraint $\alpha_{12} \gg v_0$ holds. Technically, however, evaluation of the integral for this case involves serious difficulties.

5. DISCUSSION

If there is no direct axion–fermion coupling in the tree approximation (*aee*), the Primakoff effect–induced synchrotron axion emission considered in Section 3 is a dominant mechanism of axion generation in the case of an ultrarelativistic motion of an electron in a magnetic field. As a matter of fact, its role can be assessed in very strong magnetic fields of about 10^{12}–10^{14} G, which are possible only in the shells of neutron stars [15]. Under such conditions, however, it is necessary to take into account, in addition, the presence of a dense photon gas of temperature in the range 10^8–10^{10} K, in which case the crossed process $\gamma e \longrightarrow ae$, which proceeds through an intermediate resonance photon state and which is also caused by the Primakoff effect [16], becomes possible. A comparison of the present result as given by (29) with the results from [16] shows that the contribution of the synchrotron mechanism to the axion emissivity is smaller by a few orders of magnitude. It is obvious that, in the presence of direct coupling (*aee*), the process $e \longrightarrow ea$ in an external field is always dominant over the process $e \longrightarrow e\gamma a$ considered here, the dependence on the parameter χ being the same in the two cases.

From the viewpoint of practice, the results from Section 4 as applied to calculating the axion emissivity of the Sun seem more interesting. The Primakoff effect caused by the interaction of blackbody radiation of temperature 1.3 keV at the center of the Sun with the fluctuating electric field of charged particles (electrons, protons) at a concentration of about 10^{26} cm^{-3} proves to be a dominant mechanism of solar-axion generation in this case as well. According to the results presented in [2], the axion emissivity L_a of the Sun is given by

$$L_a \approx 10^{-3} L_\odot (g_\gamma 10^{10}\ \text{GeV})^2, \quad (38)$$

where $L_\odot = 3.86 \times 10^{33}$ erg/s is the photon emissivity. In the case being considered, the condition of applicability of expression (35) is satisfied approximately at k_0 values up to 1 keV [in expressions (36) and (37), it is then necessary to go over to the limit $s \longrightarrow 1$ and to consider ν values much less than unity]. In the above energy range, an evaluation of the axion emissivity within the standard solar model [17] yields a result that is nearly three orders of magnitude less than the expression in (38). However, the emissivity in (38) is an integrated one at a mean axion energy of about 4 to 5 keV, and the contribution of the generation mechanism considered here is commensurate, in the energy region extending to 1 keV, with that which is generally accepted. It should be noted, however, that both the experiments being presently conducted and the planned experiments are aimed at detecting axions by their conversion into x-ray photons in the energy region around

a few keV and higher. Thus, the above comment will become of practical importance, should searches for solar axions be performed at lower energies as well.

ACKNOWLEDGMENTS

I am grateful to Yu.O. Yakovlev for technical assistance.

REFERENCES

1. R. D. Reccei and H. R. Quinn, Phys. Rev. Lett. **38**, 1440 (1977).
2. K. van Bibber, P. M. McIntyre, D. E. Morris, and G. G. Raffelt, Phys. Rev. D **39**, 2089 (1989).
3. F. T. Avignone III *et al.*, Yad. Fiz. **61**, 1237 (1998) [Phys. At. Nucl. **61**, 1137 (1998)].
4. M. Minowa, Yad. Fiz. **61**, 1217 (1998) [Phys. At. Nucl. **61**, 1117 (1998)].
5. G. G. Raffelt, Phys. Rep. **198**, 1 (1990).
6. G. G. Raffelt, *Stars as Laboratories for Fundamental Physics* (Univ. of Chicago Press, Chicago, 1996).
7. A. V. Borisov and V. Yu. Grishina, Zh. Éksp. Teor. Fiz. **106**, 1553 (1994) [JETP **79**, 837 (1994)].
8. V. V. Skobelev, Zh. Éksp. Teor. Fiz. **112**, 25 (1997) [JETP **85**, 13 (1997)].
9. V. V. Skobelev, Yad. Fiz. **61**, 2236 (1998) [Phys. At. Nucl. **61**, 2123 (1998)].
10. R. D. Peccei, *CP Violation* (World Sci., Singapore, 1989).
11. L. D. Landau and E. M. Lifshitz, *The Classical Theory of Fields* (Nauka, Moscow, 1967; Pergamon, Oxford, 1975).
12. I. S. Gradshteyn and I. M. Ryzhik, *Table of Integrals, Series, and Products* (Nauka, Moscow, 1971; Academic, New York, 1980).
13. V. V. Skobelev, Zh. Éksp. Teor. Fiz. **107**, 322 (1995) [JETP **80**, 170 (1995)].
14. A. A. Sokolov, I. M. Ternov, and V. G. Bagrov, in *Synchrotron Radiation* (Nauka, Moscow, 1976), p. 18.
15. A. D. Kaminker, K. P. Levenfish, and D. G. Yakovlev, Pis'ma Astron. Zh. **17**, 1090 (1991) [Sov. Astron. Lett. **17**, 450 (1991)].
16. A. V. Borisov and K. V. Zhukovskii, Yad. Fiz. **58**, 1298 (1995) [Phys. At. Nucl. **58**, 1218 (1995)].
17. J. Bahcall *et al.*, Rev. Mod. Phys. **54**, 767 (1982).

Translated by A. Isaakyan

Physics of Atomic Nuclei, Vol. 63, No. 11, 2000, pp. 1969–1972. From Yadernaya Fizika, Vol. 63, No. 11, 2000, pp. 2061–2064.

ELEMENTARY PARTICLES AND FIELDS
Theory

Some Comments on the Branching Ratios for $\bar{n}p$ Annihilation into $\pi\pi$, $K\bar{K}$, and $\pi\eta$ Channels*

A. E. Kudryavtsev**
Institute of Theoretical and Experimental Physics, Bol'shaya Cheremushkinskaya ul. 25, Moscow, 117259 Russia
Received September 27, 1999; in final form, December 16, 1999

Abstract—We present some remarks on the $\bar{n}p$ partial branching ratios in flight at low momenta of antineutrons measured by the OBELIX Collaboration. A comparison is made to the known branching ratios from the $p\bar{p}$-atomic states. The branching ratio for the reaction $\bar{n}p \longrightarrow \pi^+\pi^0$ is found to be suppressed in comparison to what follows from the $p\bar{p}$ data. It is also shown that there is no so-called dynamical $I = 0$ amplitude suppression for the process $N\bar{N} \longrightarrow K\bar{K}$. *© 2000 MAIK "Nauka/Interperiodica".*

1. SOME USEFUL DEFINITIONS

Let us first consider the $N\bar{N}$ system. By definition, $|I, I_3\rangle$ is the isospin wave function of the $N\bar{N}$ system with isospin I and its projection I_3. Using the notation of [1], we write the following relations between the physical states $|N\bar{N}\rangle$ and states of definite isospin $|I, I_3\rangle$:

$$|p\bar{p}\rangle = \frac{1}{\sqrt{2}}[|1, 0\rangle - |0, 0\rangle],$$
$$|n\bar{n}\rangle = \frac{1}{\sqrt{2}}[|1, 0\rangle + |0, 0\rangle]. \quad (1)$$

On the contrary, in terms of physical states the wave function $|I, I_3\rangle$ is sought for the isosinglet state as

$$|0, 0\rangle = -\frac{1}{\sqrt{2}}[|p\bar{p}\rangle + |n\bar{n}\rangle], \quad (2)$$

and for the isotriplet as

$$|1, -1\rangle = |n\bar{p}\rangle, \quad |1, 0\rangle = \frac{1}{\sqrt{2}}[|p\bar{p}\rangle - |n\bar{n}\rangle],$$
$$|1, 1\rangle = |\bar{n}p\rangle. \quad (3)$$

Each wave function is normalized as

$$\langle N\bar{N}|N\bar{N}\rangle = 1, \quad \langle I, I_3|I, I_3\rangle = 1.$$

Let us also define the wave function for the hadron final state $|a\rangle$ with definite isospin I: $|a\rangle_I$. We shall use the notation $\hat{V}_a^I$ for the transition operator from the initial $|I, I_3\rangle_{N\bar{N}}$ state to $|a\rangle_I$, and

$$V_a^I = {}_I\langle a|\hat{V}_a^I|I, I_3\rangle_{N\bar{N}} \quad (4)$$

is a matrix element for this operator. It does not depend on I_3. Evidently,

$$\hat{V}_a^I|J, J_3\rangle_{N\bar{N}} = 0$$

in the case $I \neq J$.

2. MATRIX ELEMENTS FOR THE TRANSITIONS $N\bar{N} \longrightarrow \pi\pi$ AND $N\bar{N} \longrightarrow K\bar{K}$

Consider only the transitions to the final $\pi\pi$ states from the initial $N\bar{N}$ S wave ($^3S_1$). In this case, the $\pi\pi$ system is produced in the $I = 1$ isospin state. So there is only one operator $\hat{V}_\pi^1$. The expansion of the $|\pi\pi\rangle$ wave function in terms of the states with definite isospin has the form

$$|\pi^+\pi^-\rangle = \frac{1}{\sqrt{3}}|0, 0\rangle + \frac{1}{\sqrt{2}}|1, 0\rangle + \frac{1}{\sqrt{6}}|2, 0\rangle,$$
$$|\pi^+\pi^0\rangle = \frac{1}{\sqrt{2}}|1, 1\rangle - \frac{1}{\sqrt{2}}|2, 1\rangle. \quad (5)$$

Thus, using definitions (1), (3), and (4), we get

$$\langle\pi^+\pi^0|\hat{V}_\pi^1|\bar{n}p\rangle = \frac{1}{\sqrt{2}}V_\pi^1,$$
$$\langle\pi^+\pi^-|\hat{V}_\pi^1|p\bar{p}\rangle = \frac{1}{2}V_\pi^1. \quad (6)$$

This means that the process $p\bar{p} \longrightarrow \pi^+\pi^-$ is to be suppressed at least by a factor of two in comparison to $\bar{n}p \longrightarrow \pi^+\pi^0$.

* This article was submitted by the author in English.
** e-mail: KUDRYAVTSEV@vxitep.itep.ru

Let us now consider the transitions into $K\bar{K}$ final states. The isospin wave functions for $K\bar{K}$ states have the following form:

$$|K^+K^-\rangle = \frac{1}{\sqrt{2}}[|1,0\rangle - |0,0\rangle],$$
$$|K^0\bar{K}^0\rangle = -\frac{1}{\sqrt{2}}[|1,0\rangle + |0,0\rangle], \quad (7)$$

$$|K^+\bar{K}^0\rangle = |1,1\rangle, \quad |K^0K^-\rangle = -|1,-1\rangle. \quad (8)$$

In this case, the $|K\bar{K}\rangle$ final state is indeed a mixture of both $I = 0$ and $I = 1$ isospin states ($I_3 = 0$). Hence, both operators, $\hat{V}_K^1$ and $\hat{V}_K^0$, make a contribution to this reaction and

$${}_K\langle 1, I_3|\hat{V}_K^1|1, I_3\rangle_{N\bar{N}} = V_K^1,$$
$${}_K\langle 0,0|\hat{V}_K^0|0,0\rangle_{N\bar{N}} = V_K^0.$$

We can calculate the matrix elements between the physical states in terms of V_K^1 and V_K^0:

$$\langle K^+K^-|\hat{V}_K|p\bar{p}\rangle = \frac{V_K^0 + V_K^1}{2},$$
$$\langle K^0\bar{K}^0|\hat{V}_K|p\bar{p}\rangle = \frac{V_K^0 - V_K^1}{2}, \quad (9)$$

$$\langle K^+\bar{K}^0|\hat{V}_K|\bar{n}p\rangle = V_K^1. \quad (10)$$

The matrix elements (9) and (10) are related to the corresponding partial cross sections:

$$\sigma = 4\pi\frac{q}{k}|\langle f|V|i\rangle|^2,$$

where q and k are the final and initial c.m. momenta. We get agreement for the expression (10) with what is given in [1], but expressions (9) differ from that of [1]. Namely, by redefining the operators according to Eq. (32) of [1], we get

$$\sigma(p\bar{p} \longrightarrow K^+K^-) + \sigma(p\bar{p} \longrightarrow K^0\bar{K}^0) = |A_0|^2 + |A_1|^2 \quad (11)$$

and

$$\sigma(\bar{n}p \longrightarrow K^+\bar{K}^0) = 2|A_1|^2. \quad (12)$$

Notice that the factor of 2 on the right-hand side of Eq. (12) is not present in Eq. (35) in [1]. Historically, this factor was also lost in [2, 3], and this error was reproduced later in some review papers, see, e.g., [4, 5]. That is why the conclusion [1–3] on $I = 0$ amplitude suppression seems to be incorrect and is to be revised. We shall discuss this problem in Section 4.

3. SOME RELATIONS BETWEEN BRANCHING RATIOS IN $p\bar{p}$- AND $\bar{n}p$-ANNIHILATION PROCESSES

Let us first consider the $\pi\pi$ case. By definition of the branching ratio, we have

$$\mathrm{Br}_{\pi^+\pi^0}(\bar{n}p) = \frac{\sigma(\bar{n}p \longrightarrow \pi^+\pi^-)}{\sigma(\bar{n}p \longrightarrow \mathrm{all})}$$

and a similar expression for the $p\bar{p}$ case. So the ratio of branching ratios is

$$\frac{\mathrm{Br}_{\pi^+\pi^0}(\bar{n}p)}{\mathrm{Br}_{\pi^+\pi^-}(\bar{p}p)} = \frac{\sigma(\bar{n}p \longrightarrow \pi^+\pi^0)}{\sigma(\bar{n}p \longrightarrow \mathrm{all})} : \frac{\sigma(\bar{p}p \longrightarrow \pi^+\pi^-)}{\sigma(\bar{p}p \longrightarrow \mathrm{all})}. \quad (13)$$

Notice that, at low energies, we have if only the S-wave contributes,

$$\sigma(p\bar{n} \longrightarrow \pi^+\pi^0) = 4\pi\frac{3}{4}\left|\langle\pi\pi|\hat{V}_\pi^1|p\bar{n}\rangle\right|^2\frac{q}{k} \quad (14)$$

and

$$\sigma(p\bar{p} \longrightarrow \pi^+\pi^-) = 4\pi\frac{3}{4}C^2(k)\left|\langle\pi\pi|\hat{V}_\pi^1|p\bar{p}\rangle\right|^2\frac{q}{k}. \quad (15)$$

Here, $C^2(k)$ is the Gamow factor,

$$C^2(k) = \frac{2\pi}{ka_\mathrm{B}}\Big/\left[1 - \exp\left(-\frac{2\pi}{ka_\mathrm{B}}\right)\right],$$

and $a_\mathrm{B} = 57.6$ fm is the $p\bar{p}$ Bohr radius. Taking into account (13)–(15), we get

$$\frac{\mathrm{Br}_{\pi^+\pi^0}(\bar{n}p)}{\mathrm{Br}_{\pi^+\pi^-}(\bar{p}p)} = \frac{\left|\langle\pi^+\pi^0|\hat{V}_\pi^1|\bar{n}p\rangle\right|^2}{\left|\langle\pi^+\pi^-|\hat{V}_\pi^1|\bar{p}p\rangle\right|^2} \times \frac{[\beta C^{-2}(k)\sigma^{\mathrm{ann}}(p\bar{p} \longrightarrow \mathrm{all})]}{[\beta\sigma^{\mathrm{ann}}(\bar{n}p \longrightarrow \mathrm{all})]} \approx 2R, \quad (16)$$

where R is now a well-defined and finite quantity:

$$R = \frac{\lim\limits_{k\to 0}[\beta C^{-2}(k)\sigma^{\mathrm{ann}}(p\bar{p})]}{\lim\limits_{k\to 0}[\beta\sigma^{\mathrm{ann}}(\bar{n}p)]}. \quad (17)$$

From the experimental data of [6, 7], we get the value of R at low momenta of the incident antiproton ($p_\mathrm{lab} = 50$–70 MeV/c):

$$R = \frac{32 \pm 2}{25.3 \pm 1.0} \approx 1.26 \pm 0.10. \quad (18)$$

Notice that this value coincides with what follows from the experimental data on annihilation of antiprotons on deuterons [8]. Thus, we conclude that the data [7] on the total annihilation $\bar{n}p$ cross section are in agreement with the results of quite independent experiments

for the annihilation of antiprotons on deuterons [8]. One can find a more detailed discussion of the quantity R extracted from different data on deuterons and some heavier nuclei in the review paper of Bendiscioli and Kharzeev [9].

The case of kaons looks very similar. Using (9) and (10), as well as the definition of the ratio R (17), one gets the following relation between branching ratios for the reactions $p\bar{p} \longrightarrow K^+K^-$, $p\bar{p} \longrightarrow K^0\bar{K}^0$, and $\bar{n}p \longrightarrow K^+\bar{K}^0$:

$$\frac{|V_K^1|^2 + |V_K^0|^2}{2|V_K^1|^2} = R\frac{\mathrm{Br}(p\bar{p} \longrightarrow K^+K^-) + \mathrm{Br}(p\bar{p} \longrightarrow K^0\bar{K}^0)}{\mathrm{Br}(\bar{n}p \longrightarrow K^+\bar{K}^0)}. \quad (19)$$

4. ANALYSIS OF THE EXPERIMENTAL SITUATION

In [7], the branching ratio for the reaction $\bar{n}p \longrightarrow \pi^+\pi^0$ in the momentum interval 50–150 MeV/c (S wave) was found to be

$$\mathrm{Br}(\bar{n}p \longrightarrow \pi^+\pi^0) = (2.3 \pm 0.4) \times 10^{-3}. \quad (20)$$

This value is to be compared with what follows from the $p\bar{p}$-atomic experiment for the reaction $p\bar{p} \longrightarrow \pi^+\pi^-$. The separation of the S- and P-wave contributions to the last reaction was provided in [10, 11]. For the branching ratio into the $\pi^+\pi^-$ channel from the atomic S state we get $(2.37 \pm 0.23) \times 10^{-3}$ [10] and $(2.04 \pm 0.17) \times 10^{-3}$ [11].

Substituting these numbers into (16), we get an evident contradiction. This means that something is wrong with the branching ratios. If one believes the experimental branching ratios for both $\bar{n}p$ and $\bar{p}p$ channels, the only possible way to solve the problem is to suggest that the $p\bar{p}$-atomic wave function at small distances has an abnormal admixture of the $\bar{n}n$ component. We shall discuss this hypothesis in the next section.

Let us now discuss the case of kaons. The only information on the branching ratio $N\bar{N} \longrightarrow K\bar{K}$ for isospin $I = 1$ channel was for a long time available from the old data for absorption of antiprotons on deuterons [12],

$$\mathrm{Br}(\bar{p}n \longrightarrow K^0K^-) = (1.47 \pm 0.21) \times 10^{-3}.$$

Nowadays, the OBELIX collaboration gives [7] (S wave)

$$\mathrm{Br}(\bar{n}p \longrightarrow K^+K_S) = (0.92 \pm 0.23) \times 10^{-3}.$$

This means that the branching ratio into $K^+\bar{K}^0$ is

$$\mathrm{Br}(\bar{n}p \longrightarrow K^+\bar{K}^0) = 2\mathrm{Br}(\bar{n}p \longrightarrow K^+K_S) = (1.84 \pm 0.46) \times 10^{-3}.$$

It is seen that this last number for the branching ratio does not contradict the old data by Bettini *et al.* [12].

At the same time, from the ASTERIX experiments [3, 13] we have

$$\mathrm{Br}(p\bar{p} \longrightarrow K^+K^-) = (1.08 \pm 0.05) \times 10^{-3},$$

$$\mathrm{Br}(p\bar{p} \longrightarrow K^0\bar{K}^0) = (0.83 \pm 0.05) \times 10^{-3}.$$

Using these values and taking into account Eq. (19), we get

$$|V_K^0| \approx 1.3|V_K^1|. \quad (21)$$

So we conclude that there is no evidence for any suppression of the $I = 0$ amplitude for the reaction $N\bar{N} \longrightarrow K\bar{K}$ in the S wave. The dynamical selection rule for this process declared in [1–5] is the consequence of incorrect formulas for the branching ratios used in [1, 2].

Let us also discuss the case of the $\pi\eta$ channel. From the experimental data reported in [7], it follows that in the momentum interval 150–250 MeV/c (P wave)

$$\mathrm{Br}(\bar{n}p \longrightarrow \pi^+\eta) = (0.99 \pm 0.22) \times 10^{-3}.$$

At the same time, from [10] we have

$$\mathrm{Br}(p\bar{p} \longrightarrow \pi^0\eta) = (7.7 \pm 1.13) \times 10^{-4}.$$

So again we arrive the conclusion that the ratio

$$\frac{\mathrm{Br}(\bar{n}p \longrightarrow \pi^+\eta)}{\mathrm{Br}(\bar{p}p \longrightarrow \pi^0\eta)}$$

is significantly less than $2R$ [see (16)].

5. A POSSIBLE SOLUTION OF THE PROBLEM FOR THE $N\bar{N} \longrightarrow \pi\pi$ BRANCHING RATIOS

In line with [1, 14, 15], we assume that the wave function for a $p\bar{p}$ atom at small distances is a superposition of $|p\bar{p}\rangle$ and $|n\bar{n}\rangle$ configurations, i.e.,

$$|\psi_{\mathrm{at}}\rangle = \frac{1}{\sqrt{1+\epsilon^2}}[|p\bar{p}\rangle + \epsilon|n\bar{n}\rangle]. \quad (22)$$

In terms of the states of definite isospin, this means that

$$|\psi_{\mathrm{at}}\rangle = \frac{1}{\sqrt{2(1+\epsilon^2)}}[(1-\epsilon)|1, 0\rangle - (1+\epsilon)|0, 0\rangle]. \quad (23)$$

So it follows immediately that

$$\frac{\mathrm{Br}(\psi_{\mathrm{at}} \longrightarrow \pi^+\pi^-)}{\mathrm{Br}(\bar{n}p \longrightarrow \pi^+\pi^0)} = \frac{(1-\epsilon)^2}{2(1+\epsilon^2)R}. \quad (24)$$

The case $\epsilon = 0$ corresponds to the usual suggestion of the absence of the $n\bar{n}$ component in the $p\bar{p}$ atom. In the limit $\epsilon = -1$, the atomic state is that of definite isos-

pin $I = 1$. Substituting the experimental numbers for the $\pi\pi$ branching ratios (see Section 4), we conclude that it is possible to fit the parameter ϵ so Eq. (23) is justified. For example, taking $\mathrm{Br}(p\bar{p} \longrightarrow \pi^+\pi^-) = 1.87$ (lower limit) and $\mathrm{Br}(\bar{n}p \longrightarrow \pi^+\pi^0) = 2.7$ (upper limit), we get $\epsilon = -2.24$, which corresponds to the value of the mixing angle $\cos\alpha = 1/\sqrt{1+\epsilon^2}$, where $\alpha \approx 66°$. This means that the admixture of the $\bar{n}n$ component should be large to fit the experimental data.

6. CONCLUSION

The data on the $\bar{n}p$ total annihilation cross section presented by the OBELIX collaboration [7] are in agreement with the data on the value of the ratio R determined from the absorption of antiprotons on deuterons (see [6] and references in [8]).

The branching ratios for the reactions $\bar{n}p \longrightarrow \pi^+\pi^0$ and $\bar{n}p \longrightarrow \pi^+\eta$ at low energies [7] seem to be too large in comparison to what follows from the analysis of the known branching ratios for the $p\bar{p}$ atom.

The branching ratio for the reaction $\bar{n}p \longrightarrow K^+K_S$ is in agreement with the known branching ratio for the reaction $\bar{p}n \longrightarrow K^0K^-$ from the deuteron data [12]. There is no suppression of the $I = 0$ $N\bar{N} \longrightarrow K\bar{K}$ reaction amplitude in the S wave (no specific dynamical selection rule).

Some admixture of the $|n\bar{n}\rangle$ component in the $p\bar{p}$-atomic wave function may help in solving problems with the branching ratio into two pions and $\pi\eta$. However, to solve this problem, the admixture should be large enough.

ACKNOWLEDGMENTS

I am very grateful to G. Bendiscioli, B. Giacobbe, B.O. Kerbikov, A. Rotondi, A. Zenoni, and A. Zoccoli for a stimulating discussion on the preliminary results of this study.

This work was supported in part by the Russian Foundation for Basic Research (project no. 96-15-96578).

REFERENCES

1. J. Jaenicke, B. Kerbikov, and H. Pirner, Z. Phys. A **339**, 297 (1991).
2. R. Landua, in *Proceedings of the Proeuropean Symposium on Proton–Antiproton Interactions and Fundamental Symmetries, Mainz, 1988*; Nucl. Phys. B (Proc. Suppl.) **8**, 179 (1989).
3. M. Doser *et al.*, Phys. Lett. B **215**, 792 (1988).
4. C. Amsler and F. Myhrer, Annu. Rev. Nucl. Sci. **41**, 219 (1991).
5. C. Dover, T. Gutsche, M. Maruyama, and A. Faessler, Prog. Part. Nucl. Phys. **29**, 87 (1992).
6. A. Bertin *et al.*, Phys. Lett. B **369**, 77 (1996).
7. OBELIX Collab. (B. Giacobbe), A talk given at the LEAP'96 Conference, Dinkelsbuhl, Germany, 1996; A. Bertin *et al.*, Nucl. Phys. B (Proc. Suppl.) **56A**, 227 (1997).
8. R. Bizzarri *et al.*, Nuovo Cimento A **22**, 225 (1974); T. Kalogeropulos *et al.*, Phys. Rev. D **22**, 2585 (1980); J. Riedelberger *et al.*, Phys. Rev. C **40**, 2717 (1989).
9. G. Bendiscioli and D. Kharzeev, Riv. Nuovo Cimento **17** (6), 1 (1994).
10. K. Peters, in *Proceedings of the LEAP'94 Conference, Bled, Slovenia, 1994* (World Sci., Singapore, 1994), p. 3.
11. C. J. Batty, Nucl. Phys. A **601**, 425 (1996).
12. A. Bettini *et al.*, Nuovo Cimento A **62**, 1038 (1969).
13. M. Doser *et al.*, Nucl. Phys. A **486**, 493 (1988).
14. J. Carbonell, G. Ihle, and J. M. Richard, Z. Phys. A **334**, 329 (1989).
15. E. Klempt, Phys. Lett. B **244**, 122 (1990).

Physics of Atomic Nuclei, Vol. 63, No. 11, 2000, pp. 1973–1975. From Yadernaya Fizika, Vol. 63, No. 11, 2000, pp. 2065–2067.

ELEMENTARY PARTICLES AND FIELDS
Theory

Quark Model and Production of Neutral Strange Secondaries in Neutrino and Antineutrino Beams*

I. N. Erofeeva, V. S. Murzin, V. A. Nikonov[1)], and Yu. M. Shabelski[1)]

Institute of Nuclear Physics, Moscow State University, Vorob'evy gory, Moscow, 119899 Russia

Received June 29, 1999; in final form, January 18, 2000

Abstract—Experimental data on K^0 and Λ production in ν and $\bar{\nu}$ beams are compared with the predictions of a quark model assuming that the direct production of secondaries dominates. Disagreement of these predictions with the data suggests that there exists a considerable resonance-decay contribution to the multiplicities of product particles. *© 2000 MAIK "Nauka/Interperiodica".*

1. INTRODUCTION

It is well known that, in soft hadron–hadron collisions, the production of resonances makes an important contribution to the multiplicity of stable secondaries (such as pions and kaons). For example, in the additive quark model, the probability of direct production of a secondary hadron having spin J is proportional to the factor $2J + 1$, which means that the main parts of pions, kaons, etc. are produced via decay of vector, tensor, and higher spin resonances. These results are in reasonable agreement [1] with the experimental data on soft hadron–hadron collisions.

However, the information about the role of resonance production in hard processes is not sufficient. The mechanisms of multiparticle production in soft and hard processes can be different. So, in the present paper, we will consider the role of resonances in neutral strange secondary production in deep-inelastic interactions of high-energy neutrinos and antineutrinos with protons and neutrons.

2. EXPERIMENTAL DATA

For comparison with the quark model (QM) predictions, the experimental data [2] of the E632 collaboration were used. The experiment was done at the Fermilab Tevatron. The detector was a 15-ft bubble chamber filled with a liquid neon–hydrogen mixture which also served as the target. The bubble chamber was exposed to a neutrino beam. The neutrino beam was formed by the quadrupole triplet train, which focused secondary particles produced by the interactions of 800-GeV protons from the Tevatron.

The data sample consisted of 6459 events (5416 νNe interactions and 1043 $\bar{\nu}$Ne interactions). The neutrino interactions with a single nucleon were picked out by using a criterion of selection such as the mass of the target [3]. It allowed us to select the interactions with the peripheral nucleon or neutrino interactions without the intranuclear cascades. The neutrino–nucleon interactions could be attributed to neutrino–proton and neutrino–neutron interactions by using the total charge of the hadronic system (Table 1). This material was used for the determination of the numbers of generated K^0 and Λ particles, as well as their production rates (or parts) relative to the different groups of events (νp, νn, $\bar{\nu} p$, and $\bar{\nu} n$) (Table 2). These production rates are the results of dividing the number of K^0 and Λ particles by the total number of events in each group. In the data sample of vees of Table 2, the corrections for losses of K^0 and Λ particles caused by methodological sources (the limited volume of the bubble chamber, scanning and fitting efficiency, etc.) [2] were not taken into consideration. The statistical errors have been cited. Nevertheless, the correction coefficients taking into account these effects must be the same for the neutrino–proton and neutrino–neutron interactions.

3. QUARK MODEL PREDICTIONS

We will consider only the events with the charged current interactions (CC). In the case of interactions with sea quarks, each type of particle and antiparticle is produced in virtually the same proportion indepen-

Table 1. Experimental data from E632

Reaction	$\nu(\bar{\nu})$Ne	$\nu(\bar{\nu})N$	$N(K^0)$	$N(\Lambda)$
νp	5416	739	47	15
νn		1273	84	38
$\bar{\nu} p$	1043	282	20	7
$\bar{\nu} n$		179	7	8

* This article was submitted by the authors in English.

[1)] Petersburg Nuclear Physics Institute, Russian Academy of Sciences, Gatchina, 188350 Russia.

Table 2. Comparison of QM production probabilities with the experimental multiplicities of directly produced K^0 and Λ at large x_F

Reaction	K^0 (QM) in units of w_K	K^0 (exp.), $x_F < -0.2$	Λ (QM) in units of w_Λ	Λ (exp.), $x_F < -0.4$
νp	~0	0.008 ± 0.003	~0	0.004 ± 0.002
νn	≈1	0.005 ± 0.002	≈1	0.011 ± 0.003
$\bar{\nu} p$	≈1	0.004 ± 0.004	≈1	0.004 ± 0.004
$\bar{\nu} n$	≈2	$0.000 \pm ?$	~0	$0.000 \pm ?$

dently of their isospin projection (say, we expect equal multiplicities of K^+, K^0, $\bar{K}^0$, and K^-). However, the secondaries produced with comparatively large negative Feynman x (x_F) in the laboratory frame should contain valence quarks of the target nucleus in the target fragmentation region; therefore, different kinds of kaons should be produced with different probabilities. For the model prediction, we will use the fact that a neutrino interacts with a valence d quark, which transforms into a u quark, whereas an antineutrino interacts with a u quark, which transforms into a d quark. Thus, we have the following configurations:

$$\nu p \longrightarrow uu + u', \quad (1)$$

$$\bar{\nu} n \longrightarrow dd + d', \quad (2)$$

$$\bar{\nu} p \longrightarrow ud + d', \quad (3)$$

$$\nu n \longrightarrow ud + u'. \quad (4)$$

Here, q' means the fast quark in the laboratory frame which absorbs a W boson and determines the fragmentation in the current region. Another two quarks determine the fragmentation of the valence remnant into secondaries with comparatively large x_F in the target hemisphere.

One can see from (1)–(4) that, say, direct production of K^0 ($d\bar{s}$) with comparatively large x_F should be suppressed in process (1), where there are no valence d quarks, in comparison to another reactions. In process (2), where there are two valence d quarks, it should be about two times larger than in the cases of (3) and (4). However, if a significant part of K^0 can be produced via decay of $K^*(890)^+$ and $K^*(890)^0$, the yields of K^0 with large x_F can be more or less equal in all considered processes.

A similar situation appears in the case of secondary Λ-baryon production with large x_F. The direct Λ (containing two initial valence quarks u and d) can be produced with equal probabilities in processes (3) and (4), and their production should be suppressed in reactions (1) and (2). However, in the case of Λ production via $\Lambda\pi$ decay of isotriplet resonance $\Sigma(1385)$, the multiplicities of large-x_F Λ should be of the same order in all reactions (1)–(4).

4. COMPARISON OF THE DATA WITH QM ESTIMATES

Here, we compare the experimental results on neutral kaons and Λ hyperons in the production of ν and $\bar{\nu}$ beams with quark model predictions. The QM multiplicities of strange secondaries, assuming only direct production of a kaon containing one valence quark of the incident target nucleon and direct production of Λ containing two valence quarks of the target nucleon, are presented in Table 2. Here, w_K and w_Λ are the probabilities of K^0 and Λ production in the processes of fragmentation (or recombination) of one and two valence quarks of the target nucleon, respectively. Let us recall that, in the case of large contributions of resonance decay, the multiplicities of K^0 and Λ can be more or less equal (the exact values of their ratios are model-dependent).

One can compare the QM probability estimates with the experimental multiplicities of K^0 for $x_F < -0.2$ and of Λ for $x_F < -0.4$.

It is clear that the data for both K^0 and Λ production do not agree with these QM predictions for the direct mechanism of secondary production. Say, the multiplicity of K^0 in $\bar{\nu} n$ interactions should be equal to the sum of their multiplicities in νn and $\bar{\nu} p$ interactions, i.e., $\simeq 0.005 \pm 0.002$, which is in disagreement with the experimental value. The most natural explanation is a large resonance contribution to the multiplicities of neutral strange secondaries which changes the predictions depending on the model of resonance contributions. This idea has been discussed before (see, for example, [4]).

5. CONCLUSION

We compare the experimental data on K^0 and Λ production in ν and $\bar{\nu}$ beams on proton and neutron targets with the predictions of the quark model assuming that their direct production dominates. Disagreement of these predictions with the data allows us to suppose that there exists a considerable resonance decay contribution to the multiplicities of produced secondaries. Unfortunately, the experimental statistics are insufficient for numerical estimations.

ACKNOWLEDGMENTS

This work was supported in part by the Russian Foundation for Basic Research (project nos. 96-15.96764 and 99-02-16578) and by NATO OUTR. LG 971390.

REFERENCES

1. V. V. Anisovich, M. N. Kobrinsky, J. Nyiri, and Yu. M. Shabelski, in *Quark Model and High Energy Collisions* (World Sci., Singapore, 1985), p. 435.
2. D. DeProspo, M. Kalelkar, M. Aderholz, *et al.*, Phys. Rev. D **50**, 6691 (1994).
3. E. S. Vataga, V. S. Murzin, *et al.*, Preprint No. 97-13/464, NIIYaF MGU (Institute of Nuclear Physics, Moscow State University, Moscow, 1997).
4. V. V. Anisovich, M. G. Huber, M. N. Kobrinsky, and B. Ch. Metsch, Phys. Rev. D **42**, 3045 (1990).

Physics of Atomic Nuclei, Vol. 63, No. 11, 2000, pp. 1976–1982. Translated from Yadernaya Fizika, Vol. 63, No. 11, 2000, pp. 2068–2074.

ELEMENTARY PARTICLES AND FIELDS
Theory

Solving a Relativistic Quasipotential Equation for a Nonlocal Separable Interaction

Yu. D. Chernichenko
Gomel State Technical University, Gomel, Belarus
Received June 3, 1999; in final form, February 1, 2000

Abstract—Within the relativistic quasipotential approach to quantum field theory, a method is developed for solving a quasipotential equation for a nonlocal separable quasipotential simulating the interaction of two relativistic particles of unequal masses. © *2000 MAIK "Nauka/Interperiodica".*

1. INTRODUCTION

Nonlocal separable potentials are of interest and value not only because the Schrödinger equation can be solved for a great number of such potentials, but also because they are extensively used in nuclear physics and in many-body problems. In particular, nonlocal separable interactions were invoked in applying Faddeev equations to the three-body problem. The approach relying on such potentials proved to be seminal in solving inverse problems [1]. However, this approach cannot be applied to essentially relativistic systems [2, 3]. By way of example, we indicate that, for systems consisting of light quarks, the contribution of relativistic corrections to the interaction Hamiltonian is commensurate with the main, nonrelativistic, term. A relativistic description is also necessary in dealing with radiative decays of mesons and nucleon resonances, where the energy of the emitted photon may be commensurate with or even greater than the constituent quark mass.

The quasipotential approach proposed in [4] proved to be a viable tool for constructing a relativistic description of two-particle systems [5]. In the present study, a finite-difference quasipotential equation involving a nonlocal separable quasipotential simulating the interaction between two relativistic spinless particles of unequal masses ($m_1 \neq m_2$) is solved within the quasipotential approach developed in [6]. The approach relies on the equation constructed in [7] for the amplitude of scattering of two relativistic particles of unequal masses. In the system of units where $\hbar = c = 1$, this equation is given by

$$A(\mathbf{p}', \mathbf{q}') = -\frac{\mu}{2\pi}\tilde{V}(\mathbf{p}', \mathbf{q}'; E_{q'}) + (2\pi)^{-3}\int d\Omega_{k'}\frac{\tilde{V}(\mathbf{p}', \mathbf{k}'; E_{q'})A(\mathbf{k}', \mathbf{q}')}{\sqrt{S_{q'}} - \sqrt{S_{k'}} + i\varepsilon}, \quad (1)$$

where $d\Omega_{k'} = d\mathbf{k}'/\sqrt{1 + (\mathbf{k}'/m')^2}$, $E_{q'} = \sqrt{m'^2 + \mathbf{q}'^2}$, and $\mu = m'^2/(m_1 + m_2)$.

It represents a relativistic generalization of the Lippmann–Schwinger equation in the spirit of Lobachevski geometry, which is realized on the upper half of the mass hyperboloid $p'^2 = m'^2$, and describes the scattering of an effective relativistic particle of mass $m' = \sqrt{m_1 m_2}$ with a relative 3-momentum $\mathbf{k}'$ on the quasipotential $\tilde{V}(\mathbf{p}', \mathbf{q}'; E_{q'})$, the total c.m. energy of the particles involved being proportional to the energy of one effective relativistic particle of mass m' [7],

$$\sqrt{S_{k'}} = \sqrt{m_1^2 + \mathbf{k}^2} + \sqrt{m_2^2 + \mathbf{k}^2} = \frac{m'}{\mu}\sqrt{m'^2 + \mathbf{k}'^2}.$$

We further introduce the wave function

$$\Psi_{q'}(\mathbf{p}') = (2\pi)^3\sqrt{1 + (\mathbf{p}'/m')^2}\,\delta(\mathbf{p}' - \mathbf{q}') - \frac{2\pi}{\mu}\frac{A(\mathbf{p}', \mathbf{q}')}{\sqrt{S_{q'}} - \sqrt{S_{p'}} + i\varepsilon}. \quad (2)$$

Instead of (1), we then arrive at the differential form of the relativistic Schrödinger equation for the wave function $\Psi_{q'}(\mathbf{p}')$ in the momentum representation. Specifically, we have

$$(\sqrt{S_{q'}} - \sqrt{S_{p'}})\Psi_{q'}(\mathbf{p}') = (2\pi)^{-3}\int d\Omega_{k'}\tilde{V}(\mathbf{p}', \mathbf{k}'; E_{q'})\Psi_{q'}(\mathbf{k}'). \quad (3)$$

A transition from the momentum representation to configuration space is accomplished with the aid of the coordinate-representation wave function [7, 8]

$$\psi_{q'}(\mathbf{r}) = (2\pi)^{-3}\int d\Omega_{p'}\xi(\mathbf{p}', \mathbf{r})\Psi_{q'}(\mathbf{p}'). \quad (4)$$

The functions

$$\xi(\mathbf{p}', \mathbf{r}) = \left(\frac{p_0' - \mathbf{p}'\cdot\mathbf{n}}{m'}\right)^{-1 - irm'},$$

$$p_0' = E_{p'} = \sqrt{m'^2 + \mathbf{p}'^2}, \quad \mathbf{r} = r\mathbf{n}, \quad |\mathbf{n}| = 1,$$

play the role of relativistic plane waves and satisfy the equation

$$(\sqrt{S_{q'}} - H_0)\xi(\mathbf{q}', \mathbf{r}) = 0, \quad (5)$$

where

$$H_0 = \frac{m'^2}{\mu}\left[\cosh\left(\frac{i\lambda'\partial}{\partial r}\right) + \frac{i\lambda'}{r}\sinh\left(\frac{i\lambda'\partial}{\partial r}\right) - \frac{\lambda'^2}{2r^2}\Delta_{\theta,\varphi}\exp\left(\frac{i\lambda'\partial}{\partial r}\right)\right].$$

Here, $\Delta_{\theta,\varphi}$ is the angular part of the Laplace operator, while $\lambda' = 1/m'$ is the Compton wavelength associated with the effective particle. By applying the Shapiro transformation (4) to Eq. (3) and taking into account Eq. (5), we obtain

$$(\sqrt{S_{q'}} - H_0)\psi_{q'}(\mathbf{r}) = \int d\mathbf{r}' V(\mathbf{r}, \mathbf{r}'; E_{q'})\psi_{q'}(\mathbf{r}'), \quad (6)$$

where

$$V(\mathbf{r}, \mathbf{r}'; E_{q'}) = (2\pi)^{-6}\int d\Omega_{p'} d\Omega_{k'} \xi(\mathbf{p}', \mathbf{r})\tilde{V}(\mathbf{p}', \mathbf{k}'; E_{q'})\xi^*(\mathbf{k}', \mathbf{r}').$$

Obviously, Eq. (5) represents an analog of the differential Schrödinger equation for particles interacting via a nonlocal potential and having unequal masses.

Thus, the fact that, within the quasipotential approach being considered, the total c.m. energy of two nonrelativistic particles of unequal energies can be represented in a form proportional to the energy of an effective relativistic particle of mass m', whence it follows that the energy denominator in the relativistic Lippmann–Schwinger equation (1) can be treated as a single-particle one, makes it possible to reduce the relativistic problem of two bodies of unequal masses to a one-body problem. The present study is devoted to precisely solving and investigating Eq. (6) and to formulating the Levinson theorem for bound states in the case of nonlocal separable quasipotentials.

2. WAVE FUNCTION AND PHASE SHIFT

For a separable interaction, we can choose the representation [9]

$$V(\mathbf{r}, \mathbf{r}'; E_{q'}) \equiv V(\mathbf{r}, \mathbf{r}') = \sum_{l=0}^{\infty}(2l+1)\sum_{n=1}^{N_l}\varepsilon_{nl} v_{nl}(r) v_{nl}(r') P_l\left(\frac{\mathbf{r}\cdot\mathbf{r}'}{rr'}\right). \quad (7)$$

Expanding the wave function $\psi_{q'}(\mathbf{r})$ in terms of partial waves as

$$\psi_{q'}(\mathbf{r}) = \sum_{l=0}^{\infty}(2l+1) i^l \frac{\varphi_l(\chi', r)}{r} P_l\left(\frac{\mathbf{q}'\cdot\mathbf{r}}{q'r}\right), \quad (8)$$

we can recast Eq. (6) into the form

$$\left[\cosh\left(i\lambda'\frac{d}{dr}\right) + \frac{\lambda'^2 l(l+1)}{2r^{(2)}}\exp\left(\frac{i\lambda' d}{dr}\right) - \cosh\chi'\right]\varphi_l(\chi', r) + \frac{1}{2}\sum_{n=1}^{N_l}\varepsilon_{nl} V_{nl}(r)\int_0^{\infty} dr' V_{nl}(r')\varphi_l(\chi', r') = 0, \quad (9)$$

where $\sqrt{S_{q'}} = (m'^2/\mu)\sqrt{1 + (\mathbf{q}'/m')^2} = (m'^2/\mu)\cosh\chi'$, $V_{nl}(r) = \sqrt{8\pi\mu/m'^2}\, r v_{nl}(r)$, $\varepsilon_{nl} = \pm 1$, and $r^{(2)} = r(r + i\lambda')$.

For the sake of simplicity, we further restrict our consideration to the case where only one separable term corresponds to each l ($N_l = 1$). In this case, Eq. (9) assumes the form

$$\left[\cosh\left(i\lambda'\frac{d}{dr}\right) + \frac{\lambda'^2 l(l+1)}{2r^{(2)}}\exp\left(\frac{i\lambda' d}{dr}\right) - \cosh\chi'\right] \times \varphi_l(\chi', r) + \frac{1}{2}\varepsilon_l V_l(r)\int_0^{\infty} dr' V_l(r')\varphi_l(\chi', r') = 0, \quad (10)$$

where $V_l(r) = \sqrt{8\pi\mu/m'^2}\, r v_l(r)$ and $\varepsilon_l = \pm 1$. A solution that obeys Eq. (10) and the boundary condition

$$\varphi_l(\chi', 0) = 0 \quad (11)$$

will be sought by applying the integral Hankel transformation [9]:

$$\tilde{\varphi}_l(\chi', \chi) = \int_0^{\infty} dr \varphi_l(\chi', r) S_l^*(\chi, r)/Q_l(\coth\chi), \quad (12)$$

$$\varphi_l(\chi', r) = \frac{2}{\pi}\int_0^{\infty} d\chi Q_l(\coth\chi)\tilde{\varphi}_l(\chi', \chi) S_l(\chi, r), \quad (13)$$

$$\tilde{V}_l(\chi) = \int_0^{\infty} dr V_l(r) S_l^*(\chi, r)/Q_l(\coth\chi), \quad (14)$$

$$V_l(r) = \frac{2}{\pi}\int_0^{\infty} d\chi Q_l(\coth\chi)\tilde{V}_l(\chi) S_l(\chi, r). \quad (15)$$

Here, $Q_l(z)$ is a Legendre function of the second kind.

It should be noted that the function $S_l(\chi', r)$ appears to be a solution to Eq. (10) in the case where the interaction is switched off ($\varepsilon_l = 0$), simultaneously satisfying the orthonormality and completeness conditions [8]

$$\frac{2}{\pi}\int_0^{\infty} dr S_l(\chi', r) S_l^*(\chi, r) = \delta(\chi' - \chi),$$

$$\frac{2}{\pi}\int_0^\infty d\chi S_l(\chi, r)S_l^*(\chi, r') = \delta(r - r').$$

By applying transformations (13) and (15) to Eq. (10), we arrive at

$$(\cosh\chi' - \cosh\chi)\tilde{\varphi}_l(\chi', \chi) = \frac{1}{2}\varepsilon_l N_l(\chi')\tilde{V}_l(\chi), \quad (16)$$

where

$$N_l(\chi') = \int_0^\infty dr V_l(r)\varphi_l(\chi', r). \quad (17)$$

Let us now set

$$V_l(r) = \nu_l(r)U_l(r), \quad (18)$$

where $\nu_l(r) = (-1)^{l+1}(r/\lambda')^{(l+1)}/(-r/\lambda')^{(l+1)}$, $(r/\lambda')^{(l)} = i^l\Gamma(l - ir/\lambda')/\Gamma(-ir/\lambda')$, and $\Gamma(z)$ is a gamma function. Suppose that the relativistic integral Hankel transformation is valid for the function $U_l(r)$:

$$\tilde{U}_l(\chi) = \int_0^\infty dr U_l(r)S_l^*(\chi, r)/Q_l(\coth\chi), \quad (19)$$

$$U_l(r) = \frac{2}{\pi}\int_0^\infty d\chi Q_l(\coth\chi)\tilde{U}_l(\chi)S_l(\chi, r). \quad (20)$$

We further consider that, for real-valued l and χ, the relation $S_l^*(\chi, r) = \nu_l(r)S_l(\chi, r)$ holds [10]. Instead of (17), we therefore have

$$N_l(\chi') = \frac{2}{\pi}\int_0^\infty d\chi Q_l^2(\coth\chi)\tilde{\varphi}_l(\chi', \chi)\tilde{U}_l(\chi). \quad (21)$$

For a unique solution to Eq. (16) to exist, it is necessary that

$$rV_l(r) \in L_1(0, \infty). \quad (22)$$

Let us consider this point in some detail. The functions $S_l(\chi, r)$ possess the well-known properties [8, 10]

$$S_l(\chi, r) \approx \sin(\chi r/\lambda' - \pi l/2), \quad \chi r/\lambda' \longrightarrow \infty, \quad (23)$$

$$S_l(\chi, r) \approx (r/\lambda')Q_l(\coth\chi)e^{-i\pi l/2}, \quad r \longrightarrow 0. \quad (24)$$

By virtue of these, the condition in (22) means that the function $\tilde{V}_l(\chi)$ is continuous everywhere, whereas the function $Q_l(\coth\chi)\tilde{V}_l(\chi)$ is differentiable for all nonnegative χ. Moreover, it follows from (14) that

$$Q_l(\coth\chi)\tilde{V}_l(\chi) = O(1), \quad |\chi| \longrightarrow \infty; \quad (25)$$

$$\tilde{V}_l(\chi) = O(1), \quad \chi \longrightarrow 0, \quad (26)$$

provided that the condition in (22) is satisfied. It is obvious that, by virtue of (18), the function $\tilde{U}_l(\chi)$ also possesses the aforementioned property.

For scattering states ($E_{q'}/m' = \cosh\chi' \geq 1$), the relevant solution to Eq. (16) is given by

$$\tilde{\varphi}_l(\chi', \chi) = \frac{\pi}{2}\frac{\sinh\chi'}{Q_l^2(\coth\chi')}\delta(\cosh\chi' - \cosh\chi) + \frac{1}{2}\varepsilon_l N_l(\chi')\mathrm{P}\frac{\tilde{V}_l(\chi)}{\cosh\chi' - \cosh\chi}, \quad (27)$$

where P is the principal-value symbol. The factor in front of the delta function was chosen in accordance with the normalization of the wave function; that is, in the absence of interaction ($\varepsilon_l = 0$), the representation in (13) must lead to the expression $\varphi_l(\chi', r) = S_l(\chi', r)/Q_l(\coth\chi')$. Substituting (27) into (13) and (21), we obtain

$$\varphi_l(\chi', r) = \frac{S_l(\chi', r)}{Q_l(\coth\chi')} + \frac{1}{\pi}\varepsilon_l N_l(\chi')\mathrm{P}\int_0^\infty d\chi Q_l(\coth\chi)\frac{\tilde{V}_l(\chi)S_l(\chi, r)}{\cosh\chi' - \cosh\chi}, \quad (28)$$

$$N_l(\chi') = \tilde{U}_l(\chi')\left[1 + \mathrm{P}\frac{1}{2}\int_0^\infty d\chi\frac{A_l(\chi)}{\cosh\chi - \cosh\chi'}\right]^{-1}, \quad (29)$$

$$A_l(\chi) = \frac{2}{\pi}\varepsilon_l Q_l^2(\coth\chi)\tilde{U}_l(\chi)\tilde{V}_l(\chi). \quad (30)$$

Since the functions $\tilde{V}_l(\chi)$ and $\tilde{U}_l(\chi)$ are differentiable, the principal values of the integrals exist; by virtue of the conditions in (25) and (26), each integral involved is convergent both at the upper and at the lower limit. Thus, a conclusion that can be drawn from the above is the following: provided that the condition in (22) is satisfied, relations (28)–(30) determine the unique solution to equation (10) with the boundary condition (11).

The asymptotic behavior of the wave function $\varphi_l(\chi', r)$ can be found by representing expression (28) in the form

$$\varphi_l(\chi', r) = \frac{\sin(r\chi'/\lambda' - \pi l/2)}{Q_l(\coth\chi')} - \varepsilon_l N_l(\chi')\mathrm{Re}\frac{1}{2i\pi}\mathrm{P}\int_{-\infty}^\infty d\chi Q_l(\coth\chi)\frac{\tilde{V}_l(\chi)}{\cosh\chi - \cosh\chi'} \times \exp(ir\chi/\lambda' - i\pi l/2), \quad r\chi'/\lambda' \longrightarrow \infty.$$

This representation follows from the asymptotic expression (23) and from the fact that the integrand on the right-hand side of (28) is an even function of χ.

Making use of the relation

$$\frac{1}{\alpha - i\eta} = i\pi\delta(\alpha) + \mathrm{P}\left(\frac{1}{\alpha}\right), \quad \eta \longrightarrow +0,$$

we obtain

$$\varphi_l(\chi', r) = \frac{\sin(r\chi'/\lambda' - \pi l/2)}{Q_l(\coth\chi')} - \varepsilon_l N_l(\chi')\mathrm{Re}\left\{\frac{1}{2i\pi}\right.$$
$$\times \int_{-\infty}^{\infty} d\chi \frac{Q_l(\coth\chi)\tilde{V}_l(\chi)\exp(ir\chi/\lambda' - i\pi l/2)}{\cosh\chi - \cosh\chi' - i\eta}$$
$$- \frac{Q_l(\coth\chi')\tilde{V}_l(\chi')}{2\sinh\chi'}[\exp(ir\chi'/\lambda' - i\pi l/2)$$
$$\left. - \exp(-ir\chi'/\lambda' + i\pi l/2)]\right\},$$
$$\eta \longrightarrow +0.$$

The integral in the last equality can easily be calculated by applying the Cauchy residue theorem in the upper half-plane of the variable χ ($\mathrm{Im}\chi \geq 0$):

$$\frac{1}{2i\pi}\int_{-\infty}^{\infty} d\chi \frac{Q_l(\coth\chi)\tilde{V}_l(\chi)\exp(ir\chi/\lambda')}{\cosh\chi - \cosh\chi' - i\eta}$$
$$= \sum_{n=0}^{\infty} \mathrm{res}\left[\frac{Q_l(\coth z)\tilde{V}_l(z)\exp(izr/\lambda')}{\cosh z - \cosh\chi' - i\eta},\right.$$
$$\left. z = \mathrm{arccosh}(\cosh\chi' + i\eta) + 2\pi n i\right]$$
$$+ \sum_{n=1}^{\infty} \mathrm{res}\left[\frac{Q_l(\coth z)\tilde{V}_l(z)\exp(izr/\lambda')}{\cosh z - \cosh\chi' - i\eta},\right.$$
$$\left. z = -\mathrm{arccosh}(\cosh\chi' + i\eta) + 2\pi n i\right]$$
$$= \frac{Q_l(\coth\chi')\tilde{V}_l(\chi')\exp(i\chi' r/\lambda')}{\sinh\chi'} + O(e^{-2\pi r/\lambda'}),$$
$$\eta \longrightarrow +0.$$

Here, we have considered that the functions sinhz and Q_l(cothz) are periodic with a period of $2\pi i$. Taking into account the last result, we find that the asymptotic behavior of the wave function is given by

$$\varphi_l(\chi', r) = \frac{\sin(r\chi'/\lambda' - \pi l/2)}{Q_l(\coth\chi')} - \varepsilon_l N_l(\chi')$$
$$\times \frac{Q_l(\coth\chi')\tilde{V}_l(\chi')\cos(r\chi'/\lambda' - \pi l/2)}{\sinh\chi'} + O(e^{-2\pi r/\lambda'}), \quad (30a)$$
$$r\chi'/\lambda' \longrightarrow \infty.$$

For arbitrary l, the asymptotic behavior of the wave function is

$$\varphi_l(\chi', r) = \frac{\sin(r\chi'/\lambda' - \pi l/2)}{Q_l(\coth\chi')}$$
$$+ \frac{\cos(r\chi'/\lambda' - \pi l/2)\tan\delta_l(\chi')}{Q_l(\coth\chi')}, \quad (30b)$$
$$r\chi'/\lambda' \longrightarrow \infty.$$

By comparing these two asymptotic equalities, we find that the phase shift can be determined from the equation

$$\tan\delta_l(\chi') = -\frac{\pi}{2}\sinh^{-1}\chi' A_l(\chi')\left[1 + \mathrm{P}\frac{1}{2}\int_0^{\infty} d\chi \frac{A_l(\chi)}{\cosh\chi - \cosh\chi'}\right]^{-1}. \quad (31)$$

We now notice that the equality in (20) can be recast into the form

$$V_l(r) = \frac{2}{\pi}\int_0^{\infty} d\chi Q_l(\coth\chi)\tilde{U}_l(\chi)S_l^*(\chi, r).$$

It follows that the complex-valued functions $\tilde{V}_l(\chi)$ and $\tilde{U}_l(\chi)$ are related by the equation

$$\int_0^{\infty} d\chi Q_l(\coth\chi)\tilde{V}_l(\chi)S_l(\chi, r)$$
$$= \int_0^{\infty} d\chi Q_l(\coth\chi)\tilde{U}_l(\chi)S_l^*(\chi, r).$$

This equation, together with the condition requiring that the phase shift and, hence, the function $A_l(\chi)$ be real-valued, leads to the equality

$$\tilde{V}_l^*(\chi) = \pm\tilde{U}_l(\chi),$$

which is equivalent to the condition

$$V_l^*(r) = \pm V_l(r).$$

The separable quasipotential $V(\mathbf{r}, \mathbf{r}')$ involves products of the form $\varepsilon_l V_l(r)V_l(r')$; therefore, it follows from the last condition that the quasipotential must be real-valued:

$$V_l^*(r) = V_l(r). \quad (32)$$

This implies that

$$\tilde{V}_l^*(\chi) = \tilde{U}_l(\chi). \quad (33)$$

The expression in (30) then takes the form

$$A_l(\chi) = \frac{2}{\pi}\varepsilon_l Q_l^2(\coth\chi)\left|\tilde{V}_l(\chi)\right|^2. \quad (34)$$

3. BOUND STATES AND LEVINSON THEOREM

Suppose that there exists at least one bound state at energy $E' = E_{q'}/m' = \cosh\chi'$. The relevant solution to Eq. (16) is then given by

$$\tilde{\varphi}_l(\chi', \chi) = -\frac{1}{2}\varepsilon_l N_l(\chi')\mathrm{P}\frac{\tilde{V}_l(\chi)}{\cosh\chi' - E'}. \quad (35)$$

Substituting this solution into (21), we arrive at the following equation for eigenvalues:

$$1 + \frac{1}{2}\mathrm{P}\int_0^\infty \frac{d\chi A_l(\chi)}{\cosh\chi - E'} = 0. \quad (36)$$

From the condition requiring the existence of bound states, it follows that Eq. (36) must have at least one solution. Hence, the function $A_l(\chi)$ must be real-valued, which leads to the condition in (33). From (34) and (36), it follows that the value of $\varepsilon_l = -1$ corresponds to the bound state whose energy lies in the range $0 \le E' = E_i' < 1$.

At the same time, Eq. (36) may have solutions at $\varepsilon_l = \pm 1$ for bound states at energies satisfying the inequality $E' = E_R' \ge 1$.

Let us consider the *s* wave ($l = 0$). Suppose that there exists a bound state at an energy satisfying the condition

$$0 \le E_i' = \cosh\chi_i' = \cos\kappa_i' < 1 \quad (\chi_i' = i\kappa_i').$$

From (35) and (36), it follows that a bound state at such an energy value exists, provided that

$$\varepsilon_0 = -1, \quad \frac{2}{\pi}\int_0^\infty d\chi \tilde{V}_0^2(\chi) > 1. \quad (37)$$

Obviously, the boundary condition (11) is then satisfied; the wave function as determined from (13) and (35) at $\varepsilon_0 = -1$ and $l = 0$ can be represented as

$$\varphi_0(\chi_i', r) = \frac{N_0(\chi_i')}{2\pi i}\int_{-\infty}^{\infty} d\chi Q_0(\coth\chi)\frac{\tilde{V}_0(\chi)\exp(ir\chi/\lambda')}{\cosh\chi - E_i'}.$$

The asymptotic behavior of this function can be determined by applying the Cauchy residue theorem in performing integration in the upper half-plane of the variable χ. As a result, we arrive at

$$\varphi_0(\chi_i', r) = N_0(\chi_i')$$

$$\times\sum_{n=0}^{\infty}\mathrm{res}\left[\frac{Q_0(\coth z)\tilde{V}_0(z)\exp(izr/\lambda')}{\cosh z - E_i'}, z = \chi_i' + 2\pi n i\right]$$

$$= \frac{\kappa_i'}{\sin\kappa_i'}\frac{N_0(\chi_i')\tilde{V}_0(\chi_i')\exp(-r\kappa_i'/\lambda')}{1 - \exp(-2\pi r/\lambda')}.$$

On the basis of this relation, we obtain

$$\varphi_0(\chi_i', r) \approx \exp(-\kappa_i' r/\lambda'), \quad r/\lambda' \longrightarrow \infty.$$

Let us now consider $l = 0$ bound states at energies in the region $E_R' = \cosh\chi_R' \ge 1$. In this case, Eq. (36) can have solutions at $\varepsilon_0 = \pm 1$ and $l = 0$. If such a solution exists, it can be shown with the aid of (30a) that the asymptotic behavior of the wave function is given by

$$\varphi_0(\chi_R', r) = -\varepsilon_0 N_0(\chi_R')\frac{Q_0(\coth\chi_R')\tilde{V}_0(\chi_R')\cos(r\chi_R'/\lambda')}{\sinh\chi_R'}$$

$$+ O(\exp(-2\pi r/\lambda')),$$

$$r/\lambda' \longrightarrow \infty.$$

From this relation, it follows that the wave function asymptotically tends to zero, provided that

$$\tilde{V}_0(\chi_R') = 0. \quad (38)$$

Since the boundary condition (11) is also satisfied, a bound state corresponds to the energy value $E_R' = \cosh\chi_R'$.

Summarizing the above results and using expression (31), we conclude that, at the bound-state energy equal to E_R', the decreasing phase shift takes the value of πn, where n is an integer. This is so, because, at $E_R' = \cosh\chi_R'$, the numerator and the denominator of the expression on the right-hand side of (31) are both equal to zero by virtue of conditions (36) and (38). It should be noted, however, that the function $A_0(\chi)$, which is determined by expression (34), has a zero of order not lower than two at the point χ_R', whereas the denominator in (31) has a simple zero. But if the denominator in (31) does not vanish at $\chi' = \chi_R'$, the phase shift proves to be tangent to the straight line $\delta_0 = \pi n$ from above or from below, not intersecting it; that is, there is an extremum. Thus, we conclude that, if the phase-shift curve intersects the straight line $\delta_0 = \pi n$ from above and if the conditions in (36) and (38) are satisfied, there is a bound state at the energy value of $E_R' = \cosh\chi_R'$.

Bound states for $l > 0$ can be analyzed by following a procedure that is similar to that used to treat the case of the *s* wave. By doing this, we arrive at results analogous to those presented above. By using the estimate in (25) and expression (31), we now conclude that $\tan\delta_l(\infty) = 0$. For this reason, we choose $\delta_l(\chi')$ in such a way as to ensure fulfillment of the equality $\delta_l(\infty) = 0$. From here and from the continuity of the phase shift in χ', we obtain the Levinson theorem for the case of a separable quasipotential ($l \ge 0$). It reads

$$\delta_l(0) - \delta_l(\infty) = \delta_l(0) = (\nu_l + n_l)\pi, \quad (39)$$

where ν_l is the number of bound states whose energies lie in the region $E'_{Rn} \geq 1$, $n = 0, 1, 2, \ldots, \nu_l - 1$, while n_l is the number of bound states at energies in the range $0 \leq E'_{ik} < 1$, $k = 0, 1, 2, \ldots, n_l - 1$.

4. APPLICATIONS

By way of example, we will use the above results to find the conditions ensuring the existence of bound states and scattering states for the quasipotential ($l = 0$)

$$V_0(r) = \alpha\delta(r-a), \quad \alpha, a > 0, \tag{40}$$

and draw a comparison with the corresponding results emerging from a nonrelativistic treatment for the same quasipotential. Obviously, the image of the quasipotential in (40) has the form

$$\tilde{V}_0(\chi') = \frac{\alpha \sin a\chi'}{\chi'}. \tag{41}$$

Let us find a bound state at an energy in the range $0 \leq E'_i < 1$, $E'_i = \cos\kappa'_i$, $0 < \kappa'_i \leq \pi/2$. In accordance with the conditions in (36) and (37), the bound state in question is then determined as a solution to the equation

$$\pi - \kappa'_i - \frac{\pi \sinh 2a(\pi - \kappa'_i)}{\sinh 2\pi a} - \frac{2\pi}{\alpha^2}\sin\kappa'_i = 0, \quad 0 < \kappa'_i \leq \frac{\pi}{2}, \tag{42}$$

under the condition

$$a\alpha^2 > 1. \tag{43}$$

At the same time, scattering states that occur at energies taking values in the region $E'_{Rn} = \cosh\chi'_{Rn} \geq 1$ and which are determined as simultaneous solutions to Eqs. (36) and (38) satisfy the equation ($\varepsilon_0 = 1$)

$$1 - \frac{\alpha^2}{2\pi}\frac{\chi'_{Rn}}{\sinh\chi'_{Rn}} = 0, \quad \chi'_{Rn} = \pm\pi n/a, \quad n = 1, 2, \ldots . \tag{44}$$

Equation (44) admits the existence of two scattering states at energies in the region

$$E'_{Rn} = \cosh\chi'_{Rn} > 1, \quad \chi'_{Rn} = \pm\pi n/a, \quad n = 1, 2, \ldots,$$

under the condition

$$\alpha^2 > 2\pi. \tag{45}$$

The value found for the energy of a scattering state, E'_{Rn}, possesses the following properties: (i) If the well width a does not change, the growth of the parameter α leads to the growth of the scattering-state energy E'_{Rn}, and vice versa. (ii) If the parameter α is fixed, changes in the parameter a lead to changes in the level specified by n, but the quantity $|\chi'_{Rn}| = \pi n/a$ remains unchanged. Thus, the energy levels in question are quantized as functions of the parameters a and α according to Eq. (44) under the condition in (45).

In the nonrelativistic case, which was considered in [1], the same image (41) corresponds to the quasipotential in (40) at $\chi' = k$. In this case, the bound state at a negative energy $k^2 = -\kappa^2 < 0$ also exists only under the condition in (43), but it is determined as a solution to the equation

$$1 - \alpha^2 e^{-a\kappa}\frac{\sinh a\kappa}{\kappa} = 0. \tag{46}$$

At the same time, there are no scattering states at nonnegative energies $k^2 \geq 0$ in the nonrelativistic case.

5. CONCLUSION

Within the relativistic quasipotential approach to quantum field theory, a method has been developed for solving a finite-difference quasipotential equation involving a nonlocal separable quasipotential that simulates the interaction between two relativistic spinless particles of unequal masses. This has permitted finding an explicit expression for the phase shift, determining the conditions under which bound and scattering states may exist, and formulating the Levinson theorem. The proposed approach relies on the possibility of representing the total c.m. energy of two relativistic particles of unequal masses as an expression proportional to the energy of an effective relativistic particle of mass m'.

As an application of the results obtained in the present study, we have analyzed the conditions of existence of bound and scattering states for a delta-function quasipotential and performed a comparison with the nonrelativistic case. It has been shown that, in contrast to the nonrelativistic case, relativistic effects in particle scattering on a delta-function quasipotential manifest themselves in the formation of scattering states.

ACKNOWLEDGMENTS

I am grateful to Yu.S. Vernov, V.I. Savrin, R.N. Faustov, and A.M. Shirokov for interest in this study and for enlightening discussions on the results presented here.

REFERENCES

1. K. Chadan and P. C. Sabatier, *Inverse Problems in Quantum Scattering Theory* (Springer-Verlag, New York, 1977; Mir, Moscow, 1980).
2. R. Barbieri, R. Kogerler, Z. Kunszt, and R. Gatto, Nucl. Phys. B **105**, 125 (1976).
3. R. McClary and N. Byers, Phys. Rev. D **28**, 1692 (1983).
4. A. A. Logunov and A. N. Tavkhelidze, Nuovo Cimento **29**, 380 (1963).

5. V. O. Galkin, A. Yu. Mishurov, and R. N. Faustov, Yad. Fiz. **55**, 1080 (1992) [Sov. J. Nucl. Phys. **55**, 608 (1992)]; Yad. Fiz. **55**, 2175 (1992) [Sov. J. Nucl. Phys. **55**, 1207 (1992)].
6. V. G. Kadyshevsky, Nucl. Phys. B **6**, 125 (1968).
7. V. G. Kadyshevskiĭ, M. D. Mateev, and R. M. Mir-Kasimov, Yad. Fiz. **11**, 692 (1970) [Sov. J. Nucl. Phys. **11**, 388 (1970)].
8. V. G. Kadyshevskiĭ, R. M. Mir-Kasimov, and N. B. Skachkov, Fiz. Élem. Chastits At. Yadra **2**, 635 (1972) [Sov. J. Part. Nucl. **2** (3), 69 (1972)].
9. Yu. D. Chernichenko, Preprint No. 88-27/48, NIIYaF MGU (Institute of Nuclear Physics, Moscow State University, Moscow, 1988).
10. I. V. Amirkhanov, G. V. Grusha, and R. M. Mir-Kasimov, Fiz. Élem. Chastits At. Yadra **12**, 651 (1981) [Sov. J. Part. Nucl. **12**, 262 (1981)].

Translated by A. Isaakyan

Physics of Atomic Nuclei, Vol. 63, No. 11, 2000, pp. 1983–1987. Translated from Yadernaya Fizika, Vol. 63, No. 11, 2000, pp. 2075–2079.

ELEMENTARY PARTICLES AND FIELDS
Theory

Reconstructing a Separable Interaction within the Relativistic Quasipotential Approach

Yu. D. Chernichenko
Gomel State Technical University, Gomel, Belarus
Received June 3; 1999; in final form, February 1, 2000

Abstract—Within the relativistic quasipotential approach to quantum field theory, a method is developed according to which a nonlocal separable quasipotential that represents the interaction between two relativistic particles of unequal masses can be reconstructed on the basis of the phase shift and bound-state energies. *© 2000 MAIK "Nauka/Interperiodica".*

It was proven by Gelfand and Levitan [1, 2], Marchenko [3], and Krein [4, 5] that the inverse problem can in principle be solved within nonrelativistic theory. They reduced the problem to linear integral equations in two versions, which served as a basis for a further development of inverse-problem theory. The most comprehensive survey of this theory was given in the monographs of Chadan and Sabatier [6] and Zakhariev and Suzko [7].

In the majority of studies, however, the problem of reconstructing the underlying interaction is formulated on the basis of the nonrelativistic Schrödinger equation, so that the important problem of reconstructing interactions for essentially relativistic systems—in particular, within the relativistic quasipotential approach [8]—has yet to be solved conclusively.

Within the quasipotential approach proposed in [9], the problem being discussed is treated here for the case where a nonlocal separable quasipotential simulating the interaction between two relativistic spinless particles of unequal masses ($m_1 \neq m_2$) must be reconstructed on the basis of the phase shift and bound-state energies. The approach developed here relies on the expression that was found by the present author for the phase shift and which has the form [10] (we use the system of units where $\hbar = c = 1$)

$$\tan\delta_l(\chi') = -\frac{\pi}{2}\sinh^{-1}\chi' A_l(\chi')\left[1 + \mathrm{P}\frac{1}{2}\int_0^\infty d\chi \frac{A_l(\chi)}{\cosh\chi - \cosh\chi'}\right]^{-1}, \quad (1)$$

where the quantity χ' is defined via the relation

$$E_{q'} = m'\sqrt{1 + (\mathbf{q}'/m')^2} = m'\cosh\chi', \quad m' = \sqrt{m_1 m_2},$$

and

$$A_l(\chi') = \frac{2}{\pi}\varepsilon_l Q_l^2(\coth\chi')\left|\tilde{V}_l(\chi')\right|^2, \quad \varepsilon_l = \pm 1. \quad (2)$$

Here, $Q_l(z)$ is a Legendre function of the second kind.

In order to find the quasipotential $V_l(r)$ on the basis of the phase shift $\delta_l(\chi')$, it is necessary to solve the integral equation (1) for the function $A_l(\chi')$. After that, the function $\tilde{V}_l(\chi')$ is determined from Eq. (2). The quasipotential $V_l(r)$ is then reconstructed by performing the relativistic Hankel transformation

$$V_l(r) = \frac{2}{\pi}\int_0^\infty d\chi Q_l(\coth\chi)\tilde{V}_l(\chi)S_l(\chi, r). \quad (3)$$

It should be noted that the function $S_l(\chi, r)$ is a free solution to a finite-difference quasipotential equation in configuration space [11].

In particular, the relativistic Hankel transformation (3) at $l = 0$ reduces to the conventional Fourier transformation

$$V_0(r) = \frac{2}{\pi}\int_0^\infty d\chi\chi\tilde{V}_0(\chi)\sin r\chi.$$

We assume that the phase shift $\delta_l(\chi')$ in Eq. (1) is a function continuous in the sense of Hölder with a positive index and that, for $\chi' \longrightarrow \infty$, it behaves as

$$\delta_l(\chi') = O(e^{-\gamma\chi'}), \quad l \geq 0, \quad \gamma > 1. \quad (4)$$

These constraints are necessary and sufficient for the quasipotential to satisfy the conditions

$$rV_l(r) \in L_1(0, \infty), \quad (5)$$

which ensures the uniqueness of the solution to the problem at hand.

It should be noted that, if the phase shift intersects the straight lines $\delta_l(\chi') = \pi n$ (n is an integer) from below as χ' increases, the inverse problem has no solutions. We therefore assume that, as χ' increases, the phase shift $\delta_l(\chi')$ intersects the straight lines $\delta_l(\chi') = \pi n$ ($n = 0, 1, 2, \ldots$) from above.

1063-7788/00/6311-1983$20.00

Suppose that there exist ν_l ($l \geq 0$) bound states at energies satisfying the conditions

$$E'_{Rn} = m'\cosh\chi'_{Rn} \geq m', \quad n = 0, 1, \ldots, \nu_l - 1.$$

We then have

$$\delta_l(0) = \pi\nu_l. \tag{6}$$

In this case, the phase shift at large energy values appears to be a negative quantity of small magnitude ($\varepsilon_l = +1$), while the bound-state energies $E'_{Rn} \geq m'$ are found by using the same values of χ' at which the phase shift $\delta_l(\chi')$ intersects the straight lines $\delta_l(\chi') = \pi n$ from above as χ' increases; that is,

$$\delta_l(\chi'_{Rn}) = \pi n, \quad n = 0, 1, 2, \ldots, \nu_l - 1. \tag{7}$$

The integral equation (1) can be reduced to the form

$$A_l(\operatorname{arccosh} x)g_l^{-1}(x) = 1 + \frac{1}{\pi}\mathrm{P}\int_1^\infty dt \frac{\psi_l(t)h_l^*(t)}{t-x}, \tag{8}$$

where $x = \cosh\chi'$ and where we introduced the following notation:

$$\begin{aligned}
\psi_l(x) &= A_l(\operatorname{arccosh} x)g_l^{-1}(x) \\
&\times [1 + (i\pi/2)g_l(x)(x^2-1)^{-1/2}], \\
g_l(x) &= -(2/\pi)(x^2-1)^{1/2}\tan\Delta_l(x), \\
\Delta_l(x) &= \delta_l(\operatorname{arccosh} x), \\
h_l(x) &= (\pi/2)g_l(x)(x^2-1)^{-1/2} \\
&\times [1 - (i\pi/2)g_l(x)(x^2-1)^{-1/2}]^{-1} \\
&= -\sin\Delta_l(x)\exp(-i\Delta_l(x)).
\end{aligned} \tag{9}$$

With the aid of the representation

$$1/(\alpha - i0) = i\pi\delta(\alpha) + \mathrm{P}(1/\alpha),$$

Eq. (8) can be recast into the form

$$\psi_l(x) = 1 + \frac{1}{\pi}\int_1^\infty dt \frac{\psi_l(t)h_l^*(t)}{t-x-i0}. \tag{10}$$

Let us consider the function

$$H_l(z) = 1 + \frac{1}{\pi}\int_1^\infty dt \frac{\psi_l(t)h_l^*(t)}{t-z}. \tag{11}$$

If the function $\psi_l(x)$ is continuous in the sense of Hölder and if the integral in Eq. (11) converges, the function $H_l(z)$ is analytic in the complex plane of the variable z with the cut from 1 to $+\infty$; in addition, the relation

$$\lim_{|z|\to\infty} H_l(z) = 1 \tag{12}$$

holds in all directions. Hence, a solution to the integral equation (10) can be represented as

$$\psi_l(x) = H_l(x_+) \equiv \lim_{\eta\to+0} H_l(x + i\eta), \quad 1 \leq x \leq \infty. \tag{13}$$

By substituting the solution in (13) into the expression for the discontinuity suffered by the function $H_l(z)$ upon traversing the cut,

$$\begin{aligned}
H_l(x_+) - H_l(x_-) &= 2i\psi_l(x)h_l^*(x) \\
&= -2i\sin\Delta_l(x)\exp(i\Delta_l(x))\psi_l(x),
\end{aligned}$$

we arrive at the homogeneous Riemann–Hilbert equation for the function $H_l(z)$:

$$H_l(x_+)\exp(2i\Delta_l(x)) - H_l(x_-) = 0, \quad 1 \leq x \leq \infty. \tag{14}$$

A particular solution satisfying Eq. (14) and the condition in (12) has the form

$$\tilde{H}_l(z) = \exp[\omega_l(z)], \tag{15}$$

where

$$\omega_l(z) = -\frac{1}{\pi}\int_1^\infty dt \frac{\Delta_l(t)}{t-z}. \tag{16}$$

We also have the relation

$$\lim_{|z|\to\infty} \omega_l(z) = 0,$$

which holds in all directions, as follows from the assumptions on the behavior of the phase shift and from the condition in (4). Moreover, the function specified in (16) is defined everywhere on the cut, perhaps with the exception of the point $z = 1$, where its behavior is given by

$$\omega_l(z) = (1/\pi)\Delta_l(1)\ln|1-z| + \Omega_l(z). \tag{17}$$

Here, the function $\Omega_l(z)$ is finite for $z \longrightarrow 1$, while $\Delta_l(1) = \delta_l(0) = \pi\nu_l$ (there are ν_l bound states at energies lying in region $E'_{Rn} = m'\cosh\chi'_{Rn} \geq m'$, $n = 0, 1, \ldots, \nu_l - 1$). Therefore, the function $H_l(z)$ has a zero of order ν_l at the point $z = 1$.

Thus, we conclude that, according to (13), (15), and (16), the relevant solution to the nonhomogeneous integral equation (10) has the form

$$\tilde{\psi}_l(x) = \exp[\alpha_l(x) - i\Delta_l(x)], \tag{18}$$

where

$$\alpha_l(x) = -\frac{1}{\pi}\mathrm{P}\int_1^\infty dt \frac{\Delta_l(t)}{t-x}. \tag{19}$$

It should be noted that the function given by (18) is regular at $x = 1$ (it has a zero of order ν_l at this point), is continuous in the sense of Hölder with the same index as the phase shift, and is bounded for $x \longrightarrow +\infty$. (All this is consistent with the a priori assumptions on its

properties.) Finally, this function is a solution to Eq. (10) since, according to the Cauchy theorem, we have

$$\frac{1}{\pi}\int_1^\infty dt\frac{\tilde{\psi}_l(t)h_l^*(t)}{t-x-i0}$$

$$= \lim_{\eta\to+0,\,R\to+\infty}\frac{1}{2\pi i}\left[\int_\Gamma dz\frac{\tilde{H}_l(z)}{z-x-i\eta}-\int_{C_R} dz\frac{\tilde{H}_l(z)}{z-x-i\eta}\right]$$

$$= \tilde{H}_l(x_+)-1 = \tilde{\psi}_l(x)-1,$$

where Γ is the closed contour consisting of a circle of radius R, two banks of the cut from 1 to R (obviously, the contour goes in opposite directions along these banks), and a circle C_η having a radius η and a center at the point $z = 1$. The contribution of the integral along the circle C_η tends to zero for $\eta \longrightarrow +0$ since the function $\tilde{H}_l(z)$ is regular at the point $z = 1$.

Let us now find a general solution to the homogeneous equation

$$\psi_{l0}(x) = \frac{1}{\pi}\int_1^\infty dt\frac{\psi_{l0}(t)h_l^*(t)}{t-x-i0}. \tag{20}$$

For this, we will now consider the function

$$H_{l0}(z) = \frac{1}{\pi}\int_1^\infty dt\frac{\psi_{l0}(t)h_l^*(t)}{t-z}, \tag{21}$$

which is analytic in the complex plane of the variable z with the cut from 1 to $+\infty$ and which obeys the relation

$$\lim_{|z|\to\infty} H_{l0}(z) = 0 \tag{22}$$

in all directions. The relevant solution to the integral equation (20) has the form (13), as before, while the function $H_{l0}(z)$ satisfies the homogeneous Riemann–Hilbert equation (14). A general solution to this equation will be sought in the form

$$H_{l0}(z) = \sum_{k=1}^{m} A_{k-1}\frac{\exp(\omega_l(z))}{(z-1)^k}. \tag{23}$$

Substituting (23) into (14) and requiring that the function $H_{l0}(z)$ be finite at $z = 1$, we obtain $m = \nu_l$. Hence, we have

$$\psi_{l0}(x) = H_{l0}(x_+)$$

$$= \sum_{k=1}^{\nu_l}(A_{k-1}/(x-1)^k)\exp[\alpha_l(x)-i\Delta_l(x)]. \tag{24}$$

It is obvious that, in just the same way as in the case of a particular solution, integration along the contour Γ shows that the function in (24) satisfies Eq. (14) and possesses all the required properties.

Therefore, a general solution to the integral equation (10) has the form

$$\psi_l(x) = \exp[\alpha_l(x)-i\Delta_l(x)]$$

$$\times\sum_{k=1}^{\nu_l}(1+A_{k-1}/(x-1)^k). \tag{25}$$

By using the notation in (9) and rearranging the sum as a product, we can recast the solution in (25) into the form

$$A_l(\chi') = -(2/\pi)\sinh\chi'\sin\delta_l(\chi')$$

$$\times\exp[\alpha_l(\cosh\chi')]\prod_{n=0}^{\nu_l-1}(1+B_n/(\cosh\chi'-1)), \tag{26}$$

where

$$\alpha_l(\cosh\chi')$$

$$= -(1/\pi)\mathrm{P}\int_0^\infty d\chi\sinh\chi\delta_l(\chi)/(\cosh\chi-\cosh\chi'). \tag{27}$$

In order to determine the constants B_n in (26), we note that, in accordance with the definition in (2), the function $A_l(\chi')$ is of fixed sign at all values of χ'; since $\varepsilon_l = +1$, it must be positive. At the same time, the phase shift changes sign at the bound-state energies $E'_{Rn} = m'\cosh\chi'_{Rn} \geq m'$. Hence, the function $A_l(\chi')$ retains a plus sign, provided that

$$B_n = 1-\cosh\chi'_{Rn}, \quad n = 0, 1, \ldots, \nu_l-1.$$

Instead of (26), we will then have

$$A_l(\chi') = -(2/\pi)\sinh\chi'\sin\delta_l(\chi')\exp[\alpha_l(\cosh\chi')]$$

$$\times\prod_{n=0}^{\nu_l-1}(1-(\cosh\chi'_{Rn}-1)/(\cosh\chi'-1)). \tag{28}$$

Thus, the solution in (28) is completely determined by the phase shift since χ'_{Rn} is also determined by the behavior of the phase shift. Moreover, it follows from expressions (27) and (28) that the function $A_l(\chi')$ is continuous in the sense of Hölder and that, for $\chi' \longrightarrow +\infty$, it behaves as

$$e^{-(\gamma-1)\chi'}, \quad \gamma > 1,$$

provided that the phase shift satisfies condition (4). This in turn implies that the quasipotential $V_l(r)$ satisfies condition (5).

The case where $\varepsilon_l = -1$ and where there are ν_l bound states whose energies lie in the region

$$E'_{Rn} = m'\cosh\chi'_{Rn} \geq m', \quad n = 0, 1, \ldots, \nu_l-1,$$

and n_l bound states whose energies satisfy the condition

$$0 \le E'_{ik} = m'\cos\kappa'_{ik} < m', \quad k = 0, 1, \ldots, n_l - 1$$

is considered in the same way.

By virtue of the Levinson theorem, we have

$$\delta_l(0) = \pi(\nu_l + n_l).$$

In accordance with expression (17), the function $H_l(z)$ therefore has a zero of order $(\nu_l + n_l)$ at $z = 1$. Further following the same line of reasoning as that adopted for the case of $\varepsilon_l = +1$ and considering that the solution $A_l(\chi')$ must now retain a minus sign for all values of χ' ($\varepsilon_l = -1$), we obtain

$$A_l(\chi') = -(2/\pi)\sinh\chi'\sin\delta_l(\chi')\exp[\alpha_l(\cosh\chi')] \times \prod_{n=0}^{\nu_l - 1}\left(1 - \frac{\cosh\chi'_{Rn} - 1}{\cosh\chi' - 1}\right)\prod_{k=0}^{n_l - 1}\left(1 + \frac{1 - \cos\kappa'_{ik}}{\cosh\chi' - 1}\right). \quad (29)$$

Thus, the function $A_l(\chi')$ is completely determined by the phase shift and bound states, and its sign is opposite to the sign of the phase shift for $\chi' \longrightarrow +\infty$.

In order to reconstruct the quasipotential $V_l(r)$ by means of the transformation in (3), it is necessary to know the complex-valued function $\tilde{V}_l(\chi')$, but expression (2) specifies only its absolute value for $l > 0$. Nonetheless, $\tilde{V}_l(\chi')$ is completely determined by the function $A_l(\chi')$, because the latter controls all bound states, the zeros of this function. These zeros occur either on the real axis ($E'_{Rn} \ge m'$) or on the imaginary axis ($0 \le E'_{ik} < m'$) in the complex plane of the variable χ'. Owing to this, we can introduce the function

$$\hat{V}_l(\chi') = \prod_{k=0}^{n_l - 1}\left(\frac{\chi' + i\kappa'_{ik}}{\chi' - i\kappa'_{ik}}\right)Q_l(\coth\chi')\tilde{V}_l(\chi')/A_l^{\text{as}}, \quad (30)$$

where n_l is the number of bound states whose energies lie in the region

$$0 \le E'_{ik} = m'\cos\kappa'_{ik} < m', \quad \chi'_{ik} = i\kappa'_{ik},$$

and A_l^{as} is the asymptotic form of the function

$$\left|Q_l(\coth\chi')\tilde{V}_l(\chi')\right| = \sqrt{(\pi/2)\varepsilon_l A_l(\chi')}$$

for $|\chi'| \longrightarrow \infty$.

The function $\hat{V}_l(\chi')$ is analytic in the region $\mathrm{Im}\chi' > 0$; is continuous for $\mathrm{Im}\chi' \ge 0$; and satisfies the condition

$$\hat{V}_l(\chi') = 1 + o(1), \quad |\chi'| \longrightarrow \infty, \quad (31)$$

provided that the condition in (5) is met. In addition, the function $\hat{V}_l(\chi')$ vanishes nowhere for $\mathrm{Im}\chi' > 0$. Therefore, the function $\ln\hat{V}_l(\chi')$ is analytic in the region $\mathrm{Im}\chi' > 0$ and tends to zero at infinity by virtue of the estimate in (31). We can then apply the integral Hilbert transformation to the real and the imaginary part of the function $\ln\hat{V}_l(\chi')$, setting

$$Q_l(\coth\chi')\tilde{V}_l(\chi') = \left|Q_l(\coth\chi')\tilde{V}_l(\chi')\right|\exp(i\Phi_l(\chi')).$$

We then obtain

$$\mathrm{Im}\ln\hat{V}_l(\chi') = -(1/\pi)\mathrm{P}\int_{-\infty}^{+\infty} d\chi\frac{\mathrm{Re}\ln\hat{V}_l(\chi)}{\chi - \chi'} = i\ln\left(\left|Q_l(\coth\chi')\tilde{V}_l(\chi')\right|/A_l^{\text{as}}\right) - \frac{1}{\pi}\int_{-\infty}^{\infty} d\chi\frac{\ln\left(\left|Q_l(\coth\chi)\tilde{V}_l(\chi)\right|/A_l^{\text{as}}\right)}{\chi - \chi' - i0}. \quad (32)$$

Combining (32) with the expression for

$$\mathrm{Re}\ln\hat{V}_l(\chi') = \ln\left(\left|Q_l(\coth\chi')\tilde{V}_l(\chi')\right|/A_l^{\text{as}}\right),$$

we now obtain the formula

$$\ln\hat{V}_l(\chi') = \frac{1}{2\pi i}\int_{-\infty}^{\infty} d\chi\frac{\ln(\pi\varepsilon_l A_l(\chi)/2(A_l^{\text{as}})^2)}{\chi - \chi'}, \quad (33)$$

which is valid in the region $\mathrm{Im}\chi' > 0$. From expressions (30) and (33), it eventually follows that

$$Q_l(\coth\chi')\tilde{V}_l(\chi') = A_l^{\text{as}}\prod_{k=0}^{n_l - 1}\left(\frac{\chi - i\kappa'_{ik}}{\chi' + i\kappa'_{ik}}\right) \times \exp\left\{\frac{1}{2\pi i}\int_{-\infty}^{\infty} d\chi\frac{\ln(\pi\varepsilon_l A_l(\chi)/2(A_l^{\text{as}})^2)}{\chi - \chi'}\right\}. \quad (34)$$

This equation is valid for $\mathrm{Im}\chi' > 0$.

Thus, a solution to the inverse problem exists and is completely determined if the function $A_l(\chi')$ is found on the basis of the phase shift and bound-state energies for $l \ge 0$.

To summarize, we note that the method proposed here to reconstruct a nonlocal separable quasipotential simulating the interaction between two relativistic spinless particles of unequal masses actually reduces to a one-body problem. This is due to the possibility of representing, within the relativistic quasipotential approach to quantum field theory, the total c.m. energy of two relativistic particles of unequal masses as an expression proportional to the energy of an effective relativistic particle of mass m'.

ACKNOWLEDGMENTS

I am grateful to Yu.S. Vernov, V.I. Savrin, and A.M. Shirokov for a permanent interest in this study and for enlightening discussions on the results presented here.

REFERENCES

1. I. M. Gel'fand and B. M. Levitan, Dokl. Akad. Nauk SSSR **77**, 557 (1951).
2. I. M. Gel'fand and B. M. Levitan, Izv. Akad. Nauk SSSR, Ser. Mat. **15**, 309 (1951).
3. V. A. Marchenko, Dokl. Akad. Nauk SSSR **104**, 695 (1955).
4. M. G. Kreĭn, Dokl. Akad. Nauk SSSR **76**, 21 (1951).
5. M. G. Kreĭn, Dokl. Akad. Nauk SSSR **76**, 345 (1951).
6. K. Chadan and P. C. Sabatier, *Inverse Problems in Quantum Scattering Theory* (Springer-Verlag, New York, 1977; Mir, Moscow, 1980).
7. B. N. Zakhariev and A. A. Suzko, *Direct and Inverse Problems: Potentials in Quantum Scattering* (Énergoatomizdat, Moscow, 1985; Springer-Verlag, Berlin, 1990).
8. A. A. Logunov and A. N. Tavkhelidze, Nuovo Cimento **29**, 380 (1963).
9. V. G. Kadyshevsky, Nucl. Phys. B **6**, 125 (1968).
10. Yu. D. Chernichenko, Preprint No. 88-27/48, NIIYaF MGU (Institute of Nuclear Physics, Moscow State University, Moscow, 1988).
11. V. G. Kadyshevskiĭ, R. M. Mir-Kasimov, and N. B. Skachkov, Yad. Fiz. **9**, 462 (1969) [Sov. J. Nucl. Phys. **9**, 265 (1969)].

Translated by A. Isaakyan

Physics of Atomic Nuclei, Vol. 63, No. 11, 2000, pp. 1988–1992. From Yadernaya Fizika, Vol. 63, No. 11, 2000, pp. 2080–2084.

ELEMENTARY PARTICLES AND FIELDS
Theory

Estimating the Particle–Antiparticle Correlation Effect for Pion Production in Heavy-Ion Collisions*

I. V. Andreev

Lebedev Institute of Physics, Russian Academy of Sciences, Leninskiĭ pr. 53, Moscow, 117924 Russia

Received June 22, 1999; in final form, December 21, 1999

Abstract—Back-to-back $\pi\pi$ correlations arising owing to the evolution of the pionic field in the course of the pion-production process are estimated for central heavy-ion collisions at moderate energies. © *2000 MAIK "Nauka/Interperiodica".*

1. INTRODUCTION

It is usually suggested that in high-energy heavy-nucleus collisions, an excited volume is formed which undergoes evolution and subsequent decay into free final particles. Particles existing in the excited volume represent a part of the medium, being quasiparticles rather than free particles. So the form of their energy spectrum $E_{\mathbf{k}}$ may differ essentially from that of free particles $E^0_{\mathbf{k}} = (\mathbf{k}^2 + m^2)^{1/2}$. It was noted (see [1–4]) that this feature leads to the appearance of specific back-to-back particle–antiparticle correlations (PAC effect). No practical estimations of the pionic PAC effect is known to us.

Below we consider central heavy-nucleus collisions at moderate (a few GeV per nucleon in the laboratory system) energies. In this case, the excited volume consists mainly of nucleons and pions (at least, at the late stage). We consider final-state pion correlations. The PAC effect is determined through the evolution parameter $r(\mathbf{k})$ and depends on two factors: first, to what extent the pionic energy $E_{\mathbf{k}}$ is modified and, second, what the characteristic time t_0 of the energy spectrum evolution is. Our numerical estimations showed [4] that pion modification in the course of hadronic matter evolution (say expansion, cooling) is too slow to give a sizable PAC effect. So we consider only the fast breakup of hadronic matter into free pions (freeze-out) as a source of PAC. Usually the breakup is considered as an instantaneous process (neglecting its time duration t_0), thus ensuring the maximal PAC effect. However, the PAC effect under consideration is sensitive to rather small time intervals of the order of 1 fm. So below we estimate PAC for finite t_0.

2. HBT AND PAC EFFECTS

In this section, we describe in parallel the main features of identical particle correlations (Hanbury-Brown–Twiss (HBT) effect) and PAC taking into account pion energy modification. The reason for the PAC effect is the time evolution of the medium in which the (quasi)particles propagate. The corresponding problem is similar to that of a quantum oscillator with variable frequency. The solution of this problem can be represented in the form of the Bogolyubov transformation [5] of the creation and annihilation operators

$$\begin{aligned} a(\mathbf{k}, t) &= u(\mathbf{k})a(\mathbf{k}, 0) + v(\mathbf{k})b^\dagger(-\mathbf{k}, 0), \\ b^\dagger(-\mathbf{k}, t) &= v(\mathbf{k})a(\mathbf{k}, 0) + u(\mathbf{k})b^\dagger(-\mathbf{k}, 0), \end{aligned} \tag{1}$$

where $a(\mathbf{k}, t)$, $a^\dagger(\mathbf{k}, t)$, $b(\mathbf{k}, t)$, and $b^\dagger(\mathbf{k}, t)$ are time-dependent annihilation and creation operators of particles and antiparticles and the Bogolyubov coefficients $u(\mathbf{k})$, $v(\mathbf{k})$ satisfy the equation

$$|u(\mathbf{k})|^2 - |v(\mathbf{k})|^2 = 1 \tag{2}$$

preserving canonical commutation relations. The Bogolyubov coefficients $u(\mathbf{k})$, $v(\mathbf{k})$ are taken to be real-valued and $|\mathbf{k}|$-dependent. So we use a parametrization

$$u(\mathbf{k}) = \cosh r(\mathbf{k}), \quad v(\mathbf{k}) = \sinh r(\mathbf{k}) \tag{3}$$

introducing the evolution parameter $r(\mathbf{k})$ (for more details, see [4]).

To present the results in a simple form, we use here a simplified description of the excited hadronic volume (particle source). So the following expressions represent a limiting case of those in [1, 4].[1)] The volume is suggested to be homogeneous, motionless (neglect of the flow), isotopically symmetric, and large enough (heavy nuclei). Under these conditions, the single-particle

* This article was submitted by the author in English.

[1)] The sign of one of the two momenta $\mathbf{p}_1$, $\mathbf{p}_2$ on the right-hand side of the second of Eq. (14) in [1] must be changed. Then Eqs. (13) and (14) of that paper will be applicable for neutral pions. This erroneous sign appeared because of neglect of the difference between a relativistic quantum field and a simple set of quantum oscillators in [1].

1063-7788/00/6311-1988$20.00

inclusive cross section can be written in a simple form:

$$N(\mathbf{k}) = \frac{1}{\sigma}\frac{d\sigma}{d^3k} = \langle a^\dagger(\mathbf{k})a(\mathbf{k})\rangle = \frac{V}{(2\pi)^3}[n(\mathbf{k}) + (2n(\mathbf{k}) + 1)\sinh^2 r(\mathbf{k})], \quad (4)$$

where $a^\dagger$ and a are creation and annihilation operators of the final-state pions, V is the volume of the source, $n(\mathbf{k})$ is the level occupation number (for example, Bose distribution), and $r(\mathbf{k})$ is the evolution parameter.

Two-particle inclusive cross sections are given by the expressions

$$\frac{1}{\sigma}\frac{d^2\sigma^{++}}{d^3k_1 d^3k_2} = \langle a_1^\dagger a_2^\dagger a_1 a_2\rangle = \langle a_1^\dagger a_1\rangle\langle a_2^\dagger a_2\rangle + \langle a_1^\dagger a_2\rangle\langle a_2^\dagger a_1\rangle \quad (5)$$

for like-sign charged (identical) pions (HBT effect),

$$\frac{1}{\sigma}\frac{d^2\sigma^{+-}}{d^3k_1 d^3k_2} = \langle a_1^\dagger b_2^\dagger a_1 b_2\rangle = \langle a_1^\dagger a_1\rangle\langle b_2^\dagger b_2\rangle + \langle a_1^\dagger b_2^\dagger\rangle\langle a_1 b_2\rangle \quad (6)$$

for charged particle–antiparticle ($\pi^+\pi^-$) pairs (PAC), and

$$\frac{1}{\sigma}\frac{d^2\sigma^{00}}{d^3k_1 d^3k_2} = \langle a_1^\dagger a_2^\dagger a_1 a_2\rangle = \langle a_1^\dagger a_1\rangle\langle a_2^\dagger a_2\rangle + \langle a_1^\dagger a_2\rangle\langle a_2^\dagger a_1\rangle + \langle a_1^\dagger a_2^\dagger\rangle\langle a_1 a_2\rangle \quad (7)$$

for neutral pion pairs (both HBT and PAC) with

$$\langle a^\dagger(\mathbf{k}_1)a(\mathbf{k}_2)\rangle = [n(\mathbf{k}) + (2n(\mathbf{k}) + 1)\sinh^2 r(\mathbf{k})]F(\mathbf{k}_1 - \mathbf{k}_2), \quad (8)$$

$$\langle a(\mathbf{k}_1)b(\mathbf{k}_2)\rangle = \sinh 2r(\mathbf{k})\left[n(\mathbf{k}) + \frac{1}{2}\right]F(\mathbf{k}_1 + \mathbf{k}_2) \quad (9)$$

(the same for $\langle a(\mathbf{k}_1)a(\mathbf{k}_2)\rangle$ in the case of neutral pions). In (8) and (9), $F(\mathbf{k}_1 \pm \mathbf{k}_2)$ represents the Fourier transform of the source volume at the breakup stage. It is a sharply peaked function of $\mathbf{k}_1 \pm \mathbf{k}_2$ (at zero momentum) having a characteristic scale of the order of the inverse size of the source, this scale being much less than the characteristic scales of the pion momentum distribution $n(\mathbf{k})$ and evolution parameter $r(\mathbf{k})$. So the last two functions may be evaluated at any of the momenta $\mathbf{k}_1, \mathbf{k}_2 \approx \pm\mathbf{k}$ (we suggest that the process is $\mathbf{k} \longrightarrow -\mathbf{k}$ symmetric, for example, collision of identical nuclei at the center-of-mass system). Evidently, pion–pion interaction effects are not present in (6) and (7); it is supposed (as usual) that they can be separated from exposed PAC and HBT correlations.

Relative two-particle correlation functions which are measured in the experiment are given by

$$C_2^{++}(\mathbf{k}_1, \mathbf{k}_2) = 1 + \frac{|\langle a^\dagger(\mathbf{k}_1)a(\mathbf{k}_2)\rangle|^2}{N(\mathbf{k}_1)N(\mathbf{k}_2)}, \quad (10)$$

$$C_2^{+-}(\mathbf{k}_1, \mathbf{k}_2) = 1 + \frac{|\langle a(\mathbf{k}_1)b(\mathbf{k}_2)\rangle|^2}{N(\mathbf{k}_1)N(\mathbf{k}_2)}, \quad (11)$$

$$C_2^{00}(\mathbf{k}_1, \mathbf{k}_2) = 1 + \frac{|\langle a^\dagger(\mathbf{k}_1)a(\mathbf{k}_2)\rangle|^2}{N(\mathbf{k}_1)N(\mathbf{k}_2)} + \frac{|\langle a(\mathbf{k}_1)a(\mathbf{k}_2)\rangle|^2}{N(\mathbf{k}_1)N(\mathbf{k}_2)}. \quad (12)$$

Introducing the normalized form factor of the prebreakup volume,

$$F(\mathbf{k}_1 \pm \mathbf{k}_2) = \frac{V}{(2\pi)^3}G(\mathbf{k}_1 \pm \mathbf{k}_2), \quad G(0) = 1, \quad (13)$$

we therefore get

$$C^{++}(\mathbf{k}_1, \mathbf{k}_2) = 1 + G^2(\mathbf{k}_1 - \mathbf{k}_2), \quad (14)$$

$$C^{+-}(\mathbf{k}_1, \mathbf{k}_2) = 1 + c(\mathbf{k})G^2(\mathbf{k}_1 + \mathbf{k}_2), \quad (15)$$

$$C^{00}(\mathbf{k}_1, \mathbf{k}_2) = 1 + G^2(\mathbf{k}_1 - \mathbf{k}_2) + c(\mathbf{k})G^2(\mathbf{k}_1 + \mathbf{k}_2) \quad (16)$$

with

$$c(\mathbf{k}) = \left(\frac{\sinh r(\mathbf{k})\cosh r(\mathbf{k})(2n(\mathbf{k}) + 1)}{\sinh^2 r(\mathbf{k})(2n(\mathbf{k}) + 1) + n(\mathbf{k})}\right)^2, \quad (17)$$

where (14) gives the usual HBT effect and (15) describes the PAC effect. Both of them contain the same form factor $G(\mathbf{k})$ (in our approximation) ensuring the same-direction $\pi^+\pi^+$ correlations and back-to-back $\pi^+\pi^-$ correlations. Neutral pions show both kinds of correlations, being identical particles and simultaneously antiparticles to themselves.

As can be seen from (17), the PAC effect is determined through the evolution parameter $r(\mathbf{k})$. In turn, the evolution parameter depends on the time duration t_0 of the pion energy evolution. For very small characteristic times t_0, the expression for $r(\mathbf{k})$ is universal [1]:

$$r_m = \frac{1}{2}\ln\left(\frac{E_\mathbf{k}^0}{E_\mathbf{k}}\right), \quad t_0 = 0, \quad (18)$$

where $E_\mathbf{k}$ is the pion energy at the prebreakup moment and $E_\mathbf{k}^0$ is the free pion energy. For larger t_0, the evolution parameter lessens and depends on unknown details of the breakup process. For estimation of $r(\mathbf{k})$, we shall use the model expression of [4]:

$$r(\mathbf{k}) = \frac{1}{2}\ln\left(\frac{\tanh(\pi E_\mathbf{k}^0 t_0/2)}{\tanh(\pi E_\mathbf{k} t_0/2)}\right). \quad (19)$$

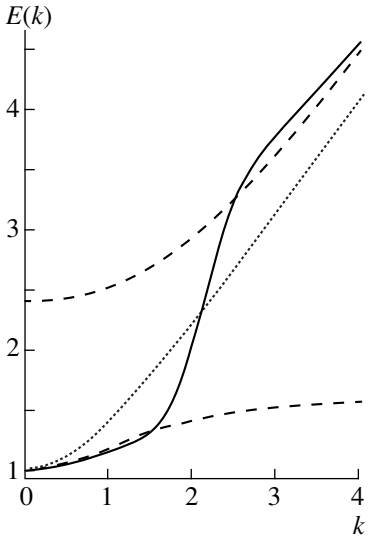

Fig. 1. Quasipion energy in nucleon medium (with $\rho = 0.5\rho_n$) calculated through pseudopotential (solid curve) and polarization operators (dashed curves), together with the free pion energy (dotted curve). All the values are taken in pion mass units.

Below, we estimate the evolution parameter $r(\mathbf{k})$ and the factor $c(\mathbf{k})$ in (17) which determines the strength of the PAC effect.

3. ESTIMATING PAC IN FINITE NUCLEON-DENSITY MATTER

To evaluate PAC, one has to know the pion energy spectrum $E_\mathbf{k}$ in finite nucleon-density matter. The simplest way to find the energy spectrum is the use of the notion of the pseudopotential [6]. It is determined as an effective potential in which the pions propagate, and it is given by the forward scattering amplitude $f(\mathbf{k})$ of the pions on the particles of the medium

$$U(\mathbf{k}) = -4\pi\rho\langle f(\mathbf{k})\rangle, \quad (20)$$

where ρ is the density of the medium particles and the amplitude $f(\mathbf{k})$ is averaged over the states of the medium particles.

In finite nucleon-density matter, $f(\mathbf{k})$ is mainly the πN-scattering amplitude. The main contribution to the amplitude is given here by P-wave scattering dominated by delta resonance. The corresponding momentum-dependent effective potential for isotopically symmetric (number of protons is equal (close) to the number of neutrons) matter may be taken in the form (see also [7, 8])

$$U(\mathbf{k}) = -\frac{8}{9}f_\Delta^2\frac{M_\Delta E_\Delta}{Mm^2}\frac{\mathbf{k}^2}{E_\Delta^2 - \mathbf{k}^2 - m^2} \quad (21)$$

with

$$f_\Delta^2/4\pi = 0.37, \quad (22)$$

$$E_\Delta = (M_\Delta^2 - M^2 - iM_\Delta\Gamma_\Delta)/2M = (2.4 - 0.5i)m, \quad (23)$$

where f_Δ is the empirical $\pi N\Delta$ coupling constant, m is the pion mass, M is the nucleon mass, and M_Δ and Γ_Δ are the mass and width of the delta resonance. Equations (21)–(23) represent the sum of the direct and exchange πN-scattering diagrams with delta resonance in the intermediate state where we neglected nucleon velocities and omitted terms containing the inverse nucleon mass (first order M^{-1} terms give only a few percent correction to E_Δ). The pion energy in the nucleon matter is now given by the equation

$$E_\mathbf{k}^2 = m^2 + \mathbf{k}^2 + U(\mathbf{k}). \quad (24)$$

It is shown in Fig. 1 for nucleon density ρ equal to one-half of the nuclear matter density (energies and momenta are taken in pion mass units).

Let us note that (24) has the form of the pionic dispersion equation with substitution of the effective potential $U(\mathbf{k})$ for the pionic polarization operator $\Pi(\mathbf{k}, E_\mathbf{k})$, which depends on both momentum $\mathbf{k}$ and energy $E_\mathbf{k}$. The polarization operator $\Pi(\mathbf{k}, E_\mathbf{k})$ in the same approximation is given by (21) with substitution of the energy squared $E_\mathbf{k}^2$ for $\mathbf{k}^2 + m^2$ in the denominator of (21), and the pion spectrum (excitations having pion quantum numbers) is then given by the self-consistent solution of the resulting dispersion equation. At first sight, the resulting pion energy spectrum [7] differs essentially from that of (24), containing at least two branches shown in Fig. 1 by dashed curves (original pion and delta-hole mixed states tend to be intersecting ones in the limit of zero coupling constant f_Δ). However, when considering the effects of the pion-energy evolution, one must use two pieces of these two branches which correspond to true pions and we essentially return to the single branch given by (24); see solid curve in Fig. 1. The vicinity of the would-be intersection point (the resonant point $\mathbf{k}_{\rm res}^2 + m^2 = \mathrm{Re}\,E_\Delta^2$, $k_{\rm res} = 2.1m$), where these two descriptions still differ, does not contribute in any case (here, $r(k_{\rm res}) = 0$ and the imaginary part of the pion energy is maximal and large). All that justifies the use of the pseudopotential $U(\mathbf{k})$ for calculation of the evolution parameter $r(\mathbf{k})$ (introduction of the polarization operator $\Pi(\mathbf{k}, E_\mathbf{k})$ would require a reformulation of the scheme of calculation of the evolution effects).

To evaluate the evolution effects, it is necessary to specify the level population $n(\mathbf{k})$, the nucleon density ρ at breakup, and the time duration t_0 of the breakup stage of the process. The level population can be estimated from thermal analysis of the data on momentum spectra of secondary particles. When extracted from the slope of the spectra, the apparent temperature gradually increases with energy and seems to saturate at around 140 MeV at a beam energy $E_L \approx 10$ GeV (see [9], for example). Below, the level population will be approximated by a Bose distribution with temperature 120 MeV

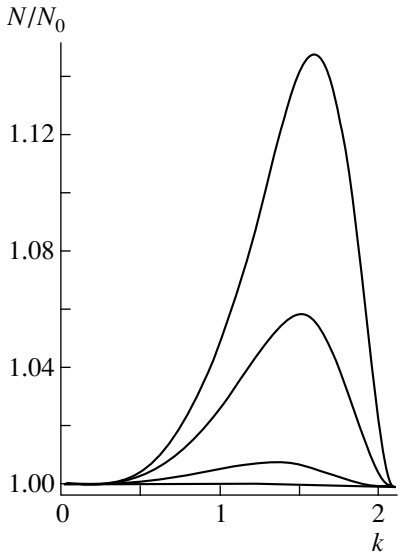

Fig. 2. Enhancement of the single-particle inclusive cross section due to the evolution effect at nucleon density $\rho = 0.5\rho_n$ for $t_0 = 0$, 0.5, 1.0, 1.5 fm (from top to bottom); momentum k is taken in pion mass units.

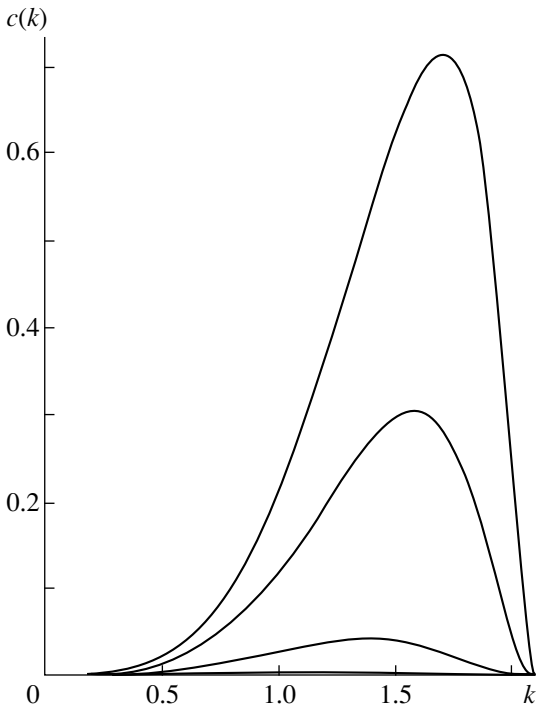

Fig. 3. Relative strength of the PAC effect (see (15)–(17)) at nucleon density $\rho = 0.5\rho_n$ for $t_0 = 0$, 0.5, 1.0, 1.5 fm (from top to bottom); momentum $k = |\mathbf{k}_1 - \mathbf{k}_2|/2$ is taken in pion mass units.

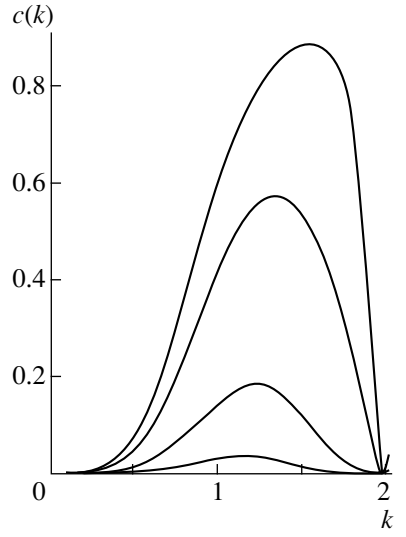

Fig. 4. The same as in Fig. 3 for nucleon density $\rho = \rho_n$.

corresponding to a beam energy of about a few GeV per nucleon,

$$n(\mathbf{k}) = (\exp(E_\mathbf{k}/T) - 1)^{-1}, \quad T = 120 \text{ MeV}. \quad (25)$$

It seems reasonable to take the nucleon density ρ to be slightly less than nuclear matter density ρ_n. So below, we present estimations for two values of ρ which we consider as limiting ones, $\rho = 0.5\rho_n$ and $\rho = \rho_n$. The time duration t_0 is left as a free parameter.

One more problem is the permissible range of the pion momenta $\mathbf{k}$, where the potential $U(\mathbf{k})$ given by (21) (that is, the corresponding scattering amplitude) may be used. Evidently, this is a low-energy potential applicable at the most at $k \le (3–4)m$. Furthermore, the imaginary part of the potential must not exceed the difference between the quasipion energy and free pion energy. This leaves us a small momentum region $k \le 1.5m$ where the calculation of the PAC effect seems to be reliable. It must also be noted that just above the delta resonance energy ($k_{\text{res}} = 2.1m$), there is another source of back-to-back pairs, that is, ρ-meson decay ($k = (2.5 \pm 0.5)m$ for free ρ mesons). So the PAC effect under consideration is an additional possible source of the correlated $\pi\pi$ pairs active at lower energies.

Calculation of the evolution parameter $r(\mathbf{k})$ according to (18) and (19), together with (21)–(24), shows that in the case under consideration, it is rather small, being zero at $k = 0$ and at $k = k_{\text{res}} = 2.1m$ and reaching the maximal values

$$r_{\max}(\mathbf{k}) = 0.16 \text{ at } k = 1.6m \text{ for } \rho = 0.50\rho_n, \quad t_0 = 0;$$
$$r_{\max}(\mathbf{k}) = 0.22 \text{ at } k = 1.5m \text{ for } \rho = 0.75\rho_n, \quad t_0 = 0;$$
$$r_{\max}(\mathbf{k}) = 0.30 \text{ at } k = 1.3m \text{ for } \rho = 1.00\rho_n, \quad t_0 = 0.$$

The function $r(\mathbf{k})$ decreases fast when the characteristic time t_0 increases and vanishes at $t_0 \approx 2$ fm.

The enhancement of single-particle inclusive cross sections arising due to the evolution effect is shown in Fig. 2, where the distribution $N(\mathbf{k})$ given by (4), over the nonenhanced ($r = 0$) value $N_0(\mathbf{k})$, is depicted for different values of the characteristic time t_0 for nucleon

density $\rho = 0.5\rho_n$ (pion momenta in Figs. 2–4 are taken in pion mass units). At higher nucleon densities, the enhancement rises, reaching at $\rho = \rho_n$ the maximal values 1.37 at $t_0 = 0$, 1.21 at $t_0 = 0.5$ fm, 1.05 at $t_0 = 1.0$ fm, and 1.02 at $t_0 = 1.5$ fm.

The results for the factor $c(\mathbf{k})$ in (15)–(17), which gives the strength of the PAC effect, are shown in Figs. 3 and 4. As can be seen, the PAC effect can be essential if the characteristic breakup time t_0 is small enough ($t_0 < 1$ fm). The presence or absence of PAC can serve as a measure of the time duration t_0, about which we have no other information. Contrary to single-particle enhancement, which can have various origins, the PAC effect can be unambiguously identified through measurement of the excess of, say, zero-rapidity (in the center-of-mass system) small-momentum anticorrelated particle–antiparticle pairs.

4. CONCLUSION

Estimation of the pionic PAC effect in heavy-nucleus collisions shows that it can serve as a substantial source of low-energy back-to-back $\pi^+\pi^-$ and $\pi^0\pi^0$ pairs (also ensuring an enhancement of single-particle pion distributions) if the breakup (freezeout) time is small enough.

REFERENCES

1. I. V. Andreev and R. M. Weiner, Phys. Lett. B **373**, 159 (1996).
2. M. Asakawa and T. Csorgo, Heavy Ion Phys. **4**, 233 (1996).
3. H. Hiro-Oka and H. Minakata, Phys. Lett. B **425**, 129 (1998).
4. I. V. Andreev, Mod. Phys. Lett. A **14**, 459 (1999).
5. N. N. Bogoliubov, Bull. Acad. Sci. USSR, Phys. Ser. **11**, 77 (1947).
6. M. Goldberger, and K. Watson, *Collision Theory* (Wiley, New York, 1964; Mir, Moscow, 1967).
7. A. B. Migdal, Rev. Mod. Phys. **50**, 107 (1978).
8. E. Oset, H. Toki, and W. Weise, Phys. Rep. **83**, 281 (1982).
9. H. G. Ritter, in *Proceedings of 5th International Workshop on Relativistic Aspects of Nuclear Physics, Rio de Janeiro* (World Sci., Singapore, 1997), p. 89.

Physics of Atomic Nuclei, Vol. 63, No. 11, 2000, pp. 1993–1998. From Yadernaya Fizika, Vol. 63, No. 11, 2000, pp. 2085–2090.

ELEMENTARY PARTICLES AND FIELDS
Theory

Multichannel Phase-Equivalent Transformation and Supersymmetry*

A. M. Shirokov and V. N. Sidorenko[1)], *****

Institute of Nuclear Physics, Moscow State University, Vorob'evy gory, Moscow, 119899 Russia

Received June 8,1999; in final form, November 12, 1999

Abstract—A phase-equivalent transformation of local interaction is generalized to the multichannel case in the direct-scattering problem. Generally, the transformation does not change the number of bound states in the system and their energies. For a special choice of the parameters involved, however, the transformation removes one of the bound states and is equivalent to the multichannel supersymmetry transformation recently proposed by J.M. Sparenberg and D. Baye (1997). With the aid of the transformation, it is also possible to add a bound state to the discrete spectrum of the system at a given energy $E < 0$ if the angular momentum $l \geq 2$ in at least one of the coupled channels. © *2000 MAIK "Nauka/Interperiodica".*

1. INTRODUCTION

Nucleon–nucleon, nucleon–cluster, and cluster–cluster potentials are an input for various microscopic calculations of nuclear structure and reactions. Unfortunately, the exact form of the potentials describing these interactions is unknown. It is conventionally supposed that the available scattering data and bound state properties can be fitted with approximately the same accuracy by different local potentials. For example, there are a lot of so-called realistic *NN* potentials on the market describing *NN* scattering and deuteron properties with high accuracy. Moreover, a description of phenomenological data can be achieved with potentials very different in structure. In particular, meson-exchange *NN* potentials of the Nijmegen kind [1] are known to have a short-range repulsive core in a triplet *s* wave. The same high-quality description of the nucleon–nucleon data is provided by the latest versions of the Moscow potential [2, 3] that does not have a repulsive core but instead is deeply attractive in the triple *s* wave at short distances and supports an additional forbidden state. The possibility of alternative descriptions of various cluster–cluster and nucleon–cluster interactions by means of repulsive-core and deeply attractive potentials with forbidden states is also well known (see, e.g., the discussion in [2] and references therein).

Principally, it is possible to distinguish experimentally between alternative potentials by studying their off-shell properties in interactions with an additional particle. The simplest probe is the photon, and as it was shown in [4–6], the proton–proton bremsstrahlung reaction $pp \longrightarrow pp\gamma$ in the energy range of 350–400 MeV can be used to discriminate between various *NN* potentials. However, the $pp \longrightarrow pp\gamma$ reaction has not been examined experimentally in this energy range.

Another possibility is to study the properties of three- and four-body systems bound by two-body potentials of interest. From this point of view, it looks like we do not have satisfactory nucleon–nucleon, cluster-nucleon, and cluster–cluster potentials at present. It is well known that none of the realistic *NN* potentials provides proper binding of tritium or ^{3}He. There have been successful attempts in generating phenomenological three-nucleon interactions tuned to fit the properties of light nuclei [7] (see also [8] and references therein). However, as it was shown in the detailed study of Picklesimer *et al.* [9], the effect of three-nucleon forces consistent with realistic two-body ones on the binding energy of the triton is canceled by the effects of virtual excitations of Δ isobars, etc. Hence, the trinucleon cannot be satisfactorily described using known realistic two-body potentials supplemented by three-body potentials consistent with them. All calculations within three-body cluster models also fail to reproduce the correct binding energy of three-cluster nuclear systems with known local cluster–cluster and cluster–nucleon potentials fitted to the corresponding scattering data.

To design a potential consistent with two-body phenomenological data and providing the correct binding of few-body systems, it seems promising to make use of phase-equivalent transformations depending on a continuous parameter(s). Some attempts in this direction have been performed using nonlocal phase-equivalent transformations. The results of these attempts are encouraging: in [10], an oversimplified *NN* potential providing a satisfactory description of *s*-wave *NN* scattering data was fitted to exactly reproduce the triton binding energy, while in [11], realistic $n\alpha$ potentials were tuned to reproduce various ^{6}He properties, including the binding energy within the $\alpha + n + n$ cluster

* This article was submitted by the authors in English.

** e-mail: shirokov@npi.msu.su

*** e-mail: sidorenko@goa.bog.msu.su

1) Moscow State University, Vorob'evy gory, Moscow, 119899 Russia.

model. The interactions suggested in [10, 11] are nonlocal ones. Various applications (see, e.g., [12, 13]) of local phase-equivalent transformations to few-body problems were restricted to the supersymmetry transformation [14–16] that removes one of the bound states in a two-body system. The supersymmetry transformation does not contain parameters and cannot be used for fine tuning of the interaction of interest.

However, a local phase-equivalent transformation which preserves the number of bound states and depends on a continuous parameter exists and is well known in the inverse scattering theory [17]. To the best of our knowledge, so far nobody has used it in few-body calculations. This transformation was developed for a single-channel case only and cannot be applied without some approximations to realistic *NN* interactions that mix triplet *s* and *d* partial waves. Another drawback of the transformation is that it involves a bound-state wave function and, thus, cannot be used to modify *nn* and *pp* interactions and the *np* interaction in all "nondeuteron" partial waves.

Recently, Sparenberg and Baye [18] suggested a multichannel supersymmetry transformation. We use some ideas of [18] to derive a multichannel phase-equivalent transformation which depends on continuous parameters. The transformation can be treated as a generalization of both the single-channel phase-equivalent transformation [17] and the multichannel supersymmetry transformation of [18]. Generally, the transformation does not change the number of bound states in the system and their energies. However, with a special choice of the parameters, the transformation removes one of the bound states and becomes equivalent to the multichannel supersymmetry transformation suggested in [18]. If the angular momenta in all coupled channels are less than two, a parameter-dependent family of local interactions phase-equivalent to the given initial one can be constructed by means of the transformation, even in the case when the system does not have a bound state. If the angular momentum is $l \geq 2$ in at least one of the coupled channels, the transformation can be used to add a bound state to the discrete spectrum of the system at a given energy $E < 0$. Having a bound state, one can construct a family of phase-equivalent potentials and afterwards remove the bound state by the supersymmetry version of the transformation. Thus, the suggested transformation can be used in a multichannel case to produce phase-equivalent interactions without any restriction on the structure of the discrete spectrum of the system. In particular, the transformation can be applied to the realistic *NN* interaction in all partial waves.

2. GENERAL FORM OF LOCAL MULTICHANNEL PHASE-EQUIVALENT TRANSFORMATION

Multichannel scattering and bound states are described by the Schrödinger equation

$$\sum_j (H_{ij} - E\delta_{ij})\varphi_j(E, r) = 0, \tag{1}$$

where indices i and j label the channels, E is the energy,

$$H_{ij} = \frac{\hbar^2}{2m}\left[-\frac{d^2}{dr^2} + \frac{l_i(l_i+1)}{r^2}\right]\delta_{ij} + V_{ij}(r) \tag{2}$$

is the Hamiltonian, m is the reduced mass, and l_i stands for the angular momentum in the channel i. We suppose that the potential $V_{ij}(r)$ (i) is Hermitian and (ii) tends asymptotically at large distances to a diagonal constant matrix,

$$V_{ij}(r) \xrightarrow[r\to\infty]{} \epsilon_i\delta_{ij}, \tag{3}$$

where ϵ_i is a threshold energy in the channel i. We suppose that $\epsilon_1 = 0$ and $\epsilon_i \geq \epsilon_j$ if $i > j$.

The boundary conditions for the wave functions are

$$\varphi_i(E, 0) = 0, \tag{4}$$

$$\varphi_i(E, \infty) < \infty. \tag{5}$$

Except for the discussion in Section 3.3, we suppose that there is at least one bound state in the system at the energy E_0. The corresponding wave function $\varphi_i(E_0, r)$ is supposed to be normalized:

$$\sum_i \int_0^\infty \varphi_i^*(E_0, s)\varphi_i(E_0, s)ds = 1, \tag{6}$$

where "$*$" denotes complex conjugation. Of course, $\varphi_i(E_0, r)$ fits a more severe boundary condition for $r \longrightarrow \infty$ than (5):

$$\varphi_i(E_0, \infty) = 0. \tag{7}$$

We define the transformed potential $\tilde{V}_{ij}(r)$ as

$$\tilde{V}_{ij}(r) = V_{ij}(r) + v_{ij}(r), \tag{8}$$

where

$$v_{ij}(r) = -2C\frac{\hbar^2}{2m}\frac{d}{dr}\frac{\varphi_i(E_0, r)\varphi_j^*(E_0, r)}{A + C\sum_k \int_a^r |\varphi_k(E_0, s)|^2 ds} \tag{9}$$

and A, C, and a are arbitrary real parameters.

The main result of this paper can be formulated as the following statement.

The wave function

$$\tilde{\varphi}_i(E, r) = \varphi_i(E, r) - C\varphi_i(E_0, r)\frac{\sum_k \int_a^r \varphi_k^*(E_0, s)\varphi_k(E, s)ds}{A + C\sum_k \int_a^r |\varphi_k(E_0, s)|^2 ds} \tag{10}$$

fits the nonhomogeneous multichannel Schrödinger equation

$$\sum_j (\tilde{H}_{ij} - E\delta_{ij})\tilde{\varphi}_j(E, r) = C\frac{\hbar^2}{2m}\frac{\varphi_i(E_0, r)}{A + C\sum_k \int_a^r |\varphi_k(E_0, s)|^2 ds}\mathcal{W}(E_0, E; a), \quad (11)$$

where the Hamiltonian

$$\tilde{H}_{ij} = \delta_{ij}\frac{\hbar^2}{2m}\left[-\frac{d^2}{dr^2} + \frac{l_i(l_i+1)}{r^2}\right] + \tilde{V}_{ij}(r) \quad (12)$$

and the quasi-Wronskian

$$\mathcal{W}(E_0, E; a) \equiv \sum_k [\varphi_k^*(E_0, a)\varphi_k'(E, a) - \varphi_k^{*\prime}(E_0, a)\varphi_k(E, a)]. \quad (13)$$

We use the prime to denote derivatives: $f' \equiv df/dr$.

To prove the statement, one can verify (11) by the direct calculation of $\sum_j (\tilde{H}_{ij} - E\delta_{ij})\tilde{\varphi}_j(E, r)$ using definitions (8)–(10) and (12) and other formulas given above, as well as the fact that the interaction $V_{ij}(r)$ is Hermitian, $V_{ij}^*(r) = V_{ji}(r)$. The calculation is lengthy but straightforward.

It is clear from (10) and (7) that the suggested transformation is phase-equivalent at any energy $E > 0$; all the bound states supported by the initial potential V_{ij} are preserved by the transformation, since the wave functions $\tilde{\varphi}_i(E_b, r)$ for the corresponding energies $E_b < 0$ (including E_0) fit both boundary conditions (4) and (7). However, the denominator in the last term in (10) should be nonzero at any distance r; therefore, one should be accurate in assigning values to arbitrary parameters A, C, and a. This requirement can be easily satisfied in a wide and continuous range of parameter values.

3. PARTICULAR CASES OF THE PHASE-EQUIVALENT TRANSFORMATION

3.1. Homogeneous Schrödinger Equation

Of course, we are mostly interested in phase-equivalent transformations that result in the homogeneous Schrödinger equation

$$\sum_j (\tilde{H}_{ij} - E\delta_{ij})\tilde{\varphi}_j(E, r) = 0 \quad (14)$$

instead of the nonhomogeneous Schrödinger equations (11). To derive the transformation leading to (14), we can search for the parameters A, C, and a providing zero values of the right-hand side of (11). The choice $C = 0$ brings us to the equivalent (contrary to phase-equivalent) transformation that is of no interest. Thus, we should search for the parameters that fit the equation

$$\mathcal{W}(E_0, E; a) = 0. \quad (15)$$

Two obvious solutions of (15) are $a = 0$ and $a = \infty$. Various other solutions of (15) can be found for particular potentials $V_{ij}(r)$. However, the nonzero finite solutions a of (15) are energy-dependent. With the solutions $a(E)$ of (15), we can obtain energy-dependent potentials $\tilde{V}_{ij}(E; r)$ phase-equivalent to the initial energy-independent potential $V_{ij}(r)$. It may be interesting for some applications, but we shall not discuss the energy-dependent transformation and shall concentrate our attention on the solutions $a = 0$ and $a = \infty$.

The case $a = 0$ presents a generalization of the single-channel phase-equivalent transformation from [17]. For the bound state at the energy E_0, the wave function obtained by means of the transformation is of the form

$$\tilde{\varphi}_i(E_0, r) = \frac{A\varphi_i(E_0, r)}{A + C\sum_j \int_0^r |\varphi_j(E_0, s)|^2 ds}. \quad (16)$$

The wave function (16) is not normalized. The normalization constant can be easily calculated. The normalized bound-state wave function is

$$\sqrt{\frac{A+C}{A}}\tilde{\varphi}_i(E_0, r) = \frac{\sqrt{A(A+C)}\varphi_i(E_0, r)}{A + C\sum_j \int_0^r |\varphi_j(E_0, s)|^2 ds}. \quad (17)$$

It is interesting that the components of the bound-state wave function in all channels are modified by the transformation synchronously: all the components $\varphi_i(E_0, r)$ are multiplied by the same factor $\sqrt{A(A+C)}\,(A + C\sum_j \int_0^r |\varphi_j(E_0, s)|^2 ds)^{-1}$. Nevertheless, the relative weight of the components $\varphi_i(E_0, r)$ in the norm of the total multichannel wave function can be changed by the transformation.

Let us now discuss the case of $a = \infty$. The transformed wave function in this case is of the form

$$\tilde{\varphi}_i(E, r) = \varphi_i(E, r) - \frac{C\varphi_i(E_0, r)\sum_j \int_\infty^r \varphi_j^*(E_0, s)\varphi_j(E, s) ds}{A + C\sum_j \int_\infty^r |\varphi_j(E_0, s)|^2 ds}. \quad (18)$$

If $E \neq E_0$, the functions $\varphi_i(E, r)$ and $\varphi_i(E_0, r)$ are orthogonal:

$$\int_0^\infty \varphi_i^*(E_0, s)\varphi_i(E, s)ds = 0. \quad (19)$$

With the help of (19) and (6), we can rewrite (18) as

$$\tilde{\varphi}_i(E, r) = \varphi_i(E, r) - \frac{C\varphi_i(E_0, r)\sum_j \int_0^r \varphi_j^*(E_0, s)\varphi_j(E, s)ds}{A - C + C\sum_j \int_0^r |\varphi_j(E_0, s)|^2 ds}. \quad (20)$$

It is seen from (20) that the case of $a = \infty$ is identical (up to the redefinition of the parameter $A \longrightarrow A + C$) to the case of $a = 0$ if $E \neq E_0$. It is clear, however, that after the redefinition of the parameter $A \longrightarrow A + C$, the potential $V_{ij}(r)$ obtained with $a = \infty$ becomes equivalent to the potential $V_{ij}(r)$ corresponding to the case of $a = 0$. Hence, the case of $a = \infty$ appears to be equivalent to the case of $a = 0$ at any energy E, including $E = E_0$. To demonstrate this explicitly, let us examine the wave function $\tilde{\varphi}_i(E_0, r)$ in the case of $a = \infty$. Replacing E by E_0 in (18), we obtain

$$\tilde{\varphi}_i(E_0, r) = \frac{A\varphi_i(E_0, r)}{A + C\sum_j \int_\infty^r |\varphi_j(E_0, s)|^2 ds} \quad (21)$$

or, equivalently,

$$\tilde{\varphi}_i(E_0, r) = \frac{A\varphi_i(E_0, r)}{A - C + C\sum_j \int_0^r |\varphi_j(E_0, s)|^2 ds}. \quad (22)$$

Replacing A by $A + C$ and normalizing the wave function (22), we obtain expression (17).

3.2. Supersymmetry

Let us discuss a particular choice of parameters: $C = 1$, $a = \infty$, and $A = 1$. The wave function in this case is

$$\tilde{\varphi}_i(E, r) = \varphi_i(E, r) + \frac{\varphi_i(E_0, r)\sum_j \int_r^\infty \varphi_j^*(E_0, s)\varphi_j(E, s)ds}{\sum_j \int_0^r |\varphi_j(E_0, s)|^2 ds} \quad (23)$$

or

$$\tilde{\varphi}_i(E, r) = \varphi_i(E, r) - \frac{\varphi_i(E_0, r)\sum_j \int_0^r \varphi_j^*(E_0, s)\varphi_j(E, s)ds}{\sum_j \int_0^r |\varphi_j(E_0, s)|^2 ds}. \quad (24)$$

Equation (23) can be used at any energy E, while (24) is applicable only if $E \neq E_0$. In the case of $E = E_0$, the wave function can be rewritten in a simpler form as

$$\tilde{\varphi}_i(E_0, r) = \frac{\varphi_i(E_0, r)}{\sum_j \int_0^r |\varphi_j(E_0, s)|^2 ds}. \quad (25)$$

Equation (23) is just Eq. (4) of [18]. In [18], Sparenberg and Baye suggested a multichannel supersymmetry transformation. Thus, Eqs. (24) and (25) describe the multichannel supersymmetry transformation, or, in other words, the multichannel supersymmetry transformation is a particular case of the phase-equivalent multichannel transformation discussed in this paper that corresponds to the particular choice of the parameters. Let us discuss how it works.

It is clear from (25) that $|\tilde{\varphi}_i(E_0, r)| \longrightarrow \infty$ as $r \longrightarrow 0$. Hence, at the energy E_0, the wave function $\tilde{\varphi}_i(E_0, r)$ does not match the required boundary condition (4) at $r = 0$. At the same time, $\tilde{\varphi}_i(E_0, r)$ fits the boundary condition (7) at $r = \infty$. Therefore, it is impossible to construct another solution of the Schrödinger equation (14) consistent with both boundary conditions at the energy $E = E_0$. As a result, the phase-equivalent transformation removes the bound state at $E = E_0$. At the same time, it is clear from (24) that for all energies $E \neq E_0$, the zero in the denominator arising in the limit $r \longrightarrow 0$ is canceled by the zero in the numerator and the wave function (24) matches the boundary conditions at the origin and at infinity both at once. Thus, the transformation in this case removes the bound state at $E = E_0$ but none of the other bound states, while the S-matrix at any energy $E > 0$ is unchanged.

Of course, the supersymmetry transformation can also be formulated in the case of $a = 0$. It is interesting that the bound state in this case is removed by a different mechanism. Suppose that $A = 0$ and that C is arbitrary. The wave function at any energy E in this case may be written as (24). However, it is seen that, at $E = E_0$, the wave function $\tilde{\varphi}_i(E_0, r) \equiv 0$.

We used the boundary condition (4) to construct the supersymmetry transformation: the bound state is removed because, for some particular parameter values, the wave function $\tilde{\varphi}_i(E_0, r)$ diverges at the origin and appears to be inconsistent with (4). One can sup-

pose that it is also possible to use the boundary condition at $r = \infty$ to remove the bound state and to construct another supersymmetry transformation. This is not so. Let us discuss the case of $a = \infty$, $A = 0$, and arbitrary C. As is seen from (18), $\tilde{\varphi}_i(E_0, r) \equiv 0$ in this case; thus, the bound state is removed. However, the transformation is no longer phase-equivalent. Indeed, at energies $E > E_0$, the last term in (18) does not vanish when $r \longrightarrow \infty$ and provides an additional phase shift, or, in other words, it modifies the S matrix.

3.3. Inverse Supersymmetry

We shall refer to a transformation that adds a bound state to the discrete spectrum of the system and leaves unchanged the S matrix and the energies of all bound states supported by the initial Hamiltonian as the inverse supersymmetry transformation.

Let us suppose that there is no bound state at the energy $E_0 < 0$. By $\varphi_i(E_0, r)$, we now denote the wave function at energy E_0 that matches the boundary condition (7) at infinity but diverges at the origin as r^{-l_i} (see, e.g.,[2)] [19]), where l_i is the angular momentum in the channel i.

With $\varphi_i(E_0, r)$, we can use our transformation to obtain the homogeneous Schrödinger equation (14) in the case of $a = \infty$. The transformed wave function $\tilde{\varphi}_i(E, r)$ is given by (18). It is seen from (18) that $\tilde{\varphi}_i(E, r)$ does not diverge at the origin and matches the boundary conditions, both at the origin and at infinity, at any energy $E \neq E_0$. For $E = E_0$, the transformed wave function $\tilde{\varphi}_i(E_0, r)$ is given by (21). It is clear that $\tilde{\varphi}_i(E_0, r)$ at the origin is proportional to $r^{2L - l_i - 1}$, where $L = \max\{l_i\}$. Hence, $\tilde{\varphi}_i(E_0, r)$ matches the boundary condition (4) if $L \geq 2$ and is not consistent with (4) if $L \leq 1$. Therefore, our transformation with $\varphi_i(E_0, r)$ irregular at the origin is the inverse supersymmetry transformation in the case of $L \geq 2$. In the case of $L \leq 1$, the transformation appears to be a phase-equivalent transformation that does not make use of the bound state and can be applied to a system that does not support a bound state. If the transformation is applied to the free Hamiltonian with $V_{ij}(r) \equiv 0$ in the s or p partial wave, it produces a nonzero "transparent" potential $\tilde{V}_{ij}(r)$ that provides the phase shift $\delta = 0$ at any energy E. The multichannel version of the transformation couples s and p partial waves to produce a two-channel "transparent" interaction that provides the S matrix of the form $S_{ij} = \delta_{ij}$.

[2)]The r^{-l} divergence of the wave functions at the origin is derived in [19] for the single-channel case only. However, the derivation of the r^{-l} rule from [19] can be easily generalized to the multichannel case, at least for the potentials that do not diverge at the origin.

It is interesting that the inverse supersymmetry transformation is not unique: we have three parameters E_0, A, and C that provide a family of inverse supersymmetry partner potentials. Contrary to it, the supersymmetry transformation is unique; however, it can be used in combination with the phase-equivalent transformation to construct a family of potentials phase-equivalent to the initial one but not supporting one of the bound states.

4. CONCLUSION

We derived a multichannel phase-equivalent transformation that can be used without restrictions on the structure of the discrete spectrum of the system in various scattering problems like *NN* scattering, nucleon–cluster, or cluster–cluster scattering. The multichannel supersymmetry and inverse supersymmetry transformations appear to be particular cases of the suggested general phase-equivalent transformation corresponding to particular choices of the parameter values. The inverse supersymmetry transformation is possible if only the orbital angular momentum $l_i \geq 2$ in at least one of the coupled channels. It is interesting to note that, from the point of view of the *NN* system, this means that a deep attractive *NN* potential, supporting an additional forbidden state like the Moscow *NN* potential, can be constructed through the inverse supersymmetry transformation of the realistic meson-exchange potential with a repulsive core only due to the *d*-wave admixture in the deuteron wave function.

By using the suggested transformation, one can construct a family of phase-equivalent potentials depending on continuous parameters. Such families may be very useful for fine tuning of the interaction aimed to fit not only two-body observables but also three- and few-body ones. If the system has at least one bound state, the phase-equivalent potential family is constructed using formulas (8) and (9) directly. One can construct phase-equivalent single- or multichannel potential families also in the case when there are no bound states in the system: if all channel orbital angular momenta $l_i \leq 1$, one can directly apply the transformation with the irregular function $\varphi_i(E_0, r)$; if at least one of the channel orbital angular momenta $l_i \geq 2$, one can produce a bound state using inverse supersymmetry at the first stage and remove the bound state at the final stage by using the supersymmetry version of the transformation. Thus, one can, for example, construct a family of phase-equivalent potentials for any combination of coupled partial waves in the *NN* system.

It should be noted that our method allows to one construct the family of phase-equivalent potentials with given properties of the spectrum in the multichannel case without use of Gelfand–Levitan–Marchenko procedure applied in the inverse scattering problem (for example, see [20]).

We hope that the suggested transformation will be useful in various few-body applications.

ACKNOWLEDGMENTS

We are grateful to A.I. Mazur, A. Mondragon, V.N. Pomerantsev, D.L. Pursey, Yu.F. Smirnov, J.P. Vary, and T.A. Weber for stimulating discussions.

This work was supported in part by the Competitive Center at St. Petersburg State University and by the State Program "Universities of Russia."

Note added in proof. Some of the problems discussed here were also considered in [21]. In particular, it was found there that it is impossible to add a bound state in the case of $L < 2$.

REFERENCES

1. V. G. J. Stoks, R. A. M. Klomp, C. P. F. Terheggen, *et al.*, Phys. Rev. C **49**, 2950 (1994).
2. V. I. Kukulin and V. N. Pomerantsev, Prog. Theor. Phys. **88**, 159 (1992).
3. V. I. Kukulin, V. N. Pomerantsev, A. Faessler, *et al.*, Phys. Rev. C **57**, 535 (1998).
4. V. G. Neudatchin, N. A. Khokhlov, A. M. Shirokov, and V. A. Knyr, Yad. Fiz. **60**, 1086 (1997) [Phys. At. Nucl. **60**, 971 (1997)].
5. A. M. Shirokov, in *Proceedings of the XI International Workshop on Quantum Field Theory and High Energy Physics, Moscow, 1997*, Ed. by B. B. Levtchenko, p. 397.
6. N. A. Khokhlov, V. A. Knyr, V. G. Neudatchin, and A. M. Shirokov, Nucl. Phys. A **629**, 218 (1998).
7. B. S. Pudliner, V. R. Pandharipande, J. Carlson, *et al.*, Phys. Rev. C **56**, 1720 (1997).
8. R. B. Wiringa, Nucl. Phys. A **631**, 70c (1998).
9. A. Picklesimer, R. A. Rice, and R. Brandenburg, Phys. Rev. Lett. **68**, 1484 (1992); Phys. Rev. C **45**, 547, 2045, 2624 (1992); **46**, 1178 (1992).
10. A. M. Shirokov, Yu. F. Smirnov, and S. A. Zaytsev, Rev. Mex. Fis. **40** (1), 74 (1994).
11. Yu. A. Lurie and A. M. Shirokov, Izv. Akad. Nauk, Ser. Fiz. **61**, 2121 (1997).
12. E. Garrido, D. V. Fedorov, and A. S. Jensen, nucl-th/9903004.
13. H. Fiedeldey, S. A. Sofianos, A. Papastylianos, *et al.*, Phys. Rev. C **42**, 411 (1990).
14. A. A. Andrianov, N. V. Borisov, and M. V. Ioffe, Phys. Lett. A **105**, 19 (1984).
15. C. V. Sukumar, J. Phys. A **18**, 2937 (1985).
16. D. Baye, Phys. Rev. Lett. **58**, 2738 (1987).
17. R. G. Newton, *Scattering Theory of Waves and Particles* (Springer-Verlag, New York, 1982, 2nd ed.; Mir, Moscow, 1969).
18. J. M. Sparenberg and D. Baye, Phys. Rev. Lett. **79**, 3802 (1997).
19. L. D. Landau and E. M. Lifshitz, *Course of Theoretical Physics*, Vol. 3: *Quantum Mechanics: Non-Relativistic Theory* (Nauka, Moscow, 1989; Pergamon, New York, 1977).
20. B. N. Zakhariev and A. A. Suzko, *Direct and Inverse Problems: Potentials in Quantum Scattering* (Énergoatomizdat, Moscow, 1985; Springer-Verlag, Berlin, 1990).
21. B. N. Zakhariev and V. M. Chabanov, Fiz. Élem. Chastits At. Yadra **30**, 277 (1999) [Phys. Part. Nucl. **30** (1999)].

Physics of Atomic Nuclei, Vol. 63, No. 11, 2000, pp. 1999–2003. Translated from Yadernaya Fizika, Vol. 63, No. 11, 2000, pp. 2091–2095.

ELEMENTARY PARTICLES AND FIELDS
Theory

Spin Effects in Two-Body Hadronic Decays of the B_c Mesons

O. N. Pakhomova and V. A. Saleev[1)]

Samara State University, ul. Akademika Pavlova 1, Samara, 443011 Russia

Received November 4, 1999; in final form, March 2, 2000

Abstract—Spin effects in the weak two-body hadronic decays of the B_c and B_c^* mesons into J/ψ and $\rho(\pi)$ mesons are considered within the model of hard one-gluon exchange between quarks at high momentum transfers. It is shown that the polarization of the J/ψ meson in the decays of the B_c^* meson differs substantially from that in the decays of the B_c meson. The decay widths of the B_c^* meson differ significantly from the widths of the B_c meson. © *2000 MAIK "Nauka/Interperiodica".*

1. INTRODUCTION

The B_c meson was first observed by the CDF collaboration at FNAL in collisions occurring in $\sqrt{s} = 1.8$ TeV [1], and an estimate of its mass was given in the same study. This initiated experimental investigations into unique properties of heavy quarkonia involving quarks of different flavors. The experimental result for the B_c-meson mass, $m_{B_c} = 6.40 \pm 0.39 \pm 0.13$ GeV, is in agreement with the theoretical predictions based on nonrelativistic quark models [2] and on QCD sum rules [3]. The predicted splitting of the $^3S_1$ and $^1S_0$ levels in the $\bar{b}c$ system is 0.05–0.07 GeV, which is much smaller than the current experimental error in the B_c-meson mass.

According to calculations within the nonrelativistic model for heavy quarkonium that were performed to order α_s^4 in perturbative QCD, the ratio of the cross sections for the production of B_c^* and B_c mesons is about 2 to 3 [4]. At the same time, the same ratio estimated on the basis of the fragmentation mechanism of B_c-meson production is about 1.3 [5]. Thus, the ability to discriminate experimentally between events leading to the production of B_c^* mesons and events leading to the production of B_c mesons is of prime importance for testing models that claim for correctly describing the production of B_c mesons.

A peak in the mass spectrum of the $J/\psi l\nu_l$ ($l = e, \mu$) system produced in the semileptonic decay

$$B_c \longrightarrow J/\psi + l + \nu_l, \tag{1}$$

where J/ψ is detected by its leptonic decay mode $J/\psi \longrightarrow l^+l^-$, is a signals of B_c-meson production [1]. In what is concerned with detection, the two-body hadronic decays featuring a J/ψ meson in the final state,

$$B_c \longrightarrow J/\psi\rho(\pi), \tag{2}$$

are preferable B_c-meson decay channels.

According to the theoretical estimates given in [6], the branching fraction for this decay mode is about 1%.

A feature peculiar to the two-body hadronic decays (2) of the B_c meson is that the decaying $\bar{b}$ antiquark and the spectator c quark are both heavy. This being so, high momentum transfers to the spectator quark ($k^2 \gg \Lambda^2_{\mathrm{QCD}}$) are required for a $c\bar{c}$ pair to form a bound state. Under this condition, the wave functions of the initial B_c meson and the final J/ψ meson cannot overlap sizably, so that the spectator approach is inapplicable in this case. In support of this conjecture, we note that the gluon virtuality in the decay processes (2) is estimated as

$$k^2 \approx -\frac{m_2}{4m_1}((m_1 - m_2)^2 - m_3^2) \approx -1.2\ \mathrm{GeV}^2,$$

where m_1, m_2, and m_3 are the masses of B_c, J/ψ, and $\rho(\pi)$, respectively; therefore, it is necessary to invoke the hard-exchange formalism [7].

2. MODEL OF HARD EXCHANGE

Within the hard-exchange approximation allowing for one-gluon exchange with a c quark in the initial state, the exclusive decay modes $B_c^+ \longrightarrow J/\psi\pi^+(\rho^+)$ and $B_c^+ \longrightarrow \eta_c\pi^+(\rho^+)$ were first considered in [6], where it was shown that the decay amplitudes calculated under the assumption that hard t-channel exchange is dominant are twice as great as the amplitudes calculated in the spectator approach. However, an arith-

[1)] Samara State University, ul. Akademika Pavlova 1, Samara, 443011 Russia, and Nayanova Municipal University, Samara, Russia.

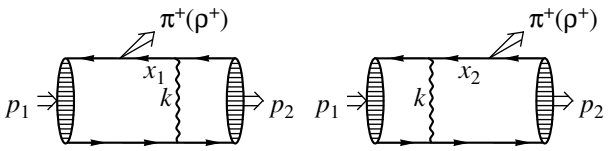

Feynman diagrams for the decays B_c^* (B_c) $\longrightarrow$ $J/\psi\rho(\pi)$.

metic error was made there in calculating the decay width $\Gamma(B_c^+ \longrightarrow \eta_c\pi^+)$ and the branching ratio $\Gamma(B_c^+ \longrightarrow \eta_c\pi^+)/\Gamma(B_c^+ \longrightarrow J/\psi\pi^+)$. Moreover, neither the decays of the B_c^* meson nor J/ψ production in various polarization states was considered in [6].

Within the hard-exchange approximation, the amplitudes for the decays B_c (B_c^*) $\longrightarrow$ $J/\psi\rho(\pi)$ are represented by the diagrams in the figure. Here, we perform our analysis in the nonrelativistic approximation, which implies that the 4-velocities of the quarks in a heavy meson are equal, whence it follows that, in the B_c meson of 4-momentum p_1, the momenta of the quarks are given by

$$p_c = \frac{m_c}{m_b + m_c}p_1, \quad p_{\bar{b}} = \frac{m_b}{m_b + m_c}p_1,$$

and that, in the J/ψ meson of 4-momentum p_2, the momenta of the quarks are

$$p_c = \frac{1}{2}p_2, \quad p_{\bar{c}} = \frac{1}{2}p_2.$$

Provided that the binding energy is disregarded, the constituent quark masses can be expressed in terms of the meson masses as

$$m_c = \frac{m_2}{2}, \quad m_b = m_1 - \frac{m_2}{2}.$$

In order to go over from the amplitude for bound-state production to the amplitude for the production of a quark–antiquark pair in which the quark and the antiquark have the same 4-velocity $v = p/m$, it is sufficient to make the substitution

$$V^i(v)\bar{U}^j(v) \longrightarrow \hat{a}\frac{(1+\hat{v})}{2}\frac{fm}{2\sqrt{3}}\frac{\delta^{ij}}{\sqrt{3}},$$

where $\hat{a} = \gamma_\mu\varepsilon^\mu$ (ε^μ is the polarization 4-vector) in the case of a vector meson and $\hat{a} = \gamma^5$ in the case of a pseudoscalar meson; f is the leptonic meson decay constant, which is related to the meson wave function at the origin by the equation

$$f = \sqrt{\frac{12}{m}}|\Psi(0)|;$$

and $\delta^{ij}/\sqrt{3}$ is the color factor considering that the quark and the antiquark in the meson are in the color-singlet state.

The effective four-fermion Hamiltonian describing nonleptonic decays of the type $b \longrightarrow c\pi(\rho)$ has the form

$$\mathcal{H}_{\text{eff}}(b \longrightarrow c\pi(\rho)) = \frac{G_F}{\sqrt{2}}V_{bc}a_1\bar{c}(x)\gamma_\mu(1-\gamma_5)b(x)A^\mu_{\pi,\rho}(x), \tag{3}$$

where $A^\mu_\pi(x) = if_\pi p^\mu_\pi e^{ipx}$ and $A^\mu_\rho(x) = if_\rho m_\rho\varepsilon^\mu(\lambda)e^{ipx}$, λ, f_π, and f_ρ being, respectively, the polarization of the vector meson, the leptonic decay constant for the π meson, and the leptonic decay constant for the ρ meson; $a_1 \approx \frac{1}{2}(C^b_+(m) + C^b_-(m))$, the coefficients $C^b_\pm(m)$ taking into account strong-interaction corrections to the effective four-fermion vertex due to hard gluons at the scale m; G_F is the effective Fermi constant; and V_{bc} is an element of the Cabibbo–Kobayashi–Maskawa matrix. We note that the negligibly small final-state interactions are discarded in the effective Hamiltonian (3).

With allowance for (3), the amplitude for the decay process $B_c^* \longrightarrow J/\psi\rho$, which is represented by the Feynman diagrams in the figure, assumes the form

$$\begin{aligned} M(B_c^* \longrightarrow J/\psi\rho) &= \frac{G_F}{\sqrt{2}}V_{bc}\frac{16\pi\alpha_s}{3}m_3 f_3\frac{f_1 m_1}{2\sqrt{3}} \\ &\times \frac{f_2 m_2}{2\sqrt{3}}\frac{a_1}{8k^4}\mathrm{tr}\Big[\hat{\varepsilon}_2(1+\hat{v}_2)\gamma^\alpha\hat{\varepsilon}_1(1-\hat{v}_1) \\ &\times(\hat{\varepsilon}_3(1-\gamma_5)(-\hat{x}_1+m_c)\gamma^\alpha \\ &+\frac{m_2}{m_1}\gamma^\alpha(-\hat{x}_2+m_b)\hat{\varepsilon}_3(1-\gamma_5))\Big], \end{aligned} \tag{4}$$

where the quantities carrying indices 1, 2, and 3 refer to B_c^*, J/ψ, and ρ, respectively, and where

$$\begin{aligned} \hat{x}_1 &= m_2\hat{v}_2 - \frac{m_2}{2}\hat{v}_1, \\ \hat{x}_2 &= m_1\hat{v}_1 - \frac{m_2}{2}\hat{v}_2, \\ k^2 &= \frac{m_2^2}{2}(1-y), \\ y &= (v_1v_2) = \frac{m_1^2+m_2^2-m_3^2}{2m_1m_2}. \end{aligned} \tag{5}$$

For the decay of the pseudoscalar B_c meson, $\hat{\varepsilon}_1$ in (4) must be replaced by γ_5, and the substitution $\hat{\varepsilon}_3 \longrightarrow \hat{v}_3$ must additionally be made if a π meson is produced in

the decay under study. In the B_c-meson rest frame, we have

$$\begin{aligned} v_1 &= (1, 0, 0, 0), \\ v_2 &= \frac{1}{m_2}(E_2, 0, 0, |\mathbf{p}_2|), \\ v_3 &= \frac{1}{m_3}(m_1 v_1 - m_2 v_2), \\ E_2 &= \frac{m_1^2 + m_2^2 - m_3^2}{2m_1}, \\ |\mathbf{p}_2| &= \sqrt{E_2^2 - m_2^2}. \end{aligned} \tag{6}$$

In the limit $m_3 = 0$, we obtain

$$E_2 \approx \frac{m_1^2 + m_2^2}{2m_1} \quad \text{and} \quad |\mathbf{p}_2| \approx \frac{m_1^2 - m_2^2}{2m_1}.$$

Summation over the polarizations of vector particles is performed by the formula

$$\sum_{L,T} \varepsilon_\mu^*(v)\varepsilon_\nu(v) = -g_{\mu\nu} + v_\mu v_\nu. \tag{7}$$

If the product J/ψ meson is longitudinally polarized, its polarization 4-vector can be represented as

$$\varepsilon_L^\mu(p) = \frac{p^\mu}{m} - \frac{mn^\mu}{(np)}, \tag{8}$$

where $n^\mu = (1, -\mathbf{p}/|\mathbf{p}|)$, so that $(nn) = 0$ and $(np) = E + |\mathbf{p}|$.

The use of the auxiliary 4-vector n^μ makes it possible to perform summation over the transverse and the longitudinal polarization of J/ψ in a manifestly covariant way:

$$\varepsilon_L^{*\mu}(v)\varepsilon_L^\nu(v) = v^\mu v^\nu - \frac{v^\mu n^\nu + v^\nu n^\mu}{(vn)} + \frac{n^\mu n^\nu}{(vn)^2}, \tag{9}$$

$$\sum_T \varepsilon_T^{*\mu}(v)\varepsilon_T^\nu(v) = -g_{\mu\nu} + \frac{v^\mu n^\nu + v^\nu n^\mu}{(vn)} - \frac{n^\mu n^\nu}{(vn)^2}. \tag{10}$$

3. RESULTS OF THE CALCULATIONS

The width with respect to the decay $B_c^* \longrightarrow J/\psi\rho$ is expressed in terms of the quantity $\overline{|M|^2}$ that is obtained from the squared modulus of the relevant amplitude by performing summation over the polarizations of the outgoing particles and averaging over the polarizations of the B_c^* meson. Specifically, we have

$$\Gamma(B_c^* \longrightarrow J/\psi\rho) = \frac{|\mathbf{p}_2|}{8\pi m_1^2}\overline{|M|^2}. \tag{11}$$

Making use of formulas (4)–(11), we arrive at

$$\begin{aligned} &\Gamma(B_c^* \longrightarrow J/\psi\rho) \\ &= G_F^2|V_{bc}|^2\frac{4\pi\alpha_s^2}{81}\frac{f_1^2 f_2^2 f_3^2}{m_1^4 m_2^6}\frac{|\mathbf{p}_2|}{(1-y)^4}a_1^2 F(B_c^*), \end{aligned} \tag{12}$$

$$\begin{aligned} &\Gamma(B_c \longrightarrow J/\psi\rho) \\ &= G_F^2|V_{bc}|^2\frac{4\pi\alpha_s^2}{81}\frac{f_1^2 f_2^2 f_3^2}{m_1^4 m_2^6}\frac{|\mathbf{p}_2|}{(1-y)^4}a_1^2 F(B_c), \end{aligned} \tag{13}$$

where $f_1 = f_{B_c} = f_{B_c^*}$, $f_2 = f_{J/\psi}$, $f_3 = f_\rho = f_\pi$, $m_1 = m_{B_c}$, $m_2 = m_{J/\psi}$, $m_3 = m_\rho$,

$$\begin{aligned} 3F(B_c^*) &= m_3^8 + 2m_3^6(13m_1^2 - 2m_1m_2 - m_2^2) \\ &+ 2m_3^4(-19m_1^4 - 18m_1^3m_2 - 16m_1^2m_2^2 + 2m_1m_2^3 + m_2^4) \\ &+ 2m_3^2(-3m_1^6 + 18m_1^5m_2 + m_1^4m_2^2 - 20m_1^3m_2^3 \\ &+ 11m_1^2m_2^4 + 2m_1m_2^5 - m_2^6) + 17m_1^8 + 4m_1^7m_2 \\ &- 32m_1^6m_2^2 - 12m_1^5m_2^3 + 14m_1^4m_2^4 + 12m_1^3m_2^5 \\ &- 4m_1m_2^7 + m_2^8, \end{aligned}$$

$$\begin{aligned} F(B_c) &= m_3^8 + 2m_3^6m_1(5m_1 + 8m_2) \\ &+ m_3^4(-19m_1^4 - 56m_1^3m_2 + 6m_1^2m_2^2 - 8m_1m_2^3 - 3m_2^4) \\ &+ 2m_3^2(2m_1^6 + 20m_1^5m_2 - 3m_1^4m_2^2 - 16m_1^3m_2^3 \\ &+ 16m_1^2m_2^4 - 4m_1m_2^5 + m_2^6) \\ &+ 4m_1^4(m_1^4 - 2m_1^2m_2^2 + m_2^4). \end{aligned}$$

In the limit $m_3 = 0$ and $m_{B_c^*} = m_{B_c}$, we obtain

$$\begin{aligned} \frac{\Gamma(B_c^* \longrightarrow J/\psi\rho)}{\Gamma(B_c \longrightarrow J/\psi\rho)} &= \frac{\Gamma(B_c^* \longrightarrow J/\psi\pi)}{\Gamma(B_c \longrightarrow J/\psi\pi)} \\ &\approx \frac{1}{12}(17 + 4x + 2x^2 - 4x^3 + x^4) = 1.58, \end{aligned} \tag{14}$$

where $x = m_2/m_1$.

A precise computation with $m_3 = m_\rho = 0.77$ GeV at $m_{B_c^*} = 6.3$ GeV and $m_{B_c} = 6.25$ GeV yields

$$\frac{\Gamma(B_c^* \longrightarrow J/\psi\rho)}{\Gamma(B_c \longrightarrow J/\psi\rho)} \approx 1.35, \tag{15}$$

$$\begin{aligned} \frac{\Gamma(B_c^* \longrightarrow J/\psi\rho)}{\Gamma(B_c^* \longrightarrow J/\psi\pi)} &\approx 3.05, \\ \frac{\Gamma(B_c \longrightarrow J/\psi\rho)}{\Gamma(B_c \longrightarrow J/\psi\pi)} &\approx 3.43. \end{aligned} \tag{16}$$

The polarization of the J/ψ mesons in the decay processes (2) can be determined through the angular distribution of the leptons produced in the decay $J/\psi \longrightarrow l^+l^-$. We denote by θ the angle between the vector of J/ψ polarization and the lepton-momentum vector. In the J/ψ rest frame, the angular distribution of the leptons, $d\Gamma/d\theta(J/\psi \longrightarrow l^+l^-)$, then has the form

$$\frac{d\Gamma}{d\theta}(J/\psi \longrightarrow l^+l^-) \sim 1 + \alpha\cos^2\theta, \tag{17}$$

where

$$\alpha = \frac{\Gamma_T - 2\Gamma_L}{\Gamma_T + 2\Gamma_L},$$

Γ_T and Γ_L being the widths with respect to the B_c (B_c^*) decays into, respectively, the transversely and the longitudinally polarized J/ψ meson. We do not present here exact analytic expressions for the widths Γ_T and Γ_L calculated with allowance for the nonvanishing masses of the π and ρ mesons because they are rather cumbersome. However, the expressions for α are simplified considerably in the limit of $m_3 = 0$ to become

$$\begin{aligned}\alpha(B_c^* \longrightarrow J/\psi\rho) &= \alpha(B_c^* \longrightarrow J/\psi\pi)\\ &\approx \frac{7 - 4x - 2x^2 + 4x^3 - x^4}{9 + 4x + 2x^2 - 4x^3 + x^4} = 0.45\end{aligned} \tag{18}$$

$$\alpha(B_c \longrightarrow J/\psi\rho) = \alpha(B_c \longrightarrow J/\psi\pi) \approx -1. \tag{19}$$

With allowance for the nonzero value of the ρ-meson mass, we obtain

$$\alpha(B_c^* \longrightarrow J/\psi\rho) \approx 0.40 \tag{20}$$

$$\alpha(B_c \longrightarrow J/\psi\rho) \approx -0.85. \tag{21}$$

The probability that the J/ψ meson retains the polarization of the B_c^* meson is governed by the parameter

$$\xi = \frac{\Gamma_{T\to T}}{\Gamma_{T\to T} + \Gamma_{T\to L}}, \tag{22}$$

where $\Gamma_{T\to T}$ is the width with respect to the decay of a transversely polarized B_c^* meson into a transversely polarized J/ψ meson and $\Gamma_{T\to L}$ is the width with respect to the decay of a transversely polarized B_c^* meson into a longitudinally polarized J/ψ meson. In the limit of $m_3 \approx 0$, we have

$$\xi(B_c^* \longrightarrow J/\psi\rho) \approx \xi(B_c^* \longrightarrow J/\psi\pi) = 1. \tag{23}$$

The calculation under the assumption that the ρ-meson mass does not vanish yields

$$\xi(B_c^* \longrightarrow J/\psi\rho) = 0.97.$$

At $f_{B_c} = f_{B_c^*} = 0.44$ GeV, $f_{J/\psi} = 0.54$ GeV, $f_\pi = 0.14$ GeV, $f_\rho = 0.22$ GeV, $V_{bc} = 0.04$, $G_F = 1.166 \times 10^{-5}$ GeV^{-2}, and $\alpha_s \approx 0.33$ [6], we obtain (in units of 10^{-6} eV)

$$\Gamma(B_c \longrightarrow J/\psi\rho) \approx 30.1a_1^2, \tag{24}$$

$$\Gamma(B_c^* \longrightarrow J/\psi\rho) \approx 40.2a_1^2, \tag{25}$$

$$\Gamma(B_c \longrightarrow J/\psi\pi) \approx 8.75a_1^2, \tag{26}$$

$$\Gamma(B_c^* \longrightarrow J/\psi\pi) \approx 13.4a_1^2. \tag{27}$$

Apart from the factor of $a_1^2 \approx 1.21$, which takes into account hard corrections to the vertex of four-fermion interaction, our decay-width values in (24)–(27) agree with the results obtained in [8, 9] for the decays $B_c \longrightarrow J/\psi\rho(\pi)$. However, the width with respect to the weak decay $B_c^* \longrightarrow J/\psi\rho(\pi)$ is much smaller than the width with respect to the electromagnetic transition $B_c^* \longrightarrow B_c\gamma$, the latter being estimated at 60 eV in [8]. Because of this, it is next to impossible to study experimentally the weak modes of B_c^* decay.

4. CONCLUSION

The results of this study can be summarized as follows. It has been shown that the decay widths $\Gamma(B_c^* \longrightarrow J/\psi\rho)$ and $\Gamma(B_c^* \longrightarrow J/\psi\pi)$ of the vector B_c^* meson are, respectively, 1.35 and 1.58 times as great as the corresponding decay widths of the pseudoscalar B_c mesons. The product J/ψ mesons are transversely polarized in B_c^* decays ($\alpha = 0.40$ for $B_c^* \longrightarrow J/\psi\rho$ and $\alpha = 0.45$ for $B_c^* \longrightarrow J/\psi\pi$) and are longitudinally polarized in B_c decays ($\alpha = -0.85$ for $B_c \longrightarrow J/\psi\rho$ and $\alpha \approx -1.0$ for $B_c \longrightarrow J/\psi\pi$). The ratio of the B_c^* and the J/ψ polarization is nearly equal to unity in the decay $B_c^* \longrightarrow J/\psi\pi$ and is 97% in the decay $B_c^* \longrightarrow J/\psi\rho$.

ACKNOWLEDGMENTS

We are grateful to V.V. Kiselev for enlightening comments and for information about new theoretical results concerning the widths with respect to the decays $B_c \longrightarrow J/\psi\rho(\pi)$.

This work was supported in part by the Russian Foundation for Basic Research (project no. 98-15-96040), by the Ministry for Higher Education of the Russian Federation (grant no. 98-0-6.2-53), and by the program Russian Universities—Basic Research.

REFERENCES

1. CDF Collab. (F. Abe *et al.*), Fermilab-pub-98/157-E; hep-ex/9805034.
2. E. Eichten and C. Quigg, Phys. Rev. D **49**, 5845 (1994); **52**, 1726 (1995); S. S. Gerstein *et al.*, Phys. Rev. D **51**, 3613 (1995); S. N. Gupta and J. M. Johnson, Phys. Rev. D **53**, 312 (1996).
3. S. Narison, Phys. Lett. B **210**, 238 (1988); P. Colangelo, G. Nardulli, and N. Paver, Z. Phys. C **57**, 43 (1993); V. V. Kiselev, Nucl. Phys. B **406**, 340 (1993).
4. A. V. Berezhnoy *et al.*, Yad. Fiz. **58**, 730 (1995) [Phys. At. Nucl. **58**, 672 (1995)]; **59**, 742 (1996) [**59**, 709 (1996)]; K. Kolodziej *et al.*, Phys. Lett. B **355**, 337 (1995); C. H. Chang and Y. Q. Chen, Phys. Rev. D **48**, 4086 (1993); A. P. Martynenko and V. A. Saleev, Phys. Rev. D **54**, 1891 (1996).
5. E. Braaten *et al.*, Phys. Rev. D **48**, R5049 (1993).
6. V. V. Kiselev, Preprint No. 96-41 (Institute for High Energy Physics, Protvino, 1996); hep-ph/9605451.
7. S. J. Brodsky and G. P. Lepage, Phys. Rev. D **22**, 2157 (1980).
8. S. S. Gerstein *et al.*, hep-ph/9803433.
9. V. V. Kiselev, private communication.

Translated by R. Rogalyov

Physics of Atomic Nuclei, Vol. 63, No. 11, 2000, p. 2004. Translated from Yadernaya Fizika, Vol. 63, No. 11, 2000, p. 2096.

XXIX International Conference on the Physics of Charged-Particle Interaction with Crystals May 31–June 2, 1999, Moscow

The XXIX International Conference on the Physics of Charged-Particle Interaction with Crystals took place in May–June 1999 at the Institute of Nuclear Physics, Moscow State University. Traditionally, attention there was given primarily to basic phenomena and processes in the interaction of accelerated particles with targets formed by ordered structures and to general problems in the physics of fast-ion interaction with matter.

Some results obtained recently in these realms are of fundamental importance. These include those that emerged from detailed investigations into particle channeling, the shadow effect, the resonance coherent excitation of ions, electromagnetic radiation from channeled electrons, and a wide variety of coherent effects in electromagnetic processes. These effects formed a basis for evolving new procedures of a considerable potential for experimental studies both in atomic and nuclear physics and in solid-state physics. At present, these new methods are being extensively used to explore processes involving high-energy elementary particles. Analysis of the phenomena considered at the present conference ensured a qualitatively new level in applying ion beams as a research tool. In particular, contemporary semiconductor technologies are based on the use of these methods.

The investigations being discussed have been vigorously developing in a number of leading research institutions and universities in the Commonwealth of Independent States of the former Soviet Union. In previous years, research groups from these institutions performed pioneering investigations and obtained results that were commonly recognized. The conferences traditionally held at Moscow State University play a substantial role in coordinating these investigations. Scientists from almost all states of the former Soviet Union and, as a rule, leading researchers from other foreign countries systematically participate in this conference.

Since the proceedings of the XXIX Conference are published in 2000, it is worthwhile to dwell upon the program of the next (XXX) conference, which will occur in 2000 and which is expected to be especially extensive. It will consist of four sections. The first section will include general issues of the physics of orientation phenomena and of their application in fundamental investigations. Among these, mention should be made of the dynamics of charged-particle scattering in ordered media, coherent inelastic processes accompanying particle interactions with crystal atoms, and problems associated with the physics of ion–atom collisions (like energy losses, as well as excitation and ionization phenomena). Unique possibilities for measuring nuclear-reaction times and detailed analyses of crystal defects and of the distribution of impurity atoms stand out among applications. Recently, some results of paramount importance have been obtained in studying structural transitions in high-temperature superconductors by using orientation effects. The potential of the channeling effect is widely used to govern beams at high-energy accelerators and to solve some problems in elementary-particle physics. The relevant problems will also be discussed at the conference.

The second section will be devoted to electromagnetic radiation from particles in crystals. A wide variety of phenomena has attracted the attention of many research groups experimenting at high-energy accelerators. Here, applied investigations are aimed at creating sources of electromagnetic radiation with unique spectral characteristics in the x-ray and gamma-ray ranges.

The third section will cover the application of methods based on orientation phenomena in various fields of physics to research and applied problems.

The fourth section will deal with problems associated with ion-beam-induced modifications to the properties of substances. Of particular interest are phenomena observed near solid-state surfaces. The conference to be held in 2000 will pay special attention to these phenomena because research institutions that have hitherto focused only on the problems of the physics of orientation phenomena are now extending the subject of their investigations to cover the fundamental problem of creating new materials. A dedicated section for discussing processes that occur in solids under the effect of intense beams of elementary particles will be organized at the conference.

Chairman of the Organizing Committee,
Professor A.F. Tulinov

1063-7788/00/6311-2004$20.00

Physics of Atomic Nuclei, Vol. 63, No. 11, 2000, pp. 2005–2007. Translated from Yadernaya Fizika, Vol. 63, No. 11, 2000, pp. 2097–2100.

XXIX INTERNATIONAL CONFERENCE ON THE PHYSICS OF CHARGED-PARTICLE INTERACTION WITH CRYSTALS

Spectral Structure of Polarization Radiation from Relativistic Electrons in Aluminum

S. V. Blazhevich[1)], V. K. Grishin, B. S. Ishkhanov, N. N. Nasonov[1)], G. S. Nefedov, V. P. Petukhov, and V. I. Shvedunov

Institute of Nuclear Physics, Moscow State University, Vorob'evy gory, Moscow, 119899 Russia

Received December 10, 1999; in final form, February 11, 2000

Abstract—Collective effects in polarization bremsstrahlung generated by relativistic electrons in a polycrystalline aluminum foil are studied experimentally on the basis of the 2.4-MeV electron accelerator installed at the Institute of Nuclear Physics (Moscow State University, Moscow). A peak structure found in this polarization bremsstrahlung for the first time is in agreement with theoretical predictions. © *2000 MAIK "Nauka/Interperiodica".*

1. INTRODUCTION

Polarization bremsstrahlung results from a variable polarization of atomic electrons that is induced by the electromagnetic field of fast charged particles [1]. Owing to its special features, polarization bremsstrahlung is one of the most interesting processes observed in collisions of charged particles with atoms. By way of example, we indicate that, in the x-ray region of photon energies between a few keV and a few tens of keV, which is of importance for various applications, polarization bremsstrahlung comes to be of a collective character because the polarization process involves coherently all atomic electrons. Owing to this, the radiation intensity integrated over the angles of observation per atom is equal to that of conventional bremsstrahlung. However, angular anisotropy is less pronounced in the case of polarization bremsstrahlung than in the case of conventional bremsstrahlung. We can therefore expect that, in the interaction of fast particles with atoms, radiation at observation angles larger than $1/\gamma$, where γ is the Lorentz factor for incident electrons, will be dominated by polarization bremsstrahlung.

In the above energy region, the effective impact parameter at which the motion of an incident particle generates polarization bremsstrahlung is commensurate with atomic dimensions and, hence, with interatomic distances in condensed media. Therefore, the properties of polarization bremsstrahlung are expected to be rather sensitive to the structure of condensed substances. In particular, a tight correlation between the properties of polarization bremsstrahlung and the structure of amorphous and polycrystalline condensed media was predicted in [2].

Unfortunately, experiments studying polarization bremsstrahlung were performed predominantly in the region of resonance atomic frequencies (see [1]), where correlations between atoms are insignificant. At the Institute of Nuclear Physics in Moscow (Moscow State University) and at the Institute of Nuclear Physics in Tomsk (Tomsk Polytechnic University), experimental investigations into coherent processes in polarization bremsstrahlung generated by relativistic particles employed 6.7-MeV electrons incident on amorphous targets [3] and 900-MeV electrons incident on heavy-metal targets [4], respectively.

This article reports on new results coming from an experimental investigation of the spectral distribution of polarization bremsstrahlung from a polycrystalline aluminum foil exposed to relativistic electrons. The ensuing discussion also covers the results from [3, 4].

2. DESCRIPTION OF THE EXPERIMENT

The experiment made use of a 2.4-MeV electron beam from the continuous linear electron accelerator installed at the Institute of Nuclear Physics (Moscow State University, Moscow). The beam of cross-sectional area 2×2 mm^2 was incident on a 2-μm-thick aluminum foil arranged in a vacuum chamber at an angle of 45° with respect to the beam trajectory. The electrons that traversed the target were then absorbed in a Faraday cup. The target was fixed on a movable bench with a remote control. The quality of the incident beam was monitored with the aid of a special TV camera and a screen covered with luminophore and positioned in the same chamber. Photons emitted in electron–target interactions were recorded by a cooled SiLi detector within a small solid angle of 1.5 msr. The detector, which had an energy resolution of 200 eV, was oriented at a right angle to the beam and was positioned at a distance of 0.5 m from the target. As was mentioned above, this geometry allowed us to obtain an optimum proportion between polarization bremsstrahlung and

[1)] Belgorod State University, Studencheskaya ul. 12, Belgorod, 308007 Russia.

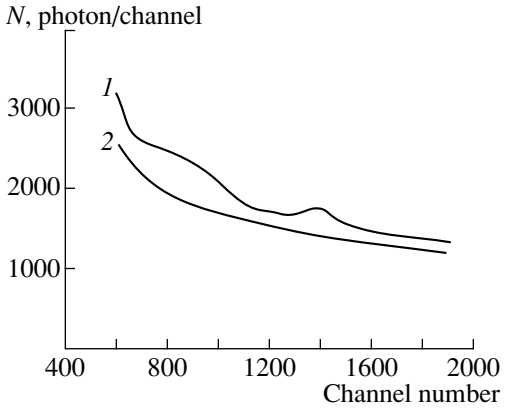

Fig. 1. Experimental spectrum of x-ray radiation generated by 2.4-MeV electrons in an aluminum target 2 μm thick (spectral section above the *K*-line of aluminum): (*1*) main signal and (*2*) external background.

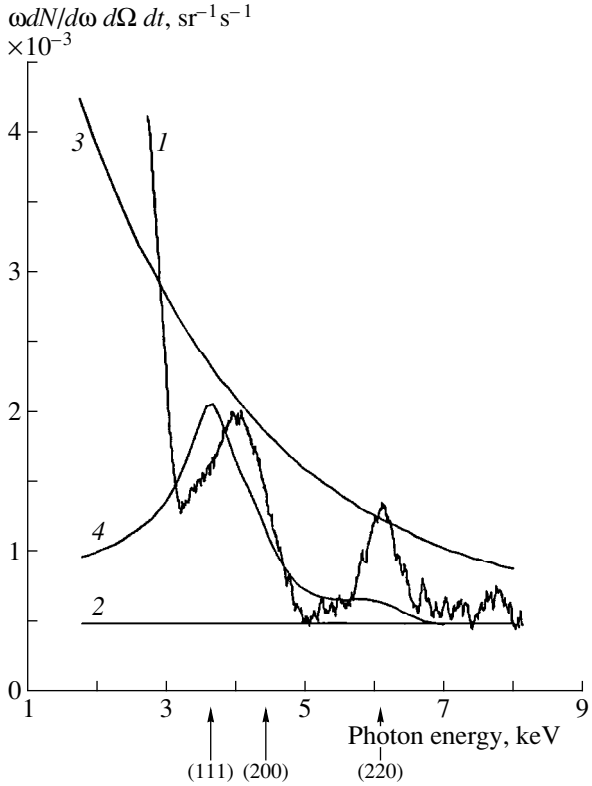

Fig. 2. Spectral distribution of polarization-bremsstrahlung intensity: (*1*) experimental data upon external-background subtraction; (*2*) conventional-background intensity; and (*3*, *4*) calculated intensities of polarization bremsstrahlung and conventional background in an amorphous and in a polycrystalline aluminum target, respectively.

conventional bremsstrahlung—the former is dominant here, since the latter is characterized by a high degree of angular anisotropy. There was also a small lead screen in the chamber, which allowed us to cover the detector along the line-of-sight direction toward the target. In that case, the detector recorded the actual external background arising in the chamber owing to target irradiation with the accelerated beam. Moreover, additional magnets shielded the detector from scattered electrons.

The photon flux was measured at a beam current whose maximum value did not exceed 10 nA, whereby nonlinear distortions were avoided in accumulating spectral data. The use of the continuous mode of accelerator operation permitted considerably reducing the time required to accumulate a statistically reliable data sample and minimizing the effect of the facility time drift.

Several runs of measurements of polarization bremsstrahlung were performed. In the first runs, whose results were reported in [5, 6], polarization bremsstrahlung for moderately relativistic electrons was separated for the first time. Because of a high background level, however, it was impossible to perform a reliable analysis of the structure of polarization bremsstrahlung. In the subsequent runs reported here, the measurements were performed at an appreciably reduced level of the external background.

Curve *1* in Fig. 1 represents a typical energy spectrum of x-ray photons according to the latest experiment. Apart from polarization radiation proper, this spectrum contains conventional bremsstrahlung and a background. The background is shown by curve *2* in Fig. 1 (the results are presented with due regard to radiation absorption in the target and the spectral sensitivity of the detector; however, the relevant corrections were insignificant in the energy region being considered). A dominant contribution to the total radiation flux comes from the peak that corresponds to the *K*-line of the aluminum characteristic radiation and which occurs in the region around 1.5 keV. This peak exceeds the level of radiation in the neighboring photon-energy region by a factor of about 3. In Fig. 1, we do not therefore display the *K*-line region in the overall spectrum.

3. DISCUSSION OF THE RESULTS

Figure 2 shows the resulting energy (frequency) spectrum of the observed-radiation intensity upon background subtraction (curve *1*). For the sake of comparison, we also show a few curves (*2–4*) calculated under conditions complying with the experimental conditions of radiation collimation. Curve *2* describes the spectrum of conventional-bremsstrahlung intensity—in the energy region being considered, it appears to be a horizontal line. Curves *3* and *4* represent the spectra of polarization-bremsstrahlung intensity in amorphous and in polycrystalline aluminum, respectively, the contribution of conventional-bremsstrahlung intensity being taken into account for each spectrum. The curves in question were calculated on the basis of the theoretical relations from [2].

According to the results of the calculations (see also [1]), the spectral distributions of polarization

bremsstrahlung in amorphous and polycrystalline media differ markedly. In the coherent region, polarization bremsstrahlung in a polycrystalline medium has a peak structure, whose origin is similar to that in the case of Debye–Scherrer peaks observed in the scattering of an x-ray flux in a polycrystalline medium. In the photon-energy range 1–8 keV, there are three peaks at 3.75, 4.33, and 6.12 keV (these are their mean energies) corresponding to the coherent scattering of the incident-electron field on the (111), (200), and (220) aluminum crystallographic planes at a Wolf–Bragg angle of 45° in the experiment. For moderately relativistic electrons, the peaks are rather broad, the heights of the peak maxima decreasing fast as their mean energy becomes higher. Therefore, the (111) and (200) peaks are poorly resolved, merging into the first peak on curve *4* in Fig. 2.

Comparing the curves in Fig. 2, we can conclude that polarization bremsstrahlung can be singled out reliably from experimental data and that the character of this radiation is governed by the polycrystalline structure of a target material. The positions of the peaks on the measured curve are in agreement with the predictions. The measured yield of polarization bremsstrahlung in the vicinity of the (111) and (200) peaks also complies with theoretical values. The main discrepancy between theoretical predictions and experimental data, which is observed in the vicinity of the (220) peak, can be attributed tentatively to coherent Bragg reflection from the surface texture of the target and to the background of the iron *K*-line, which comes into play as the result of rescattering of secondary particles on the chamber walls.

Thus, experimental results confirm that the spectral properties of polarization bremsstrahlung generated by relativistic electrons in polycrystalline and in amorphous media differ considerably, in contrast to what is observed for conventional bremsstrahlung [7]. Bearing in mind previous experimental data on the behavior of polarization bremsstrahlung from relativistic electrons in amorphous carbon [3], we can state that the mechanism of this radiation is highly sensitive to the structure of the medium. This is supported by our preliminary data from the measurements of polarization bremsstrahlung in other media. This circumstance is of considerable importance for developing new methods for a structural analysis of substances.

The above conclusions also supplement substantially the results of Verzilov *et al.* [4], who studied radiation generated by 900-MeV electrons in heavy metals that was observed at an angle of 19° with respect to the electron trajectory. In heavy metals, the upper boundary of the coherent region of bremsstrahlung radiation falls within the region around 100 keV because, there, the effective radius of the atomic electron shell, $R = a_0/Z^{1/3}$ (where a_0 is the Bohr radius and Z is the charge number of the atomic nucleus), is less than an angstrom. On this basis, the radiation recorded in [4] near 50 keV was interpreted as polarization bremsstrahlung. However, no correlation between the properties of this radiation and the structures of the medium was found. The possible reason for this is that, under the conditions of the experiment reported in [4], the region of lower polarization-bremsstrahlung energies, where the structure of the medium could be operative, was close to the detection threshold of about 20 keV (we used a more informative presentation of the results than that in [4], displaying the intensity values instead of the flux densities of x-ray photons, whereby the conventional-bremsstrahlung intensity representing a horizontal line—see, for example, curve *2* in our Fig. 2—can be singled out easily).

4. CONCLUSION

Two important features of polarization bremsstrahlung have been revealed for the first time in the present article:

(i) The spectral distribution of polarization bremsstrahlung generated by relativistic electrons in polycrystalline substances has a clear-cut peak structure.

(ii) The yield of polarization bremsstrahlung is suppressed noticeably outside the peak region.

ACKNOWLEDGMENTS

We are grateful to V.M. Agranovich and B.M. Bolotovskiĭ for enlightening discussions on the results presented in this article.

This work was supported by the Russian Foundation for Basic Research (project no. 96-02-17109).

REFERENCES

1. M. Ya. Amusia, V. M. Buimistrov, *et al.*, *Polarization Bremsstrahlung of Particles and Atoms* (Plenum, New York, 1992).
2. N. Nasonov, Nucl. Instrum. Methods Phys. Res. B **145**, 19 (1998).
3. S. Blazhevich, A. Chepurnov, V. Grishin, *et al.*, Phys. Lett. A **211**, 309 (1996).
4. K. Yu. Amosov, V. A. Verzilov, I. E. Vnukov, *et al.*, Pis'ma Zh. Éksp. Teor. Fiz. **63**, 145 (1996) [JETP Lett. **63**, 153 (1996)].
5. S. Blazhevich, V. Grishin, N. Nasonov, *et al.*, in *Proceedings of EPAC'98, Stokholm, 1998*, p. 2458.
6. S. V. Blazhevich, V. K. Grishin, B. S. Ishkhanov, *et al.*, Vestn. Mosk. Univ., Ser. 3: Fiz., Astron., No. 6, 50 (1998).
7. M. L. Ter-Mikaelian, *High-Energy Electromagnetic Processes in Condensed Media* (Akad. Nauk Arm. SSR, Yerevan, 1969; Wiley, New York, 1972).

Translated by E. Kozlovskiĭ

Physics of Atomic Nuclei, Vol. 63, No. 11, 2000, pp. 2008–2010. Translated from Yadernaya Fizika, Vol. 63, No. 11, 2000, pp. 2101–2104.

XXIX INTERNATIONAL CONFERENCE ON THE PHYSICS OF CHARGED-PARTICLE INTERACTION WITH CRYSTALS

Dynamical-Diffraction Effects in Parametric Radiation

V. P. Voronov, N. V. Kamyshachenko, N. N. Nasonov, and V. A. Nasonova

Belgorod State University, Studencheskaya ul. 12, Belgorod, 308007 Russia

Received February 11, 2000

Abstract—An analytic theory is developed for dynamical-diffraction effects in x-ray radiation from a relativistic electron traversing a thin single crystal. It is shown that such dynamical effects may be responsible for a glaring discrepancy between recent experimental data and the traditional theory of parametric x-ray radiation.

1. INTRODUCTION

Parametric x-ray radiation [1–4] arises owing to the scattering of the Coulomb field of a fast particle moving in a medium characterized by a periodic dielectric permittivity, $\varepsilon(\omega, \mathbf{r}) = 1 + \chi_0(\omega) + \sum_{\mathbf{g}} \chi_{\mathbf{g}}(\omega) e^{i\mathbf{g}\cdot\mathbf{r}}$, where ω is the photon energy, while $\mathbf{g}$ is a reciprocal-lattice vector. The dynamical theory of x-ray diffraction in a crystal [5] or its simplified version, kinematical theory (perturbation theory), is usually used to describe this radiation. Previous investigations of the spectral and angular distributions of relevant x-ray photons propagating along the direction of Bragg scattering revealed good agreement between experimental data on parametric radiation and kinematical theory. Here, the absence of dynamical effects is due to the fact that, in the case of parametric x-ray radiation, the necessary condition of synchronism between the emitted photon and the radiating particle, $\omega = \mathbf{k}\cdot\mathbf{v}$ ($\mathbf{k}$ is the photon wave vector, and $\mathbf{v}$ is the velocity of the radiating particle), is satisfied only off the region of the dynamical maximum in the Bragg scattering of the pseudophoton field of a particle on the set of atomic crystal planes.

Of particular interest in connection with the aforesaid is the experimental result reported recently by Freudenberger *et al.* [6], who measured, in Bragg geometry, the orientation dependence of the yield of collimated parametric x-ray radiation generated by 87-MeV electrons in a Si crystal (111). At the maximum of this orientation dependence, the measured yield is eight times as great as the theoretical prediction, the orientation angle corresponding to the experimental maximum being 2.8 times smaller than that which follows from the theory of parametric radiation.

The objective of the present study is to develop an analytic theory of the dynamical scattering of the electromagnetic field of a relativistic electron traversing a thin single crystal. On the basis of our results, we will attempt to explain the experimental results presented in [6] and propose a new scheme for generating x-ray radiation.

2. GENERAL RELATIONS

Let us consider the structure of the electromagnetic field excited by a relativistic electron traversing a thin crystal whose reflecting crystallographic plane (which is specified by a reciprocal-lattice vector $\mathbf{g}$) is parallel to the crystal surface (see Fig. 1). Within the two-wave approximation of the dynamical theory of diffraction [5], the Fourier amplitude of the electric field, $\mathbf{E}_{\mathbf{k}\omega} = \frac{1}{(2\pi)^4}\int d^3r\,dt\,\mathbf{E}(\mathbf{r}, t)e^{-i\mathbf{k}\cdot\mathbf{r}+i\omega t}$, is sought in the form of the sum of the direct and diffracted waves, $\mathbf{E}_0 = \sum_{\lambda=1}^{2}\mathbf{e}_{\lambda 0}E_{\lambda 0}$ and $\mathbf{E}_{\mathbf{g}} = \sum_{\lambda=1}^{2}\mathbf{e}_{\lambda\mathbf{g}}E_{\lambda\mathbf{g}}$, respectively, where the polarization vectors are given by $\mathbf{e}_{10} = \mathbf{e}_{1\mathbf{g}} \approx \mathbf{k}\times\mathbf{g}$, $\mathbf{e}_{20} \approx \mathbf{k}\times\mathbf{e}_{10}$, $\mathbf{e}_{2\mathbf{g}} \approx \mathbf{k}_g\times\mathbf{e}_{10}$, and $\mathbf{k}_g = \mathbf{k} + \mathbf{g}$. Determining the free and forced solutions to the Maxwell equations for the Fourier amplitudes of the relevant fields within and outside the crystal and finding unknown coefficients from the boundary conditions at

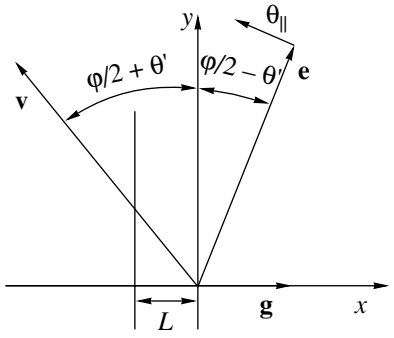

Fig. 1. Geometry of the parametric-radiation process. The following notation is adopted in this figure: $\mathbf{v}$ is the velocity of the radiating particle, $\mathbf{n} = \mathbf{e}\left(1 - \frac{1}{2}\theta^2\right) + \boldsymbol{\theta}$ is a unit vector in the direction of radiation ($\mathbf{e}\cdot\boldsymbol{\theta} = 0$), θ' is the orientation angle measured with respect to the position of the exact Bragg resonance, L is the crystal thickness, $\mathbf{g}$ is a reciprocal-lattice vector, and $\theta_{\|}$ is the absolute value of the projection of the vector $\boldsymbol{\theta}$ onto a direction parallel to the reaction plane.

1063-7788/00/6311-2008$20.00 © 2000 MAIK "Nauka/Interperiodica"

the crystal surface, one obtains the conventional (rather cumbersome) expression for the distribution of the radiation with respect to spectral and angular variables in Bragg geometry (see, for example, [3, 4]).

In the theory of parametric x-ray radiation, a traditional approach relies on the asymptotic formula for the above distribution. This formula describes the yield of parametric x-ray radiation associated with the scattering of the equilibrium Coulomb field of a fast particle over the entire crystal thickness. Because of the screening of the equilibrium field due to the polarization of medium electrons, the yield of this radiation is saturated fast with increasing energy of the radiating particle (density effect in parametric x-ray radiation [7]).

By analyzing the general formula for the yield of parametric x-ray radiation generated by a relativistic electron traversing the surface of a crystal, it was shown in [8] that there is additional radiation due to the dynamical scattering of transition radiation from this electron in the crystal. A generalization of the problem considered in [8] to the case of a finite-thickness crystal was given in [9, 10], where the relevant results were obtained from a numerical analysis. In the present study, we describe the process analytically on the basis of an asymptotic approach, which is opposite, in a sense, to that which is adopted in the conventional theory of parametric x-ray radiation.

In the general expression for the distribution of the radiation with respect to the spectral and angular variables, we first single out terms representing the contribution of transition radiation (such terms are always discarded in the asymptotic formula for parametric x-ray radiation). After some simple algebra, we obtain

$$\omega\frac{dN_\lambda}{d\omega d^2\theta} = \frac{e^2}{\pi^2}\frac{\Omega_\lambda^2}{(\gamma^{-2}+\Omega^2)^2}R(\zeta_\lambda,\delta_\lambda),$$
$$R = \frac{\left|\sinh^2(\delta_\lambda\sqrt{1-\zeta_\lambda^2})\right|}{\left|1-\zeta_\lambda^2\right| + \left|\sinh^2(\delta_\lambda\sqrt{1-\zeta_\lambda^2})\right|}, \quad (1)$$

where λ is the polarization subscript, $\Omega_1 = \theta_\perp$, $\theta_\parallel = 2\theta' + \theta_\parallel$, γ is the Lorentz factor, $\zeta_\lambda = (\omega_b'/\omega_b - 1)/\beta_\lambda$, $\beta_\lambda = 2\omega^2|\chi_g\|\alpha_\lambda|/g^2$, $\alpha_1 = 1$, $\alpha_2 = \cos\varphi$, $\omega_b' = \omega_b(1 + (\theta' + \theta_\parallel)\cot(\varphi/2))$, $\omega_b = g/2\sin(\varphi/2)$, and $\delta_\lambda = \beta_\lambda gL/2$.

The ensuing analysis will rely on expression (1), which differs markedly from that traditionally used in the theory of parametric x-ray radiation. This expression describes radiation correctly for $\gamma^2|\chi_0| = \gamma^2\omega_0^2/\omega^2 \gg 1$ since, under the conditions being considered, the angular distribution in (1) ($\Delta\Omega \approx \gamma^{-1}$) is concentrated almost completely in the region of a dip in the angular distribution of conventional parametric x-ray radiation ($\Omega \leq \omega_0/\omega$, $\omega_0/\omega \gg \gamma^{-1}$, where ω_0 is the plasmon frequency in the medium) that is generated by a particle over the entire crystal thickness and which is suppressed by the density effect.

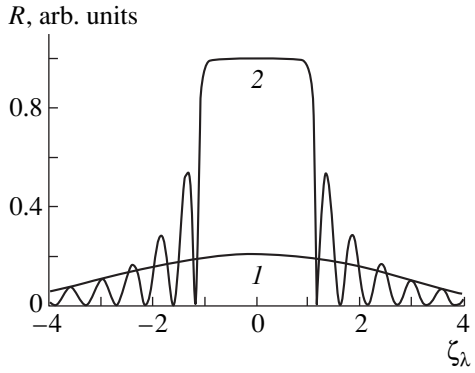

Fig. 2. Universal frequency dependence of the coefficient of the dynamical reflection of the field of a fast particle from a crystal at δ_λ = (*1*) 0.5 and (*2*) 5.

We note that the factor $e^2\Omega_\lambda^2\pi^{-2}(\gamma^{-2} + \Omega^2)^{-2}$ in (1) describes the angular distribution of the vacuum Coulomb field of a relativistic electron and that the quantity $R(\zeta_\lambda, \delta_\lambda)$ corresponds to the coefficient of the dynamical reflection of the field from the crystal. The reason why the dynamical regime of reflection is realized here is that, in the present case, the process involves free transition-radiation photons (rather than bound pseudophotons, as in conventional parametric x-ray radiation), whose distribution with respect to spectral and angular variables differs only slightly from the distribution of pseudophotons in a vacuum for $\omega \ll \gamma\omega_0$ (recall that we consider precisely this region of frequencies). The dependence $R(\zeta_\lambda, \delta_\lambda)$, which characterizes the intrinsic linewidth of the radiation being discussed, is illustrated in Fig. 2.

The crystal-thickness dependence of the radiation yield is a very important characteristic. Integrating expression (1) with respect to ω, we obtain

$$\frac{dN_\lambda}{d^2\theta} = \frac{e^2}{\pi^2}\beta_\lambda\frac{\Omega_\lambda^2}{(\gamma^{-2}+\Omega^2)^2}F(\delta_\lambda),$$
$$F(\delta_\lambda) = \frac{2}{\pi}\int_0^\infty \frac{dx\left|\sinh^2(\delta_\lambda\sqrt{1-x^2})\right|}{\left|1-x^2\right| + \left|\sinh^2(\delta_\lambda\sqrt{1-x^2})\right|}. \quad (2)$$

According to the curve in Fig. 3, the yield of the radiation being considered is saturated at a crystal thickness approximately equal to the extinction length for Bragg scattering.

By comparing the theoretical result in (2) with the experimental data from [6], we find that there is agreement for the values of the orientation angle θ' that correspond to the maximum of the orientation dependence of the radiation yield; in addition, it turns out that the calculated radiation yield at the maximum of the radiation dependence is approximately twice as large as the

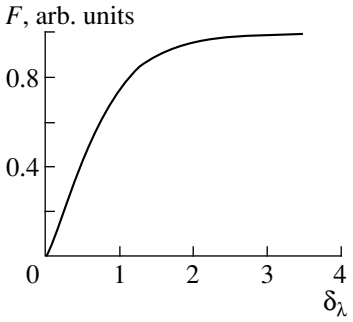

Fig. 3. Universal crystal-thickness dependence of the radiation yield.

measured value. The latter may be due to a sizable interference contribution of conventional parametric x-ray radiation {in the experiment reported in [6], the crystal thickness was comparatively large, while the coefficient $\gamma\omega_0/\omega$ exceeded unity insignificantly (it was about 2.5)}.

Performing a two-dimensional integration of expression (1) with respect to θ, we find the spectrum of a noncollimated radiation in the form

$$\frac{dN_\lambda}{d\omega} = \frac{e^2}{2}\beta_\lambda F(\delta_\lambda) T_\lambda(\omega),$$

$$T_1 = \left[\omega_b^2\gamma^{-2}\cot^2\frac{\varphi}{2} + \left(\omega - \omega_b\left(1 - \theta'\cot\frac{\varphi}{2}\right)\right)^2\right]^{-1/2}, \quad (3)$$

$$T_2 = \frac{\left(\omega - \omega_b\left(1 - \theta'\cot\frac{\varphi}{2}\right)\right)^2}{\left[\omega_b^2\gamma^{-2}\cot^2\frac{\varphi}{2} + \left(\omega - \omega_b\left(1 - \theta'\cot\frac{\varphi}{2}\right)\right)^2\right]^{3/2}}.$$

Expressions (2) and (3) show that, under the condition $\omega \ll \gamma\omega_0$, both the angular width $\Delta\theta \approx \gamma^{-1}$ and the relative spectral width $\Delta\omega/\omega \approx \gamma^{-1}$ of the radiation being considered are much less than the corresponding quantities for conventional parametric x-ray radiation.

From (2), it follows that the total number of emitted photons is

$$N_\lambda = \frac{e^2}{4}\beta_\lambda F(\delta_\lambda)\left[\ln(1+\gamma^2\theta_d^2) - \frac{\gamma^2\theta_d^2}{1+\gamma^2\theta_d^2}\right], \quad (4)$$

where θ_d is the angular dimension of the collimator. On the basis of expression (4), it can be concluded that, in the crystal-thickness region $L < 4/(g\beta_\lambda)$, where the effect of saturation is not yet observed, the total yield of the radiation being considered is on the same order of magnitude as the total yield of conventional parametric x-ray radiation.

A considerable excess of the distribution of our radiation with respect to spectral and angular variables over the analogous quantity for the conventional parametric x-ray radiation (by a factor of about $\gamma^2\omega_0^2/\omega_b^2 \gg 1$ at $L \approx L_{opt} = 4/g\beta_\lambda$) can be used to develop an efficient source of quasimonochromatic pencil-like x-ray radiation.

The proposed source consists of a set of thin crystals (of thickness $L \approx L_{opt}$) positioned in a vacuum along the trajectory of a beam of radiating electrons, the distance T between the neighboring crystals being greater than the radiation-formation length in a vacuum, also known as the coherence length $l_{coh} = 2\gamma^2/\omega_b$. In this case, photons are emitted in each crystal independently and propagate in a vacuum at a large angle with respect to the electron trajectory without undergoing photoabsorption (here, the total thickness of the system, $L_{tot} = NL_{opt}$, N being the number of crystals, may considerably exceed the photoabsorption length, which restricts the yield of radiation in conventional x-ray sources, where photons propagate along the trajectory of particles radiating in a medium).

ACKNOWLEDGMENTS

The present study was stimulated by discussions with B.M. Bolotovskiĭ and M.L. Ter-Mikaelian on the physics of free-photon and pseudophoton scattering in a medium.

This work was supported in part by the Ministry for Higher Education of the Russian Federation (grant no. 97-07.2-151) and by the Russian Foundation for Basic Research (project no. 99-02-18183).

REFERENCES

1. Ya. B. Faĭnberg and N. A. Khizhnyak, Zh. Éksp. Teor. Fiz. **32**, 883 (1957) [Sov. Phys. JETP **5**, 720 (1957)].
2. M. L. Ter-Mikaelian, *High-Energy Electromagnetic Processes in Condensed Media* (Akad. Nauk Arm. SSR, Yerevan, 1969; Wiley, New York, 1972).
3. V. G. Baryshevskiĭ and I. D. Feranchuk, Zh. Éksp. Teor. Fiz. **61**, 944 (1971) [Sov. Phys. JETP **34**, 495 (1971)].
4. G. M. Garibyan and C. Yang, Zh. Éksp. Teor. Fiz. **61**, 930 (1971) [Sov. Phys. JETP **34**, 502 (1971)].
5. Z. G. Pinsker, *Dynamical Scattering of X-rays in Perfect Crystals* (Nauka, Moscow, 1972).
6. J. Freudenberger, H. Genz, V. Morokhovskii, and A. Richter, in *Abstracts of the International Workshop in Radiation Physics with Relativistic Electrons, Tabarz, Germany, June 1998*, p. 24.
7. N. Nasonov and A. Safronov, in *Proceedings of the International Symposium RREPS-93, Tomsk, Russia, October 1993*, p. 87.
8. A. Caticha, Phys. Rev. A **40**, 4322 (1989).
9. X. Artru and P. Rullhusen, Nucl. Instrum. Methods Phys. Res. B **145**, 1 (1998).
10. X. Artru, in *Abstracts of the International Workshop in Radiation Physics with Relativistic Electrons, Tabarz, Germany, June 1998*, p. 32.

Translated by A. Isaakyan

Physics of Atomic Nuclei, Vol. 63, No. 11, 2000, pp. 2011–2014. Translated from Yadernaya Fizika, Vol. 63, No. 11, 2000, pp. 2105–2108.

XXIX INTERNATIONAL CONFERENCE ON THE PHYSICS OF CHARGED-PARTICLE INTERACTION WITH CRYSTALS

Collimator-Size Effect on the Parametric-Radiation Spectrum

N. V. Kamyshanchenko, I. N. Kuzmenko, N. N. Nasonov, and V. A. Nasonova

Belgorod State University, Studencheskaya ul. 12, Belgorod, 308007 Russia

Received February 11, 2000

Abstract—It is shown that, by varying the angular size of a collimator, the spectral distribution of parametric x-ray radiation can be split into two isolated peaks and that the center of the spectral distribution of this radiation is shifted in frequency in response to an increase in the collimator size. It is also predicted that an increase in the angular size of the collimator will lead to a substantial modification of the character of the orientation dependence of the radiation spectrum. © *2000 MAIK "Nauka/Interperiodica".*

1. INTRODUCTION

The motion of a fast charged particle in a crystal is accompanied by the scattering of its Coulomb field by atomic electrons of the crystal. Owing to the periodic arrangement of atoms in the crystal lattice, this scattering has a coherent character. Parametric x-ray radiation [1–4] generated under such conditions has a number of unique characteristics: it has a quasimonochromatic spectrum; it has a pencil-like character, propagating at a large angle with respect to the radiating-particle velocity; and the energy of the photons constituting this radiation can be smoothly changed.

Since the energy of a photon emitted in parametric x-ray radiation is tightly related to the angle of radiation observation, the properties of this radiation depend substantially on the collimator (or radiation-detector) sizes. The objective of this study is to analyze in detail the spectral and orientation properties of parametric x-ray radiation versus angular sizes of the collimator. We will show that these properties undergo qualitative changes with increasing collimator sizes.

2. GENERAL RELATIONS

Presently, the theory of parametric x-ray radiation has been firmly established. In a number of studies, the validity of its description on the basis of perturbation theory (kinematical approximation) was demonstrated theoretically and confirmed experimentally. Following [2] and using conventional methods, we find that the distribution of the intensity of parametric x-ray radiation with respect to spectral and angular variables can be represented as

$$\omega\frac{dN}{dtd\omega d^2\theta} = \frac{8\pi Z^2 e^6 n_0^2 |S(\mathbf{g})|^2 e^{-g^2u^2}}{m^2(1+g^2R^2)^2} \times \frac{[\mathbf{v}(\mathbf{g}\cdot\mathbf{v}) - \mathbf{g}(1-\sqrt{\varepsilon}(\mathbf{n}\cdot\mathbf{v}))/\varepsilon]^2 - [(\mathbf{n}\cdot\mathbf{g})(\mathbf{g}\cdot\mathbf{v}) - (\mathbf{n}\cdot\mathbf{g})(1-\sqrt{\varepsilon}(\mathbf{n}\cdot\mathbf{v}))/\varepsilon]^2}{[g^2(1-\sqrt{\varepsilon}(\mathbf{n}\cdot\mathbf{v})) + 2\sqrt{\varepsilon}(\mathbf{n}\cdot\mathbf{g})(\mathbf{g}\cdot\mathbf{v})]^2} \frac{1}{1-\sqrt{\varepsilon}(\mathbf{n}\cdot\mathbf{v})} \delta\left(\omega - \frac{\mathbf{g}\cdot\mathbf{v}}{1-\sqrt{\varepsilon}(\mathbf{n}\cdot\mathbf{v})}\right), \quad (1)$$

where $\mathbf{g}$ is a reciprocal-lattice vector that specifies the reflecting crystallographic plane; $S(\mathbf{g})$ is a structural factor; $e^{-g^2u^2}$ is the Debye–Waller factor; n_0 is the density of crystal atoms; Z is the number of electrons in the atom; R is the screening radius; $\varepsilon = 1 - \omega_0^2/\omega^2$, ω_0 being plasmon frequency; $\mathbf{n}$ is a unit vector in the direction of emitted-photon momentum; and $\mathbf{v}$ is the velocity of the radiating particle. The disposition of the vectors $\mathbf{g}$, $\mathbf{v}$, and $\mathbf{e}$ lying in the same plane is shown in Fig. 1. The vector $\mathbf{n}$ is given by

$$\mathbf{n} = \mathbf{e}\left(1 - \frac{1}{2}\theta^2\right) + \boldsymbol{\theta}, \quad \mathbf{e}\cdot\boldsymbol{\theta} = 0, \quad \boldsymbol{\theta} = \boldsymbol{\theta}_\perp + \boldsymbol{\theta}_\parallel, \quad (2)$$

where $\theta_\parallel$ and $\theta_\perp$ are, respectively the parallel and perpendicular components of the two-dimensional vector $\boldsymbol{\theta}$ appearing to be the angular variable in the distribution of the radiation. The orientation angle θ' is measured from the position of the exact Bragg resonance. A change in θ' corresponds to a rotation of the crystal as a discrete unit about the axis orthogonal to the plane of the figure. The angle between the vectors $\mathbf{v}$ and $\mathbf{e}$ remains unchanged upon this rotation.

In terms of the variables $\boldsymbol{\theta}$ and θ', formula (1) takes the conventional form in the kinematical theory of parametric x-ray radiation; that is,

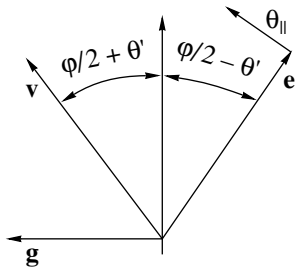

Fig. 1. Geometry of the parametric-radiation process (**v** is the radiating-particle velocity, while **g** is a reciprocal-lattice vector).

$$\omega\frac{dN}{dtd\omega d^2\theta} = \frac{e^2\omega_0^4|S(\mathbf{g})|^2e^{-g^2u^2}}{\pi g^2(1+g^2R^2)^2} \times\frac{\theta_\perp^2+(2\theta'+\theta_\parallel)^2\cos^2\varphi}{(\gamma^{*-2}+\theta_\perp^2+(2\theta'+\theta_\parallel)^2)^2} \times\delta\left[\omega-\omega_b\left(1+(\theta'+\theta_\parallel)\cot\frac{\varphi}{2}\right)\right], \quad (3)$$

where $\gamma^* = \gamma(1+\gamma^2\omega_0^2/\omega^2)^{-1/2}$, $\gamma = (1-v^2)^{-1/2} \gg 1$, and $\omega_b = g/2\sin(\varphi/2)$ is the Bragg frequency in whose neighborhood the spectrum of the radiation is concentrated.

Expression (3) (or expressions similar to it) is widely used to describe experimental results. In doing this, it is implied that the angular size of the radiation collimator is sufficiently small. In the following, we will study the collimator-size effect on the spectrum of the detected radiation.

We consider the case of a rectangular collimator:

$$-\frac{1}{2}\Delta\theta_\parallel < \theta_\parallel < \frac{1}{2}\Delta\theta_\parallel, \quad -\frac{1}{2}\Delta\theta_\perp < \theta_\perp < \frac{1}{2}\Delta\theta_\perp.$$

Performing a two-dimensional integration in (3) with respect to θ, we obtain the observed radiation spectrum in the eventual form

$$\omega\frac{dN}{d\omega} = N_0F(x, y, \lambda_\perp, \lambda_\parallel),$$

$$N_0 = \frac{2e^2\omega_0^4}{\pi g^3}\frac{|S(\mathbf{g})|^2e^{-g^2u^2}\gamma^*L\sin^2(\varphi/2)}{(1+g^2R^2)^2\cos(\varphi/2)},$$

$$F = \frac{1}{\sqrt{1+(x+y)^2}}\left\{\left[1+\frac{(x+y)^2\cos^2\varphi}{1+(x+y)^2}\right]\right. \quad (4)$$

$$\times\arctan\left(\frac{\lambda_\perp}{\sqrt{1+(x+y)^2}}\right)-\left[1-\frac{(x+y)^2\cos^2\varphi}{1+(x+y)^2}\right]$$

$$\left.\times\frac{\lambda_\perp(1+(x+y)^2)^{-1/2}}{1+\lambda_\perp(1+(x+y)^2)^{-1}}\right\}\sigma(x-y+\lambda_\parallel)\sigma(y+\lambda_\parallel-x),$$

where $x = \gamma^*\tan(\varphi/2)(\omega/\omega_b - 1)$, $y = \gamma^*\theta'$, $\lambda_\perp = \frac{1}{2}\gamma^*\Delta\theta_\perp$, $\lambda_\parallel = \frac{1}{2}\gamma^*\Delta\theta_\parallel$, $\sigma(Z)$ is the Heaviside function, and L is the crystal thickness assumed to be much smaller than the photoabsorption length.

Below, the universal function F is used in our analysis of the effect of the parameters $\lambda_\parallel$ and $\lambda_\perp$ on the spectrum and on the orientation dependence of the radiation yield.

3. DISCUSSION

Let us first consider the properties of the radiation in the limiting case of $\lambda_\perp \ll 1$, $\varphi \neq \pi/2$. Formula (4) is then simplified considerably to become

$$F \approx 2\lambda_\perp\cos^2\varphi\frac{(x+y)^2}{[1+(x+y)^2]^2} \times\sigma(x-y+\lambda_\parallel)\sigma(y+\lambda_\parallel-x), \quad (5)$$

whence we can see that, under the conditions being considered, the shape and the amplitude of the spectrum depend substantially on the parameters $\lambda_\parallel$ and y. For $\lambda_\parallel \ll 1$, the spectrum represents a narrow line ($\Delta x = 2\lambda_\parallel \ll 1$) centered at the point $x = y$. The corresponding energy of the emitted photon is given by

$$\omega = \omega_b(1+\theta'\cot(\varphi/2)). \quad (6)$$

This expression is usually used in the theory of parametric x-ray radiation.

The amplitude of the spectral line is determined by the value of the orientation parameter y in accordance with the factor $4y^2/(1+4y^2)^2$ following from (5) for $\lambda_\parallel \ll 1$. This factor describes the orientation dependence of the radiation yield with two peaks at $y = \pm 1/2$ (it is typical of parametric x-ray radiation).

Let us now consider the case of $\lambda_\parallel \longrightarrow \infty$ (slit collimator). The spectrum is then described by the formula

$$F \approx 2\lambda_\perp\cos^2\varphi\frac{(x+y)^2}{[1+(x+y)^2]^2}, \quad (7)$$

which follows from (5) and which predicts two substantial modifications to the spectrum in relation to the preceding case. From Eq. (7), we can see that, in the case being considered, the spectrum represents a symmetric curve having two peaks at $x = \pm 1 - y$. The width of the spectral distribution is large, $\Delta x \geq 1$, and it is centered at $x = -y$, which corresponds to the emitted-photon energy

$$\omega = \omega_b(1-\theta'\cot(\varphi/2)). \quad (8)$$

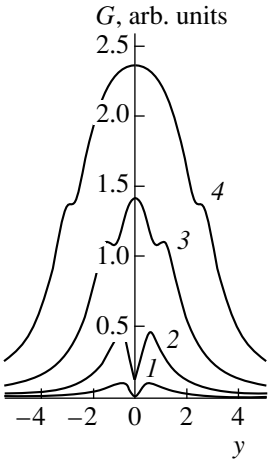

Fig. 2. Universal orientation dependence of the radiation yield for $\lambda_\perp \ll 1$ at $\lambda_\parallel$ = (*1*) 0.1, (*2*) 0.5, (*3*) 2, and (*4*) 5.

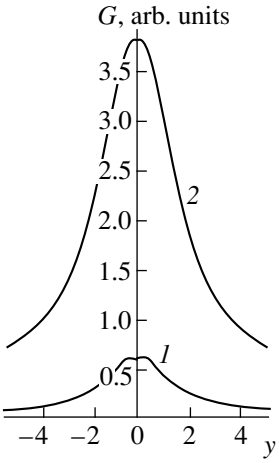

Fig. 3. Universal orientation dependence of the radiation yield for $\lambda_\perp \longrightarrow \infty$ and $\varphi = \pi/8$ at $\lambda_\parallel$ = (*1*) 0.3 and (*2*) 2.

It follows that, when we go over from a pointlike to a slit collimator, the spectrum of parametric x-ray radiation is split; concurrently, line broadening and a shift of the spectral-distribution center occur, the latter being dependent on the orientation angle. For this splitting, $\Delta\omega_p$, and the shift of the distribution center, $\Delta\omega_c$, we have

$$\Delta\omega_p = 2\omega_b\gamma^{*-1}\cot\frac{\varphi}{2}, \quad \Delta\omega_c = 2\omega_b\theta'\cot\frac{\varphi}{2}. \qquad (9)$$

Integrating the function F in (5) with respect to x, we obtain the orientation dependence of the radiation yield in the form

$$G(y, \lambda_\parallel) = \int dxF = \lambda_\perp\cos^2\varphi\Big[\arctan(2y+\lambda_\parallel) - \arctan(2y-\lambda_\parallel) - \frac{(2y+\lambda_\parallel)}{1+(2y+\lambda_\parallel)^2} + \frac{(2y-\lambda_\parallel)}{1+(2y-\lambda_\parallel)^2}\Big]. \qquad (10)$$

The function G shown in Fig. 2 for various values of the parameter $\lambda_\parallel$ exhibits a qualitative variation in the orientation dependence of the yield of parametric x-ray radiation with increasing angular size of the collimator in the reaction plane. With increasing $\lambda_\parallel$, the orientation curve that is typical of parametric x-ray radiation and which has two peaks at small values of $\lambda_\parallel$ transforms into an orientationally independent constant.

Formulas (5)–(9) are not valid in the particular case of $\varphi = \pi/2$. For this value of the emission angle φ, it follows from (4) that

$$F = \frac{2}{3}\frac{\lambda_\perp^3}{[1+(x+y)^2]^2}\sigma(x-y+\lambda_\parallel)\sigma(y+\lambda_\parallel-x). \qquad (11)$$

An analysis of this formula by a method similar to that used above leads to results that are by and large analogous to those in the preceding case, but the spectral distribution of radiation does not undergo splitting here.

Let us now consider another limiting case, that of $\lambda_\perp \longrightarrow \infty$. From (4), we then obtain

$$F = \frac{\pi}{2}\frac{1}{\sqrt{1+(x+y)^2}}\Big[1+\frac{(x+y)^2\cos^2\varphi}{1+(x+y)^2}\Big] \times \sigma(x-y+\lambda_\parallel)\sigma(y+\lambda_\parallel-x). \qquad (12)$$

It can easily be verified that, in the case being considered, the radiation spectrum transforms from a narrow line of width $2\lambda_\parallel$ for $\lambda_\parallel \ll 1$ into a bell-like curve of width $\Delta x \geq 1$ for $\lambda_\parallel \longrightarrow \infty$. However, only in the emission-angle region $\varphi < \pi/4$ does the spectral curve split into two peaks, but these peaks are rather weak. In response to an increase in the collimator size, the center of the spectral distribution of the radiation shows a shift of the same magnitude as in the preceding case of $\lambda_\perp \ll 1$.

The orientation dependence of the radiation yield is given by the formula

$$G(y, \lambda_\parallel) = \int dxF = (1+\cos^2\varphi)[\operatorname{arcsinh}(2y+\lambda_\parallel) - \operatorname{arcsinh}(2y-\lambda_\parallel)] - \cos^2\varphi\Big[\frac{(2y+\lambda_\parallel)}{\sqrt{1+(2y+\lambda_\parallel)^2}} - \frac{(2y-\lambda_\parallel)}{\sqrt{1+(2y-\lambda_\parallel)^2}}\Big], \qquad (13)$$

which follows from (11). The curves that represent the dependence $G(y)$ for various values of $\lambda_\parallel$ and φ are shown in Figs. 3 and 4.

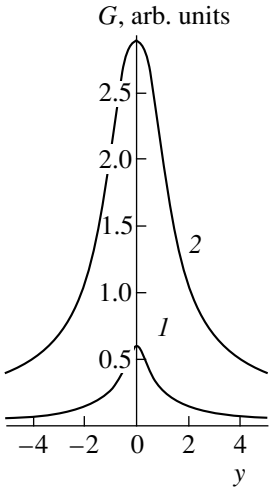

Fig. 4. As in Fig. 3, but for $\varphi = \pi/2$.

4. CONCLUSION

The spectral and orientation characteristics of parametric x-ray radiation depend substantially on the angular sizes of the radiation collimator.

With increasing collimator size in the reaction plane, the spectral distribution of the radiation broadens, while its center undergoes a shift.

If a slit collimator, with the slit being oriented along the reaction plane, is used, the observed radiation spectrum splits into two isolated peaks.

An increase in the angular size of the collimator can radically change the orientation dependence of the yield of parametric x-ray radiation (a trend toward weakening of this dependence is observed).

The above effects are of a simple geometric origin. The angular distribution (3) of the reflex of parametric x-ray radiation is bell-shaped and has a dip at its center (this is the angular structure of transverse pseudophotons of the Coulomb field of a relativistic particle that are reflected by a crystal). Because of the presence of a delta function in (3), there is a tight correlation here between the energy of the emitted photon, on one hand, and the values of the angle of radiation observation in the reaction plane, $\theta_\parallel$, and the orientation angle θ', on the other hand. Owing to the above features, the shape of the observed spectrum and its orientation dependence are determined by the degree of overlap of the reflex of parametric x-ray radiation and the collimator. If the aperture of the collimator is small in relation to the intrinsic width of the angular distribution of parametric x-ray radiation, the observed spectrum is narrow, and the orientation dependence is similar to the angular distribution of parametric x-ray radiation. On the other hand, no orientation dependence is observed if the collimator is open completely; as to the corresponding spectrum, which features all possible photon energies, it can have a dip (at specific transverse sizes of the collimator, $\Delta\theta_\perp$, and specific values of the emission angle φ) caused by the absence of photons emitted through the mechanism of parametric x-ray radiation in the direction of Bragg scattering.

ACKNOWLEDGMENTS

This work was supported in part by the Ministry for Higher Education of the Russian Federation (grant no. 97-07.2-155).

REFERENCES

1. Ya. B. Faĭnberg and N. A. Khizhnyak, Zh. Éksp. Teor. Fiz. **32**, 883 (1957) [Sov. Phys. JETP **5**, 720 (1957)].
2. M. L. Ter-Mikaelian, *High-Energy Electromagnetic Processes in Condensed Media* (Akad. Nauk Arm. SSR, Yerevan, 1969; Wiley, New York, 1972).
3. V. G. Baryshevskiĭ and I. D. Feranchuk, Zh. Éksp. Teor. Fiz. **61**, 944 (1971) [Sov. Phys. JETP **34**, 495 (1971)].
4. G. M. Garibyan and C. Yang, Zh. Éksp. Teor. Fiz. **61**, 930 (1971) [Sov. Phys. JETP **34**, 502 (1971)].

Translated by V. Bukhanov

Physics of Atomic Nuclei, Vol. 63, No. 11, 2000, pp. 2015–2017. Translated from Yadernaya Fizika, Vol. 63, No. 11, 2000, pp. 2109–2111.

XXIX INTERNATIONAL CONFERENCE ON THE PHYSICS OF CHARGED-PARTICLE INTERACTION WITH CRYSTALS

Possibility of Deflecting Relativistic-Ion Beams by Bent Single Crystals

A. A. Greenenko[1)] and N. F. Shul'ga*

Ukrainian Research Center Kharkov Institute for Physics and Technology, ul. Akademicheskaya 1, Kharkov, 310108 Ukraine

Received December 10, 1999; in final form, February 11, 2000

Abstract—The propagation of high-energy ions through a bent single crystal near a crystallographic axis is investigated. The results of these investigations reveal that a new mechanism of ion-beam deflection is possible in this case. This mechanism is based on multiple ion scattering by atomic strings in a bent crystal. The results obtained from a computer simulation of the effect are also presented. The effect is shown to depend strongly on the particle charge. *© 2000 MAIK "Nauka/Interperiodica".*

1. INTRODUCTION

The deflection of beams of high-energy positively charged particles via the mechanism of planar channeling in bent crystals is a well-studied effect, which is used in practice [1, 2]. In [3–5], it was indicated that there exists another mechanism of beam deflection by a bent crystal, that which is based on the multiple scattering of particles by atomic strings. A feature peculiar to this mechanism is that, in scattering by atomic strings, beam deflection is possible both for channeled and for above-barrier particles; at the same time, only for channeled particles is this possible in the case of motion along bent crystallographic planes. Moreover, a beam incident on a bent crystal at a small angle with respect to a crystallographic axis can undergo both deflection and splitting. It is important to note that not only elementary-particle beams but also beams of multiply charged ions can be deflected by bent crystals [6]. In the latter case, the value of the charge affects substantially the deflection of the charged-particle momentum [6, 7]. In the present study, we analyzed the mechanism of deflection of relativistic-ion beams due to multiple particle scattering on atomic strings in a bent crystal.

2. SIMULATION PROCEDURE AND BASIC RESULTS

The possibility of deflecting ion beams that traverse a bent crystal near a crystallographic axis was considered both analytically and on the basis of a numerical simulation. The problem at hand can be treated analytically in the case where the conditions of dynamical chaos are realized in the scattering process [8]. But in the general case, it is necessary to apply methods of a numerical simulation. For this purpose, we developed a computer code for simulating the propagation of charged particles through a bent crystal near a crystallographic axis [4, 8]. The propagation of particles through a crystal is considered as a step-by-step two-dimensional motion in the plane orthogonal to the direction of the crystallographic axis in the total field of atomic strings. A continuous potential of atomic strings can be computed on the basis of the Mollier approximation for the potential of an individual atom. At each step, we computed both coherent and incoherent particle scattering, the former being caused by an averaged continuous potential. Incoherent scattering is associated with the distinction between the actual potential of a string and the averaged potential. This distinction is due to the thermal displacements of lattice atoms from equilibrium positions and to lattice electrons. Incoherent scattering changes the transverse energy of the scattered particle. It is taken into account under the assumption of a Gaussian distribution of computed quantities.

An analytic consideration of charged-particle propagation through a bent crystal near a crystallographic axis shows [8] that the effect of beam deflection by a crystal is possible under the condition

$$\alpha = \frac{L}{R_{\psi_c}}\frac{l_\perp}{R_{\psi_c}} < 1, \qquad (1)$$

where L is the crystal thickness, R is the radius of curvature of its bend, ψ_c is the critical angle of axial channeling, and $l_\perp$ is the length over which the distribution of particles with respect to the azimuthal angle is established as the result of multiple scattering. For $\psi \le \psi_c$, we have the approximate relation $l_\perp \approx (\psi_c n d a_{\mathrm{TF}})^{-1}$, where n is the density of atoms, d is the interatomic spacing along the direction of motion (z axis), and a_{TF} is the radius of screening of the atomic potential.

Since $\alpha \sim \psi_c^{-3}$ and $\psi_c \sim \sqrt{Z_i}$, the mechanisms of propagation through a bent crystal can be very different

[1)] Ukrainian Research Center Kharkov Institute for Physics and Technology, ul. Akademicheskaya 1, Kharkov, 310108 Ukraine and Belgorod State University, Studencheskaya ul. 12, Belgorod, 308007 Russia.

* e-mail: shulga@kipt.kharkov.ua

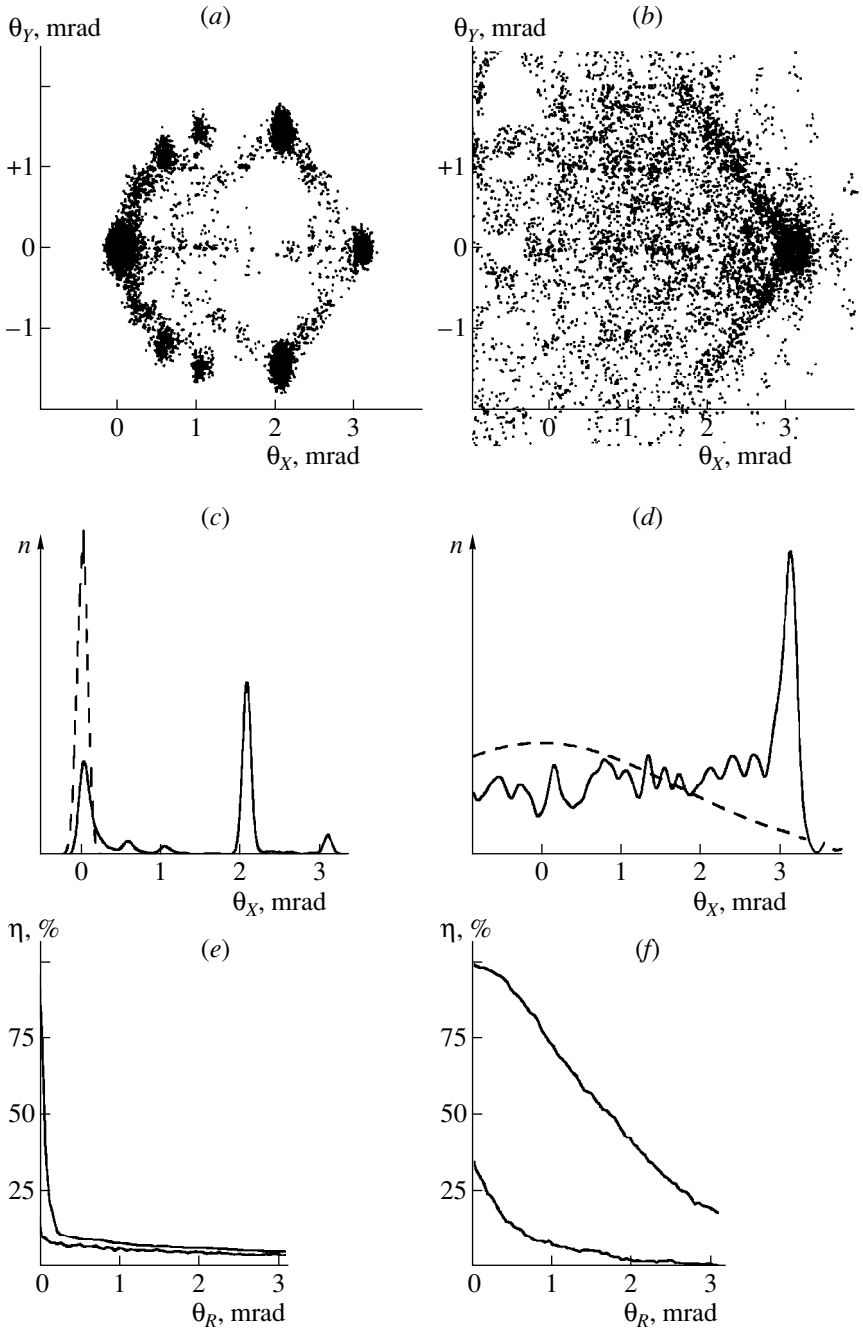

Fig. 1. Propagation of 450-GeV beams of (*a*, *c*, *e*) protons and (*b*, *d*, *f*) U^{+92} ions through a bent silicon crystal whose thickness is of $L = 3$ cm and whose radius of curvature is of $R = 10$ m near its ⟨110⟩ axis: (*a*, *b*) angular distributions of particles leaving the crystal, (*c*, *d*) horizontal profile of the beam leaving the crystal, and (*e*, *f*) fractions of (upper curves) deflected and (lower curves) hyperchanneled particles versus the crystal thickness. The dashed curves in Figs. 1*c* and 1*d* represent the profiles of the beams that traversed a 3-cm layer of amorphous silicon. The coordinates of the initial-beam center, the beam divergence, the coordinates specifying the crystal-axis direction at the downstream surface of the crystal, the beam dimensions, and the observation base were, respectively, $(\theta_X, \theta_Y) = (0, 0)$, 3×10^{-6} rad, $(\theta_X, \theta_Y) = (3.1, 0, 0)$ mrad, 1×2 mm^2, and 4 m.

for protons and for multiply charged ions. By way of example, we indicate that, for a beam of 450-GeV particles incident on a silicon single crystal along the ⟨110⟩ axis at $L = 3$ cm and $R = 10$ m (which corresponds to the parameters of the CERN experiment studying the axial deflection of protons [9]), we have $\alpha_p = 80$ for protons and $\alpha_U = 0.1$ for uranium ions. Taking into account the condition in (1), we conclude that, for the above values of the beam and crystal parameters, the mechanism of deflection via multiple scattering on single-crystal strings must be operative for ions and inoperative for protons. This theoretical prediction is fully

confirmed by the results of a numerical simulation (for a proton beam, the results of the simulation are in good agreement with the experimental data from [9]). Figure 1 shows the results of our computer simulation for the above conditions.

Our results demonstrate that the angular distributions of protons that traversed a single crystal differ considerably from the analogous distribution for multiply charged uranium ions. The direction of the crystallographic axis at the downstream surface of the crystal is taken here to correspond to $\theta_R = 3$ mrad. In the case of ions, a significant fraction of beam particles (about 20%) are deflected through this angle, following the bend of the crystallographic axis. It is predominantly the above-barrier particles that undergo deflection under such conditions (see Fig. 1*f*). Among protons, only the hyperchanneled particles are deflected in the case being considered (see Fig. 1*e*). Initially, the fraction of hyperchanneled protons is much less than that in the case of ions because the depth of the two-dimensional potential well is much greater for ions than for protons. The results of our simulation reveal, however, that the process of dechanneling is more vigorous for ions than for protons; as a result, the beam of uranium ions leaving the crystal does not contain hyperchanneled particles. Our analysis of the numerical data shows that this effect is due to a sharp intensification of incoherent scattering on lattice electrons with increasing particle charge. Thus, the deflection mechanism associated with multiple scattering on bent atomic strings is operative for multiply charged ions. Indeed, strong incoherent scattering, which suppresses the deflection of hyperchanneled particles (both in the axial and in the planar case), leaves the possibility for the axial deflection of above-barrier particles.

Symmetric peaks in the distribution of protons (see Figs. 1*a*, 1*c*) are associated with particles captured in planar channels. This capture occurs when the deflected particles cease to follow the axis and results in the possible splitting of the beam into several isolated fractions. A gradual escape of particles from the trajectory along the axis occurs when the deflection conditions are impaired—that is, when the parameter α approaches unity with increasing crystal thickness. The fractions captured by planes are localized when the capture of new particles is terminated—that is, when $\alpha > 1$; this inequality can be considered as the condition under which the effect of beam spitting is realized.

Thus, the propagation of relativistic multiply charged ions through a bent crystal differs considerably from the propagation of protons and must be considered separately. The results obtained here show that the above effects can be investigated at the GSI ion accelerator.

ACKNOWLEDGMENTS

This work was supported by the Foundation for Basic Research and the Ministry for Science and Education of Ukraine (projects Landau–Pomeranchuk–Migdal effect and QSU 082231) and by the Russian Foundation for Basic Research (project no. 98-02-16160).

REFERENCES

1. *Relativistic Channeling*, Ed. by R. A. Carrigan, Jr., and J. A. Ellison (Plenum, New York, 1987), NATO ASI Ser., Ser. B, Vol. 165.
2. V. M. Biryukov, V. I. Kotov, and Yu. A. Chesnokov, Usp. Fiz. Nauk **164**, 1017 (1994) [Phys. Usp. **37**, 937 (1994)].
3. J. F. Bak, P. R. Jensen, W. Madsboll, *et al.*, Nucl. Phys. B **242**, 1 (1984).
4. A. A. Greenenko and N. F. Shul'ga, Nucl. Instrum. Methods Phys. Res. B **90**, 179 (1994).
5. A. A. Grinenko and N. F. Shul'ga, Poverkhnost **12**, 58 (1995).
6. G. Arduni, C. Biino, M. Clement, *et al.*, CERN SL/97-43 (DI), 1997.
7. N. F. Shul'ga, A. I. Akhiezer, V. I. Truten', and A. A. Greenenko, Phys. Scr. **218**, 172 (1999).
8. A. I. Akhiezer, N. F. Shul'ga, V. I. Truten', *et al.*, Usp. Fiz. Nauk **165**, 1165 (1995) [Phys. Usp. **38**, 1119 (1995)].
9. A. Baurichter, K. Kirsebom, V. Medenwaldt, *et al.*, Nucl. Instrum. Methods Phys. Res. B **115**, 172 (1996).

Translated by V. Bukhanov

Physics of Atomic Nuclei, Vol. 63, No. 11, 2000, pp. 2018–2020. Translated from Yadernaya Fizika, Vol. 63, No. 11, 2000, pp. 2112–2114.

XXIX INTERNATIONAL CONFERENCE ON THE PHYSICS OF CHARGED-PARTICLE INTERACTION WITH CRYSTALS

Ionization Energy Losses of Fast Charged Particles Produced in Matter

N. F. Shul'ga[1), *] and V. V. Syshchenko

National Research Center, Kharkov Institute for Physics and Technology, Akademicheskaya ul. 1, Kharkov, 310108 Ukraine

Received December 10, 1999; in final form, February 11, 2000

Abstract—Ionization energy losses of an ultrarelativistic electron produced in matter are considered. The interference of the proper Coulomb field of the product particle and the electromagnetic wave that this particle emits is shown to be significant at impact-parameter values that make a dominant contribution to the ionization energy losses. The effect is shown to exert virtually no influence on the ionization energy losses of the particle. © *2000 MAIK "Nauka/Interperiodica".*

1. Ionization energy losses of clusters formed by fast charged particles occurring at small distances from one another may differ significantly from the total ionization energy losses of the individual particles constituting the cluster if these particles are far from one another. This distinction is associated with the interference of the electromagnetic fields created by the particles of the cluster at distances that contribute significantly to ionization energy losses. Such a situation emerges, for example, when a high-energy electron–positron pair is produced in matter [1]. The point is that the characteristic angles of divergence of a high-energy pair produced in matter are very small. It follows that, over rather long a time interval, the transverse distance between the particles of the pair will be small in relation to the maximum impact-parameter values of $\rho_{max} \sim v/\omega_p$, ($v$ is the particle velocity, and ω_p is the plasmon frequency) that contribute significantly to the ionization energy losses of the individual particles of the pair. The electromagnetic fields of the electron and the positron of the product pair compensate each other partly at distances of v/ω_p the from the pair in the transverse direction; therefore, the ionization energy losses of such a cluster are smaller than the ionization energy losses of the individual particles. By way of example, we indicate that, at photon energies of $\hbar\omega \sim 100$ GeV, characteristic angles of divergence of the particles forming the pair are estimated as $\theta_\pm \sim 4mc^2/\hbar\omega \sim 2 \times 10^{-5}$ rad, so that the reduction of the ionization energy losses of the product pair must manifest itself at longitudinal distances of $l \sim \rho_{max}/\theta_\pm \sim 0.05$ cm from the pair-production vertex. This effect was observed in cosmic rays [1].

A similar effect occurs in the Coulomb explosion of fast molecules in a thin layer of matter [2]. The similarity of these two processes was noticed in [3].

For a long time, the electromagnetic field surrounding a high-energy charged particle (electron) produced in matter can differ significantly from the normal proper field of a similar particle that moves at a constant speed in the same direction [4, 5]. The effect is determined by the interference of the Coulomb field of the electron and the field of the electromagnetic wave that this electron emits. An ultrarelativistic electron emits waves predominantly at small angles with respect to its velocity, $\theta \sim mc^2/E$, where E is the electron energy. As a result, an electron, with its Coulomb field, and the emitted electromagnetic wave will be at small distances from each other for a long period of time; hence, the effect of interference between the two fields will be significant. In this sense, the electron and the electromagnetic wave emitted by it can be treated as a cluster formed by the Coulomb field of the electron and the emitted electromagnetic wave. Such clusters manifest themselves in many processes associated with radiation from ultrarelativistic electrons in matter, such as coherent radiation from relativistic electrons in oriented crystals and the Landau–Pomeranchuk effect, which consists in the suppression of bremsstrahlung from ultrahigh-energy electrons in amorphous media (see, for example, [5]). There naturally arises the question of whether such a cluster can manifest itself in ionization energy losses of a particle in a medium. This is the problem to be addressed in the present article.

2. We consider some special features of the evolution of the field of a particle following its production in matter and the ionization energy losses of the particle in this case. First, we analyze the evolution of the field of a high-energy particle produced in a medium, neglecting the dielectric properties of the medium.

We assume that a charged particle is instantaneously produced at the time instant $t = 0$ with a finite velocity $\mathbf{v}$.

* e-mail: shulga@kipt.kharkov.ua

1) National Research Center, Kharkov Institute for Physics and Technology, Akademicheskaya ul. 1, Kharkov, 310108 Ukraine and Belgorod State University, Studencheskaya ul. 12, Belgorod, 308007 Russia.

The potentials of the particle field are determined by the equations ($c = 1$)

$$\left(\nabla^2 - \frac{\partial^2}{\partial t^2}\right)\varphi(\mathbf{r}, t) = -4\pi e\delta(\mathbf{r} - \mathbf{v}t)\Theta(t), \quad (1)$$

$$\left(\nabla^2 - \frac{\partial^2}{\partial t^2}\right)\mathbf{A}(\mathbf{r}, t) = -4\pi e\mathbf{v}\delta(\mathbf{r} - \mathbf{v}t)\Theta(t), \quad (2)$$

where $\Theta(t)$ is the Heaviside step function. Solutions to Eqs. (1) and (2) can be represented in terms of the Fourier integrals

$$\varphi(\mathbf{r}, t) = \frac{e}{2\pi^2}\mathrm{Re}\int\frac{d^3k}{k(k - \mathbf{k}\cdot\mathbf{v})}e^{i\mathbf{k}\cdot\mathbf{r}}(e^{-i\mathbf{k}\cdot\mathbf{v}t} - e^{-ikt}), \quad (3)$$

$$\mathbf{A}(\mathbf{r}, t) = \frac{e}{2\pi^2}\mathbf{v}\mathrm{Re}\int\frac{d^3k}{k(k - \mathbf{k}\cdot\mathbf{v})}e^{i\mathbf{k}\cdot\mathbf{v}t}(e^{-i\mathbf{k}\cdot\mathbf{v}t} - e^{-ikt}). \quad (4)$$

These solutions can also be recast into the form

$$\varphi(\mathbf{r}, t) = \Theta(t - r)\varphi_0(\mathbf{r}, t), \quad (5)$$

$$\mathbf{A}(\mathbf{r}, t) = \Theta(t - r)\mathbf{A}_0(\mathbf{r}, t), \quad (6)$$

where φ_0 and $\mathbf{A}_0$ determine the conventional Coulomb field of a charged particle that moves at a velocity $\mathbf{v}$,

$$\varphi_0(\mathbf{r}, t) = \frac{e}{[(z - vt)^2 + \rho^2\gamma^{-2}]^{1/2}}, \quad (7)$$

$$\mathbf{A}_0(\mathbf{r}, t) = \frac{e\mathbf{v}}{[(z - vt)^2 + \rho^2\gamma^{-2}]^{1/2}}. \quad (8)$$

Here, $\gamma = (1 - v^2)^{-1/2}$ is the Lorentz factor, the z axis is aligned with $\mathbf{v}$, and $\boldsymbol{\rho}$ is a radius vector in the plane orthogonal to $\mathbf{v}$.

The first terms in (3) and (4) describe the potentials of the conventional Coulomb field of a particle that moves at a velocity $\mathbf{v}$. The second terms describe the field of the emitted wave for $t \longrightarrow \infty$. In each term in (3) and (4), the main contribution to the integrals with respect to $\mathbf{k}$ in every comes from $\mathbf{k}$ whose directions are close to the direction of $\mathbf{v}$—more specifically, from the region where the characteristic angle θ between $\mathbf{k}$ and $\mathbf{v}$ is $\theta \sim \gamma^{-1}$. For such $\mathbf{k}$, the relevant Fourier components of the surrounding field are suppressed over the time period from $t = 0$ to $t < (k - \mathbf{k}\cdot\mathbf{v})^{-1} \sim 2\gamma^2/k$ in relation to those in the region $t > 2\gamma^2/k$. This means that, over the period $\Delta t \sim 2\gamma^2/k$, the particle is in a "semibare" state deprived of its normal Coulomb field. Considering that the main contribution to the ionization energy losses of the particle comes from the region $k > \omega_p/v$, we can expect that the ionization energy losses are suppressed over the time interval $\Delta t \sim 2\gamma^2/k$. For electron energies of $E_e \sim 100$ GeV, we have $v\Delta t \sim 10^2$ cm.

Direct calculations reveal, however, that there is no such effect—that is, the ionization energy losses of the electron reach their normal value after a lapse of the time $\Delta t \sim \rho_{\max}/v$. By using relations (5) and (6), we can indeed show (in accordance with the Bohr method for calculating the ionization energy losses [6]) that the energy losses of a particle at distances $z \gg \rho_{\max}$ from its production vertex in matter are given by

$$T = T_0\left(1 - \frac{1}{\ln(\rho_{\max}/\rho_{\min})}\frac{\rho_{\max}^2}{4z^2} + \ldots\right), \quad (9)$$

where

$$T_0 = \frac{\omega_p^2 e^2}{v}\ln\frac{\rho_{\min}}{\rho_{\max}} \quad (10)$$

and $\rho_{\min}$ is the minimum impact-parameter value that contributes significantly to the ionization energy losses. This value is determined on the basis of quantum considerations and is about p^{-1}, where p is the projectile momentum.

From Eq. (9), we can see that, at $z \gg \rho_{\max}$, the correction to the conventional expression T_0 for the energy lost by the particle in matter owing to the prolonged existence of the electron in the "semibare" state is small. That the ionization energy losses increase within a time interval smaller than the time over which the normal Coulomb field of the electron is recovered can be explained by the fact that the splash Δ of the field strength at $t = r$ [see Eqs. (5) and (6)] compensates for the decrease in the ionization energy losses that is associated with the absence of the field for distances $r > t$.

3. Let us now take into account the dielectric properties of the medium. In this case, Eqs. (1) and (2) assume the form [7]

$$\hat{\varepsilon}\left(\nabla^2 - \hat{\varepsilon}\frac{\partial^2}{\partial t^2}\right)\varphi(\mathbf{r}, t) = -4\pi e\delta(\mathbf{r} - \mathbf{v}t)\Theta(t), \quad (11)$$

$$\left(\nabla^2 - \hat{\varepsilon}\frac{\partial^2}{\partial t^2}\right)\mathbf{A}(\mathbf{r}, t) = -4\pi e\mathbf{v}\delta(\mathbf{r} - \mathbf{v}t)\Theta(t). \quad (12)$$

If the dielectric permittivity is given by

$$\varepsilon(\omega) = 1 - \frac{\omega_p^2}{(\omega + i0)^2}, \quad (13)$$

solutions to these equations can be represented as

$$\varphi(\mathbf{r}, t) = \frac{e}{2\pi^2}\mathrm{Re}\int\frac{d^3k}{k^2}e^{i\mathbf{k}\cdot\mathbf{r}}\left\{-\frac{\omega_p e^{-i\mathbf{k}\cdot\mathbf{v}}}{\omega_p - \mathbf{k}\cdot\mathbf{v}} + \frac{\omega_p e^{-i\omega_p t}}{\omega_p - \mathbf{k}\cdot\mathbf{v}}\right.$$
$$\left. + \frac{\sqrt{k^2 + \omega_p^2}e^{-i\mathbf{k}\cdot\mathbf{v}t}}{\sqrt{k^2 + \omega_p^2} - \mathbf{k}\cdot\mathbf{v}} - \frac{\sqrt{k^2 + \omega_p^2}}{\sqrt{k^2 + \omega_p^2} - \mathbf{k}\cdot\mathbf{v}}e^{-i\sqrt{k^2 + \omega_p^2}t}\right\}\Theta(t), \quad (14)$$

$$\mathbf{A}(\mathbf{r}, t) = \frac{e}{2\pi^2}v\mathrm{Re}\int d^3k e^{i\mathbf{k}\cdot\mathbf{r}}$$
$$\times\left\{\frac{e^{-i\mathbf{k}\cdot\mathbf{v}t}}{\sqrt{k^2 + \omega_p^2}(\sqrt{k^2 + \omega_p^2} - \mathbf{k}\cdot\mathbf{v})}\right. \quad (15)$$

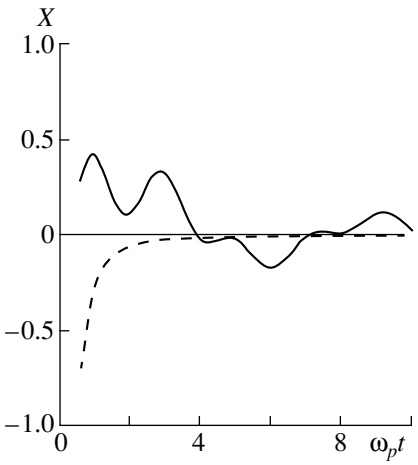

Quantity X calculated according to the expressions (dashed curve) (9) and (solid curve) (16) versus $\omega_p t$.

$$-\frac{e^{-i\sqrt{k^2+\omega_p^2}t}}{\sqrt{k^2+\omega_p^2}(\sqrt{k^2+\omega_p^2}-\mathbf{k}\cdot\mathbf{v})}\Bigg\}\Theta(t).$$

It can easily be seen that, for $\omega_p \longrightarrow 0$, Eqs. (14) and (15) reduce to Eqs. (3) and (4). Calculating the ionization energy losses on the basis of the method described in [7], we obtain

$$T = T_0 + \frac{e^2\omega_p}{v}\frac{\sin(\omega_p t)}{t} - \frac{e^2\omega_p^2}{v} \tag{16}$$
$$\times[\mathrm{ci}(\omega_p t)\sin^2(\omega_p t) - \mathrm{si}(\omega_p t)\cos^2(\omega_p t)],$$

where

$$\mathrm{ci}(x) = -\int_x^\infty \frac{\cos t}{t}dt = C + \ln x + \int_0^x \frac{\cos t - 1}{t}dt,$$

$$\mathrm{si}(x) = -\int_x^\infty \frac{\sin t}{t}dt = -\frac{\pi}{2} + \int_0^x \frac{\sin t}{t}dt,$$

and $C = \ln\gamma = 0.577$ is the Euler constant.

The quantity $X = (v/\omega_p^2 e^2)(T - T_0)$, which determines the deviation of the ionization energy losses of the "semibare" electron from the normal energy losses in accordance with expressions (9) and (16), is displayed in the figure as a function of $\omega_p t$.

For electron energies of $E_e \sim 1$ GeV, $(v/\omega_p^2 e^2)T_0 \sim 17$; therefore, the difference of the T value computed according to (16) and T_0 at distances of a few ω_p^{-1} (that is, a few $\rho_{\max}$ for ultrarelativistic particles) is within 2%.

Thus, we see that the prolonged existence of an electron deprived of its normal Coulomb field has virtually no effect on the ionization energy loss of a particle in a medium. We emphasize, however, that the semibare-electron effect is significantly manifested in the radiation from relativistic particles [8].

ACKNOWLEDGMENTS

This work was supported by the Russian Foundation for Basic Research (project no. 98-02-16160) and by the Ministry for Higher Education of the Russian Federation (project no. 97-0-143-5).

REFERENCES

1. A. E. Chudakov, Izv. Akad. Nauk SSSR, Ser. Fiz. **19**, 651 (1955).
2. W. Brandt, A. Ratkowski, and H. Ritchie, Phys. Rev. Lett. **33**, 302, 1325 (1974).
3. N. F. Shul'ga and V. V. Syshchenko, Phys. Lett. A **165**, 175 (1992).
4. E. L. Feĭnberg, Zh. Éksp. Teor. Fiz. **50**, 202 (1966) [Sov. Phys. JETP **23**, 132 (1966)].
5. A. I. Akhiezer and N. F. Shul'ga, *Electrodynamics of High Energy in Matter* (Nauka, Moscow, 1993).
6. J. D. Jackson, *Classical Electrodynamics* (Wiley, New York, 1975; Inostrannaya Literatura, Moscow, 1965).
7. L. D. Landau and E. M. Lifshitz, *Electrodynamics of Continuous Media* (Nauka, Moscow, 1992; Pergamon, New York, 1984).
8. N. F. Shul'ga and S. P. Fomin, Phys. Lett. A **114**, 148 (1986).

Translated by M. Kobrinsky

Physics of Atomic Nuclei, Vol. 63, No. 11, 2000, pp. 2021–2024. Translated from Yadernaya Fizika, Vol. 63, No. 11, 2000, pp. 2115–2118.

XXIX INTERNATIONAL CONFERENCE ON THE PHYSICS OF CHARGED-PARTICLE INTERACTION WITH CRYSTALS

Relativistic-Electron Scattering on an Atomic String of a Crystal at Ultrasmall Angles of Particle Incidence on a String

N. F. Shul'ga[1), *] and V. I. Truten'

State Research Center Kharkov Institute for Physics and Technology, ul. Akademicheskaya 1, Kharkov, 310108 Ukraine

Received December 10, 1999; in final form, February 11, 2000

Abstract—The classical and quantum scattering of fast electrons on an atomic string of a crystal is considered at angles of particle incidence on the string that are much smaller than the critical angle of axial channeling. The investigation was performed within the simplest approximation of the continuous atomic-string potential in the form of a cutoff Coulomb potential. For this case, the azimuthal scattering of particles at an angle exceeding 180° in the plane orthogonal to the string axis is shown to be possible for all impact-parameter values. It is demonstrated that, in particle scattering on a string, an effect can occur that is similar to the Ramsauer–Townsend effect, which consists in a considerable reduction of the total cross section for slow-electron scattering on atoms. *© 2000 MAIK "Nauka/Interperiodica".*

1. INTRODUCTION

When a fast charged particle is incident on an atomic string of a crystal at a small angle ψ with respect to its axis, correlations between successive collisions of the particle with string atoms are of importance. Because of these correlations, the particle is scattered predominantly at the azimuthal angle φ in the plane orthogonal to the string axis [1]. At angles of particle incidence that exceed the critical angle of axial channeling, ψ_c, typical values of the azimuthal scattering angle are small. However, these typical values of the azimuthal scattering angle increase with decreasing angle ψ, achieving 180° at $\psi \sim \psi_c$. Of particular interest is scattering of negatively charged particles on an atomic string because, at all possible values of the angle ψ, such particles can approach closely the string axis, undergoing intense interactions with the string field.

In the present study, we analyze special features of the scattering of a negatively charged particle on an atomic string of a crystal at ultrasmall angles of particle incidence on the string. The study is performed within the simplest approximation relying on a continuous potential of the atomic string in the form of a cutoff Coulomb potential. It is shown that, in the region $\psi \ll \psi_c$, the character of particle scattering on a string changes drastically with decreasing ψ. In particular, it turns out that, at some value of $\psi = \psi_g$ ($\psi_g \ll \psi_c$), the classical angle of particle scattering is 180° for all impact-parameter values. This effect is similar to the effect of giant glory in slow-electron scattering on an atom [2]. For $\psi < \psi_g$, the angle of particle scattering on the string is shown to exceed 180° for all impact-parameter values resulting in scattering.

We have considered quantum aspects of particle scattering on an atomic string. For $\psi < \psi_g$, the quantum-scattering cross section can oscillate considerably about the classical value over the entire range of azimuthal scattering angles. This effect is similar to the generalized Ramsauer–Townsend effect for slow-electron scattering on atoms at a large angle [3, 4].

We also investigate the scattering cross section as a function of the angle φ. At small angles ψ, the total scattering cross section is shown to have a rather complicated structure. In particular, this cross section appears to have a deep minimum at a certain value of ψ. This result is similar to the Ramsauer–Townsend effect, which consists in a considerable reduction of the total cross section for slow-electron scattering on an atom (see [3]).

2. QUANTUM- AND CLASSICAL-SCATTERING CROSS SECTIONS

The motion of a fast charged particle incident on an atomic string of a crystal at a small angle ψ with respect to its axis (z axis) is determined primarily by a continuous string potential—that is, by the potential of string atoms that is averaged along the z axis [5, 6]. The z component of the momentum is conserved in this field, so that the particles undergo scattering only at the azimuthal angle φ in the (x, y) plane, which is orthogonal to the string axis. As a result, we arrive at the two-dimensional problem of particle scattering on a potential $U(\rho)$ in the (x, y) plane, where $\rho = \sqrt{x^2 + y^2}$.

This formulation of the problem is valid both for the quantum and for the classical treatment of the process of particle scattering on an atomic string. In classical

[1)] National Research Center Kharkov Institute for Physics and Technology, ul. Akademicheskaya 1, Kharkov, 310108 Ukraine and Belgorod State University, Studencheskaya ul. 12, Belgorod, 308007 Russia.

* e-mail: shulga@kipt.kharkov.ua

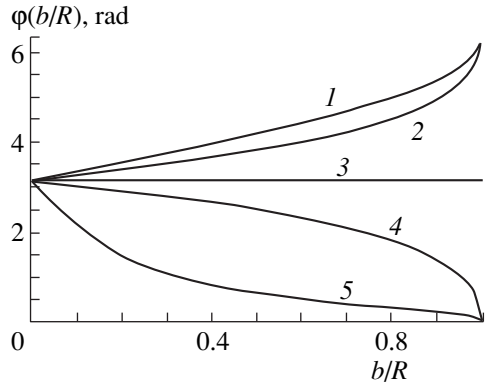

Fig. 1. Deflection function $\varphi = \varphi(b/R)$ (R is the cutoff radius of the string potential) for electron scattering by an atomic string of a silicon crystal at ψ = (*1*) $0.05\psi_c$, (*2*) $0.2\psi_c$, (*3*) ψ_g, (*4*) $0.4\psi_c$, and (*5*) $0.8\psi_c$.

mechanics, the angle of azimuthal particle scattering in the field $U(\rho)$ is given by [1]

$$\varphi(b) = \pi - 2b\int_{\rho_0}^{\infty}\frac{d\rho}{\rho^2}\left(1 - \frac{U(\rho)}{\varepsilon_\perp} - \frac{b^2}{\rho^2}\right)^{-1/2}, \qquad (1)$$

where b is the string impact parameter, $\varepsilon_\perp = \varepsilon\psi^2/2$ is the transverse particle energy, ε is the particle energy, and ρ_0 is the minimum distance between the particle and the string axis.

If the function $\varphi(b)$ is known, we can find the cross section for classical particle scattering on the string, $\frac{d\sigma_c}{d\varphi}$, at angles in the interval $(\varphi, \varphi + d\varphi)$. The result is

$$\frac{d\sigma_c}{d\varphi} = L\psi\left|\frac{d\varphi}{db}\right|^{-1}, \qquad (2)$$

where L is the string length.

The cross section for quantum particle scattering on the atomic-string field has the form [1]

$$\frac{d\sigma}{d\varphi} = \frac{L\psi}{2\pi p_\perp}\left|\sum_{l=-\infty}^{\infty} e^{il\varphi}(e^{2i\eta_l} - 1)\right|^2, \qquad (3)$$

where η_l are phase shifts for scattering on the field $U(\rho)$ and $p_\perp = \varepsilon\psi$. Summation is performed over the integral values of the angular momentum in the transverse plane.

In the semiclassical approximation, the phase shifts η_l are given by

$$\eta_l = \int_{\rho_0}^{\infty} d\rho\sqrt{p_\perp^2 - 2\varepsilon U(\rho) - l^2\rho^{-2}} - \int_{\rho_0}^{\infty} d\rho\sqrt{p_\perp^2 - l^2\rho^{-2}}, \qquad (4)$$

where ρ_0 is the root of the radicand (at $l = 0$, we have $\rho_0 = 0$).

According to (3), the total cross section for particle scattering on the string is

$$\sigma_{\text{tot}} = \frac{4L\psi}{p_\perp}\sum_{l=-\infty}^{\infty}\sin^2\eta_l. \qquad (5)$$

In order to find the scattering cross section, it is necessary to know the form of the function $U(\rho)$. The continuous potential of the atomic string has a rather complex form; therefore, simpler forms of the potential energy $U(\rho)$ are often used to approximate the potential of the particle interaction with the string.

For the function $U(\rho)$, we use here the form (see [1, 5, 7])

$$U(\rho) = \begin{cases} -\alpha\left(\frac{1}{\rho} - \frac{1}{R}\right), & \rho \le R \\ 0, & \rho > R, \end{cases} \qquad (6)$$

where $\alpha = U_0 a$, a being the Thomas–Fermi radius of the screening of the atomic potential $U_0 = \pi Ze^2/2d$ (here, $Z|e|$ and e are the charges of the atomic nucleus and the electron, respectively, and d is the spacing between the string atoms), while R is the cutoff radius of the string potential.

Functions of the form $U(\rho) = \alpha/\rho$ are often used in the theory of particle channeling in crystals [5, 7]. In this approximation, the potential $U(\rho)$ is cut off at the distance equal to half the spacing between the nearest atomic strings of the crystal.

The problem of particle scattering on the potential (6) was also considered in studying slow-electron scattering on atoms [2, 3, 8].

3. RESULTS AND DISCUSSION

Formulas (1)–(5) allow us to study particle scattering on an atomic string within the quantum and within the classical framework.

The calculated deflection function $\varphi = \varphi(b)$ for a negatively charged particle scattered by an atomic string is shown in Fig. 1 at various values of the parameter ψ/ψ_c, where $\psi_c = \sqrt{2U_0/\varepsilon}$ is the critical angle of axial channeling.

Our results reveal that the character of particle scattering on an atomic string changes significantly at $\psi \sim \psi_g$, where $\psi_g = \sqrt{\alpha/\varepsilon R}$.

For $\psi > \psi_g$, $\varphi(b)$ is a monotonically decreasing function of the impact parameter, the particles being scattered here at angles that do not exceed 180°.

At $\psi = \psi_g$, the particles are scattered at $\varphi(b) = 180°$ for all impact-parameter values. This effect is similar to the effect of giant glory in slow-electron scattering on atoms [2].

For $\psi < \psi_g$, $\varphi(b)$ is a monotonically increasing function of the impact parameter, the particles being scat-

tered at angles in excess of 180° at all impact-parameter values.

Figure 2 shows the differential cross sections for the scattering of 10-MeV electrons incident on an atomic string of a silicon crystal at angles of $\psi = (a)\ 0.8\psi_c$ and $(b)\ 0.2\psi_c$ with respect to the $\langle 100 \rangle$ axis. These values of ψ correspond to the angles of particle incidence such that $\psi > \psi_g$ in the former case (a) and $\psi < \psi_g$ in the latter case (b). The values of $F = (La\psi)^{-1}\dfrac{d\sigma}{d\varphi}$ are plotted along the ordinate. The thin and the thick curve correspond to the calculations by formulas (2) (classical scattering) and (3) (quantum scattering), respectively. The cutoff radius of the potential was taken to be $R = 0.96$ Å, which corresponds to half the mean spacing between the atomic strings in the plane orthogonal to the $\langle 100 \rangle$ axis of a silicon crystal.

These results show that, at $\psi = 0.8\psi_c$, the quantum and classical cross sections coincide over a considerable region of scattering angles; modest oscillations of the quantum-scattering cross section about the values of the classical-scattering cross section in the region of small scattering angles are caused by diffraction effects in particle scattering on the localized string potential.

At $\psi = 0.2\psi_c$, the classical cross section increases monotonically with increasing scattering angle. Here, the quantum cross section develops sizable oscillations about the values of the classical cross section over the whole region of scattering angles. The oscillations are caused by a significant contribution to the scattering cross section (3) from terms associated with small values of the quantum number l. These oscillations are similar to those that occur in the generalized Ramsauer–Townsend effect for slow-electron scattering on atoms at large angles [3, 4].

Figure 3 displays the total cross section for the scattering of 10-MeV electrons on an atomic string of the silicon crystal [see Eq. (5)] as a function of the angle of particle incidence on the string. Here, the quantity $G = (2RL\psi)^{-1}\sigma_{tot}$ is plotted along the ordinate. Our results demonstrate that the total cross section has a rather complicated structure in the region of small angles ψ. In the region of large values of ψ ($\psi \geq \psi_c$), the total cross section decreases smoothly with increasing ψ. In the region of small ψ, the cross section exhibits sharp variations. The reason for this is that the contributions of some terms drop out from the sum over l (5) when ψ decreases.

The total cross section is close to zero at $\psi \sim 0.04\psi_c$. This effect is analogous to the Ramsauer–Townsend effect, which consists in a significant decrease in the total cross section for slow-electron scattering on atoms in a certain region of particle energies (see [3] and references therein).

In conclusion, we note that the above special features of electron scattering on the string field are peculiar not only to the approximation of the string field in the form (6) but also to other approximations that fall off fast with increasing distance.

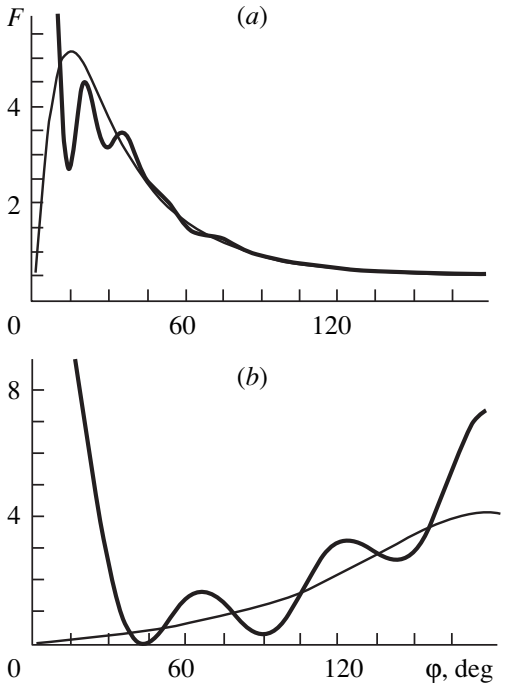

Fig. 2. Differential cross sections for the scattering of 10-MeV electrons incident on an atomic string of a silicon crystal at angles of $\psi = (a)\ 0.8\psi_c$ and $(b)\ 0.2\psi_c$ with respect to the $\langle 100 \rangle$ axis. The values of $F = (La\psi)^{-1}\dfrac{d\sigma}{d\varphi}$ are plotted along the ordinate. The thin and the thick curve represent the results of the calculations by formulas (2) (classical scattering) and (3) (quantum scattering), respectively.

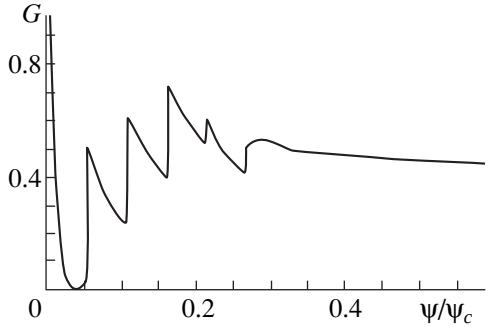

Fig. 3. Total cross section for the scattering of 10-MeV electrons on an atomic string of a silicon crystal as a function of the angle of incidence. The values of $G = (2RL\psi)^{-1}\sigma_{tot}$ and of ψ/ψ_c are plotted along the ordinate and the abscissa, respectively.

ACKNOWLEDGMENTS

This work was supported in part by the Ukrainian Foundation for Basic Research, by the International

Science and Educational Program of Ukraine (project Landau–Pomeranchuk–Migdal effect and QSU 082231), and by the Russian Foundation for Basic Research (project no. 98-02-16160).

REFERENCES

1. A. I. Akhiezer and N. F. Shul'ga, *High-Energy Electrodynamics in Matter* (Nauka, Moscow, 1993).
2. Yu. N. Demkov and J. Los, Phys. Lett. A **46**, 13 (1974).
3. N. F. Mott and H. S. W. Massey, *The Theory of Atomic Collisions* (Clarendon, Oxford, 1965; Mir, Moscow, 1969).
4. William F. Egelhoff, Jr., Phys. Rev. Lett. **71**, 2883 (1993).
5. J. Lindhard, Usp. Fiz. Nauk **99**, 249 (1969).
6. D. S. Gemmell, Rev. Mod. Phys. **46**, 129 (1974).
7. I. A. Golovchenko, Phys. Rev. B **13**, 4672 (1976).
8. F. M. Morse, Rev. Mod. Phys. **4**, 577 (1932).

Translated by E. Kozlovskiĭ

Physics of Atomic Nuclei, Vol. 63, No. 11, 2000, pp. 2025–2028. Translated from Yadernaya Fizika, Vol. 63, No. 11, 2000, pp. 2119–2122.

XXIX INTERNATIONAL CONFERENCE ON THE PHYSICS OF CHARGED-PARTICLE INTERACTION WITH CRYSTALS

Simulating the Spectrum and the Polarization Characteristics of Coherent Radiation from Ultrarelativistic Electrons in a Diamond Crystal

V. I. Truten'

National Research Center Kharkov Institute for Physics and Technology, ul. Akademicheskaya 1, Kharkov, 310108 Ukraine

Received December 10, 1999; in final form, February 11, 2000

Abstract—On the basis of a computer simulation, it is shown that, in the spectrum of radiation from ultrarelativistic electrons in oriented crystals, new maxima can appear in the low-frequency region in addition to ordinary coherent maxima. This effect is due to the influence of high-index planes on the radiation in question. The aforementioned new maxima manifest themselves not only in the spectrum but also in the polarization characteristics of the radiation. *© 2000 MAIK "Nauka/Interperiodica".*

1. INTRODUCTION

Relativistic electrons moving in a crystal at a small angle to one of the crystal planes closely packed with atoms can induce coherent and interference phenomena in their radiation. Owing to these effects, the radiation spectrum exhibits sharp peaks at which the radiation is characterized by a high intensity and by a polarization [1–5]. With increasing particle energy, the positions of those peaks are shifted fast toward the high-frequency region. From an energy value of about 100 GeV, the coherent maxima are localized in the region where photon energies are close to the energy of radiating electrons [6–8].

It was indicated in [9] that, for specific orientations of the crystal axes and planes, the spectrum of coherent radiation from ultrarelativistic electrons exhibits, in addition to ordinary peaks, some new peaks in the low-frequency region. The intensity and polarization of the radiation at these new peaks are close to those at the ordinary peaks. The origin of these peaks is associated with the influence of the weakly packed crystal planes on coherent radiation.

This result was obtained in the approximation of a nearly straight electron trajectory in a crystal. However, the motion of a particle in a crystal can have a rather complicated character. In particular, it can be either regular or chaotic in the periodic field of a crystal lattice. Therefore, there arises the problem of whether these peaks can indeed arise under the conditions of actual particle dynamics in a crystal. In the present article, this problem is considered on the basis of a simulation of coherent radiation from relativistic electrons in a crystal.

From the results of this simulation, it follows that the actual dynamics of electron motion does not destroy coherent peaks induced by the effect of weakly packed crystal planes.

Among other things, these results demonstrate that the new peaks in the coherent-radiation spectrum can be observed not only at ultrahigh energies but also at particle energies of about 1 GeV.

2. SPECIAL FEATURES OF COHERENT RADIATION FROM ULTRARELATIVISTIC ELECTRONS MOVING NEAR CRYSTAL PLANES

Basic results of the theory of coherent radiation from relativistic electrons moving in a crystal were obtained in the first Born approximation [1, 4, 5]. However, the conditions of its applicability are soon violated as the energy ε of the radiating particle is increased or as the angles of its incidence with respect to the crystal axes and planes—ψ and θ, respectively—are decreased [8, 10]. At the same time, the radiation from a particle moving in a crystal can be described in the semiclassical approximation over a broad range of energies ε and of angles ψ and θ. In the semiclassical approximation, the cross section for this radiation can be expressed in terms of the classical trajectory of the radiating particle. If, within the coherence length, the trajectory in question is close to a straight line, the spectral density of coherent radiation in a crystal coincides with the corresponding result obtained in the Born approximation [5–8, 10] and is given by

$$\omega\frac{d\sigma}{d\omega} = \frac{2e^2\delta\varepsilon'}{m^2\Delta\varepsilon}\sum_{\mathbf{g}}|S(\mathbf{g})|^2\frac{\mathbf{g}_\perp^2}{g_\parallel^2} \times\left[1+\frac{\omega^2}{2\varepsilon\varepsilon'}-2\frac{\delta}{g_\parallel}\left(1-\frac{\delta}{g_\parallel}\right)\right]|U_\mathbf{g}|^2 e^{-\bar{u}^2\mathbf{g}^2}, \quad (1)$$

where ε and ε' are, respectively, the initial and the final energy of the radiating electron; m is the electron mass; $\omega = \varepsilon - \varepsilon'$ is the radiated-photon energy; $\delta = \omega m^2/2\varepsilon\varepsilon'$; Δ is the elementary-cell volume, $S(\mathbf{g})$ is the structural

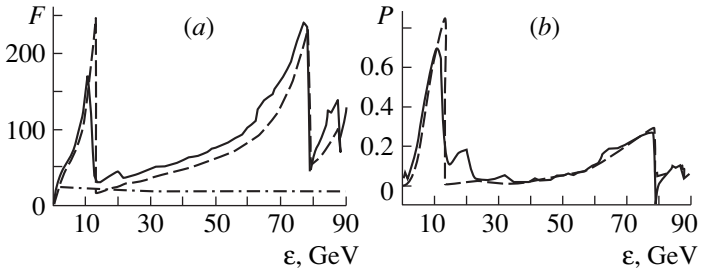

Fig. 1. (*a*) Spectrum and (*b*) polarization of coherent radiation from $\varepsilon = 100$ GeV electrons in a diamond crystal at $\psi = 2.5 \times 10^{-3}$ rad and $\alpha = 0.199$ (the values of $F = \frac{1}{nL\sigma_0}\frac{dE}{d\omega}$, where $\sigma_0 = Z^2e^6m^{-2}$, are plotted along the ordinate in Fig. 1*a*): (solid curves) results of our simulation, (dashed curves) results of the calculation according to (1), and (dash-dotted curve) results of the calculation according to the Bethe–Heitler formula.

factor; **g** is a reciprocal-lattice vector, $\mathbf{g}_\parallel$ and $\mathbf{g}_\perp$ being its components parallel and orthogonal to the initial-electron momentum **p**; $U_\mathbf{g}$ is the Fourier component of the potential of a single atom in a crystal; and $\overline{u^2}$ is the mean-square amplitude of lattice thermal vibrations. Summation in (1) is performed over vectors **g** that satisfy the condition $g_\parallel \geq \delta$. We use the system of units where $\hbar = c = 1$.

In the situation commonly considered within the theory of coherent radiation, an electron moves in a crystal at a small angle ψ with respect to one of the closely packed crystal axes (taken to be the *z* axis). The expressions for $g_\parallel$ and $\mathbf{g}_\perp$ can then be represented as

$$g_\parallel = g_z + \psi(g_y\cos\alpha + g_x\sin\alpha), \quad \mathbf{g}_\perp^2 = g_x^2 + g_y^2, \quad (2)$$

where α is the angle between the initial-electron-momentum component orthogonal to the *z* axis and the *y* axis.

When an electron traverses a crystal, there can arise the situation where it moves simultaneously at a small angle ψ with respect to the one of the crystal axes ($\psi \ll 1$) and at a small angle α with respect to the one of the crystal planes ($\alpha \ll 1$). This case is of particular interest since it will be shown below that, under such conditions, there exists a region of the angles ψ and α and of the energies ε where the coherent-radiation spectrum develops, in addition to conventional peaks, new peaks at which the intensity and the polarization of the radiation are rather high. These peaks in the coherent-radiation spectrum, which are induced by the effect of crystal planes whose order is higher than that of the plane near which the electron moves, are highly sensitive to small variations in the angle α.

In order to demonstrate this, we consider the coherent radiation from $\varepsilon = 100$ GeV electrons moving in a diamond crystal at an angle of $\psi = 2.5 \times 10^{-3}$ rad with respect to the $\langle 001\rangle$ axis, the angle α between the particle-momentum projection onto the (001) plane and the (110) crystallographic plane being $\alpha \approx 0.2$. The results of the calculations for (*a*) the spectrum and (*b*) the polarization of the coherent radiation from such electrons are depicted in Fig. 1 by dashed curves. An analysis of these results reveals that, in the case under consideration, in addition to ordinary coherent peaks in the frequency region $\omega \geq 0.8\varepsilon$, a new peak appears in the low-frequency region $\omega < 0.8\varepsilon$ and that this new peak is characterized by a high radiation intensity.

Let us now focus on some features of the radiation process that are responsible for the emergence of this maximum.

The main peak in the coherent-radiation spectrum at $\omega \sim 0.8\varepsilon$ is associated with the contribution to the radiation cross section from the reciprocal-lattice vector having the components $g_z = g_y = 0$ and $g_x = 4\pi\sqrt{2}/a$, where *a* is the lattice constant (the *x* and *y* axes are aligned with the $\langle 110\rangle$ and $\langle 1\bar{1}0\rangle$ crystallographic axes, respectively). This peak is due to the interference of the electromagnetic waves radiated by the electron in collisions with crystal planes parallel to the (110) plane.

The peak in the coherent-radiation spectrum at low frequencies is controlled by the contribution to the cross section from the vector **g** whose components are $g_z = 0$, $g_y = -4\pi\sqrt{2}/a$, and $g_x = 20\pi\sqrt{2}/a$. This peak emerges owing to the interference of the electromagnetic waves radiated by the electron in collisions with the crystal planes parallel to the (320) plane.

Under variations of about 0.02 in α, the low-frequency peak disappears, while the coherent-radiation peak at $\omega \sim 0.8\varepsilon$, which is dominant under the conditions being considered, remains virtually intact.

Thus, we can see that, in the case under consideration, a significant contribution to the radiation comes not only from the main crystallographic plane (110) but also from the rather "weak" (320) plane. Here, we are dealing with the situation where a particle moves in a crystal at small angles to two different crystallographic planes with the result that there arise two different peaks in the coherent-radiation spectrum, each being

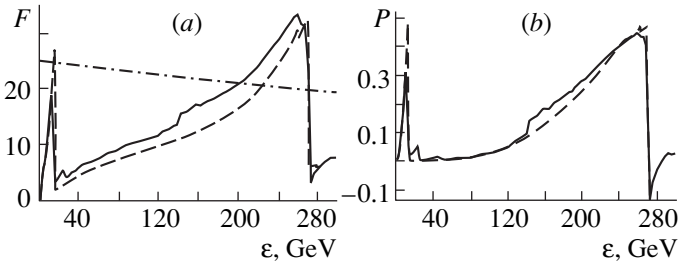

Fig. 2. As in Fig. 1, but for $\varepsilon = 1$ GeV and $\psi = 2.5 \times 10^{-2}$ rad.

characterized by a high intensity and by a high degree of the linear polarization of the radiation.

3. SIMULATING COHERENT RADIATION IN A CRYSTAL

The above results were obtained within the dipole approximation of the quantum theory of radiation. Moreover, it was required that the particle trajectory in a crystal be close to a straight line. The last approximation soon becomes invalid as the angle of particle incidence on the crystal with respect to one of the crystallographic axes is decreased. Moreover, the motion of a particle in a crystal with respect to the atomic strings of the crystal, which are aligned with the z axis, may be either regular or chaotic. Further, the character of this motion can affect pronouncedly the interference properties of the coherent radiation from the particle. Since the particle trajectory in a crystal is rather complicated, a simulation of the motion and the radiation under the conditions of actual dynamics in the crystal is of particular importance.

Within the semiclassical approximation of QED, the spectral density of the radiation can be expressed in terms of the classical trajectory of the particle in a crystal. Provided that the conditions under which the radiation from a particle moving in a crystal can be considered in the dipole approximation are satisfied, the spectral density and the polarization of the coherent radiation, the quantities that are obtained by averaging the spectral density of the coherent radiation and the degree of its polarization over various particle trajectories, can be represented as

$$\left\langle \frac{dE}{d\omega} \right\rangle = \frac{e^2\omega}{4\pi}\frac{\varepsilon^2+\varepsilon'^2}{\varepsilon\varepsilon'}\int_\delta^\infty \frac{dq}{q^2}\left[1-2\frac{\delta}{q}\left(1-\frac{\delta}{q}\right)\frac{2\varepsilon\varepsilon'}{\varepsilon^2+\varepsilon'^2}\right] \times \langle |\mathbf{W}(q)|^2\rangle, \quad (3)$$

$$P = \frac{e^2\omega\delta^2}{2\pi}\int_\delta^\infty \frac{dq}{q^4}\langle \mathbf{W}_x^2(q) - \mathbf{W}_y{}^2(q)\rangle \times \left[\left\langle \frac{dE}{d\omega}\right\rangle + \left(\frac{dE}{d\omega}\right)_{\text{incoh}}\right]^{-1}, \quad (4)$$

where

$$\mathbf{W}(q) = \int_{-\infty}^{\infty} dt\, \dot{\mathbf{v}}_\perp(t) e^{iqt} \quad (5)$$

is the Fourier component of the transverse component of the particle acceleration, while $(dE/d\omega)_{\text{incoh}}$ is the spectral density of incoherent radiation. The recoil effect in radiation has been taken into consideration in (3)–(5).

We are interested in the radiation of frequencies that are less than or about the frequency corresponding to the first coherent peak in the radiation spectrum. In this region of frequencies, the condition $\omega \ll \varepsilon\varepsilon'\psi/m^2R$ (R is the screening radius) is satisfied, which enables us to represent $\mathbf{W}(q)$ in the form

$$\mathbf{W}(q) = \sum_n \vartheta_n e^{iqt_n}\mathbf{n}, \quad (6)$$

where ϑ_n is the scattering angle in the nth collision between the particle and the atomic string that is parallel to the z axis, while t_n is the time instant at which this collision occurs. The quantities ϑ_n and t_n can be found by solving the equation of motion for the electron in the field of the continuous potential of an atomic string in a crystal [5, 11].

Expressions (3)–(6) make it possible to develop a method for numerically simulating the motion of electrons in a crystal and the coherent radiation from them under the conditions ensuring either a regular or a chaotic pattern of particle motion. On the basis of this method, we can analyze the effect of the character of particle motion in a crystal on the interference properties of coherent radiation and, in particular, reveal the role of "weak" crystallographic planes in the coherent-radiation process.

Along with (*a*) the coherent-radiation spectrum and (*b*) the polarization degree both calculated according to (1), Fig. 1 displays the results of our simulation for the properties of radiation under the same conditions (solid curves). The simulation was performed for a diamond crystal of thickness $L \sim 50$ μm.

It can be seen that the results of the simulation comply well with the corresponding results obtained according to (1). This means that, in the case being con-

sidered, the actual dynamics of electrons in a crystal does not destroy the coherent peaks induced by the effect of "weak" crystallographic planes.

The effect considered here manifests itself at lower electron energies as well. Figure 2 displays the results of the simulation and of the calculations according to (1) for the spectral characteristics of the coherent radiation from $\varepsilon = 1$ GeV electrons at $\psi = 2.5 \times 10^{-2}$ rad and at the same value of α as before. In this case, the effect is not so pronounced: the radiation intensity at the coherent peaks is on the same order of magnitude as the incoherent-radiation intensity. As to the polarization of the radiation, it is quite sizable at either coherent peak.

Our results demonstrate that new peaks in the coherent radiation can appear not only at energies of $\varepsilon \sim 100$ GeV but also at much lower energies. In order to observe this effect experimentally, one needs electron beams of angular divergence $\Delta\theta$ not greater than $\psi\Delta\alpha$, where $\Delta\alpha$ is the interval of angles α where the peaks under consideration do exist.

ACKNOWLEDGMENTS

I am grateful to N.F. Shul'ga for a stimulating discussion on the problems considered here.

This work was supported in part by the Ukrainian State Foundation for Basic Research (project Landau–Pomeranchuck–Migdal effect).

REFERENCES

1. H. Uberall, Z. Naturforsch. A **17**, 332 (1960).
2. G. Diambrini, Rev. Mod. Phys. **40**, 611 (1968).
3. U. Timm, Fortschr. Phys. **17**, 765 (1971).
4. M. L. Ter-Mikaelian, *High-Energy Electromagnetic Processes in Condensed Media* (Wiley, New York, 1972; Akad. Nauk Arm. SSR, Yerevan, 1969).
5. A. I. Akhiezer and N. F. Shul'ga, *High-Energy Electrodynamics in Matter* (Nauka, Moscow, 1993).
6. H. Bilokon, G. Bologna, *et al.*, Nucl. Instrum. Methods **204**, 299 (1983).
7. V. N. Baĭer, V. M. Katkov, and V. M. Strakhovenko, *High-Energy Spectromagnetic Processes in Oriented Single Crystals* (Nauka, Novosibirsk, 1989).
8. A. I. Akhiezer, V. I. Truten', and N. F. Shul'ga, Nucl. Instrum. Methods Phys. Res. B **67**, 207 (1992).
9. N. F. Shul'ga, V. I. Truten', and V. V. Syshchenco, Phys. Lett. B **327**, 306 (1994).
10. A. I. Akhiezer, V. F. Boldyshev, and N. F. Shul'ga, Fiz. Élem. Chastits At. Yadra **10**, 52 (1979) [Sov. J. Part. Nucl. **10**, 19 (1979)].
11. A. I. Akhiezer, V. I. Truten', and N. F. Shul'ga, Phys. Rep. **203**, 289 (1991).

Translated by O. Chernavskaya

Physics of Atomic Nuclei, Vol. 63, No. 11, 2000, pp. 2029–2032. Translated from Yadernaya Fizika, Vol. 63, No. 11, 2000, pp. 2123–2126.

XXIX INTERNATIONAL CONFERENCE ON THE PHYSICS OF CHARGED-PARTICLE INTERACTION WITH CRYSTALS

Investigation of Resonance Diffractive Radiation from Relativistic Electrons in Conducting Periodic Targets

I. E. Vnukov, B. N. Kalinin, P. V. Karataev, G. A. Naumenko, A. P. Potylitsin, and O. V. Chefonov

Nuclear Physics Institute, Tomsk Polytechnic University, pr. Lenina 2a, Tomsk 50, 634050 Russia

Received December 10, 1999; in final form, February 11, 2000

Abstract—Optical resonance diffractive and transition radiation from 200-MeV electrons in conducting periodic targets with spaced strips are investigated experimentally at the Tomsk synchrotron. The orientation and spectral properties of the radiation are measured. © *2000 MAIK "Nauka/Interperiodica".*

Electromagnetic radiations stemming from a dynamical perturbation of atomic electron shells and free electrons by the electromagnetic field of a charged particle traveling in a medium (polarization radiation) include transition radiation, diffractive radiation, Cherenkov radiation, parametric x-ray radiation, and polarization bremsstrahlung. In contrast to all others, diffractive radiation arises when relativistic particles pass in close proximity to the target edge, at a distance of about $\gamma\lambda$, where γ is the particle Lorentz factor and λ is the wavelength of the emitted radiation. Interest in this type of radiation is associated with the possibility of using it for nondisturbing beam diagnostics [1] and with the possibility of generating monochromatic-radiation beams in the millimeter and submillimeter ranges [2].

In recent years, attention in theoretical studies has been focused on resonance diffractive radiation as a useful subject for experimental investigations [3–6]. At observation angles $\theta > \gamma^{-1}$, the formation length for diffractive radiation that is generated by ultrarelativistic particles ($\gamma \gg 1$) and which belongs to the optical wavelength range becomes sufficient for applying periodic targets in order to obtain monochromatic radiation and to increase its intensity [6]. Periodic targets (that is, gratings whose profile was obtained by periodically deforming a continuous surface) for diffractive-radiation generation were first employed to study the Smith–Purcell effect [7–9]. As was shown in [3], the use of a periodic structure formed by spaced narrow metal strips ($h \sim \gamma\lambda$) could increase considerably the intensity of the radiation being discussed.

The first experiment that studied millimeter diffractive radiation generated by a beam of relativistic electrons was performed in 1995 [10]. Optical diffractive radiation was first observed in the experiment reported in [11] and performed in a beam of 200-MeV electrons from the SIRIUS synchrotron. According to [12, 13], inverse transition radiation in the optical range shows a great promise for beam diagnostics. It can be hoped that beam diagnostics with periodic targets (see above) will extend the applicability range of the method, simultaneously reducing multiple particle scattering in the target to a considerable degree, since some initial particles will pass through the target gaps in this case.

The intensity of resonance diffractive radiation is given by [3]

$$\frac{d^2W}{d\omega d\Omega} = F_1F_2F_3,$$

where F_1 is the intensity of diffractive radiation from a semi-infinite plane; F_2 is a factor that takes into account interference from the different edges of a single target element; and F_3 is a factor that takes into account interference from the different target elements,

$$F_3 = \exp[(1-N)\alpha_0]\left\{\frac{\sin^2\left(\frac{N\phi_0}{2}\right) + \sinh^2\left(\frac{N\alpha_0}{2}\right)}{\sin^2\left(\frac{\phi_0}{2}\right) + \sinh^2\left(\frac{\alpha_0}{2}\right)}\right\}.$$

Here,

$$\alpha_0 = \left(\frac{2\pi d\sin\theta_0}{\gamma\beta\lambda}\right)\sqrt{(1+\gamma^2\theta_X^2)},$$

$$\phi_0 = \left(\frac{2\pi d}{\lambda}\right)\left[\cos(\theta_Y - \theta_0) - \frac{\cos\theta_0}{\beta}\right],$$

where θ_0 is the target-orientation angle, θ_X and θ_Y are the observation angles, d is the period of the target, λ is the radiation wavelength, and N is the number of grating periods.

At small grating-inclination angles such that $\alpha_0 \ll 1$, the radiation spectrum develops appreciable maxima caused by the periodicity of the target in the longitudinal direction. The condition under which there arises a resonance can be written as

$$\phi_0 = \left(\frac{2\pi d}{\lambda}\right)\left[\cos(\theta_Y - \theta_0) - \frac{\cos\theta_0}{\beta}\right],$$

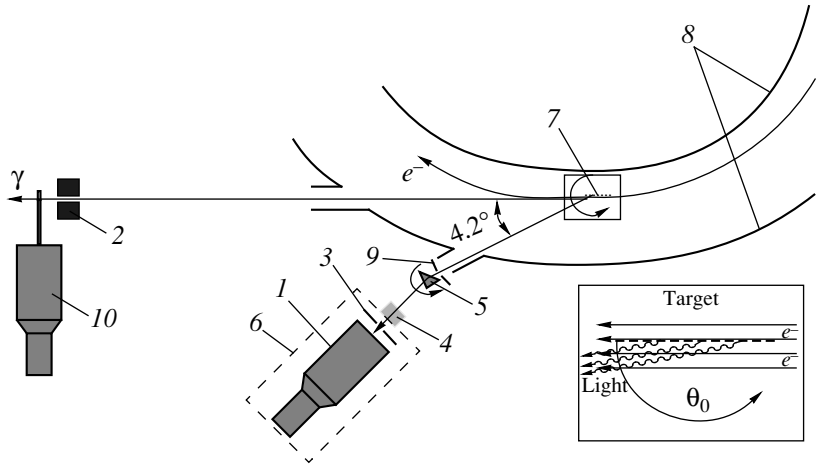

Fig. 1. Layout of the experimental setup: (*1*) phototube, (*2*, *3*, *9*) collimators, (*4*) mirror, (*5*) prism, (*6*) detection unit, (*7*) target, (*8*) accelerator chamber, and (*10*) scintillation counter.

where k is an integral number representing the order of diffraction. It can be expected that the above condition of the emergence of a resonance remains valid in the case where a relativistic particle traverses an inclined grating, irrespective of whether it passes through the grating gap or through a strip.

In 1998, Haberle *et al.* [14] studied experimentally resonance optical inverse transition radiation. Their measurements, which employed a continuous periodic target, were performed with electrons incident on the target at large angles, in which case the efficiency of the use of a resonance was reduced considerably.

In the experiments at the Tomsk synchrotron, orientation dependences and the spectra of resonance diffractive radiation from 200-MeV electrons were measured for planar aluminum targets having a thickness of 30 μm and forming gratings of period 0.2, 0.4, or 0.8 mm at an angle of 4.2° with respect to the direction of electron motion. The experiment was performed in the internal beam of the accelerator. In order to suppress the synchrotron-radiation contribution, a mode was implemented where the electron spill onto the target was short (about 10 μs). The beam spill was dumped at the stage of growth of the accelerator magnetic field. In this case, the pitch of the electron helix was 40 μm. The angular spread of the electron beam was σ_θ = 2.3 mrad. Figure 1 shows the layout of the experimental setup.

Accelerated electrons were dumped onto a periodic target (*7*) manufactured from polished aluminum and placed on a two-coordinate goniometer in the straight section of the accelerator.

An optical spectrometer recorded radiation generated by electrons at an angle of 4.2° with respect to the electron beam. The spectrometer was based on a collimator (*9*) and an optical prism (*5*), which expands the radiation under study in the energy spectrum. The expansion interval necessary for obtaining a frequency resolution of 10% was recorded by a detection system (*6*) that consisted of a phototube (*1*) and a collimator (*3*). The PMT-110 phototube with a sensitivity to light of 5.5×10^{-5} A/lm was used in the experiment. The spectral-sensitivity region of the photocathode in the phototube used was 300–900 nm. In order to reduce the background, the detection unit was removed from the plane of the electron-beam orbit by means of a mirror (*4*) and was arranged vertically.

The spectrum was scanned by rotating the prism. The frequency calibration of the spectrometer was performed by using calibrated photodiodes. Figure 2 shows the calibration curve. The spectral efficiency of the spectrometer was determined on the basis of the spectrum of transition radiation from a continuous target (see below).

A scintillation counter (*10*) was employed to monitor the measurement by bremsstrahlung. The beams of bremsstrahlung and of optical radiation were collimated to 1.5 and 1.05 mrad, respectively. (This was done with collimators *2* and *3*.)

Figure 3 shows the orientation dependence of the intensity of inverse transition radiation for a continuous target rotated about the vertical axis. The FWHM value, which was determined by the divergence of the electron beam, the angular aperture of the detector, and the intrinsic divergence of transition radiation, was $2.44\,\gamma^{-1}$. The maximum of the orientation dependence (at θ_0 = 2.1°) corresponds to the peak of the mirror reflection of transition radiation.

Figure 4 shows the spectrum of the inverse optical transition radiation according to measurements at the maximum of the orientation dependence. Such measurements are necessary for determining the efficiency of the spectrometric setup. From Fig. 4, it can be seen that the spectrum of inverse optical transition radiation is not a constant, in contradiction with theoretical predictions. The maximum transition-radiation yield lies

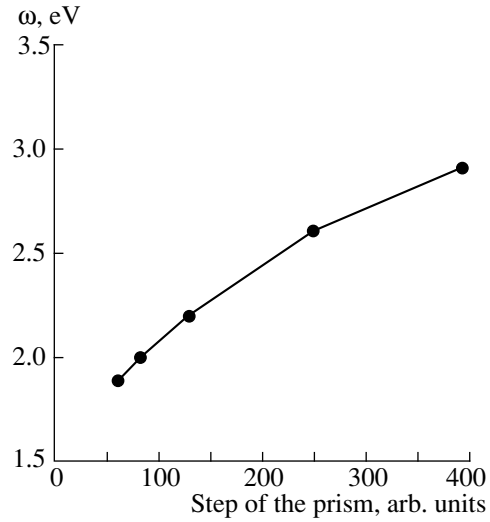

Fig. 2. Spectrometer-calibration curve.

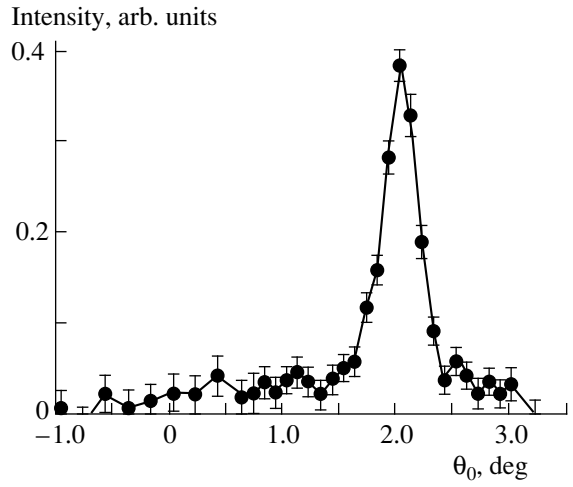

Fig. 3. Orientation dependence of the inverse-transition-radiation intensity for a rotating continuous target.

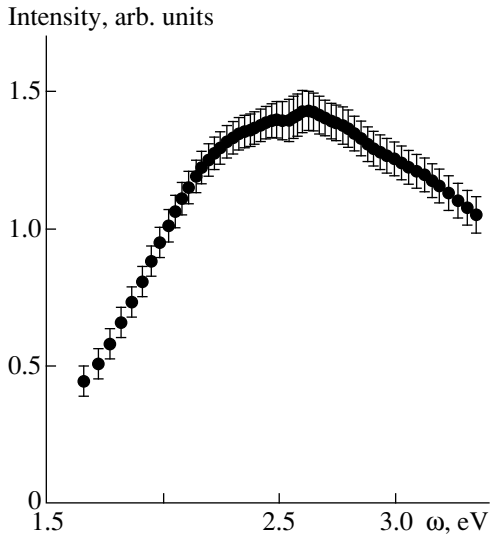

Fig. 4. Spectrum of inverse optical transition radiation for a continuous target oriented at the angle of $\theta_0 = 2.1°$.

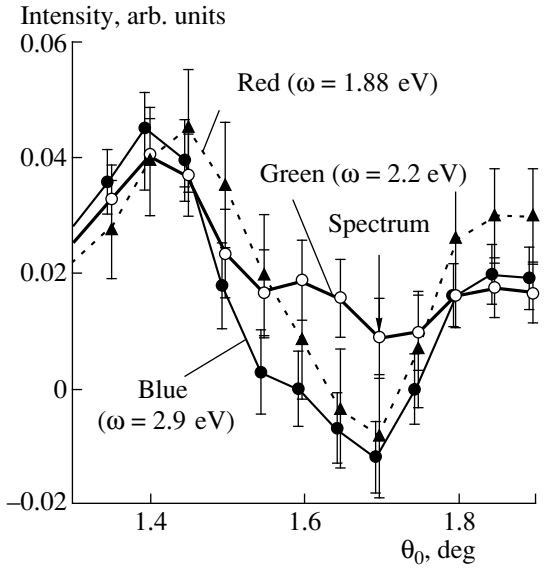

Fig. 5. Orientation dependence of the yield of optical resonance diffractive radiation for a periodic target of period 0.8 mm.

in the energy range between 2.2 and 3 eV; this is due to the special features of the photocathode in the phototube used and to the optical properties of the spectrometric channel.

The orientation dependence of the optical resonance diffractive radiation from electrons incident on a periodic target of period 0.8 mm is displayed in Fig. 5 for angles in the range between 1.3° and 1.9°. In analyzing this dependence, we can see that, for different wavelengths, the orientation curves behave somewhat differently, which is associated with the dynamical process of diffractive-radiation formation. The most pronounced distinction between the dependences on spectral and angular variables is observed at the orientation angle of $\theta_0 = 1.72°$. Figure 6 shows the optical-radiation spectrum for this orientation angle, the correction for the spectrometer efficiency being included. The maximum of the spectral distribution corresponds to the first order of resonance diffractive radiation, and its width is due primarily to grating defects (according to our estimates, the angular spread of the grating strips is $\sigma = 0.85°$).

The results of the present experimental studies can be summarized as follows:

(i) We have evolved an experimental setup for measuring the orientation and spectral properties of optical radiation from relativistic electrons.

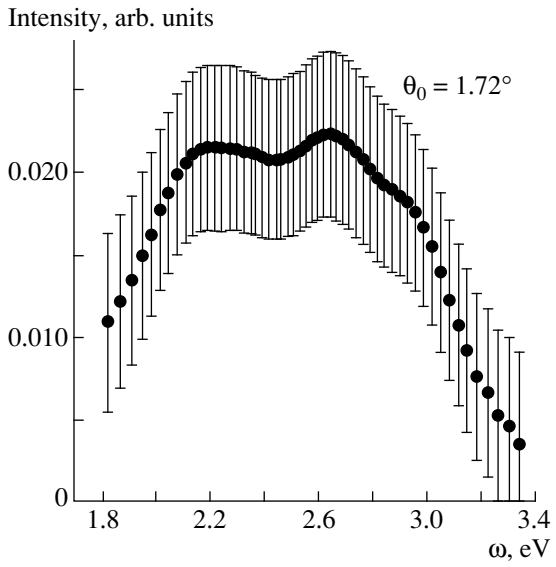

Fig. 6. Spectrum of optical resonance polarization radiation for a periodic target.

(ii) We have measured the orientation and spectral dependences of the optical resonance polarization radiation from 200-MeV electrons traversing a conducting target formed by spaced strips.

(iii) In order to ensure a correct comparison of experimental and theoretical results, future studies must be performed with targets characterized by a small scatter of strip orientations with respect to the grating plane.

ACKNOWLEDGMENTS

This work was supported in part by the Russian Foundation for Basic Research (project nos. 98-02-17994 and 99-02-16884).

REFERENCES

1. M. C. Lampel, Nucl. Instrum. Methods Phys. Res. A **385**, 19 (1997).
2. Y. Shibata, S. Hasebe, K. Ishi, *et al.*, Phys. Rev. E **57**, 1061 (1998).
3. A. P. Potylitsyn, Phys. Lett. A **238**, 112 (1998).
4. A. P. Potylitsyn, Nucl. Instrum. Methods Phys. Res. B **145**, 169 (1998).
5. A. P. Potylitsyn, Nucl. Instrum. Methods Phys. Res. B **145**, 60 (1998).
6. B. M. Bolotovskiĭ, Tr. Fiz. Inst. Akad. Nauk SSSR **140**, 95 (1982).
7. G. Doucas, J. H. Mulvey, M. Omori, *et al.*, Phys. Rev. Lett. **69**, 1761 (1992).
8. K. J. Woods, J. E. Walsh, R. E. Stoner, *et al.*, Phys. Rev. Lett. **74**, 3808 (1995).
9. K. Ishi, Y. Shibata, T. Takahashi, *et al.*, Phys. Rev. E **51**, R5212 (1995).
10. Y. Shibata, S. Hasebe, K. Ishi, *et al.*, Phys. Rev. E **52**, 6787 (1995).
11. I. E. Vnukov, B. N. Kalinin, G. A. Naumenko, *et al.*, Pis'ma Zh. Éksp. Teor. Fiz. **67**, 760 (1998) [JETP Lett. **67**, 802 (1998)].
12. X. K. Maruyama, M. J. Hellstrem, C. B. Reid, *et al.*, Nucl. Instrum. Methods Phys. Res. B **79**, 788 (1993).
13. R. B. Fiorito, D. W. Rule, *et al.*, Phys. Rev. E **51**, 2759 (1995).
14. O. Haberle, P. Henry, and P. Rullhusen, in *Proceedings of BEAMS'98, Haifa, Israel, June 7–12, 1998.*

Translated by E. Kozlovskiĭ

Physics of Atomic Nuclei, Vol. 63, No. 11, 2000, pp. 2033–2036. Translated from Yadernaya Fizika, Vol. 63, No. 11, 2000, pp. 2127–2130.

XXIX INTERNATIONAL CONFERENCE ON THE PHYSICS OF CHARGED-PARTICLE INTERACTION WITH CRYSTALS

Calculation of the Volume Polarization Field of a Relativistic Particle

V. A. Aleksandrov, A. S. Sabirov, and G. M. Filippov

Chuvash State University, Moskovskiĭ pr. 15, Cheboksary, 428015 Russia

Received December 10, 1999; in final form, February 11, 2000

Abstract—The polarization fields of a relativistic particle moving in a homogeneous medium are calculated. The results are illustrated by graphs that show the behavior of the electric and magnetic fields in the reference frame comoving with the particle. The behavior of the fields at large distances from the particle is analyzed. *© 2000 MAIK "Nauka/Interperiodica".*

1. INTRODUCTION

Polarization fields generated by a charged particle moving in a solid can significantly affect some processes accompanying the propagation of atomic or molecular ions, neutral atoms, and molecules through solid films. In particular, special features of high- and low-energy peaks and alignment of ions along the velocity direction in the Coulomb explosion of molecular ions (see, for example, [1, 2]) are usually explained by introducing the concept of the wake potential. The pattern of the energy losses of clusters formed by charged particles can also strongly depend on the wake potentials of each particle. There is every reason to believe that polarization fields are important in studying various phenomena associated with the motion of relativistic atoms, ions, or nuclei through solid-state targets [3].

Polarization fields (or wake potentials) were calculated by many authors within various models (see, for example, [4, 5]), so that some aspects of this problem have been clarified to a considerable extent. As to the polarization fields of relativistic particles, their general theory based on the formalism of dielectric functions has been known for a long time (see, for example, [6]). However, specific calculations of fields in the vicinity of a moving particle are incomplete [7]. It is well known that, in the laboratory frame, the electric field of a moving particle is distorted in such a way that the transverse components increase by a factor of γ, where γ is the Lorentz factor. In addition to the electric field, there arises a proper magnetic field, which increases with increasing particle velocity. In the reference frame comoving with the particle, there exists only an ordinary Coulomb field. When a particle moves in a medium, fast charges arise in any reference frame, producing a magnetic field. In the reference frame comoving with the particle, this is a purely polarization field. If the energy of the particle and, hence, its Lorentz factor, increase, we can expect that the transverse components of the fields will be significantly enhanced, irrespective of the reference frame where these fields are specified. The first specific calculations of the polarization fields in the comoving reference frame revealed that the electric polarization field increases with the Lorentz factor, but that, in the direction of the velocity vector, the longitudinal and the transverse dielectric function cause cancellation of the leading terms, which are proportional to γ. The field is stretched linearly in γ along the direction of motion, so that the deceleration force increases only in proportion to a logarithm of the Lorentz factor. We do not know any specific calculations of the magnetic polarization fields. In this article, we are going to fill this gap partly. The magnetic field formed in the vicinity of a relativistic particle can considerably exceed maximum fields obtained under laboratory conditions; therefore, they can significantly affect various polarization phenomena in clusters, fast atoms, and molecular ions.

2. POLARIZATION FIELDS OF RELATIVISTIC PARTICLES

In the reference frame comoving with a relativistic charged particle, its field must be static; therefore, it is sufficient to calculate the scalar potential and the magnetic field to characterize this field. From general considerations, it is clear that the magnetic field must be axisymmetric and must be directed, according to the corkscrew rule, along a circle whose center occurs on the symmetry axis. Specifically, it is given by (hereafter, we use the system of atomic units)

$$H_\varphi(\rho, z') = -\gamma^2 \frac{Zv}{\pi c}\int_{-\infty}^{\infty} dq_z \int_0^\infty dq_\perp \frac{q_\perp^2}{q_\perp^2 + k_z^2} e^{iq_z z'} J_1(q_\perp \rho) \times \left[\frac{1}{\varepsilon_l(\mathbf{k}, \omega)} - 1 - \frac{v^2}{c^2}\frac{k_z^2(\varepsilon_{tr}(\mathbf{k}, \omega) - 1)}{q_\perp^2 + k_z^2(1 - \varepsilon_{tr}(\mathbf{k}, \omega)v^2/c^2)}\right], \quad (1)$$

where $\varepsilon_l = (k, \omega)$ and $\varepsilon_{tr}(k, \omega)$ are, respectively, the longitudinal and the transverse permittivity of the

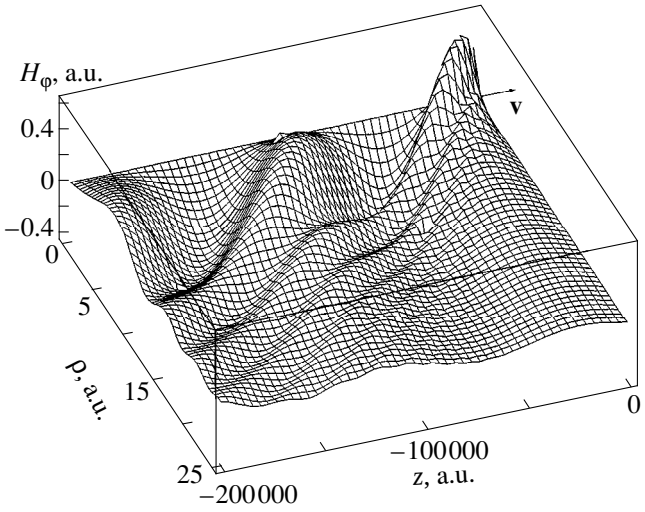

Fig. 1. Magnetic field H_φ in the vicinity of a particle in the reference frame comoving with it ($\gamma = 100$) as a function of the coordinates ρ and z. All quantities are measured in atomic units. A particle with charge $Z = 1$ moves in carbon ($r_S = 1.53$ a.u. is the average spacing between electrons in the electron gas of carbon).

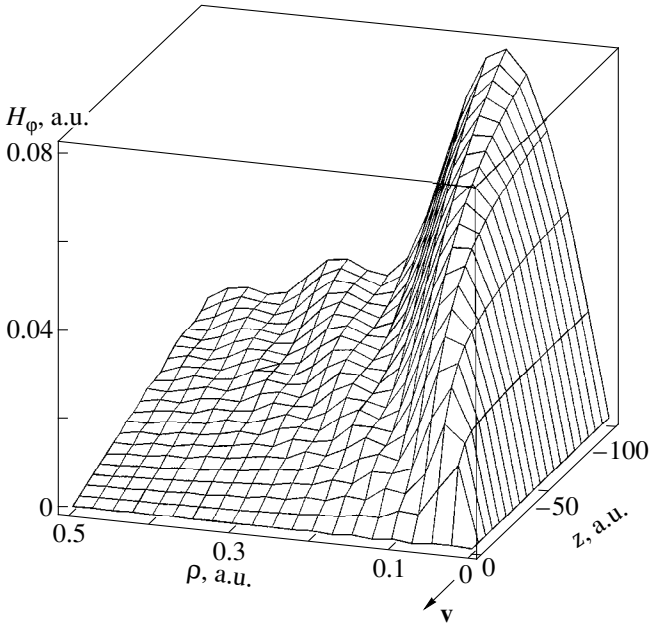

Fig. 2. As in Fig. 1, but in the nearest vicinity of the particle.

medium; $\omega = vk_z$; $\mathbf{q} = (q_\perp, q_z)$; $\mathbf{k} = (q_\perp, \gamma q_z)$; $z' = \gamma(z - vt)$; $\rho = \sqrt{x^2 + y^2}$; J_n is a Bessel function of nth order; Z is the charge of the particle; v is its velocity; the z axis is directed along the velocity; and c is the speed of light. In the reference frame comoving with the particle, the electric-field potential, which determines the electric field by the equality $\mathbf{E}_{\rm pol} = -\mathrm{grad}\,\Phi_{\rm pol}$, has the form

$$\Phi_{\rm pol}(\rho, z) = \gamma^2 \frac{Z}{\pi}\int\int \frac{q_\perp dq_\perp dq_z}{q_\perp^2 + k_z^2} J_0(q_\perp \rho) e^{iq_z z'} \times \left[\frac{1}{\varepsilon_l} - 1 - \frac{v^4}{c^4}\frac{q_\perp^2 k_z^2}{q^2}\frac{\varepsilon_{\rm tr} - 1}{q_\perp^2 + k_z^2(1 - \varepsilon_{\rm tr} v^2/c^2)}\right], \quad (2)$$

where the notation is identical to that in Eq. (1). Since the vector potential is independent of time in the comoving reference frame, it does not contribute to the electric field, which is therefore a purely potential field. The transverse and the longitudinal dielectric permittivity, which appear in Eqs. (1) and (2), can be calculated in some cases. By way of example, we indicate that, for a dense electron gas, they are described quite accurately by the Lindhard formulas [8]. For a solid-state target, the dielectric permittivities within the microscopic theory proposed in [9] take into account the excitations and polarizations of atomic cores. So far, the quantities in (1) and (2) have not been calculated for the cases being considered. Below, we make use of simplified model expressions for the dielectric functions such that (i) $\varepsilon_l(q, \omega), \varepsilon_{\rm tr}(q, \omega) \longrightarrow 1$ when $q \longrightarrow \infty$ or $\omega \longrightarrow \infty$; (ii) for $q \longrightarrow \infty$, the energies of longitudinal elementary excitations must tend to the free-electron energy; (iii) in the limit $q \longrightarrow 0$, the frequencies of the longitudinal and the transverse modes must coincide; and (iv) $q \longrightarrow \infty$, the energy of the transverse collective mode must tend to the free-photon energy.

The simplest form of the dielectric functions that satisfy conditions (i)–(iv) is

$$\varepsilon_l(q, \omega) = 1 - \frac{\omega_0^2}{\omega^2 + \omega_0^2 - \omega_q^2}; \quad \varepsilon_{\rm tr}(q, \omega) = 1 - \frac{\omega_0^2}{\omega^2}, \quad (3)$$

where ω_0 is the plasmon frequency and $\omega_q = \omega_0 + q^2/2$.

In this case, the expressions for the fields can be reduced to single integrals; for example, we have

$$H_\varphi = \frac{v}{c} Z \frac{\omega_0^2}{v^2}\int_0^\infty \frac{dq_\perp q_\perp^2 J_1(q_\perp \rho)}{q_\perp^2 + \omega_0^2/v^2} \times \left\{\frac{\exp(-|z|\sqrt{q_\perp^2 + \omega_0^2/c^2})}{\sqrt{q_\perp^2 + \omega_0^2/c^2}} + \gamma \Lambda(\rho, z, q_\perp)\right\},$$

where

$$\Lambda(\rho, z, q_\perp) = \frac{1}{v\sqrt{|q_\perp^2 + 2\omega_0 - v^2|}}\frac{1}{q_\perp^2 + 2\omega_0} \times \{\theta(q_\perp - \sqrt{v^2 - 2\omega_0}) e^{-|z|}\sqrt{q_\perp^2 + 2\omega_0 - v^2/\gamma} \times \left[(2v^2 - \omega_0)\sqrt{q_\perp^2 + 2\omega_0 - v^2}\sin\left(\frac{|z|v}{\gamma}\right) + v(2v^2 - q_\perp^2 - 3\omega_0)\cos\left(\frac{|z|v}{\gamma}\right)\right]$$

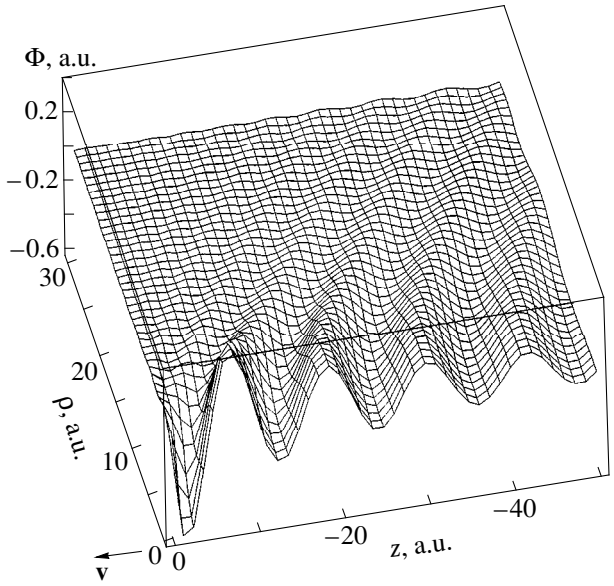

Fig. 3. Scalar potential of the polarization field in the vicinity of a nonrelativistic particle ($v = 2$ a.u. $\approx 4.39 \times 10^6$ m/s).

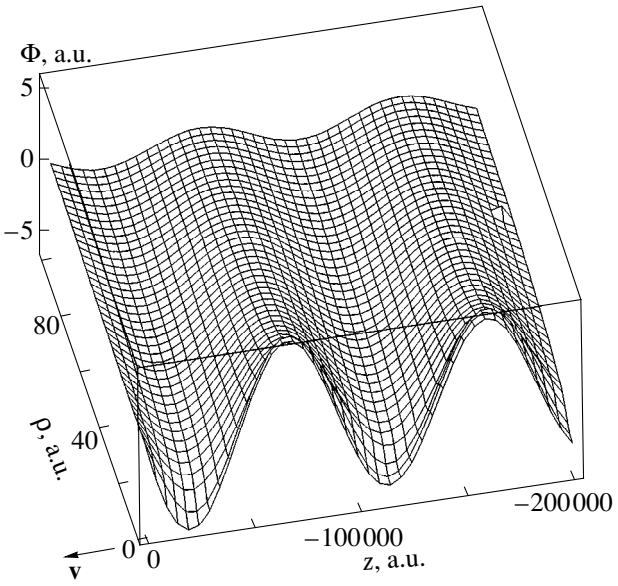

Fig. 4. As in Fig. 3, but for a relativistic ($\gamma = 100$) particle.

$$+\theta(\sqrt{v^2-2\omega_0}-q_\perp)[(2v^2-\omega_0)\sqrt{v^2-q_\perp^2-2\omega_0}$$
$$-\operatorname{sgn}(z)v(2v^2-q_\perp^2-3\omega_0)]$$
$$\times\sin\left(\frac{|z|}{\gamma}(v+\operatorname{sgn}(z)\sqrt{v^2-q_\perp^2-2\omega_0})\right)\Bigg\},$$

$\theta(\xi)$ is the Heaviside step function, and $v > \sqrt{2\omega_0}$. The scalar potential can reduced to the form

$$\Phi = -\gamma Z\frac{\omega_0^2}{v^2}\int_0^\infty \frac{dq_\perp q_\perp J_0(q_\perp\rho)}{q_\perp^2+\omega_0^2/v^2}\Lambda(\rho, z, q_\perp)$$
$$+Z\int_0^\infty dq_\perp J_0(q_\perp\rho)\left(-e^{-q_\perp|z|}+\frac{q_\perp^3\exp(-|z|\sqrt{q_\perp^2+\omega_0^2/c^2})}{(q_\perp^2+\omega_0^2/v^2)\sqrt{q_\perp^2+\omega_0^2/c^2}}\right).$$

Figures 1 and 2 display the functions $H_\varphi(\rho, z)$ for the motion of a proton in a carbon film. Figures 3 and 4 show the scalar potential whose gradient determines the polarization electric field in the reference frame comoving with the proton. At large distances from the particle, the peaks of wavelike field perturbations do not show a typical "retardation" at relativistic energies in relation to the nonrelativistic case (compare Fig. 3 at $v = 2$ and Fig. 4 at $\gamma = 100$). The reason for this is that, for $\gamma \gg 1$, the field propagates at large distances, where long-wave transverse and longitudinal excitations of arbitrarily large phase velocities are dominant. Physically, the particle brings the entire electron subsystem of a solid into synchronous motion in this case. If the behavior of the field at small distances is inspected more closely, a characteristic retardation of the field in relation to the particle can be observed for $\gamma \gg 1$ (see Fig. 5). In the chosen model, the exact expression for the force decelerating the particle has the form.

$$F_b = \frac{Z^2\omega_0^2}{v^2}\ln\left[\frac{\gamma^2[\sqrt{v^2(1-\omega_0/c^2)^2-2(\omega_0/\gamma^2)(1-\omega_0/2c^2)}+v(1-\omega_0/c^2)]^2}{2\omega_0(1-\omega_0/2c^2)}\right].$$

3. POLARIZATION FIELDS OF A MOVING ATOM

Expressions (1) and (2), which were obtained for a pointlike charge, can be generalized quite straightforwardly for a more complicated charge distribution. By way of example, we indicate that, for an atom where the electron density-distribution is steady-state and is characterized by the Fourier components $\rho_e(\mathbf{q})$, we arrive at

$$\Phi_{\text{pol}}(\mathbf{x}') = \frac{\gamma^2}{2\pi^2}\int\frac{d^3q}{q_\perp^2+k_z^2}e^{i\mathbf{q}\cdot\mathbf{x}'}(Z-\rho_e(\mathbf{q}))$$
$$\times\left[\frac{1}{\varepsilon_l}-1-\gamma^2\frac{v^4}{c^4}\frac{q_\perp^2q_z^2}{q^2}\frac{\varepsilon_{\text{tr}}-1}{q_\perp^2+k_z^2(1-\varepsilon_{\text{tr}}v^2/c^2)}\right], \quad (4)$$

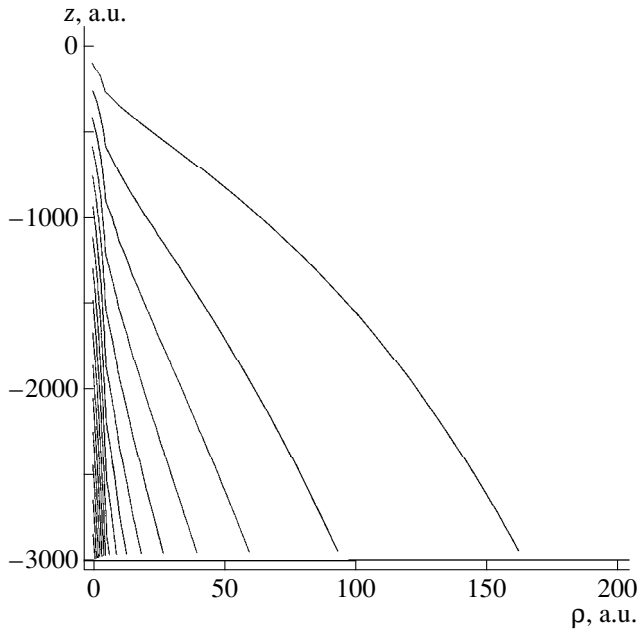

Fig. 5. Contour plot of the scalar potential at small distances from a relativistic particle ($\gamma = 100$).

$$\mathbf{H}(\mathbf{x}') = -i\gamma^2\frac{1}{2\pi^2 c}\int\frac{d^3q}{q_\perp^2 + k_z^2}e^{i\mathbf{q}\cdot\mathbf{x}'}[\mathbf{q}\times\mathbf{v}](Z-\rho_e(\mathbf{q})) \times\left[\frac{1}{\varepsilon_l} - 1 - \gamma^2\frac{v^2}{c^2}\frac{q_z^2(\varepsilon_{tr}-1)}{q_\perp^2 + k_z^2(1-\varepsilon_{tr}v^2/c^2)}\right]. \quad (5)$$

If $\rho_e(\mathbf{q})$ is axisymmetric with respect to the z axis, expressions (4) and (5) reduce to double integrals of the types in (1) and (2).

Expressions (4) and (5) do not involve the self-interaction of charges because the polarization fields express the effect of medium particles on external particles moving through a medium. In calculating the state of each electron in an atom, we must therefore take fully into account the fields given by (4) and (5). Because of the mutual screening of the charges involved, these fields are suppressed in relation to the case of the motion of an individual charge, but this is so only at large distances from an atom. At small distances, which correspond to large q, the polarization fields are not subject to strong screening and can significantly affect the states of atomic electrons. Therefore, estimates of these fields and their configurations are of considerable interest for experimentalists investigating the propagation of atomic particles through solid films.

Detailed calculations of fields for this case are now in progress.

REFERENCES

1. D. S. Gemmell, J. Remillieux, J.-C. Poizat, *et al.*, Phys. Rev. Lett. **34**, 1420 (1975).
2. M. P. Carpenter, R. W. Dunford, D. S. Gemmell, *et al.*, Phys. Rev. A **55**, 2090 (1997).
3. V. V. Okorokov, in *Proceedings of the XXVII International Conference on the Physics of Charged-Particle Interaction with Crystals* (Mosk. Gos. Univ., Moscow, 1997), p. 20.
4. P. M. Echenique, R. H. Ritchie, and W. Brandt, Phys. Rev. B **20**, 2567 (1979).
5. Y. Yamadzaki, in *Proceedings of the NATO Advanced Study Institute on the Interaction of Charged Particles with Solids and Surfaces, Alicante, Spain, 1990*, Ed. by A. Gras-Marti *et al.* (Plenum, New York, 1991; Vysshaya Shkola, Moscow, 1994).
6. L. D. Landau and E. M. Lifshitz, *Electrodynamics of Continuous Media* (Nauka, Moscow, 1982; Pergamon, New York, 1984).
7. Yu. V. Budnikov, A. S. Sabirov, and G. M. Filippov, Fiz. Tverd. Tela (Leningrad) **24**, 195 (1982) [Sov. Phys. Solid State **24**, 107 (1982)].
8. J. Lindhard, Mat. Fys. Medd. K. Dan. Vidensk. Selsk. **28** (8), 1 (1954).
9. V. A. Aleksandrov and G. M. Filippov, in *Proceedings of the XXI All-Union Conference on the Physics of Charged-Particle Interaction with Crystals* (Mosk. Gos. Univ., Moscow, 1992), p. 57.

Translated by M. Kobrinsky

Physics of Atomic Nuclei, Vol. 63, No. 11, 2000, pp. 2037–2040. Translated from Yadernaya Fizika, Vol. 63, No. 11, 2000, pp. 2131–2134.

XXIX INTERNATIONAL CONFERENCE ON THE PHYSICS OF CHARGED-PARTICLE INTERACTION WITH CRYSTALS

Transitions in an Atom Moving along a Metal Surface

V. A. Aleksandrov, A. S. Sabirov, and G. M. Filippov

Chuvash State University, Moskovskiĭ pr. 15, Cheboksary, 428015 Russia

Received December 10, 1999; in final form, February 11, 2000

Abstract—The probabilities of transitions in atoms moving along a metal surface are calculated. © *2000 MAIK "Nauka/Interperiodica".*

1. INTRODUCTION

Excitation and ionization that occur in an atom reflected from a metal surface and which are due to the surface polarization of a solid and to the generation of surface quasiparticles were considered in [1]. The experiments reported in [2] demonstrated that the state of an atom moving at a certain distance from a surface can undergo changes. In the present study, the probabilities of transitions in an atom that are induced by its interaction with surface modes are theoretically estimated for the case where the atom moves near the surface without coming into contact with it. In particular, we consider in detail the case where the direction of motion is parallel to the surface. Our calculation in the first and in the second order of perturbation theory revealed that, upon moving along metal surface for a short time interval, a hydrogen atom undergoes a transition from the 2*s* state to the 2*p* state, the transition probability being sufficient for detecting the resulting radiation. We believe that the experimental results reported in [2] (so-called Sokolov effect) can be explained on this basis.

2. BRIEF REVIEW OF RELEVANT THEORY

Surface electromagnetic fields that arise owing to the generation of surface plasmons or to the polarization of their vacuum play a substantial role in various surface phenomena. The theory of surface plasmons (more precisely, plasmon-polaritons) was reviewed in detail elsewhere [3, 4]. In the present study, we focus on the excitation of an atom moving along a metal surface. Let H_{int} be the Hamiltonian of atom interaction with the field of surface plasmons, and let the atom be initially in the ϕ_{2s} state characterized by zero total angular momentum. The state of the atom at an arbitrary instant of time can be roughly treated as a coherent mixture of the 2*s* and 2*p* states whose angular momenta are 0 and 1, respectively,

$$\Psi = (\alpha\phi_{2s} + \beta\phi_{2p}e^{-i\Delta Et})e^{-i\varepsilon_2 t}. \quad (1)$$

Here, ΔE is the Lamb shift, while ε_2 is the energy of the excited state of the hydrogen atom. In the two-state approximation considered here, the time-dependent coefficients in the expansion in Eq. (1) satisfy the set of equations

$$i\dot{\alpha} = (H_{\text{int}})_{sp}\beta, \quad i\dot{\beta} = (H_{\text{int}})_{ps}\alpha. \quad (2)$$

Solving the set of Eqs. (2), we find that the coefficients α and β depend periodically on time. This result can be treated as a special case of so-called quantum beating. Another type of quantum beating was observed in the experiments that were reported in [2] and which employed a beam of hydrogen atoms in state (1) with $|\alpha| \gg |\beta|$. Once the atoms had traveled a distance L in a vacuum, the beam was transmitted through a facility that changed the number of 2*p* atoms owing to the transitions of a small fraction of 2*s* atoms. As a result, there arose a coherent mixture including two groups of the 2*p* atoms shifted in phase by the constant $\Delta EL/v$. If the amplitude of the 2*p* atoms in the initial beam was equal to β and if the amplitude of the second group of such atoms is β', the experimentally observed intensity of the leading line in the Lyman series is proportional to

$$I = |\beta|^2 + |\beta'|^2 + 2|\beta\beta'|\cos(\Delta EL/v + \arg(\beta^*\beta')). \quad (3)$$

The resulting beats are due to the Lamb shift. The contrast of the relevant interference pattern is determined by the ratio

$$\eta = \frac{I_{\max} - I_{\min}}{\bar{I}} = 4\frac{|\beta\beta'|}{|\beta|^2 + |\beta'|^2}. \quad (4)$$

3. CALCULATION OF THE TRANSITION PROBABILITY

We now proceed to calculate the probabilities of the transitions from the 2*s* state to the 2*p* state in a hydrogen atom moving along the surface, assuming that these transitions are due to atom interaction with the fields of surface electromagnetic excitations. We will consider first-order processes in which the atomic transition is accompanied by the generation of a surface plasmon, second-order processes involving a virtual surface plasmon, and processes caused by the nonuniformity of the surface polarization fields of the atom.

1063-7788/00/6311-2037$20.00

We assume that the atom moves along an infinite planar metal surface at a distance a from it and the field of surface plasmons is switched on abruptly at the instant $t = 0$. This formulation of the problem simulates the experimental situation where the atoms fly above the restricted surface region.

The Hamiltonian of atom interaction with the field of surface plasmons can be represented as

$$\hat{H}_{\text{int}} = \int [\delta(\mathbf{x} - \mathbf{x}_0(t)) - \hat{\rho}_e(\mathbf{x}, t)]\hat{\varphi}_s(\mathbf{x}, t)d^3\mathbf{x},$$

where the operator of the potential of the surface-plasmon field has the form

$$\hat{\varphi}_s(\mathbf{x}, t) = \sum_{\mathbf{q}_\parallel} g_{\mathbf{q}_\parallel} e^{-q_\parallel |z|}(\hat{s}_{\mathbf{q}_\parallel} e^{i\mathbf{q}_\parallel \cdot \mathbf{r}} + \hat{s}^+_{\mathbf{q}_\parallel} e^{-i\mathbf{q}_\parallel \cdot \mathbf{r}}).$$

Here, $\mathbf{x} = \{\mathbf{r}, z\}$, $\mathbf{x}_0(t) = \mathbf{a} + \mathbf{v}t$ is the equation of the trajectory of an atom moving along the metal surface $z = 0$ at a distance a, $\mathbf{q}_\parallel$ is the plasmon momentum parallel to the surface, and $g_{\mathbf{q}_\parallel}$ is the coupling constant. The z axis, which is orthogonal to the surface, is directed from the metal to the vacuum; the velocity $\mathbf{v}$ is parallel to the y axis; and the x axis is chosen to be the axis of angular-momentum quantization (Fig. 1).

In the first order of perturbation theory, the probability of the $2s \longrightarrow 2p$ transition has the form

$$W_m^{(1)} = \sum_{\mathbf{q}_\parallel} g_{\mathbf{q}_\parallel}^2 \left| \int_0^t dt' \int_{-\infty}^{\infty} \frac{dq_z}{2\pi} \frac{2q_\parallel}{q_\parallel^2 + q_z^2} e^{i(\omega_s + \omega_{fi})t' - i\mathbf{q} \cdot \mathbf{x}_0(t')} (\delta_{fi} - \langle \varphi_{21m} | e^{i\mathbf{q} \cdot \mathbf{r}} | \varphi_{200} \rangle) \right|^2, \quad (5)$$

where φ_{200} and φ_{21m} are the wave functions of, respectively, the $2s$ and the $2p$ state of the hydrogen atom; ω_s is the surface-plasmon energy; and $\omega_{fi} = \varepsilon_{2p} - \varepsilon_{2s} = \Delta E$.

At large times t, the transition probability decreases asymptotically with increasing atom-to-surface distance in inverse proportion to the distance cubed:

$$\begin{bmatrix} W_0^{(1)}(t) \\ W_{\pm 1}^{(1)}(t) \end{bmatrix} = \frac{9}{16\omega_s a^3} \begin{bmatrix} 2 \\ 3 \end{bmatrix}. \quad (6)$$

In the second order of perturbation theory, the transition of the hydrogen atom from the $2s$ state to the $2p$ state is accompanied by the excitation of a virtual plasmon, which is then absorbed. The probability of this process is given by

$$W^{(2)}(t) = \left| \sum_{n, \mathbf{q}_\parallel} g_{\mathbf{q}_\parallel}^2 \int_0^t dt_1 \int_0^{t_1} dt_2 e^{-i\omega_s(t_1 - t_2)} \int_{-\infty}^{\infty} \frac{dq_z}{2\pi} \frac{2q_\parallel}{q_\parallel^2 + q_z^2} A_{fn}(\mathbf{q}, t_1) \int_{-\infty}^{\infty} \frac{dq_z'}{2\pi} \frac{2q_\parallel}{q_\parallel^2 + q_z'^2} A_{ni}(-\mathbf{q}', t_2) \right|^2, \quad (7)$$

where $A_{fi}(\mathbf{q}, t) = e^{i\omega_{fi}t + i\mathbf{q} \cdot \mathbf{x}_0(t)}(\delta_{fi} - \langle f | e^{-i\mathbf{q} \cdot \mathbf{x}} | i \rangle)$ and $\mathbf{q}' = (\mathbf{q}_\parallel, q_z')$.

The following circumstances are of importance in calculating the probability by formulas (5) and (7): (i) Since the Lamb shift is small, the probability approaches slowly a steady-state regime. (ii) If the velocity of the atom is less than the minimum phase velocity of surface plasmons (as was the case in the experiment reported in [2]), the plasmons are not excited, in which case the probabilities of first-order processes asymptotically tend to constant values for $t \longrightarrow \infty$; at the same time, the probabilities of second-order processes involving a virtual surface plasmon increase in proportion to t at large times. (iii) At small values of t, when the steady-state regime has not yet been established, the relevant probabilities may be nonlinear functions of time. (iv) Formulas (5) and (7) were derived under the assumption that the atom undergoes a transition from the $2s$ state to the $2p$ state; when the population of the $2p$ state becomes commensurate with the population of the $2s$ state, the inverse transitions begin to occur. In this case, quantum beats between the $2s$ and $2p$ states arise, their frequency being dependent on the distance a. For this reason, expressions (5) and (7) can be treated as the probabilities of the corresponding transitions only in the case where $W^{(1)}$ and $W^{(2)}$ are much less than unity. If $W^{(1)}$ or $W^{(2)}$ are about or greater than unity, the probability that the atom is in the $2p$ state is on the order of unity in accordance with the relevant solutions to equations of the type in (2).

Numerical estimates reveal that, for $a \leq q_c^{-1}$, where q_c is the endpoint momentum of the surface plasmon, a dominant contribution to the transition probability comes from the intermediate state $n = |100\rangle$. However, this contribution is exponentially suppressed in the region $a \gg q_c^{-1}$, where the intermediate state $n = |210\rangle$ makes a dominant contribution, which decreases in proportion to a^{-8} for $a \longrightarrow \infty$. For this reason, the probability $W^{(2)}$ was calculated by taking into account both the intermediate state $|100\rangle$ and the intermediate state $|210\rangle$. According to our estimates, other intermediate

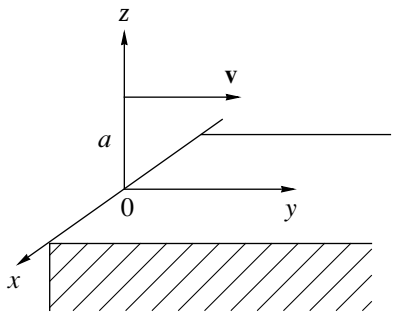

Fig. 1. Geometry of the motion of an atom over the metal surface.

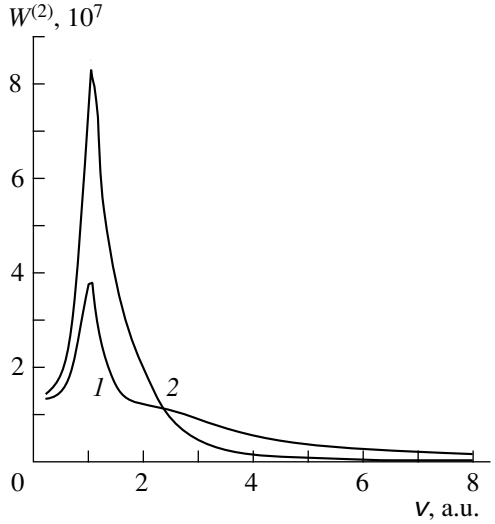

Fig. 2. Probabilities $W^{(2)}$ of second-order transitions to the (*1*) $|21-1\rangle$ and (*2*) $|211\rangle$ states of a hydrogen atom moving along a gold surface at the distance of $a = 1$ a.u. for the time $t = 10^6$ a.u. versus the atom velocity. The first-order contribution is negligibly small here.

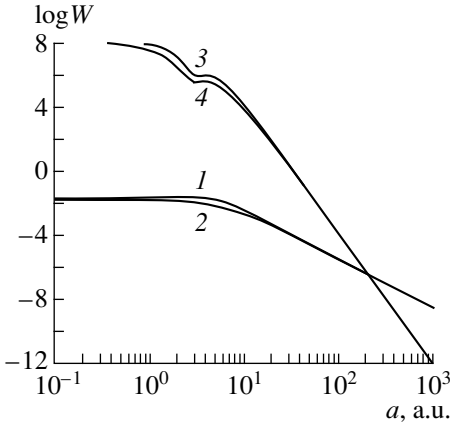

Fig. 3. (*1*, *2*) Probabilities $W^{(1)}$ of first-order transitions to, respectively, the $|211\rangle$ and the $|21-1\rangle$ state of a hydrogen atom moving along a gold surface at the velocity of $v = 1$ a.u. for the time $t = 10^6$ a.u. and (*3*, *4*) probabilities $W^{(2)}$ of second-order transitions to the same states versus the distance from the surface.

states yield small corrections to the contributions of these two states under the conditions prevalent in the experiment reported in [2]. In the second order, the probability was calculated as the squared modulus of the sum of the contributions to the total transition amplitude from all included intermediate states. The transition probabilities calculated in the second order of perturbation theory are displayed in Fig. 2 versus the atom velocity at a fixed distance from the surface. The peak position corresponds to the velocity value of $(\varepsilon_{2p} - \varepsilon_{1s} + \omega_s)/q_c$. The transition probabilities calculated in the first and in the second order of perturbation theory are shown in Fig. 3 versus the atom-to-surface distance for two final states $|21 \pm 1\rangle$. It can be seen from this figure that the probabilities $W^{(1)}$ and $W^{(2)}$ are much less than unity for $a > 30$ a.u. Near the surface, the probability $W^{(2)}$ may take large values, depending on the duration of the motion of the atom over the metal surface. Typical time dependences of the probabilities $W^{(1)}$ and $W^{(2)}$ are given by the following estimates: (i) $W^{(2)} \sim t^2$ for $1 \ll t \ll 1/\Delta E$; (ii) $W^{(2)} \sim t$ for $t \gg 1/\Delta E$; and (iii) $W^{(1)} \sim t^2$ for $t \longrightarrow 0$ and attains fast (within $t \sim 10^2$–10^4 a.u.) a constant value for $v < v_{cr}$, where v_{cr} was estimated here at about 1.5 a.u. (which is less than the atom velocity of about 0.94 a.u. in Sokolov's experiments).

4. DISCUSSION

Our calculations have demonstrated that, owing to the interaction with electromagnetic surface modes of a solid, an atom moving near it can undergo transitions from one state to another without directly colliding with surface atoms. Thus, the phenomenon being considered is of a collective origin. Since the surface polarization field exists in a vacuum at distances from the surface that are much greater than atomic dimensions, the probability of first-order transitions decreases with increasing distance from the surface in inverse proportion to the distance cubed, in contrast to what is known for collisions between neutral atoms, where this decrease is exponential (see, for example, [5]). In the second order, the contributions of some intermediate states decrease exponentially with increasing a, whereas others exhibit a power-law dependence.

According to our estimates, the integrated probability of the transition of beam atoms from the 2*s* state to the 2*p* state is about 10^{-3} under actual experimental conditions, which is sufficient for detecting the effect via the observation of the resulting dipole radiation.

ACKNOWLEDGMENTS

We are grateful to A.F. Tulinov, who proposed the subject for this research.

REFERENCES

1. V. A. Aleksandrov and G. M. Filippov, Fiz. Khim. Obrab. Mater. **4**, 5 (1998).
2. B. B. Kadomtsev, *Dynamics and Information* (Usp. Fiz. Nauk, Moscow, 1997).
3. *Surface Polaritons*, Ed. by V. M. Agranovich and D. L. Mills (North-Holland, Amsterdam, 1982; Nauka, Moscow, 1985).
4. G. M. Filippov, Izv. Vyssh. Uchebn. Zaved., Fiz. **1**, 94 (1995).
5. V. A. Kvlividze and S. S. Krasil'nikov, *Introduction to the Physics of Atomic Collisions* (Mosk. Gos. Univ., Moscow, 1985).

Translated by R. Tyapaev

Physics of Atomic Nuclei, Vol. 63, No. 11, 2000, pp. 2041–2044. Translated from Yadernaya Fizika, Vol. 63, No. 11, 2000, pp. 2135–2138.

XXIX INTERNATIONAL CONFERENCE ON THE PHYSICS OF CHARGED-PARTICLE INTERACTION WITH CRYSTALS

Measurement of Spin Rotation in Particle Channeling as a Means for Experimentally Testing the Correctness of the Method for Deriving the Equation of Motion for a Spin

A. J. Silenko

Institute of Nuclear Problems, Belarussian State University, Minsk, Belarus

Received December 10, 1999

Abstract—Two alternative approaches to deriving the equation of motion for a spin are compared. It is shown that the conventional approach leads to the conclusion that the spin of a positron is rotated through a large angle as the result of planar positron channeling in a straight crystal. The quantum-mechanical approach based on the Foldy–Wouthuysen transformation predicts no spin rotation in this case. Experimental measurements can reliably discriminate between the two methods for deriving the equation of motion for a spin. © *2000 MAIK "Nauka/Interperiodica".*

1. INTRODUCTION

In the past few years, considerable advances have been made in measurements of spin rotation for polarized particles channeled through a bent crystal [1, 2]. Experiments of this type make it possible to determine the magnetic moments of short-lived particles [3]. In order to interpret correctly relevant experimental data, one needs detailed information about the motion of particle spins in the nonuniform field of crystals. In [1, 2], the motion of a spin was calculated on the basis of the Bargmann–Michel–Telegdi (BMT) equation [4]. A conventional method for deriving this equation relies on the assumption that the 4-velocity vector u^μ is orthogonal to the polarization 4-vector a^μ [4, 5],

$$u^\mu a_\mu = 0. \tag{1}$$

However, a generalization of this method to the case of a nonuniform field gives rise to terms in the equation of motion for a spin that are proportional to the first derivatives of the strengths of the electric and magnetic fields [6, 7]. Such terms appear in the respective quantum equations as well if these equations are derived by using relation (1) [8, 9]. The use of this relation as an auxiliary condition in deriving the quantum equation of motion for a spin can be avoided by going over to the Foldy–Wouthuysen representation. Since the polarization operator is known in this representation, the equation of motion for a spin can readily be derived by computing the commutator of the polarization operator and the Hamiltonian [10, 11].[1)] The resulting equation represents an exact quantum analog of the BMT equation, and it does not involve the first derivatives of the field strengths. There are no such derivatives in the equations from [11, 14] either, where they were obtained on the basis of classical electrodynamics without resort to the condition in (1). However, the equation from [11, 14] differs from the BMT equation even for a uniform field.

Of course, the theoretical concept based on the orthogonality of the velocity and polarization 4-vectors seems appealing, because it defines the polarization vector and, hence, the particle spin in quite a natural and simple way. However, there arises the question of whether this semiclassical model conforms to an exact quantum description.

It will be shown below that the two alternative approaches to describing particle polarization, which lead to qualitatively different types of motion of a spin in a nonuniform field, can be discriminated experimentally by studying spin motion in the planar channeling of ultrarelativistic particles in straight crystals.

We use here the system of units in which $\hbar = c = 1$.

2. EQUATION OF MOTION OF A SPIN IN A NONUNIFORM FIELD

By differentiating the orthogonality condition (1) for the velocity and polarization 4-vectors with respect to the proper time τ, we obtain a relation between the equation of motion of a particle and the equations of motion of its spin [5]:

$$a_\mu \frac{du^\mu}{d\tau} = -u_\mu \frac{da^\mu}{d\tau}. \tag{2}$$

The equation of motion of the particle involves terms proportional to the first derivatives of the field strengths. These terms are due to the drawing of a magnetic dipole into the domain of a stronger field or forcing it out of such a domain, depending on the orientation of the magnetic momentum. In accordance with Eqs. (1) and (2), this gives rise to terms involving the

[1)] The expressions for the Hamiltonian in the Foldy–Wouthuysen representation that were obtained in [10, 12, 13] are consistent.

1063-7788/00/6311-2041$20.00 © 2000 MAIK "Nauka/Interperiodica"

first derivatives of the field strengths in the equation of motion for a spin as well. For this reason, the equation of motion of a spin in a nonuniform electromagnetic field (Good–Nyborg equation [6, 7]) has the form

$$\frac{da^\mu}{d\tau} = 2\mu F^{\mu\nu}a_\nu - 2\mu' u^\mu F^{\nu\rho}u_\nu a_\rho - \frac{\mu}{m}u^\mu a^\rho a^\nu u^\lambda \frac{\partial G_{\nu\lambda}}{\partial x^\rho}, \quad (3)$$

which is dictated by the equation for motion of the particle and by the condition in (2). The notation used in Eq. (3) is the following: μ is the total magnetic moment; $\mu' = \mu - e/2m$ is the anomalous magnetic moment; $F^{\mu\nu} = (-\mathbf{E}, \mathbf{H})$ is the strength tensor of the electromagnetic field; $G^{\nu\lambda} = (-\mathbf{H}, -\mathbf{E})$ is its dual;

$$D^\mu = O^\mu_\nu \frac{\partial}{\partial x_\nu} = \frac{\partial}{\partial x_\mu} - u^\mu u_\nu \frac{\partial}{\partial x_\nu},$$
$$O^\mu_\nu = \delta^\mu_\nu - u^\mu u_\nu,$$

and δ^μ_ν is a Kronecker delta. The last term in (3) describes spin precession caused by the nonuniformity of the field. The respective equation for the polarization 3-vector $\boldsymbol{\xi}$ has the form [6]

$$\frac{d\boldsymbol{\xi}}{dt} = \left(\frac{e}{\epsilon} + 2\mu'\right)[\boldsymbol{\xi}\times\mathbf{H}] + \frac{2\mu'\epsilon}{\epsilon + m}(\mathbf{v}\times\mathbf{H})\cdot[\mathbf{v}\times\boldsymbol{\xi}] + \left(\frac{e}{\epsilon + m} + 2\mu'\right)[\boldsymbol{\xi}\times[\mathbf{E}\times\mathbf{v}]] + \frac{\mu\epsilon}{m(\epsilon + m)}[\boldsymbol{\xi}\times[\mathbf{v}\times\nabla]]\left\{(\boldsymbol{\xi}\cdot[\mathbf{E}\times\mathbf{v}]) + (\boldsymbol{\xi}\cdot\mathbf{H}) - \frac{\epsilon}{\epsilon + m}(\boldsymbol{\xi}\cdot\mathbf{v})(\mathbf{v}\cdot\mathbf{H})\right\}. \quad (4)$$

Thus, the conventional method for deriving the equation of motion for a spin on the basis of condition (1) leads to Eq. (4), which involves the first derivatives of the field strengths. In the case of a uniform field, Eq. (4) reduces to the BMT equation. In contrast to Eq. (4), the quantum equation of motion for a spin as derived with the aid of the Foldy–Wouthuysen representation does not involve terms with the first derivatives of the field strengths other than those appearing in the BMT equation. In the semiclassical approximation, it has the form [11]

$$\frac{d\boldsymbol{\xi}}{dt} = \left(\frac{e}{\epsilon} + 2\mu'\right)[\boldsymbol{\xi}\times\mathbf{H}] + \frac{2\mu'\epsilon}{\epsilon + m}(\mathbf{v}\cdot\mathbf{H})[\mathbf{v}\times\boldsymbol{\xi}] + \left(\frac{e}{\epsilon + m} + 2\mu'\right)[\boldsymbol{\xi}\times[\mathbf{E}\times\mathbf{v}]]. \quad (5)$$

Equation (5) differs both from Eq. (4) and from the quantum equations of motion for a spin that were derived in [8, 9] with the aid of condition (1).

As to the equation derived in [11, 14] within classical electrodynamics without resort to condition (1), what is of importance here is that it is inconsistent with Eq. (5), which was derived by the methods of quantum theory. To put it differently, the semiclassical and the classical description of spin motion are inconsistent with the quantum description (see [11, 14]). In what follows, it is demonstrated that this conclusion holds not only for spin-1/2 particles.

3. MOTION OF A PARTICLE SPIN IN PLANAR CHANNELING THROUGH A CRYSTAL

It was shown in [15] that, from the Good equation (4), it follows that, in the planar channeling of an ultrarelativistic positron through a straight crystal, the positron spin is rotated through a large angle. For heavier particles, this effect is less pronounced. Here, we study the rotation of the spin of particles moving in a crystal at an arbitrary velocity, taking into account the oscillatory character of particle motion in the crystal field.

It is well known that the motion of relativistic particles channeled through a crystal can be adequately described in the semiclassical approximation, whereas the motion of a spin is of essentially a quantum character. In the case of channeling through a straight crystal, the equation of motion of a spin as obtained from the Good equation (4) has the form

$$\frac{d\boldsymbol{\xi}}{dt} = 2\left(\frac{\mu_0}{\gamma + 1} + \mu'\right)[\boldsymbol{\xi}\times[\mathbf{E}\times\mathbf{v}]] + \frac{\mu\gamma}{m(\gamma + 1)}[\boldsymbol{\xi}\times[\mathbf{v}\times\nabla]](\boldsymbol{\xi}\cdot[\mathbf{E}\times\mathbf{v}]), \quad (6)$$

where $\mu_0 = e/2m$ is the Dirac magnetic moment and $\gamma = \epsilon/m$ is the Lorentz factor. The quantum equation of motion for a spin from [11] differs from Eq. (6) in that the former does not contain the last term from the latter. Let the x axis be orthogonal to the system of crystallographic planes, and let the y axis be aligned with the particle velocity. In this case, Eq. (6) can be reduced to the form

$$\frac{d\boldsymbol{\xi}}{dt} = 2\left(\frac{\mu_0}{\gamma + 1} + \mu'\right)\frac{\sqrt{\gamma^2 - 1}}{\gamma}E_x[\boldsymbol{\xi}\times\mathbf{e}_z] - \frac{4\pi\mu(\gamma - 1)}{m\gamma}\rho\xi_z[\boldsymbol{\xi}\times\mathbf{e}_z], \quad (7)$$

where $\rho = \frac{1}{4\pi}\frac{dE_x}{dx}$ is the charge density.

In planar channeling, a particle executes oscillatory motion along the x axis. For this reason, the electric field in the reference frame comoving with the particle

is a nearly sinusoidal function of time. In this case, the first term in Eq. (7) is a large quantity developing rapid oscillations, whereas the second term is a comparatively small quantity close to a constant. Such equations can readily be solved by the Kapitza method [16]. Let us represent vector $\boldsymbol{\xi}$ as the sum of the two terms,

$$\boldsymbol{\xi} = \boldsymbol{\Theta} + \boldsymbol{\eta},$$

where $\boldsymbol{\Theta}$ is a quantity slowly varying over a typical time on the order of the period of spin precession, T, and $\boldsymbol{\eta}$ is a quantity rapidly oscillating with a frequency Ω $|\boldsymbol{\Theta}| \gg |\boldsymbol{\eta}|$. Upon averaging over the time interval t satisfying the condition $1/\Omega \ll t \ll T$, we obtain $\langle\boldsymbol{\Theta}\rangle = \boldsymbol{\Theta}$, $\langle\boldsymbol{\eta}\rangle = 0$, and $\langle\dot{\boldsymbol{\eta}}\rangle = 0$.[2)] Equation (7) then breaks down into two equations

$$\frac{d\boldsymbol{\Theta}}{dt} = 2\left(\frac{\mu_0}{\gamma+1} + \mu'\right)\frac{\sqrt{\gamma^2-1}}{\gamma}\langle E_x[\boldsymbol{\eta}\times\mathbf{e}_z]\rangle - \frac{4\pi\mu(\gamma-1)}{m\gamma}\langle\rho\rangle\Theta_z[\boldsymbol{\Theta}\times\mathbf{e}_z], \quad (8)$$

$$\frac{d\boldsymbol{\eta}}{dt} = 2\left(\frac{\mu_0}{\gamma+1} + \mu'\right)\frac{\sqrt{\gamma^2-1}}{\gamma}E_x[\boldsymbol{\Theta}\times\mathbf{e}_z].$$

We now solve the second equation and substitute the result into the first one. Since the averaged value of the time derivative of a quantity varying within a bounded region is zero, we arrive at

$$\left\langle E_x(t)\int E_x(t)dt\right\rangle = \frac{1}{2}\left\langle\frac{d}{dt}\left(\int E_x(t)dt\right)^2\right\rangle = 0.$$

Hence, the oscillating term does not contribute to the rotation of the polarization vector, and the equation of motion for a spin takes the form

$$\frac{d\boldsymbol{\Theta}}{dt} = -\frac{4\pi\mu(\gamma-1)}{m\gamma}\langle\rho\rangle\Theta_z[\boldsymbol{\Theta}\times\mathbf{e}_z]. \quad (9)$$

Equation (9) is deduced from the Good–Nyborg equation (3). From the BMT equation, which is consistent with quantum theory [10, 11], it follows that the angle of rotation of the polarization vector nearly vanishes.[3)]

From Eq. (9), it follows that not only does the polarization vector $\boldsymbol{\xi}$ execute small-amplitude high-frequency oscillations, but that it is also rotated at the angular velocity

$$\boldsymbol{\omega} = \frac{4\pi\mu(\gamma-1)}{m\gamma}\langle\rho\rangle\Theta_z\mathbf{e}_z \approx \frac{4\pi\mu(\gamma-1)}{m\gamma}\langle\rho\rangle\xi_z\mathbf{e}_z.$$

This relation is consistent with the formula for ultrarelativistic particles ($\gamma \gg 1$) from [15].

The spin-rotation angle per unit distance traveled by the particle is given by

$$\frac{d\Phi}{dl} = \frac{1}{v}\frac{d\Phi}{dt} = \frac{4\pi\mu}{m}\sqrt{\frac{\gamma-1}{\gamma+1}}\langle\rho\rangle\xi_z. \quad (10)$$

In the case of planar channeling through a bent crystal, the spin-rotation angles per unit length for oppositely polarized particle beams differ by the quantity

$$\frac{8\pi\mu}{m}\sqrt{\frac{\gamma-1}{\gamma+1}}\langle\rho\rangle.$$

4. DISCUSSION OF THE RESULTS

Thus, there are two alternative approaches to deriving the equation of motion for a spin that lead to qualitatively different results. The conventional method, which is based on condition (1) and which is used in the majority of studies, leads to the emergence of terms in the equation of motion for a spin that involve the first derivatives of the field strengths. No such terms arise in the equation derived by the quantum method that employs the Foldy–Wouthuysen transformation, so that spin motion is described here by the BMT equation. It can be shown that, within the quantum approach, conditions (1) and (2) do not hold because the equation of motion for a particle as derived by using the Hamiltonian in the Foldy–Wouthuysen representation (see [10]) involves the first derivatives of the field strengths.

Equation (1) determines the polarization 3-vector $\boldsymbol{\xi}$ in the noninertial reference frame comoving with the particle [11, 14] because it is only in this reference frame that the spatial components of the 4-vector u^μ are equal to zero and $a^\mu = (0, \boldsymbol{\xi})$. If the vector $\boldsymbol{\xi}$ is defined in an inertial reference frame coincident at one instant of time with the reference frame comoving with the particle, its time dependence, which determines the form of the equation of motion, will be different [11].

There arises the question as to which of these two alternative methods for deriving the equation of motion for a spin is correct. A reliable answer to this question can be found experimentally. For this purpose, it is sufficient to measure the change in the polarization of a relativistic-positron beam upon its planar channeling through a straight crystal. From (3), (4), and (10), it follows that the spin vector rotates in this case through a sizable angle about the z axis, which is orthogonal to the system of crystallographic planes and to the particle velocity. This angle can be measured to a sufficient precision. For Si, Ge, and W single crystals, the values obtained with aid of (10) for the spin-rotation angle per unit distance traveled by channeled ultrarelativistic ($\gamma \gg 1$) positrons in a direction parallel to the (110) plane at $\xi_z = a$ ($a \leq 1$) are $41a$, $28a$, and $77a$ rad cm^{-1}, respectively. These estimates, obtained at temperature $T = 293$ K, are consistent with those obtained in [15]. In the case of a heavier particle, the effect is much less pronounced (see [15]).

From the BMT equation, it follows that there is virtually no spin rotation in planar channeling through a

[2)] Here, angular brackets denote averaging over the time period t satisfying the above condition.

[3)] The spin-rotation effect described in [17] is very small.

straight crystal. Only depolarization of the beam does occur [18].

No information about observation of spin rotation in channeling through a straight crystal can be found in the literature. Nonobservation of such spin rotation in dedicated experiments, should it be reliably established, would imply that the motion of a spin in a nonuniform field cannot be adequately described on the basis of the known classical and semiclassical approaches. This would cast some doubt upon the applicability of the BMT equation to spin-1 and spin-3/2 particles because this equation was derived by the methods of quantum theory only for the case of spin-1/2 particles. For this reason, it is of fundamental importance to develop a rigorous quantum theory of spin motion in an electric field for the case of higher spins ($s \geq 1$). A comprehensive theoretical investigation of this problem is required for determining the magnetic moments of these particles from experiments based on channeling. The validity of the BMT equation for higher spin particles can be tested experimentally. Measurements of the rotation of the relativistic-deuteron spin in planar channeling though a bent crystal seems to be the best test in this field. In implementing such experiments, it is necessary to take into account spin oscillations described in [19].

5. CONCLUSION

We have performed a comparative analysis of two alternative methods for deriving the equation of motion for a spin. It has been shown that the conventional approach leads to the conclusion that the spin of a positron traveling through a planar channel in a straight crystal is rotated through a large angle. The quantum approach based on the Foldy–Wouthuysen transformation predicts no spin rotation in this case. Thus, experimental measurements are needed to find out which of the two methods for deriving the equation of motion for a spin is correct. The question of whether the BMT equation is applicable to the case of higher spin particles ($s \geq 1$) can also be solved experimentally.

REFERENCES

1. D. Chen, I. F. Albuquerque, V. V. Baublis, *et al.*, Phys. Rev. Lett. **69**, 3286 (1992).
2. A. V. Khanzadeev, V. M. Samsonov, R. A. Carrigan, and D. Chen, Nucl. Instrum. Methods Phys. Res. B **119**, 266 (1996).
3. V. G. Baryshevskiĭ, Pis'ma Zh. Tekh. Fiz. **5**, 182 (1979) [Sov. Tech. Phys. Lett. **5**, 73 (1979)].
4. V. Bargmann, L. Michel, and V. L. Telegdi, Phys. Rev. Lett. **2**, 435 (1959).
5. V. B. Berestetskiĭ, E. M. Lifshitz, and L. P. Pitaevskiĭ, *Quantum Electrodynamics* (Nauka, Moscow, 1989; Pergamon, Oxford, 1982).
6. R. H. Good, Phys. Rev. **125**, 2112 (1962).
7. P. Nyborg, Nuovo Cimento **31**, 1209 (1964); **32**, 1131 (1964).
8. A. I. Solomon, Nuovo Cimento **26**, 1320 (1962).
9. E. Plante, Nuovo Cimento, Suppl. **4**, 246, 291 (1966); **5**, 944 (1967).
10. A. Ya. Silenko, Teor. Mat. Fiz. **105**, 46 (1995).
11. A. Ya. Silenko, Poverkhnost, No. 2, 111 (1997).
12. E. I. Blount, Phys. Rev. **128**, 2454 (1962).
13. A. I. L'vov, Preprint No. 344 (Lebedev Institute of Physics, Russian Academy of Sciences, 1987), p. 33.
14. A. Ya. Silenko, Poverkhnost, No. 5, 97 (1998).
15. V. G. Baryshevskiĭ and A. O. Grubich, Yad. Fiz. **37**, 1093 (1983) [Sov. J. Nucl. Phys. **37**, 648 (1983)].
16. L. D. Landau and E. M. Lifshitz, *Mechanics* (Nauka, Moscow, 1988; Pergamon, New York, 1988).
17. A. Ya. Silenko, Zh. Éksp. Teor. Fiz. **107**, 1240 (1995) [JETP **80**, 690 (1995)].
18. V. G. Baryshevsky, Nucl. Instrum. Methods Phys. Res. B **44**, 266 (1990).
19. V. G. Baryshevsky, J. Phys. G **19**, 273 (1993).

Translated by R. Rogalyov

Physics of Atomic Nuclei, Vol. 63, No. 11, 2000, pp. 2045–2047. Translated from Yadernaya Fizika, Vol. 63, No. 11, 2000, pp. 2139–2141.

XXIX INTERNATIONAL CONFERENCE ON THE PHYSICS OF CHARGED-PARTICLE INTERACTION WITH CRYSTALS

Quadrupole and Contact Interaction of Relativistic Particles with the Electric Field of Crystals

A. J. Silenko

Institute of Nuclear Problems, Belarussian State University, Minsk, Belarus

Received December 10, 1999

Abstract—The Hamiltonian for the quadrupole and the contact interaction of relativistic particles with an electrostatic field is found. The equation of motion for the particle spin is derived. © *2000 MAIK "Nauka/Interperiodica"*.

1. INTRODUCTION

The quadrupole moment of a particle with a spin $I \geq 1$ is responsible for very special properties of the motion of its spin in external fields. There occur spin oscillations consisting in alteration to the spin projection [1]. There is such an effect even in channeling or quasichanneling in straight crystals, and it can be employed to determine the quadrupole moments of short-lived particles [1]. Usually, this concerns relativistic or ultrarelativistic particles; therefore, it is necessary to take exactly into account relativistic effects in deriving the equation of motion for a spin. In [1], the equation of motion for a spin was derived by the standard approach, which consists in a transition from the particle rest frame to the laboratory frame with allowance for Thomas precession. However, it was indicated in [2, 3] that this approach can yield incorrect results because it relies on the incorrect assumption that the 4-velocity vector u^μ is orthogonal to the polarization 4-vector a^μ: $u^\mu a_\mu = 0$ (see [4–6]). In the present article, the equation of motion for the spin of a particle having a quadrupole moment is derived by constructing the Hamiltonian by a method that takes rigorously into account relativistic effects and by employing the canonical equation of rotational motion [3].

2. THEORETICAL ANALYSIS

Particles moving in the electrostatic field of a crystal are involved in the quadrupole and in the contact interaction. The terms in the Hamiltonian that are responsible for these interactions are given by

$$\mathcal{H} = \frac{1}{6}Q_{ij}\frac{\partial^2\phi}{\partial X_i \partial X_j} + \frac{1}{6}\tau\frac{\partial^2\phi}{\partial X_i^2}, \quad (1)$$

where ϕ is the scalar potential of the crystal field; Q_{ij} and τ are, respectively, the tensor of the quadrupole moment of the moving particle and the mean square of its charge radius; and $X_i (i = 1, 2, 3)$ are the c.m. coordinates of this particle. Summation is performed here over dummy indices. For nonrelativistic particles, we have $Q_{ij} = Q_{ij}^{(0)}$ and $\tau = \tau^{(0)}$, where

$$Q_{ij}^{(0)} = \int \rho(\mathbf{r}^{(0)})(3x_i^{(0)}x_j^{(0)} - \delta_{ij}r^{(0)2})dV^{(0)},$$
$$\tau^{(0)} = \int \rho(\mathbf{r}^{(0)})r^{(0)2}dV^{(0)}. \quad (2)$$

Hereafter, the superscript (0) labels quantities defined in the particle rest frame, while $\mathbf{r}^{(0)}$ and $x_i^{(0)}$ $(i = 1, 2, 3)$ are, respectively, the radius vector and the coordinates of the charges that constitute the particle and which are distributed with the density $\rho(\mathbf{r}^{(0)})$. Upon going over to operators, the tensor of the quadrupole moment is expressed in terms of the particle-spin operator as

$$Q_{ij}^{(0)} = \frac{3Q^{(0)}}{2I(2I-1)}\left[I_iI_j + I_jI_i - \frac{2}{3}I(I+1)\delta_{ij}\right], \quad (3)$$

where I is the particle spin $(I \geq 1)$, I_i are the spin-operator projections, and $Q^{(0)}$ is the quadrupole moment.

For moving particles, the quantities Q_{ij} and τ are given by the expressions

$$Q_{ij} = \int \rho(\mathbf{r})(3x_ix_j - \delta_{ij}r^2)dV, \quad \tau = \int \rho(\mathbf{r})r^2dV, \quad (4)$$

which are similar to (2). This follows from the relativistic invariance of the elementary charge $de = \rho(\mathbf{r})dV$,

$$\rho(\mathbf{r})dV = \rho(\mathbf{r}^{(0)})dV^{(0)}. \quad (5)$$

The transformation of the quantities Q_{ij} and τ is controlled by the relativistic length-contraction law. Owing to this law, moving particles, which are spherically symmetric in their rest frame, assume the shape of an oblate ellipsoid in the laboratory frame. Consequently, their effective quadrupole moment is not zero [7].

We use the well-known expression for the relativistic transformation of lengths in the covariant form

$$x_i = x_i^{(0)} - \frac{\gamma}{(1+\gamma)}\beta_i\beta_k x_k^{(0)}, \quad \beta_i = \frac{v_i}{c}, \quad v_i = \frac{dX_i}{dt}, \quad (6)$$

1063-7788/00/6311-2045$20.00 © 2000 MAIK "Nauka/Interperiodica"

where $\gamma = 1/\sqrt{1-\beta^2}$ is the Lorentz factor. We then have (see [7])

$$x_i x_j = x_i^{(0)} x_j^{(0)} - \frac{\gamma}{(1+\gamma)}(\beta_i x_j^{(0)} + \beta_j x_i^{(0)})\beta_k x_k^{(0)} + \frac{\gamma^2}{(1+\gamma)^2}\beta_i\beta_j\beta_k\beta_l x_k^{(0)} x_l^{(0)}. \quad (7)$$

From expressions (2), (4), (5), and (7), it follows that

$$Q_{ij} = Q_{ij}^{(0)} - \frac{\gamma}{\gamma+1}(\beta_i\beta_k Q_{kj}^{(0)} + \beta_j\beta_k Q_{ki}^{(0)}) + \frac{\gamma^2}{(\gamma+1)^2}\beta_i\beta_j\beta_k\beta_l Q_{lk}^{(0)} + \frac{1}{3}\delta_{ij}\beta_k\beta_l Q_{lk}^{(0)} - \left(\beta_i\beta_j - \frac{1}{3}\delta_{ij}\beta^2\right)\tau^{(0)},$$
$$\tau = \left(1 - \frac{1}{3}v^2\right)\tau^{(0)} - \frac{1}{3}\beta_k\beta_l Q_{lk}^{(0)}. \quad (8)$$

Relations (8) determine the quadrupole and contact interaction of the particle with the electrostatic field. Upon going over to operators, the velocity $\mathbf{v}$ can be replaced by the momentum operator $\mathbf{p} = -i\hbar\nabla$ according to the relation

$$\mathbf{v} = \frac{\mathbf{p}}{\gamma m} = \frac{c\mathbf{p}}{(m^2c^2 + \mathbf{p}^2)^{1/2}},$$

where m is the particle mass. As a rule, the relativistic motion of a particle in a crystal can be described semiclassically, while the motion of a spin is always of a quantum character.

The equation of motion for a spin is determined by the commutator of the spin operator $\mathbf{I}$ and the Hamiltonian,

$$\frac{d\mathbf{I}}{dt} = i[\mathcal{H} \times \mathbf{I}]. \quad (9)$$

According to (3), the character of spin motion is controlled by the operator $Q_{ij}^{(0)}$, but it is independent of $\tau^{(0)}$. We have the commutation relation

$$[Q_{ij}^{(0)}, I_k] = i(e_{kli}Q_{jl}^{(0)} + e_{klj}Q_{ij}^{(0)}), \quad (10)$$

where e_{kli} is an antisymmetric tensor.

According to (8)–(10), the spin motion caused by the quadrupole moment of the particle is described by the equation

$$\frac{dI_k}{dt} = \frac{1}{3\hbar}\left[e_{kin}Q_{jn}^{(0)} - \frac{\gamma}{\gamma+1}(e_{kjn}Q_{mn}^{(0)} + e_{kmn}Q_{nj}^{(0)})\beta_i\beta_m + \frac{\gamma^2}{(\gamma+1)^2}e_{kmn}Q_{ln}^{(0)}\beta_i\beta_j\beta_l\beta_m\right]\frac{\partial^2\phi}{\partial X_i\partial X_j}. \quad (11)$$

3. DISCUSSION OF THE RESULTS

Equation (11) describes the motion of the particle spin in an electrostatic field. In general, it does not coincide with that which is presented in [1], the distinctions being quite pronounced for relativistic particles. In the case of planar or axial channeling—this case is of particular interest for practical application—it is, however, possible to neglect, for a first approximation, the velocity components in the plane orthogonal to the direction of channeling. If the particles move along the z-axis direction, then $v_x, v_y \ll v_z$ and $\partial^2\phi/\partial Z^2 = 0$. In this case, the external field is transverse with respect to the particle motion, and Eq. (11) reduces to the form

$$\frac{dI_k}{dt} = \frac{1}{3\hbar}e_{kin}Q_{jn}^{(0)}\frac{\partial^2\phi}{\partial X_i\partial X_j}. \quad (12)$$

Equation (12) coincides with that obtained by Baryshevsky and Shechtman [1], who performed a detailed analysis of spin motion, which is of an oscillatory character in the case of channeling or quasichanneling in straight crystals. From (8) and (11), it follows that, for relativistic particles, the contributions to spin oscillations from the quadrupole and from the contact interaction are on the same order of magnitude owing to the presence of the term $\beta_k\beta_l Q_{lk}^{(0)}/3$ in expression (8) for τ. It can be seen from (12), however, that the resulting motion of the spin does not depend on the velocity. This effect can be explained in the following way: the contraction of the longitudinal size of a charged particle moving along the z axis does not change the energy of its interaction with the transverse electric field since this energy is determined by the coordinates x and y, respectively.

The second and the third term in the bracketed expression on the right-hand side of (11) can affect sizably the motion of the spin in particle scattering.

Equations (11) and (12) do not describe the spin motion associated with the existence of the particle magnetic moment. The corresponding contribution to the spin motion is pronounced in the case of channeling in bent crystals, but it is negligibly small in the case of channeling in straight crystals (see [8]).

4. CONCLUSION

The Hamiltonian for the quadrupole and the contact interactions of relativistic particles having a spin $I \geq 1$ with an electrostatic field has been constructed. This has enabled us to derive the equation of motion for a spin. In the case where moving particles undergo channeling or quasichanneling in bent crystals, the equation obtained here coincides with that presented in [1].

REFERENCES

1. V. G. Baryshevsky and A. G. Shechtman, Nucl. Instrum. Methods Phys. Res. B **83**, 250 (1993).
2. A. Ya. Silenko, Poverkhnost, No. 2, 111 (1997).
3. A. Ya. Silenko, Poverkhnost, No. 5, 97 (1998).
4. V. B. Berestetskiĭ, E. M. Lifshitz, and L. P. Pitaevskiĭ, *Quantum Electrodynamics* (Nauka, Moscow, 1989; Pergamon, Oxford, 1982).
5. R. H. Good, Phys. Rev. **125**, 2112 (1962).
6. P. Nyborg, Nuovo Cimento **31**, 1209 (1964).
7. A. Ya. Silenko, Izv. Akad. Nauk, Ser. Fiz. **63**, 997 (1999).
8. A. Ya. Silenko, Zh. Éksp. Teor. Fiz. **107**, 1240 (1995) [JETP **80**, 690 (1995)].

Translated by O. Chernavskaya

Physics of Atomic Nuclei, Vol. 63, No. 11, 2000, pp. 2048–2050. Translated from Yadernaya Fizika, Vol. 63, No. 11, 2000, pp. 2142–2144.

XXIX INTERNATIONAL CONFERENCE ON THE PHYSICS OF CHARGED-PARTICLE INTERACTION WITH CRYSTALS

Rotation of the Spin of a Charged Particle with an Anapole Moment in Planar Channeling

A. J. Silenko

Institute of Nuclear Problems, Belarussian State University, Minsk, Belarus

Received December 10, 1999

Abstract—Interaction of relativistic particles possessing an anapole moment with an electric field of a crystal is studied. The equation of motion of a spin is derived. The spin-rotation angle in planar channeling is found.

1. INTRODUCTION

In the channeling of a charged particle, its spin is rotated about its momentum owing to parity-violating weak interaction [1–3]. It will be shown below that there is a similar effect caused by the interaction of the anapole moment of a moving particle or nucleus with the electrostatic field of a crystal.

An anapole moment, whose existence was predicted by Zel'dovich [4], is one of the static moments of the magnetic type. However, the existence of an anapole moment stems from parity nonconservation. For this reason, the magnitude of the anapole moment is determined by weak interaction. An account of the theory of the anapole moment was given in [5–7].[1)] The anapole moment was observed experimentally in [8].

The motion of a particle with an anapole moment in an electrostatic field gives rise both to quadrupole [7, 9] and to contact interaction. In [7, 9], their strengths were computed to terms of order v/c, where v is the particle velocity. In the present study, an exact relativistic expression for the Hamiltonian describing the interaction of the anapole moment of a particle with an electrostatic field is derived, which makes it possible to find the equation of motion for a spin. We use the system of units in which $\hbar = c = 1$.

2. THEORETICAL ANALYSIS

We proceed from the expression given in [10] for the Hamiltonian describing the interaction of a relativistic particle having a magnetic moment $\boldsymbol{\mu}$ with an electromagnetic field. If there is only an electric field, the interaction Hamiltonian is given by

$$\mathcal{H}_{\rm int} = -\frac{1}{\epsilon}\boldsymbol{\mu}\cdot[\mathbf{E}\times\mathbf{P}], \qquad (1)$$

where ϵ is the kinetic energy of the particle; $\mathbf{P}$ is the generalized momentum; $\mathbf{E} = -\nabla\varphi$; and $\mathbf{E}$ and ϕ are, respectively, the strength and the potential of the electric field. It should be emphasized that the magnetic moment $\boldsymbol{\mu}$ is determined in the reference frame instantaneously comoving with the particle under consideration. To a sufficient degree of precision, we have $\mathbf{P} = \epsilon\mathbf{v}$, where $\mathbf{v}$ is the particle velocity. As a rule, the motion of a relativistic particle in a crystal can be adequately described in the semiclassical approximation, whereas the motion of a spin is always of essentially a quantum character.

The interaction of the anapole moment with an external field can be considered on the basis of the simplified model where the anapole moment is assumed to be formed by pointlike magnetic dipoles. The anapole moment can be defined by one of the following two equivalent formulas [6, 7]:

$$\mathbf{a} = -\pi\int r^2\mathbf{j}\,dV, \quad \mathbf{a} = 2\pi\int(\mathbf{r}\cdot\mathbf{j})\mathbf{r}\,dV. \qquad (2)$$

In this case, the radius vector of an element of the current of density $\mathbf{j}$ can be represented in the form

$$\mathbf{r} = \mathbf{r}^{(0)} + \mathbf{r}', \quad |\mathbf{r}'| \ll |\mathbf{r}^0|,$$

where $\mathbf{r}^{(0)}$ is the radius vector of the center of the magnetic dipole and $\mathbf{r}'$ is the radius vector of the current element with respect to this center. Upon integration with respect to $\mathbf{r}$, expression (2) takes the form

$$\mathbf{a} = 2\pi\sum\mathbf{r}^{(0)}\times\boldsymbol{\mu}. \qquad (3)$$

In contrast to magnetic moments, the strength of the electric field $\mathbf{E}$ in (1) is defined in the laboratory frame. Suppose that $\mathbf{r}' = \mathbf{R} + \mathbf{r}$, where $\mathbf{r}'$ is the radius vector of the center of the magnetic dipole, $\mathbf{R}$ is the radius vector of the center of the particle having an anapole moment, and $\mathbf{r}$ is the end-to-end vector from the center of the particle to the center of the magnetic dipole. The quantity $\mathbf{E} = \mathbf{E}(\mathbf{r}')$ is the field strength at the point where the magnetic dipole resides. Expanding it in a power series to terms of order r/R inclusive, where r is on the order

[1)] The anapole moment (anapole) is also known as a toroidal dipole.

of the particle radius, we obtain

$$E_i(\mathbf{r}') = E_i(\mathbf{R}) - x_j \frac{\partial^2 \phi(\mathbf{R})}{\partial X_i \partial X_j}, \quad (4)$$

where summation over dummy indices is implied. The quantities x_i must be expressed in terms of the quantities $x_i^{(0)}$ defined in the reference frame comoving with the particle. In our manipulations, we make use of the relativistic formula for coordinate transformations in the covariant form

$$x_i = x_i^{(0)} - \frac{\gamma}{(1+\gamma)c^2} v_i v_k x_k^{(0)}, \quad v_i = \frac{dX_i}{dt}, \quad (5)$$

where $\gamma = (1 - v^2/c^2)^{-1/2}$ is the Lorentz factor. We then sum products of the form $x_i^{(0)} \mu_j$ over the magnetic dipoles that form the anapole moment (the magnetic dipoles are assumed to be pointlike). Since the intrinsic quadrupole magnetic moment of the particle is zero, we have

$$x_i^{(0)} \mu_j + x_j^{(0)} \mu_i = 0. \quad (6)$$

The terms in the Hamiltonian that are responsible for the interaction of the anapole moment with an electrostatic field can be found by summation over the magnetic dipoles with the aid of Eqs. (3)–(6). The result is

$$\mathcal{H}_{\text{int}} = \frac{1}{6} Q_{ij} \frac{\partial^2 \phi}{\partial X_i \partial X_j} + \frac{1}{6} \tau \frac{\partial^2 \phi}{\partial X_i^2},$$

$$Q_{ij} = \frac{3}{4\pi\gamma}(a_i v_j + a_j v_i) + \frac{3\gamma}{2\pi(\gamma+1)} v_i v_j (\mathbf{a}\cdot\mathbf{v}) \quad (7)$$

$$- \frac{1}{2\pi} \delta_{ij} (\mathbf{a}\cdot\mathbf{v}), \quad \tau = -\frac{1}{\pi} \mathbf{a}\cdot\mathbf{v}.$$

The anapole moment of a particle at rest is $\mathbf{a} = a_0 \mathbf{I}/I$, where $\mathbf{I}$ is the spin operator and

$$a_0 = e\kappa_a \frac{G}{\sqrt{2}\alpha} \frac{(I+1/2)(-1)^{I+1/2-l}}{I+1}. \quad (8)$$

Here, e is an elementary charge, G is the Fermi constant, α is the fine-structure constant, and κ_a is a dimensionless factor [6].

The quantities Q_{ij} and τ are, respectively, the effective quadrupole moment of the particle and the mean square of its charge radius; they manifest themselves in the case of a moving anapole moment. Formula (7) defines a parity-violating interaction.

3. DISCUSSION OF THE RESULTS

Let us consider the case of planar channeling and chose the z axis to be orthogonal to the system of crystallographic planes. The component of the particle velocity along the z axis can be neglected. Expression (7) for the interaction Hamiltonian then takes the form

$$\mathcal{H}_{\text{int}} = -\frac{1}{4\pi I} a_0 (\mathbf{I}\cdot\mathbf{v}) \frac{\partial^2 \phi}{\partial Z^2}.$$

The equation of motion of a spin is determined by the commutator of the operator $\mathbf{I}$ and the Hamiltonian. Upon evaluating this commutator, we arrive at

$$\frac{d\mathbf{I}}{dt} = i[\mathcal{H}_{\text{int}}, \mathbf{I}] = \boldsymbol{\omega} \times \mathbf{I},$$

where ω is the angular velocity of spin rotation. In the case being considered, it is given by

$$\boldsymbol{\omega} = -\frac{1}{4\pi I} a_0 \frac{\partial^2 \phi}{\partial Z^2} \mathbf{v}. \quad (9)$$

The spin of a particle is rotated about its velocity. The spin-rotation angle per unit length traveled by the particle is

$$\frac{d\Phi}{dl} = \frac{1}{v} \frac{d\Phi}{dt} = \frac{\omega}{v}.$$

It is independent of the velocity, its absolute value being given by

$$\frac{d\Phi}{dl} = \frac{1}{4\pi I} \left| a_0 \frac{\partial^2 \phi}{\partial Z^2} \right|.$$

The anapole moments of elementary particles and nuclei are on the order of G or G/α [6, 11, 12]. The calculations revealed that, both for elementary particles (including the electron and the positron) and for nuclei, the spin-rotation angle per unit length traveled by a particle in planar channeling is $d\Phi/dl \sim 10^{-9}$–10^{-11} rad/cm. This estimate shows that the spin-rotation angles caused by anapole moments and by weak interaction [2, 3] are on the same order of magnitude. The precision of current experiments is not sufficient for detecting such small angles.

4. CONCLUSION

The Hamiltonian describing the interaction of the anapole moment of a relativistic particle with an electrostatic field has been derived. The motion of a particle having an anapole moment gives rise to parity-violating quadrupole and contact interactions. The equation of motion of a spin has been obtained. The spin-rotation angles caused by anapole moments are on the same order of magnitude as those caused by weak interaction.

REFERENCES

1. V. G. Baryshevskiĭ, Vestsi Akad. Navuk Belarusi, Ser. Fiz.-Énerg. Navuk, No. 2, 49 (1992).
2. A. Ya. Silenko, Poverkhnost, No. 11, 91 (1995).

3. A. J. Silenko, Nucl. Instrum. Methods Phys. Res. B **114**, 259 (1996).
4. Ya. B. Zel'dovich, Zh. Éksp. Teor. Fiz. **33**, 1531 (1957) [Sov. Phys. JETP **6**, 1184 (1957)].
5. V. M. Dubovik and A. A. Cheshkov, Fiz. Élem. Chastits At. Yadra **5**, 791 (1974) [Sov. J. Part. Nucl. **5**, 318 (1974)].
6. I. B. Khriplovich, *Nonconservation of Parity in Atomic Phenomena* (Nauka, Moscow, 1988).
7. G. N. Afanas'ev, Fiz. Élem. Chastits At. Yadra **24**, 512 (1993) [Phys. Part. Nucl. **24**, 219 (1993)].
8. M. C. Noecker, B. P. Masterson, and C. E. Wieman, Phys. Rev. Lett. **61**, 310 (1988).
9. A. J. Silenko, Prog. Theor. Phys. **101**, 875 (1999).
10. A. Ya. Silenko, Poverkhnost, No. 5, 97 (1998).
11. N. Dombey and A. D. Kennedy, Phys. Lett. B **91**, 428 (1980).
12. W. C. Haxton and E. M. Henley, Phys. Rev. Lett. **63**, 949 (1989).

Translated by R. Rogalyov